

KIT SCIENTIFIC REPORTS 7548

Nuclear Fusion Programme

Annual Report of the Association
Karlsruhe Institute of Technology/EURATOM

January 2009 - December 2009

I. Pleli (ed.)

Nuclear Fusion Programme

Annual Report of the Association Karlsruhe Institute of Technology/EURATOM

January 2009 - December 2009

**Karlsruhe Institute of Technology
KIT SCIENTIFIC REPORTS 7548**

Nuclear Fusion Programme

Annual Report of the Association
Karlsruhe Institute of Technology/EURATOM

January 2009 - December 2009

I. Pleli
(ed.)

Impressum

Karlsruher Institut für Technologie (KIT)
KIT Scientific Publishing
Straße am Forum 2
D-76131 Karlsruhe
www.ksp.kit.edu

KIT – Universität des Landes Baden-Württemberg und nationales
Forschungszentrum in der Helmholtz-Gemeinschaft



Diese Veröffentlichung ist im Internet unter folgender Creative Commons-Lizenz
publiziert: <http://creativecommons.org/licenses/by-nc-nd/3.0/de/>

KIT Scientific Publishing 2010
Print on Demand

ISSN 1869-9669

Overview

Introduction

The limitation and environmental impact of fossil fuels consumption does require new ways of energy supply. The worldwide energy demand will substantially increase in the course of this century in particular in populous countries such as China and India. In this strongly competitive environment the dependence of the European Union on imported energy (presently about 53% of the total energy used is imported) is predicted to increase to even higher levels over the next decades. Nuclear fusion offers an option of an environmental benign energy source with favourable safety features and almost unlimited fuel resources.

Nuclear fusion research is aiming to generate the physical and technical basis of a fusion power station which, similar to the sun, gains energy from the fusion of light atoms. In order to attain ignition of the fuel, a mixture of deuterium/tritium (isotopes of hydrogen), will be confined by strong magnetic fields and heated up to more than 100 million degrees.

The construction of the experimental reactor ITER in Cadarache/France in the framework of a worldwide project marks the next big step on the way to a fusion power station. For the first time a fusion power of 500 Mega Watt will be generated by a long burning plasma and applied technologies will undergo extended tests.

The Karlsruhe Institute of Technology (KIT) is working in the framework of the European Fusion Programme, as the successor of the Forschungszentrum Karlsruhe GmbH (FZK). KIT actually is the result of the merger of FZK and the University of Karlsruhe. The Association KIT-EURATOM is developing key technologies in the areas of superconducting magnets, microwave heating systems (Electron-Cyclotron-Resonance-Heating, ECRH), the deuterium-tritium fuel cycle, He-cooled breeding blankets, a He-cooled divertor and structural materials, as well as refractory metals for high heat flux applications including a major participation in the preparation of the international IFMIF project. Furthermore, investigations and modelling on plasma wall interactions are carried out.

The results from experimental activities such as the tests of high temperature superconducting current leads in the test facility TOSKA, the quasi-stationary gyrotron operation and the operation of fuel cycle subsystems and components with deuterium-tritium have already been utilised for the design work for ITER or the construction of the stellarator Wendelstein 7-X.

With the construction of ITER new challenges have to be mastered by the EURATOM-Associations. While up to now concepts for components and systems have been developed and their functionality has been tested in laboratory scale or semi-technical scale, now plant components have to be constructed for fabrication by the industry and their integration into the plant has to be supported. In order to effectively deploy personal and financial resources consortia of European Association Laboratories have been formed which will bear the responsibility for the realisation of components and systems in accordance with the procurement packages of ITER. The Association KIT-EURATOM is leading a consortium for the construction of the European test blanket module (TBM) systems, as well as two others on the construction of the upper port plug ECRH microwave launcher and the European share of the inner fuel cycle of ITER. Moreover, KIT is also involved in consortia of EURATOM-Associations for the development and procurement of gyrotrons providing microwaves of 170 GHz and 2 MW output power for ITER, for nuclear data development and for the development of the ITER bolometer diagnostics. Furthermore, the already existing co-operation with industrial companies is being intensified.

The design and construction of ITER components and subsystems need to be supported by experiments such as prototype testing, validation of scale up factors and additional R&D. For this purpose a helium loop HELOKA is being constructed which not only serves for experi-

mental investigations of the TBM, but also as a pilot loop in view of the loops to be installed in ITER for the cooling of test blanket modules.

The demonstration power station DEMO constitutes the next step beyond ITER which is supposed to be planned after some years of ITER operation. In the framework of a European DEMO study the Association KIT-EURATOM is developing the so-called multi-module blanket concept which promises reduced plant shutdown times during remotely controlled exchange of blankets and thus contributes to increased plant availability.



Helium Loop Karlsruhe – Low pressure (HELOKA-LP) for testing the High Flux Test Module for IFMIF

Furthermore, a helium cooled divertor for DEMO is under development.

About 230 professionals and technicians are involved in the fusion programme of the Association KIT-EURATOM with additional support of technical departments.

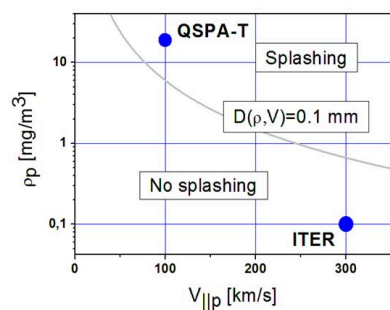
Progress from January 2009 to December 2009 is reported here. More information is available from the programme management and from the responsible scientists. The website <http://www.fusion.kit.edu/english/index.php> offers further access to the fusion activities of KIT.

Plasma Wall Interaction

In ITER and DEMO the disruptions and edge localised modes (ELMs) can result in brittle destruction (BD), melt motion and vaporization of the tungsten (W), CFC and beryllium (Be) wall surfaces of the plasma facing components (PFCs). To clarify tolerable transients and also for disruption mitigation by massive gas injection, computer codes are being developed at KIT. The damages to the wall as well as the impact of eroded and injected atoms on the plasma are modelled.

The magneto-hydrodynamics and radiation code TOKES is used to calculate toroidally symmetric plasma contamination, plasma fluxes onto the wall and sputtered, vaporized and injected atoms in the vessel. The thermo-mechanic code PEGASUS is used to simulate the brittle destruction of CFC and W. The fluid dynamics code MEMOS simulates the melt motions on W and Be surfaces. The wall damage by the runaway electrons is simulated with the Monte-Carlo code ENDEP. Main models for BD and melt motion have been validated against experiments on plasma guns, electron beams and tokamak facilities.

The simulations allowed the main conclusions that for the divertor PFCs, a maximum tolerable ELM energy density 0.5 MJ/m^2 can be predicted. In addition, W has large risk of cracking, especially in case of surface melting, building crack meshes of cell sizes from 0.1 up to 2 mm depending on applied loads. W melt splashing is probable when taking into account the Lorentz force of electric cross-currents. The beryllium wall can withstand only rather small loads below 0.5 MJ/m^2 .



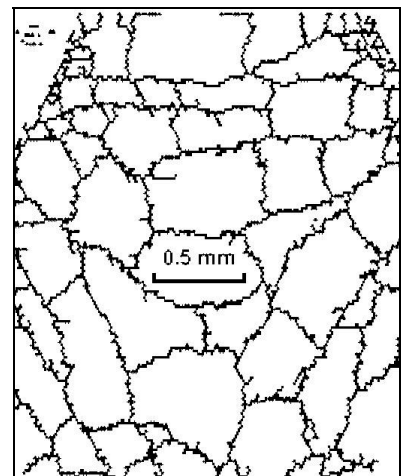
Plot of plasma density vs. melt velocity with melt splashing threshold

The new MEMOS calculations were focused mainly on the threshold and magnitude of **melt splashing under repetitive heat loads** in order to optimize the design of the tungsten macrobrush targets. It is concluded that after the expected ITER transient loads, melt splashing on the surface would not occur. The figure demonstrates the calculated margin of splashing threshold.

In a joint effort of the theoretical KIT team and the experimental TEXTOR team at FZJ, a check was undertaken of the earlier MEMOS prediction that some rounding of the castellation corners of W-brush targets would prevent the bridging of the brush tiles. The experiment suggested adjustment of MEMOS to the particular experimental geometry in order to calculate the bridging threshold.

For the thermo-mechanics code PEGASUS, a model for **W surface cracking under pulsed heat loads** below the melting threshold Q_{th} was developed and validated against experiments on plasma gun facility QSPA-Kh50. After transient loads with $Q < 1 \text{ MJ/m}^2$ (below tungsten melting threshold) the crack mesh on W surface develops, with crack mesh sizes of the order of 0.5 mm in agreement with the measured values.

The code MEMOS was applied for preliminary simulations of the behaviour of **lithium plasma facing components** under ITER conditions. The simulations showed that Li cannot be used in the ELMy H-mode operation. Even small ELMs completely remove Li away from a W substrate. A vapour shield in front of a Li film is not effective.



Calculated crack pattern on the numerical W surface; $Q = 0.45 \text{ MJ/m}^2$

Heating and Current Drive - ECRH

Microwaves produced in gyrotron tubes and delivered to the plasma by a system of mirrors and waveguides are an efficient tool for plasma heating (Electron Cyclotron Resonance Heating, ECRH) as well as, in combination with suitable steering devices, for plasma stabilisation by counteracting local plasma instabilities.



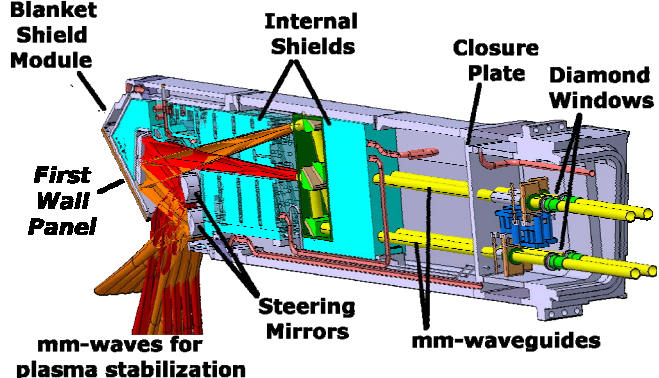
Front-end of the W7-X plug-in antenna with the launching mirrors

The complete **ECRH system for Wendelstein 7-X** will be provided by KIT in cooperation with EU partners. The 1 MW, continuous wave (CW), 140 GHz series gyrotrons have been developed with Thales Electron Devices. To solve unexpected problems with parasitic oscillations, a dedicated R&D programme was conducted at KIT using a modular step-frequency tuneable gyrotron. In result, a robust beam tunnel which efficiently suppresses the parasitic oscillations was developed. At IPP Greifswald, the existing parts of the ECRH system was used for testing of special components like a compact long-pulse high-power diplexer and new CW absorber loads. Also the stability of the output beam of the gyrotrons, which is of particular importance during the first second where the frequency is changed by a few 100 MHz, has been investigated. Progress has been made in assembling and testing the W7-X ECRH plug-in antenna modules. Based upon the experience with the W7-X ECRH system, KIT is participating in the European Gyrotron Consortium (EGYC), for the development of the **2 MW, CW, 170 GHz coaxial cavity gyrotron for ITER**.

Advanced beam tunnel designs with the potential of enhanced suppression of parasitic oscillations in the cavity were investigated using a modular step-frequency tuneable short pulse gyrotron. In the new design the copper rings of the beam tunnel were modified by introducing irregular corrugations. This version did not show any beam tunnel parasitic oscillations, even at a beam current well above the design value. For the first time the brazing of a down-scaled elliptical CVD diamond disk was finished successfully. This offers the possibility to braze a diamond disk of realistic size in Brewster configuration.

In a detailed **design study for a 170 GHz 4 MW coaxial-cavity gyrotron**, the designs for the major gyrotron components (electron gun, coaxial-cavity; quasi-optical system for two output RF beams and collector) are being developed. Extensive optimizations on the geometry of the interaction cavity have been performed to achieve highest efficiencies and acceptable low wall losses.

The conceptual design of the **ITER ECRH Upper Launcher** for plasma-stabilization by mm-waves, earlier developed within the ECHULA group together with CRPP, FOM, INR and IPP, had matured to the so-called "Mitre-Bend" design proven by simulations of regular launcher operation but also of critical plasma disruptions. The design was considered as mature enough to enter the Preliminary Design Review (PDR) at ITER. In result, the quality of the design was proven, as the absence of any potential show stoppers was stated, together with a few 3rd order comments (further reading can be found in the ITER newsline #109).



The ITER ECRH "Mitre-Bend" Upper Launcher Design

Magnet Structure and Integration

Based on rich experience from the test of the ITER TF model coil and the design, construction and testing of the ITER current lead demonstrator, KIT took responsibility for the procurement of high temperature superconducting (HTS) current leads for Wendelstein 7-X as well as for JT-60SA. The W7-X current lead prototypes have been constructed during 2009 with a subsequent test that will be performed in 2010. With respect to future fusion power stations, the application of high temperature superconducting coils is a promising target and KIT is preparing the use of novel High Tc Superconductors for fusion magnets.

For W7-X, in total 14 **HTS current leads** are required with a maximum design current of 18.2 kA. TOSKA will be used for the test of the W7-X prototype current leads. In addition 6 leads for a maximum current of 26 kA and 20 leads with a maximum current of 20 kA are



W7-X current lead prototype

required for the JT-60SA TF and CS magnets, respectively. To come to a fast and economic testing sequence, the Current Lead Test Facility Karlsruhe (CuLTKa) is under construction. The present planning expects the readiness of CuLTKa until end of 2011. With the availability of this facility, the series testing of W7-X and JT-60SA current leads will be moved from TOSKA to CuLTKa.



KIT quench detectors UNIQLD (type: 3410) during burn-in



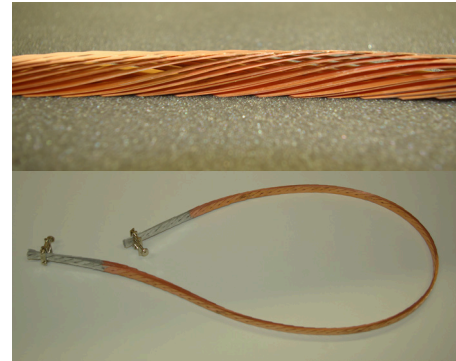
Cryogenic testing: Full-size tube mounted within testing rig

The development of a **quench detection system** for the magnets of W7-X was successfully terminated with the external production of ~ 600 quench detection units. A quench detection system for ITER has been discussed and preliminary technical specifications were developed.

Mechanical testing, especially tensile and shear were performed at **cryogenic temperatures** for different parts of magnet structures of ITER including the pre-compression ring. In detail: Tensile tests of full size butt welded Toroidal Field Coil conduit material, fracture toughness experiments with specimens of Poloidal Field Coil conduit material samples, tensile tests on pre-compression-ring material (glass fibre epoxy), bending tests on samples made from 3x3 Cable-in-Conduit Conductor (CICC) array material. In addition, numerous tests for W7-X have been performed at low temperature.

tests of full size butt welded Toroidal Field Coil conduit material, fracture toughness experiments with specimens of Poloidal Field Coil conduit material samples, tensile tests on pre-compression-ring material (glass fibre epoxy), bending tests on samples made from 3x3 Cable-in-Conduit Conductor (CICC) array material. In addition, numerous tests for W7-X have been performed at low temperature.

Roebel-cables Assembled from Coated Conductors (RACC) are developed as high current low AC loss conductors for application in windings and magnets. The development is concentrating on two different routes, one with 10-12 mm wide cables for the application regime of 2-5 kA (77 K and s.f.), and narrow 4 mm cables for currents up to 2 kA. The narrow cables will serve as strands for future Rutherford Cable concepts with > 20 kA transport current. For 12 mm wide cables, currents up to 2.6 kA were demonstrated, 4 mm cables achieved currents up to 1.3 kA. An important innovation in both cable types is multi-stacking applied in the strands as a very effective design to increase the transport current.



A 2.6 kA HTS RACC-cable with 1.1 m length (upper fig.) and view to the spliced strands showing multistacking of strands

Breeding Blanket and Divertor

A central element of KIT's long term programme towards a fusion power reactor is the design, analyses, qualification and manufacturing of a solid breeder blanket, i.e. the Helium Cooled Pebble Bed (HCPB), and of the Helium Cooled divertor. The HCPB blanket concept is part of the Test Blanket Module (TBM) programme for ITER and included in the F4E procurement. Several activities are performed also for the second EU TBM, namely the Helium Cooled Lithium Lead (HCLL) concept developed by CEA.

The institutions working on the European TBM programme have organised themselves in the **European Test Blanket Module Consortium of Associates** (KIT, CEA; ENEA, CIEMAT, RMKI and NRI) with KIT providing the project leader and hosting the central support team. The TBM-CA has started grant work for F4E in 2009. Main activities performed in KIT are: (1) Definition of an Experimental & Simulation Programme for reliable HCPB TBS Test Programme in ITER, (2) Conceptual Design of the HCPB TBM, (3) Preliminary plan for the Manufacturing of a HCPB TBM, (4) Conceptual Design of the HCLL- and HCPB-Helium Cooling System for ITER. In addition, contributions for the definition of MHD Experiments for the HCLL TBM, for non-destructive testing in TBM manufacturing and for the development of the Tritium Technology for the TBM auxiliary systems have been performed in 2009.



HELOKA vacuum vessel



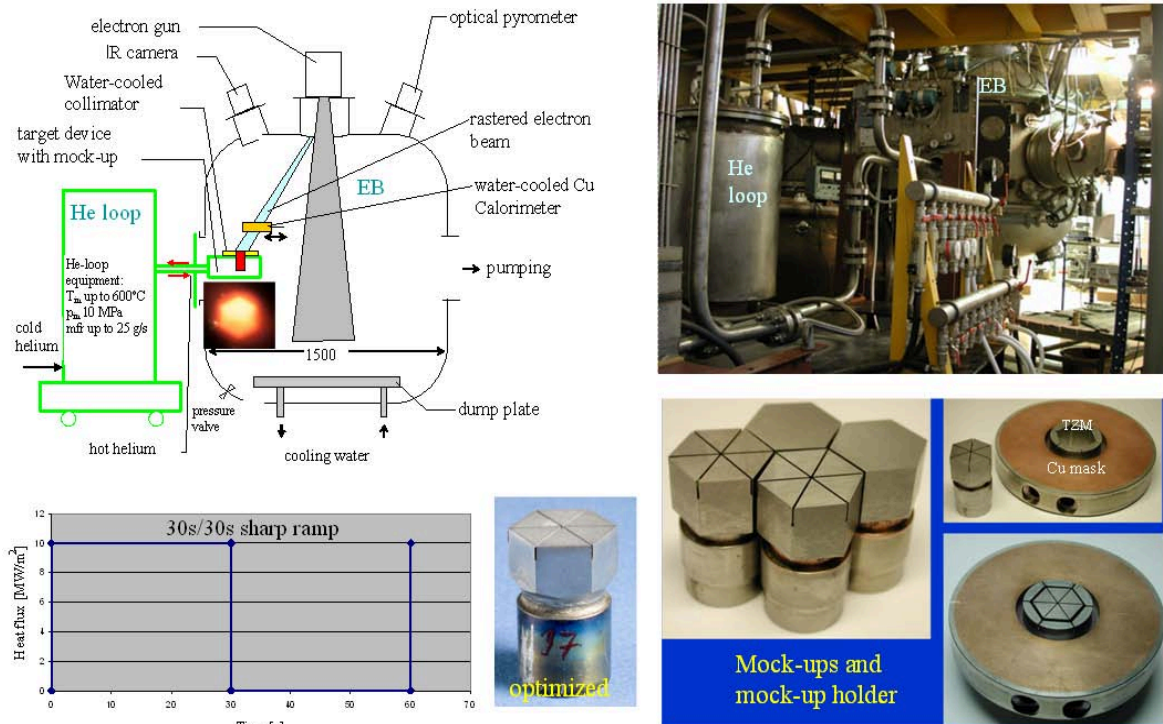
The out-of-pile qualification of large blanket mock-ups under high pressure He cooling is one of the major challenges in the breeder blanket development programme. To this end, the **HELOKA-High Pressure /TBM loop** is being set up at KIT. The construction was started in April

2009 and the assembly of the piping is almost finalized. In addition, the vacuum vessel for containing the test modules has been manufactured.

Ceramics Breeder and Neutron Multiplier Materials are being developed and characterised for the solid breeder blanket. The development of Be-Ti alloys, an advanced high-performance neutron multiplier was continued in 2009 with laboratory-scale tests aimed to produce samples and studying their relevant properties. The development of lithium orthosili-

cate pebbles has been continued in collaboration with Schott AG, Mainz, including materials characterisation and a study of recycling strategies taking into account different activation scenarios in a reactor. As the two materials are used in form of a pebble bed, the modelling of pebbles and pebble beds has been developed further, using both simulations of collective behaviour of pebble beds and crush load experiments on single pebbles.

In the development of the **KIT Helium Cooled Divertor**, the current work is focussed on technological studies on fabrication, integration, and high heat flux (HHF) tests of divertor 1-finger and 9-finger mock-ups, to demonstrate feasibility of manufacturing and to prove the performance of the design. The tests were performed in a combined electron beam and He



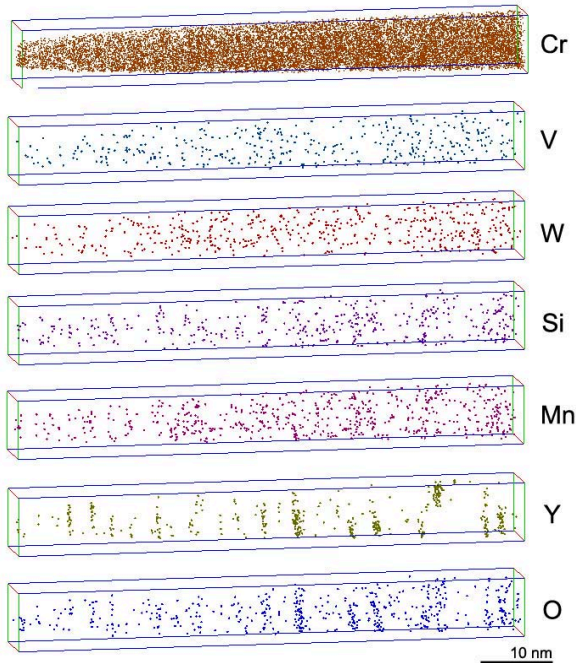
Combined He loop and TSEFEY test facility at Efremov for the KIT He cooled divertor testing

loop facility at Efremov. Three HHF test series were successfully performed till now. Neither sudden destruction, nor completely broken mock-ups (brittle failure), nor recrystallisation of the W thimble was observed in any of the mock-ups in any test. The latest series of successfully tested mock-ups survived outstandingly more than 200 cycles under 10 MW/m^2 in total without any damages. The upcoming HHF 1-finger test series 2010 ff will aim at reaching the breakthrough of 10 MW/m^2 and 1000 cycles by continuing testing the mock-ups from last test series, as well as testing new mock-ups manufactured with a refined technology in KIT and Efremov.

Structural Materials - Development and Characterisation

High performance materials are indispensable for economical and environmentally acceptable operation of fusion power reactors. In line with the EFDA and the F4E paths towards ITER, TBMs and DEMO reactor development, the current activities are concentrated on further improvement of EUROFER by reduction of critical elements, procurement of EUROFER for the fabrication of ITER Test Blanket Modules (TBMs) mock-ups, post irradiation examination of neutron irradiated EUROFER, development and characterization of nanoscaled oxide dispersion strengthened steels, as well as development and characterization of improved W-alloys.

During the last few years considerable improvement has been made in the definition and **fabrication of reduced activation ferritic-martensitic steels (RAFM)**. Studies for further reduction of impurities included: (i) activation analysis by FISPACT code calculations to check the influence of different radiologically undesired elements, (ii) impurity evaluation with steel producing companies, and (iii) Round Robin experiments for the chemical analysis of the radiologically the undesired elements Nb, Mo, Al, Ni, Cu, and Co with participation of six different industrial and research laboratories. The different pathways how the detrimental elements find their way into the final RAFM steel product were analysed. These findings were used in the production of a new 11 ton EUROFER 97-3 heat and lead to a considerable reduction of the Nb content.



Oxide dispersion strengthened ferritic-martensitic steel ODS-EUROFER 97 irradiated at 330 °C up to ~30 dpa in the fast neutron reactor BOR-60 was studied by **topographic atom probe** in the as-irradiated state and after additional annealing at 500 °C. A high number density of ultra fine (~1-3 nm in diameter) nano-clusters enriched in yttrium, oxygen, manganese and chromium were observed. Although the composition of the clusters differs from that for the unirradiated state, it can be concluded that even after 30 dpa irradiation at 330 °C, the Y₂O₃ particles remain quite stable, despite the fact that the concentration of yttrium and oxygen in the matrix increases several times after irradiation. The recovery annealing at 500 °C for 3 hours decreases the number density of clusters compared to the pre-irradiated state. However, the composition of Y-O clusters after annealing was closer to the irradiated state than to the unirradiated.

Specimens of EUROFER 97 have been neutron irradiated at HFR Petten up to an average dose of 16.3 dpa at irradiation temperatures of 250 °C, 300 °C, 350 °C, 400 °C and 450 °C. Broad based **quantitative TEM examinations** have been performed. A new result is that a clear maximum of the irradiation hardening occurs at an irradiation temperature of ~300 °C. This maximum has been confirmed now by tensile and Charpy tests and hardness measurements and can be explained by correlating the irradiation induced dislocation loop density with tensile and DBTT data.

Advanced blanket concepts like the HCPB or gas cooled divertor concepts require operational temperatures of 700 to 750° C or even more. **Reduced activation ferritic (RAF) ODS-steels** such as Fe-(12-14)Cr-(2-3)W-(0.2-0.5)Ti-(0.2-0.5)Y₂O₃ being developed in USA, Japan and Europe for fission and fusion applications appear promising for fulfilling the requirements. By improving several steps of the production route, a variety of elemental compositions and production routes have been screened. Property correlations have been established between the microstructure and mechanical properties.

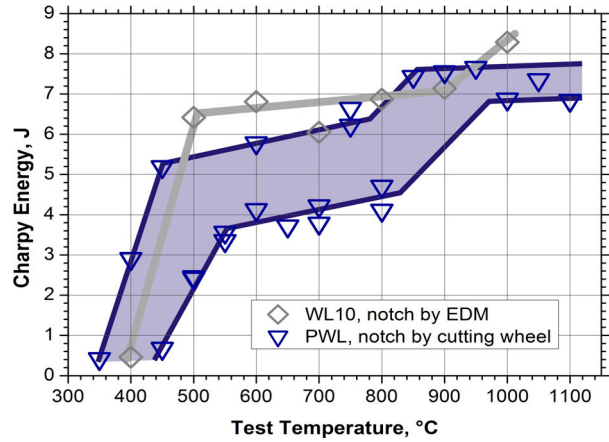
One of the most critical issues of **tungsten based alloys** in connection with structural applications is the required ductile-to-brittle transition temperature (DBTT) after irradiation of less than 600° C (measured by EU standard mini-Charpy tests). A comprising study has been performed to characterize different tungsten materials with respect to their applicability for structural divertor parts. In summary, there are three types of fractures: (i) brittle (below ~500° C), (ii) delamination (~500-900° C), and (iii) ductile (above ~900° C) for pure tungsten (PWL in the figure), while W alloys such as W-1%La₂O₃ (WL10) does not even become completely ductile at all. The reason for the still high ductile transition temperature is not brittle fracture but an extended range of delamination fracture. Additional examinations revealed that notches prepared by electro discharge machining produce more surface micro-cracks than notches produced by sawing or milling. Such micro-cracks promote delamination fracture, as has been demonstrated by a comparison with un-notched specimens and with specimens without micro-cracks (notch fabrication by sawing).

Structural Materials – Mechanical Behaviour and Reliability

Structural materials to be used for in-vessel components of future fusion power plants, in particular blanket and divertor, will be subject to complex thermo-mechanical loading and very high irradiation doses. Characterization and modelling of their mechanical behaviour under these loading conditions is mandatory for their reliable use. Therefore, extensive mechanical testing is conducted to collect comprehensive knowledge about the deformation, damage and toughness behaviour of structural materials in the reference as well as in the irradiated states. The irradiated states are investigated within the post irradiation examinations (PIE) of irradiation programs, for RAFM steels SPICE, ARBOR I and ARBOR II. The PIE are partly performed at the KIT Fusion Materials Laboratory (FML) which provides the hot cells infrastructure for testing and characterization of irradiated materials including optical and electron microscopy and various small specimen technologies for instrumented indentation, Charpy impact, tensile, creep, and LCF testing.

Beside the determination of design relevant data, properties and limits constitutive models are developed to describe the behaviour observed, providing a material design interface which allows reliable lifetime prediction for components. The modelling has recently been extended for taking into account the effect of helium, which cannot be covered by the irradiation experiments due to the lack of fusion neutron spectrum in the irradiation facilities currently available.

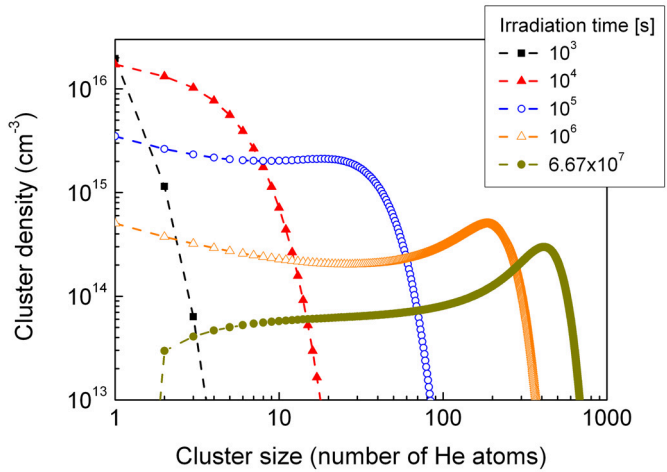
The investigations consider base materials as well as their welded and diffusion bonded joints, whose behaviour is strongly dependent on the processing parameters and the result-



Scattering of Charpy energy of tungsten materials as a result of notch fabrication and material production

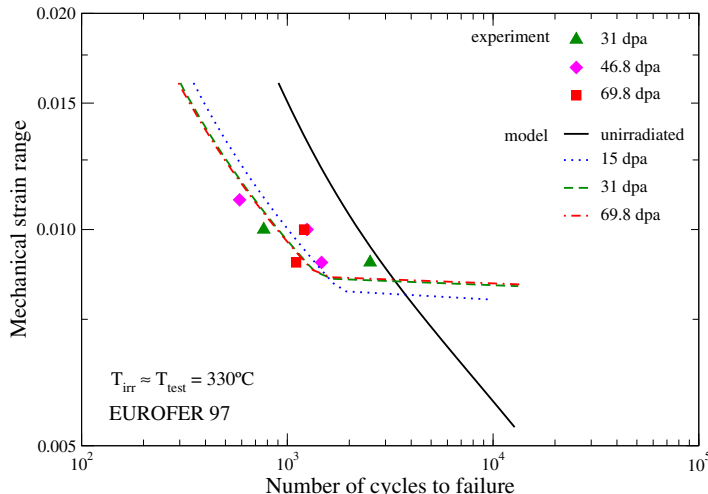
ing quality. For the characterization of the joints quality non-destructive testing is qualified by evaluating the limits of detectable defects.

In the almost completed PIE of the **irradiation programs ARBOR I and ARBOR II**, the tensile, Charpy and LCF behaviour of the RAFM steels, EUROFER 97, EUROFER 97 HT (Heat Treated) and F82H mod after 30 dpa and 70 dpa, respectively, are characterized. For considering the influence of helium, a phenomenological model is developed to describe **helium cluster/bubble growth kinetics** under irradiation. The model allows, for given helium production rates, the calculation of the evolution of helium clusters as it is demonstrated for the 83 wppm ^{10}B doped EUROFER 97 irradiated within the SPICE irradiation program. Thereby, a peak at a cluster size of 410 helium atoms corresponding to a bubble size of 2.1 nm is predicted which is in a good agreement with microstructural observations.



Model calculation for the evolution of helium clusters with irradiation time in 83 wppm ^{10}B doped model alloy

Within the SPICE irradiation program. Thereby, a peak at a cluster size of 410 helium atoms corresponding to a bubble size of 2.1 nm is predicted which is in a good agreement with microstructural observations.



Influence of high dose irradiation on the low cycle fatigue of EUROFER 97

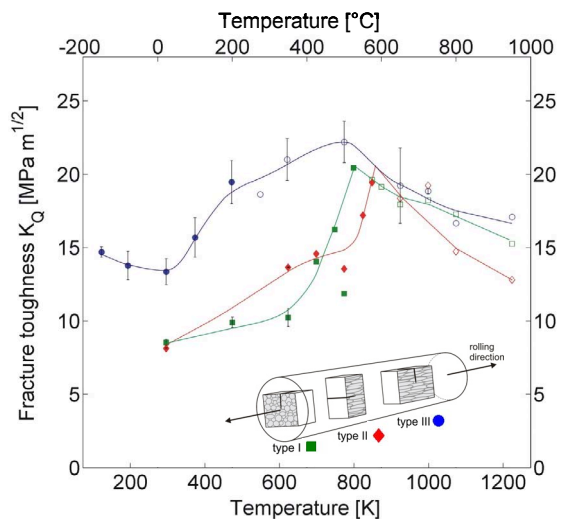
tion of the constitutive behaviour of RAFM steels during and after neutron irradiation under low cycle fatigue conditions. Applying the model to predict the low cycle fatigue behaviour of irradiated EUROFER 97, the negative influence of irradiation on the fatigue lifetime at high strain ranges could be reproduced fairly well. At low strain ranges, the model predicts higher fatigue lifetimes and even endurance for irradiated EUROFER 97 which however is not yet verified by the experiments.

To ensure high quality joints, the **ultrasonic non-destructive testing (NDT)** is being evaluated by determining the limits of detectable defects in different types of joints. The examinations on welded specimens with artificial, differently arranged and sized defects showed that in welding seams of typical blanket structures flaws of 0.2 mm in size are detectable with automated immersion ultrasonic testing. In diffusion bonded seams, the limit of detectable

Evaluating the deformation data obtained within the irradiation programs, a physics-based model describing the irradiation induced hardening has been developed and successfully applied to EUROFER 97 and F82H mod determining its parameters for these materials. The model does not only allow the determination of hardening due to neutron irradiation, but also of its alteration under inelastic deformation and high temperature dwell conditions. Its coupling with the model describing the deformation and damage behaviour of RAFM steels in the un-irradiated state provides a powerful tool for the prediction

flaw size can be even 0.1 mm provided the distance between the surface and the diffusion bonded seem is less than 5 mm.

In view on the application of tungsten and tungsten alloys as structural material in the helium cooled divertor for DEMO, the **fracture mechanical behaviour** of polycrystalline rolled tungsten is characterized considering its anisotropic microstructure. The largest fracture toughness and the lowest DBTT are observed for the specimens extracted in the longitudinal orientation, when the crack propagates transverse to the rolling direction through the elongated grains, yielding a transcrystalline cleavage.



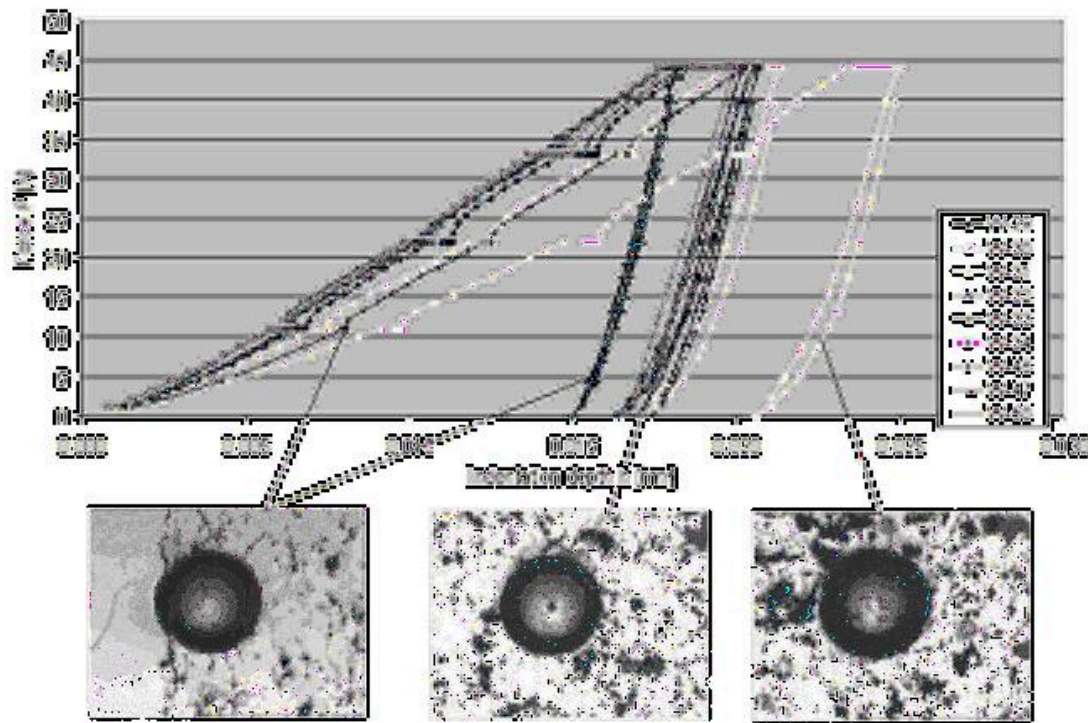
Fracture toughness of tungsten for the three different crack orientations with respect to the rolling direction

Structural Materials – Processing and Compatibility

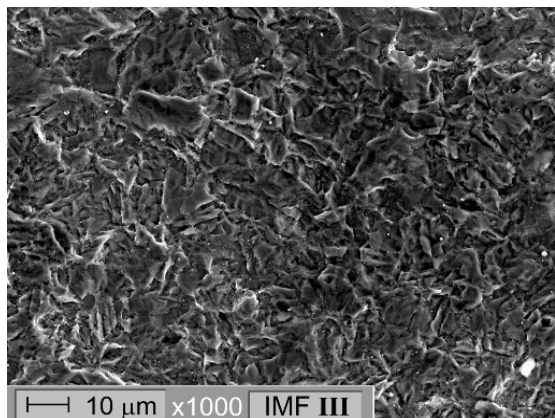
Along with the development and characterisation of tungsten and tungsten based alloys directed towards the potential use as structural materials for a helium-cooled divertor, processing and fabrication technology development are pursued. Work is structured into fabrication process development, process characterization, machining, joining and mock-up testing. Compatibility towards liquid breeder Pb-Li is an important requirement for ferritic-martensitic steels like EUROFER in the HCLL blanket concept.

Powder Injection Moulding (PIM) offers a large potential for mass production of near-net-shape parts with high precision. A new feedstock with 50 vol.-% solid load of a binary W-powder particle system was successfully developed. First W-PIM experiments showed a good mouldability of micro parts. Also a suitable pre-sintering and HIP process chain has been developed. The finished samples show a high density and hardness.

A modified commercial indentation device installed in a hot cell of the Fusion Materials Laboratory (FML) in combination with a neural network based analysis method allows identifying the material parameters of a **unified visco-plasticity model** with nonlinear isotropic and kinematic hardening from small metal specimens. The applicability of the method for bulk material and even for porous tungsten coatings could be demonstrated with indents made in a cross-section of a polished W-coating deposited on a EUROFER substrate (plasma-spray).



Load-depth curves for a porous W-coating deposited on EUROFER by plasma-spray. The interface between tungsten and EUROFER can be seen in the lower left micrograph



SEM image of tungsten layer on EUROFER steel

Electrolytes based on **ionic liquids (IL)**, which are molten salt systems with drastically reduced melting temperatures, can open new paths in electro-chemical deposition, assuming a suitable combination of IL plus metal salt can be designed for deposition of refractory metals, e.g. W, Ta or Ti. Such a system has been identified for W deposition on EUROFER. The ionic liquid used was the commercially available IL, Ethyl-Methyl-Imidazolium Chloride (EMIM-Cl), which was already seen as a suitable electrolyte for Al-deposition on EUROFER for formation of corrosion and tritium permeation barriers. The affinity of tungsten deposition from such systems is higher than for Al from Al-

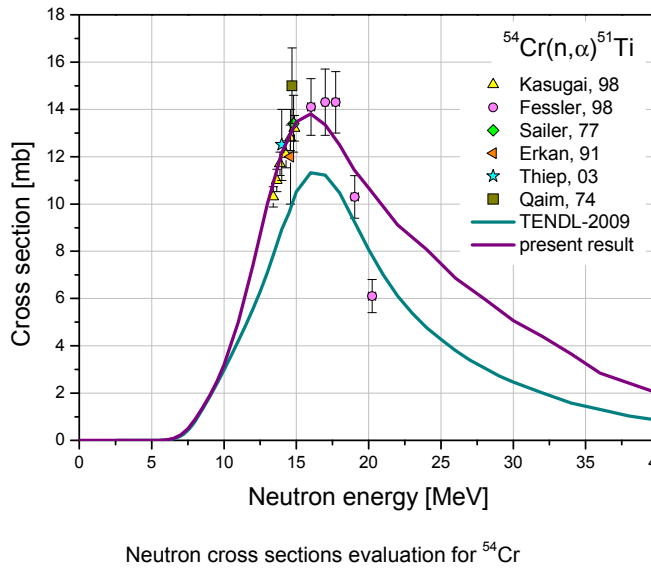
systems, so it was possible to deposit metallic layers with a thickness of roughly 20 μm for the first time. This result indicates that the electrolytes of type IL open the path for electro-chemical deposition of refractory metals which can be used as diffusion barriers in brazing or as filler metals directly.

Nuclear Data

The activities in this field comprise theoretical and experimental work aiming at the provision of a qualified nuclear data base and validated computational tools for neutronics calculations of fusion systems. The KIT contribution to the theoretical activities is on the evaluation of general purpose nuclear cross section data, the qualification of new and updated data evaluations through computational benchmark analyses including sensitivity/uncertainty analyses and the development of advanced computational schemes for sensitivity calculations based on the Monte Carlo technique.

The experimental activities are aimed at providing the experimental data base required for the validation of the computational tools and data applied in fusion neutronics calculations. The current focus is on activities devoted to the experimental validation of Test Blanket Module (TBM) design calculations by means of a neutronics mock-up experiment and on cross-section validation experiments relevant for IFMIF. In addition, advanced measurement techniques are being explored which could later be used in neutronics experiments on TBMs in ITER.

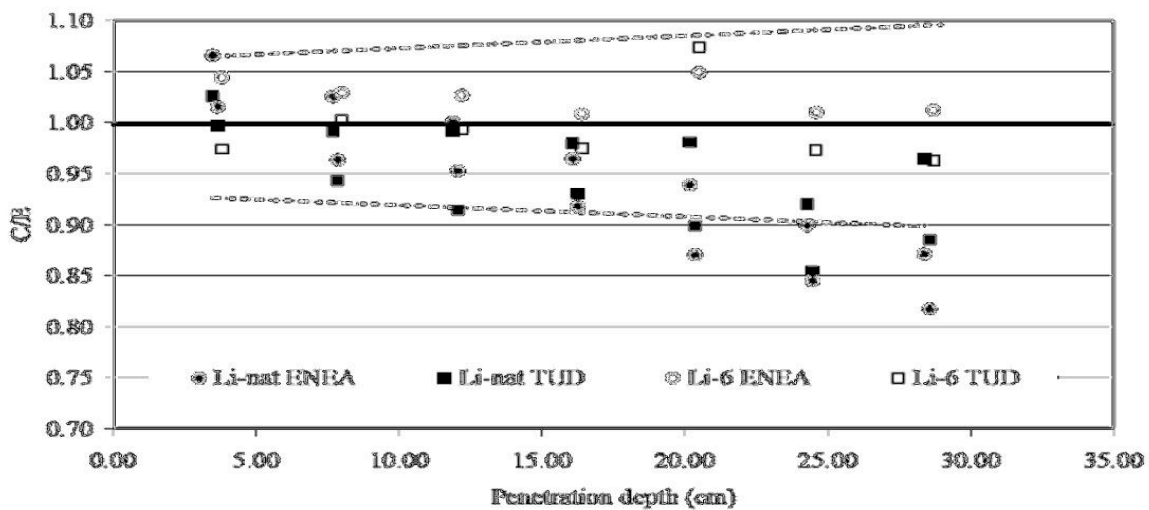
In the frame of the TBM-related work, the **Monte Carlo sensitivity code MCSEN** is being prepared as a release version for external users. MCSEN has been used to perform sensitivity and uncertainty of the HCLL-TBM mock-up experiment, conducted at the Frascati Neutron Generator (FNG), and of the HCLL-TBM in ITER. The calculated uncertainties of nuclear responses such as the tritium production were shown to be at a level of 2 to 4%.



Cross-section data evaluations were performed for the ^{50}Cr , ^{53}Cr and ^{54}Cr isotopes interacting with neutrons up to the energy of 200 MeV. A new evaluation methodology was developed to this end, comprising the generation of uncertainty information by means of the novel Unified Monte Carlo method.

A dedicated neutronics experiment has been performed on a mock-up of the Helium-Cooled Lithium-Lead (HCLL) TBM Test Blanket Module (TBM) in collaborative effort of ENEA Frascati, KIT (using the TU Dresden (TUD) neutron laboratory), JSI, Ljubljana and AGH, Cracow, for the comparison of calculated and measured **tritium production**

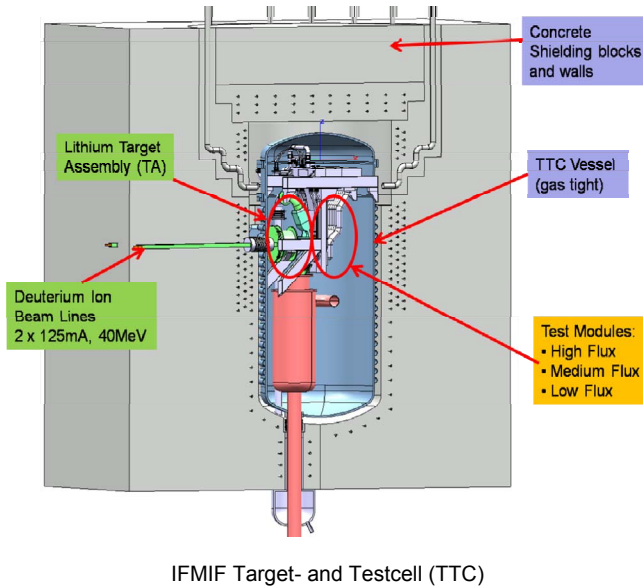
rates (TPR), applying two different methods of measurement. In result, coherence of the different methods is quite good for low penetration depths of the neutrons in the breeder material, however declines at higher penetration depths.



Calculation/Experiment (C/E) comparison of the tritium production rate measurements using Li_2CO_3 pellets

International Fusion Materials Irradiation Facility (IFMIF)

In the Engineering Validation and Engineering Design Activity (EVEDA) for the International Fusion Material Irradiation Facility IFMIF, which is an element of the Broader Approach activities launched jointly among Europe and Japan, the German contribution, provided by KIT, includes engineering tasks for the IFMIF Testcell and the IFMIF High Flux Test Module, as well as the neutronics analysis for the IFMIF Creep Fatigue Test Module.



IFMIF Target- and Testcell (TTC)

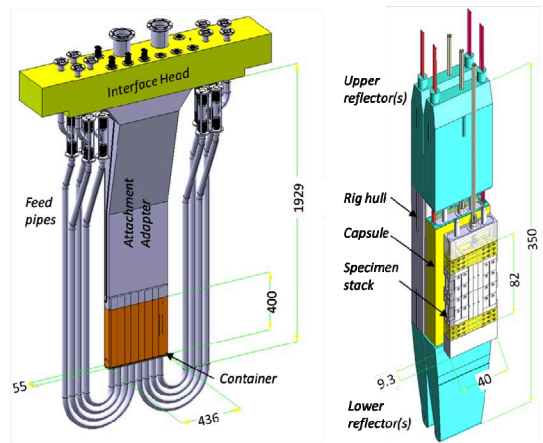
The IFMIF Target- and Testcell (TTC) will contain the lithium target neutron source and the test modules. Within a concrete pit, which has a radiation shielding function, there is the TTC vessel, which is gas tight to allow a controlled inner atmosphere, and to provide a barrier against hazardous materials, such as lithium, NaK, and radioactive contaminants. The High Flux Test Module (HFTM) is the irradiation device for miniaturized ("small specimen" – SSTM) samples. The HFTM is positioned directly behind the neutron source inside the TTC.

The irradiation capsule, which contains a set of material specimen for irradiation inside the HFTM, was already developed and analysed to a considerable degree of maturity. New efforts were concentrated on the fittings for the filling and emptying of the NaK liquid metal (employed to improve the heat conduction from the specimen to the capsule surface), the specimen insertion and retrieval procedure, and the placement and specification of the welding seams. These activities were of high priority in the project, in order to launch the production of the irradiation capsules for the irradiation tests foreseen in the BR2 test reactor.

The HFTM Container and the attachment adapter have been optimized for fabrication. Especially the welding capability of the components has been improved, by adapting the material strengths. The new geometry has been taken as a basis for new CFD and FEM models. CFD calculations of the temperature fields in the structure have been performed for the standard case of specimen temperatures.

The cylindrical vessel type test cell design (MTC) has been developed further, with reduced space requirements. A major issue is the choice of the insulation material to be employed for electrical connectors. The best choices are either PEEK or epoxy resins. Improvement of the shielding of the connectors will be a major challenge for further TTC development.

The **HELOKA-LP test facility** is dedicated to the test of the HFTM under 1:1 operation conditions. This facility has been constructed in cooperation with industry. In 2009, this facility has been finalized and tested. It was proven, that the facility can sustain all specified operation points foreseen for the HFTM mock-up, and stay within the given tolerances for mass



HFTM and the irradiation rigs

flow, inlet pressure, and temperature. Next steps are the training of the personnel and fine tuning of the facility, and the construction of the test section port, which will connect the HFTM mock-ups to the facility.

Fuel Cycle – Vacuum Pumping

Since two decades, KIT has been developing vacuum pumping systems for fusion reactors. The concept of cryogenic pumping based on cryosorption at activated charcoal has been developed and successfully demonstrated, and is now the common technology used for all primary vacuum pumping systems at ITER. As these cryopumps are part of the European procurement package for ITER, KIT has been entrusted with the development of the complete build-to-print packages and the elaboration of the detailed design of the large cryogenic pumping systems of the ITER torus, the ITER cryostat and the ITER NBI.

With the replacement of experienced KIT vacuum staff who moved to ITER, new topics, especially cryogenic thermohydraulics and transient pressure loss estimations as well as vacuum flow simulation, were taken up. In both areas, KIT has now acquired the leading role in fusion.

The **detailed design work for the cryopumps** of ITER was started in 2009. KIT will provide the complete build-to-print package of the torus cryopumps and the Heating-NBI cryopump. Both cryopump designs are unique and will be validated by a prototype each. The HNB prototype pump will be manufactured and tested in the NBI test facility MITICA which is under construction at Consorzio RFX, Padova, Italy.

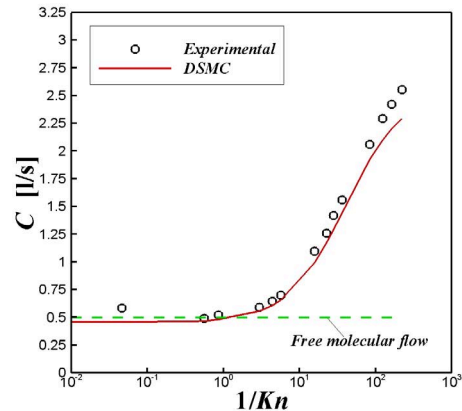


TIMO-2 facility: flexible cryogenic transfer lines

To prepare the tests of the prototype of the torus cryopump at KIT, the test facility TIMO-2 was upgraded in order to be able to replicate two novel ITER operational requirements, namely the direct supply with cryogenic helium gas at 100 K and the supply with supercritical helium at 4.35 K (instead of 4.5 K). Furthermore, the existing rigid cryotransfer lines were replaced by flexible ones designed according to special ITER requirements, to allow for rapid interchange from one pump to the other, which is of prime importance for the expected acceptance testing phase of the serial pumps. The figure is showing TIMO-2 during final acceptance of the cryolines. The TIMO upgrade project will be finished during 2010. TIMO-2 will replicate ITER operation conditions for the large-scale ITER pumps in the same way as TIMO did in the past for the 50% model pump.

The detailed design of the pre-production torus cryopump made excellent progress. The main challenge of this activity is to design this prototypical pump in such a way that it can be optionally used at ITER as a spare pump. This requires elaborating a design in compliance with design codes and standards which are all still emerging at ITER. The main focus of the work done in 2009 was therefore to freeze requirements and to define the input basis for the whole work.

A special highlight was the progress in modelling of vacuum flows throughout the whole range of the Knudsen number, in an efficient collaboration with the Hellenic Fusion Association, Volos that could be regarded as template for successful EFDA stimulated collaboration in Europe. Fusion devices typically feature very complex vacuum systems. The achievable net pumping speed and effective vacuum conductance of such a system is of major importance and therefore, a thorough and encompassing study of the flow conditions is mandatory. For that purpose, the system is represented as a network of channels, and the predicted quality of performance is directly given by the quality describing the channel flow. In the last decade, excellent progress has been made in modelling fully developed flows in long channels, but a typical fusion vacuum system comprises mainly shorter channels where the flow is developing and end effects must not be ignored. Hence, to provide a thorough basis for channel flow prediction, a parametric programme has been launched for the first time, focusing on the experimental and numerical investigation of gas flows through short tubes at variable finite length. The benchmark result, i.e., the agreement between the computational method (DSMC - Direct Simulation Monte Carlo) and experimental values, is excellent. The vacuum flow activities will be continued and it is planned to use the results to support the design of the ITER gas injection systems.



Conductance vs. Knudsen number for short tubes

Fuel Cycle – Tritium Plant

The water de-tritiation system (WDS) and the isotopic hydrogen separation system (ISS) are European contributions to the ITER tritium plant. Both systems have been set up at technical scale in the Tritium Laboratory of KIT during the last years in order to investigate the behaviour of single components under various working conditions and configurations, as well as the dynamic interaction of WDS and ISS. Specific data derived from the experiments are being currently incorporated in the design of the respective systems for ITER.



ISS: The opened Cold-Box with a view on the condenser

Further fusion research activities at TLK are related to the test blanket modules for ITER in terms of tritium removal from gas streams of high flow rate. The aim is to identify a process which can easily be upgraded to DEMO relevant flow rates (factor of more than 100 compared to ITER).

In view of the **ITER ISS** a special packing designated for the cryogenic distillation column was evaluated in terms of liquid hold-up and separation performance in comparison to two standard packings. All three were tested in round-the-clock measurement phases lasting for several days each with different hydrogen/ deuterium mixings and different operational parameters. The aim of these experiments was on the one hand to determine the separation performance of the different packings and on the other hand to calculate the liquid hold-up as a function of the given parameters. The liquid hold-up should be as low as possible to minimise the tritium

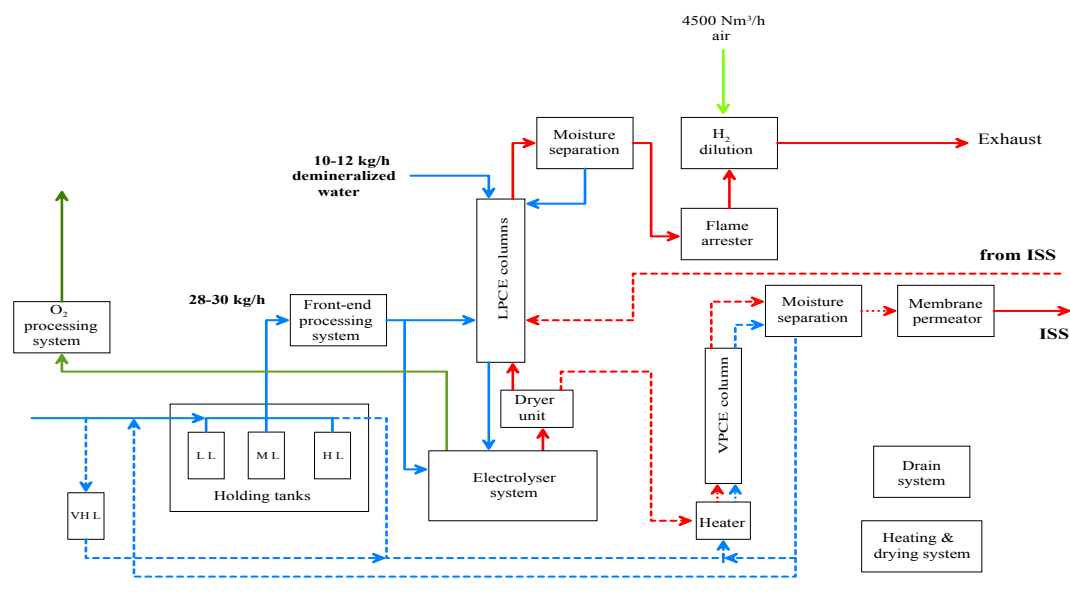


Structured metal gauze packing for ISS

inventory in the future ITER ISS. One important result was that the design of the columns (e.g. re-distributor) has a considerable influence on the liquid hold-up and on the operability of the whole facility.

The endurance tests of the **WDS facility** were directed towards long term operation of critical components needed for the design of the ITER WDS. The results confirm that the level of tritium decontamination remains stable over the testing period. This indicates that there is almost no loss in performance or degradation of the catalyst/packing mixture material of the liquid phase catalytic exchange (LPCE) column over the years. For the Solid Polymer Electrolyser units applied in the WDS facility, no signs of structural damage caused by tritium decay could be found. The structural integrity was preserved in all cases.

As a result of design integration activities, ITER requested an update of the **ISS-WDS process design**. A new design has been proposed, integrating a vapour phase catalytic exchange (VPCE) column. The advantages this additional component is bringing are the reduction of the tritium activity in the water to be fed to the WDS (to gain longer life-times of electrolyzers) and the possibility of processing highly tritiated water which could cause disposal problems during the operation of ITER.



Enhanced configuration of the ITER WDS incorporating a VPCE column

Contents

	Page
Overview	i - xix
Plasma Wall Interaction	1
Development of the PWI Basis in Support of Integrated High-Z Scenarios for ITER (WP09-PWI-05).....	3
Demonstration of Liquid Plasma-facing Components: Modelling Lithium Melting Damage with the Code MEMOS (WP9-PWI-06)	8
Mitigation of Disruption Loads for ITER (WP9-PWI-08)	10
Head Load in ITER Relevant ELM Scenarios (WP09-PWI-09).....	13
Physics: Heating and Current Drive - ECRH	17
Development of the European Gyrotron („CCGDS6“) (F4E-2008-GRT-08(PMS-H.CD)-01).....	19
Microwave Heating for Wendelstein 7-X	29
ECR Heating and Current Drive – Step-Tunable Gyrotron Development	36
Design Studies towards a 170 GHz 4 MW Coaxial-Cavity Gyrotron (EFTS EC-Tech – Contract No. 042636 (FU06))	42
Electron Cyclotron Systems Technology for ITER (EFTS EC-Tech-Contract No. 042636 (FU06))	45
Design, Analysis and Testing of the Upper Launcher for the ITER-ECH&CD System (EFDA/06-1406 - TW6-TPHE-ECHULB4 and TW6-TPHE-ECHULA).....	48
Production of the ITER EC Upper Port Plug Preliminary Design Review Documentation (structural, diamond window and integration) and Completion of Welding Tests for the Port Plug Structure (F4E-2009-OPE-051 (PMS-H.CD))	50
Goal Oriented Training Programme "Outgassing Measurements for ITER ECRH Upper Launcher" (WP08-GOT-ITER-PPE (FU07-CT-2008-00047))	53
Project funded by the Ministry for Education and Research (BMBF): Manufacturing of ITER ECH Upper Port Plug Structural System Prototypes	58
Magnet Structure and Integration	63
Materials Cryogenic Testing (EFDA/07-1704-1604 – TW6-TMSM-CRYOGT).....	65
Current Leads for Wendelstein 7-X and JT-60SA	71
Definition of Procedures for Coil Electrical Testing and PF Transient Analysis (EFDA/06-1522 – TW6-TMSC-COILMO)	75
Quench Detection System for Fusion Magnets	79
Development of HTS-Roebel Cables	82
Cryogenic Infrastructure	85
Breeding Blanket and Divertor	89
Construction of the High Pressure Helium Loop (HELOKA-HP/TBM) for Testing of TBMs (TW5-TTB-001).....	91
Components and Instrumentation Development for TBM (TW2-TTBB-007b).....	93
Manufacturing and Testing of a FW Channel Mock-up for Experimental Investigation of Heat Transfer with He at 80 bars and Reference Cooling Conditions. Comparison with Numerical Modeling (TW5-TTBB-001 D 10)	98
Manufacturing and Testing of Mock-ups for Investigation of Coolant Flow in the Manifold System of HCPB TBM (GRICAMAN Experiments) (TW5-TTBB-003 D 1)	103

	Page
Design and Development of the European Test Blanket Modules (TBM) Systems ("TBM08G1") (F4E-2008-GRT-09(PNS-TBM)-01)	109
Fusion Researcher Fellowships - WP08-FRF-FZK/Cismondi	125
Goal Oriented Training Programme "Breeding Blanket Developments for Fusion Reactors" (WP08-GOT-EUROBREED (FU07-CT-2008-00047)	128
Helium Cooled Pebble Bed: Breeder and Neutron Multiplier Materials.....	131
Modelling of Pebbles and Pebble Beds.....	134
Procurement and Quality Control of Lithium Orthosilicate Pebbles – OSi 08.....	136
DEMO Divertor: Fabrication, Joining, and High Heat Flux Component Testing (WP08-09-MAT-WWALLOY, Activity 1.....	143
Structural Materials - Development and Characterisation.....	149
Investigation of Options to Reduce Critical Elements in Low Activation Ferritic/ Martensitic Steels (EFDA/05-1244 – TW4-TTMS-RedAct).....	151
Support and Follow-up of the EFDA/06-1903 Art. 7 Contract for Procurement of EUROFER for the TBM Fabrication Technology Trials and Mock-ups (EFDA/06-1520 – TW6-TTB-EUROFER).....	153
Characterisation of Reference EU-ODS-EUROFER Batch: Optimisation of Heat Treatment, Ageing Behaviour and Microstructural Characterisation (TW5-TTMS-006 D 10).....	155
Fabrication and Irradiation of FE-54 Enriched Samples to Study the Influence of He/dpa Ratio on Materials Degradation Up to Medium Dose Level (TW4-TTMS-001 D 1, TW5-TTMS-001 D 2)	159
Tomographic Atomic Probe Analysis of EUROFER Materials Irradiated in the ARBOR Irradiation Campaign (TW5-TTMS-001 D 4)	163
TEM Examination of Microstructure & Nano-Chemistry of Neutron Irradiated EUFOFER 97 Specimens (15 dpa HFR) (WP08-09-MAT-REMEV, Activity 5)	170
Nano Composited Ferritic Steels for HT Application: Identification of Promising Candidate Alloy Compositions and Respective Fabrication Routes According to the Outcome of the 2004 Study. Production of Different Laboratory Batches (14%Cr) (TW5-TTMS-006 D 5, TW5-TTMS-006 D 7)	174
Developing the Present Generation of ODS Nano-structured Ferritic Steels (WP08-09-MAT-ODSFS, Activity 1)	181
Coordination of the EFDA Fusion Materials Topical Group and Fundamental Studies on Mechanical Properties of W-alloy (WP08-09-MAT-WWALLOY).....	185
Development of Improved W-alloys for Application in a Power Plant with He Cooled Divertor (TW4-TTMA-002 D 2, TW5-TTMA-002 D 2).....	190
Structural Materials – Mechanical Behaviour and Reliability	195
Fast Reactor Irradiation up to 30 dpa, at 340°C of Tensile, Charpy and LCF RAF/M Specimens, Completion of the PIE (TW2-TTMS-001b D 9).....	197
Mechanical Post Irradiation Examinations of FZK-Specimens Irradiated in the ARBOR-2 Experiment in the BOR 60 Reactor (TW5-TTMS-001 D 10)	198
Creep-fatigue Lifetime Prediction Rules for Irradiated (TW2-TTMS-005b D 4).....	201
Quantitative TEM & SEM Investigation of Irradiated Specimens from SPICE (HFR) and ARBOR 1 (BOR-60) (WP08-09-MAT-REMEV, Activity 5).....	204
Qualification of Welded Joints by LCF Testing (TW6-TTMS-004 D 3)	208
Experimental Determination of the Slip Systems and Dislocation Glide Properties of Pure α -Fe (WP08-09-MAT-REMEV, Activity 4).....	214
Define and Perform Accompanying Experiments to D 5 (e.g. creep crack growth at 550°C) (TW5-TTMS-005 D 6)	217
Qualification of NDT (non-destructive detection techniques) for Evaluation of Limits of Detectable Cracks (TW6-TTMS-005 D 5)	219

	Page
SSTT: Continuation of the Modeling of the Ductile Region – Transferability of Small Size Specimens to Standard Size and FW Applications (TW6-TTMS-005 D 12)	220
Fracture-mechanical Characterization of W-Alloy (W-Ti, W-V, W-Ta) in the Interesting Temperature Window for fusion Applications (RT-1300°C) (WP08-09-MAT-WWALLOY; Activity 2).....	222
Preliminary RT Test of Unirradiated Specimens Thin Foil Tensile Specimens in View of Future PIE – Comparison to Standard Tensile Test (TW5-TTMA-002 D 5)	227
Mechanical Characterization of W-Armour Materials (WP08-09-MAT-WWALLOY, Activity 3).....	229
Operation of the Fusion Materials Laboratory (Underlying Technology)	230
 Structural Materials – Processing and Compatibility	 233
Corrosion Resistance of Bare and Coated EUROFER in Liquid PbLi.....	235
PM Production and PIM of Tungsten and Tungsten Alloys (WP08-09-MAT-WWALLOY, Activity 2).....	241
W-Alloy Development for Structure Application and Characterization (WP08-09-MAT-WWALLOY, Activity 2).....	244
Electro-chemical Machining (ECM) of Tungsten and Tungsten Alloys (WP08-09-MAT-WWALLOY, Activity 1)	246
Development of W-EUROFER & W-W Brazed Joints. Commercial Joint Deposited by Electro-chemical Methods: (i) Aqueous Electrolytes and (ii) Organic Electrolytes (WP08-09-MAT-WWALLOY, Activity 1)	253
 Nuclear Data	 261
Nuclear Data: Benchmark Experiments to Validate EFF/EAF Data (EFDA/07-1704-1631 - TW6-TTMN-002B)	263
Improvement of Nuclear Data, Development of Tools and Experiments/Validation in Support of ITER Activities (F4E-2008-GRT-014-01 (ES-AC) - Action 1, NUDATA_Files)	274
Nuclear Data Studies/Experiments in Support of TBM Activities (F4E-2008-GRT-014-02 (ES-AC) - Action 2, NUDATA_Exper).....	279
Assessment of the Suitability of Neutron and Gamma Detectors in the Future Experiment at JET for the Validation of Shutdown Dose Rate Prediction - Characterization of a CdTe Gamma-ray Detector for Measurements at JET (JW9-FT-5.31)	286
 International Fusion Materials Irradiation Facility (IFMIF)	 289
Broader Approach Activities: IFMIF Test Cell and High Flux Test Module	291
Broader Approach Activities: IFMIF EVEDA – Material Responses in Creep-fatigue Samples and Heating Bodies irradiated at IFMIF CFTM	297
 Fuel Cycle – Vacuum Pumping	 301
Upgrade of TIMO Facility (TW5-TTFF-VP 58, F4E-2009-GRT-019-01).....	303
Completion of Final Design for the Prototype Torus Cryopump and Testing in TIMO-2 to Qualify the Design (F4E-2009-GRT-018-01)	307
Instrumentation for ITER Cryopumps and Cold Valve Boxes (F4E-2009-GRT-020-01)	311
Conductance Modelling of ITER Divertor and Torus Pumping Duct (EFDA/06-1498 – TW6-TTFF-VP 68).....	313
Development of a New Collisional Flow Monte Carlo Method.....	317
Design Activities for the first ITER HNB Injector (F4E-2008-GRT-011; F4E-2009-GRT-032).....	319
Investigation of Vacuum Gas Flows for Nuclear Fusion Applications (Fusion Researcher Fellowships - WP08-FRF-FZK/Varoutis).....	324

	Page
Fuel Cycle – Tritium Plant	329
Endurance Tests of Water Detritiation System (TW6-TTFD-TR 64)	331
Functional and Performance Evaluation of Sulzer CY Packing in View of ITER-ISS (F4E-2009-GRT-023-01)	333
Testing of Isotope Separation System (ISS) with the WDS (TW6-TTFD-TR 63)	336
Update of ITER-ISS-WDS Process Design – 1 (EFDA/06-1510 – TW6-TTFD-TPI 55)	338
Development and Customization of CATIA V5 for Tritium Plant Systems (EFDA/06-1514 – TW6-TTFD-TR 65)	340
Goal Oriented Training Programme “Tritium Technologies for the Fusion Fuel Cycle” (WP08-GOT-TRI-TOFFY, FU07-CT-2008-00047)	341
Safety	343
Combined Hydrogen and Dust Explosion and Mitigation Experiments and Model Development. Validation and Application to ITER and New Analysis of Explosion Reference Events (F4E-2008-GRT-01-01 (ES-SF))	345
Appendix I KIT Departments Contributing to the Fusion Programme	349
Appendix II Fusion Programme Management Staff.....	351
Appendix III Glossary	353

Plasma Wall Interaction

Development of the PWI Basis in Support of Integrated High-Z Scenarios for ITER (WP09-PWI-05)

WP09-PWI-05-02/FZK/BS

Introduction

In the future tokamak ITER, plasma edge localized modes (ELMs) and disruptions of the plasma confinement may result in vaporization and melting of the divertor and first wall surfaces made of beryllium and tungsten, the ITER target reference materials. For transient heat loads below the melting threshold, the surface cracking remains an issue for ITER design.

For modelling the melt motion damage including bulk heat transport, the incompressible fluid dynamics code MEMOS was applied. The new calculations with MEMOS were mainly focused for the magnitudes and the threshold of melt splashing under repetitive heat loads, in order to optimize the W-macrobrush target design. Furthermore, MEMOS has been validated melt splashing experiments at the plasma gun QSPA-T facility, and applied for supporting the numerical modelling of the melt damage to W targets in the ITER simulation experiments at the tokamak TEXTOR.

The tungsten surface cracking under ELM heat loads below the melting threshold was simulated with the thermomechanic code PEGASUS. Comparisons with experimental observation for the tungsten cracking below the melting threshold at the plasma gun QSPA-Kh-50 facility have been done.

Simulations of melt motion damages using the code MEMOS

ITER transient loads at the divertor surface		
Disruptions (duration $\Delta t \sim 3$ ms)		
Type of transient	Max impact energy, Q_{max}	Max current, J_{max}
	MJ/m ²	MA/m ²
Maximal	30	30
Typical	10	5
Mitigated	1.5 (First wall)	0
ELMs ($\Delta t \sim 0.5$ ms)		
Uncontrolled	15	30
'Half-controlled'	2	5
Controlled	1	5

There are many parameters for which the W melt damage after ITER ELMs and disruptions has to be estimated. The most important ones are the impact energy Q [MJ/m²], the pulse duration Δt [ms], and the electric current through the target J [MA/m²] (see the table). The separatrix strike point (SSP) movement magnitude δ [cm], the normal pressure p_{\perp} [bar] and the tangential pressure p_{\parallel} [bar] as well as the heat loads to small lateral parts of W-brush Q_{lat} [MJ/m²] are also involved in the benchmark ITER modelling with MEMOS. Recently, the code

was mainly applied for bulk targets, taking into account the SSP point motion ($\delta = 5$ cm), the cross currents, the tangential pressure and the lateral loads. The heat load dependencies in time and the space earlier calculated with the MHD code FOREV together with the pulse shapes such as rectangular and triangular ones and some special reference shape have been used. The consequences of one typical ITER disruption strongly depend on these parameters. The recent MEMOS calculations showed that diverse damage parameters vary in wide ranges. The disruption damage can be characterized by the melt velocity $V_{melt} \sim 0.2 - 0.5$ m/s, the melt thickness $H \sim 33$ to 60 μ m, the magnitude of melt mountains h_+ up to 16 μ m and the crater depth h_- up to 5 μ m. For ITER ELMs up to $Q = 1.6$ MJ/m², $V_{melt} < 0.36$ m/s, H up to 44 μ m, h_+ up to 50 μ m at the reference pulse shape, and h_- up to 6.2 μ m were obtained in the simulations. After many transients those parameters will be significantly increased.

As an example, Fig. 1 demonstrates the erosion profile on the surface of a bulk tungsten target after multiple disruptions of $Q = 15 \text{ MJ/m}^2$ and $\Delta t = 5 \text{ ms}$ (at $\delta = 5 \text{ cm}$). After 100 disruptions, the crater depth reaches 1.5 mm ($\delta = 5 \text{ cm}$) or 5 mm (at $\delta = 0 \text{ cm}$). The MEMOS results are summarized in special tables for assisting in ITER design.

The validation of the code MEMOS against experimental data obtained in recent QSPA-T experiments has been continued. In the W splashing experiments, the maximum plasma pressure of normal pulse incidence (pulse duration 0.5 ms, stream radius 3 cm) was varied from 2.3 to 4 bar, with heat load values from 1.6 to 2.2 MJ/m². W droplets appear after the plasma pulse with a delay of 3 ms, rather isotropically, with velocities U up to 20 m/s and sizes D up to 60 μm . From the experiments it follows that the plasma velocity along the surface, $V_{\parallel p}$, is equal to e.g. 100 km/s (for 1.6 MJ/m²), the plasma density ρ_p is $\sim 20 \text{ mg/m}^3$, and the melt layer thickness is 50 μm .

Numerical simulations demonstrated a reasonable agreement with the experimental data on the droplet sizes and droplet velocities, and allowed projections towards the melt splashing at ITER conditions. Further development of the melt splashing model was done starting from approximation of experimental droplet sizes and velocities with analytical distribution functions of the Upper Limit Log Normal distribution type:

$$f(x) \propto \exp(-\delta(\ln(C(x_{\max}/x-1))^2)$$

Fig. 2 demonstrates the experimental and the approximated distributions of the droplet velocity.

Assuming the Kelvin-Helmholtz (KH) instability as the mechanism of droplet emission, the model parameters were fitted to the experiments. The relevant ITER parameters are $V_{\parallel p} \sim 300 \text{ km/s}$ and $\rho_p \sim 0.1 \text{ mg/m}^3$, and from the KH-model the melt splashing velocity $V_m \approx 1 \text{ m/s}$ is derived. Projecting the KH-model upon ITER transient loads below the vapour shield threshold, the conclusion can be drawn that the melt splashing would not occur (see Fig. 3). With the vapour shield, no prediction is yet done.

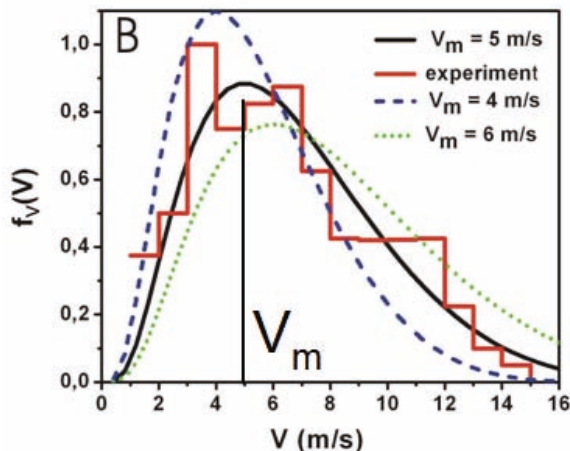


Fig. 2: Velocity distribution of W droplets ($Q = 1.6 \text{ MJ/m}^2$, $p_{\perp} = 2.3 \text{ bar}$).

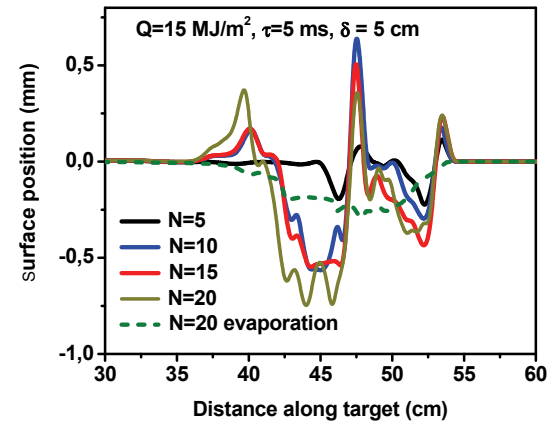


Fig. 1: Erosion profiles after N disruptions.

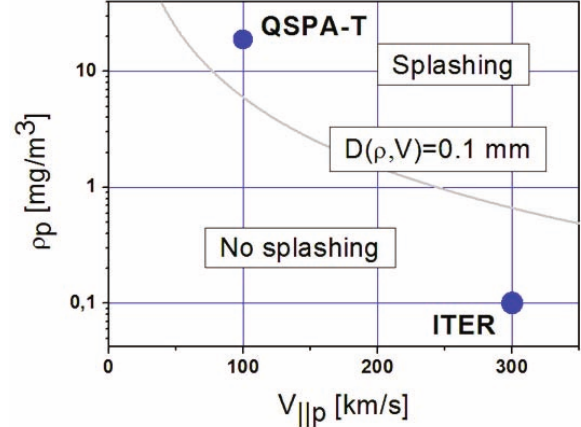


Fig. 3: The melt splashing threshold (the melt thickness D is constant).

TEXTOR relevant activity: The joint work of FZK / KIT and TEXTOR teams was based on an attempt of checking the earlier MEMOS prediction that some rounding of the castellation corners of the W-brush target prevents bridging of the brush tiles. The bridging has to be avoided, because it increases the wall load by eddy currents during the disruption. In current TEXTOR W-experiments, the melt mountains up to 2 mm on the edges of W-brushes of 5 and 10 mm width at rounding radii $R = 0$ mm and $R = 1$ mm were achieved, however no bridging occurred (not even at $R = 0$). The experiment suggested adjustment of MEMOS to the particular experimental geometry in order to calculate the bridging threshold, taking into account the $J \times B$ force and the plasma pressure gradient as the most important causes of the violent melt motion. The joint experimental/modelling program was agreed.

Simulation of tungsten armour cracking using the code PEGASUS

Modelling for W surface cracking under pulsed heat loads below the melting threshold at 0.57 MJ/m 2 has been developed. The Kelvin-Voigt model for viscose-elastic deformations has been implemented in the code PEGASUS. The model has been validated against the plasma gun QSPA-Kh50 using the experimental results for room temperature W exposed to pulsed plasma heat loads of $Q = 0.45$ MJ/m 2 .

In these experiments, after a few pulses a mesh of cracks of typical sizes of 0.3 to 1 mm developed at the surface, which was heated up to 3000 K. The mesh remained stable during 200 shots (see Fig. 4), but the width of the cracks increased with the shot number, reaching about 10 μ m. Then, at larger shot numbers, the surface started to melt, probably due to some deterioration of thermoconductivity. The melting results in additional small cracks inside the cells of the original mesh. Increasing Q results in substantial melting and drastically increased crack width (see Fig. 5).

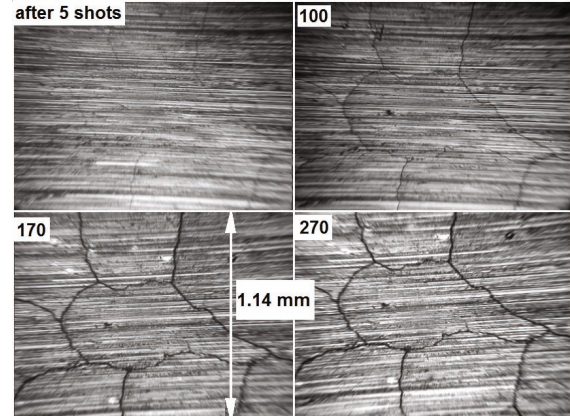


Fig. 4: Mesh of cracks in W after many shots at the plasma gun QSPA-Kh50. The crack pattern does not change.

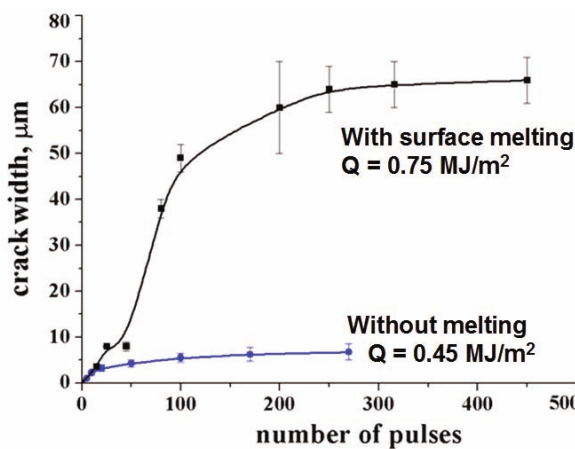


Fig. 5: Crack average width vs. shot number.

thus deformations of the material there. At the high final temperature, the deformations are substantially plastic, i.e. the viscosity of W decreases, allowing some stress relaxation in the sub-surface, but not as complete as when melting occurs. The following decrease of temperature increases again the viscosity and thus fixes the material deformation during the cooling, and the material relaxation results in a large tensile stress σ which produces the cracks when exceeding some threshold σ_c .

The reason for cracking of any material close to the surface heated by severe heat loads is a thermostress produced in the sample due to a temperature gradient. A steep temperature gradient is generated, and the faster the heating rate, the steeper the gradient. It seems that cracking is absent in the stationary regime, and occurs under off normal events only. The cracking during the melting phase was analysed earlier with PEGASUS. Now, the code's model focuses on the pre-melting shots. The crack appearance can be described as follows. During the fast heating, some compressive thermostress appears in a thin (~ 50 μ m) sub-surface layer, because of non-homogeneous thermal expansion and

The PEGASUS thermal conduction model bases on the conductivity k as a function of local temperature. The data on k is available up to the melting point temperature. The stress tensor σ_{ik} is proportional to the deformation tensor u_{ik} , and at large stress values (determined by the Mises criterion), the stress additionally becomes proportional to the time derivative du_{ik}/dt :

$$\sigma = Eu + \theta \left(\frac{\|\sigma\|}{\sigma_y} - 1 \right) \eta \frac{\partial u}{\partial t}$$

Here, E is the material constant tensor comprising the Young's, Poisson's and shear modules, η is the viscosity tensor, and σ_y is the yield strength of the Mises criterion. The data on E is available up to 3000 K. One can also assume σ_y and $\sigma_c/10$ as 1 MPa for 2500 K and 20 MPa for 3000 K.

The data on η is lacking. Therefore, η is used as the fitting parameter in the validation of PEGASUS against the experiments. Typically, in the experiment σ is of few GPa. Thus σ_y and σ_c are negligible. That allowed model simplification, and yielded a solution of the type:

$$u \sim \frac{\sigma_{\max}}{E} \left(1 - \exp \left(-\frac{t}{\tau} \right) \right), \quad \tau = \frac{\eta}{E}$$

Using the experimental time $\tau = 0.25$ ms, $\eta = \tau E = 45$ s-MPa was obtained. Using these values for the parameters of the model, PEGASUS simulations have been performed. They demonstrated gradual development of the crack widths in the stable net pattern that appeared on the numerical W sample below the melting point (Fig. 6). The average crack mesh size is 0.5 mm, and the maximum crack width is 7 μ m (in agreement with the measured value).

Conclusions

The code MEMOS was applied for further modelling of melting and splashing in a wide range of transient load parameters at the surfaces of the tungsten macrobrush and bulk targets. In the case of disruptions, the melt erosion can reach a thickness of 1 cm, which is comparable with the target thickness. For ELMs, the experimentally observed melt splashing is predicted not to occur at ITER conditions. Plasma gun experiments allowed the validation of the new plasticity model implemented in the code PEGASUS. Further modelling of the W erosion for transient heat loads at varying surface geometries, and benchmarking the codes against available plasma gun and tokamak data is necessary.

Staff:

B.N. Bazylev
 I.S. Landman
 S.E. Pestchanyi

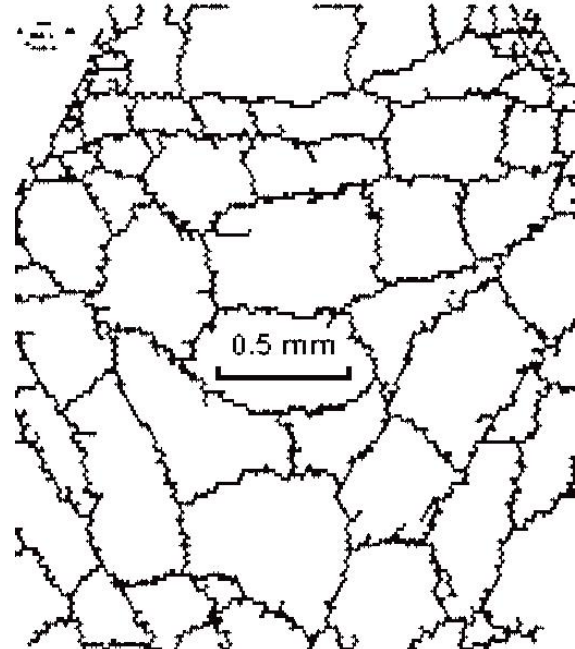


Fig. 6: Numerical cracks on a W surface.

Literature:

- [1] B. Bazylev, I. Landman, A. Loarte, N.S. Klimov, V.L. Podkorytov, V.M. Safronov, Droplet Emission from Tungsten Melt Layer under Transients. Experiments and Modelling. 12th International Workshop on Plasma Facing Materials and Components for Fusion Applications (PFMC-12), 11-14 May 2009, Juelich, Germany. Accepted for publication in *Physica Scripta*.
- [2] S. Pestchanyi, I. Garkusha, I. Landman, Simulation of tungsten armour cracking due to small ELMs in ITER. Presented at the conference ISFNT-9, Dalian, China, October 2009 for publication.
- [3] N. Klimov, V. Podkorytov, A. Zhitlukhin, D. Kovalenko, B. Azylev, G. Janeschitz, I. Landman, S. Pestchanyi, G. Federici, A. Loarte, M. Merola, J. Linke, T. Hirai, J. Compan, Experimental study of PFCs erosion under ITER-like transient loads at plasma gun facility QSPA. *Journal of Nuclear Materials* 390-391 (2009) 721-726.
- [4] B. Bazylev, G. Janeschitz, I. Landman, S. Pestchanyi, A. Loarte, G. Federici, M. Merola, A. Zhitlukhin, V. Podkorytov, N. Klimov, J. Linke, T. Hirai, Experimental validation of 3D simulations of tungsten melt erosion under ITER-like transient loads, *Journal of Nuclear Materials*, 390-391 (2009) 810-813.
- [5] I.E. Garkusha, et al. (incl. I.S. Landman), Experimental study of plasma energy transfer and material erosion under ELM-like heat loads, *Journal of Nuclear Materials*, 390-391 (2009) 814-817.
- [6] R.J. Hawryluk, et al. (incl. I.S. Landman), Principal physics developments evaluated in the ITER design review, *Nuclear Fusion* 49 (2009) No. 065012.
- [7] I.E. Garkusha, et al. (incl. I.S. Landman), Damage to preheated tungsten targets after multiple plasma impacts simulating ITER ELMs, *Journal of Nuclear Materials*, 386 (2009) 127-131.
- [8] B. Bazylev, G. Janeschitz, I. Landman, S. Pestchanyi, A. Loarte, Erosion simulation of first wall beryllium armor under ITER transient heat loads, *Journal of Nuclear Materials*, 386 (2009) 919-921.
- [9] B. Bazylev, G. Janeschitz, I. Landman, et al. Experimental and theoretical investigation of droplet emission from tungsten melt layer, *Fusion Engineering and Design*, 84 (2009) 441-445.

Acknowledgement

This work, supported by the European Communities under the Contract of Association between EURATOM and Karlsruhe Institute of Technology (KIT), was carried out within the framework of the European Fusion Development Agreement. The views and opinions expressed herein do not necessarily reflect those of the European Commission.

Demonstration of Liquid Plasma-facing Components: Modelling Lithium Melting Damage with the Code MEMOS (WP09-PWI-06)

WP09-PWI-06-01/FZK/BS

Preliminary numerical modelling with the incompressible fluid dynamics code MEMOS for lithium plasma facing components (PFC) has been performed. This work was motivated by the Li activity on the tokamak FTU at ENEA Frascati, where a liquid lithium limiter (LLL) with a capillary porous system (CPS) is installed. A heating system increases the Li temperature above the melting point at 450 C. The liquid Li flows, through capillaries of 15 μm radius within a network of wires of 30 μm diameter, from a reservoir to the plasma facing surface. As a result, a thin lithium film coating forms on the chamber wall during the discharge; this process is called the 'lithization'. The impact of the hot confined plasma on the limiter surface produces Li ions in the vessel by physical sputtering and by evaporation.

At present, it appears too early for trying to extrapolate to ITER the FTU conditions for liquid PFC sputtering experiments. ITER is anticipated to operate in the H-mode of plasma confinement, where the plasma edge localized modes (ELMs) may result in melting and vaporization erosion at the divertor and first wall surfaces even in the case of tungsten PFCs (W melting point is 3600 K). Thus, obviously quite different aspects of the lithization, e.g. melt motion under the $J \times B$ force, should be most important in ITER. The capillary boundary conditions at the bottom of the lithium film are not yet implemented in MEMOS. However, it seems that for the transients, the CPS will not be effective as a compensator of melt layer evaporation or melt removal, and thus the inflow of Li from the CPS can be neglected in the preliminary simulations. Anyway, the removal of the Li film from the main chamber wall, that can be a Be or a W armour, should be addressed at first.

Therefore, in this study we simulated the melt motion and the evaporation at the Li surface, assuming a Li film on an impermeable tungsten substrate. The MEMOS simulations showed that even the mitigated ELMs with an impact energy Q below 0.5 MJ/m², which are not immediately dangerous for the W target, can severely destroy the Li target. In the simulations, the melt motion processes involving the mechanisms of tangential $J \times B$ - and pressure gradient forces are taken into account. An initial thickness of 40 μm was assumed for the Li coating. The initial temperature T_0 was chosen as 500 K (to simulate the molten Li film) and 300 K (to include Li melting during the transient). The applied force and the energy flux correspond to a rectangular pulse.

First simulations showed that even a small ITER ELM of $Q = 0.5 \text{ MJ/m}^2$ produces immediate removal of the Li film from the W mount during a time shorter than the ELM duration of 0.5 ms. Therefore, to demonstrate a significant melt motion effect, we chose reducing the ELM size down to $Q = 0.1 \text{ MJ/m}^2$.

Fig. 1 demonstrates the effect of the melt motion caused by the tangential pressure $p_{\text{par}} = 1 \text{ mbar}$, showing the melt wave after 1 ms. Fig. 2 shows the influence of the $J \times B$ force on the depth of the resolidification crater (at 300 K) in the applied magnetic field of 5 T, and Fig. 3 the influence of the tangential pressure.

Based on these MEMOS simulations, we conclude that both solid and molten Li behave similarly. Even small ELMs completely remove the Li from the W substrate. The simulations also showed that there is no vapour shield developing in front of Li film.

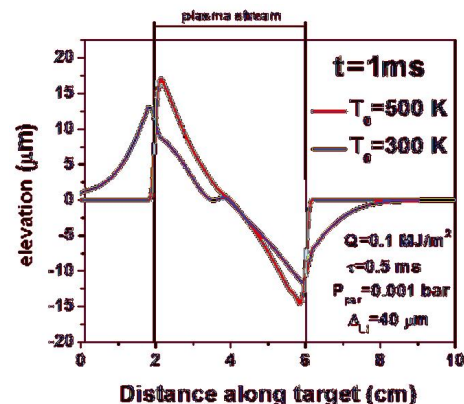


Fig. 1: Effect of tangential pressure on Li film dynamics.

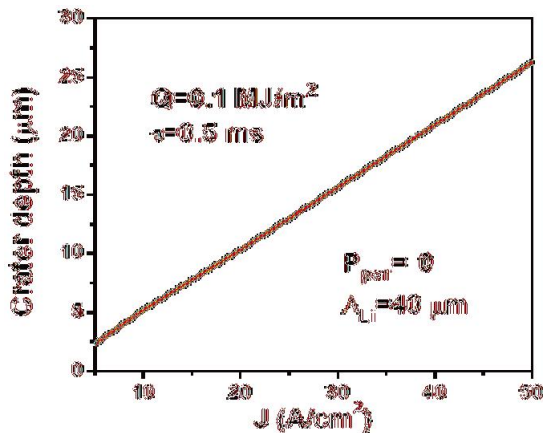


Fig. 2: Crater depth vs. cross-current J.

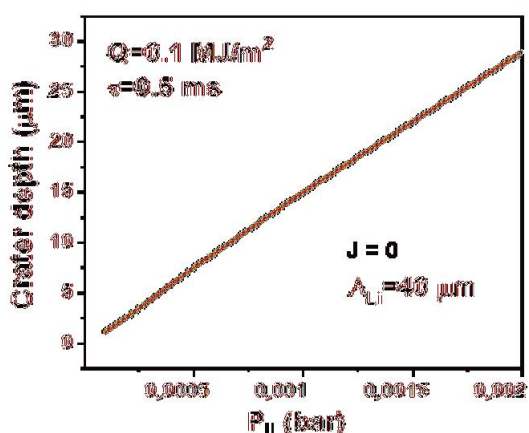


Fig. 3: Crater depth vs. tangential pressure.

Staff:

B.N. Bazylev
I.S. Landman

Acknowledgement

This work, supported by the European Communities under the Contract of Association between EURATOM and Karlsruhe Institute of Technology (KIT), was carried out within the framework of the European Fusion Development Agreement. The views and opinions expressed herein do not necessarily reflect those of the European Commission.

Mitigation of Disruption Loads for ITER (WP09-PWI-08)

WP09-PWI-08-01/FZK/BS

Introduction

With the available disruption mitigation techniques, a significant part of the released energy of the confined plasma impacts on the first wall. For example, when the massive gas injection (MGI) is used, the radiative load can be up to 2 MJ/m^2 on a 1 ms time scale, which can result in melting of beryllium plasma facing components (PFCs). Thus, the capabilities of MGI are limited. During MGI the plasma resistance increases drastically, producing strong longitudinal electric field and resulting in runaway electrons, the impact of which on the wall can also cause melting. A detailed numerical analysis in order to predict the margin of application of the technique is therefore necessary.

The mitigated ITER ELMs still can produce significant damages to Be PFCs, due to the mechanisms of melt motion such as the tangential plasma pressure, the $\mathbf{J} \times \mathbf{B}$ force and following the Raleigh-Taylor (RT) instability. In result, a molten layer of up to 1 mm thickness can be splashed away from Be surface.

Energy deposition into the Be PFCs of ITER by the runaway electrons generated during disruptions was simulated with the Monte-Carlo energy deposition code ENDEP. The incompressible fluid mechanics code MEMOS was also employed to evaluate PFC melting due to runaway electron energy deposition. The simulations of the PFC damage under the runaways' impact were carried out for small inclination angles of the impacting electrons with respect to the PFC surface in a realistic ITER design geometry. The transversal energy E_{tr} of runaway electrons varies in a wide range, however remaining much lower than the full energy E_e (see Fig. 1)

In addition, Be melting and splashing after small ITER ELMs were numerically simulated with MEMOS, and the application of both codes to the heating of graphite surfaces at the tokamak JET is described as well. That modelling approach was aimed at supporting and interpreting JET runaway experiments, and also at predictions of the possible Be wall damages in ITER.

Beryllium wall erosion under plasma and runaways' impacts

In the code ENDEP diverse mechanisms of slowing down of relativistic electrons in a bulk target are implemented, accounting for secondary avalanche processes as well. The slowing down occurs in a magnetic field that is inclined under a small angle α of 1.5 deg w.r.t. to the target surface (in accordance with the ITER specifications). In the runaway simulations, the following parameters were assumed: Impact energy $Q \sim 20 \text{ MJ/m}^2$, pulse duration $\Delta t = 0.1 \text{ s}$, full electron energy $E_e = 15 \text{ MeV}$ and transversal energy E_{tr} up to 3 MeV. According to the ENDEP simulations, at $E_{tr} = 0$ half of the energy is reflected back, and the energy deposition is mainly near the surface. At $E_{tr} > E_e/5$, 80% and more of the impacting energy is absorbed (see Fig. 2).

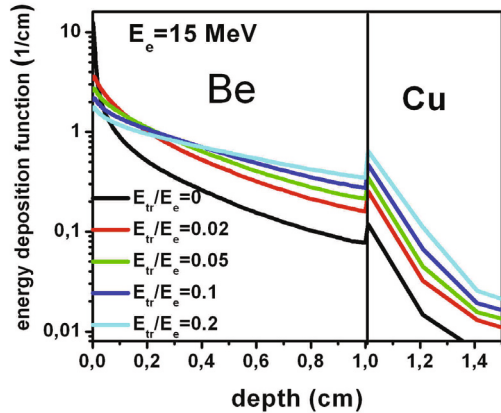


Fig. 1: Distribution of energy deposition of runaway electrons in case of Be plate mounted on the copper cooling structure.

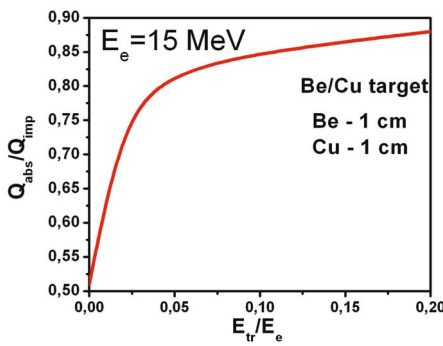


Fig. 2: Absorbed energy fraction vs. E_{tr}/E_e .

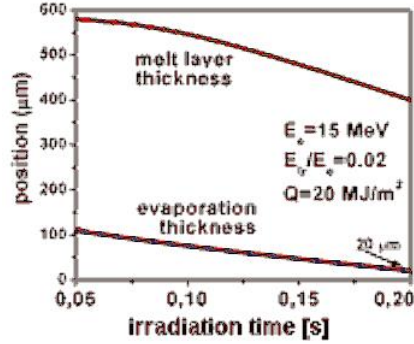


Fig. 3: The melt layer gets thinner with increasing Δt .

The runaway caused heating was calculated with MEMOS for $E_{tr} = E_e/50$, bulk target, Q up to 30 MJ/m^2 , Δt up to 0.2 s (rectangular pulse) and initial wall temperature 500 K. Under these conditions, the beryllium surface temperature reaches 2350 K, and the evaporation is significant. The depth of the melt pool does not exceed 0.7 mm, and about 20% of melt layer vaporizes (see Fig. 3). It is to note that without taking into account the evaporation, the melt pool thickness would reach 2 mm. If assuming the Kelvin-Helmholtz (KH) instability, the molten mass should be splashed away.

According to the MEMOS numerical simulations for assessing the impact of ITER ELMs, a Be macrobrush geometry of a structure size D below 3 cm decreases the melt velocity V by several times compared to the bulk Be target. For example, for an ELM of $Q = 1 \text{ MJ/m}^2$ impact energy and $\Delta t = 0.5 \text{ ms}$ pulse duration, the tangential pressure gradient produces melt velocities V of $\sim 1 \text{ m/s}$ ($D = 1 \text{ cm}$) and $\sim 7 \text{ m/s}$ ($D = 8 \text{ cm}$), the bulk target roughness is $6 \mu\text{m}$. The $J \times B$ force of the cross-current J causes an increase of V proportionally to J and Δt : E.g., $V \approx 3 \text{ m/s}$ for $B = 5 \text{ T}$, $J = 10 \text{ MA/m}^2$ and $\Delta t = 0.5 \text{ ms}$. Fig. 4 demonstrates the proportionality of V and J . The halo current of an ITER disruption of 10 ms duration can be estimated as $J = 0.5 \text{ MA/m}^2$, and thus, the melt velocity again is $V \approx 3 \text{ m/s}$. Longitudinal currents can cause the RT instability, which effectively removes the melt layer. Splashing already occurs for $J > 4 \text{ kA/m}^2$, which is much less than the expected magnitude of $J \approx 0.1 \text{ MA/m}^2$.

Supporting numerical simulations for JET

The numerical simulations for JET have been performed in the frame of the JET work program during the modelling month of the experimental campaign C27b (September 2009). The codes ENDEP and MEMOS have been used. The simulations are necessary for a better understanding of the mechanisms of surface damage under the action of runaway electrons generated during JET disruptions and the mitigated disruption initiated by MGI. The comparison of numerical simulation results with the JET experimental data is also necessary for further validation of the KIT codes developed for the prediction of the first wall runaway damage under ITER conditions.

The parameters of runaway electrons such as the energy spectrum, the energy flux and the inclination angles were defined on the basis of experimental data. Then, the energy deposition functions of electrons inside the graphite were calculated with ENDEP (Fig. 5). Final-

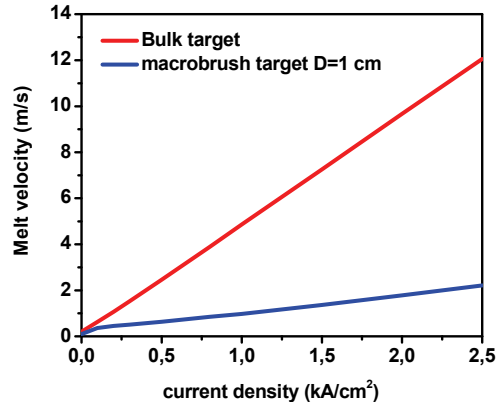


Fig. 4: The maximum of the melt motion velocity vs. the cross-current for bulk and macrobrush targets for the reference Type I ELM scenario with $Q = 1.25 \text{ MJ/m}^2$ and $\Delta t = 0.5 \text{ ms}$.

ly, the results of the runaway electron action were calculated with MEMOS, namely the distributions of the temperature inside the graphite target, for different energy fluxes and spectral energies of electrons. The dependence of the surface temperature on the heat loads caused by the runaway electrons is shown in Fig. 6 for an exponential energy distribution function $f \sim \exp(-E_e/E_d)$, with $E_d = 8$ MeV, $E_{tr}/E_e = 0.05$, and an inclination angle of the magnetic field to the armour surface $\alpha = 10$ deg.

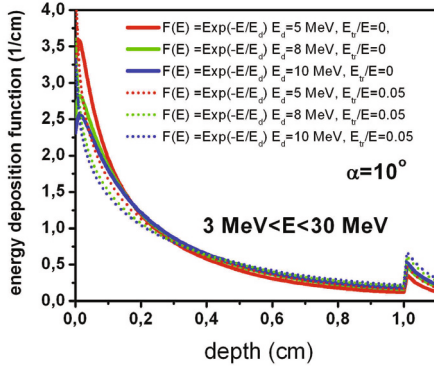


Fig. 5: Energy deposition function of runaway electrons inside graphite armour (with Cu mount) for different electron energy distribution functions.

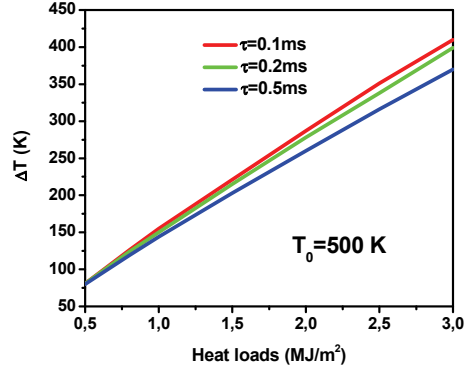


Fig. 6: The graphite surface temperature as a function of the heat loads caused by the runaway electrons of different pulse durations.

So far, only a preliminary comparison between the numerical simulation results and the experimental data was done. The results of the numerical simulations have been presented at the meeting of the JET campaign.

Conclusions

The numerical work carried out for the beryllium first wall of ITER revealed that the vaporization of Be significantly decreases the melt depth (2 mm \rightarrow 0.7 mm), in turn decreasing the splashing removal of Be caused by the $J \times B$ forces of eddy currents. Thus, considering the evaporation is significant for assessing the Be surface damage properly. However, splashing still can remain important, which should be a critical issue to be taken into account in the ITER design. The results obtained provide useful benchmarks for the first wall damage, but more work is needed for further development of MEMOS in order to investigate in more detail the Be splashing dynamics. The work should be continued, also in frame of further cooperation between KIT and JET which is reasonable and necessary.

Staff:

B.N. Bazylev
I.S. Landman

Literature:

[1] B. Bazylev, Yu. Igitkhanov, I. Landman, S. Pestchanyi, A. Loarte, Erosion simulation of first wall beryllium armour after ITER transient heat loads and runaway electrons action, 14th International Conference on Fusion Reactor Materials (ICFRM-14), Sep 6-11 2009, Sapporo, Japan, presented for publication.

Acknowledgement

This work, supported by the European Communities under the Contract of Association between EURATOM and Karlsruhe Institute of Technology (KIT), was carried out within the framework of the European Fusion Development Agreement. The views and opinions expressed herein do not necessarily reflect those of the European Commission.

Heat Load in ITER Relevant ELM Scenarios (WP09-PWI-09)

WP09-PWI-09-02/FZK/BS

Introduction

In 2009, the modelling of hot plasma and radiation impacts, generally aiming at tolerable ELMs and mitigated disruptions on the divertor plates and the main chamber wall in ITER, using the MHD codes FOREV (developed for CFC wall) and TOKES, has been focused on the first wall radiation impact and plasma contamination by the impurities. At this stage, the decision was taken to cease the development of FOREV and concentrate the work upon the tokamak code TOKES, because TOKES is exceeding the capabilities of FOREV. In particular, TOKES is suitable not only for CFC, but also for other wall materials like beryllium and tungsten.

Furthermore, TOKES can be used to address the problem of the radiation wall load during massive gas injection (MGI), that is currently relevant for ITER. However, this application requires further elaboration of the code, in order to allow the two-dimensional description of plasma cooling on a millisecond time scale. Focussing on MGI as the most important target for the current work implied adding the chemical elements neon and argon to the available inventory of TOKES gas species, which was done. In MGI, there is contact of the hot, confined plasma with the cold, dense injected gas, which makes the problem similar to the vapour shield problem in the plasma-wall contact case. The model of a 2D toroidally symmetric multi-fluid plasma is now under generalization, and currently includes as fast cross-diffusion the non-equilibrium expansion of a two-fluid plasma of deuterium and argon (or neon) along the magnetic field lines. In near future, the generalized TOKES, this year aiming at the MGI problem, will be applied for further investigations of the consequences of the impact of ITER ELMs on the tokamak wall.

The injected noble gas G is ionized in the confined deuterium plasma, the contamination of the core plasma results in a fast loss of plasma energy by radiation, and the radiation wall load as well as the fast plasma transport are calculated. The newly developed TOKES MGI model at first was compared with the tokamak DIII-D. Then, predictive simulations for ITER were performed, leading to the conclusion that after the radiation flush, the wall temperature can exceed the beryllium melting point in front of the jet entry.

Simulation of massive gas injection with TOKES

Tokamak experiments demonstrated effective ionization of G-atoms ($G = Ne, Ar, He$) during MGI. The subsequent MHD activity causes thermal quenching (TQ) within a few ms, when the ionization front reaches the magnetic surface of safety factor $q = 2$, and a toroidally symmetric flush of radiation. On the short time scale, the ionization of G-atoms localized near the jet entry can result in plasma parameters strongly varying on the poloidal coordinate y . For example, the electron temperature T_e decreases drastically near the jet. This can significantly decrease the ionization rate resulting in deep jet penetration. In the low temperature region, the Spitzer diffusion of the plasma can become significant, which increases the thickness of the scrape-off layer (SOL). Therefore, the 1D plasma model of TOKES for the cross-coordinate x was generalized to include also the dependences on y (see Fig. 1).

The code TOKES was developed for the integrated simulation on the discharge time scale (10^3 s), however permitting multiple ELMs, which allows application of the code also for the MGI problem. Generally, the magnetic field in TOKES can evolve together with the confined plasma, and the currents are recalculated after each time step. The fluids are ionized plasma species, from hydrogen isotopes to tungsten, of different charge states and bound electron excitation states. The detailed species description in the confinement region allowed the implementation of a non-stationary corona model, including radiation losses and dynamically

changing ion populations N_{mzk} , with m being the isotope index from H, D, T to W. z is the charge state and k the index of bound electron levels.

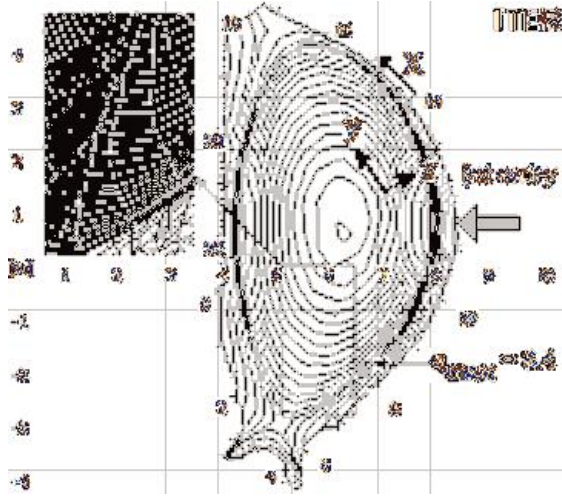


Fig. 1: TOKES layout for MGI simulations: The contours in the tokamak vessel show the magnetic surfaces. The rectangular fragment demonstrates the two-dimensional mesh of plasma cells and the triangle-based mesh for neural atoms in the SOL. The capital X designates the wall coordinate; x- and y-orts are orthogonal.

The particular features of the MGI simulation are as follows. With short TQ, the magnetic field is assumed fixed and the conventional plasma transport neglected. The MGI-induced MHD thermal transport in TOKES is based on a phenomenological diffusive approach. The plasma upgrade for 2D required sacrificing the available non-stationary radiation model, replacing it by opacity tables, and fixing the ion charge states (e.g. $z_{Ar} = 10$). The gas is injected from a toroidally symmetric location, horizontally towards the magnetic axis (see Fig. 1), and assuming a given inflow $\Gamma_G(t)$. For adequate simulation of the G-atoms, the basic triangular mesh in the poloidal plane is drastically refined in the vicinity of the jet trajectory (minimum cell size 5 mm). The Euler's equations for the longitudinal expansion of the fluids, as well as 2D diffusion- and thermal conduction equations are solved numerically.

transport, the calculations were compared with an MGI experiment with argon on DIII-D in 2007. In the experiment, the TQ duration is about 0.3 ms. For comparison, all spatial data of the ITER configuration of TOKES were multiplied by the factor 0.25, the toroidal magnetic field by 0.4, the plasma current by 0.1, and initial experimental plasma profiles were used.

The calculated radiation flux is about 3 times shorter than that in the experiment (see Fig. 2). The discrepancy is attributed to the jet entry location (in DIII-D, it is near the top of the vessel, which increases the time for passing through the vessel) and to the opacity model currently used. The non-stationary 2D radiation model would probably result in a longer TQ and thus better fit the experiment. It is to note that in the TOKES' non-stationary 1D plasma model, the injected gas reaches its maximum charge states on a time scale of 1 ms.

For ITER, simulations using the opacity approach appear suitable, because the TQ duration can be longer than that of DIII-D. Therefore, the MGI for ITER was simulated in order to predict the maximum temperature of the beryllium first wall during the radiation flush. An initial Be wall temperature of 500 K was assumed. For MGI in ITER, a TQ time of 2 ms was obtained, where the maximum wall temperature after the radiation flush exceeded the Be melting point of 1566 K (see Fig. 3). Fig. 4 demonstrates the calculated highly inhomogeneous distribution of the radiation power over the wall.

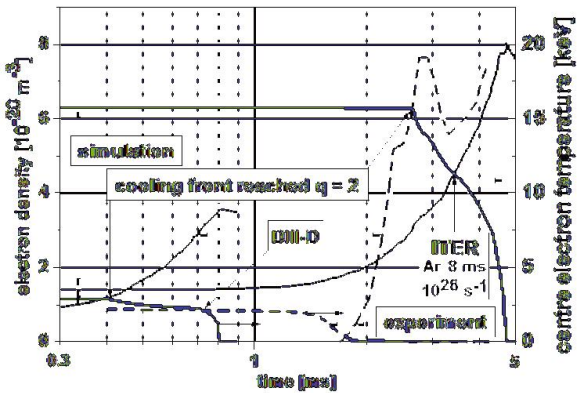


Fig. 2: Comparison of the current MGI simulation with the DIII-D experiment, and the simulation of MGI for ITER.

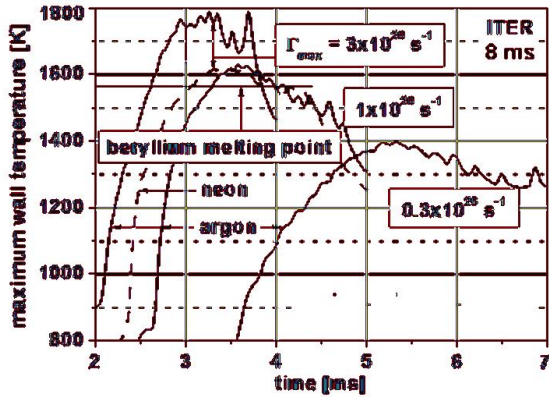


Fig. 3: Wall temperature near the wall coordinate $X = 10.8$ m for ITER.

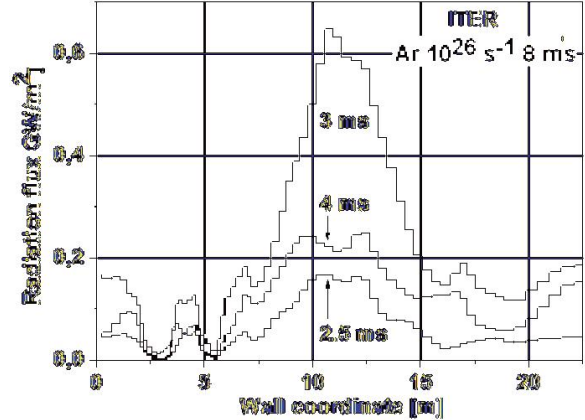


Fig. 4: Wall radiation flux for ITER.

Conclusions

The 2D simulations showed that for the massive gas injection, thermal quench times shorter than 5 ms should be avoided for the Be wall, which is possible if an optimal amount of injected gas is chosen (~ 10 g Ar or Ne entering the vessel prior TQ end). This study presents preliminary TOKES modelling results for MGI. As next step, it is necessary to adjust the available non-stationary radiation loss model to the new 2D plasma model. The further comparison with modern tokamaks such as JET, DIII-D and ASDEX UG implies implementing the corresponding locations of injectors, which in the model currently are located in the horizontal midplane. The results obtained provide useful benchmarks of MGI simulations, but more work is needed for further development of the code in order to reach reliable integrated modelling, including plasma and surface aspects like the injector gas dynamics in the vessel.

Staff:

I.S. Landman
S.E. Pestchanyi

Literature:

- [1] I.S. Landman, S.E. Pestchanyi, Yu. Igitkhanov, R. Pitts, Modelling of Wall and SOL Processes and Contamination of ITER Plasma after Impurity Injection with the Tokamak Code TOKES, Presented at the conference ISFNT-9, Dalian, China, October 2009 for publication.
- [2] I.S. Landman, G. Janeschitz, Modelling of SOL transport and radiation losses for ITER with the integrated tokamak code TOKES, Journal of Nuclear Materials, 390-391 (2009) 384-387.
- [3] S. Pestchanyi, I. Landman, Experimental verification of FOREV-2D simulations for the plasma shield, Journal of Nuclear Materials, 390-391 (2009) 822-825.
- [4] V.M. Safronov, N.I. Arkhipov, I.S. Landman, et al., Evaporation and vapour shielding of CFC targets exposed to plasma heat fluxes relevant to ITER ELMs, Journal of Nuclear Materials, 386 (2009) 744-746.
- [5] I.S. Landman, G. Janeschitz, Modelling of radiation impact on ITER beryllium wall, Journal of Nuclear Materials, 386 (2009) 915-918.

Acknowledgement

This work, supported by the European Communities under the Contract of Association between EURATOM and Karlsruhe Institute of Technology (KIT), was carried out within the framework of the European Fusion Development Agreement. The views and opinions expressed herein do not necessarily reflect those of the European Commission.

Physics: Heating and Current Drive – ECRH

Development of the European Gyrotron ("CCGDS6") (F4E-2008-GRT-08(PMS-H.CD)-01)

Introduction

The development of a 2 MW, CW, 170 GHz coaxial cavity gyrotron for ITER is pursued within the European Gyrotron Consortium (EGYC, consisting of CRPP, Switzerland; KIT, Germany; HELLAS, Greece; CNR and ENEA, Italy), which acts as scientific partner for F4E, and in co-operation with ISSP, Latvia. The goal of the development is making available sources for 170 GHz ECH & CD at ITER providing 8 MW CW power, to supply the EU contingent on ECH & CD sources in ITER. In contrast to other contributors to ITER ECH & CD, the EU plans to provide sources with 2 MW RF power per unit (ITER minimum specification: 1 MW) for reduced cost and space requirements, to be able to double the system power if requested and to establish the – essentially more powerful - coaxial technology.

While the industrial gyrotron prototype, built by Thales Electron Devices (TED, France), is tested at CRPP, KIT provides support to the development and the tests through component design, analysis and simulation, as well as both low and high power tests. The tests are done with the modular short-pulse pre-prototype gyrotron at KIT. In particular, KIT is solely responsible for the design of cavity, uptaper and mode converter system, and is involved in gun, beam tunnel and collector design.

In parallel to the coaxial 2 MW gyrotron activities, a 1 MW conventional cavity design is in preparation as fallback solution. This backup design intends to support the strategic decision about keeping the 2 MW design or switching to a conventional 1 MW design, which will be taken end of 2010 after the next series of prototype experiments.

Status of work at the beginning of 2009

In autumn 2008, the experiments with the first coaxial 2 MW prototype at CRPP were stopped without major success. It had not been possible to operate the device in long pulse, and even in short pulse (1 – 2 ms) the output power was limited to 1.4 MW due to a lack of high voltage standoff. After opening the tube, several damages were found which could not be explained. Specifications were reached only in the collector validation: The heat load capacity of the collector and the cooling system was verified to be at least 2.2 MW (in RF-less tests).

At the same time, the tests at KIT with the short-pulse pre-prototype, which was equipped with a comparable electron gun and the same cavity, uptaper and mode converter, were partly successful: An output power of 1.4 MW at 23 % efficiency was reached in a reduced power operating point, to be compared with expected 1.5 MW, and an undesired low frequency oscillation (265 MHz) was successfully suppressed. However, another parasitic oscillation, now at an RF of about 160 GHz, reduced output power and efficiency slightly, and the fact that the limited magnetic field strength of the KIT magnet enforced operation at reduced parameters was unsatisfying and inhibited the demonstration of 2 MW RF power at high efficiency, and an efficient support for solving the problems of the prototype.

Finally, the mode converter, featuring a conventional helically deformed launcher antenna, was found to be insufficient, since it delivered an output beam with only 77% Gaussian mode content, in contrast to the prediction of 86 % and the ITER specification of >95% (the original plan was to add phase correcting mirrors to increase the simulated 86 % to the required 95 %). A new design code for innovative launcher types, based on arbitrary wall deformations, was already in work, and a first improved launcher had just been built and verified in cold test. In contrast to helically deformed launchers, launchers with arbitrary wall deformations are more suitable for typical coaxial cavity modes with relative caustic radius smaller than 0.5.

Driven by all of these problems, a further effort for the 1 MW backup design, which was stopped at the stage of a feasibility study in March 2008, was planned.

Achievements in 2009

High power tests with the pre-prototype

To overcome the limitation in magnetic field strength of the Oxford Instruments magnet used at KIT, an additional normal conduction (NC) coil was wound directly onto the pre-prototype gyrotron body, which allowed for an increase from 6.72 T to about 6.9 T in coil current pulses of some 10 seconds. In parallel, the electron gun design was modified for nominal operation at 90 kV, while at lower magnetic field the operation point had been limited to 80 kV by the achievable relativistic cyclotron frequency. With these improvements, 1.8 MW at 27 % efficiency were achieved in first experiments in January. At the same time, a corrugated beam tunnel as investigated later in the step-tunable gyrotron was employed (see Fig. 1). However, since the RF output power in these tests was actually limited by the NC coil power supply, no definite improvement could be attributed to that change.

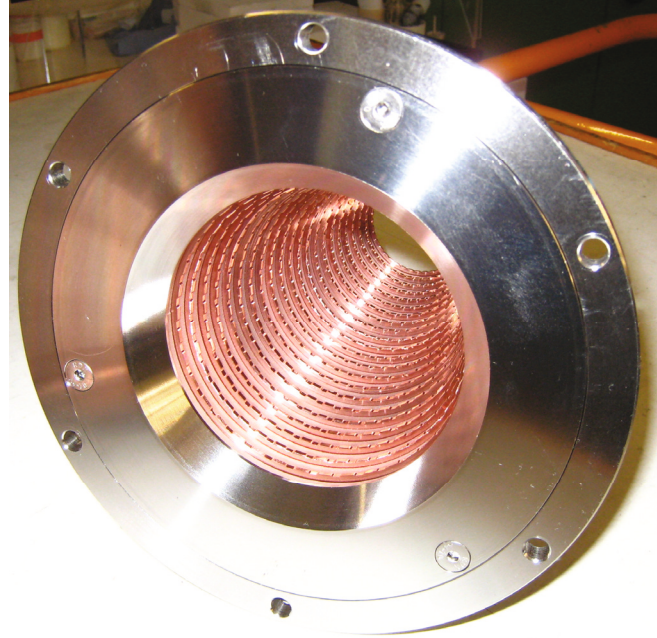


Fig. 1: New beam tunnel prototype with irregularly corrugated copper rings.

In the following experimental setup in summer, a more powerful source for the NC coil was used. With these changes and with the new mode converter system (see below), the RF output power finally reached 2.2 MW at an efficiency of 30 %, which is world record for a 170 GHz CW-relevant gyrotron design (see Fig. 2). Thus, the feasibility of a stable single-mode operation above 2 MW was demonstrated, and was in good agreement with simulations. In particular, the comparison to the simulation shows that at this power, the edge of the stable single-mode operation was reached, and a further power increase via voltage is inhibited by mode competition. This is the first time that this limit was actually demonstrated experimentally, while in earlier experiments, the output power was limited by other factors. Using a newly developed spectral measurement system, it was now also possible to prove that no RF parasitic oscillation appeared any more. Instead, a new low frequency parasitic oscillation at 112 MHz was observed, which does not seem to deteriorate the gyrotron operation.

For completeness, it should be noted that due to 3.3 % RF absorption in the short pulse vacuum barrier windows of the pre-prototype (made from fused silica or silicon nitride), an even higher power of 2.3 MW at 31 % efficiency can be expected using the standard long pulse diamond window with negligible loss. Note that all efficiencies given here are without depressed collector.

In the experiments during summer, the new mode converter system with improved launcher was installed and tested, yielding 95.5 % Gaussian mode content in the high power measurements, in good agreement with simulation and low power tests (see Fig. 3). The level of stray radiation in the gyrotron was measured to be 7 ± 2 %, to be compared to 8 ± 2 % for the old mode converter system. Even though this is a slight improvement, the reduction of stray

radiation is not as good as expected, which raises the question for other sources of stray radiation, different from the mode converter system.

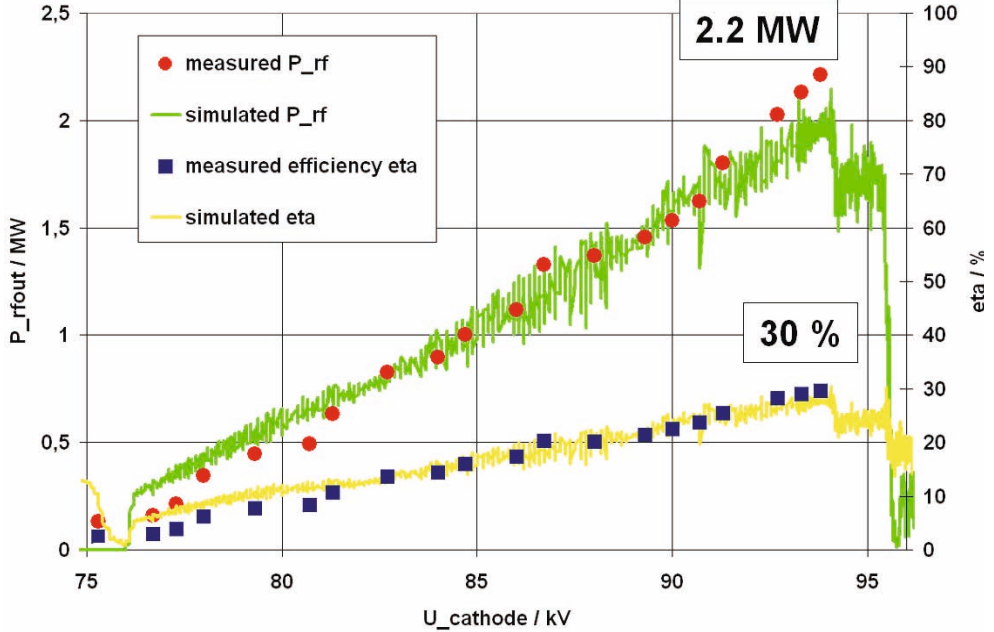


Fig. 2: Gyrotron output power and efficiency vs. cathode voltage measured and calculated at the nominal magnetic field of 6.88 T.

However, the ITER specifications are fulfilled now by this system. Still, the launcher development was taken further to next designs which promise up to 99.3 % Gaussian mode content.

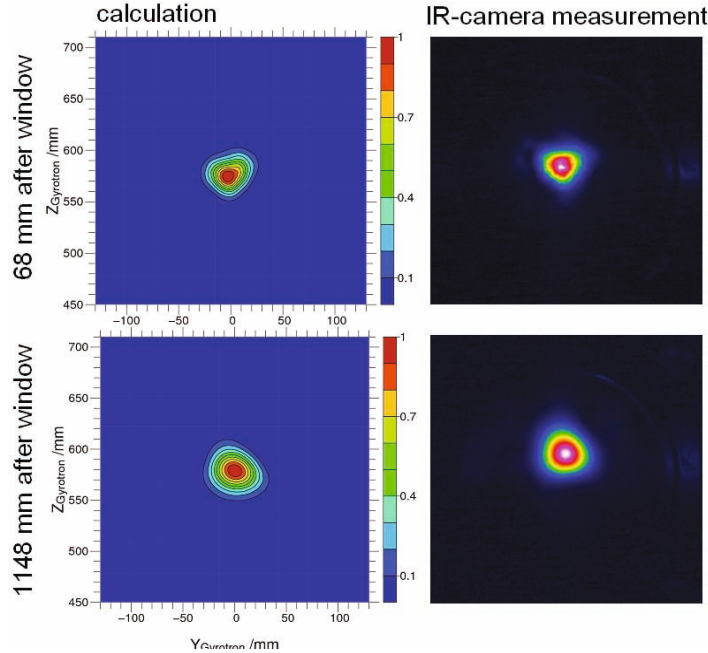


Fig. 3: Calculation (left) and high-power measurement (right, using a PVC target and an IR camera) of the mm-wave beam profile for the gyrotron operation at 170 GHz in the TE34,19 mode.

The experimental campaign in summer was concluded in August with broadband tests of the pre-prototype. To do this, the tube was equipped with a broadband silicon nitride Brewster window. Preliminary tests were done at 141.3 GHz and 143.3 GHz, reaching 1.8 MW at 26 % efficiency and 1.25 MW at 23 %, respectively (see Fig. 4). These values have not been optimised experimentally because of time constraints. Improvement seems possible – the simulation predicts RF powers above 2 MW for a variety of frequencies between 130 GHz and 170 GHz (even up to 210 GHz, if the magnetic field is available). First measurements of the RF output beam qualitatively showed a good shape, but must be continued for a reliable calculation of the Gaussian mode content (see Fig. 5).

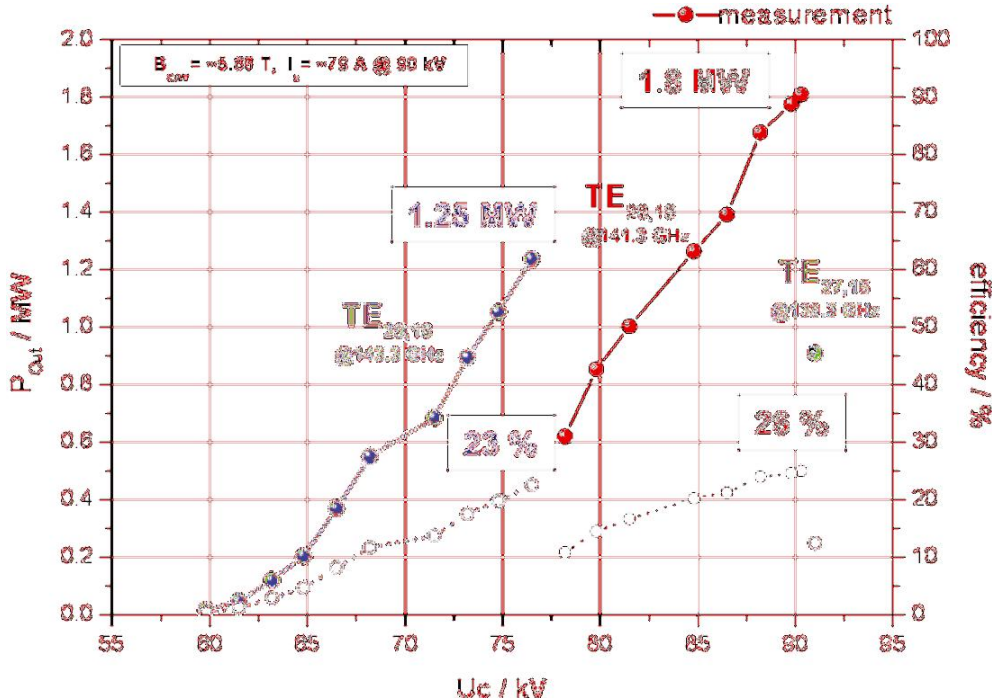


Fig. 4: RF output power (bold) and efficiency (faint) for $\text{TE}_{28,16}$ (141.3 GHz) and $\text{TE}_{29,16}$ (143.3 GHz) vs. acceleration voltage.

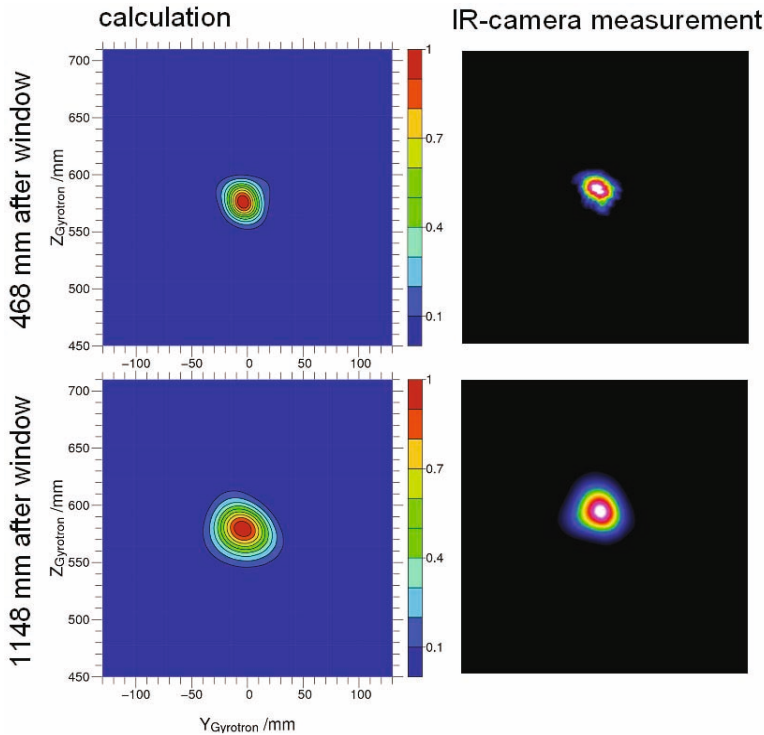


Fig. 5: Calculation (left) and high-power measurement (right, using a PVC target and an IR camera) of the mm-wave beam profile for the gyrotron operation at 143.4 GHz in the $\text{TE}_{29,16}$ mode.

sign is comparably good as the former pre-prototype gun. In particular, 1.6 MW power with 26% efficiency have been obtained in line with previous results.

The latest experimental campaign in October and November was conducted to verify the new electron gun design for the refurbishment of the long pulse prototype, featuring in particular a small diameter beam tunnel as a shield for "halo electrons". These experiments were derogated by a small leak in the water cooling circuit of the RF absorbers in the mirror box, inhibiting conditioning. After the detection of the leak, evacuation of the cooling circuit and some more weeks of conditioning, it was possible to reach nominal electron beam parameters, despite the vacuum conditions which were still bad. The RF measurements taken at somewhat reduced parameters resulted in similar values as with the previous gun, indicating that the new gun de-

Improvements on theoretical models, codes and designs

The high power experiments and refurbishment design activities are generally accompanied and supported by work on the theoretical models, the codes and corresponding design improvements. During 2009, the work done on electron gun, beam tunnel, cavity and mode converter required enhancements in theoretical approaches for the understanding of these devices.

As reported above, the 2008 experiments with the industrial prototype at CRPP had a rather negative result. This was attributed to flaws in the electron gun design concerning electron velocity spread and potential traps. Consequently, the electron gun for the prototype refurbishment was completely redesigned, which was done under the responsibility of CRPP, however with essential input from KIT. To gain a better understanding of the effect of trapped electrons, beamless tests were done with the pre-prototype, which indicated clearly the appearance of undesired vacuum currents in the presence of potential traps. In addition, the gun simulation code ESRAY was extended for simulation of trapped electrons. The final electron gun design is not verified by experiment yet, however can be considered as the best design studies according to current knowledge. This is one result of the intense collaboration among CRPP and KIT.

The work on the beam tunnel is described in the chapter about the step-tunable gyrotron. The resulting improved beam tunnel structure was successfully employed in the coaxial gyrotron as well.

The cavity and uptaper of the coaxial gyrotron are not changed for refurbishment, since their suitability was proved in the experiment. Still, the simulation codes for the gyrotron interaction, namely SELFT, have been enhanced by introducing better averaging schemes for carrier frequency and azimuthal electron distributions. Such details may appear unimportant, but turn out to be crucial for realistic simulations – the good agreement between simulation and measurement as shown in Fig. 2 is only possible with these improvements in such high order mode regimes. The important point is to gain trust in the simulations for the next designs. It should be noted that the gyrotron interaction and beam tunnel work was done in strong collaboration with HELLAS and ISSP.

The improvements in the launcher design have already been mentioned above. The new code TWL_DO, which was written to design launchers with arbitrary wall deformations by iteratively solving the scalar diffraction integral equation, has been steadily enhanced, yielding an even better next launcher design. Further work on the tools for the quasi-optical mode converter system is done to include tapers in the simulation, to allow for faster and more flexible simulations and to provide a better data exchange between codes. One point to be emphasized is the inclusion of reflection and transmission calculation in the TWL_DO launcher design code, which, together with other tools, should help in determining the stray radiation.

Progress with the 1 MW back-up design

The 1 MW back-up design, interrupted in March 2008 at the stage of a feasibility study, was included in the current F4E grant to be taken further and to reach a final design state. Within this topic, the existing W7-X collector design was investigated for suitability at 170 GHz and under RF modulation, increasing the heat load at the collector to 1.45 MW. It is estimated that this heat load can be handled, but only when transverse electron beam sweeping is employed.

The cavity model design was supplemented by and fitted to a non-linear uptaper with sufficiently low mode conversion. Since this geometry shows sufficient mode stability and safety

margin at the desired operating point, it is considered the final design. This work has been done in collaboration with HELLAS and ISSP.

For a final electron gun design, a decision about the shape of the magnetic field must be taken. Originally, use of the existing magnet at CRPP ("ASG-magnet") had been foreseen. Then, it was decided to replace this magnet because of its excessive helium consumption. This opens the chance to specify a magnetic field profile that can be provided by KIT magnets, too. The advantage is that then the relevant gyrotron components, in particular the electron guns, of pre-prototype and prototype can be made not only similar or comparable, but identical. This is important whenever a problem in the inflexible and expensive prototypes needs to be investigated in a modular short-pulse tube like the pre-prototype – for example, it turned out that the differences between first prototype and pre-prototype gun were too big, even though the guns were considered comparable. Consequently, the problems of the first prototype could not be investigated using the pre-prototype. However, the decision for a particular magnetic field shape under various boundary conditions is difficult and is not done yet. First gun designs by CRPP show that several field configurations are possible. The final decision about the field shape and the gun will be made cooperatively among CRPP and KIT.

Conclusions and prospects

The successful 2.2 MW short pulse experiments and the good results with the new mode converter system have solved two basic problems of the 2 MW coaxial gyrotron project for ITER: It is proven now that the chosen mode can be operated stably at the desired power and above, and that a suitable output beam can be generated. These are essential steps in this project, which give hope for successful accomplishment.

The main purpose of the future activities within this project is to support the long pulse prototype experiment, which will start again with the delivery of the refurbished prototype to CRPP in July 2010, aiming at 1 s pulses. The experimental and theoretical work in late 2010 should for this reason be flexibly adapted to the results of the prototype experiment.

Apart from that, several questions are still open or need experimental validation: An efficiency of 50 % is expected with depressed collector (at 30 % efficiency without depression), but needs experimental verification. Furthermore, using a depressed collector is the first precondition for increasing the pulse length of the pre-prototype, which in nominal operation currently is limited by the power supply to 1 ms. As it can be expected that a modular experimental gyrotron will be required as investigation tool during the whole series production of the ITER gyrotrons, it would also make sense to increase the pulse length of the pre-prototype as far as reasonable, in order to make the important effects of beam neutralisation and thermal influence visible in experiments at KIT. Even without the damage through the leakage, the currently used electron gun reaches the end of its lifetime. Furthermore, the whole pre-prototype construction needs to be modified to fit into the new magnet at KIT (the fast step-tunable magnet, to be delivered in early 2010). This magnet reaches a field of up to 7.2 T, so the normal conducting coil can be removed. These major changes should be taken as a good possibility to reconsider a design with increased pulse length.

Regarding the mode converter, the next launcher design needs to be realised in hardware and verified. Apart from that, an experiment with an alternative Russian launcher design will be performed, and other ways for improving the mode converter system are under investigation, too. It will be important to clarify the source of the additional stray radiation. This problem will be tackled both in experiment and in simulation.

As shown by the first experiments on step frequency tuning, operation of the pre-prototype at different frequencies in different modes is a topic of highest interest. These experiments will be taken further to determine whether it is in fact possible to operate this gyrotron in a variety

of modes between 130 GHz and 170 GHz above 2 MW and with a high Gaussian mode content.

All these experimental approaches will need an appropriate support on the theoretical and simulation side. In particular, better and well-verified modelling of stray radiation is needed. Moreover, work will be done for improved modelling of both low frequency and RF parasitic oscillations, as well as for particle traps and beam neutralisation processes.

Finally, the 174 GHz 1 MW experiment with a 140 GHz W7-X gyrotron, which was foreseen in 2009, may be pursued as a first step to an alternative backup solution. This is possible only under the condition that a W7-X gyrotron can be made available for such tests.

Staff:

K. Baumann
E. Borie
J. Flamm
G. Dammertz
G. Gantenbein
H. Hunger
S. Illy
J. Jin
S. Kern
R. Lang
W. Leonhardt
M. Losert
D. Mellein
B. Piosczyk
T. Rzesnicki
A. Samartsev
A. Schlaich
M. Schmid
R. Schneider
W. Spieß
J. Szczesny
M. Thumm
J. Weggen

Literature:

- [1] Albajar, F., Bonicelli, T., Saibene, G., Alberti, S., Fasel, D., Goodman, T., Hogge, J.P., Pagonakis, I., Porte, L., Tran, M.Q., Avramides, K., Vomvoridis, J., Claesen, R., Santinelli, M., Dumbrajs, O., Gantenbein, G., Kern, S., Illy, S., Jin, J., Piosczyk, B., Rzesnicki, T., Thumm, M., Henderson, M., Cirant, S., Latsas, G., Tigelis, I.: Review of the European programme for the development of the gyrotron for ITER. Lohr, J. [Editor] Proc. of the 15th Joint Workshop on Electron Cyclotron Emission and Electron Cyclotron Resonance Heating, Yosemite National Park, Calif., March 10-13, 2008, Singapore : World Scientific Publ., 2009 S.415-21; ISBN 978-981-281-463-0
- [2] Borie, E., Kern, S.: On the effect of RF-space charge on the beam-field interaction in gyrotrons. Journal of Infrared, Millimeter and Terahertz Waves, 30(2009) S.915-23; DOI:10.1007/s10762-009-9520-8
- [3] Braune, H., Erckmann, V., Illy, S., Laqua, H.P., Noke, F., Purps, F., Schmid, M.: Advanced transverse field collector sweeping for high power gyrotrons. Litvak, A.G. [Editor] Strong Microwaves : Sources and Applications , Proc. of the 7th Internat. Workshop, Nizhny Novgorod, July 27 - August 2, 2008, Vol.1 S.149-53; Nizhny Novgorod : Russian Academy of Sciences, 2009, ISBN 978-5-8048-0083-4
- [4] Braune, H., Erckmann, V., Illy, S., Laqua, H.P., Michel, G., Noke, F., Purps, F., W7-X ECRH Teams at IPP and FZK: Transverse field collector sweeping for the W7-X gyrotrons. Modulation techniques. 34th Internat. Conf. on Infrared, Millimeter, and Terahertz Waves (IRMMW-THz 2009), Busan, Korea, September 21-25, 2009
- [5] Darbos, C., Henderson, M., Albajar, F., Bigelow, T., Bonicelli, T., Denisov, G.G., Heidinger, R., Hogge, J.P., Kobayashi, N., Piosczyk, B., Rao, S.L., Rasmussen, D., Saibene, G., Sakamoto, K., Takahashi, K.:

Progress status of the ITER electron cyclotron H&CD system. 5th IAEA Technical Meeting on ECRH Physics and Technology for Large Fusion Devices, Gandhinagar, IND, February 18-20, 2009, Book of Abstracts S.34

[6] Darbos, C., Henderson, M., Albajar, F., Bigelow, T., Bonicelli, T., Chavan, R., Denisov, G., Farina, D., Gandini, F., Heidinger, R., Hogge, J.P., Kern, S., Kobayashi, N., Ramponi, G., Rao, S.L., Rasmussen, D., Saibene, G., Sakamoto, K., Sauter, O., Scherer, T., Takahashi, K., Zohm, H.: ECRH system for ITER. 18th Topical Conf. on Radio Frequency Power in Plasmas, Gent, B, June 24-26, 2009, Book of Abstracts S.35

[7] Darbos, C., Henderson, M., Albajar, F., Bigelow, T., Bonicelli, T., Chavan, R., Denisov, G.G., Fasel, D., Heidinger, R., Hogge, J.P., Kobayashi, N., Piosczyk, B., Rao, S.L., Rasmussen, D., Saibene, G., Sakamoto, K., Takahashi, K., Thumm, M.: Progress in design and integration of the ITER electron cyclotron H&CD system. Fusion Engineering and Design, 84(2009) S.651-55, DOI:10.1016/j.fusengdes.2009.02.007

[8] Gantenbein, G., Rzesnicki, T., Alberti, S., Goodman, T., Hogge, J.P., Illy, S., Jin, J., Kern, S., Piosczyk, B., Samartsev, A., Thumm, M.: Status of development of high power coaxial-cavity gyrotron at FZK. 5th IAEA Technical Meeting on ECRH Physics and Technology for Large Fusion Devices, Gandhinagar, IND, February 18-20, 2009

[9] Gantenbein, G., Dammertz, G., Erckmann, V., Illy, S., Kern, S., Rzesnicki, T., Kasperek, W., Piosczyk, B., Samartsev, A., Schlaich, A., Thumm, M.: Recent investigations on stable operation of high-power gyrotrons. US-EU-JPN RF Heating Technology Workshop, Dazaifu-City, Fukuoka, J, September 16-18, 2009, Book of Abstracts S.11

[10] Goodman, T.P., Alberti, S., Droz, E., Fasel, D., Hogge, J.P., Jawla, S., Porte, L., Siravo, U., Tran, M.Q., Albajar, F., Bonicelli, T., Benin, P., Bethuys, S., Lievin, C., Cirant, S., Dumbrajs, O., Gantenbein, G., Illy, S., Jin, J., Kern, S., Piosczyk, B., Rzesnicki, T., Thumm, M.: First experimental results from the EU 2 MW coaxial cavity ITER gyrotron prototype. Lohr, J. [Editor] Proc. of the 15th Joint Workshop on Electron Cyclotron Emission and Electron Cyclotron Resonance Heating, Yosemite National Park, Calif., March 10-13, 2008, Singapore : World Scientific Publ., 2009 S.515-22; ISBN 978-981-281-463-0

[11] Henderson, M., Albajar, F., Alberti, S., Baruah, U., Bigelow, T., Becket, B., Bertizzolo, R., Bonicelli, T., Bruschi, A., Caughman, J., Chavan, R., Cirant, S., Collazos, A., Darbos, C., deBaar, M., Denisov, G., Farina, D., Gandini, F., Gassman, T., Goodman, T.P., Heidinger, R., Hogge, J.P., Jean, O., Kajiwara, K., Kasperek, W., Kasugai, A., Kern, S., Kobayashi, N., Landis, J.D., Moro, A., Nazare, C., Oda, J., Paganakis, I., Platania, P., Plaum, B., Poli, E., Porte, L., Piosczyk, B., Ramponi, G., Rao, S.L., Rasmussen, D., Ronden, D., Saibene, G., Sakamoto, K., Sanchez, F., Scherer, T., Shapiro, M., Sozzi, C., Spaeh, P., Straus, D. Sauter, O., Takahashi, K., Tanga, A., Temkin, R., Thumm, M., Tran, M.Q., Zohm, H., Zucca, C.: Recent progress in the ITER EC H&CD system. US-EU-JPN RF Heating Technology Workshop, Dazaifu-City, Fukuoka, J, September 16-18, 2009, Book of Abstracts S.5

[12] Henderson, M., Albajar, F., Alberti, S., Baruah, U., Bigelow, T., Becket, B., Bertizzolo, R., Bonicelli, T., Bruschi, A., Caughman, J., Chavan, R., Cirant, S., Collazos, A., Darbos, C., deBaar, M., Denisov, G., Farina, D., Gandini, F., Gassman, T., Goodman, T.P., Heidinger, R., Hogge, J.P., Jean, O., Kajiwara, K., Kasperek, W., Kasugai, A., Kern, S., Kobayashi, N., Landis, J.D., Moro, A., Nazare, C., Oda, J., Paganakis, I., Platania, P., Plaum, B., Poli, E., Porte, L., Piosczyk, B., Ramponi, G., Rao, S.L., Rasmussen, D., Ronden, D., Saibene, G., Sakamoto, K., Sanchez, F., Scherer, T., Shapiro, M., Sozzi, C., Spaeh, P., Straus, D. Sauter, O., Takahashi, K., Tanga, A., Temkin, R., Thumm, M., Tran, M.Q., Zohm, H., Zucca, C.: An overview of the ITER electron cyclotron H&CD system. 34th Internat. Conf. on Infrared, Millimeter, and Terahertz Waves (IRMMW-THz 2009), Busan, Korea, September 21-25, 2009

[13] Henderson, M.A., Beckett, B., Darbos, C., Kobayahsi, N., Saibene, G., Albajar, F., Bonicelli, T., Alberti, S., Chavan, D., Fasel, D., Goodman, T.P., Pagonakis, I.G., Sauter, O., Cirant, S., Farina, D., Ramponi, G., Heidinger, R., Piosczyk, B., Thumm, M., Rao, S.L., Kajiwara, K., Sakamoto, K., Takahashi, K., Denisov, G., Bigelow, T., Rasmussen, D.: A revised ITER EC system baseline design proposal. Lohr, J. [Editor] Proc. of the 15th Joint Workshop on Electron Cyclotron Emission and Electron Cyclotron Resonance Heating, Yosemite National Park, Calif., March 10-13, 2008, Singapore: World Scientific Publ., 2009 S.458-64, ISBN 978-981-281-463-0

[14] Hogge, J.P., Goodman, T.P., Alberti, S., Albajar, F., Avramides, K.A., Benin, P., Bethuys, S., Bin, W., Bonicelli, T., Bruschi, A., Cirant, S., Droz, E., Dumbrajs, O., Fasel, D., Gandini, F., Gantenbein, G., Illy, S., Jawla, S., Jin, J., Kern, S., Lavanchy, P., Lievin, C., Marletaz, B., Marmillod, P., Perez, A., Piosczyk, B., Pagonakis, I., Porte, L., Rzesnicki, T., Siravo, U., Thumm, M., Tran, M.Q.: First experimental results from the European Union 2-MW coaxial cavity ITER gyrotron prototype. Fusion Science and Technology, 55(2009) S.204-12

- [15] Jawla, S., Hogge, J.P., Alberti, S., Goodman, T., Piosczyk, B., Rzesnicki, T.: Infrared measurements of the RF output of 170-GHz/2-MW coaxial cavity gyrotron and its phase retrieval analysis. *IEEE Transactions on Plasma Science*, 37(2009) S.414-24, DOI:10.1109/TPS.2008.2011488
- [16] Jin, J., Thumm, M., Piosczyk, B., Kern, S., Flamm, J., Rzesnicki, T.: High efficient quasi-optical mode converter for coaxial ITER gyrotron. *10th Internat. Vacuum Electronics Conf. (IVEC 2009)*, Roma, I, April 28-30, 2009; Proc.on CD-ROM S.279-80, Piscataway, N.J. : IEEE, 2009, ISBN 978-1-4244-3499-2
- [17] Jin, J., Thumm, M., Piosczyk, B., Kern, S., Rzesnicki, T., Flamm, J.: A new method for the design of quasi-optical launchers for high power gyrotrons. *36th International Conference on Plasma Science (ICOPS) and 23rd Symposium on Fusion Engineering (SOFE-23)*, San Diego, Calif., May 31 - June 5, 2009
- [18] Jin, J., Thumm, M., Piosczyk, B., Kern, S., Flamm, J., Rzesnicki, T., Li, G.: A new method for the design of quasi-optical mode converter for high power gyrotron. *21st Joint Russian-German Workshop on ECRH and Gyrotrons*, Greifswald, May 11-16, 2009
- [19] Jin, J., Thumm, M., Piosczyk, B., Kern, S., Flamm, J., Rzesnicki, T.: Novel numerical method for the analysis and synthesis of the fields in highly oversized waveguide mode converters. *IEEE Transactions on Microwave Theory and Techniques*, 57(2009) S.1661-68, DOI:10.1109/TMTT.2009.2021878
- [20] Jin, J., Thumm, M., Piosczyk, B., Kern, S., Li, G., Rzesnicki, T.: Highly efficient quasi-optical mode converter for coaxial ITER gyrotron at FZK. *34th Internat. Conf. on Infrared, Millimeter, and Terahertz Waves (IRMMW-THz 2009)*, Busan, Korea, September 21-25, 2009
- [21] Kern, S., Avramides, K.A.: Improving gyrotron interaction calculations. *34th Internat. Conf. on Infrared, Millimeter, and Terahertz Waves (IRMMW-THz 2009)*, Busan, Korea, September 21-25, 2009
- [22] Kern, S., Borie, E.: On the effect of RF-space charge on the beam-field interaction in gyrotrons. *34th Internat. Conf. on Infrared, Millimeter, and Terahertz Waves (IRMMW-THz 2009)*, Busan, Korea, September 21-25, 2009
- [23] Kern, S., Schlaich, A., Flamm, J., Gantenbein, G., Latsas, G., Rzesnicki, T., Samartsev, A., Thumm, M., Tigelis, I.: Investigations on parasitic oscillations in megawatt gyrotrons. *34th Internat. Conf. on Infrared, Millimeter, and Terahertz Waves (IRMMW-THz 2009)*, Busan, Korea, September 21-25, 2009
- [24] Kern, S., Alberti, S., Beringer, M.H., Borie, E., Braune, H., Dammertz, G., Dumbrajs, O., Erckmann, V., Flamm, J., Giguet, E., Gantenbein, G., Hogge, J.P., Illy, S., Jin, J., Laqua, H.P., Legrand, F., Leonhardt, W., Lievin, C., Michel, G., Piosczyk, B., Prinz, H.O., Rzesnicki, T., Schmid, M., Thumm, M., Tran, M.Q.: Gyrotrons for fusion plasma heating - status of development at the Forschungszentrum Karlsruhe (FZK). *Jahrestagung Kerntechnik 2009*, Dresden, 12.-14.Mai 2009 Berlin : INFORUM GmbH, 2009, CD-ROM Paper 801
- [25] Kern, S., Flamm, J., Gantenbein, G., Illy, S., Jin, J., Piosczyk, B., Prinz, O., Rzesnicki, T., Thumm, M., Dumbrajs, O.: Status of experiments on the EU 2MW coaxial cavity ITER gyrotron pre-prototype at FZK. Lohr, J. [Editor] *Proc. of the 15th Joint Workshop on Electron Cyclotron Emission and Electron Cyclotron Resonance Heating*, Yosemite National Park, Calif., March 10-13, 2008, Singapore: World Scientific Publ., 2009 S.523-28, ISBN 978-981-281-463-0
- [26] Li, G., Jin, J., Kern, S., Thumm, M.: Frequency and mode characteristics of an oversized quasi-optical launcher towards a step tunable coaxial-cavity gyrotron. *KIT PhD Symp.*, Karlsruhe, 18.März 2009
- [27] Pagonakis, I.G., Hogge, J.P., Goodman, T., Alberti, S., Piosczyk, B., Illy, S., Tzesnicki, T., Kern, S., Lievin, C.: Gun design criteria for the refurbishment of the first prototype of the EU 170GHz/2MW/CW coaxial cavity gyrotron for ITER. *34th Internat. Conf. on Infrared, Millimeter, and Terahertz Waves (IRMMW-THz 2009)*, Busan, Korea, September 21-25, 2009
- [28] Porte, L., Alberti, S., Albajar, f., Avramides, K.A., Benin, P., Bin, W., Bonicelli, T., Bruschi, A., Cirant, S., Droz, E., Dumbrajs, O., Fasel, D., Gandini, F., Goodman, T.P., Hogge, J.P., Illy, S., Jawla, S., Jin, J., Kern, S., Lievin, C., Marletaz, B., Marmillod, P., Pagonakis, I., Perez, A., Piosczyk, B., Rzesnicki, T., Siravo, U., Thumm, M., Tran, M.Q.: Testing and development of a 1MW/170GHz coaxial-cavity gyrotron for ITER and the CRPP gyrotron test stand. *5th IAEA Technical Meeting on ECRH Physics and Technology for Large Fusion Devices*, Gandhinagar, IND, February 18-20, 2009, Book of Abstracts S.28

- [29] Rzesnicki, T., Piosczyk, B., Gantenbein, G., Jin, J., Kern, S., Samartsev, A., Thumm, M.: 170 GHz, 2 MW coaxial cavity gyrotron for ITER. Recent results obtained with a short pulse tube. 10th Internat. Vacuum Electronics Conf.(IVEC 2009), Roma, I, April 28-30, 2009, Proc. on CD-ROM S.277-78, Piscataway, N.J. : IEEE, 2009, ISBN 978-1-4244-3499-2
- [30] Rzesnicki, T., Piosczyk, B., Gantenbein, G., Jin, J., Kern, S., Samartsev, A., Thumm, M. : Towards the 2 MW RF output power of the coaxial cavity gyrotron pre-prototype for ITER. 36th International Conference on Plasma Science (ICOPS) and 23rd Symposium on Fusion Engineering (SOFE-23), San Diego, Calif., May 31 - June 5, 2009
- [31] Rzesnicki, T., Piosczyk, B., Gantenbein, G., Jin, J., Kern, S., Samartsev, A., Thumm, M.: Major progress in the development of the 2 MW coaxial-cavity gyrotron for ITER. 34th Internat. Conf. on Infrared, Millimeter, and Terahertz Waves (IRMMW-THz 2009), Busan, Korea, September 21-25, 2009
- [32] Samartsev, A., Gantenbein, G., Dammertz, G., Flamm, J., Kern, S., Rzesnicki, T., Schlaich, A., Thumm, M.: Characterization of parasitic oscillations in multifrequency gyrotron. 21st Joint Russian-German Workshop on ECRH and Gyrotrons, Greifswald, May 11-16, 2009
- [33] Schmid, M., Gantenbein, G., Thumm, M.: Operation of the FZK gyrotron high voltage supplies and plans for future upgrades. 21st Joint Russian-German Workshop on ECRH and Gyrotrons, Greifswald, May 11-16, 2009
- [34] Schmid, M., Hrabal, D., Piosczyk, B., Thumm, M.: Past and future upgrades of the gyrotron high voltage cathode power supplies at the Forschungszentrum Karlsruhe. Fusion Engineering and Design, 84(2009) S.1734-38, DOI:10.1016/j.fusengdes.2009.01.059
- [35] Thumm, M.: Progress on gyrotrons for ITER and future fusion reactors. 18th Topical Conf. on Radio Frequency Power in Plasmas, Gent, B, June 24-26, 2009, Book of Abstracts S.8-9
- [36] Thumm, M.: High power microwaves for fusion plasma heating. 12th Internat. Conf. on Microwave and High Frequency Heating (AMPERE 2009), Karlsruhe, September 7-10, 2009
- [37] Thumm, M., Rzesnicki, T., Piosczyk, B., Flamm, J., Gantenbein, G., Illy, S., Jin, J., Kern, S., Samartsev, A., Schlaich, A.: 2 MW, 170 GHz pre-prototype coaxial-cavity gyrotron for ITER. US-EU-JPN RF Heating Technology Workshop, Dazaifu-City, Fukuoka, J, September 16-18, 2009, Book of Abstracts S.10

Acknowledgement

This work was supported by Fusion for Energy under the grant contract No. F4E-2008-GRT-08(PMS-H.CD)-01 with collaboration by EPFL, Switzerland; HELLAS, Greece; CNR, Italy and ENEA, Italy. The views and opinions expressed herein reflect only the author's views. Fusion for Energy is not liable for any use that may be made of the information contained therein.

Microwave Heating for Wendelstein 7-X

Introduction

In the recent years electron cyclotron resonance systems have been established as a standard method for localised heating (ECRH) or current drive (ECCD) in fusion relevant plasmas. Thus, ECRH will be the basic day-one heating system for the stellarator W7-X, which is currently under construction at IPP Greifswald. In the first stage, W7-X will be equipped with a 10 MW ECRH system operating at 140 GHz in continuous wave (CW). The complete ECRH system will be provided by KIT (formerly: FZK), in cooperation with EU partners within the 'Projekt Mikrowellenheizung für W7-X' (PMW), that was established in 1998. The PMW responsibility covers the design, development, construction, installation and integrated tests of all components required for stationary plasma heating on site at IPP Greifswald. PMW also coordinates the contributions by Institut für Plasmaforschung (IPF) of the University of Stuttgart (IPF), which is responsible for the microwave transmission system and part of the HV-system, and those by the team at IPP Greifswald, which is responsible for the in-vessel components and for the in-house auxiliary systems. Furthermore, PMW benefits from the collaboration with Centre de Recherche de Physique des Plasmas (CRPP) Lausanne, Commissariat à l'Energie Atomique (CEA) in Cadarache and Thales Electron Devices (TED) in Vélizy.

A contract between CRPP Lausanne, FZK Karlsruhe / KIT and TED, Vélizy, had been settled to develop and build the continuously operating series gyrotrons. The first step of this collaboration was the development of prototype gyrotrons for W7-X with an output power of 1 MW for CW operation at 140 GHz. This step had been finished successfully.

Then, seven series gyrotrons have been ordered from the industrial company TED. First operation and long pulse conditioning of these gyrotrons are to be done at the test stand at FZK, where pulses up to 180 s at full power are possible (factory acceptance test, FAT); 30 minutes shots at full power are possible at IPP (site acceptance test, SAT). Including the pre-prototype tube, the prototype tube and the 140 GHz CPI-tube, ten gyrotrons will be available for W7-X. To operate these gyrotrons, eight superconducting magnetic systems have been ordered from Cryomagnetics Inc., Oak Ridge, USA, complementing the existing the Oxford Instruments and Accel magnets.

The project made further progress in 2009. Most of the components of the transmission system, HV-systems and in-vessel-components have been ordered, manufactured, delivered and are ready for operation at IPP Greifswald. A part of the existing ECRH system is already used to test new concepts and components for ECRH. Some delay arose in the project during the last 2 years due to unexpected difficulties in the production of the series gyrotrons.

Series Gyrotrons

The first TED series gyrotron SN1 had been tested successfully at FZK and IPP in 2005 (920 kW/1800 s). It fulfilled all the specifications; during the acceptance test no specific limitations were observed. In order to preserve the warranty, this gyrotron has been sealed, and the two prototype gyrotrons are routinely used for experiments instead.

The next series gyrotrons showed a more or less different behaviour with respect to parasitic oscillations excited in the beam tunnel region. These oscillations result in an excessive heating of the beam tunnel components, in particular of the absorbing ceramic rings. Re-opened after operation, the gyrotrons showed significant damages due to overheating of the ceramic rings and the brazing of the rings. This in general limited the pulse length in high-power operation to a few ms.

In support of the manufacturer, a dedicated R&D programme was conducted at FZK, with a scheduled completion by end of June 2009. The R&D aimed at the development of a robust beam tunnel which suppresses the parasitic oscillations efficiently. In order to validate a new beam tunnel as much as possible, tests with a structurally modified beam tunnel in a frequency step tuneable gyrotron and a coaxial cavity gyrotron have been performed. Details of the tests are presented in the chapters referring to these approaches, respectively.

The R&D programme at KIT was terminated on schedule with a clear result. The high power experiments with different beam tunnel versions in the step-frequency-tuneable gyrotron (105 – 143 GHz) and the coaxial-cavity gyrotron (170 GHz) clearly show the superiority of a beam tunnel with corrugated copper rings with respect to parasitic oscillations. Hence, KIT / FZK strongly recommended installing a beam tunnel with corrugated copper rings in all W7-X series gyrotrons.. The preliminary time schedule suggests that the gyrotron manufacturer will deliver the next gyrotron equipped with the improved beam tunnel in April 2010.

Transmission Line

The transmission line consists of single-beam waveguide (SBWG) and of multi-beam waveguide (MBWG) elements. For each gyrotron, a beam conditioning assembly of five single-beam mirrors is used. Two of these mirrors are matching the gyrotron output to a fundamental Gaussian beam with the correct beam parameters, two others are used to set the appropriate polarization needed for optimum absorption of the radiation in the plasma. A fifth mirror directs the beam to a plane mirror array, the beam combining optics, which is situated at the input plane of a multi-beam wave guide. This MBWG is designed to transmit up to seven beams (five 140 GHz beams, one 70 GHz beam plus an additional spare channel) from the gyrotron area (entrance plane) to the stellarator hall (exit plane). To transmit the power of all gyrotrons, two symmetrically arranged MBWGs will be used. At the output planes of the MBWGs, a mirror array (beam distribution optic, BDO) re-separates the beams and distributes them via two other mirrors and CVD-diamond vacuum barrier windows to individually movable antennas (launchers) in the torus. The BDOs and the consecutively arranged mirrors are mounted in so-called towers with "pinnacles" on top.

In 2008, the manufacturing of these pinnacles had almost been finished, including the shielding structures around the vacuum barrier windows, the interfaces to the stellarator ports, side absorbing screens and directional couplers integrated into the surfaces of the mirrors in front of the windows. Present work concentrates on the alignment control system in conjunction with the grating couplers.

Investigations on the stability of the output beam of the gyrotrons have been started, motivated by the fact that the W7-X gyrotrons exhibit a pronounced downward frequency chirp of a few 100 MHz until about 1 s after switch-on. This is caused by the thermal expansion of the cavity. The quasi-optical beam transmission lines – and especially the two matching mirrors – are designed based upon beam measurements during the first few milliseconds of a pulse. Any noticeable change in beam direction after switch-on would preclude the use of phase-shaping mirrors, which are currently in consideration for the final design. To investigate any beam

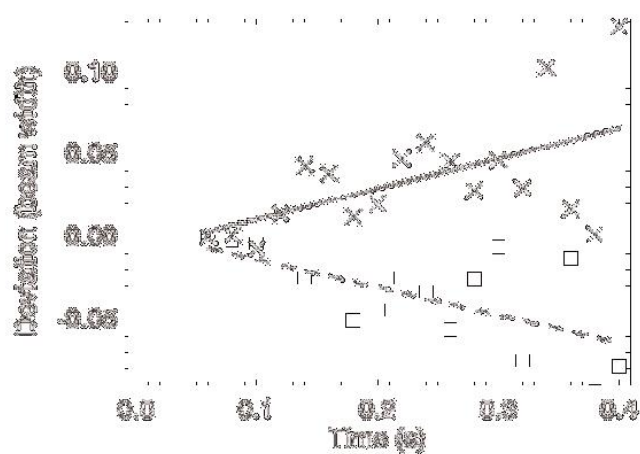


Fig. 1: Plot of the beam centre displacement (in units of beam diameter) in the x (crosses) and y (squares) direction versus time (x: vertical direction, y: horizontal direction at the gyrotron).

wandering effects, a high temperature Si_3N_4 target was subjected to a 350 ms pulse from the TED prototype gyrotron. The displacement of the beam centre is plotted in Fig. 1. While a clear displacement can be seen, the noise is too strong to decide whether the beam returns to its original position after 300 ms. Further measurements are underway.

Due to the aging of the available CW absorber loads, which leads to increased arcing problems at higher power, attempts to replace these loads have been continued. One option is the "long load" which consists of a long (> 20 m) waveguide made of stainless steel, where the power is coupled as a Gaussian beam. By appropriate down-tapering, the absorption of the waveguide is matched to the eventual power loss along the guide. After first tests employing a simple mock-up system with standard water tubes and welded connections had shown strong arcing, a second attempt with an un-cooled electro-polished tube was successful. Therefore, the design of a water-cooled version with flanged connections is underway.

As in the past years, the ECRH system could be used for testing special components. One test campaign was dedicated to the investigation of a compact long-pulse high-power diplexer. The present device ("MkII") is equipped with HE_{11} interfaces, and thus is compatible with waveguide transmission systems. It is developed for use as a combiner of the power of two gyrotrons, and as a fast directional switch (FADIS) between two outputs, and therefore is of potential interest for ITER. With the basic features determined in low power measurements at IPF Stuttgart, the MkII device was integrated in the quasi-optical transmission line of the ECRH system at IPP Greifswald for high power tests. The experimental arrangement is seen from above in Fig. 2.

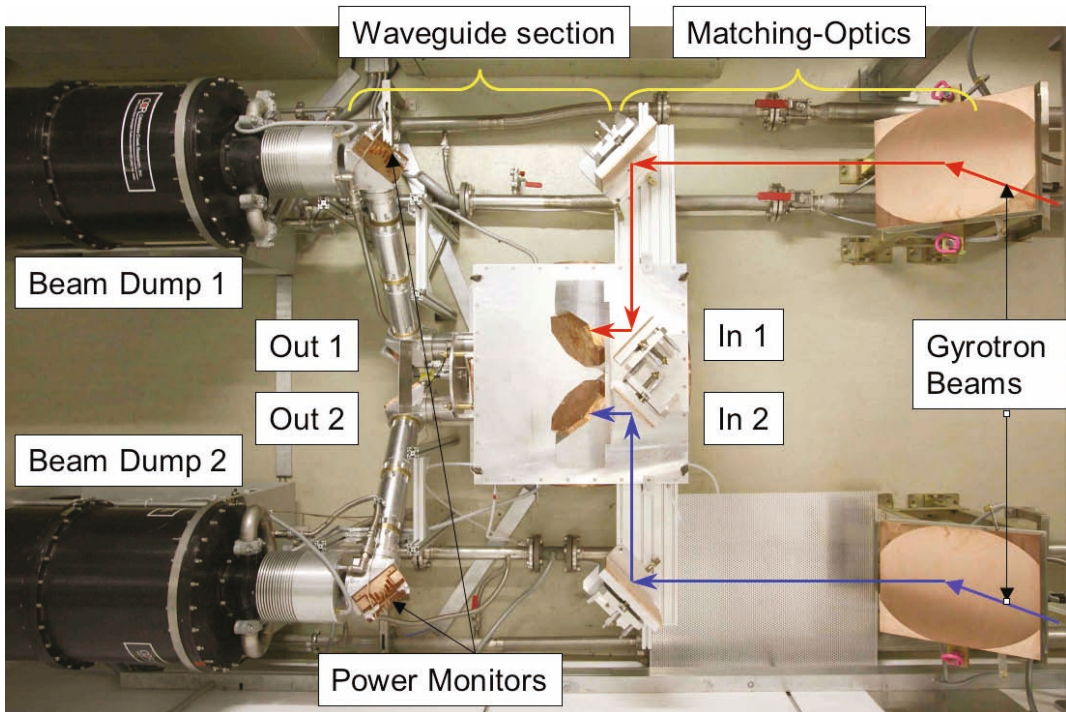


Fig. 2: Photograph of the setup in the beam duct of the ECRH system for W7-X. The compact MKII diplexer is seen in the center. The arrows indicate the beam paths of both free-space beams (In1 and In2). The waveguide outputs (Out1 and Out2) with two mitre bends in each arm are seen on the left side feeding the two CW-dummy loads (beam dump 1 and 2).

Commissioning experiments were started with one gyrotron ("Maquette") to determine the power and energy capability of the resonance frequency with various fixed settings. So far, 75 s pulses with a peak power of 500 kW were obtained; extension to 100 s at this power level seems feasible. Fast switching experiments have been performed, an example is shown in Fig. 3.

One of the resonator mirrors is equipped with a tuneable mounting for frequency tracking, the drive being a development by TNO in Delft. First tests with this feedback system could demonstrate fast tracking to the slope of the diplexer resonance, which is needed for optimum contrast of a fast switching system. Experiments for resonance tracking, which is necessary for combining the power from two gyrotrons, are in preparation.

For two of the N-ports of W7-X, "remote steering" launchers are foreseen. This is due to the fact that front steering launchers as used in the A and E ports (see chapter on launchers) will not fit into these narrow ports. The remote steering effect is based on the propagation characteristics of the modes in a square waveguide leading to imaging effects: For a proper length of the waveguide, a microwave beam at the input of the waveguide (with a defined direction set by the mirror system outside of the plasma vacuum) will exit the waveguide (near the plasma) at the same direction. For W7-X, the vacuum window, a vacuum valve as well as a mitre bend must be integrated into the 5.1 m long waveguide. To optimize the position of these components, and thus to reduce the antenna loss, calculations have been performed. Fig. 4 shows the transmission loss for various launching angles and a 25 mm gap in the waveguide as a function of the axial position; good performance is obtained in an angular rage of $\pm 12^\circ$, if the vacuum valve is situated at $z= 2.56$ m. Optimization calculations are continued to further enlarge the steering range by modifying the cross-section of the square waveguide.

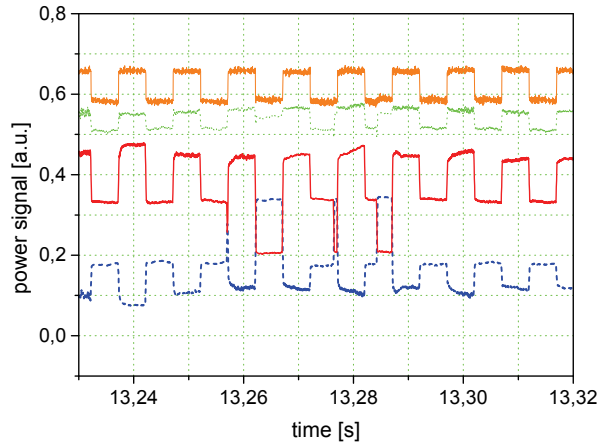


Fig. 3: Input (orange, In1) and output power signals (blue, dashed for Out1, red, solid for Out2) as well as the sum of both output power values (green, dotted). The body voltage of the gyrotron, and hence the frequency, is modulated with a square wave $\Delta U_{B1} = 1$ kV, $f_{MD} = 100$ Hz; the mean frequency is kept at the resonance slope of the diplexer.

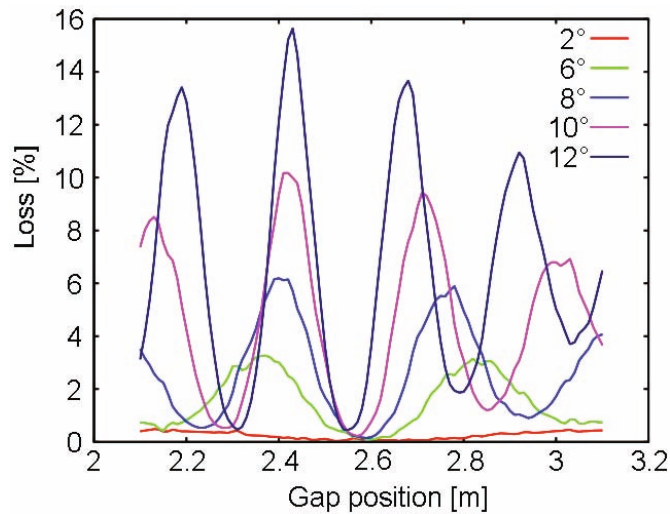


Fig. 4: Transmission losses for a 25 mm gap in the square corrugated remote steering waveguide as a function of the axial position.

In-vessel-components

The assembly of three of four ECRH plug-in antenna modules (plug-in launcher for A and E ports) was completed. The launchers containing three beam lines each were sent to Greifswald for final acceptance tests. The first two launchers passed the vacuum test in the large MISTRAL vacuum chamber successfully (see Fig. 5). The laser tracking measurement of the antenna dimensions and of the corresponding ports however revealed a collision, because the dimensions of both systems are out of tolerance. The antenna size must be reduced, while the port size has to be increased. In addition, mechanical tests of the movable antenna mirrors displayed some non-appropriately assembled bearings. A repair procedure and minor design changes have been elaborated. The launchers were sent back to KIT (BTI) for refurbishment. The ports, which are in IPP responsibility, will be re-worked for larger opening diameter at Greifswald.

The transmitted ECRH power will be measured by a waveguide array of 120 copper tubes. Four waveguide bundles will cross the vacuum-air interface in four B-type ports. The intermediate flanges for the waveguide array, consisting of 30 individual CF16 flanges for every waveguide, as well as the in-vessel waveguide support structure have been manufactured. The assembly of waveguides and ports will start at the beginning of 2010.

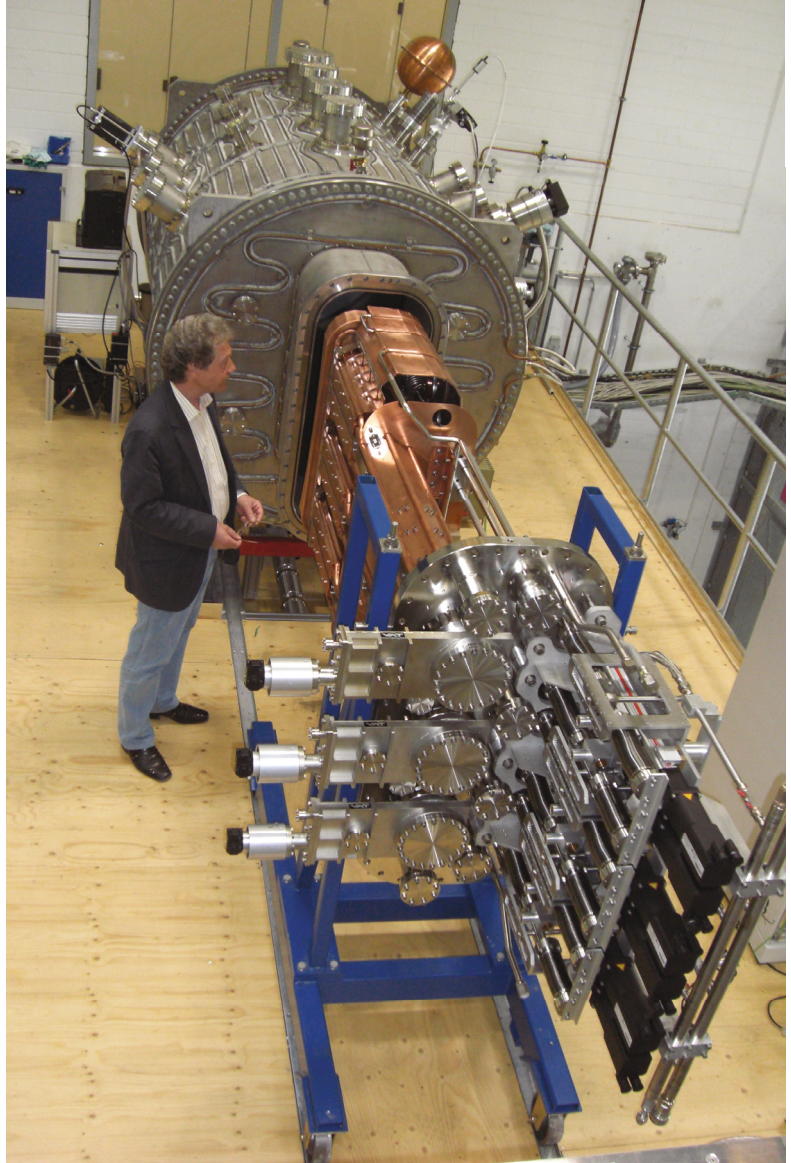


Fig. 5: Test of the launcher in the MISTRAL vacuum test chamber at IPP Greifswald.

Staff:

IHM (KIT)	IPF (University of Stuttgart)	IPP (Greifswald/Garching)
K. Baumann	P. Brand	B. Berndt
G. Dammertz	C. Lechte	H. Braune
<u>G. Gantenbein</u>	W. Kasperek	V. Erckmann (PMW)
S. Illy	H. Kumric	F. Hollmann
S. Kern	M. Krämer	L. Jonitz
M. Kupper	R. Munk	H. Laqua
R. Lang	F. Müller	G. Michel
W. Leonhardt	B. Plaum	F. Noke
M. Losert	S. Prets	F. Purps
D. Mellein	P. Salzmann	T. Schulz
S. Miksch	K.H. Schlüter	P. Uhren
A. Papenfuß	A. Zeitler	M. Weißgerber
B. Piosczyk		
A. Samartsev		
M. Schmid		
W. Spiess		
D. Strauss		
J. Szczesny		
<u>M. Thumm</u>		
J. Weggen		

Literature:

- [1] Braune, H.; Erckmann, V.; Illy, S.; Laqua, H.P.; Noke, F.; Purps, F.; Schmid, M., Advanced transverse field collector sweeping for high power gyrotrons. Litvak, A.G. [ed.], Strong Microwaves : Sources and Applications ; Proc.of the 7th Internat. Workshop, Nizhny Novgorod, Vol.1 p.149-53, Nizhny Novgorod : Russian Academy of Sciences, 2009, ISBN 978-5-8048-0083-4
- [2] Braune, H.; Erckmann, V.; Illy, S.; Laqua, H.P.; Michel, G.; Noke, F.; Purps, F.; W7-X ECRH Teams at IPP and FZK, Transverse field collector sweeping for the W7-X gyrotrons. Modulation techniques. 34th Internat. Conf. on Infrared, Millimeter, and Terahertz Waves (IRMMW-THz 2009), Busan, Korea, September 21-25, 2009
- [3] Erckmann, V.; Kasperek, W.; Gantenbein, G.; Hollmann, F.; Jonitz, L.; Noke, F.; Purps, F.; Weissgerber, M., W7-X ECRH Teams at IPP, FZK and IPF, ECRH for W7-X: transmission losses of high-power 140-GHz wave beams. Fusion Science and Technology, 55(2009) p.16-22
- [4] Erckmann, V.; Brand, P.; Braune, H.; Gantenbein, G.; Kasperek, W.; Laqua, H.P.; Lechte, C.; Marushchenko, N.B.; Michel, G.; Thumm, M.; Turkin, Y.; Weissgerber, M., ECRH Groups at IPP Greifswald, FZK Karlsruhe and IPF Stuttgart, The 10 MW, CW, ECRH-plant for W7-X: status and high power performance. Litvak, A.G. [ed.], Strong Microwaves : Sources and Applications ; Proc. of the 7th Internat. Workshop, Nizhny Novgorod, Vol.1 S.60-69, Nizhny Novgorod: Russian Academy of Sciences, 2009, ISBN 978-5-8048-0083-4
- [5] Erckmann, V.; Braune, H.; Laqua, H.P.; Marushchenko, N.B.; Michel, G.; Turkin, Y.; Weissgerber, M.; Gantenbein, G.; Thumm, M.; Brand, P.; Kasperek, W.; Lechte, C. W7-X ECRH Teams at IPP, FZK and IPF, The 10 MW, CW, ECRH-plant for W7-X: status and high power performance. Lohr, J. [Hrsg.], Proc.of the 15th Joint Workshop on Electron Cyclotron Emission and Electron Cyclotron Resonance Heating, Yosemite National Park, Singapore: World Scientific Publ., 2009 p.427-32, ISBN 978-981-281-463-0
- [6] Erckmann, V.; Kasperek, W.; Koshurinov, Y.; Lubyako, L.; Petelin, M.I.; Shchegolkov, D.Yu.; Hollmann, F.; Michel, G.; Noke, F.; Purps, F. ; ECRH Groups at IPP, IPF, IAP, FZK and IPF, Power combination of two 140-GHz gyrotrons and fast switching of the combined beam. Fusion Sci. Technol. 55 (2009) p.23-30
- [7] Gantenbein, G.; Braune, H.; Dammertz, G.; Erckmann, V.; Illy, S.; Kern, S.; Kasperek, W.; Lechte, C.; Legrand, F.; Leonhardt, W.; Lievin, C.; Michel, G.; Piosczyk, B.; Samartsev, A.; Schmid, M.; Thumm, M., Recent developments on the W7-X 140 GHz gyrotron. 21st Joint Russian-German Workshop on ECRH and Gyrotrons, Greifswald, May 11-16, 2009,

- [8] Gantenbein, G.; Dammertz, G.; Illy, S.; Kern, S.; Leonhardt, W.; Piosczyk, B.; Schmid, M.; Thumm, M.; Braune, H.; Erckmann, V.; Laqua, H.P.; Michel, G.; Kasperek, W.; Lechte, C.; Legrand, F.; Lievin, C.; Prinz, O., The 140 GHz, 1MW gyrotron - status and recent results. Lohr, J. [Hrsg.], Proc. of the 15th Joint Workshop on Electron Cyclotron Emission and Electron Cyclotron Resonance Heating, Yosemite National Park, Calif., Singapore: World Scientific Publ., 2009 p.529-34, ISBN 978-981-281-463-0
- [9] Kasperek, W.; Petelin, M.; Erckmann, V.; Bruschi, A.; Plaum, B.; Koposova, L.; Lubyako, L.; Michel, G.; Bin, W.; D'Arcangelo, O.; ECRH Groups at IPP, IPF, IAP, FZK and IFP: Compact diplexers for power combination and fast switching in ECRH systems: designs, experimental results, and system integration. 5th IAEA Technical Meeting on ECRH Physics and Technology for Large Fusion Devices, Gandhinagar, IND, February 18-20, 2009 Book of Abstracts p.23
- [10] Kasperek, W., Petelin, M.I., Erckmann, V., Bruschi, A., Noke, F., Purps, F., Hollmann, F., Koshurinov, Y., Lubyako, L., Plaum, B., Wubie, W., and ECRH groups at IPP Greifswald, FZK Karlsruhe, IFP Milano, IAP Nizhny Novgorod, and IPF Stuttgart. High-power microwave diplexers for advanced ECRH systems. *Fusion Eng. Design* 84 (2009) 1002-1005.
- [11] Kasperek, W.; Petelin, M.; Schegolkov, D.; Erckmann, V.; Bruschi, A.; Braune, H.; Hollmann, F.; Jonitz, L.; Michel, G.; Laqua, H.P.; Noke, F.; Purps, F.; Schulz, T.; Brand, P.; Plaum, B.; Wubie, W.; Kohsurinov, Y.; Lubyako, L.; Bin, W.; D'Arcangelo, O.; ECRH Groups at IPP, IPF, IAP, FZK and IFP: High power microwave diplexers for advanced ECRH systems. Litvak, A.G. [ed.], *Strong Microwaves : Sources and Applications* ; Proc. of the 7th Internat. Workshop, Nizhny Novgorod, Vol.1 S.27-39, Nizhny Novgorod : Russian Academy of Sciences, 2009, ISBN 978-5-8048-0083-4
- [12] Michel, G.; Brand, P.; Braune, H.; Erckmann, V.; Gantenbein, G.; Kasperek, W.; Laqua, H.P.; Marushchenko, N.; Oosterbeek, J.W.; Thumm, M.; Weißgerber, M., ECRH Teams at IPP, IPF and FZK, Electron cyclotron resonance heating for W7-X. 18th Topical Conf. on Radio Frequency Power in Plasmas, Gent, B, June 24-26, 2009, Book of Abstracts p.87
- [13] Thumm, M.; Braune, H.; Dammertz, G.; Erckmann, V.; Gantenbein, G.; Illy, S.; Kern, S.; Kasperek, W.; Laqua, H.P.; Lechte, C.; Legrand, F.; Leonhardt, W.; Lievin, C.; Michel, G.; Piosczyk, B.; Prinz, O.; Schmid, M., 1 MW, 140 GHz series gyrotrons for the W7-X stellarator. Litvak, A.G. [ed.], *Strong Microwaves: Sources and Applications* ; Proc. of the 7th Internat. Workshop, Nizhny Novgorod, Vol.1 p.84-94, Nizhny Novgorod : Russian Academy of Sciences, 2009, ISBN 978-5-8048-0083-4
- [14] Thumm, M.; Brand, P.; Braune, H.; Dammertz, G.; Erckmann, V.; Gantenbein, G.; Illy, S.; Kasperek, W.; Kern, S.; Laqua, H.P.; Lechte, C.; Marushchenko, N.B.; Michel, G.; Samartsev, A.; Schlaich, A.; Schmid, M.; Turkin, Y.; Weissgerber, M.; W7-X ECH Teams at KIT, IPP and IPF. 10 MW, 0.14THz, CW gyrotron and optical transmission system for fusion plasma heating. Internat. Symp. on Frontier of Terahertz Spectroscopy III: Next Generation Technology in THz Frequency Region and its Application to THz Sensitive Spectroscopy and Sensing, Fukui, J, October 22-23, 2009, Proc. p.17-22

ECR Heating and Current Drive – Step-Tuneable Gyrotron Development

Introduction

In recent years, electron cyclotron resonance heating and current drive (ECRH and ECCD) has been established as a successful instrument in magnetically confined fusion plasmas. Gyrotrons are the unique devices which meet the extraordinary requirements of those applications: output power in the MW range, 100 – 200 GHz output frequency, pulse length of several seconds up to continuous wave. Due to its excellent coupling to the plasma and the very good localisation of the absorbed RF power, ECRH is applied in present day machines and is also foreseen in large forthcoming fusion projects: it will be the main heating system for the stellarator W7-X which is currently under construction and it will play a major role in the ITER tokamak. In particular, advanced tokamaks are operated in a plasma regime where MHD instabilities, potentially limiting the performance, are present. To a large extent, the stability in a tokamak is influenced by the distribution of the internal plasma currents which can be manipulated by the injection of RF waves. The location of the absorption of RF waves of the angular frequency ω is dependent on the resonance condition $\omega - k_z v_z = \omega_c$ (k_z : z-component of the wave number, v_z : electron velocity along z-axis). Thus, by changing the wave frequency ω , the absorption can be moved to any radial position where the local cyclotron frequency of the electrons ω_c holds for the expression above.

Industrial gyrotrons in the relevant frequency range with an output power of about 1 MW are usually designed for a fixed frequency. However, frequency tuneable gyrotrons are not a standard product since these broadband tubes require additional optimisation of major components like the electron beam forming optics, cavity, quasi-optical mode converter and output window.

For experiments on plasma stabilisation at ASDEX Upgrade (IPP Garching) with advanced ECRH and ECCD, multi-frequency tuneable (105 – 143 GHz) 1-MW long-pulse gyrotrons are highly needed.

Investigations on improved beam tunnel structures

To solve unexpected problems with parasitic oscillations in the beam tunnel of the W7-X gyrotron and the coaxial 2 MW ITER tube, a dedicated test program for the investigation of different beam tunnel structures was set up. To support Thales Electron Devices (TED), the manufacturer of the W7-X gyrotron, the modular step-frequency tuneable short pulse gyrotron was used to investigate parasitic oscillations in the beam tunnel. Since this tube is equipped with a Brewster window and is designed for broadband operation with regard to all components, experiments over wide parameter ranges could be accomplished, yielding more information about the behaviour of the measured unwanted oscillations.

The step-frequency tuneable gyrotron was designed for operation in the frequency range 105 – 143 GHz in different operating modes. Frequency-step tuning is performed by changing the magnetic field and excitation of corresponding TE modes in the cavity. Typical high power operating parameters of the gyrotron are an accelerating voltage of 80 kV and a beam current of 40 A. However, beam currents up to 60 A have been used in the experiments.

In the first experimental setup, a standard, azimuthally symmetric beam tunnel as used in the W7-X gyrotron was installed as reference. This reference beam tunnel was supposed to support parasitic oscillations. In a second experimental campaign, this beam tunnel was replaced by a modified version with distorted azimuthal symmetry.

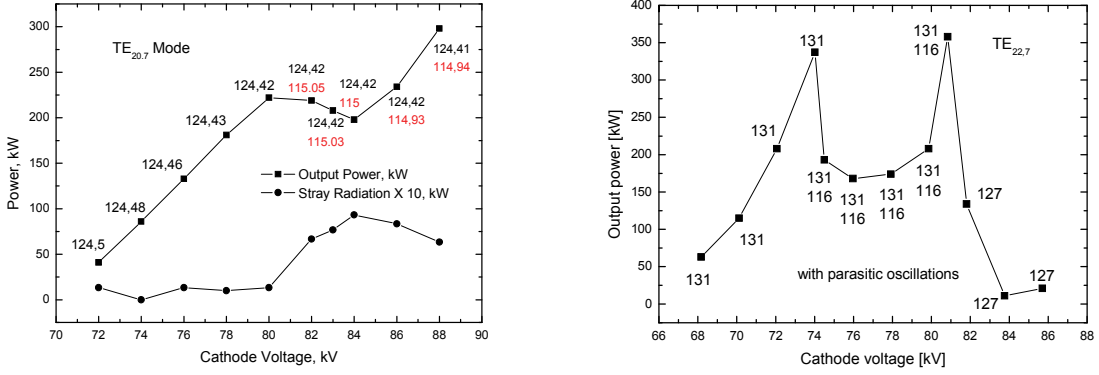


Fig. 1: Output power vs. cathode voltage for two different operating modes in the first experimental setup (reference beam tunnel).

The azimuthally symmetric reference beam tunnel showed parasitic oscillations, their influence on the behaviour of the gyrotron could clearly be seen. The first effect was a reduction in output power and efficiency, and increased stray radiation power as soon as frequencies of parasitic oscillations could be measured, as shown in Fig. 1. It can clearly be seen that the gyrotron does not show a usual behaviour; the cavity interaction of the desired operating mode is strongly degraded by the parasitic oscillation.

Further, it could be observed that the frequencies of parasitic oscillations are much more sensitive to parameter changes than the frequencies of cavity modes are. In Fig. 2 the stronger frequency dependence of parasitic oscillations on accelerating voltage and magnetic field can be seen. This shows that the unwanted oscillations are weakly attenuated circular symmetric backward waves.

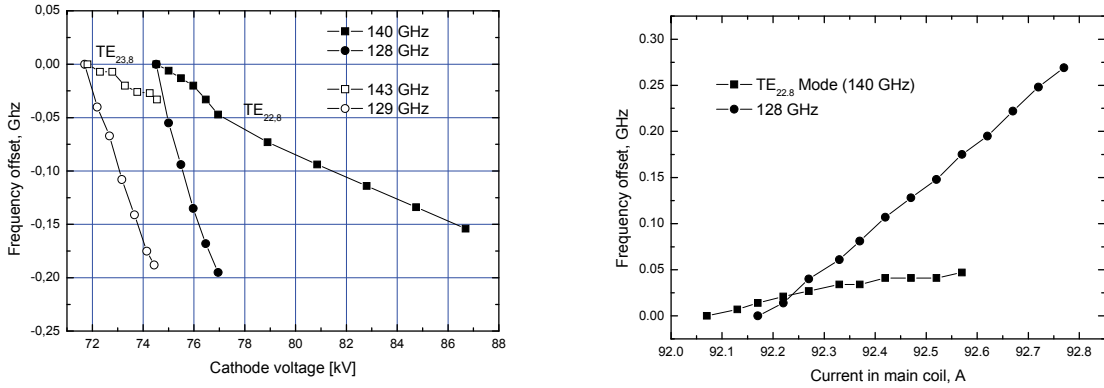


Fig. 2: Frequency variation of cavity modes and parasitic oscillations around 128 GHz vs. acceleration voltage (left) and main magnetic field (right).

In the second experimental campaign the beam tunnel was modified by removing the azimuthal symmetry in order to suppress azimuthally symmetric backward waves. This was done by introducing irregular corrugations in the copper rings with a depth of about $\lambda/4$, in order to cut azimuthal RF currents and thereby let the attenuation of the ceramics take effect on azimuthally symmetric modes, too. The number, width and periodicity of the corrugations is optimized and, together with the monotonously decreasing inner diameters of adjacent rings, this is forming a structure which avoids longitudinal periodicity. Such a structure can be considered as a grating with many different grating constants as well. This complicates the formation of a resonant field structure and effectively damps $TE_{m,p}$ modes, in particular symmetric TE modes ($m = 0$). A picture of the modified beam tunnel is given in Fig. 3.

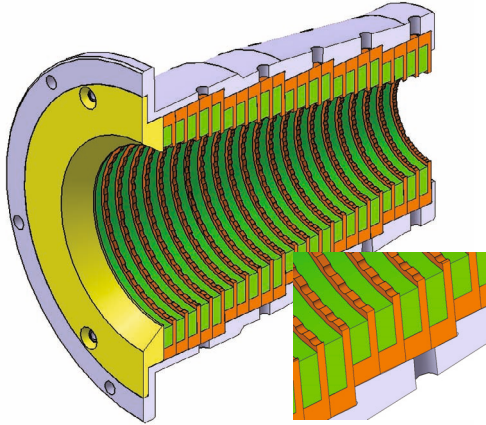


Fig. 3: Beam tunnel with corrugated Cu rings.

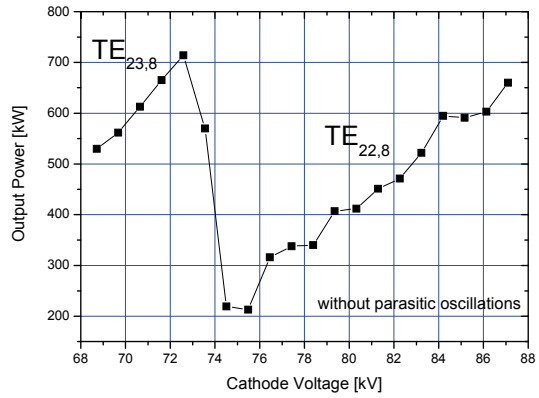


Fig. 4: RF output power of the gyrotron with the improved beam tunnel.

After introducing the improved beam tunnel, the gyrotron was operated with the same parameters. Experiments in this configuration did not show any beam tunnel parasitic oscillations as described above for the reference beam tunnel. Even at a beam current well above the design value (60 A), no beam tunnel RF oscillations in the high frequency range have been observed. A typical measurement of the RF output power for the TE_{22,8} mode, as shown in Fig. 4, indicates a usual output power behaviour versus acceleration voltage, in contrast to Fig. 2.

Quasi-optical mode converter

The quasi-optical mode converter is used for transferring the cavity mode into a Gaussian beam which fits through the window aperture. It consists of a dimpled-wall waveguide antenna, the so-called launcher, and a set of three beam-forming mirrors. For the multi-mode gyrotron, the mode converter has to be optimized to convert nine modes between TE_{17,6} (105 GHz) and TE_{23,8} (143 GHz) with different properties to a Gaussian beam which does not change its properties from mode to mode. First, the launcher's inner waveguide wall is optimized to form a Gaussian output pattern and a minimum of stray radiation. Then, the mirrors are designed to maximal power transmission through the window aperture by optimizing the diameter and position of the waist of the Gaussian beam for all modes.

In the past year the manufacturing of two mode converters (low/high power version) of the second generation was completed and both systems were characterised by low-power measurements. The mode analysis of the radiated beam of the main TE_{22,8} mode at 140 GHz after passing three focusing mirrors in the plane of the output window yielded a Gaussian content in the experiment of 89 % for both versions. This is a little bit less then what can be expected according to numerical optimisation calculations. A typical image of the measured output beam of the high power mode converter is shown in Fig. 6.

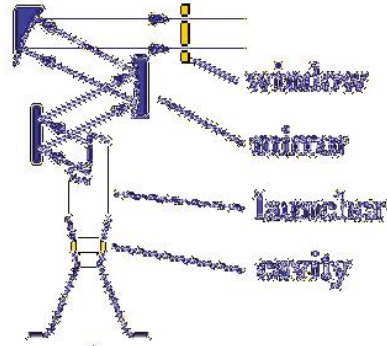


Fig. 5: Basic elements and principle of quasi-optical system.

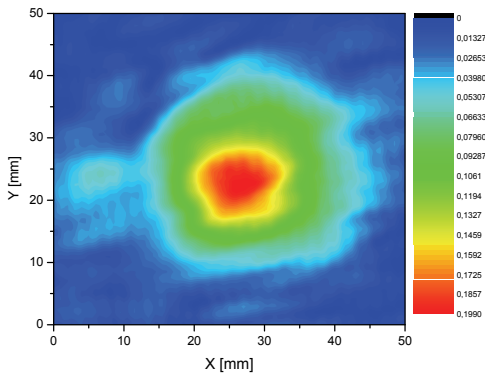


Fig. 6: RF output beam leaving the mode converter (low power measurement).

The inner surfaces of both launchers have been measured mechanically. Small differences in the manufactured devices are observed although for both versions the same data set has been used. To verify the possible consequences of the different geometry, these data have been used as an input for the Surf3D code, and mode conversion as well as field propagation in the real 3 mirror system have been calculated. The results are a Gaussian content of 90.7 % for the Cu launcher and 93.3 % for the Al launcher. In the high-power experiment, the Gaussian content of the Cu launcher was significantly smaller. Additional investigations to clarify this discrepancy are underway.

CVD-diamond Brewster window

Efficient operation for the large number of operating modes at different frequencies requires using a broadband synthetic diamond Brewster window fabricated by chemical vapour deposition (CVD). Due to the large Brewster angle of 67.2° deg, the diameter of the disk also has to be rather large, in order to provide sufficient aperture for the RF beam. One disk with a thickness of 1.7 mm and a diameter of 140 mm was developed by Element Six and already has been delivered. This disk can be used for the elliptic shape of a Brewster window with an effective aperture of 50 mm.

Because of the ellipticity, the stresses during the brazing procedure are different from those occurring with circular disks. These stresses were calculated to increase by a factor of 1.3. To investigate whether a diamond disk will sustain these stresses, brazing tests have been performed at Thales Electron Devices, using a quartz disk and a small diamond disk for which the stresses are increased compared to the circular one. In case of successful brazing, the 140 mm diamond disk will be brazed with copper cuffs, so that it will be possible to cool the disk at the edge.

In 2009 the first brazing of the small diamond disk was finished successfully; the assembly is vacuum tight. A photograph of the system is given in Fig. 7. In coordination with the industrial partner, the brazing of the real-size diamond disk will be launched.

Fast step-tunable magnet

A fast step tuneable magnet which offers the possibility to change the magnetic field in the range 4.15 – 5.67 T has been ordered. With this magnet there will be the unique possibility to change the gyrotron frequency from 105 GHz to 143 GHz in steps of approximately 3 GHz within 0.5 s every 10 s. The maximum field will be 7.2 T, thus making the magnet suitable also for the investigation of 170 GHz gyrotrons for the ITER ECRH system.



Fig. 7: CVD diamond disk Brewster angle window.



Fig. 8: Completely mounted fast step-tunable magnet during tests at the manufacturer's site.

In 2009, the coil system has been cold-tested in a test cryostat. In this cryostat the magnet has shown operation at the maximum field and fast switching of the magnetic field strength. The coil system was installed in the original cryostat and measurements of the field profile have been performed showing a good agreement with the design. The demonstration of the full specifications of the system in the original cryostat, e.g. alignment of the magnetic and geometrical axis and loss rates, is expected in the beginning of 2010.

Staff:

G. Dammertz
J. Flamm (Uni Karlsruhe)
G. Gantenbein
S. Illy
S. Kern
W. Leonhardt
J. Jin
D. Mellein
A. Papenfuss
B. Piosczyk
A. Samartsev
T. Scherer
M. Schmid
R. Schneider
W. Spieß
D. Strauss
J. Szczesny
M. Thumm

Literature

- [1] Borie, E.; Kern, S., On the effect of RF-space charge on the beam-field interaction in gyrotrons. *Journal of Infrared, Millimeter and Terahertz Waves*, 30(2009) S.915-23
- [2] Gantenbein, G.; Rzesnicki, T.; Alberti, S.; Goodman, T.; Hogge, J.P.; Illy, S.; Jin, J.; Kern, S.; Piosczyk, B.; Samartsev, A.; Thumm, M., Status of development of high power coaxial-cavity gyrotron at FZK. 5th IAEA Technical Meeting on ECRH Physics and Technology for Large Fusion Devices, Gandhinagar, IND, February 18-20, 2009
- [3] Kern, S.; Avramides, K.A., Improving gyrotron interaction calculations. 34th Internat.Conf.on Infrared, Millimeter, and Terahertz Waves (IRMMW-THz 2009), Busan, Korea, September 21-25, 2009
- [4] Kern, S.; Schlaich, A.; Flamm, J.; Gantenbein, G.; Latsas, G.; Rzesnicki, T.; Samartsev, A.; Thumm, M.; Tighe-lis, I., Investigations on parasitic oscillations in megawatt gyrotrons. 34th Internat.Conf.on Infrared, Millimeter, and Terahertz Waves (IRMMW-THz 2009), Busan, Korea, September 21-25, 2009
- [5] Kern, S.; Alberti, S.; Beringer, M.H.; Borie, E.; Braune, H.; Dammertz, G.; Dumbrajs, O.; Erckmann, V.; Flamm, J.; Giguet, E.; Gantenbein, G.; Hogge, J.P.; Illy, S.; Jin, J.; Laqua, H.P.; Legrand, F.; Leonhardt, W.; Lievin, C.; Michel, G.; Piosczyk, B.; Prinz, H.O.; Rzesnicki, T.; Schmid, M.; Thumm, M.; Tran, M.Q., Gyrotrons for fusion plasma heating - status of development at the Forschungszentrum Karlsruhe (FZK). Jahrestagung Kerntechnik 2009, Dresden, 12.-14.Mai 2009 Berlin : INFORUM GmbH, 2009 CD-ROM Paper 801

- [6] Leuterer, F.; Münich, M.; Brandl, F.; Brinkschulte, H.; Grünwald, G.; Manini, A.; Monaco, F.; Ryter, F.; Schütz, H.; Stober, J.; Wagner, D.; Kasperek, W.; Gantenbein, G.; Empacher, L.; Lechte, C.; Kumric, H.; Schüller, P.; Litvak, A.; Chirkov, A.; Denisov, G.; Fix, A.; Illin, V.; Malygin, S.; Misnikov, V.; Nichiporenko, V.; Popov, L.; Tai, E.; Zapevalov, V., Operation experience with the ASDEX upgrade ECRH system. *Fusion Science and Technology*, 55(2009) S.31-44
- [7] Prinz, O.; Arnold, A.; Gantenbein, G.; Liu, Y.H.; Thumm, M.; Wagner, D., Highly efficient quasi-optical mode converter for a multifrequency high-power gyrotron. *IEEE Transactions on Electron Devices*, 56(2009) S.828-34
- [8] Samartsev, A.; Gantenbein, G.; Dammertz, G.; Flamm, J.; Kern, S.; Rzesnicki, T.; Schlaich, A.; Thumm, M., Characterization of parasitic oscillations in multifrequency gyrotron. 21st Joint Russian-German Workshop on ECRH and Gyrotrons, Greifswald, May 11-16, 2009, Folien auf CD-ROM
- [9] Stober, J.; Franke, Th.; Grünwald, G.; Leuterer, F.; Manini, A.; Monaco, F.; Münich, M.; Neu, R.; Schütz, H.; Wagner, D.; Zohm, H.; Gantenbein, G.; Heidinger, R.; Meier, A.; Thumm, M.; Kasperek, W.; Lechte, C.; Chirkov, A.V.; Denisov, G.G.; Litvak, A.; Malygin, S.A.; Myasnikov, V.E.; Nichiporenko, V.O.; Popov, L.G.; Solyanova, E.A.; Tai, E.M.; Meo, F.; Woskov, P., On the way to a multi-frequency ECRH system for ASDEX upgrade., Lohr, J. [Hrsg.], Proc.of the 15th Joint Workshop on Electron Cyclotron Emission and Electron Cyclotron Resonance Heating, Yosemite National Park, Singapore [u.a.] : World Scientific Publ., 2009 S.433-39, ISBN 978-981-281-463-0
- [10] Wagner, D.; Stober, J.; Leuterer, F.; Sips, G.; Grünwald, G.; Monaco, F.; Münich, M.; Poli, E.; Schütz, H.; Volpe, F.; Treutterer, W.; Zohm, H.; Franke, T.; Thumm, M.; Heidinger, R.; Gantenbein, G.; Meier, A.; Kasperek, W.; Lechte, C.; Litvak, A.G.; Denisov, G.G.; Chirkov, A.; Tai, E.; Popov, L.G.; Nichiporenko, V.O.; Myasnikov, V.E.; Solyanova, E.A.; Malygin, S.A., Multi-frequency ECRH at ASDEX upgrade. Litvak, A.G. [Hrsg.], Strong Microwaves : Sources and Applications ; Proc.of the 7th Internat.Workshop, Nizhny Novgorod, Vol.2 S.304-11, Nizhny Novgorod: Russian Academy of Sciences, 2009, ISBN 978-5-8048-0083-4
- [11] Wagner, D.; Stober, J.; Franke, T.; Leuterer, F.; Poli, E.; Monaco, F.; Münich, M.; Schütz, H.; Zohm, H.; Thumm, M.; Scherer, T.; Meier, A.; Gantenbein, G.; Flamm, J.; Kasperek, W.; Lechte, C.; Höhnle, H.; Litvak, A.G.; Denisov, G.G.; Cirkov, A.; Popov, L.G.; Nichiporenko, V.O.; Myasnikov, V.E.; Tai, E.M.; Solyanova, E.A.; Malygin, S.A., Multi-frequency ECRH system at ASDEX upgrade. 34th Internat.Conf.on Infrared, Millimeter, and Terahertz Waves (IRMMW-THz 2009), Busan, Korea, September 21-25, 2009
- [12] Wagner, D.; Thumm, M.; Gantenbein, G.; Flamm, J.; Neilson, J.; Vernon, R. Multi-mode generator for the cold test of broadband quasi-optical gyrotron mode converters., US-EU-JPN RF Heating Technology Workshop, Dazaifu-City, Fukuoka, J, September 16-18, 2009, Book of Abstracts S.22
- [13] Wagner, D.H.; Stober, J.K.; Leuterer, F.; Sips, G.; Grünwald, G.; Monaco, F.; Münich, M.J.; Poli, E.; Schütz, H.; Volpe, F.; Treutterer, W.; Zohm, H.; Franke, T.; Thumm, M.; Heidinger, R.; Gantenbein, G.; Meier, A.; Kasperek, W.; Lechte, C.; Litvak, A.G.; Denisov, G.G.; Chirkov, A.; Tai, E.; Popov, L.; Nichiporenko, V.; Myasnikov, v.; Solyanova, E.; Malygin, S., Progress and first results with the new multifrequency ECRH system for ASDEX upgrade. *IEEE Transactions on Plasma Science*, 37(2009) S.395-402

Design Studies towards a 170 GHz 4 MW Coaxial-Cavity Gyrotron (EFTS EC-Tech – Contract No. 042636 (FU06))

For future fusion devices it is desirable to develop gyrotrons with highest possible unit power to reduce the costs and space requirements for new ECRH systems. Currently the 2 MW coaxial-cavity gyrotron has reached prototype status; consequently, a detailed design study for a 170 GHz 4 MW coaxial-cavity gyrotron was started in 2008. Within the Euratom Fusion Training Scheme EC-TECH No. 042636 (FU06) this work is done as the main topic of the Ph.D. thesis of a trainee. After physical and technical feasibility studies the designs for the major gyrotron components (electron gun, coaxial-cavity; quasi-optical system for a two beams output and collector) are developed. Table 1 summarizes major design parameters.

Table 1: Design requirements for a 170 GHz 4 MW CW coaxial-cavity gyrotron.

Operating frequency f_0	170 GHz
RF output power P_{out}	4 MW
Total interaction efficiency η_{tot}	> 35 % (without depressed collector)
Peak ohmic wall loading (realistic) ρ_{wall}	< 2 kW/cm ²
Loading coaxial insert (realistic) ρ_{coax}	< 0.2 kW/cm ²
Emitter current density j_{beam}	< 5 A/cm ²

In a mode selection process one well qualified mode, namely TE-52,31, was found to deliver the desired output power and frequency. Extensive optimizations on the geometry of the interaction cavity have been performed to achieve highest efficiencies and acceptable low wall losses. All calculations have been done using self-consistent and in-stationary slow-variables code packages, which are available at KIT. In addition, the tapers of the cavity have been designed using scattering matrix codes to guarantee lowest mode conversion towards the quasi-optical output launcher and lowest backward power transmission towards the electron gun. Overall mode conversion of lower than 0.25% of the total power from the main mode is possible. A typical start-up simulation with linear voltage rise considering realistic gun parameters can be seen in Fig. 1.

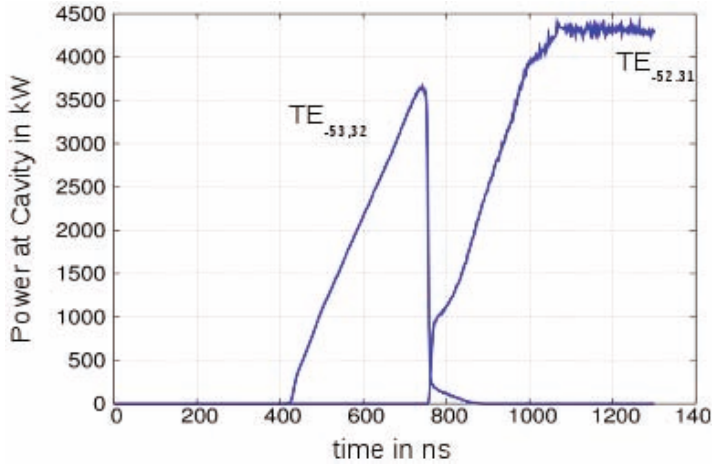


Fig. 1: Self-consistent start-up simulation for the TE-52,31 mode.

In the next step, possible diode and triode-type magnetron injection gun designs have been developed. It was possible to find suitable designs using well-known script-based optimization algorithms. Extensive parameter studies have been carried out to specify the adjustability and sensitivity of the electron beam quality to the electrical and geometrical parameters. Within a triode-type magnetron injection gun, the ratio α between the perpendicular and the axial velocity components of the electron can be smoothly tuned using the voltage applied to the modulation anode. This can be seen in Fig. 2. In addition, considering the limitation imposed by the maximum allowable electric field, the required radial dimension of a triode-type gun at the axial position of its cathode is small, compared to the diode-type gun, due to the lower modulation voltage.

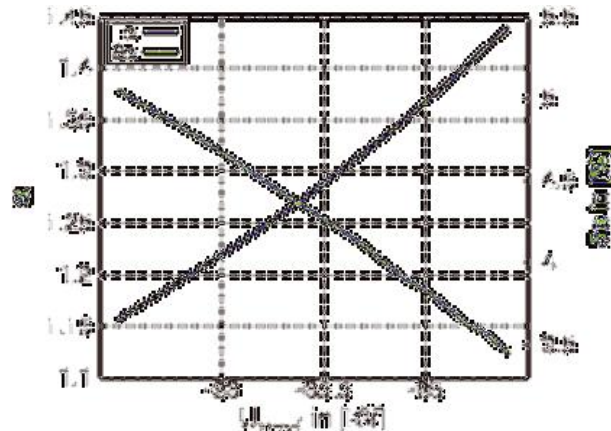


Fig. 2: Velocity ratio α and its spread over voltage applied to modulation anode.

Electron Devices (TED) in Velizy, France, which started already in 2009. Possible collector layouts will be examined considering traditional OFHC copper and new copper alloys as material. The focus will be on the development of advanced transversal and radial magnetic sweeping systems to reduce the loading of the collector wall.

Several thermo-mechanical studies will be performed to optimize the heat exchange at the collector wall and to examine long-pulse operation effects.

Staff:

M.H. Beringer
S. Illy
J. Jin
S. Kern
J.C. Rode
M. Thumm

Literature:

- [1] M.H. Beringer, S. Illy, S. Kern, M. Thumm, *Recent Design Steps Towards a 4 MW 170 GHz Coaxial Gyrotron for Future Fusion Devices*, Book of abstracts 5th IAEA Technical Meeting on ECRH Physics and Technology for Large Fusion Devices, February 2009, Gandhinagar, India, p. 29
- [2] J.C. Rode, M.H. Beringer, S. Illy, S. Kern, M. Thumm, *Magnetron Injection Guns for a 4 MW 170 GHz Coaxial Gyrotron*, Proc. 10th International Vacuum Electronics Conference, April 2009, Rome, Italy, pp. 96-97
- [3] M.H. Beringer, S. Illy, S. Kern, J.C. Rode, M. Thumm, *Recent Design Steps Towards a 4 MW 170 GHz Coaxial Cavity Gyrotron*, 21st Joint Russian-German Workshop on ECRH and Gyrotrons, May 2009, Greifswald, Germany
- [4] J.C. Rode, M.H. Beringer, S. Illy, S. Kern, B. Piosczyk, M. Thumm, *Diode and Triode Type Magnetron Injection Guns for a 4 MW 170 GHz Coaxial-Cavity Gyrotron*, 21st Joint Russian-German Workshop on ECRH and Gyrotrons, May 2009, Greifswald, Germany
- [5] J.C. Rode, *Design Study of Magnetron Injection Guns for a 4 MW 170 GHz Coaxial Gyrotron*, Diploma Thesis at the Institute for Pulsed Power and Microwave Technology at Forschungszentrum Karlsruhe and Institut fuer Hochfrequenztechnik und Elektronik at University of Karlsruhe, May 2009, Karlsruhe, Germany
- [6] M.H. Beringer, S. Illy, J. Jin, S. Kern, J.C. Rode, M. Thumm, *Further Design Steps Towards a 4 MW 170 GHz Coaxial-Cavity Gyrotron*, 34th International Conference on Infrared, Millimetre and Terahertz Waves, September 2009, Busan, Korea, T4C04

Synthetic diamond discs, which are suitable for microwave beams of up to 2 MW, are used as output windows for gyrotrons. Consequently a gyrotron with an output power of 4 MW needs two windows, and its quasi-optical system should convert the high order volume mode into two Gaussian-like output beams. For this conversion a launcher antenna with two cuts was designed using a newly developed KIT in-house code. The beams are radiated with a very high Gaussian-content of 97% and 98% (vector correlation coefficient) and have an azimuthal separation of 144°.

The next steps will be the design of the collector, which is to be done mainly during a period when the trainee is visiting Thales

Acknowledgement

This work was supported by the European Communities under the contract of Association between EURATOM and Karlsruhe Institute of Technology. The views and opinions expressed herein do not necessarily reflect those of the European Commission.

Electron Cyclotron System Technology for ITER (EFTS EC-Tech – Contract No. 042636 (FU06))

Overview

The ITER ECRH Upper Launcher for plasma-stabilization by mm-waves is subject to high heating during regular and extreme mechanical loads (Lorentz forces) during plasma disruptions. In the framework of the EURATOM Research Training Network “EC Tech”, numerical tools (finite elements modelling – FEM – and computational fluid dynamics – CFD – simulations) have been used to verify that the space requirements are fulfilled and that the cooling system is able to remove the heat deposited into the structure. As the design evolves and gets refined, more detailed analyses are necessary for more accurate calculations. To this end, a highly detailed electromagnetic sub-model has been developed for the upper port plug.

Furthermore, CFD simulations have been made also to check whether a low-viscosity silicon oil can be used as an alternative to water for the cooling of the W7-X 1MW gyrotron window.

Upper port plug

Structural simulation

The interaction between eddy currents (induced during a vertical disruption) and the magnetic field of ITER generates strong loads on the port plug structure. The design of the structure has been optimized to reduce its deflection. This goal is achieved by increasing the thickness of the walls in the rear part (where lower induction and higher stresses are located) and by removing, as far as possible w.r.t. the radiation protection requirements, the shielding blocks. In such modified configuration, the maximum displacement of the plug is ~9mm (Fig. 1). If the upper port is integrated in the simulation, then 2.6mm must be added (Fig. 2). The total displacement, 11.6mm, still fulfils the “13mm maximum” requirement defined by the gap to the neighbouring components.

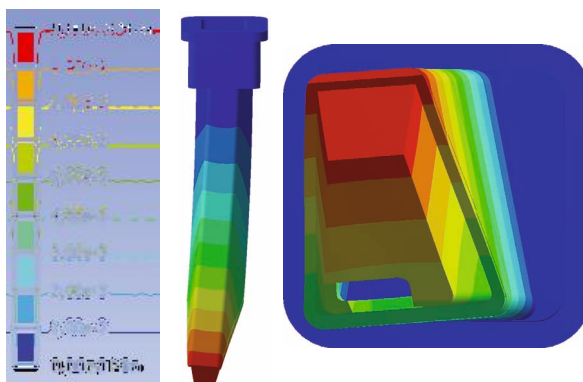


Fig. 1: Total displacement of the Upper Launcher.

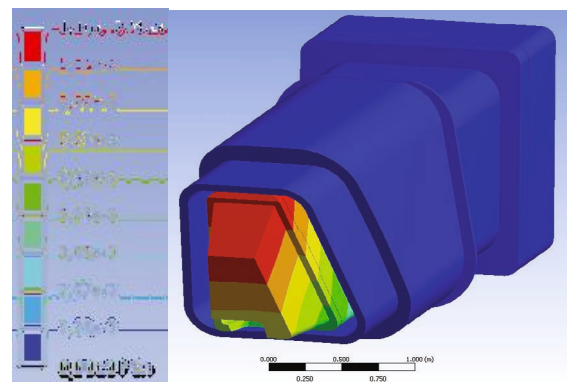


Fig. 2: Upper port integration. The deflection increases by 2.6 mm.

Improvement of the EM model

The eddy currents calculation has been made on the basis of a coarse model of the upper port plug (an example is shown in Fig. 3). The partitioning is required because of the mismatch between the geometry in the EM model and the real geometry of the port plug. Thus, better predictions can be made using a more detailed model that carefully reproduces the real geometry of the structure (at the expense of complexity). Such model has been developed and is shown in Fig. 4. It will be used for a more accurate calculation of the loads acting on the structure during VDE.

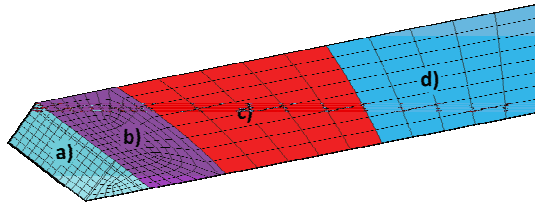


Fig. 3: EM model of the upper port plug. The geometry is only approximated.

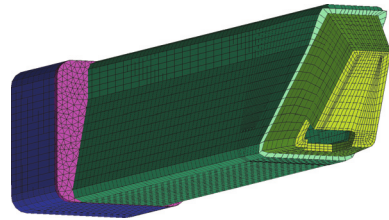


Fig. 4: Detailed EM model of the upper port plug. The real geometry is reproduced more accurately.

Blanket Shield Module (BSM) cooling

The front section of the upper port consists of a double wall structure with meandering channels for cooling. Water of 30bar pressure is flowing inside this channel for heat removal. A small portion of a corner of the BSM (corner mock-up, see Fig. 5) has been manufactured and tested at the KIT Launcher Handling Test Facility (LHT). The experimental data obtained with the prototype have been used to validate a CFD model of the same portion of the BSM. The simulation has been extended to the case of pulsed heating, by using the heat loads from the neutronics model (MCNP) described in [1]. The simulation showed that the cooling system is able to remove the heat assuring a good temperature distribution over the surfaces of the mock-up (Fig. 6).

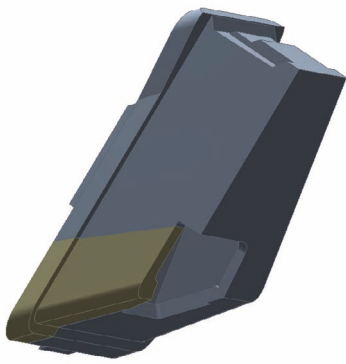


Fig. 5: Portion of the BSM where the corner mock-up has been obtained from.

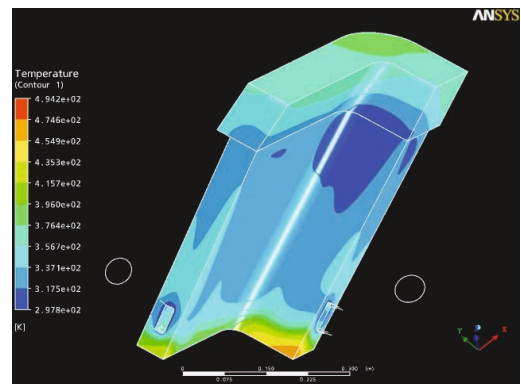


Fig. 6: Simulation of the temperature distribution in the corner mock-up during pulsed operation of ITER.

W7-X window cooling

In the diamond window assembly for the 1MW gyrotrons to be used in the stellarator W7-X, two copper cuffs are brazed to the CVD material. Because of possible corrosion of the brazing material (which would lead to window break), a silicon oil (instead of water) would be preferable as a cooling medium. CFD analyses of the cooling assembly have been performed to evaluate the performances of the DC200(R) 5cSrt silicon oil. The results indicate that this fluid would be a good alternative to water (Fig. 7 and Fig. 8).

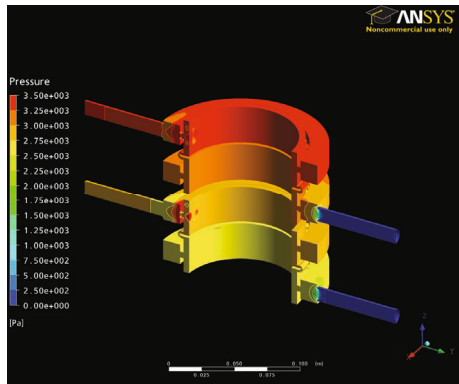


Fig. 7: Pressure distribution of water (lower model) and silicon oil (upper model) in the W7-X gyrotron window assembly.

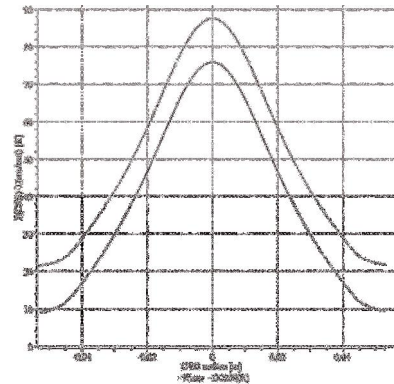


Fig. 8: Temperature distribution over the CVD window. Comparison between water (solid line) and silicon oil (dashed line).

Staff:

D. Strauß
A. Vaccaro

Literature:

[1] "Neutronic achievements in the development of the ITER upper port ECRH launcher", Arkady Serikov *et al.*, Proceedings 5th IAEA Technical Meeting, Gandhinagar, India, 2009.

Acknowledgement

This work was supported by the European Communities under the contract of Association between EURATOM and Karlsruhe Institute of Technology. The views and opinions expressed herein do not necessarily reflect those of the European Commission.

Design, Analysis and Testing of the Upper Launcher for the ITER ECH&CD System (EFDA/06-1406 - TW6-TPHE-ECHULB4 and TW6-TPHE-ECHULA)

Overview

During the TW6-TPHE-ECHULA/-B contracts, the conceptual Upper Launcher design has matured to the stage of the so-called "Mitre-Bend" design (Fig. 9), proven by simulations of regular launcher operation but also of critical plasma disruptions. Furthermore, manufacturing tests were made in a specifically built up Launcher Handling Test facility (LHT). The development could be finished in 2008 and the obtained Upper Launcher design was considered as mature enough to enter the Preliminary Design Review at ITER.

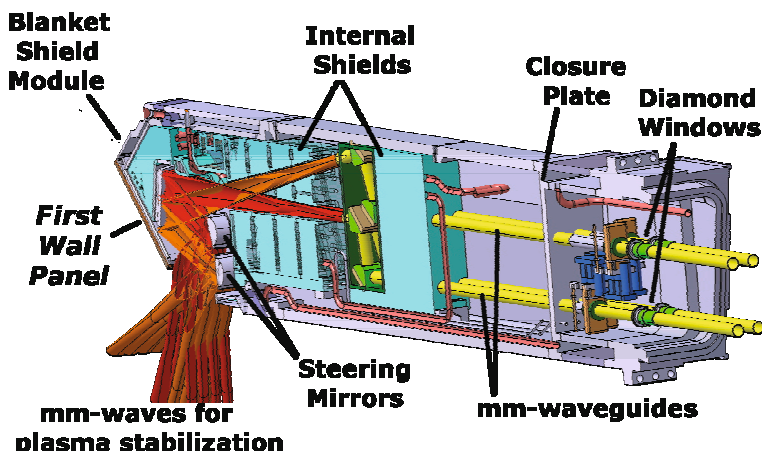


Fig. 9: The ITER ECRH "Mitre-Bend" Upper Launcher Design.

Results

In the beginning of 2009, the results were summarized and reported to F4E. Actually, the contract is being closed, while the activities have partially been continued under the contract F4E-2009-OPE-051.

Staff:

G. Aiello
W. Leonhard
A. Meier
T. Scherer
S. Schreck
A. Serikov
P. Spaeh
D. Strauß
A. Vaccaro

Literature:

- [1] T. A. Scherer, R. Heidinger, A. Meier, P. Spaeh, D. Strauss, A. Vaccaro, K. Sakamoto, K. Kajiwara, K. Takahashi (JAEA), „Prototype Testing of the Blanket Shield Module and Torus Window Assembly for the ITER ECH Upper Launcher”, 5th IAEA Technical Meeting on ECRH Physics and Technology for Large Fusion Devices”, ITER India, Gandhinagar, India, 18. – 20 Feb. 2009.
- [2] A. Vaccaro, R. Heidinger, W. Leonhardt, A. Meier, D. Mellein, T. Scherer, A. Serikov, P. Späh, D. Strauß, „Fluid dynamics and thermal analysis for the ITER ECH Upper Launcher”, 5th IAEA Technical Meeting on ECRH Physics and Technology for Large Fusion Devices”, ITER India, Gandhinagar, India, 18. – 20 Feb. 2009.

- [3] T. A. Scherer, G. Aiello, D. Strauß, S. Schreck, P. Späh, A. Meier, A. Vaccaro, „Prototyping and testing of ITER ECH upper launcher components”, 21st Joint Russian-German Workshop on ECRH and Gyrotrons (STC-Meeting), IPP Greifswald, May 11 – May 16, 2009.
- [4] P. Spaeh, R. Heidinger, K. Kleefeldt, A. Meier, T. Scherer, A. Serikov, D. Strauss, A. Vaccaro, „Structural Design of the ITER EC Upper Launcher”, 36th Intern. Conf. on Plasma Science and 23th Sympos. On Fusion Engineering (ICOPS/SOFE), San Diego (CA) 31. May – 5 June 2009.
- [5] M. Henderson, F. Albajar, S. Alberti, U. Baruah, T. Bigelow, B. Becket, R. Bertizzollo, T. Bonicelli, A. Bruschi, J. Caughman, R. Chavan, S. Cirant, A. Collazos, C. DARBOS, M. deBaar, G. Denisov, D. Farina, F. Gandini, T. Gassman, T. P. Goodman, R. Heidinger, J. P. Hogge, O. Jean, K. Kajiwara, W. Kasperek, A. Kasugai, S. Kern, N. Kobayashi, J. D. Landis, A. Moro, C. Nazare, J. Oda, I. Paganakis, P. Platania, B. Plaum, E. Poli, L. Porte, B. Piosczyk, G. Ramponi, S. L. Rao, D. Rasmussen, D. Ronden, G. Saibene, K. Sakamoto, F. Sanchez, T. Scherer, M. Shapiro, C. Sozzi, P. Spaeh, D. Strauss, O. Sauter, K. Takahashi, A. Tanga, R. Temkin, M. Thumm, M. Q. Tran, H. Zohm, C. Zucca, „An Overview of the ITER Electron Cyclotron H&CD System”, Proc. Of the 34th International Conference on IRMMW-THz Wave 2009, IEEE CFP09IMM-CDR, ISBN 978-1-4244-5417-4, Busan, Korea, 2009.
- [6] D. Wagner, J. Stober, S. Bäumel, T. Franke, F. Leuterer, E. Poli, F. Monaco, M. Münich, H. Schütz, H. Zohm, M. Thumm, T. Scherer, A. Meier, G. Gantenbein, J. Flamm, W. Kasperek, C. Lechte, H. Höhnle, A. G. Litvak, G. G. Denisov, A. Cirkov, L. G. Popov, V. O. Nichiporenko, V. E. Myasnikov, E. M. Tai, E. A. Solyanova, S. A. Malygin, „Multi-Frequency ECRH System at ASDEX Upgrade”, Proc. Of the 34th International Conference on IRMMW-THz Wave 2009, IEEE CFP09IMM-CDR, ISBN 978-1-4244-5417-4, Busan, Korea, 2009.
- [7] Theo A. Scherer, Dirk Strauss, Maika Torge, Andreas Meier, „Investigations of dielectric RF properties of ultra low loss CVD diamond disks for fusion applications”, Proc. Of the 34th International Conference on IRMMW-THz Wave 2009, IEEE CFP09IMM-CDR, ISBN 978-1-4244-5417-4, Busan, Korea, 2009.
- [8] Wagner, D.; Stober, J.; Bäumel, S.; Franke, T.; Leuterer, F.; Monaco, F.; Münich, M.; Schmid-Lorch, D.; Schütz, H.; Zohm, H.; Thumm, M.; Scherer, T.; Meier, A.; Gantenbein, G.; Flamm, J.; Kasperek, W.; Höhnle, H.; Lechte, C.; Litvak, A.G.; Denisov, G.G.; Cirkov, A.; Tai, E.M.; Popov, L.G.; Nichiporenko, V.O.; Myasnikov, V.E.; Solyanova, E.A.; Malygin, S.A., “Recent upgrades and extensions of the new multi-frequency ECRH system at ASDEX Upgrade”, US-EU-JPN RF Heating Technology Workshop, Dazaifu-City, Fukuoka, J, September; 16-18, 2009; Book of Abstracts S.14.
- [9] C. DARBOS, M. Henderson, F. Albajar, T. Bigelow, T. Bonicelli, R. Chavan, G. Denisov, D. Farina, F. Gandini, R. Heidinger, J. P. Hogge, S. Kern, N. Kobayashi, G. Ramponi, S. L. Rao, D. Rasmussen, G. Saibene, K. Sakamoto, O. Sauter, T. Scherer, D. Strauss, K. Takahashi, H. Zohm, “ECRH system for ITER”, 18th Topical Conf. on Radio Frequency Power in Plasmas, Gent, Belgium, June 24-26, p. 35, 2009.
- [10] P. Späh, R. Heidinger, K. Kleefeldt, F. Leher, A. Meier, C. Obermeier, T. Scherer, A. Serikov, D. Strauss, A. Vaccaro: Manufacturing studies of structural components for the ITER EC Upper Launcher; proceedings of the 9th ISFNT conference, 12 – 16 Oct. 2009, Dalian, China.
- [11] A. Serikov, U. Fischer, D. Grosse, R. Heidinger, P. Spaeh, D. Strauss: Nuclear safety of the ITER quasi-optical ECH launcher, SOFE 2009, San Diego, USA
- [12] A. Serikov, U. Fischer, D. Grosse, R. Heidinger, K. Kleefeldt, P. Spaeh, D. Strauss, A. Vaccaro: IEEE Transactions on Plasma Science (2009)

Acknowledgement

This work, supported by the European Communities under the contract of Association between EURATOM and Karlsruhe Institute of Technology, was carried out within the framework of the European Fusion Development Agreement. The views and opinions expressed herein do not necessarily reflect those of the European Commission.

Production of the ITER EC Upper Port Plug Preliminary Design Review Documentation (structural, diamond window and integration) and Completion of Welding Tests for the Port Plug Structure (F4E-2009-OPE-051 (PMS-H.CD))

Overview

The starting point of the contract was the ITER ECRH Upper Launcher design as delivered in the TW6-TPHE-ECHULA-B contracts. The main objectives were to integrate recent design upgrades (partially due to last minute ITER-changes of external interfaces) and to present the new design (Fig. 10) in the Preliminary Design Review at ITER which is the last major milestone before the Final Design Review followed by procurement.

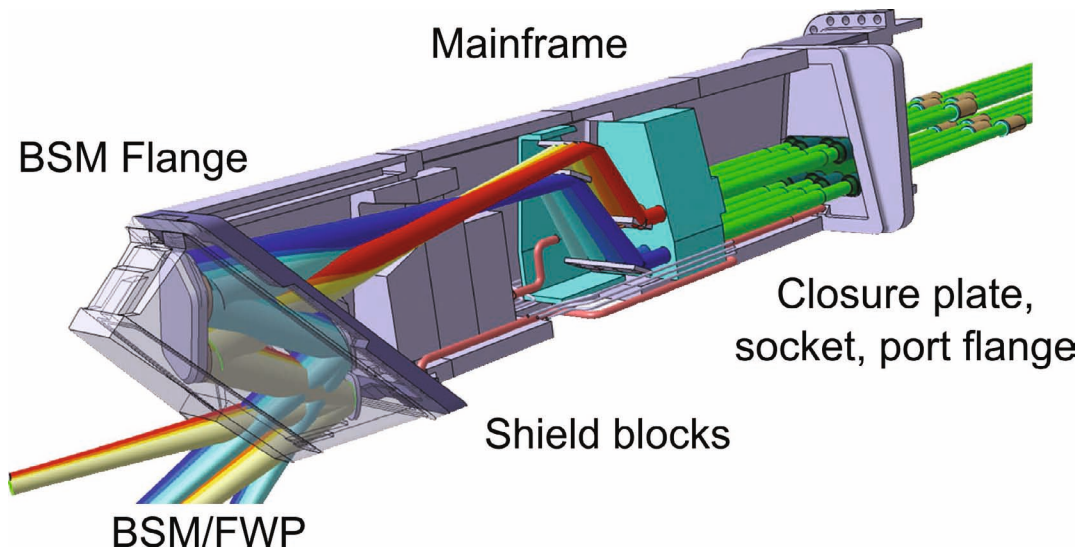


Fig. 10: Preliminary Design of the "quasi-optical" ECRH Upper Launcher for ITER.

Design upgrades

Plasma disruption mitigation

During plasma disruptions, a huge peak load is acting on the plasma facing components and, due to eddy current induction, on the other in-vessel components behind them. These eddy currents interact with the magnetic field and result in very high Lorenz forces. The upper port plug is a cantilevered structure with an overall length close to 10 m, while the gap to the neighbouring components at the first wall is limited to only 13 mm. This extreme combination of leverage and spatial confinement required design improvements of the port plug structure which are close to the physically possible. Structural strengthening generally can be achieved by adding material (thicker side walls), which at the same time leads to higher eddy current induction and therefore higher Lorenz forces. The design drivers were therefore on one hand to add material in the rear section of the plug (low induction) and on the other hand to remove material from the front section (high induction). This could be realized in the new design by increasing the wall thickness in the rear single wall section and the removal of shielding in the front section down to the acceptable limits of radiation protection. The flexibility of the design allows to nearly arbitrarily add shielding in the rear part in the case that radiation limits have to be revised (e.g. changed plasma parameters). In its current state, the design is fulfilling the gap requirement with a reasonable safety margin (< 13 mm gap, see Fig. 2).

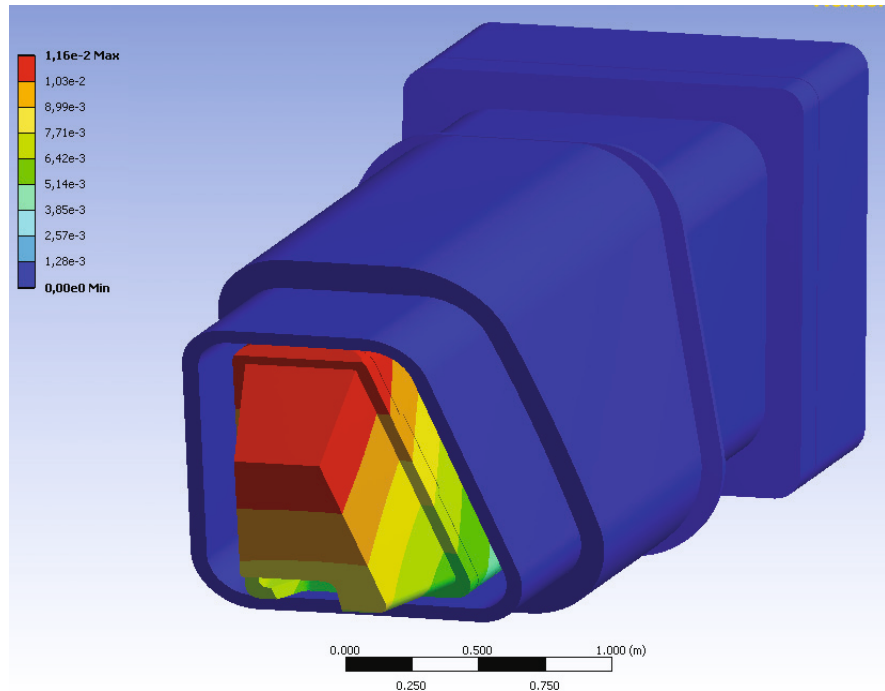


Fig. 11: Deflection of plug and port.

Enhanced plasma stabilization efficiency

The original “mitre bend” design – where the transition from waveguide beam propagation to a quasi-optical propagation occurred close to the focussing mirror in the launcher front – has been updated to a “quasi optical” design (Fig. 10), where the transition to the quasi optical beam propagation is made directly behind the waveguides in the rear section of the Launcher. As a consequence, lower losses and a higher steering range could be achieved. Especially the range increase allows the upper launchers to provide also a part of the current drive foreseen for the equatorial launcher. As a consequence, a modified equatorial launcher with both co- and counter ECCD becomes possible, allowing a better control of the plasma current profile. The new “quasi optical” design has been successfully integrated into the upgraded structural system before the Preliminary Design Review.

Adapted mainframe

A change of the cabling/waveguide/tubing layout between the upper port and the plug made an update of the cross sectional shape of the main frame necessary. Although there was a loss in available height inside the launcher, the design was proven to be flexible enough for a fast adaptation without big efforts. A benefit of the adaptation is the simpler shape of the structure, which is easier to manufacture. The flange between the mainframe and the Blanket Shield Module (BSM) has been adapted to the new geometry, and the bolting has been upgraded to the new ITER load specifications of plasma disruptions.

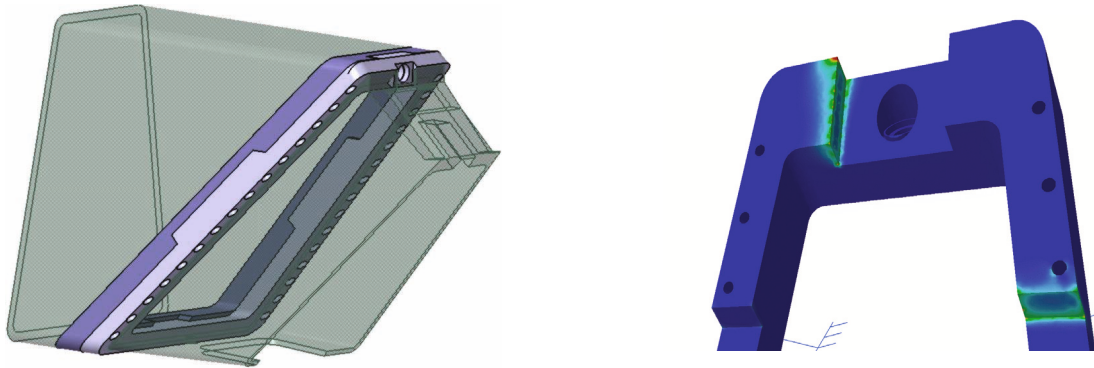


Fig. 12: BSM flange design and stress analysis of support keys.

Preliminary Design Review (PDR)

The upgraded design was presented in the PDR, where a panel of international experts reviewed the design and gave recommendations (so-called “chits”) ranging from class 1 (potential show stoppers to be resolved before going towards final design) over class 2 (issues to be resolved until the Final Design Review) and class 3 (comments). The quality of the upper launcher design has been highlighted by the absence of any potential show stoppers, and has been summarized together with a short introduction to the purpose of the four ECRH Upper Launchers in the ITER newsline #109 [1]. The further issues and comments were welcome as a useful input for the roadmap towards final design.

Staff:

G. Aiello
W. Leonhard
A. Meier
T. Scherer
S. Schreck
A. Serikov
P. Spaeh
D. Strauß
A. Vaccaro

Literature:

[1] “Launching the Launcher”, Robert Arnoux, ITER newsline #109,
<http://www.iter.org/newsline/Pages/109/1509.aspx>

Acknowledgement

This work was supported by Fusion for Energy under the service contract No. F4E-2009-OPE-051 (PMS-H.CD). The views and opinions expressed herein reflect only the author's views. Fusion for Energy is not liable for any use that may be made of the information contained therein.

Goal Oriented Training Programme “Outgassing Measurements for ITER ECRH Upper Launcher” (WP08-GOT-ITER-PPE (FU07-CT-2008-00047))

Scope

Outgassing is the gas desorption from a vacuum surface due to the temperature of the surface. Such gas will normally derive from the surface or immediate sub-surface layers of the material [1]. The measurement of the total and partial thermal outgassing rates of materials to be used for the vacuum components in ITER is necessary in order to protect the vacuum quality and reduce the contamination of the ITER plasma.

In this context, outgassing measurements have been planned for the main structural material of the ITER ECH Upper Launcher, the stainless steel SS 316L(N)-IG.

Overview of the measuring method

The selected method of measuring outgassing rates is the dynamic flow method or conductance method: the item being measured is pumped through a vacuum path with a known conductance, and the pressure difference across this path is measured. The specific thermal outgassing rate q_{th} , which is the outgassing per unit time and unit area of the desorbing surface, is given in $\text{Pa m}^3 \text{s}^{-1} \text{m}^{-2}$ by

$$q_{th} = C \cdot \frac{\Delta P}{A_r}$$

where C is the conductance, ΔP is the pressure difference across the path and A is the real area of the item. The outgassing measurements involve material samples to be inserted into a vacuum chamber and therefore, the outgassing characteristics of the chamber have to be established in a blank run immediately prior to the tests with the samples. In the formula above, the specified pressure is that obtained by subtracting the pressure reading related to the blank run from the corresponding reading related to the sample run [2].

If the speed of the pumping station used to create the necessary vacuum condition is very large as compared to the conductance, the pressure on the pump side of the vacuum path is very much lower than that on the sample side, and thus can be ignored. In this case only the pressure on the sample side of the vacuum path must be measured. A calibrated vacuum gauge measures the total pressure and the partial pressures may be determined by a calibrated mass spectrometer. Good practice requires a total pressure gauge also to be fitted downstream of the conductance path to ensure that the pressure conditions are met, but this gauge does not need to be calibrated.

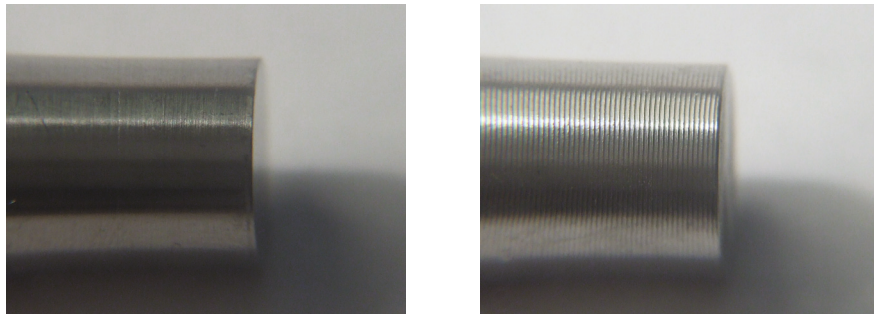
The thermal outgassing from material surfaces is temperature dependent and is also a function of the time that a surface has been exposed to vacuum (i.e. has been pumped). The outgassing results have to be presented as steady state, that is they have to be referred at the time when the rate of change of the measured outgassing rate is less than 5% over an elapsed time of 120 minutes. This is necessary in order to compare the outgassing results with the limits of outgassing rates for materials for use in ITER vacuum systems [3].

Experiment in progress

Samples and their characterization

Outgassing measurements are going to be done on samples of cylindrical shape. Up to now, SS 316L(N)-IG prototypes are not available, so SS 316 LN and SS 317 LNM samples have been chosen for the tests. They have been obtained by three different fabrication techniques: powder hot isostatic pressing, rolling, and rolling combined with solid hot isostatic pressing.

Each sample has a diameter of 10 mm and a length of 30 mm, and per each one, two different surface finishes are considered: in one case, the sample is polished (figure 1a) and in the other one, it has a surface structure with regular rills (figure 1b). This is necessary in order to take into account the effect of the surface finish on the outgassing calculations which depend on the real area of the samples.



The real surface area of the specimens has been determined by the roughness measurements performed using a non-contact optical technique: white-light is focused on the sample surface by a measuring head and the spectrum of the light scattered on the surface generates a peak in the spectrometer; the wavelength of this peak is used to determine the roughness height on the sample.

The purpose of the measurements was the determination of the surface factor of every sample, defined as

$$f_s = \frac{A_r}{A_\sigma}$$

where A_r is the real surface area and A_g is the geometrical surface area. Using f_s and the calculated geometrical area of the samples, the real one is thus obtained via the relation above. The surface factor turned out to be ~ 1.2 for the polished samples and ~ 1.8 for the ones with the rills.

The oven and its characterization

As previously specified, the outgassing is temperature-dependent and therefore, the outgassing measurements have to be done at several temperatures.

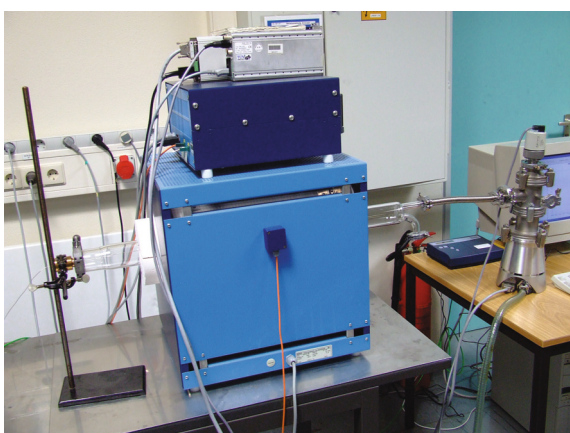


Fig. 2: Temperature calibration in vacuum

For the tests, the samples have to be put into a quartz tube of 6 cm diameter and 80 cm length. This tube is placed inside an oven connected to a proportional-integrative-derivative controller (PID controller) which allows the temperature reading of the oven. Vacuum conditions are created by a membrane pump and a turbo-molecular pump connected in series: the first pump produces the rough vacuum, while the second one creates a finer vacuum. For the moment, a Penning gauge is used to measure the pressure inside the system.

Vacuum tests have been performed for the setup without the mass spectrometer and by measuring the total inside pressure with a Pirani - cold cathode combination gauge: very good vacuum values have been reached, in the order of 1×10^{-7} mbar at several temperatures.

The temperature of the oven indicated by the PID controller does not correspond to the real temperature which occurs inside the quartz tube in the centre of the oven (i.e., where the samples have to be placed for the measurements), so a calibration was necessary.

The temperature calibration of the PID controller was done using and a K-thermocouple placed in the centre point of the oven, both at atmospheric pressure and at 1.5×10^{-7} mbar. In figure 2, the setup for the temperature calibration in vacuum condition is shown. The calibration curves obtained in both cases are shown in figure 3. The calibration has been done in the temperature range of interest for the Upper Launcher, and therefore the range covers the typical temperatures of the vacuum component during the normal operation (120-150°C) and baking operation (240°C).

During the calibration, the PID temperature was increased from 30°C up to 350°C in steps of 10°C and per each PID value, the controller was kept at this value for about 8 hours in order to reach the thermal equilibrium in the centre of the oven. The corresponding thermocouple (TC) temperature was recorded as mean value over a time period of 30 minutes (one value per second was the sampling rate of the thermocouple). The figure 3 shows that, with respect to the atmospheric pressure case, under vacuum condition the TC temperatures are higher and, as a consequence, closer to the corresponding PID temperatures; moreover they show a linear behaviour. These differences exist because during the calibration at atmospheric pressure, the extremities of the quartz tube are colder than the central part of the tube like in the vacuum case, but now are free (i.e. opened). As a consequence, natural air convective motions arise, carrying away the heat from the tube; in this way the thermocouple records lower temperatures.

For some temperatures of particular interest, i.e. temperatures in the range of normal and baking operation, the temperature profile corresponding to the length (30 mm) of the samples along the axis of the quartz tube was measured at the pressure of 1.5×10^{-7} mbar. The profiles obtained are flat, i.e., a good thermal equilibrium is reached along the samples.

Mass spectra in blank runs

Material samples have to be inserted into a vacuum chamber for outgassing measurements, and thus the outgassing characteristics of the chamber have to be determined. In the present work, the vacuum chamber is a quartz tube and mass spectra measurements at several temperatures have been performed for the experimental setup without samples.

The setup used for the measurements is shown in figure 4. The quartz tube inside the oven, is connected to a Pirani - cold cathode combination gauge on the left side, and to three components of the setup on the right side by means of an equal 4-way cross: the turbomolecular pump (which is connected in series to the membrane pump, not visible in the picture), a Pirani - cold cathode combination gauge and a quadrupole mass spectrometer.

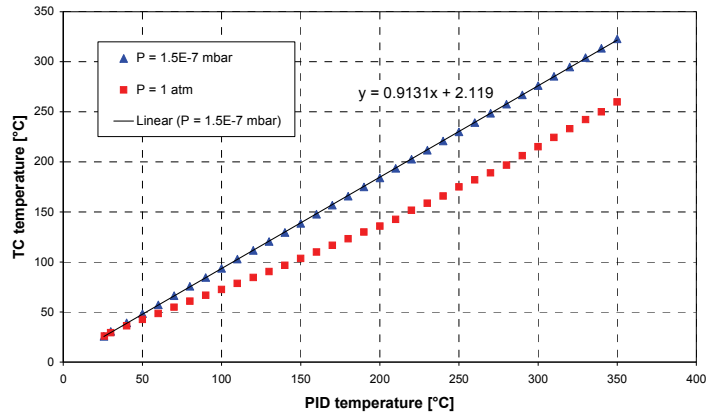


Fig. 3: Temperature calibration curves.



Fig. 4: Setup for mass spectra measurements.

have been calculated by fitting them with the Gaussian function, and these areas have been used to calculate the partial pressures. The figure 6 shows the partial pressure of H^+ as a function of the PID temperature. As expected, when the temperature increases in the system with constant volume, the partial pressures increase. According to the ideal gas law, the pressure-temperature relation should be linear. In addition, there is outgassing. Thermal desorption is an exponential function of temperature and, as a consequence introduces, non-linearity in the pressure-temperature relation.

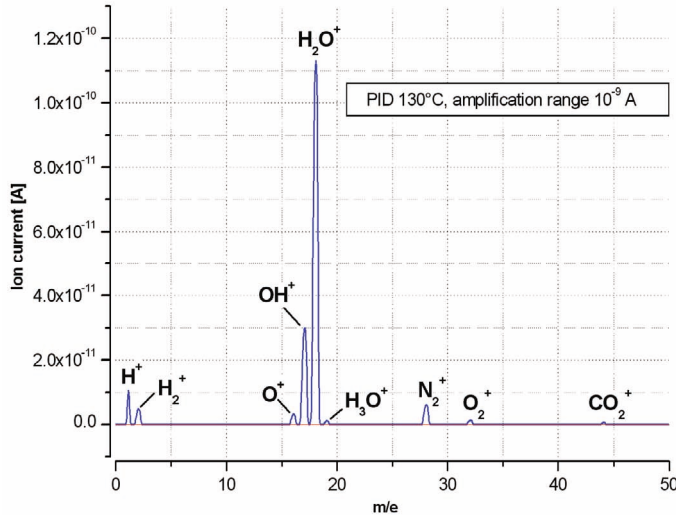


Fig. 5: Mass spectrum for 130°C PID temperature.

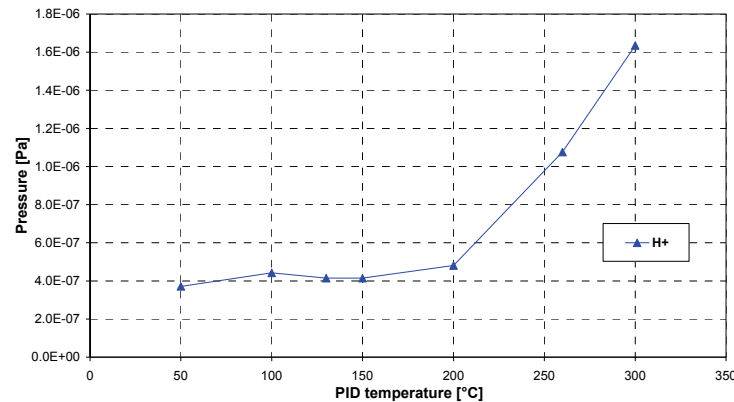


Fig. 6: Pressure-temperature relation for the H^+ peak.

Spectra have been measured at pressures in the order of 1×10^{-7} mbar, for the PID temperatures 50°C, 100°C, 130°C, 150°C, 200°C, 260°C and 300°C, and by setting the maximum value of the ion current in the measurement range to 10^{-9} A in order to appreciate the water peak.

A typical spectrum is shown in figure 5 for the PID temperature 130°C. The main peaks detected are those related to H^+ , H_2^+ , O^+ , OH^+ , H_2O^+ and N_2^+ . The percentages of water and its fragment OH are very large, so vacuum baking of the setup is necessary before the outgassing measurements. The areas under the peaks

Future steps

The experimental setup according to the selected method of measuring the outgassing rates has to be arranged: a calibrated vacuum gauge and a calibrated mass spectrometer have to be placed upstream of the conductance while the pumps (membrane pump and turbo-molecular pump connected in series) together with a non-calibrated vacuum gauge must be put downstream of the conductance path. The conductance must be very much lower than the speed of the pumping station.

The conductance is temperature dependent and, most importantly, depends on the mass of the gas species traversing the path; so it must be measured or calculated to a reasonable degree of accuracy. Before starting the outgassing measurements of the samples in different test conditions, e.g. for several temperatures and exposure times to vacuum, the outgassing measurement in a blank run has to be done immediately prior to every test.

Outgassing measurements for the SS 316L(N)-IG material must be done and the outgassing results must be compared with the limits of the outgassing rates for materials for use in ITER vacuum systems, given in the Vacuum Handbook [3], and potential consequences have to be evaluated.

Staff:

G. Aiello
T. Scherer

Literature:

- [1] ITER Vacuum Handbook Appendix 21, Glossary of vacuum terms relevant to ITER, 9 December 2008, IDM Ref: ITER_D_2F94QX.
- [2] ITER Vacuum Handbook Appendix 17, Guide to Outgassing Rates and their Measurement, 29 July 2009, ITER Ref: ITER_D_2EXDST.
- [3] ITER Vacuum Handbook, 12 June 2009, IDM Ref: ITER_D_2EZ9UM.

Acknowledgement

This work, supported by the European Communities under the contract of Association between EURATOM and Karlsruhe Institute of Technology, was carried out within the framework of the European Fusion Development Agreement. The views and opinions expressed herein do not necessarily reflect those of the European Commission.

Project funded by the Ministry for Education und Research (BMBF):

Reference: 03FUS0010

“Aufbau eines Versuchsstandes für den ECRH Upper Launcher in ITER”

Manufacturing of ITER ECH Upper Port Plug Structural System Prototypes

Introduction

The ECH launching system at the upper port level of ITER was developed under EFDA by the “ECHULA group” of EURATOM associations (ENEA/CNR Milano, CRPP Lausanne, FOM Rijnhuizen, KIT – former FZK Karlsruhe and IPP/IPF Garching/Stuttgart). The current design is based on four ECH Upper Port Plugs (UPP) for stabilising by local current drive [1] Neoclassical Tearing Modes (NTMs) and the sawtooth instability. The ECH UPPs [2] consist of the plug hull with a trapezoidal mainframe, a blanket shield module (BSM) and the first wall panel (FWP) with a cut-out for the mm-wave beams, several shield blocks for neutron shielding, a beam line with CVD-diamond windows as the first tritium barrier, and a mirror arrangement with a steering mechanism for the local current drive.

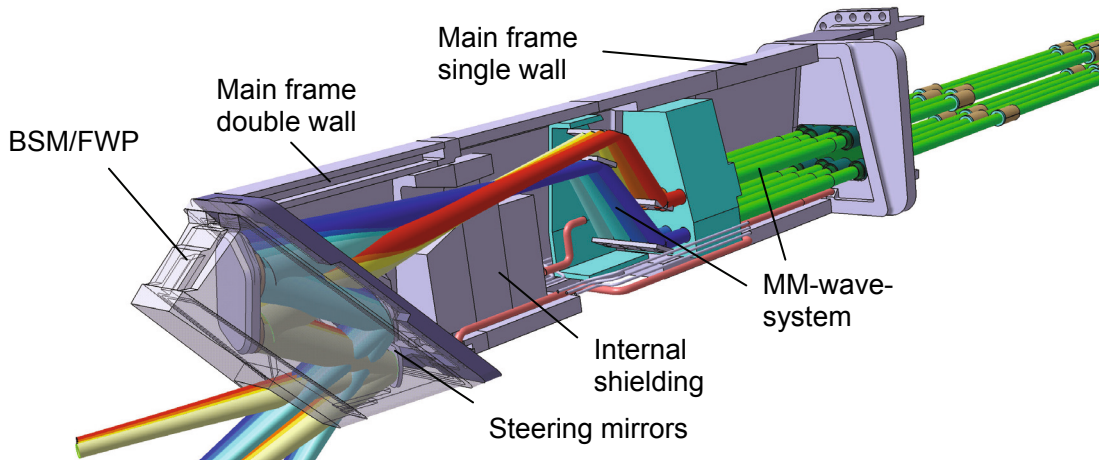


Fig. 1: The ECH Upper Port Plug launcher.

A major challenge to the structural component design is the necessity to withstand the high mechanical forces and torque moments generated by the interaction of induced currents with the strong static magnetic field [3]. The Upper Port Plug (UPP) has a length of almost 6m and is fixed as a cantilever at its back end to the Upper Port, which in turn is fixed at its front side to the vacuum vessel. The structural design has to take into account the structural integrity as well as the space requirements of the ECH system inside the launcher. With respect to the deflection of Port and Port Plug during plasma disruptions and the small gap in between those components, the need for both a rigid structure and minimum fabrication tolerance is mandatory. Therefore, the main frame of the launcher is formed by massive stainless steel structures to provide maximum moment of inertia. It is foreseen to be manufactured by a welded assembly of machined parts. To define and validate the welding of the structural system, manufacturing tests need to be performed on prototypical components [4].

Motivation for prototype manufacturing

All structural components of the ITER ECH launchers must fulfill a wide range of challenging mechanical and thermo-mechanical requirements. They have to sustain very high mechani-

cal forces, generated by plasma disruptions; by the gravity of their own and their internal components, and by pressurised cooling water. Thermal loads of up to 3 W/cm^3 apply due to radiation and volumetric neutron heating [5]. Thus, it is necessary to design a very rigid and massive structure with a wall thickness of up to 90mm. Accurate and safe welding of such massive components is not a well-described standard process, therefore tests have to be performed.

The launcher will be mounted into the upper port with a gap of 20 mm between the plug structure and the inner wall of the port. 13 mm are reserved for maximum deflection of the launcher [6] leaving a manufacturing tolerance of 3.5 mm (considering same tolerance for the port) has to be maintained for the outer wall components of the plug. Several components have to be cooled by pressurised water, leak tight weld joints for these components are required. Depending on the welding method, substantial shrinking is expected, which needs to be evaluated by manufacturing tests in advance.

To investigate manufacturing of cooled double wall components, a first prototype (the BSM corner Prototype) was manufactured and tested. The results of this task were presented in [7], [8]. For investigating the manufacturing of un-cooled structures, the so-called mainframe was selected and potential manufacturers were identified. In a tendering procedure, MAN DWE in Deggendorf, Germany, offering excellent references on plant engineering and welding assemblies of heavy components, was chosen for an industrial partnership.

Design of the single wall manufacturing prototype

The single wall section of the main frame is 3 m long and expected to be manufactured out of three segments with a length of 1m each. The thickness varies between 55 mm and 90 mm. These elements will be welded together with their face sides. Fig. 2 shows the 3D-CAD model of such a segment. In a first approach it was decided to manufacture one prototypic element with 55 mm thickness, made of the same stainless steel (SS 316L(N)IG) as it is defined in the ITER materials handbook. After a supplier survey had been done, it turned out impossible to get the use of this type of stainless steel in line with the project budget. Thus, the similar, but much more common type of steel SS 316L was chosen to be used, and because of the much lower cost of this material, manufacturing of a second prototype was possible, in order to compare the two manufacturing techniques. Certainly, the marginally different material composition will cause some minor differences of the welding parameters, but for defining the basic welding processes, it can be assumed having good compliance with the original ITER material. The most promising welding methods identified are (a) submerged TIG-welding and (b) electron-beam-welding. A benchmark test was set up to evaluate the pros and cons of these two methods.

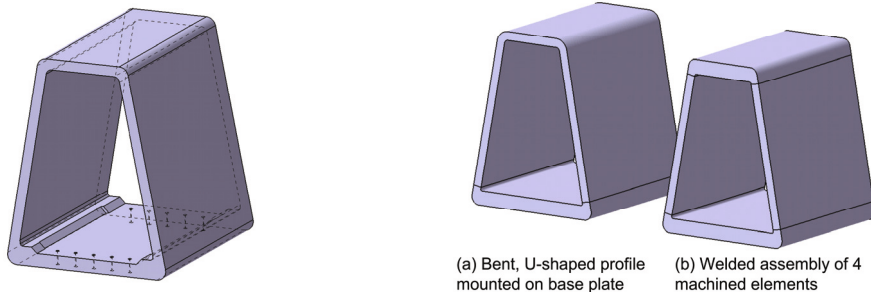


Fig. 2: 3D CAD model of the single wall prototype.

To match the trapezoidal shape with the fillets on the edges, two design principles have been considered: A big plate has to be bent twice to get a “u”-shaped profile, which must be welded onto a machined base plate (Fig. 2a). A big advantage would be the smaller number of welds, reducing the risk of shrinking. However, preliminary tests have shown that precise

bending of 55 mm steel plates would not be possible without enormous workshop equipment and a huge effort on subsequent heat treatment of the bent plate. Thus, it was decided to resort to a welded assembly of four parts: Two machined plates at top and bottom, rigidly coupled by side walls (Fig 2b). The fillets at the corners must be machined, therefore the perfectly round edges were approximated by a three-staged chamfered profile to ease manufacturing. However, for the final design the need for these fillets (e.g. because of vacuum conditions, mechanical properties, etc.) has to be proved.

The most important reason for manufacturing a prototype of the single wall main frame is gaining experience on shrinking effects, caused by welding of thick plates. It was expected (at least for the TIG-welding method), that significant shrinking would occur in vertical direction, decreasing the total height of the assembly, and also in horizontal direction, affecting the geometry of the trapezoidal profile. Two variants for the assembly of the four raw-parts were developed, where the first one features two vertical and two horizontal welds; for the second one only horizontal welds are considered (Fig. 3). The second variant was chosen though the machining effort is substantially increased, because here the shrinking process is much more predictable than for the first concept, where the welding seams are aligned in two directions.

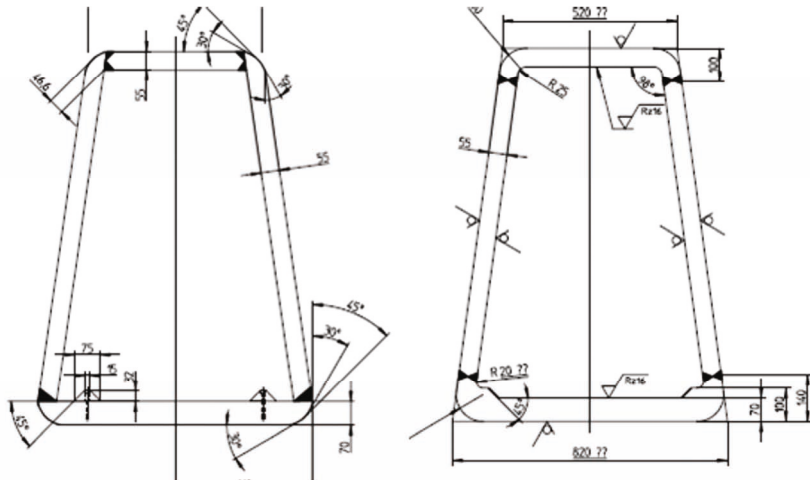


Fig. 3: Welding scheme variants of the prototype assembly.

Manufacturing process

After having established the design of the prototypes, the manufacturing process was started with the procurement of the raw parts. Quality checks showed that there are some ripple structures on the raw SS sheets, therefore the joint areas of the side walls needed additional surface machining to obtain perfect welding rims. All In-vessel components for ITER need additional surface machining because of the vacuum conditions, so this is not an additional effort; however thickness allowance on the steel sheets has to be considered. After machining the single parts, assembly schemes and welding plans were set up for both variants. For the electron-beam welded prototype, a series of test welds were performed to determine the optimum welding parameters for SS-plates with 55 mm thickness. Substantial shrinking of the component was not expected, as heat affected zone in the material is very limited. Thus, dedicated assembly frames to guarantee contour accuracy were not needed. In order to assure leak tightness of the welds and mechanical stiffness, each welded joint consists of three welding layers with different parameters. Additional extensions for setting the starting point of the weld were mounted, and the entire assembly was fixed by several spot-welds. Because of limited size of the vacuum chamber of the electron beam weld device, each weld seam was set in two successive steps. To discharge the electron beam, copper loads were mounted to the rear zone of each weld. They were removed after assembly. Fig. 4 shows the

electron beam-welded prototype. For the submerged TIG-weld prototype, a well-defined welding scheme was described to mitigate inhomogeneous deformation of the prototype. The welding parameters were set and the assembly was mounted onto a special support structure, to allow access for the welding tool, and to minimize the generation of residual stresses and shrinking in the horizontal direction. As for the electron-beam welded prototype, different types of weld seams were applied in a multi-layer configuration. Before and during the welding process, the outer contour of both prototypes was measured by means of a laser tracking system to obtain information about deformation and shrinking.

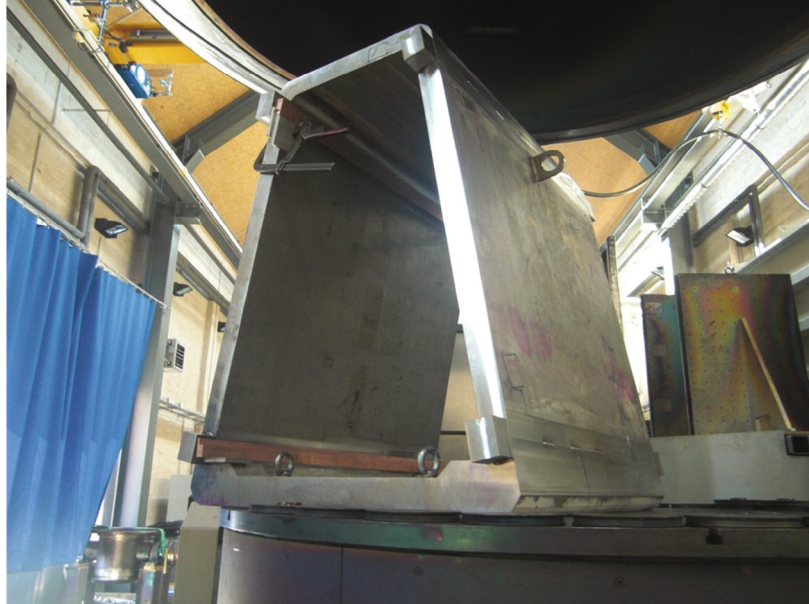


Fig. 4: Manufacturing of single wall prototype by electron-beam welding.

Analysis of manufacturing prototypes

In a first approach, both manufacturing processes were assessed to be successful. After assembly, both prototypes were measured, using again the laser tracking system. For the electron beam welded prototype, negligible vertical and horizontal deformations were observed. The submerged TIG-welded prototype showed larger deformation (as expected), but this was limited to the vertical direction. Considering this systematic effect by changing the size of the single parts, the required geometry can be perfectly matched. To evaluate the leak tightness of the welds, ultrasonic inspection, X-ray inspection and dye penetration inspection were performed. Tensile tests were made to determine the mechanical properties of the welds. Tests on residual stresses are foreseen. The evaluation of these analyses is still ongoing.

Conclusion

A conceptual design for the ITER ECH&CD upper launcher was established, and manufacturing processes for dedicated sub-components were identified. For the validation of the manufacturing processes, a first series of manufacturing tests for single and double wall components has been performed and several prototypes have been built. Analysis of contour accuracy, leak tightness and mechanical properties of the assemblies are ongoing.

Staff:

R. Heidinger
K. Kleefeldt
A. Meier
T. Scherer
A. Serikov
P. Späh
D. Strauss
A. Vaccaro

Literature:

- [1] G. Saibene et al., "Design of the ITER Electron Cyclotron Wave launcher for NTM Control", *Fusion Energy* 2006 (Proc. 21st Int. Conf. Chengdu, 2006) (Vienna: IAEA) CD-ROM file IT/P2-14
- [2] R. Heidinger et al., "Conceptual design of the ECH upper launcher system for ITER", Proceedings of the 25th Symposium on Fusion Technology, Rostock, Germany, 15th-19th September 2008, Fusion Engineering and Design Vol. 84, June 2009, Pages 284-289
- [3] D. Strauss, R. Heidinger, P. Späh, A. Vaccaro, G. Hailfinger., "Electromagnetic and structural analyses of the ECRH UPP in ITER", Yosemite National Park, CA USA, Ed. John Lohr (General Atomics Inc.) 10 – 13 March 2008, pp. 535 – 541., Proc. Of the 15th Joint Workshop on Electron Cyclotron Emission and Electron Cyclotron Resonance Heating EC15
- [4] P. Späh, R. Heidinger, K. Kleefeldt, F. Leher, A. Meier, C. Obermeier, T. Scherer, A. Serikov, D. Strauss, A. Vaccaro: Manufacturing studies of structural components for the ITER EC Upper Launcher; Proceedings of the 9th ISFNT Conference, 12 – 16 Oct. 2009, Dalian, China.
- [5] A. Serikov, U. Fischer, D. Grosse, R. Heidinger, K. Kleefeldt, P. Spaeh et al.: "Overview of recent nuclear analyses for the ITER ECH launcher in ITER", Proceedings of the 9th ISFNT Conference, 12 – 16 Oct. 2009, Dalian, China.
- [6] A. Vaccaro, R. Heidinger, W. Leonhardt, A. Meier, D. Mellein, T. Scherer, et al.: "Fluid dynamics and thermal analysis for the ITER ECH Upper Launcher", Proceedings of the 5th IAEA Technical Meeting on ECRH Physics and Technology for Large Fusion Devices, Gandhinagar, India, 18-20 Feb. 2009.
- [7] P. Späh, R. Heidinger, K. Kleefeldt, A. Meier, T. Scherer, D. Strauss, A. Vaccaro: "Prototyping studies for the Blanket Shield Module of the ITER ECH Upper Port Plug", Proceedings of the 25th Symposium on Fusion Technology, Rostock, Germany, 15th-19th September 2008, Fusion Engineering and Design Vol. 84, June 2009, Pages 1789-1793
- [8] T. Scherer, R. Heidinger, A. Meier, P. Spaeh, D. Strauss, A. Vaccaro, et al: "Prototype Testing of the Blanket Shield Module and Torus Window Assembly for the ITER ECH Upper Launcher", Proceedings of the 5th IAEA Technical Meeting on ECRH Physics and Technology for Large Fusion Devices", Gandhinagar, India, 18. – 20 Feb. 2009.

Acknowledgement

This work was financially supported by the Ministry of Research and Education (BMBF) under the grant No. 03FUS0010. The views and opinions expressed herein do not reflect necessarily those of the BMBF or the European Commission.

Magnet Structure and Integration

Materials Cryogenic Testing (EFDA/07-1704-1604 (TW6-TMSM-CRYOGT))

Background and objectives

The mechanical testing of materials for magnet components at cryogenic temperatures is needed. The following tests shall be carried out: tensile properties, fatigue properties, and thermal contraction tests for the selected magnet component materials at cryogenic temperatures (4-77 K).

For tensile, fracture toughness, and fatigue crack growth rate tests, the cryogenic test facility working at < 7 K will be used. The materials to be tested include metals, metal composites, and glass/resin composites. The tests shall be carried out at the facilities and with the equipment available at the cryogenic laboratory of KIT, CryoMaK.

Scope of contract

The scope of the contract is described as follows:

- Fatigue life tests on the chosen structural materials
- Cryogenic mechanical characterization of structural materials and welds according to the task progress
- Tensile strength and fatigue properties tests for the selected candidate structural materials at cryogenic temperature (4-7 K)
- If required thermal expansion and thermal conductivity measurements of the structural and non-structural materials at the cryogenic temperature range.

TF butt weld

To obtain the mechanical properties of full size butt welded TF conduit material five tubes (43.7 x 2 mm and 1.5 m long) with butt welds were provided for tensile test by Nippon Steel and JAEA Japan, see figure 1. As the tubes have to be clamped in a way that no slipping occurs, a special clamp is designed made from INVAR 36 and 1.4429 (316L) material to use the high strength of the material and the different thermal expansion to get a better friction and clamping force, see figure 3.



Fig. 1: Picture of the butt welded TF tubes.

Tensile tests are performed on flat tensile specimen taken of TF tube material (figure 2). The specimen are machined by EDM and tested at 4.2 K, the results are summarized in table 1. One full-size tube is tested at RT, see figure 4.



Fig. 2: Specimen TFb from base material area and TFw taken of weld area. Specimens TFw1 to 4 after test. The failure occurs within weld area.

Table 1: Results of specimens taken of base material TFb and at TF tube weld TFw.

Filename	Temperature	Young's Modulus	Yield Strength	Ultimate Tensile Strength	Uniform Elongation	Total Elongation
-	K	GPa	MPa	MPa	%	%
TFb-1	4	189.6	1006	1518	33.4	33.5
TFb-2	4	189.9	1015	1540	36.2	40.9
TFb-3	4	211.1	1034	1561	41.5	43.4
TFb-4	4	197.9	1096	1601	37.1	43.1
TFw-1	4	211.8*	1011*	1515	30.5	32.5
TFw-2	4	189.1*	986*	1512	32.8	33.1
TFw-3	4	208.1*	916*	1501	30.1	34.2
TFw-4	4	215.6*	932*	1494	28.2	28.2

* As the material is not homogeneous, the results of Young's modulus and yield strength are biased by weld area and HAZ

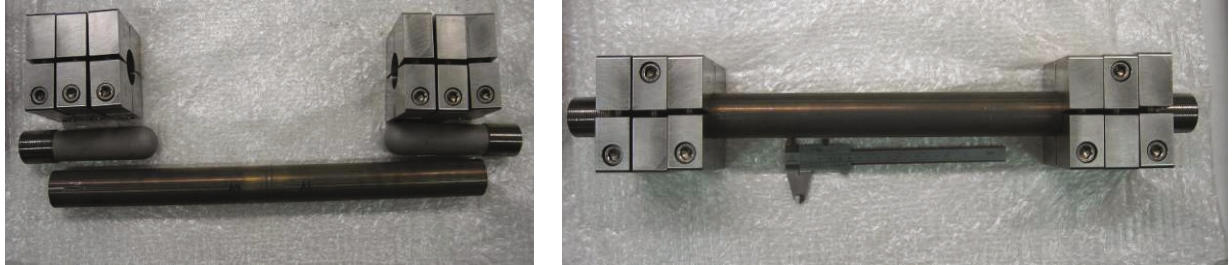


Fig. 3: Detailed view of gripping device, the diameter of the inner bolt is reduced from tip going to the thread. The ends of the tube have cut slits to deform the tube on the inner bolt by clamps.

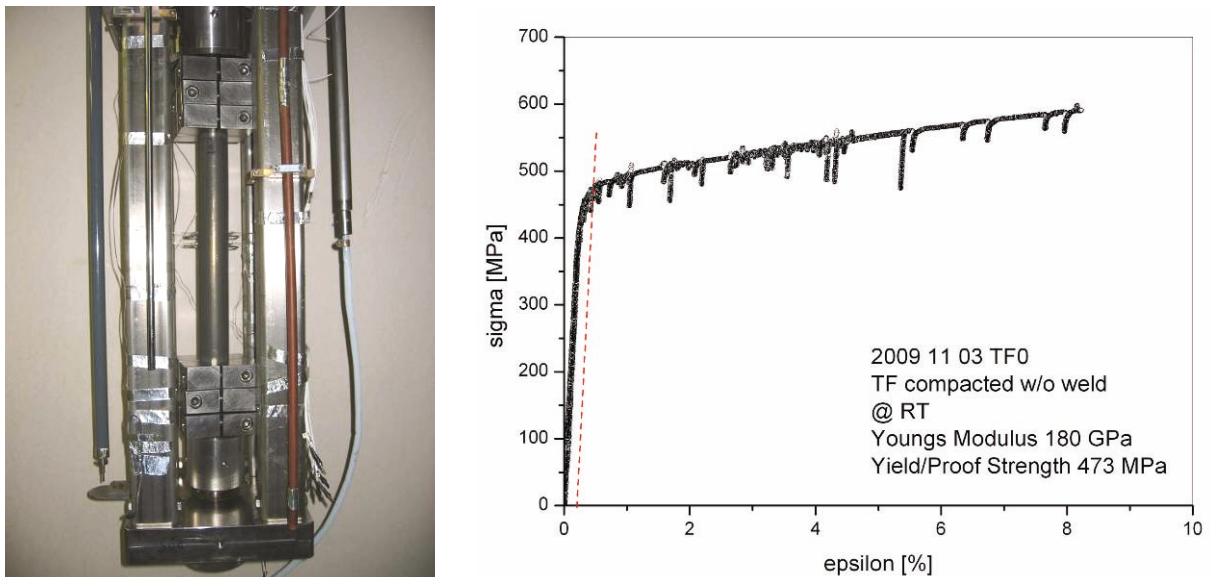


Fig. 4: Full-size tube mounted within testing rig and stress strain diagram of measurement.

PF-conduit

First PF conduit material samples were provided by ENEA, Frascati for several tests to be performed. Small size specimen and compact tension specimen were taken from this conduit to be tested according to specification by F4E. To perform fracture toughness experiments according to J-integral ASTM E 813 / JIS 2284 with 5 mm thick CT-specimen a new mounting device was fabricated.

Not compacted PF conduit material was provided and specimens were taken of this material.

The results from the tensile tests are summarized in table 2 showing typical values for uncompacted PF conduit material. However, the corner specimens show a slightly higher mechanical performance, owing to the deformation and compaction during tube manufacture within the corner region.

The J_q gives 450 N/mm resulting in $K_{IC} = 300 \text{ MPa m}^{0.5}$. The high value for K_{IC} is in good correspondence with the low determined yield strength of the face specimen in table 2 (A1-A4).

Table 2: Specimens according to PF specification (A1-A4). Additional specimens from corners (A5-A7).

Filename	Temperature	Young's Modulus	Yield Strength	Ultimate Tensile Strength	Uniform Elongation	Total Elongation
-	K	GPa	MPa	MPa	%	%
A1	4	183.8	596	1544	26.5	26.9
A2	4	177.5	583	1514	36.5	36.5
A3	4	204.4	571	1517	35.0	42.6
A4	4	178.8	575	1514	37.7	43.4
A5	4	195.0	868	1557	39.3	45.6
A6	4	207.4	867	1547	36.9	36.9
A7	4	191.7	822	1559	31.6	32.0

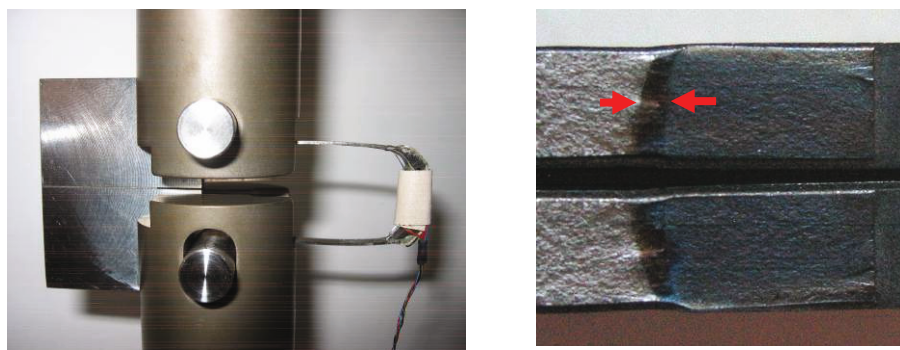


Fig. 5: On the left the mounted CT specimen on the right side the fracture area (within red arrows J-integral).

Pre-compression-ring material

Samples taken from the pre-compression-ring were provided by ENEA, Frascati for tests at cryogenic temperature. Here compression tests are foreseen on material (glass fiber epoxy

composite) taken in the different geometric directions. In figure 7 the four different sample types are shown. Figure 6 gives the stress-strain diagram of the compression tests. The results are summarized in table 3. Sample PCR2 was not measured as it is equivalent to PCR1.

Table 3

Filename	Temperature	Compression Modulus	Yield Strength	Ultimate Strength	Maximum Compression
-	K	GPa	MPa	MPa	%
PCR1	RT	56.4	-	795	1.4
PCR3	RT	19.3	144	180	1.9
PCR4	RT	20.8	158	180	1.7
PCR1	4	60.7	-	1129	1.8
PCR3	4	31.7	-	354	1.0
PCR4	4	31.5	-	492	1.5

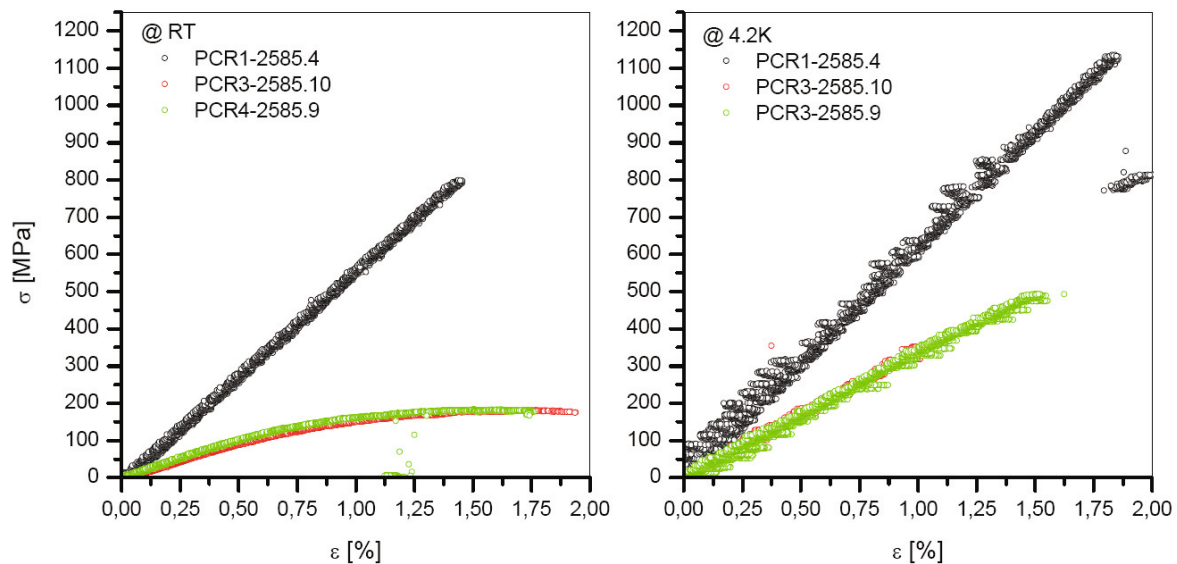


Fig. 6: Stress-strain diagram of compression tests.



Fig. 7: Showing geometry of compression sample PCR1 (steel caps), PCR2 with 8 mm diameter and PCR3 (radial), PCR4 (transversal).

Push-through experiment on 3x3 CICC array

To test the insulation material in shear mode of a 3x3 cable in conduit array of EDIPO conductor cross section, push-through technique was used to compare the results with former experiments. The measurement was done under compression using a pushing steel plate adjusted to the middle sc-CICC and a counter mask (see figure 8). From each of the two samples, using glass fabric with and without size material, three different specimens were cut with the height of 15 mm, 20 mm, and 25 mm. The specimen was cooled down force free to 4.2 K and initially loaded during measurement.



Fig. 8: Setup for the push through experiment.

In table 4 the achieved maximum load is listed and with the measured outer steel area of the conductor the shear strength is obtained. The results are similar to the ones obtained in former experiments.

From this it seems that the specimens using glass fabric with size material achieve higher shear strength values compared to the specimens using desized glass fabric. However, due to the low number of specimens (three with different height) the result has to be handled carefully. This kind of test also is not ideal to measure the real shear strength possible for the insulation material as debonding between steel conduit and insulation material occurs. Therefore bending experiments will be done on especially machined specimens to measure the interlaminar shear strength ILSS.

Table 4: Results of the push-through experiment.

Filename	Temperature	Max. Load	Area d x c*	Shear-Strength
-	K	kN	Mm ²	MPa
Glass fabric with size material ("nicht entschlichtet")				
NE-15	4	33.87	15 x 52.6	42.9
NE-20	4	37.37	20 x 52.6	35.5
NE-25	4	70.86	25 x 52.6	53.8
Glass fabric without size material ("entschlichtet")				
E-15	4	17.89	15 x 52.6	22.6
E-20	4	32.20	20 x 52.6	30.6
E-25	4	33.62	25 x 52.6	25.5

* height d and measured circumference of sc-CICC steel tube

ILSS test on special bending specimens made from 3x3 CICC array

As the push through experiment showed debonding of the steel material and the insulation material, it was decided to try to cut small size three point bending specimens from the remaining cable in conduit array material, see figure 9. Still at some samples one steel side was ripped off due to internal stress relaxation while cutting the conduit material. These specimens are with reduced thickness in table 5. As can be seen the values are significantly higher than for the push through experiments reported in table 4.

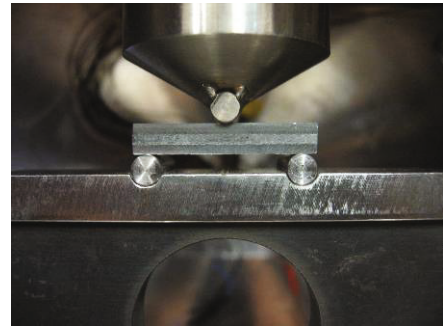


Fig. 9: Setup for the bending experiment for ILSS determination. $\sigma_{ILS} = 0.75 \text{ Pm} / (\text{b h})$.

Table 5: Results from ILSS test.

Filename	Temperature	Maximum Load P_m	ILSS σ_{ILS}	$b \times h$ / Remarks
-	K	kN	MPa	mm x mm
E01	RT	2.72	72.9	8x3.5 / desized*
E02	RT	2.40	44.1	8x5.1 / desized
E03	4	3.75	68.9	8x5.1 / desized
E01b	RT	2.77	74.2	8x3.5 / not desized*

* one steel side broke off during machining of specimen

Staff:

A. Ehrlich
K.-P. Weiss
S. Westenfelder

Acknowledgement

This work, supported by the European Communities under the contract of Association between EURATOM and Karlsruhe Institute of Technology, was carried out within the framework of the European Fusion Development Agreement. The views and opinions expressed herein do not necessarily reflect those of the European Commission.

Current Leads for Wendelstein 7-X and JT-60SA

Current Leads for Wendelstein 7-X

The stellarator W7-X presently under construction at the Greifswald branch of the Max-Planck-Institute for Plasma Physics consists of 50 non-planar and 20 planar coils with a maximum conductor current of 17.6 kA. KIT will deliver the current leads for the magnet system. In total 14 current leads are required (maximum design current $I_{\max} = 18.2$ kA, nominal current $I_{\text{nom}} = 14$ kA).

Prototype current lead manufacturing

Since the continuation of the work for the W7-X current leads in October 2008, the qualification programme for the manufacturing and assembly of all components required for the current lead assembly, e.g. by using mock-ups is almost completed. All materials and half-pieces required for the prototype current lead manufacturing are available and this is almost the case for the components required for the series production. In particular all HTS stacks will be manufactured and delivered until the end of 2009.

The brazing process for the stainless steel to copper connection at both ends of the copper heat exchanger has been optimized together with industry to obtain a good and reproducible contact.

The closure of the helium space of the heat exchanger which is a critical manufacturing step because it has to be rather tight to prevent a bypass for the helium flow, was successfully performed and checked by a pressure drop measurement using He at room temperature. It has been decided to introduce this measurement in the qualification process for the heat exchanger which will follow immediately the He leak tightness and pressure test required by the national authority (TÜV).

The soft soldering of the HTS stacks in the grooves of the 12 fold prism of the stainless steel support structure turned out to be problematic due to the tolerances of the stack thickness which could not be made as tight as required for the vacuum soldering process. Thus the procedure was changed to a soldering under nitrogen gas atmosphere and qualified in strong interaction with the supplier of the HTS stacks. Recently the coating of the soldered stacks with Parylene was qualified also together with industry. Fig. 1 left shows a picture of the HTS module for the prototype current lead.

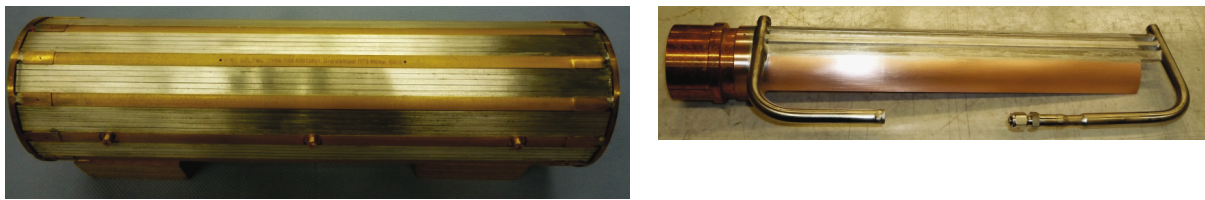


Fig. 1: Prototype of the HTS module (left) and of the cold contact including the contact cooling (right).

The Nb_3Sn inserts required for the cold contacts of the current lead were fabricated for both the prototype and series current leads, the reaction heat treatment and brazing was performed for the prototypes. Fig. 1 right shows a picture of the cold contact end including the contact cooling.

The design of the Paschen tight HV-insulation for the prototype current leads has been investigated this year by building mock-ups and is being completed now. Some emphasis has been done for the qualification of the epoxy resin to be used for the insulation regarding electrical and mechanical strength. The main result of this investigation was that the stainless

steel part which has to be insulated shall be well prepared; it turned out that Edelkorund blasting gives the best surface to have a good mechanical contact to the epoxy.

The manufacturing procedure of the HV insulation of the current lead outer vacuum tube has been carried out in closed cooperation with industry and was successfully tested under Paschen conditions.

The design and manufacturing of the Paschen tight insulation of the cold contact region (connection area of the current lead to the W7-X bus bar), the so-called "cold pot", has been manufactured together with industry, and was qualified and tested successfully. The second part of the qualification process is the dismounting and re-assembly of the cold pot from the bus bar support which is presently under investigation. Fig. 2 shows the picture of the mock-up of the cold pot including HV insulation and conductive paint layer.

The mock-ups for the components were then used to qualify the final current lead assembly. Parallel to this assembly, tools were developed and optimized for use of the manufacturing of the prototype current leads. Fig. 3 shows a picture of the current lead mock-up.

Due to the tight schedule, the qualification process using the full-size mock-ups and the manufacturing and assembly of the prototypes are done in a very close conjunction. The status is that the mock-up is completed and both prototypes will be finished for final assembly in the test cryostat end of January 2010. After installation in the test cryostat the prototype test is planned to start in April 2010.



Fig. 2: HV-insulation
mock-up - left:
glas/G10 insula-
tion, right: mock-
up covered with
conductive paint.



Fig. 3: Mock-up of the W7-X current lead.

Preparation of test facility

Due to the work performed for the refurbishment of the TOSKA facility in 2007 and 2008 for a possible series test of some of the W7-X non-planar coils, the construction work for the current lead test facility CuLTKa was delayed and can not be finished for the prototype test of the current leads in time. To keep the schedule it was decided to adapt TOSKA for the prototype test. In the mean time, the TOSKA piping was modified, the test cryostat is being completed, and the connection piece between the test cryostat and the TOSKA vessel is under construction. Fig. 4 shows a CAD drawing of the TOSKA vessel including the test cryostat and the power cables connected. A LN_2 test of TOSKA was performed in December 2009 successfully.

Parallel to this effort, the construction of CuLTKa is continued. The design of the valve box, control box, valve test box and the various transfer lines was continued. One main issue was the refurbishment of the platform located in test hall 406 which will host all cryostats together with the measurement cabin. Fig. 5 shows a picture of the platform during construction. A second issue was the high current connection between the 30 kA power supply, located in

the basement of test hall 406/2 and CuLTKa. For this purpose a channel has been made which will house the high current water cooled cables. High and low voltage electronics which are required to measure all sensors being at HV potential are under development. The present planning expects the readiness of CuLTKa until mid of 2011.

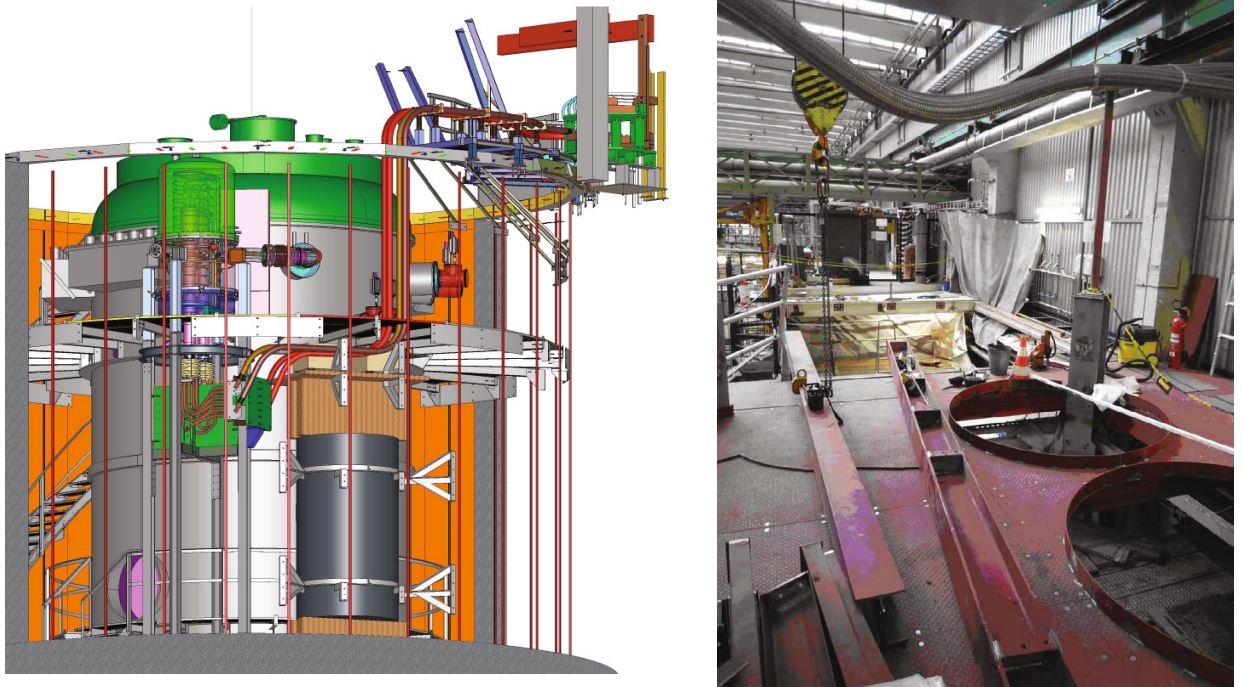


Fig. 4: CAD drawing of modification of TOSKA for prototype test of W7-X current leads including test cryostat and power cable connections.

Fig. 5: CuLTKa platform during construction (Nov 2009).

Current Leads for JT-60SA

In the frame of the Broader Approach Agreement between Japan and the EU and concomitantly to the ITER project, a satellite tokamak project called JT-60SA has been agreed. The magnet system of JT-60SA consists of 18 toroidal field coils (25.7 kA), 4 central solenoid modules (20 kA) and 7 poloidal field coils (20 kA). Following the commitment of the German Government to the EU, KIT shall design, construct and test the current leads. In total 6 leads for a maximum current of 26 kA and 20 leads with a maximum current of 20 kA, mounted in vertical, upright position are required. The plasma and basic parameters of JT-60SA are defined by Japanese and EU Satellite Tokamak Working Groups considering its mission.

The status is as follows:

- Presently the procurement arrangement for the HTS current leads for JT-60SA is being finalized by JT-60SA EU home team in conjunction with KIT. Part of the PA is the Technical Specification which is also being finalized. The Agreement of Collaboration is being finalized in parallel as well. Signature of both documents is expected at the beginning of 2010.
- The order for the HTS stacks required for the TF as well as for the CS/EF current leads has been placed. The specifications are in conjunction to those already performed for the stacks needed for the W7-X current leads.
- In conjunction to the preparation of the Technical Specification, a first design of the HTS current lead for TF coils of JT-60SA has been performed. The detailed design for both the TF as well as the PF/EF current leads will be done in 2010, after completion of the prototype current leads for W7-X and after the interfaces are agreed.

Staff:

W7-X CL:

W.H. Fietz
R. Heller
M.S. Darweschsadt
G. Dittrich
S. Fink
U. Fuhrmann
M. Gehrlein
R. Heger
M. Heiduk
C. Lange
V. Leibbrand
R. Lietzow
I. Meyer
T. Möhring
R. Müller
R. Rotondo
U. Saller
E. Specht
V. Zwecker
A. Kienzler
C. Molnar
T. Vogel
P. Wagner-Nagy

JT-60SA:

W.H. Fietz
R. Heller
B. Ganninger
M. Gehrlein
R. Heger
C. Lange
T. Möhring
U. Saller
A. Opitz

Literature:

- [1] W.H. Fietz, R. Heller, A. Kienzler, R. Lietzow, "High Temperature Superconductor Current Leads for WENDELSTEIN 7-X and JT-60SA", IEEE Transactions on Applied Superconductivity, 19 (3) (2009), 2202-2205
- [2] P. Keller, M. Schwarz, K.P. Weiss, R. Heller, A. Jung, A. Aubele, "Electromechanical and Thermal Characterization of Stacked Bi-2223 Tapes at Cryogenic Temperature", IEEE Transactions on Applied Superconductivity, 19 (3) (2009), 2893-2897
- [3] W.H. Fietz, R. Heller, A. Kienzler, R. Lietzow, "Status of HTS current leads for WENDELSTEIN 7-X and JT-60SA", Fusion Engineering and Design 84 (2-6), (2009), 776-779
- [4] M. Schwarz, K.P. Weiss, R., W.H. Fietz, "Thermal conductivity measurement of HTS tapes and stacks for current lead applications", ", Fusion Engineering and Design 84 (2-6), (2009), 1748-1750
- [5] R. Heller, A. Class, A. Batta, R. Lietzow, H. Neumann, M. Tischmacher, "Modelling of the fin type heat exchanger for the HTS current leads of W7-X 3 and JT-60SA", accepted for publication in Cryogenics

Acknowledgement

This work was financially supported by the Ministry of Research and Education (BMBF) under the grant No. 03FUS0013 and is done in the Project JT-60SA under the Broader Approach Agreement between Europe and Japan. The views and opinions expressed herein do not reflect necessarily those of the BMBF or the European Commission.

Definition of Procedures for Coil Electrical Testing and PF Transient Analysis (EFDA/06-1522 (TW6-TMSC-COILMO))

Introduction

Fast high voltage excitations on large superconducting coils can lead to internal non-linear voltage distributions or even oscillations within the coils and thus to increased high voltage stress on different locations. For the calculation of the maximum conductor, layer and ground insulation voltage of the ITER PF coils a PF CS coil model was established. For detailed analysis the PF 3 and PF 6 coils were selected, because PF 3 has the largest main radius of the PF coils and PF 6 the largest number of turns.

In addition, test procedures for ITER TF coils were established derived from a prior calculation of the transient electrical behaviour of the TF coils [1] and experiences gained in practice by testing of the ITER TF Model Coil.

Strategy on Calculation of Voltage Stress for PF coils

The calculations of voltage stress within the PF 3 and PF 6 coils were started with calculations in Finite Element Method (FEM) programme and are continued by calculations in network programme. The flow chart of the calculation strategy is shown in Fig. 1. With the specified geometry and materials the FEM-model of the coil was established. The FEM-model was used to calculate frequency

dependent inductances of the coil. The capacitances between the turns and to grounded parts of the coil were calculated analytically with formulas for parallel plate and cylindrical capacitances. The calculated values were taken into a network model of the coil as lumped elements. The values for resistances of the superconducting windings in network model were set to 100 pΩ due to the very low resistance of superconducting turns of the coil. The calculations with the network models were separated in frequency and time domain. In the frequency domain the resonance frequency of the coil was calculated, which gives the first benchmark on the electrical behaviour of the coil for different transient voltage excitations as they appear during the fast discharge. The resonance frequency for symmetrical grounding of the PF 3 coil was calculated to be 25.5 kHz and for PF 6 coil to be 32.0 kHz. The resonance frequency of the PF 3 and PF 6 coils for symmetrical grounding with instrumentation cables were calculated to be 24.4 kHz and 30.7 kHz respectively.

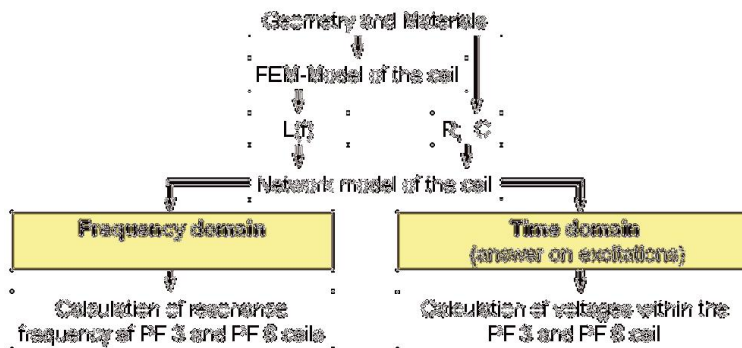


Fig. 1: Calculation strategy of voltage stress within the coil.

Networks of PF Coils and Switching Circuits

The detailed calculations of the voltage stress on different kinds of insulation within the coils in time domain makes it necessary to establish the network models of the different discharge units like Fast Discharge Unit or Switching Discharge Unit. As an example Fig. 2 shows the network model of the Fast Discharge Unit for PF 6.

After completion of the system modelling the relevant current and fault scenarios were discussed with F4E and ITER organisation and 4 different scenarios were selected for further examination:

- Fast discharge without earth fault
- Reference scenario without earth fault
- Failure case 1: Currents set to rated values, voltages set to maximum values but without booster converter, fast discharge with earth fault
- Failure case 2: Currents set to 10 kA, voltages set to maximum values with booster converter, fast discharge with earth fault.

The results of the calculations of fast discharge showed that higher voltages on the coil terminals were calculated than the values given in [2]. The maximum voltages calculated on the positive and negative terminals of PF 6 coil are 3.4 kV and -5 kV, respectively. The maximum voltage between the coil terminals was calculated to be 7.7 kV. The higher voltages on the coil terminals are caused by the discharge of the counterpulse capacitor Cc-FDU-PF6 shown in Fig. 2. This fast transient procedure was not considered in [2], where the maximum voltage between the terminals was given with 5 kV.

The maximum voltage on ground insulation within the coils during fast discharge was calculated to be 12 kV, which is even higher than the voltage on the coil terminals. Such behaviour is possible for fast transient voltage excitations within a large coil. This effect was calculated and measured on ITER Toroidal Field Model Coil (TFMC) [3].

Present activities are concentrated to a defined reference scenario in case of no fault occurrence.

In addition, high frequency measurements on low and high temperature superconductors were performed which confirm the new modelling practice with reduced PF turn resistance [4].

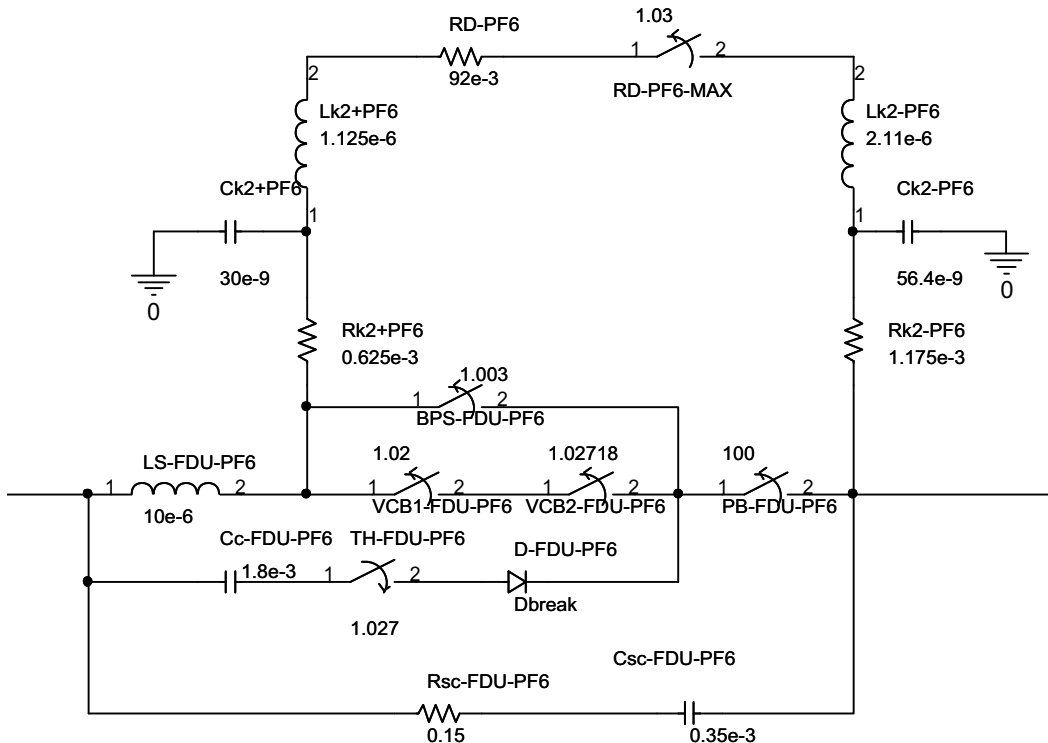


Fig. 2: Network model of the FDU of the PF 6 coil.

High Voltage Test Procedures for the ITER TF Coils

The transient electrical behaviour was investigated for fast discharge and 2 fault events in a prior study [1]. Additionally high voltage testing experience was gained during high voltage acceptance tests and the tests which were performed during two current operation phases with the ITER TF Model coil.

Derived from these experiences it is proposed for ITER TF coil high voltage acceptance test to start with a DC test followed by an impulse test. Then a further DC test should be performed. As a next step a series of DC and AC tests is proposed to test conductor, radial plate and ground insulation individually. Such a full acceptance test is recommended for all ITER TF coils after completion of fabrication under ambient conditions, for a cold test and after warm up.

For room temperature conditions a Paschen test is necessary, too. But for cryogenic conditions a Paschen test is not recommended because it would require a special cryostat.

The test voltage value is depending on the fault scenarios which are considered as to be mastered by the TF coils without damaging. The most severe fault scenario which was examined during the transient calculations assumes a malfunction (or trigger delay of several ms) of 2 neighbouring fast discharge units which causes a voltage increase in the discharge system of the 18 TF coils on certain locations. Further it is assumed that – as a consequence of this voltage increase – an earth fault occurs at one of the two locations with the maximum voltage to ground at the time with the highest voltage to ground. As a consequence a further change in the TF coil system would appear leading to further voltage increase on another TF coil. Derived from this fault scenario test voltages for ground insulation till 34 kV and for radial plate and conductor insulation till 11 kV are proposed. The compatibility of these voltage values for radial plate and conductor insulation had been shown with 10 h tests with 11 kV DC and 11 kV / $\sqrt{2}$ AC on the ITER TF model coil [5]. For ground insulation a test with 34 kV on the ITER TF model coil was not possible because the ITER TF model coil has a fault – but the principle compatibility of a test voltage of 34 kV can be derived by experiments with the Polo coil which had a ground insulation thickness similar to the present ITER TF design.

Staff:

A. Winkler
S. Fink
W. H. Fietz

Literature:

- [1] A. Fink, W. H. Fietz, A. M. Miri, X. Quan, A. Ulbricht, Study of the Transient Volt-age Behaviour of the Present ITER TF Coil Design for Determination of the Test Voltages and Procedures, Forschungszentrum Karlsruhe, Scientific Report FZKA 7053, 2004
- [2] ITER Design Description Documents, Annex 6B, 2.4 Fault and Safety Analysis, N41RI3500-11-01W0.1
- [3] S. Fink, A. Ulbricht, H. Fillinger, A. Bourquard, M. Prevot, "High voltage tests of the ITER Toroidal Field Model Coil insulation system", IEEE Transactions on Applied Superconductivity, Vol. 12, Issue 1, 2002, pp. 554-557
- [4] A. Winkler, M. Noe, Th. Schneider, Frequency Behaviour of the Impedance of Superconducting Coils, Journal of Physics: Conference Series, EUCAS 2009, to be published
- [5] S. Fink, A. Winkler, W. Fietz, M. Noe, Definition of Procedures for Coil Electrical Testing and Preparation for PF Transient Analysis, FZKA 7483, 2009

Acknowledgement

This work, supported by the European Communities under the contract of Association between EURATOM and Karlsruhe Institute of Technology, was carried out within the framework of the European Fusion Development Agreement. The views and opinions expressed herein do not necessarily reflect those of the European Commission.

Quench Detection System for Fusion Magnets

Introduction

After the successful quality assessment of the W7-X - quench detection system at test facilities of CEA/Saclay at the end of 2008, the Max Planck-Institute of Plasma Physics / IPP Greifswald performed a tender procedure for manufacturing of appr. 600 additional quench detector units (QDUs). Completion of production (executed at Prettli electronic manufacturing company located in Lübeck/Germany) is expected by the end of 2009.

The quench detection system was developed by Karlsruhe Institute of Technology (KIT) (formerly Forschungszentrum Karlsruhe GmbH), at the Institute for Data Processing and Electronics - IPE. IPE also manufactured a pilot lot of 160 detectors at its assembly facilities.

The detector properties of the production run could be verified and confirmed by repeating all tests (e.g. EMC, vibration, magnetic field and high-voltage tests) successfully.



Fig. 1: IPE quench detectors UNIQUID (type: 3410) during burn-in.

Status of the IPE contributions to W7-X quench detection

With the external production of these QDUs the contribution of IPE to the W7-X ended in 12/2009. Possible future collaborations of IPE with IPP Greifswald with respect to quench detection systems could be the upgrade of IPE's quench detection system operational software package *QVision*. Latest developments of *QVision* software are related to expanding the control room link interface (remote interface of *QVision*'s supervision operating mode).

Further objectives in 2009

Definition of requirements for a quench detection system at ITER

With the beginning of 2009 a possible application of the IPE quench detection system at ITER has been discussed and preliminary technical specifications were developed. In summary, quench detection electronics for ITER are challenging.

The requirements of ITER quench detection differ substantially in some of detectors properties from those of W7-X. The ITER requirements ask for a modification of the existing electronic design.

Quench detection specification for ITER versus W7-X
(some selected criteria)

Technical requirements	W7-X	ITER Tokamak
<i>Potential separation (detector's electronic circuit to GND)</i>	13.8 KV	30 KV minimum
<i>Isolation quench signal plug (HV-Plug)</i>	18 KV max. (1 minute)	30 KV min. (permanent)
<i>HV-Input capability</i>	500 V (channel to HVGND)	5 KV (channel to HVGND)
<i>HV-Input capability</i>	1 KV (chan. to chan.)	10 KV (chan. to chan.)
<i>Transient recording time</i>	10 sec. max.	75 sec.
<i>Large signal recording</i>	not applicable	switchable (manual or automatic)

While the details of the required potential separation have mostly been worked out in 2009 (first prototypes of dedicated DC/DC-converters with 30 KV potential separation are designed and manufactured), the dimensioning of the detector input stage to withstand high transient voltages in the range to 5 KV requires a sophisticated electronic circuit redesign. In contrast to the HV input capability, small (quench-) voltages in the mV-range have to be identified by the detector. These circumstances require a very large dynamic range of the detectors input stage.

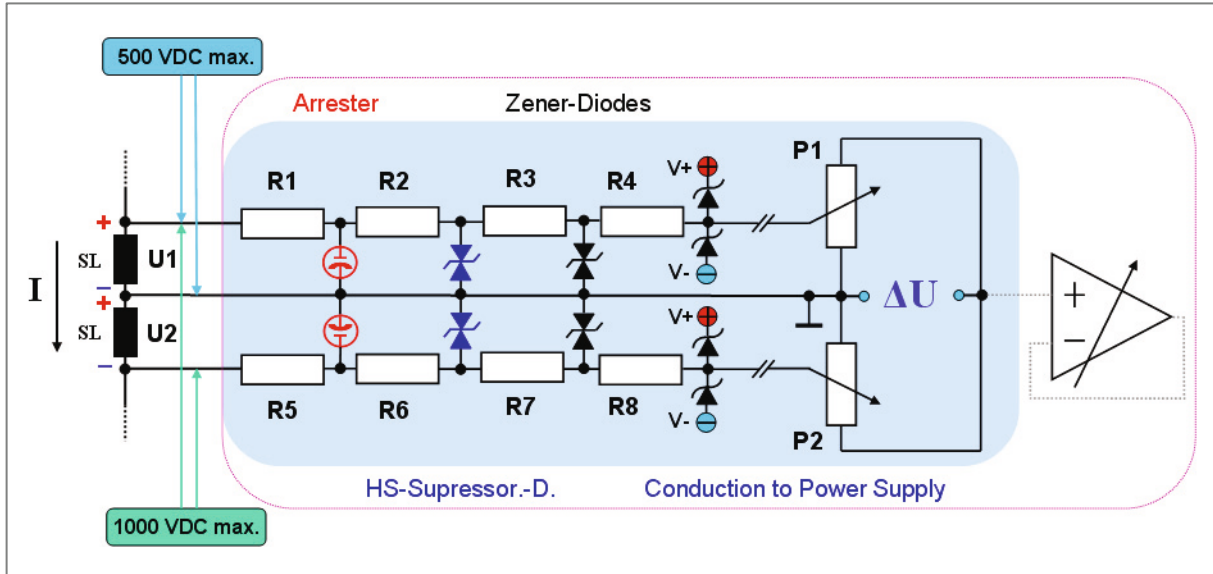


Fig. 2: Schematic of cascaded large voltage transient suppression input circuit of the present IPE quench detector UNIQU 3410.

present IPE quench detector UNIQU

Fig. 2 shows the large voltage transient suppression circuit of the present IPE quench detector. Damage of the detectors inputs is effectively prevented by the use of cascaded voltage limiting stages and additional current conduction to the detectors power supply at the last stage. The input impedance of the detector is mainly defined by the series resistors of the first stage (R1, R5).

While an input resistance of 100 kOhm (dissipation loss \approx 2 W @ 500 VDC input) is well matched to the leakage current of voltage limiting elements and input bias currents of digital potentiometer circuits, a maximum rated load of 5 KV would result in a two digit MOhm impedance at the same dissipation loss. An input impedance of 1 MOhm still would result in a power dissipation in the range of 25 W per channel (= 50 W per detector). Presently the maximum power dissipation at the IPE detector is approximately 3 W per channel. The PCB-dimensions of the detector are 100 mm * 340 mm (= 3 RU standard Euroboard module).

Starting redesign-phase of IPEs quench detector electronics at the end of 2009

To achieve a synergistic effect in developing of quench detection systems, IPE plan to reuse many components of the special board design of the present quench detector unit (type 3410). The specified properties of the ITER quench detection systems (especially large voltage input capability) will be tested based on a carefully adjusted electronic design in conjunction with new low leakage electronic devices.

IPE plan arrangements to the electronic design to obtain a high impedance of the detectors input at retention of low input offset drifts (for detecting of low voltage in the mV-range). Minimum dissipation loss is of particular importance if the present detector dimensions should be retained.

Staff:

A. Ebersoldt
K. Petry
S. Stricker
D. Tcherniakhovski

Development of HTS-ROEBEL Cables

Magnets with High Temperature Superconductors (HTS) are a promising alternative for DEMO following up ITER. Roebel-cables Assembled from Coated Conductors (**RACC**) were introduced by KIT as high current low AC conductors for application in windings of such magnets. This concept is the only so far for the second generation (2G) High Temperature Superconductors (HTS), which provides the necessary features as segmentation of the superconductor into different percolation paths (strands) which are in addition transposed along the conductor. The development is concentrating on two different routes, one with 10-12 mm wide cables for the application regime of 2-5 kA (77 K and s.f.) and narrow 4 mm wide cables for currents up to 2 kA. The narrow cables will serve as strands for future Rutherford Cables concepts with > 20 kA transport current. For 12 mm wide cables currents up to 2.6 kA were demonstrated, 4 mm wide cables achieved currents up to 1.3 kA. An important innovation in both cable types is an applied multi-stacking in the strands as a very effective design to increase the transport current.

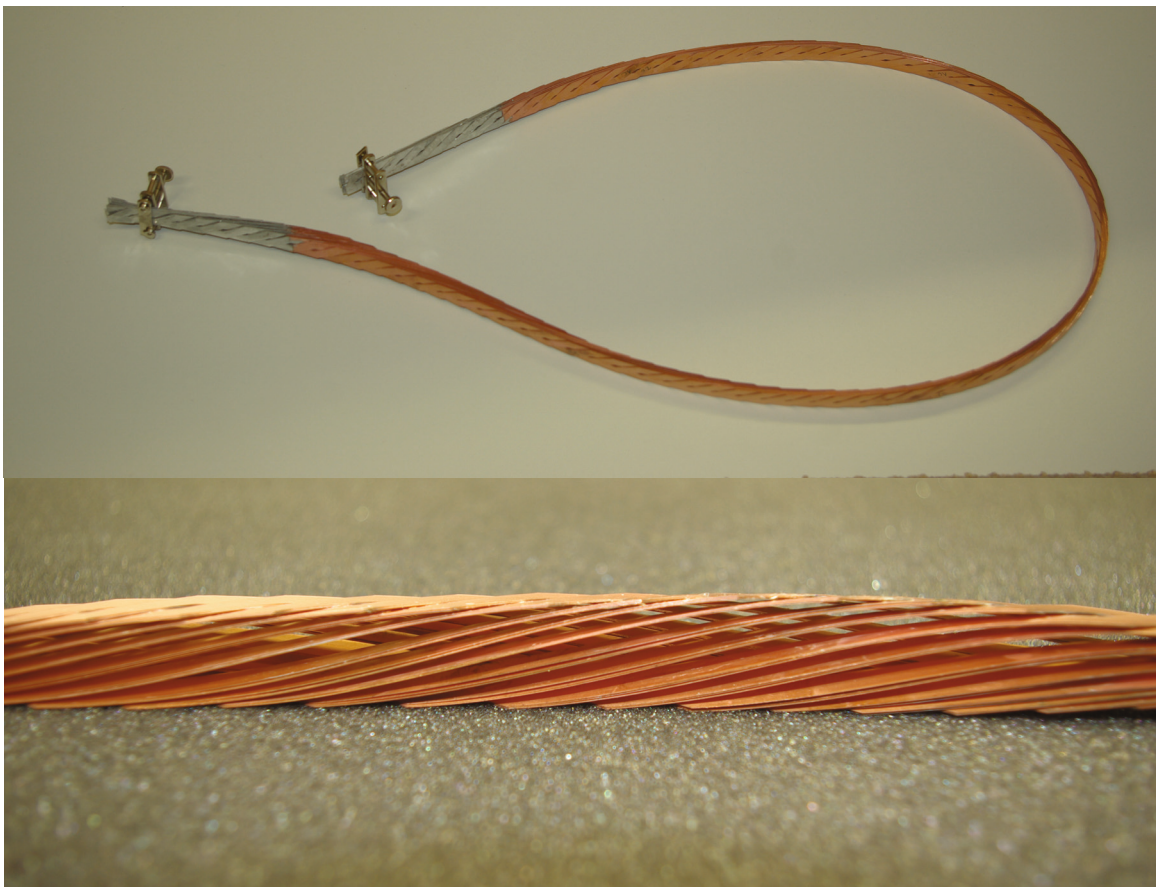


Fig. 1: A 2.6 kA HTS RACC-cable with 1.1 m length (upper fig.) and view to the spliced strands showing multistacking of strands (3-fold).

AC loss measurements were performed applying standardized pick-up-coil methods in AC fields perpendicular to the cable surface. The results, normalised to the current carrying potential, is shown in Fig. 3. The loss behaviour is well between the two approximations, the strip and ellipse cross section behaviour. The aspect ratio of the cables plays a minor role; multistacking however is proved as a powerful method to increase the cable current and to approach a square cable cross section.

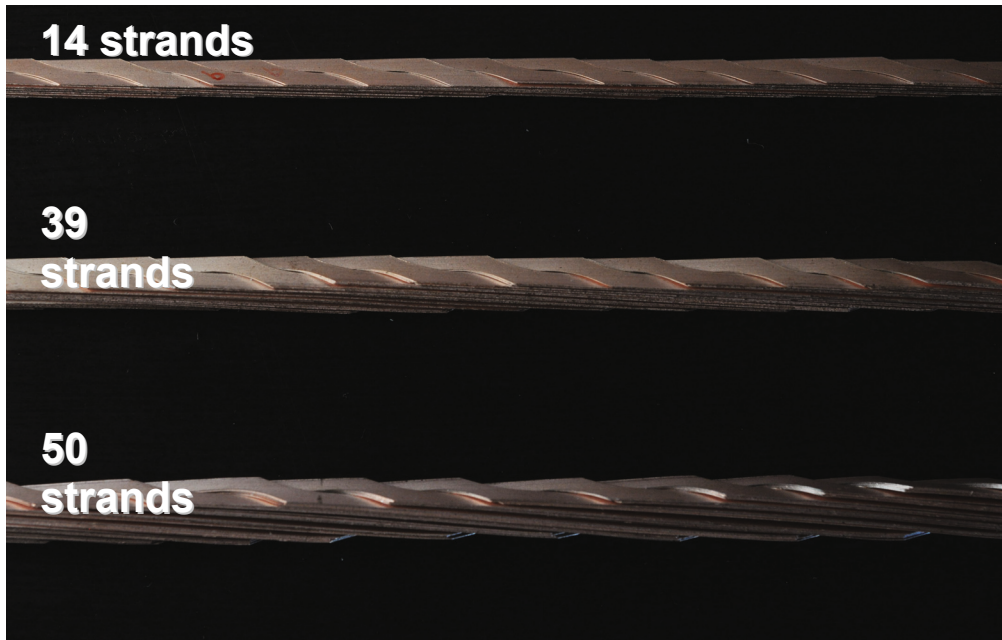


Fig. 2: Different stages of multistacking (1x, 3x, and 5x) in 4 mm wide RACC-cables with 0.46 kA, 1.1 kA and 1.3 kA transport current (77 K, s.f.)

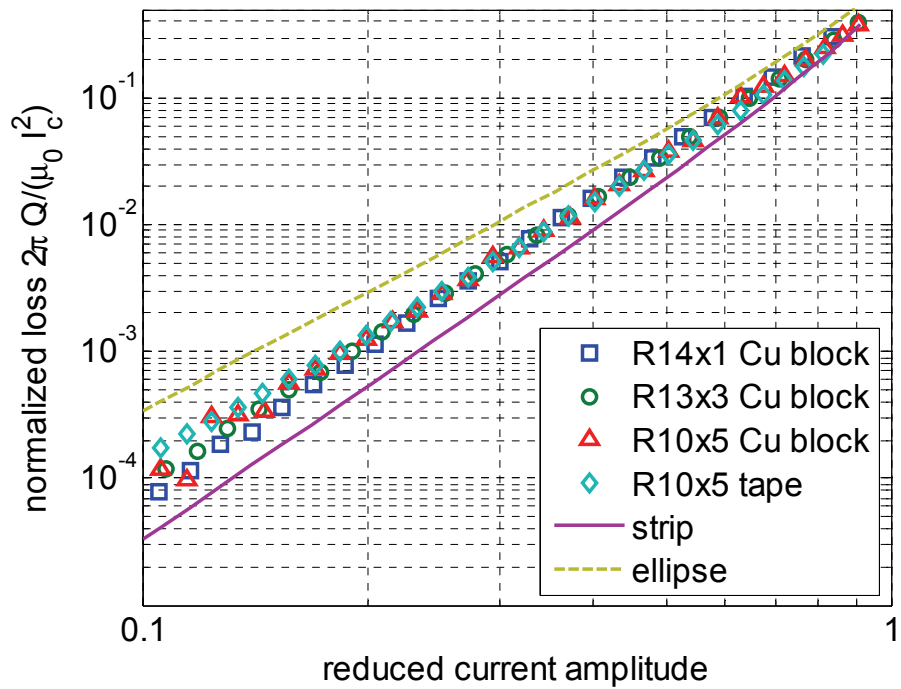


Fig. 3: AC losses measured by excitation in AC fields for the cables of figure 2 [1].

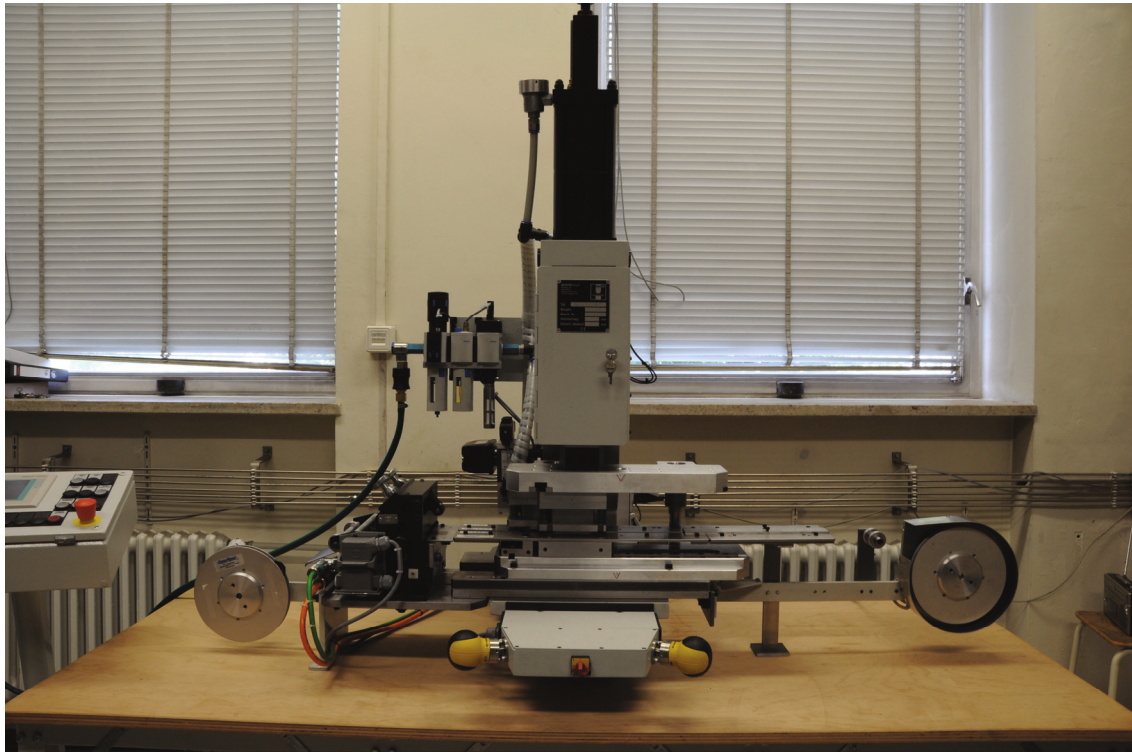


Fig. 4: Reel-to-reel automatic ROEBEL strand punching machine.

In order to come to longer lengths of cables, a reel-to-reel automatic strand punching tool was developed together with a specialized company. Operation of the device was started in July 2008. The punching technique of the former hand operated tool was used and the same accuracy was achieved. The new machine was quality approved for 4-12 mm wide tapes.

Outlook for the future: Next steps will be an optimized RACC cable with mechanical reinforcement for tests in the FBI facility, studying current vs. axial strain behaviour. Following up the automatic punching a RTR-cabling device needs to be designed and realized. Long length strands allow more complex cables as the Rutherford design [2].

Staff:

W. Goldacker
A. Drechsler
A. Kudymow
A. Kling
C. Schmidt
S. Terzieva
F. Grilli
R. Heller

Literature:

- [1] S. Terzieva, M. Vojenčiak, E. Pardo, F. Grilli, A. Drechsler, A. Kling, A. Kudymow, F. Gomory, W. Goldacker, "Transport and magnetization ac losses of ROEBEL assembled coated conductor cables: measurements and calculations" EUCAS2009 Dresden, poster
- [2] W. Goldacker, S.I. Schlachter, A. Kudymow, A. Drechsler, S. Terzieva, R. Heller, "Promising new concepts for AC CC-cables with very high currents"; CCA-Conference 2009, Barcelona, extended abstract in Proc.

Cryogenic Infrastructure

Introduction

The cryogenic infrastructure of the ITP supplies different experiments within the Institute for Technical Physics (ITeP) and other institutes of the KIT which are working for the Fusion Programme with refrigeration power or liquid helium. Such experiments in the ITeP are tests of superconductive components in the TOSKA facility, experiments for the ITER-cryopump in TIMO, and mechanical material tests in different cryostats.

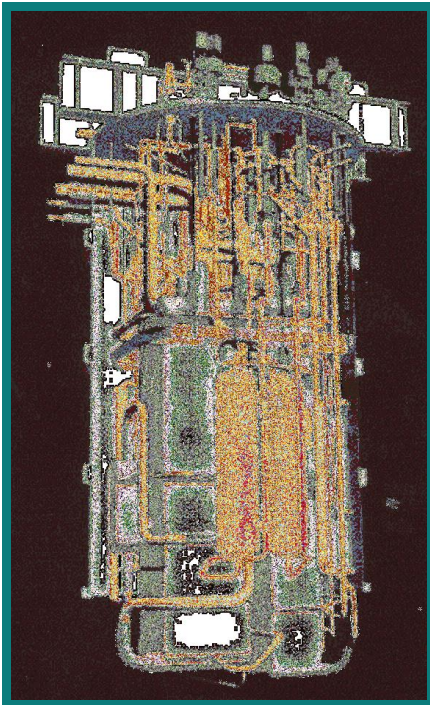


Fig. 1: Inner design of the Coldbox of the 2 kW-refrigerator.

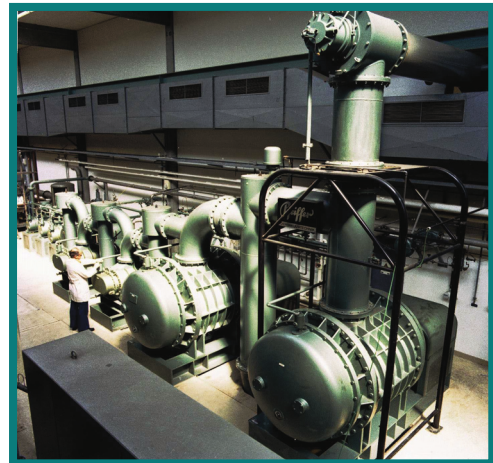


Fig. 2: 8-ary vacuum pump station of the 300 W@1.8 K-refrigerator.

For these experiments the cryogenic infrastructure comprises among other things:

- A 2 kW-refrigerator at 4.4 K with a liquefaction rate of 21 g/s (equivalent to 600 litres/h).
- A 300 W-refrigerator at 1.8 K with a liquefaction rate of 5 g/s (equivalent to 145 litres/h).
- A high pressure helium purifier working at 200 bars with a continuous purification mass flow of 14 g/s and a discontinuous purification mass flow of 28 g/s. The residual impurity content is lower than 1 ppm.
- Three recovery compressors with a pressure increase from one to 200 bars and a maximum mass flow of 26 g/s or 527 standard cubic meters respectively.
- A helium storage system consisting of:
 - stationary liquid helium vessels with a capacity of 15,000 litres or 1,875 kg respectively
 - storage tanks for impure helium with a capacity of 1,075 kg
 - storage tanks for pure helium with a capacity of 1,275 kg

The whole storage system has consequently a capacity of 4,225 kg or 23,985 standard cubic meters respectively, see Fig. 3.

- A liquid nitrogen storage vessel with a capacity of 32,650 litres for the supply of all experiments and a filling station to distribute liquid nitrogen in transport vessels.

The cryogenic infrastructure is controlled by a state-of-the-art control system based on PCS7 and WinCC. The operation of the components can be done in two control rooms or via clients installed directly at the experiments.



Fig. 3: Helium storage system.

A team of five operators, three engineers and one academic staff member is responsible for maintenance, repair, upgrading and extension of the cryogenic infrastructure for new or changed experiments.

Additional tasks are the supervision of peripheral installations such as

- Energy distribution system
- Re-cooling water unit
- Compressed air distribution system.

Also, maintenance, repair, upgrading and extension of the

- Vacuum systems
- Different safety devices like oxygen monitors

are tasks of this group.

Beyond these regularly routine work this report is focused on selected extension projects, as well as giving an overview of the cryogenic supply activities for fusion projects.

Selected maintenance and extension works

300 W (1.8 K) refrigerator

The following selected maintenance and extension work at the 300 W-refrigerator were done in 2009:

- Change of temperature sensor for the 5,000 litre LHe vessel, see Fig. 4
- New temperature sensors for the control of the water cooled oil removal
- Installation of a new mass flow meter.

2 kW (4.4 K) refrigerator

The following selected maintenance and extension works at the 2 kW-refrigerator were done in 2009:

- Upgrading and improvement of the operation stations
- Change and upgrading of vacuum measurement for thermal insulation
- Modification of the automotive valve control, the actuator and the mass flow meter of the LHe-filling-station
- Test of new turbo vacuum pumps for the thermal insulation of the Cold-box
- Modification of the working voltage

- Change of the mass flow meter for the cooling water and check with ultrasonic flow measurement method
- Change of a time relay within the control cabinet of the Freon cooling cycle together with an improvement of the ventilation of the cabinet.



Fig. 4: Change of a temperature sensor for the 5,000 litre LHe vessel of the 300 W-refrigerator.

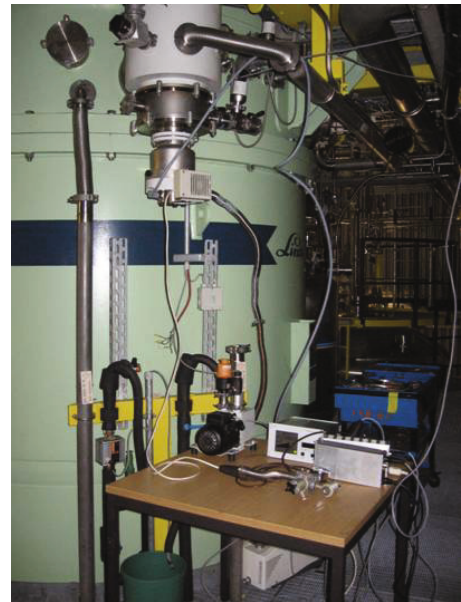


Fig. 5: Test of new vacuum pumps for the thermal insulation of the 2 kW-refrigerator.

He-recovery and purification system

The following selected maintenance and extension works at the He-recovery and purification system were done in 2009:

- Change of signals for recovery gas flow
- Connection of some control functions to the guidance system with Profibus
- Change of high pressure valves
- Inventory of gas bottles
- Changes for the noise box of the recovery compressors
 - Installation of a new ventilator
 - Change of the ventilation channels
 - Installation of a new sound absorber for the ventilator
 - Installation of a ambient air monitoring sensor system
- Revision of one recovery compressor.

Miscellaneous

- Preparation for a new connection of signals from TOSKA to the new data concentrator
- Connection of the cooling water plant to the new data concentrator
- Preparation work for the assembly of the control cabinets for CuLTKa
- Installation of a new PCS7 Engineering station.



Fig. 6: New PCS7 Engineering station.

Cryogenic supply for the Fusion Programme

The different experiments for the Fusion programme in ITeP are supplied with circa 14,200 litres liquid helium or 10,000 standard cubic meters. In addition the refrigerators ran nearly 470 hours in 2008 for the supply of refrigeration power.

For comparison, the average consumption for such experiments in the period between 2001 and 2008 is about 25,700 litres liquid helium or 18,000 standard cubic meters respectively and 2,100 hours of refrigeration power. So in 2009 we had a significantly lower consumption than the years before. This decreased consumption was caused by the time consuming structural reconstruction work for new experiments in TOSKA and TIMO which also resulted in modifications of the cryogenic infrastructure.

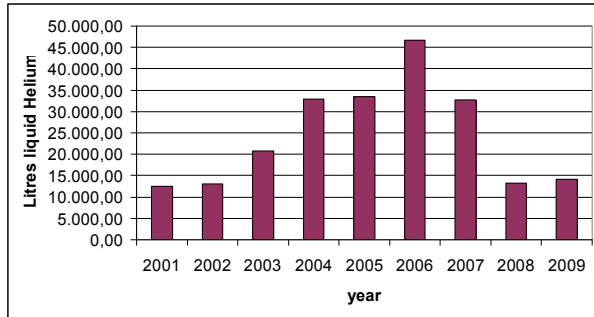


Fig. 7: Liquid Helium supply between 2001 und 2009.

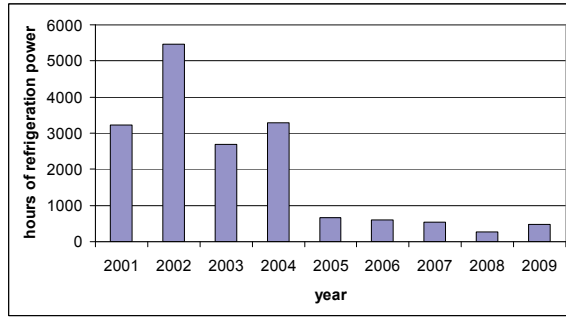


Fig. 8: Hours of refrigeration power between 2001 und 2009.

Staff:

A. Baumgärtner
S. Bobien
M. Duelli
H. Neumann
B. König
K. Metzger
E. Ternig
D. Wetzel
H. Zimmermann

Breeding Blanket and Divertor

Construction of the High Pressure Helium Loop (HELOKA-HP/TBM) for Testing of TBMs (TW5-TTB-001)

The objective of this task is to construct the HELOKA-HP/TBM loop as presented and agreed in the "EFDA HELOKA Assessment Report" in a renovated building of KIT (former FZK) comprising the purchase of loop components and supply systems, acceptance tests at the manufacturer's site, installation, commissioning and acceptance tests.

The construction of the HELOKA helium loop was started in April 2009 after the piping layout was approved by the German notified body (TÜV). The assembly of 95% of the piping is finalized. The remaining 5%, corresponding to helium circulator connecting pipes, is going to be finalized in the first half of 2010 as soon the circulator is delivered. In addition, a Dummy-Test Section has been designed and manufactured in order to close the loop when the test module is not installed. This dummy allows, in the commissioning phase, the testing of the various measurement devices (flow meter, temperature and pressure sensors) that are installed on the pipes going to and coming from the test section.



Fig. 1: Left: HELOKA construction site (hot side piping); right: test section connecting flanges.

The vacuum vessel in which the test modules are going to be installed has been manufactured and preliminary studies of the piping connecting the test module with the loop have been performed.



Fig. 2: HELOKA vacuum vessel.

All instrumentation for the helium loop (flow meters, temperature and pressure sensors) have been procured and (mechanically) installed into the loop.

The detailed design of the helium supply system has been finalized. The manufacturing of this subassembly is under way: the compressor and the valves have been procured and the contract for the helium supply construction has been awarded.

The functional design and technical specifications for the auxiliary and mains power distribution of the Helium loop, including the 750 kW electric heater and the 300 kVA turbo-circulator were finalized in the second half of the year and the tender action completed in November. The functional design and technical specifications of the control of the electric heaters, made with power thyristors, was completed also in the second half of the year and the contract awarded. The detailed design of both supplies is completed and the installation is foreseen for the end of February next year. Both electric loads will be powered from new circuit breakers, available on the market, that incorporates analogue to digital converters for the three phase voltage and current measurements as well as calculations of power factors and PROFIBUS interface with the HELOKA distributed Data Acquisition and Control System (DACS). Additionally, a local industrial WLAN was installed in the HELOKA DACS to simplify operation, maintenance and access to system drawings and documentation on the server from the field.

Staff:

S. Berberich
B.E. Ghidersa
J. Freund
E. Magnani
V. Marchese
G. Messemer
N. Prothmann

Acknowledgement

This work, supported by the European Communities under the contract of Association between EURATOM and Karlsruhe Institute of Technology, was carried out within the framework of the European Fusion Development Agreement. The views and opinions expressed herein do not necessarily reflect those of the European Commission.

Components and Instrumentation Development for TBM (TW2-TTBB-007b)

Background

The next generation of fusion machine will have to demonstrate tritium self-sufficiency, and the preliminary experiences in ITER using Test Blanket Modules (TBM) will produce important results required for the design of the DEMO breeder blanket and associated tritium processing systems.

For the Helium Cooled Pebbles Bed (HCPB) concept using lithium ceramics to produce tritium via the ${}^6\text{Li}(\text{n},\alpha){}^3\text{H}$ nuclear reaction, two adjacent helium gas loops are implemented: (a) the He purge loop consisting in the Tritium Extraction System (TES), (b) the He cooling loop equipped with a Coolant Purification System (CPS).

On-line tritium measurements mainly based on ionisation chambers are integrated all along both loops for process control and monitoring purposes. However, the precise tritium measurement here is particularly complex since tritium is present only as traces and under both molecular and oxide forms (noted Q_2 and Q_2O , respectively; Q means H,D,T). Therefore, in addition, a dedicated tritium accountancy stage (Figure 1) is mandatory as interface between the blanket tritium systems and the tritium plant. Fundamentally, the way to recover tritium within TES and CPS and the corresponding processes directly impact on the tritium accountancy stage.

Preliminary study of the tritium accountancy system as an interface between the EU TBM tritium processing systems (TES and CPS) and the ITER tritium plant systems

Based on the current design for the tritium systems in TES & CPS of ITER TBM, a preliminary design of the accountancy systems has been performed. Different approaches have been compared considering the measurement method (dynamic versus static) and the analytical techniques used, with regard to:

- Performances: sensitivity, detection limit, accuracy, time response, ...
- Operation: liability, calibration, sampling (or not), measurement time
- Integration: interfaces, space allocation
- Costs.

For the nominal TES operation, the tritium fraction in hydrogen is about 500 ppm, and hydrogen might be diluted with helium. For analytical purposes, gas chromatography has been retained as reference, mainly because it is easy to operate and maintain, and do not need high vacuum. However, the use of liquid nitrogen is required to separate the ${}^6\text{Q}_2$ isotopologues, and gas sampling is mandatory. The alternative use of Laser Raman spectroscopy (LARA) developed at TLK for the Katrin experiment has been evaluated. It would allow an on-line measurement (no sample) with remote measurement using optic fibres. Recent measurements at TLK have shown a detection limit of about 50 Pa partial pressure of tritium for a counting duration of 500 s at a laser power of 5 W. This detection limit could be improved by some orders of magnitude using a more advanced configuration, so that in principle the LARA measurement would perfectly fulfil the analytical requirements for the accountancy stage.

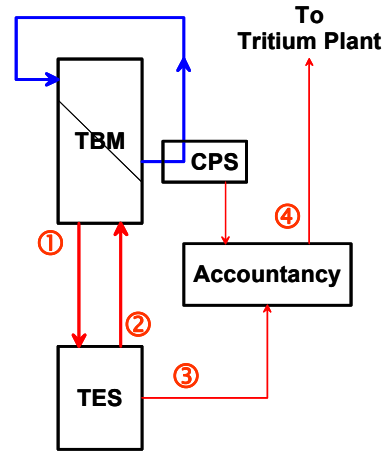


Fig. 1: Tritium management in HCPB: Tritium bred and released from the ceramic is ① extracted from the blanket in a purging mode ② removed from the purge gas ③ recovered and sent to the tritium accountancy system ④ and finally transferred to the tritium plant for further processing.

Whatever the processes used in the TES systems for tritium recovery are, it has been highlighted that the dynamic volumetric accountancy based on flow rates and activity measurements with ionisation chambers is likely not enough accurate to ensure reliable tritium tracking and precise tritium measurements mandatory for the validation of the neutronics predictions. Even if it is more demanding, a static approach based on pVT-c measurements (pressure, volume, temperature, concentration) should be implemented in order to ensure accuracy better than 10%.

As a consequence, the recovery of the tritium trapped in the Adsorption Column (AC) and the Cryogenic Molecular Sieve Bed (CMSB) needs to be carefully studied in term of load to the accountancy procedure (e.g. addition of purge gas versus vacuum pumping). It seems important to limit the dilution of molecular tritium with helium, and thus it is recommended to (a) use vacuum pumping or adopt and “indirect” regeneration for the AC (figure 2), (b) use vacuum pumping for the regeneration of the CMSB instead of a purge gas.

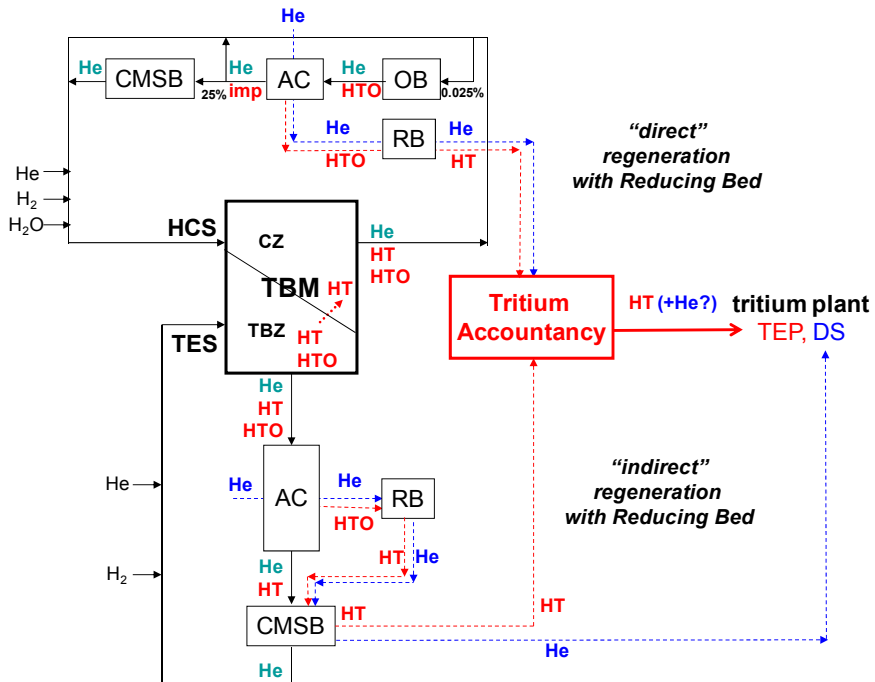


Fig. 2: Schematic representation of the tritium systems for TBM and different modes for the regeneration of the adsorption column: “direct” regeneration refers to the nominal procedure and Q_2 discharged to the tritium plant is diluted with He used for the regeneration; “indirect” regeneration enables the separation of Q_2 from He that could be discharged separately.

Finally, considering the accountancy system as interface between the blanket and the tritium plant, it seems valuable to separate in the blanket system the tritium rich streams to be sent with accountancy to the Tokamak Exhaust Processing (TEP), while the tritium depleted stream could be discharged without accountancy in the detritiation systems (DS).

Study of the possible use of a PERMCAT reactor instead of a reducing bed to recover tritium from water in the TES and CPS regeneration loops

The current design of TES and CPS comprises a reducing bed (RB) (cf. figure 2) in order to avoid water between the port cells and the tritium plant. Reduction of water over a hot metal might be in a first approach the most straightforward method. However it is not totally satisfactory with regard to operation: highly exothermic reaction, limited efficiency for conversion, limited reversibility or effort for regeneration, and production of waste.

Among different alternatives, the PERMCAT process developed at TLK is a promising candidate to recover tritium from water. The PERMCAT process relies on a catalytic membrane reactor using a hydrogen perm-selective Pd/Ag membrane, and promotes isotope exchange reactions between hydrogen and tritium bound in molecules. Operated in the so-called counter current swamping mode, PERMCAT allows a quasi complete recovery of tritium in pure molecular form (Q_2) in a one through process.

The use of PERMCAT has been carefully analysed with regard to the process and the final tritium accountancy. From the process point of view, PERMCAT is much more appropriate than water reduction, minimising waste production and ensuring efficiency higher than 99%. In addition, PERMCAT works as an “indirect regeneration” enabling to separate the feed stream into 2 different products: a tritium rich one send to the accountancy, a depleted one discharged to the detritiation systems. The fact that tritium is exclusively recovered in the molecular form (pure Q_2 not diluted with He) is another advantage for the accountancy systems. It is finally recommended to review the design of TES and CPS and to integrate PERMCAT for the tritium recovery from tritiated water in the ITER TBM systems.

Study of an alternative process for the tritium extraction system based on a combination of selective permeation and PERMCAT process

Looking towards DEMO, new proposals for tritium processing in the breeder blanket are motivated by the following points:

- The DEMO relevancy of former TES designs is questionable considering the process itself (different traps, temperature and valves cycles, use of cryogenic fluids) and the size of the components that need to be scaled-up by 3 orders of magnitude,
- The handling of both forms of tritium (Q_2 and Q_2O) requires a chemistry step upstream of the accountancy stage, which causes intrinsic difficulties (see the problematic of reduction over hot metal discussed in the previous section),
- The most recent out-pile studies for tritium release experiments performed on the last European ceramic material showed that tritium is mainly released as water; other studies have also shown that the use of hydrogen in the purging gas could reduce the long term performances for tritium extraction, so that a He purge doped with water vapour could be recommended.

On these bases, alternative options for TES have been studied. A totally new concept so-called "PERMSEL / PERMCAT" has been proposed in 2008. As shown in figure 3 it comprises as unique tritium recovery stage a PERMCAT reactor that recovers tritium from tritiated water. In combination, a perm-selective reactor for tritium removal from the He purge is implemented upstream of PERMCAT. It has the function of a pre-concentration stage that allows returning back to the blanket the main fraction of the helium depleted in tritium, whereas the smaller fraction of helium enriched in tritium is routed to PERMCAT for further processing. In principle, the PERMSEL/PERMCAT combination shows significant improvements compared to the previous designs. On the one hand, it allows a fully continuous operation at constant non-cryogenic temperatures that should improve the reliability of the systems and minimise the tritium inventory. On

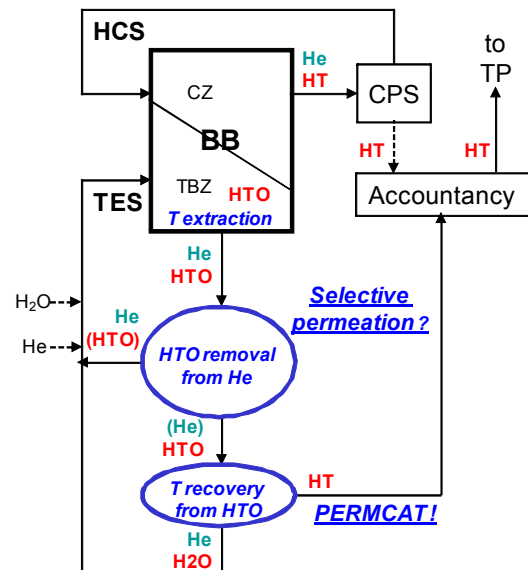


Fig. 3: Alternative concept for TES based on PERMCAT process for tritium recovery from water in combination with a pre-concentration stage using perm-selective membrane for tritium removal from the He purge gas doped with water vapour.

the other hand, if the addition of water into the He purge is workable, this would enhance the tritium release from the breeder zone, and at the same time reduce significantly the tritium permeation into the coolant. This would greatly relax the present huge requirements for tritium processing in the both TES and CPS loops. Last but not least, the tritium accountancy should be easier and more accurate since the PERMCAT provides tritium in the pure molecular form.

The PERMCAT process developed at TLK for more than one decade for the final clean-up of the Tokamak Exhaust Processing systems is presently further studied towards tritium recovery from water. Recently, a technical scale PERMCAT reactor comprising 13 Pd/Ag membranes enclosed in a common catalyst bed has been produced in collaboration with the main workshop (figure 4). Inactive (without tritium) commissioning tests have shown the best processing performances ever measured in comparison with previous reactors. This enhanced capability is attributed to the specific design of this reactor that increases, compared with previous designs, the ratio amount of catalyst / permeation area. It is verified that it is of advantage when PERMCAT is exclusively used to promote isotope exchange reactions, which is the case for the particular application of water processing.

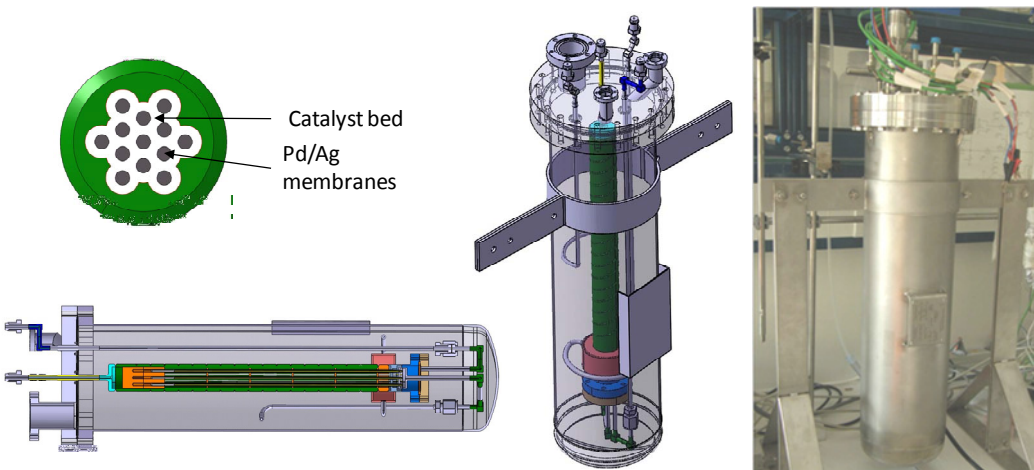


Fig. 4: Last technical scale PERMCAT reactor based on a new design comprising 13 Pd/Ag membranes enclosed in a common catalyst bed; the ratio of catalyst material / permeation area has been especially increased to process high amount of tritium bound in molecules.

In parallel, the CAPER facility at TLK is being upgraded to accommodate new components in order to produce significant flow rate of highly tritiated water and to handle the water downstream of the PERMCAT process. The first components have been installed and the tests should start early next year according to a staged approach. Using the current PERMCAT reactor of the CAPER facility (single-tube) the aim is to progressively increase the water partial pressure in the feed stream and specific activity of the water, with the final objective to produce and detritiate stoichiometric DTO for ITER application.

For the PERMSEL stage, the R&D work is still in the early preliminary phase. In collaboration with KIT Campus South (former University of Karlsruhe), a conceptual study has been performed and the following main results have been obtained:

- The feasibility and attractiveness of selective permeation has been confirmed, with major benefits in terms of very low tritium inventory with an easy and reliable operation;
- Some promising candidate materials for inorganic perm-selective membrane have been identified, especially the hydroxy-sodalite (zeolite) membranes with very small pores inaccessible for hydrogen;

- However, the lack of experimental data on permeation and selectivity for the particular case of gas composition close to the ones considered in the TES, that is the ternary mixture of He/Q₂/Q₂O has been highlighted.

The continuation of this R&D should now focus on experimental activities in order to get valuable and relevant input data to be used for simulation in order to consolidate the first promising evaluations.

Staff:

D. Demange
E. Fanghänel
K. Günther
T.L. Le
K.H Simon
R. Wagner
S. Welte
M. Kind and S. Stämmeler from KIT Campus South

Literature:

- [1] S. Welte, D. Demange, R. Wagner: "Mechanical design and first experimental results of an upgraded technical PERMCAT reactor for tritium recovery in the fuel cycle of a fusion machine", 9th International Symposium on Fusion Nuclear Technology, October 11th -16th, 2009, Dalian, China (to be published in Fusion Engineering and Design)
- [2] F. Borgognoni, D. Demange, L. Dörr, S. Tosti, S. Welte: "Processing test of an upgraded mechanical design for PERMCAT reactor", 9th International Symposium on Fusion Nuclear Technology, October 11th -16th, 2009, Dalian, China (to be published in Fusion Engineering and Design)
- [3] D. Demange, M. Glugla, K. Günther, T.L. Le, K.H. Simon, R. Wagner, S. Welte: "Counter-current isotope swamping in a membrane reactor: the PERMCAT process and its applications in fusion technology", 9th International Conference on Catalysis in Membrane Reactors, June 28th – July 2nd, 2009, Lyon, France (to be published in Catalysis Today)

Acknowledgement

This work, supported by the European Communities under the contract of Association between EURATOM and Karlsruhe Institute of Technology, was carried out within the framework of the European Fusion Development Agreement. The views and opinions expressed herein do not necessarily reflect those of the European Commission.

Manufacturing and Testing of a FW Channel Mock-up for Experimental Investigation of Heat Transfer with He at 80 bars and Reference Cooling Conditions. Comparison with Numerical Modeling (TW5-TTBB-001 D 10)

Introduction

The HETRA experiment has been motivated by corresponding three-dimensional (3D) numerical analyses which revealed significant effects of the asymmetrical heat loads on the cooling of the first wall. These analyses have shown that the heat transfer coefficient in the first wall is $\sim 15\%$ lower than predicted by one-dimensional heat transfer evaluations based on Dittus-Boelter-like correlations and that satisfactory cooling of the first wall can be achieved only with hydraulically rough channels. The verification of these computational results is going to be done on the basis of the results of the HETRA experimental campaign. A single first wall channel is going to be tested in a Helium cycle at 8MPa, while the surface heat load is represented by a set of electrical heaters. The goal of the experiment is to verify results of 3D computational analysis through: (i) detailed temperature measurements in the structure of the first wall and (ii) measurements of pressure losses in the first wall channel.

Layout of HETRA experimental facility

The main components of the HETRA experimental facility are presented in Figure 1. The facility involves one U sweep of the first wall channel. Relevant parameters of the helium coolant (pressure of 8MPa, inlet temperature of 573K and mass flow rate of 0.1kg/s) are provided by the connection of the HETRA test section to the HEBLO facility. The connection is made by two side channels (see Figure 1). As the purpose of the side channels is to provide developed flow conditions at the entrance of the heated section, their flow cross-section is identical to the one of the first wall - square 14.3x14.3mm with rounded corners (radius of 4mm). The side channels are not heated.

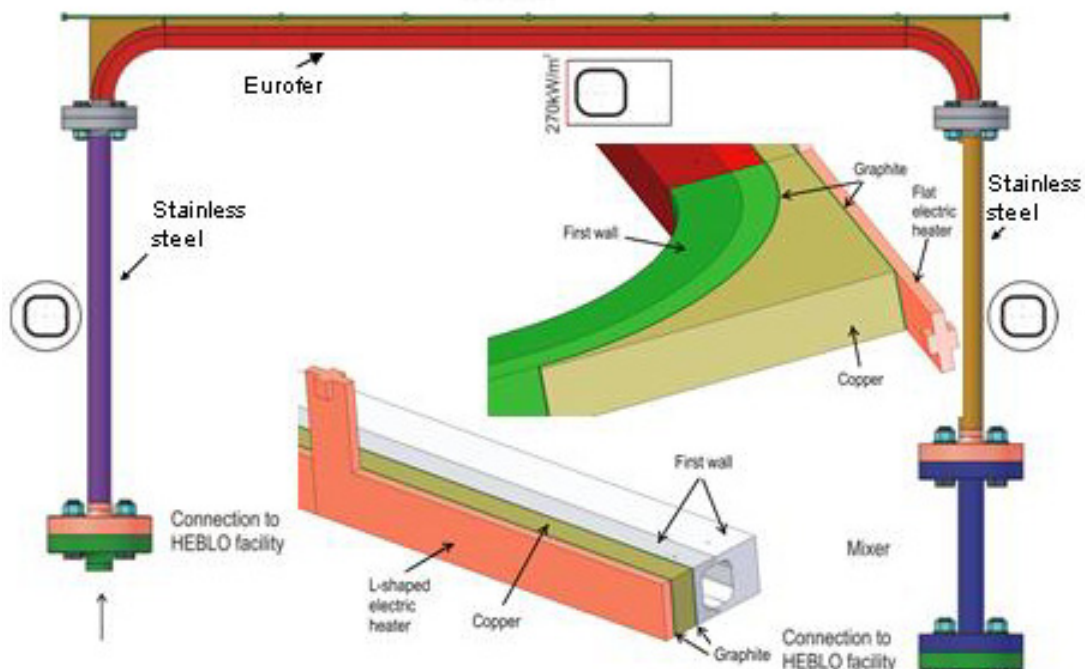


Fig. 1: Main parts of the HETRA test section. Inserts present the arrangement of the heaters at the straight channel section and at the channel bends.

The heated HETRA section involves two channel bends and a long straight section which simulates the plasma adjacent part of the first wall. This section will be heated only on the side representing the plasma facing side. The heating of the back side of the first wall which

in TBM comes from breeding units is in HETRA experiments neglected due to its multiple lower magnitude. The heat flux of 270 kW/m^2 at the plasma facing side of the first wall is simulated by a set of 8 flat ceramic heaters. Inserts in Figure 1 show the heater arrangement at the HETRA heated section. To ensure uniform heat flux and to diminish effects of imperfect thermal contact, the gap between the heaters and the first wall, will be bridged by two thin graphite layers (thickness of 0.5mm) between which a 10mm layer of copper is placed. Since the results of numerical simulations showed that one-sided heating causes significant temperature gradients over channel cross-section, at the exit of the outlet side channel a mixer is placed, which should provide a uniform helium temperature, i.e. avoid incorrect determination of fluid bulk temperature.

Fabrication and assembling of HETRA test section

The channel has been divided into the following parts for the fabrication: inlet side part, outlet side part, two bends and the straight section. As the side parts are not relevant for heat transfer, they are fabricated by erosion of the channel cross-section in stainless steel cylinders with diameter of 30mm. The wall cross-section of channel bends and the straight channel section is chosen to be relevant of the TBM first wall - a rectangle 19.3x30mm. The straight section is made by milling of channel halves in EUROFER. To fabricate channel bends, channel halves are fabricated by turning into two rings. The rings are then cut to produce 90° bends. The channel halves of both straight sections and the channel bends are welded by Electron beam welding (EB). EB welding has also been applied to connect the channel bends with the straight section



Fig. 2: HETRA channel (heated section) with installed thermocouples.

The heated channel section is connected to side channels with flanges. The flow cross section of flanges is the same as the one of the channel, so that no flow disturbances are induced at locations where the heated and not heated HETRA parts are connected. The flanges are from the same material as the corresponding channel parts. Use of flanges enables replacement of the heated section, i.e. use of different heated sections in which different roughness heights/types can be examined. In the current experimental campaign two heated sections are going to be considered: (i) a section with hydraulically smooth channel walls (surface roughness less than $4\mu\text{m}$) which is considered as a reference case and will primarily be used to verify numerical results and (ii) a section with artificially produced micro-

scopic roughness which will be used to prove reliability of the numerically based conclusion that the surface roughness of $20\mu\text{m}$ is sufficient to provide satisfactory cooling of the first wall.

Figure 2 presents a heated section with mounted thermocouples. It is noted that temperature measurements in HETRA experiments will be done only in steel since inserting of thermocouples into the channel would significantly disturb the fluid stream. The arrangement of temperature measuring positions is given in Figure 3. Therefore, 6 sets of temperature measurements will be performed along the heated section (denoted as I-VI in Figure 3). The measuring planes are positioned in the middle of the heating elements to avoid the effects of the discrete heaters. The measurements will be done applying thermocouples with diameter of 0.5mm. The thermocouples will be inserted orthogonally to the heat flux (from bottom/top side of heated section) in order to minimize temperature gradients along the thermocouple cable. The pattern of thermocouples within one measuring plane is arranged so to obtain temperature data along three constant z coordinates, i.e. corresponding temperature gradients along four lines (see insert in Figure 3). As the temperature gradients in the front (heated) channel wall are very strong, three thermocouples are placed for each measuring line in this domain. In the back (not heated) wall only two thermocouples along a measuring line are foreseen. Therefore, within each set the temperature of the steel wall could be measured at 10 positions.

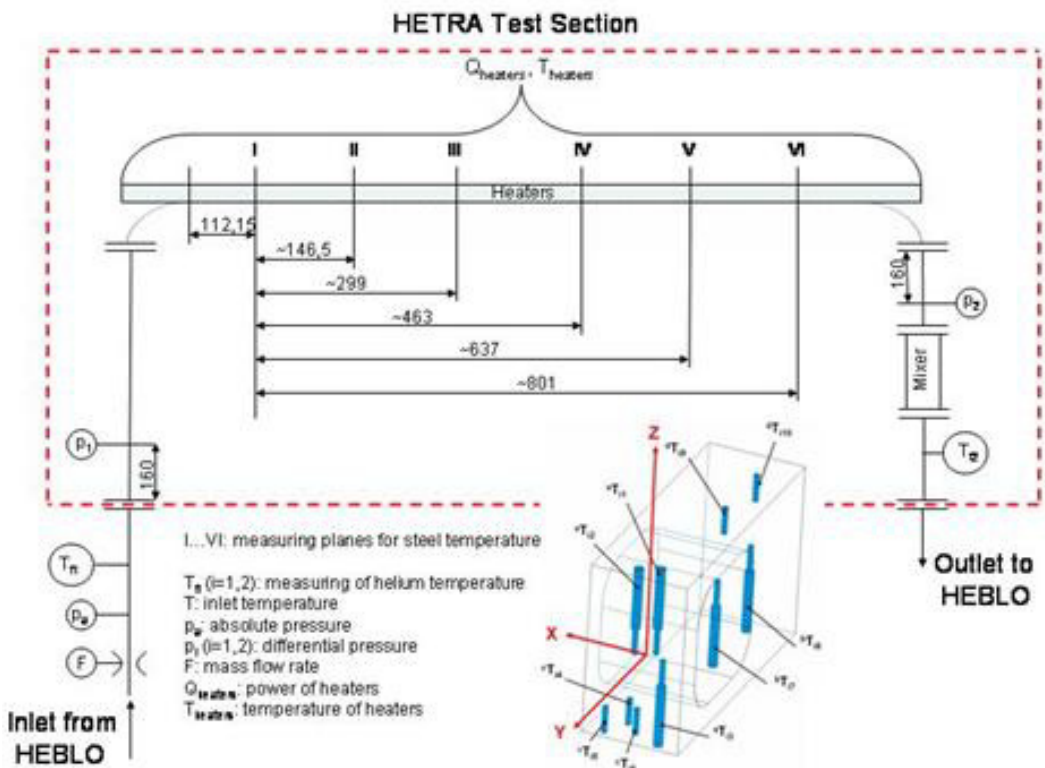


Fig. 3: HETRA measuring plan. Insert represents the pattern of thermocouples within one of the measuring planes I-VI.

Figure 4 presents the HETRA cooling channel with assembled graphite layers, copper parts and electrical heaters. Although this layout corresponds to the one foreseen by the design (see Figure 1) the section which will actually be built into the HETRA test section had to be assembled with numerous elements in order to provide the tightness of the whole arrangement (see Figure 5).

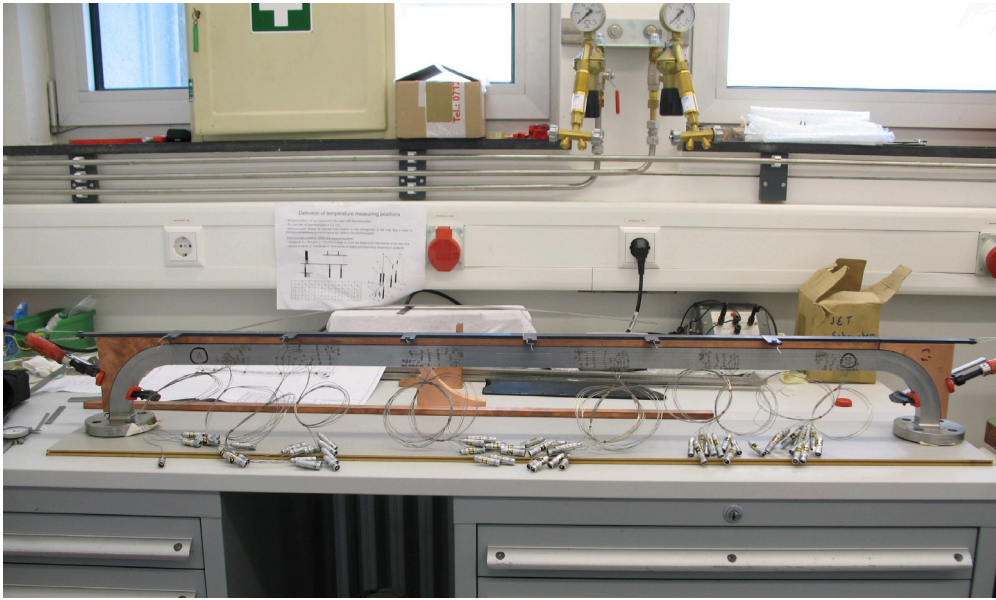


Fig. 4: HETRA channel with assembled cooper parts, graphite layers and electrical heaters.



Fig. 5: Final arrangement of HETRA channel before its insert in the vacuum tube.

The heated HETRA section is going to be thermally isolated by the use of a vacuum tube. Figure 6 presents the main parts (top image) and the installation of the vacuum tube in the HEBLO facility (bottom image). The advantage of a vacuum tube to a former design with classical thermal insulation is that an access for the thermo-camera can be made and in that way the surface temperature on three channel surfaces (which are not covered by heaters) can be recorded.

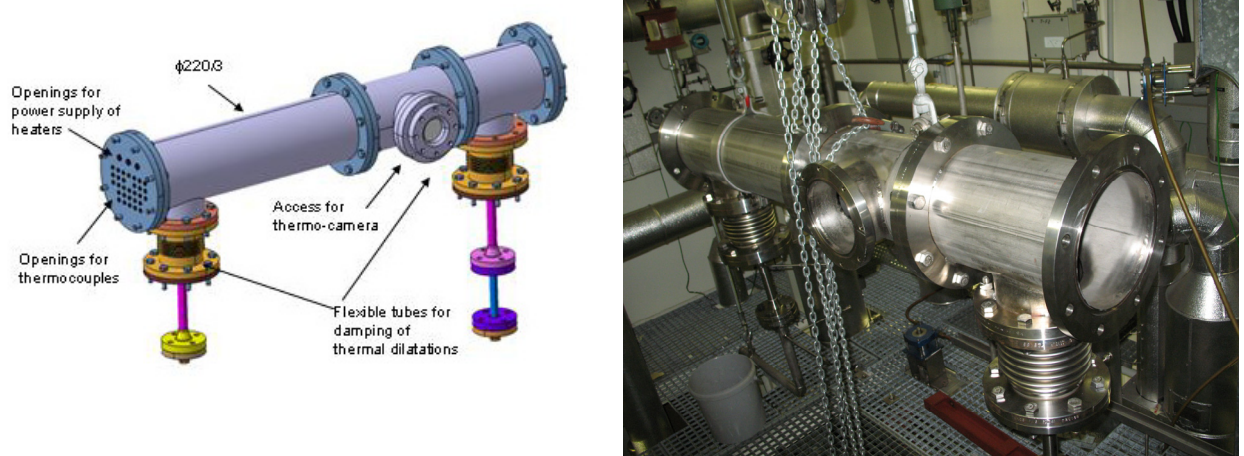


Fig. 6: CAD design of the the vacuum tube for isolation of the heated HETRA section (left) and its installation in the HEBLO facility (right).

Conclusions

The HETRA facility has been designed for the verification of numerically found effects of asymmetrical heating on the cooling of the first wall. The investigations will be performed for a portion of the first wall containing one U sweep of the cooling channel. The tests will be done in a Helium cycle at 80 bars. The heat load of 270 kW/m^2 on the surface representing plasma facing side of the first wall will be achieved by a set of electrical heaters. The numerical results will be verified through comparison with detailed temperature measurements in the steel structure. Two test sections will be applied: one with hydraulically smooth channel surface and one with artificial surface roughness. All the HETRA components are fabricated and assembled. Currently the installation of HETRA test section in HEBLO facility is undertaken. The first tests are going to be started at the beginning of 2010.

Staff:

M. Ilic
G. Messemer
K. Zinn

Acknowledgement

This work, supported by the European Communities under the contract of Association between EURATOM and Karlsruhe Institute of Technology, was carried out within the framework of the European Fusion Development Agreement. The views and opinions expressed herein do not necessarily reflect those of the European Commission.

Manufacturing and Testing of Mock-ups for Investigation of Coolant Flow in the Manifold System of HCPB TBM (GRICAMAN Experiments) (TW5-TTBB-003 D 1)

Introduction

The objective of this task is to contribute to the out-of-pile testing of Helium-Cooled-Pebble-Bed Test Blanket Module (HCPB TBM). The envisaged activity focuses on out-of-pile testing of a look-alike mock-up of the TBM manifold system, in particular to the optimization of the coolant flow.

The need for such an investigation is due to the very complicated geometry of the flow domain: large coolant collectors (so-called manifolds) that are filled with numerous flow obstacles are connected with numerous narrow channels in the form of meanders. However, by the TBM design it is foreseen that strictly defined flow rates through individual cooling components are achieved through proper definition of their hydraulic resistances. For example, the HCPB TBM design Version V.2.1-W, for which the investigation performed here are performed, the required flow distribution is as follows. The coolant, helium at 8MPa and 300°C enters the manifold 1 with mass flow rate of 1.3355kg/s, from where it should be uniformly distributed among 12 coolant channels in the first wall (FW channels). The outflow from FW channels is collected in the manifold 2 (Mf2), where the following flow distribution should take place: 0.56 kg/s flows through by-pass pipes out of the system, 0.01941kg/s flows in each of 8 vertical stiffening grids, 0.02111kg/s flows in each of 16 horizontal grids and 0.02051kg/s goes into each of 16 cap channels. The outflow from grid and cap channels is collected in manifold 3 (Mf3) and from there uniformly distributed among 16 breeding units (BU). The outflow of BU's is led into the manifold 4 where it, finally, leaves TBM. In order to find out whether such a flow distribution can take place, GRICAMAN (GRIdCAPsMANifolds) experiments are proposed.

The flow domain to be investigated in GRICAMAN experiments is defined to be the upper poloidal half of TBM bounded at the outlets of the first wall channels, at the outlets of by-pass pipes and at the inlets of breeding units, i.e. involving one half of manifold 2, cooling channels in four horizontal and eight vertical stiffening grids, 8 cooling channels within two cap halves, half of manifold 3 and inlets of 8 breeding units. Significant simplifications of the experimental facility are achieved (i) assuming that the flow is adiabatic, (ii) replacing helium with air pressurised at 3bar and ambient temperature and (iii) representing complicated stiffening grid- and cap channels by simple pipes with the equivalent flow resistances. The experiments are supported with numerical simulations by the computer code STAR-CD.

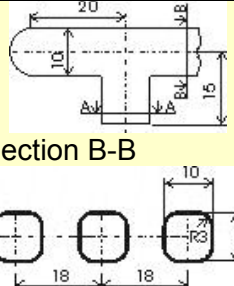
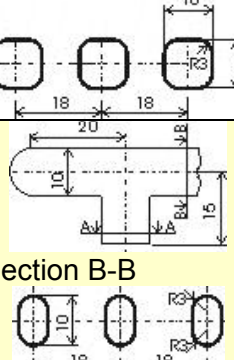
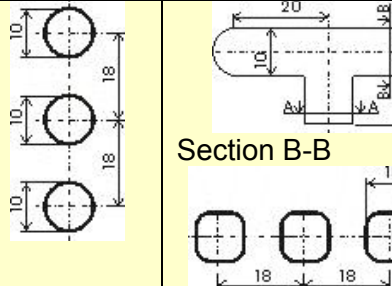
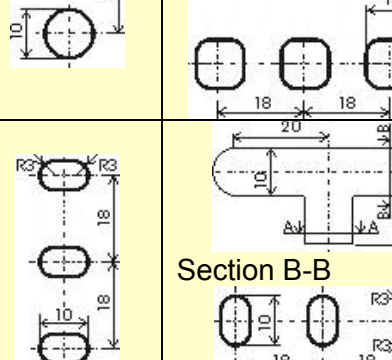
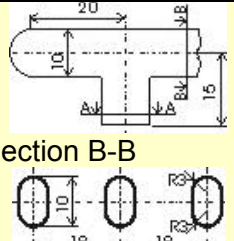
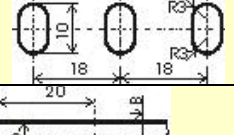
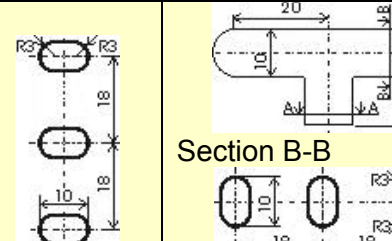
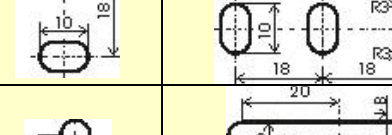
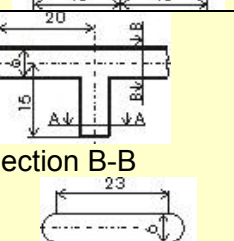
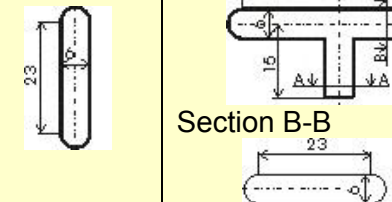
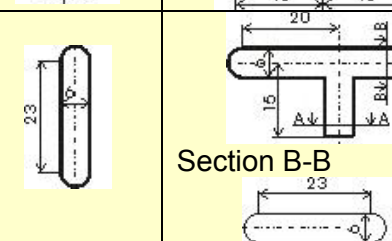
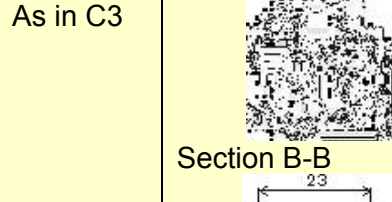
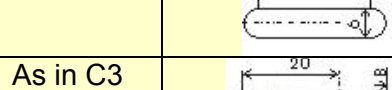
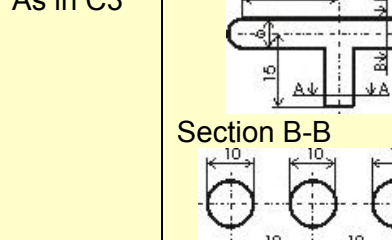
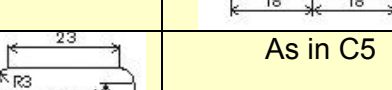
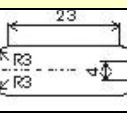
Investigation of fluid flow in cooling channels of stiffening grids and caps

As the first step in Gricaman activities detailed investigations of the fluid flow in cooling channels within caps and horizontal/vertical stiffening grids have been performed. These investigations have been done in order to estimate if the grid/cap channels as proposed in HCPB TBM V.2.1-W can provide the desired mass flow rate distribution when they are connected parallel.

The flow is investigated only numerically by the use of the code STAR-CD since the computational models for the flow in similar grid/cap channels of HCPB TBM V.1.1 have already been verified experimentally. The computations are done for designed mass flow rates, which for the case of the air at 3bar and ambient temperature have the following values: $m_{nh}=0.011507\text{kg/s}$ for horizontal grid, $m_{nv}=0.010581\text{kg/s}$ for vertical grid and $m_{nc}=0.011180\text{kg/s}$.

The computational results for geometry of grid/cap cooling channels as originally proposed in HCPB TBM V.2.1-W have shown that: (i) pressure loss in cap channels ($8p_c=2461\text{Pa}$) was significantly lower then the ones for grid channels and (ii), the pressure drop in horizontal grid channels ($8p_h=6860\text{Pa}$) is lower then in vertical grid channels ($8p_v=8900\text{Pa}$).

Table 1: Investigated geometrical arrangements of inlet/outlet leg of cap channels.

	Cap connection to manifold 2 (Inlet)	Cap connection to manifold 3 (Outlet)		8p _C (Pa)	
		Section A-A	Section A-A		
C1.	 Section B-B 	 Section B-B 	2461		
C2.	 Section B-B 	 Section B-B 	7699		
C3.	 Section B-B 	 Section B-B 	10917		
C4.	As in C3	As in C3	 Section B-B 	As in C3	8014
C5.	As in C3	As in C3	 Section B-B 	As in C5	6746
C6.	As in C3		As in C5	As in C5	5961

A simple hydraulic analysis of parallel connected channels shows that for such a configuration of cooling channels the mass flow rates are dramatically different from the ones prescribed by design. For this reason, grid/cap channels had to be redesigned. The redesigning is based on the following strategy: the geometry of horizontal grid channels is kept as proposed in HCPB TBM V.2.1-W, while the geometry of vertical grid channels and cap channels is changed to meet the requirement on hydraulic resistance which ensures proper flow distribution among the aforementioned three types of cooling channels. For an easier explanation of introduced changes grid/cap channels are divided in three domains and the following ter-

minology is used – inlet leg (channel part connected to manifold 2), outlet leg (channel part connected to manifold 3) and meander (3-channel bundle between inlet and outlet leg).

The resistance of vertical grid channels has been decreased by simple enlargement of the width of inlet/outlet leg from 20 to 29 mm, i.e. the cross-section 6x29mm (with shorter sides in the form of half circles) has been adopted. The geometry of the meander was kept as given in HCPB TBM V.2.1-W. For such a configuration of vertical grid channels pressure drop of $8p_v=7070\text{Pa}$ is evaluated.

Due to their specific connections to manifolds, the number of geometrical arrangements of inlet/outlet leg had to be investigated in order to find a geometry of cap channels that fits with the ones within grids. The results presented in Table 1 show that the satisfactory hydraulic resistance for cap channels is obtained for arrangement C5 ($8p_c=6746\text{Pa}$). It is noticed that also the cross-section of the channels in the cap meander has been changed from original 10x10mm to 6x10mm (shorter sides in the form of half circles).

Finally, a hydraulic analysis of the flow distribution in parallel connection of the redesigned grid/cap channels gave a satisfactory flow distribution: in cap $mc=1.0104\text{mcn}$, in horizontal grid $mh=1.0019\text{mhn}$ and in vertical grid $mv=0.9869\text{mvn}$ so that the redesigned grid/cap channels have been considered as proper and built in the design of Gricaman facility.

Design and fabrication of manifold boxes for GRICAMAN facility

The most complex parts of the Gricaman facility are so-called manifold boxes, which represent one half of the manifold 2 and manifold 3 of HCPB TBM in the poloidal direction. When designing the Gricaman manifolds the following strategy has been adopted: (i) the real geometry of the inner manifold space has been kept as in HCPB TBM; (ii) the real geometry of all the manifold connections (channels in the first wall, stiffening grids, caps and breeding units) has been kept at sufficient length which provides realistic flow inlet/outlet conditions; (iii) for the sake of flexibility, all components involved in Mf2 box and Mf3 box are fixed with screws – no welding is applied. The Layout of the manifold boxes for the Gricaman facility obtained in this way is presented in Figure 2 (Mf2 box) and Figure 3 (Mf3 box).

The supply of manifold box 2 with pressurized air is performed through six channels representing the outlet parts of the FW cooling channels in the upper poloidal half. The cross section of these channels is geometrically identical to the ones in the TBM (rounded square 15x15mm with radius in corners of 4mm). The FW channels in Gricaman Mf2 box are fabricated by milling channel halves in two steel plates (parts Mf2-04 and Mf2-05). For sealing O-rings are applied. The outlets of FW channels in Mf2 are drilled in the inside plate (part Mf2-04). The cross section of these outlets is a rectangle-like with total length of 20mm and two half-circle sides with diameter of 15mm. FW channels will be connected with 1" pipes which supply pressurised air via a rail with round openings (part Mf2-06) whose position corresponds to FW channels. The length of FW channels (from inlet to the outlet in Mf2 box) is 450.35mm, i.e. $\sim 28D_h$. This length should be sufficient to fulfil the purpose of FW channels - establishing of velocity profiles at inlet to Mf2 that are identical to the ones in TBM. At each channel a pressure measuring position is placed 238.5mm from channel inlet ($\sim 15D_h$).

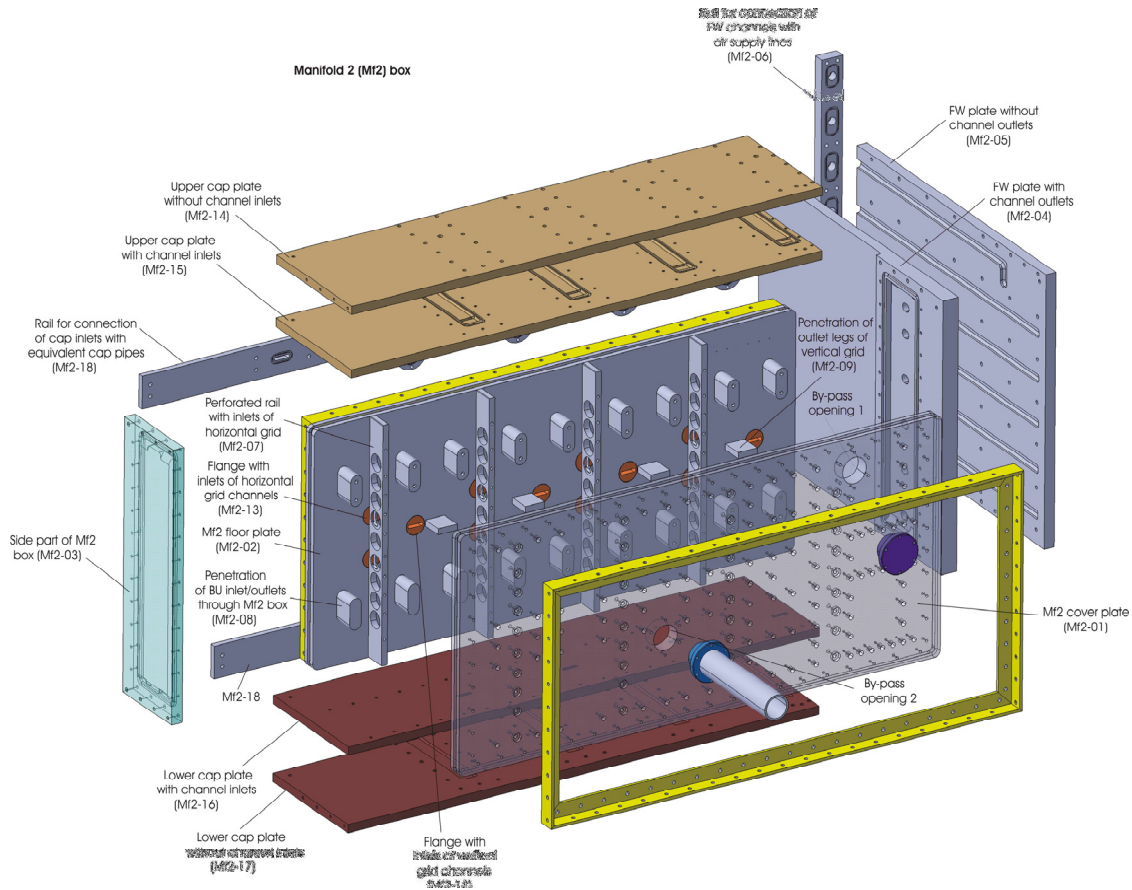


Fig. 2: Layout of Manifold 2 box for Gricaman experimental facility.

Inlet (from Mf2) and outlet (to Mf3) legs of cap channels are fabricated in the same way: halves of the cap channel cross-section are milled in two plates and the plates will be fastened to each other with screws (parts Mf2-14 – Mf2-17 in Figure 2 and parts Mf3-28-Mf3-31 in Figure 3). Sealing will be done with O-rings. The length of inlet cap channels is 174mm, that is ~20mm longer then the straight part of real cap inlet leg. At each inlet cap channel a pressure measuring position is placed at 82mm from the inlet cross-section (~8D_h). These inlet legs of cap channels will be connected with equivalent cap pipes via a rail (part Mf2-18) at which a conical flanges with outlet diameter $\frac{3}{4}$ " will be screwed. The connection of outlet cap channels with equivalent cap pipes will also be done via a flange and a rail (part Mf3-32 in Figure 3). In order to diminish the effects of strong local flow disturbances due to sudden change of channel cross-section, a single slightly diverging channel is foreseen in front of the 3-channel-chunks of outlet cap legs. The length of the chunks up to channel exit is 175mm, what is ~21D_h. At each of them a pressure measuring position is foreseen at a distance of 78mm (~10D_h) from the channel exit.

Outlet and inlet legs of grid channels are designed in the form of flanges which will be screwed to the manifold floor plates. Within these flanges a real geometry of channel cross-section (29x6mm with the shorter sides in the form of half circles) is kept in the length which corresponds to the real geometry of grid channels – 115mm for inlet and 150mm for outlet legs. The channels are fabricated by eroding in cylindrical steel pieces, what guarantees good sealing. It is noted that the real geometry of inlet/outlet legs of horizontal grid channels is completed with channel parts milled in perforated rails Mf2-07 and Mf3-23. Pressure measuring positions are foreseen at 70mm from inlet cross-section (~9D_h) at Mf2 grid flanges and at 82mm (~11D_h) from inlet cross section of Mf3 grid flanges.

Finally, inlet legs of breeding unit channels are designed similar as in the case of grid channels – flanges with eroded channels are attached to the Mf3 floor plate (parts Mf3-27 in Fig-

ure 3). The cross section of the channels is 17x50mm with short sides in the form of half circles. The length of the channels is 215mm. At each BU flange a pressure measuring position is foreseen at 168mm away from channel inlet ($\sim 6.36D_h$).

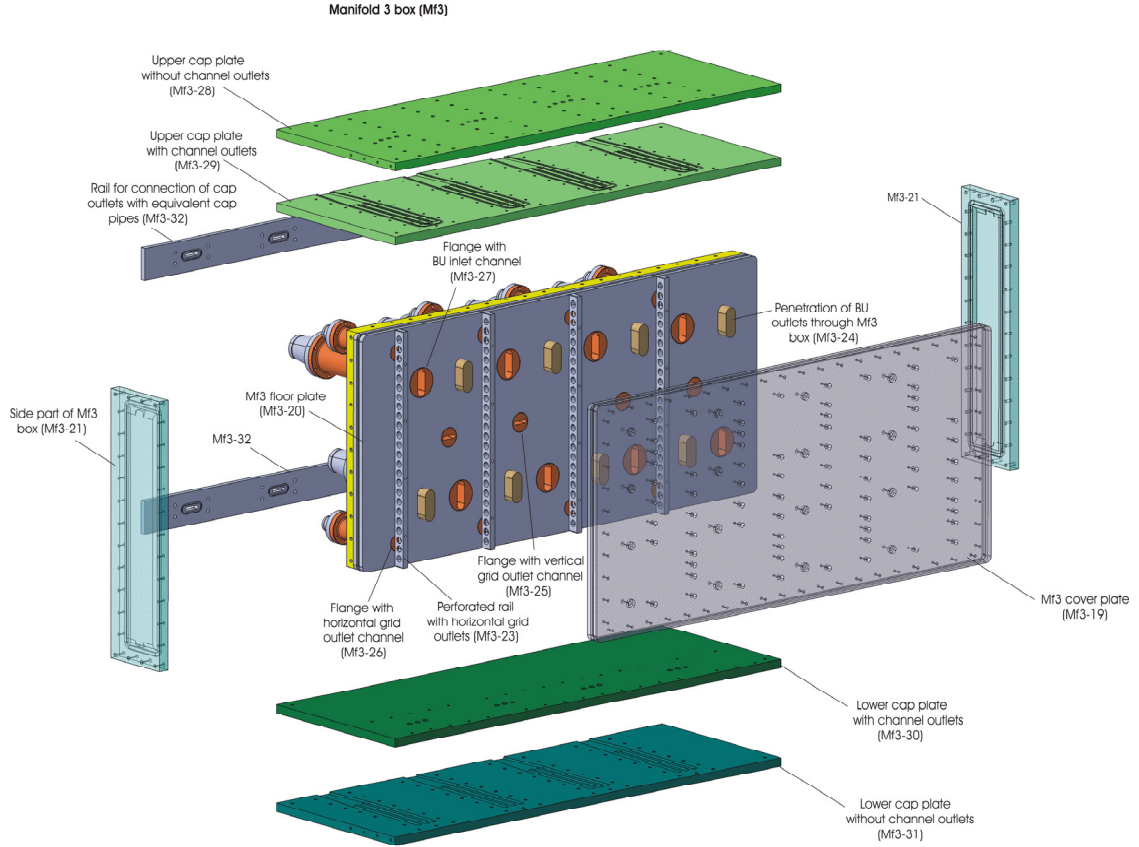


Fig. 3: Layout of Manifold 3 box for Gricaman experimental facility.

To realistically represent the inside structure of manifold fluid domains, flow obstacles are inserted which represent penetrations of BUs and vertical grid channels through Mf2 space (parts Mf2-08 and Mf2 -09 in Figure 2) i.e. penetrations of outlet BU channels in Mf3 volume (parts Mf3-24 in Figure 3).

The status of the work on Gricaman assembly is: (i) Manifold 2 and Manifold 3 boxes are designed and fabricated. (Figure 4 presents examples of already manufactured parts); (ii) Equivalent grid/cap channels have been designed. Their fabrication is foreseen starting in April 2010. In Mai 2010 pre-experiments for adjustment of the hydraulic resistance of individual channels is going to be undertaken; (iii) Assembling of Mf2 and Mf3 boxes will be started at the end of Mai 2010; (iv) Components like filter, pressure regulator, pressure vessels as well as measuring devices are purchased and delivered; (v) In June 2010 the Gricaman facility will be fully assembled and ready for measurements; (v) Numerical model is under preparation.

Conclusions

The report deals with Gricaman experimental facility for investigation of flow distribution in the coolant system of HCPB TBM. The considered flow domain is the upper poloidal half of TBM bounded at the outlets of FW channels, at the outlets of by-pass pipes and at the inlets of BU's. The facility is designed keeping real geometry of manifold 2 and manifold 3 and replacing complicated grid and cap cooling channels with simple pipes having the same flow resistance as the real channels. The flow resistance as well as internal flow distribution within

stiffening grids and cap channels has been investigated and optimised. The Gricaman assembly is expected to be completed in summer 2010.

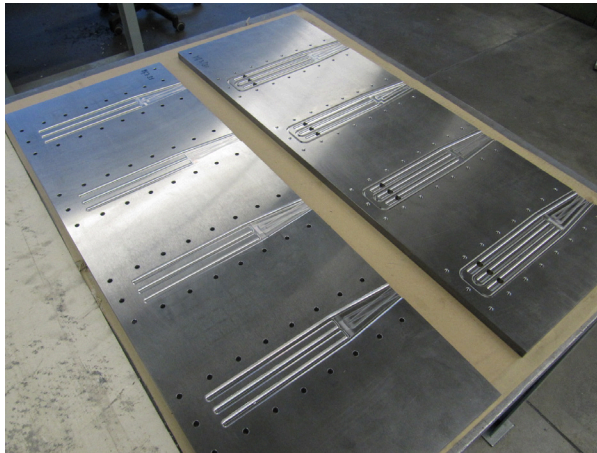


Fig. 4: Examples of already manufactured parts for Gricaman manifolds: left – plates with milled outlet legs of cap channels (parts Mf3-30 and Mf3-31 in Figure 3); manifold flanges (parts Mf2-12 and Mf2-13 in Figure 2 and Mf3-25, Mf3-26 and Mf3-27 in Figure 3).

Staff:

O. Bitz

M. Ilic

T. Kuhn

E. Stratmanns

G. Legradi (Institute for nuclear Techniques, Budapest University of Technology and Economics)

Acknowledgement

This work, supported by the European Communities under the contract of Association between EURATOM and Karlsruhe Institute of Technology, was carried out within the framework of the European Fusion Development Agreement. The views and opinions expressed herein do not necessarily reflect those of the European Commission.

Design and Development of the European Test Blanket Modules (TBM) Systems (“TBM08G1”) (F4E-2008-GRT-09(PNS-TBM)-01)

The Grant *F4E-2008-GRT-09 (PNS-TBM)* was published in the F4E web page in July 2008. The proposal of the TBM-CA was presented in September 2008 and after a negotiation phase the Grant Agreement was signed by F4E and FZK (now KIT) as coordinator organisation in December 2008. The Grant Agreement addresses and regroups most activities of the Work Programme 2008 which are directly connected to the achievement of the 2009 milestones or which are on the critical path for achievement of later milestones. These activities are technically linked together and are, by consequence, regrouped in a single action.

The general objective of the present Grant Agreement is to reach a level of design, technology development and management that allows:

- i. Validating most of the 2009 milestones identified by the ITER STAC:
 - TBM Quality management system established – 06/2009
 - TBMs system conceptual design delivered – 12/2009
 - TBM Preliminary Safety Reports delivered – 12/2009
- ii. Implementing the European TBMs project strategy and choices (some elements of the European project scope/objective are actually not addressed in IO milestones), in particular:
 - Classify the TBM Systems with respect to French/European Regulation and confirm Codes & Standards to be applied
 - Give the same orientation to both TBMs concepts (vertical) and allocate both TBMs in a single ITER Port
 - Define a common generic steel box design for both the HCLL and the HCPB concept
 - Issue the design documents under a structure that allows later update with clear traceability
 - Issue assessment documents stating the needed future analyses and technology development efforts
 - Issue technical work plan proposal and assessment in specialized areas for confirming the future strategy and project management elements (cost/schedule/time/risk)
 - Enhanced coordination between technical tasks to ensure technical consistency at the level of the TBM systems and with respect to the ITER plant.
 - Enhanced synergies between HCLL and HCPB design and technology development activities for cost/time rationalization.

On this basis, detailed objectives in each technical field have been derived and described in detailed technical specifications that accompanied the Call for Proposal. The scope of work for the present Grant Agreement has been broken down into 32 tasks representing manageable units of work for a total amount of about 185 deliverables.

In addition the ITER TBM Systems is classified as Quality Class 1 that requires the application of a complete set of Quality Management Provision. These provisions were listed in the F4E document “Management Specification”.

On February 10 and 11 2009, the kick-off meeting for the grant “F4E-2008-GRT-09 (PNS-TBM)” was held at the F4E premises at Barcelona. Thus, work has started for the first multi-beneficiary grant awarded by F4E still in 2008. The beneficiaries are the institutions which have organised themselves in the European Test Blanket Module Consortium of Associates (TBM-CA), that came into force upon signature of the related consortium agreement in November 2008. The scope, partnership, governance, organisation of work, management structure and legal framework of the collaboration were developed in a thorough process of consultation and refinement on the basis of the common commitment to the success of the TBM project. Thus, a partnership has been defined and a work distribution been elaborated that makes use of the complementary competences of the partners, covering the full scope of the TBM system development and avoiding any duplication of work. The partners in the TBM-CA, all of them EURATOM Associates or operating as Research Units under the umbrella of a EURATOM Associate, are CEA, representing the core activity for the European HCLL blanket concept, CIEMAT, leading the diagnostic engineering and CODAC activities, ENEA, having major stakes in the helium processing and testing activities, FZK (now KIT), for the European HCPB blanket concept development, NRI, leading the PbLi loop development, and RMKI, bringing in design and installation engineering competence.

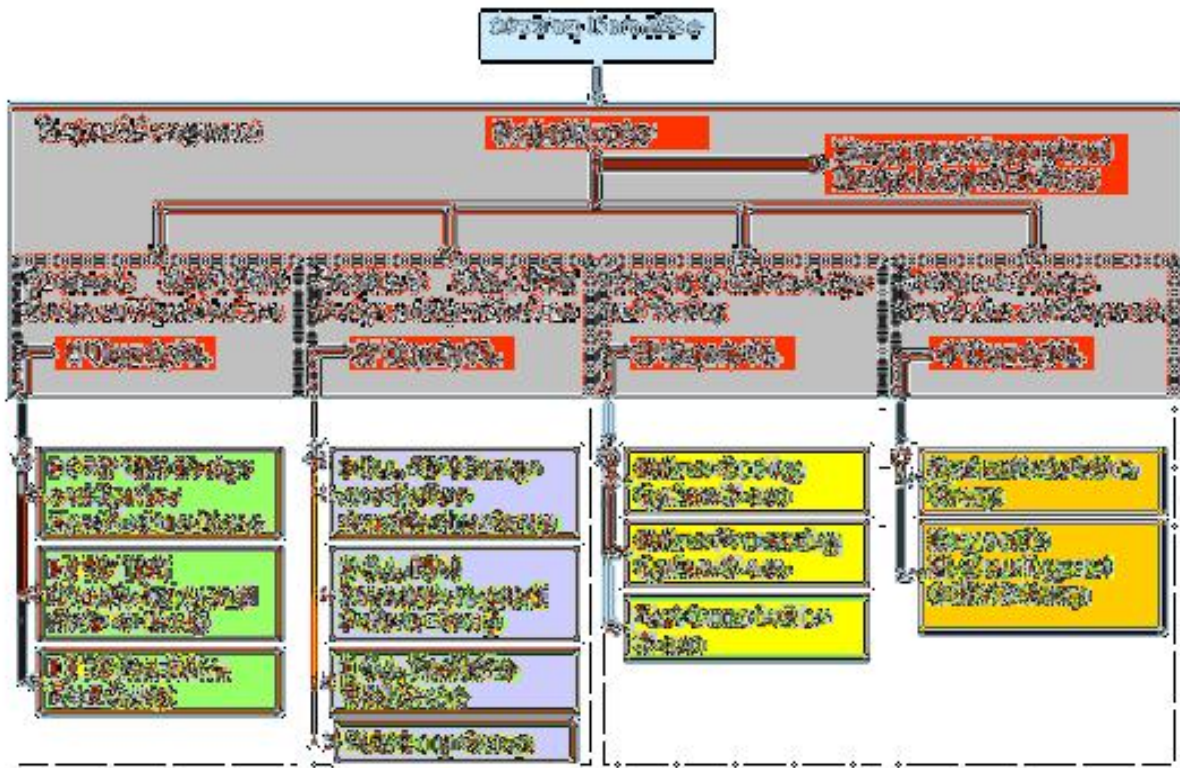


Fig. 1: Organisation Chart of the TBM-CA.

Equally important, an efficient management structure has been introduced (see Fig. 1) with a Project Leader, four Deputy Project Leaders, each of them supervising one division, and a Management Support and Design Integration Team (MDIT). The latter is the main instrument to ensure the coherence of the work and to provide all the management support tools required to keep on track a project of this complex nature. I.e., the MDIT has both technical (system engineering coordination, design integration and coordination of CAD work) and administrational (project management, control of planning, resources and funds, quality management) functions, as well as tasks towards the regulatory authorities (safety and licensing). Its most important task, of course, is to secure that there is a seamless integration of all the engineering work and to develop and secure the implementation of the quality standards, in particular that the formal tools to be used in the work (CAD, planning & scheduling,

document management) will be applied according to the same standards. The Project Leader and the MDIT are hosted by KIT, acting as coordinator in the grant agreement.

Staff of MDIT and Project Management:

L. Bankos
L.V. Boccaccini
J. Gafert
M. Ionescu-Bujor
H. Neuberger
D. Panayotov
P. Sardain (delegated by CEA)
S. Schreck

List of External Contributors:

G. Aiello (ENEA)
O. Bede (RMKI)
L. Jourd'heuil (CEA)
L. Kosek (NRI)
J-F. Salavy (CEA)
L. Sedano (CIEMAT)

In the following the work in the 4 groups led by KIT and the input from 3 smaller KIT activities, which contribute to the Division 2 (CEA leadership) and Division 3 (ENEA leadership) are illustrated:

1. HCPB Predictive Tools Group (PTG):

Experimental Programme & Simulation Capacity for reliable HCPB TBS Test Programme in ITER

The main objective of the work in the present task (Macro-Task TG-06) is to develop a sound Experimental Programme & Simulation Capacity for the HCPB-TBS to be performed in ITER over the next ten years. It includes objectives, deliverables and milestones to be done in the frame of the Fusion for Energy Call for Proposal number F4E-2008-GRT-09. The overall work is distributed in 7 different tasks, of which one (T31-3) is related to the coordination, assessment and integration of the Experimental programme, while the others (T23-2, T24-2, T26, T27-2, T28-2, T29-2) are assigned to experts in charge to define this Programme in different fields (thermo-hydraulics, neutronics, electro-magnetic, tritium transfer and cycle, pebble bed mechanics and system/coupled phenomena). An analogous Group as been established for the HCLL TBS, that includes also the field of the Magneto-Hydrodynamics and PbLi-steel Corrosion that are investigated in KIT. This Group is leaded in Saclay by our French Colleagues in the Consortium.

The development plan for HCPB Modeling Tools is created by combining the results of the "expert" tasks. The work is performed in three steps as shown in Fig. 2.

Step 1: Expression of the needs: In this first step of the work HCPB-DEMO relevant requirements have been investigated to specify which models have to be validated and what figures of merit should be considered as targets (T31.3-D1). Additionally a template was prepared to define proposals for experiments (T31.3-D2). The template has been diffused among the field coordinators responsible for the field of modeling concerned in the respective task. Proposals for experiments and tests to be performed in ITER with the aim to achieve a reliable TBMs test programme have been added to the template, for each field respectively. The lists of tests and experiments of the different fields have been agreed with F4E and the results have been listed to construct the integral HCPB TBM modeling programme. Finally a ranking of the proposed experiments is prepared, considering increasing complexity order and synthesis (for each modeling field and each HCPB TBS proposed experience) of the needs in terms of models, software, control of the environment variables and instrumentations (31.3-D3).

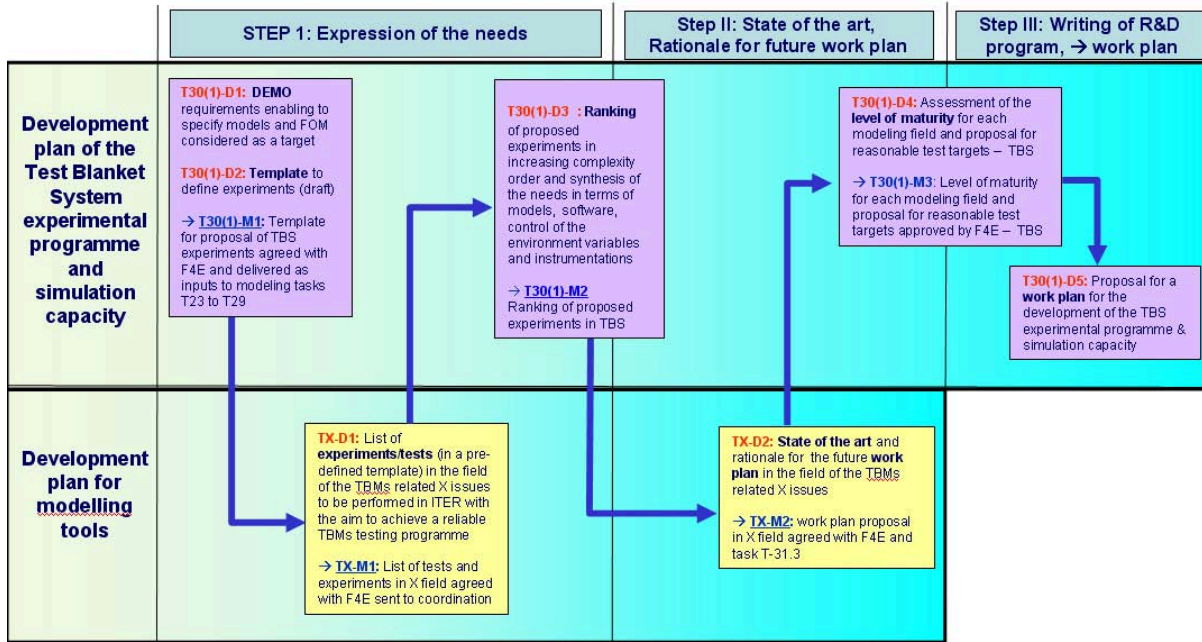


Fig. 2: Tasks objectives for PTG.

Step 2: State of the art and rationale for a future work plan: After the definition of the needs concerning the development of HCPB TBS modeling tools the proposed experiments are compared to the state-of-the-art to identify the needs of a the future work plan for each field. The work plan proposal will be agreed with F4E coordinated by the PT EGL (T23-2-, T24-2-, T26-, T27-2-, T28-2- and T29-2-M2/H2) and will be transferred to Task T31.3. Using the confirmed and approved information of each modeling field an integral R&D programme will be developed, assessing the level of maturity for each modeling field. Additionally a proposal for reasonable test targets will be prepared. Both will be reported in the frame of T-31.3-D4.

Step 3: Writing of the R&D programme/work plan: On basis of the outcome of T-31.3.1-M3 a R&D programme/work plan will be proposed including the development of the HCPB TBS experimental programme and simulation capacity (T-31.3-D5).

Staff:

A. Abou-Sena
 L. Bühler
 D. Demange
 U. Fischer
 Y. Gan
 M. Ilic
 A. Jianu
 M. Kamlah
 A. Klix
 W. Krauss
E. Magnani
 C. Mistrangelo
 P. Perslavstev
 J. Reimann

List of External Contributors:

G. Aiello (ENEA)
 M. Angelone (ENEA)
 M. Chiumentti (CIMNE)
 M. Eid (CEA)
 F. Gabriel (CEA)
 J. Jordanova (INRNE-BAS)
 A. Lyoussi (CEA)
 P. Martinez (GOT-EUROBREED Trainee)
 F. Moro (ENEA)
 C. Moreno (CIEMAT)
 L. Petrizzi (ENEA)
 M. Pillon (ENEA)
 R. Villari (ENEA)

2. HCPB TBM Design and System Specification Group (DSG): Conceptual Design of the HCPB TBM

The main objectives of the present task (Macro-Task TG-02) are to develop the design and qualification plan of the HCPB TBM generic box, of EM-TBM and IN-TBM breeder zone. Additionally the fabrication and development plan for the TBM box fabrication are addressed in the Macro-Task TG-02 (see next paragraph). The macro-task includes objectives, deliverables and milestones that are distributed in 3 different tasks: T10-1 (design of the HCPB TBM generic box), T11 (design of the BU for the EM-HCPB TBM), T12 (design of the BU for the IN-HCPB TBM). An analogous Macro-Task TG-01 has been assigned to the Design Group working in Saclay on the development of the HCLL TBM.

Detailed objectives for each sub-task are:

HCPB TBM generic box: The main structure of the HCPB TBM generic box will be common for all successive versions of TBMs to be tested in ITER. As a consequence the design of the generic box has to fulfil the functional requirements, which rely mainly on the relevancy with the DEMO blanket module for the HCPB concept. Furthermore the box integrity for normal and accidental situations has to be insured. A convergence effort is important with the TBM foreseen for the HCLL concept in order to ensure a maximum similarity of the designs within the European TBM project, and sharing of the development effort. During this year the "Confirmation of input data, software/models, correlations and material properties" (T-10-1 Step 1) and the "Preliminary generic box design and evaluation of DEMO-relevancy" (T-10-1 Step 2) have been completed.

HCPB EM and IN-TBM breeder zones: the objective is to propose a preliminary design of the breeder zone of the HCPB TBM for the so-called "Electro-Magnetic" test phase in ITER and for the so-called "Integral" test phase in ITER. During this year the first step of T11 and T12 have been completed ("First evaluation of the interest/need/limitation of electrical heating of the breeder zone and related He cooling/heating conditions, evaluation of the interest of using dummy pebble material" for T11 and "Confirmation of preliminary design parameters and related DEMO relevancy level" for T12).

The breeder zones development must closely share with the TBM generic box development the following fundamental points: (1) the outer dimensions of the breeding cells guiding available space dimensions for the breeding zone, (2) the thermal coupling between breeding cells and box structure, providing boundary conditions for both models, (3) feed-through solutions for feeding breeder units with coolant and breeder, and for connecting instrumentation, imposed by box geometry and technical choices.

In particular a methodology for the calculation of the heat power produced in the Breeder Zone and deposited on the TBM box components has been defined.

The preliminary design of the TBM box and of the TBM IN-BU performed in the frame of task 10 and 12 have been assembled in a CAD model suitable for performing neutronic analyses. The results of the neutronic analyses have been used for the preliminary thermal design assessment of the HCPB TBM. Fig. 3 shows the temperature field in steady state analyses performed with a 500 kW/m^2 uniform heat flux deposited on the First Wall. The TBM box components are modeled in details, including the cooling channels. The complexity of the model requires reducing its size: a $\frac{1}{4}$ scaled HCPB TBM is studied, using symmetry boundary conditions on the radial-poloidal and radial-toroidal cutting planes.

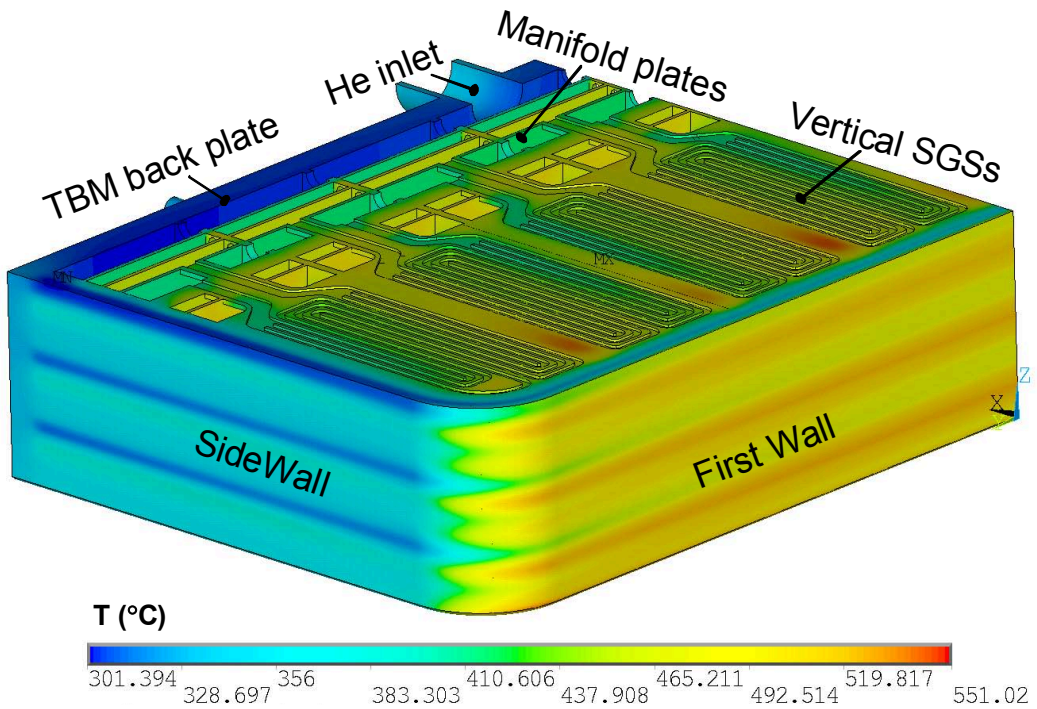


Fig. 3: Thermal design assessment of the HCPB TBM.

Staff:

O. Bitz
F. Cismundi
M. Illic
H. Neuberger

List of External Contributors:

S. Kecskes (RMKI)
B. Kiss (RMKI)
G. Legradi (RMKI)

**3. HCPB TBM Manufacturing and Material Group (MMG):
Preliminary plan for the Manufacturing of a HCPB TBM**

The scope of task T-22 (TBM Box fabrication development and qualification plan) was to investigate different strategies for manufacturing of HCPB-TBM sub-components as well as possibilities for the assembly of the TBM box. The task is sub-divided into phase 1 (Preliminary TBM box development and qualification work plan up to the realization of a TBM FMU by Industry) which was concluded in 09/2009. In the frame of this activity different scenarios for sub-component reference and alternative fabrication, as well as assembly routines have been investigated. Base of all routines is the foundation in a KIT work plan for Welding Procedure Specifications (WPS) of all assembly concerns conform to codes and standards like European PED code and the French nuclear code RCC-MR. Critical parts like distortion of FW bending has been started in order to support the development and optimization of HCPB TBM design concept. Additionally numerical analysis works for several welding routines are also started in preliminary phase of T22 task. In the frame of HCPB TBM manufacturing the main emphasis is focused on residual distortions reduction. In context of low level residual distortions after welding it seems to be more efficient to use laser or electron beam technologies. By using of high-energy welding technologies (EB, laser) smaller resultant plastic zone in weld joint should be achieved as a result of small local heat input zone. Thus smaller residual distortions may be expected in comparison with TIG or NGTIG low speed multi-pass welding technology. MIG-laser combination (so called hybrid technique) presents the multi-

pass high speed welding technology, which can be taken as other variant in future TBM box assembly activities of next grant activities.

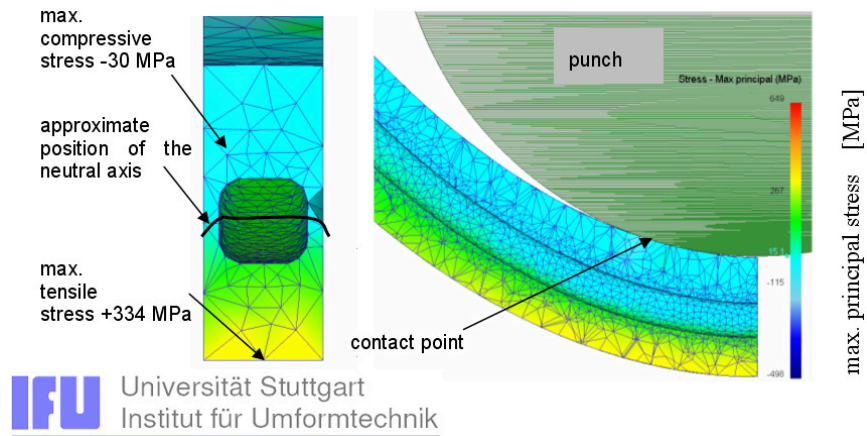


Fig. 4: Started program of bending analysis for HCPB TBM First Wall fabrication.

4. Helium Cooling System Group (HCG): Preliminary Design of the HCLL- and HCPB-Helium Cooling System for ITER

One of the activities performed by KIT as part of the F4E grant (F4E-2008-GRT-09) is the preliminary engineering design of the Helium Cooling systems for the two European TBM: HCLL and HCPB. The activities performed under this task include the generation of a new thermo-dynamic model as well as a thermo-mechanical model of the system considering updated equipment and piping layout. In the Fig. 5 below the preliminary layout of the two loops inside of the CVCS area (Level 3) of the (ITER) Tokamak building is presented.

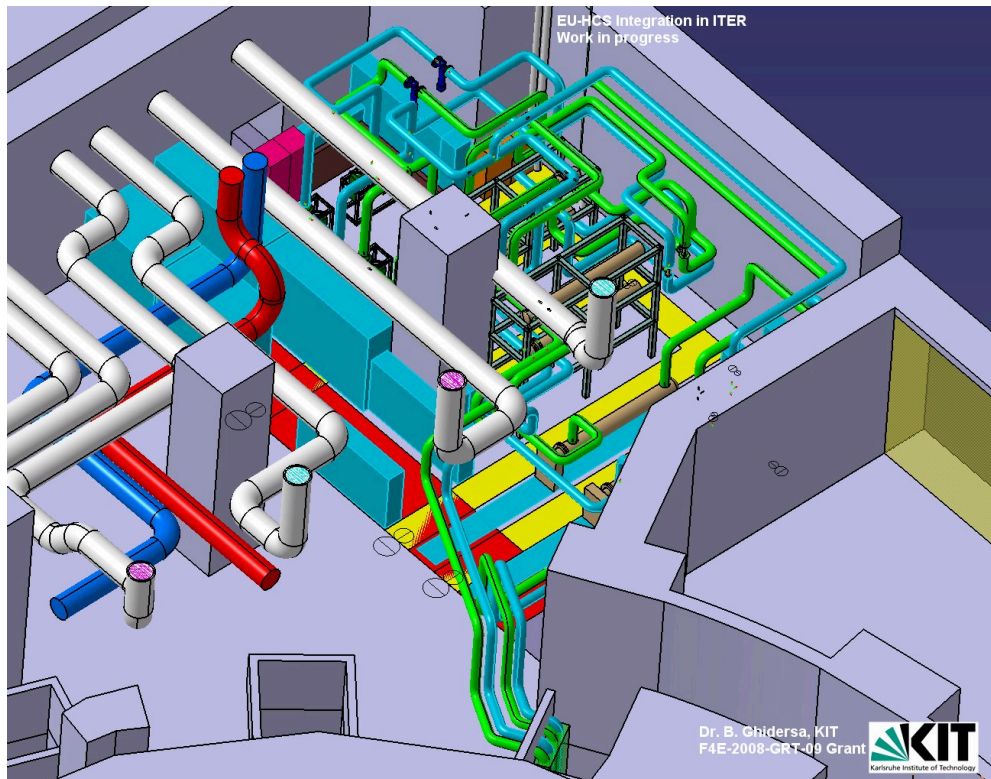


Fig. 5: Preliminary layout for the HCLL and HCPB-HCS in CVCS area of the ITER Tokamak building.

Thus, in an area with a footprint of about 158 m² the space for all major equipments has been reserved including the space for the associated power supply and control cubicles. Also, a preliminary layout of the piping system has been proposed. Various access routes (yellow stripes) and preliminary supporting structures for some of the equipments have been proposed. This new layout has been transmitted to ITER in November 2009 as a first (draft) EU-TBM-HCS layout. Currently, a first technical report concerning the preliminary loop design is prepared.

Staff:

B. E. Ghidersa
X. Jin
V. Weber

Contribution to Division 2 (CEA leadership):

5. List of MHD Experiments for HCLL TBM to be performed in ITER (D1)

A list of magneto-hydrodynamic (MHD) experiments is proposed to be performed in ITER. The main objectives include obtaining data to validate theoretical predictions of pressure and velocity distribution in the TBM as well as of the MHD pressure drop both at a local level (in specific sub-components of the PbLi circuit) and at a global level (total pressure drop). Moreover, pressure data are required to verify that the flow is equally distributed among the breeder units (BUs) that form a blanket module. Further objectives could be supplying inputs to other working fields (corrosion, tritium transport...). This could be achieved by adapting or broadening the proposed experiments according to the needs of those fields.

Indications about flow distribution in the TBM can be obtained from measurements of electric potential. Instead in order to judge about effects of inertia and electromagnetic forces on the flow across the gap at the first wall, pressure differences between connected BUs have to be assessed.

The MHD behavior of the TBM and more specifically the MHD flow within the BUs is expected to be analogous to the one in an outboard blanket module of a DEMO reactor. With a toroidal magnetic field around 4T in the ITER TBM, comparable temperatures and dimensions, it is possible to achieve in both environments similar characteristic flow parameters. Therefore the proposed experiments have a high DEMO relevance. Moreover, it would be quite difficult to perform these experiments in external facilities since it would require large experimental volume in strong toroidal magnetic fields $\geq 4T$ showing the typical radial dependence $B_t \sim r^{-1}$. Besides that, it would be necessary to consider an additional poloidal component of the magnetic field relevant for fusion applications (in a first approximation $B_p \cong 1T$ in the TBM). The proposed experiments aim at analyzing the effects of interacting phenomena that occur when the complex ITER environment is considered. Moreover, experiments for investigating mixed convection phenomena can be performed in ITER by exploiting the first wall surface heat flux coming from the plasma.

Three groups of MHD experiments are identified and described in detail. One type of tests is characterized by a forced flow driven by a given pressure difference. This requires isothermal testing conditions. Therefore such experiments are carried out during phases when there is no heat flux towards the first wall, i.e. there is no plasma. Measurements of temperature are needed to check the establishment of isothermal conditions and to define temperature dependent fluid properties. This kind of experiments allows investigating separately MHD phenomena since there is no coupling to heat transfer processes. The experimental data will be used for validating theoretical predictions of pressure and velocity distribution in the TBM.

A second type of experiments is foreseen to study buoyancy effects. For that purpose it is desirable to have clearly specified thermal boundary conditions, i.e. an imposed heat flux from one or more heated plates, and defined heat extraction through neighboring cooling plates. The given thermal flux has to simulate the volumetric heat, which is generated when neutrons are present. All these experiments are required to investigate free and mixed convection. The outcomes will be used to select and validate numerical models for magneto-convection.

The third group includes experiments with an applied thermal power and a first wall heat flux from the plasma. They should allow understanding the overall performance of the blanket under more realistic MHD and thermal conditions.

However, it can be noted that, while an experimental program for ITER is required to test technological aspects and predict synergetic effects and complex coupled phenomena, a basic research work plan is necessary as preparation for ITER applications. It includes for instance component and mock-up experiments in simulated conditions and testing of measuring equipment and instruments. This latter kind of experiments is fundamental to reach an optimization of the number of sensors to be used in ITER in order to minimize their impact on TBM design and performance and to verify the applicability of the available measuring techniques. The proposed out-of-ITER tests have been selected with precise objectives:

- a) To investigate problems that could endanger the functionality of ITER TBM.
- b) To optimize the final design of the blanket modules.
- c) To study proper instrumentation to be used for the proposed experiments.
- d) To support the development of specific features to be implemented in a numerical code. Experimental data will be organized in benchmark libraries.

HCLL TBM-related MHD Issues: State of the Art and Rationale for the Future Work Plan (D2)

With the aim of covering the gap between the present scientific and technical knowledge and the ones required to perform the proposed MHD experiments in ITER, a list of actions, defining the future research activities, is defined. In order to do that, a number of groups is identified in which the requirements for performing MHD tests in ITER are subdivided: instrumentation, out-of-ITER complementary-experiments, modeling and software. In each category the main issues are listed and separately analyzed to define the state of art of the present knowledge related to the considered problem.

It should be pointed out the importance of out-of-ITER experiments to test and develop proper instrumentation. Two kinds of experiments have to be foreseen: first, tests have to be performed to study the functionality of single sensors, second, mock-ups have to be designed and manufactured to investigate and optimize the integration of instrumentation in the TBM, to study combined effects, fabrication issues and to find out the required space for a complete installation.

The selection of diagnostic sensors and related equipment for ITER tests depends on the available space and on the complex environmental conditions (high temperature, varying magnetic field, induced currents...). For the development of measuring instruments, information about material compatibility in ITER environment should be clearly given. For measurements during a pulse, when time-dependent magnetic fields and wall heat flux occur, a sufficiently fast measuring system has to be used, which is able to follow the transient. Since replacement and repair of sensors is difficult and often impossible once the TBM system has been assembled, redundancy of instrumentation has to be guaranteed.

The requirements common to all the measuring methods can be summarized as follows:

- Applicability in the specific fusion environment (high temperatures up to 500°, intense magnetic fields, temperature and magnetic field gradients)
- Negligible impact on measurements
- Accuracy and long lifetime
- Sufficiently fast response time
- Simple replacement or redundancy

Concerning code development, capacity to simulate numerically the MHD flow distribution in the whole TBM is not achieved yet. Further development of theoretical tools is mandatory for the prediction of global 3D coupled phenomena.

It is important to remember that in ITER only outboard blanket modules can be tested. In a DEMO reactor there will be also inboard modules characterized by a more limited available space and a higher magnetic field. Numerical calculations should consider all these features and allow to foresee the requirements to pass from an ITER outboard blanket to a DEMO inboard blanket environment.

Development of a numerical code has the following global objectives:

- Interpretation of the ITER experimental data
- Support the selection of physical models, e.g. for magneto-convection and near-wall description of velocity, current and pressure
- Planning new experiments and defining features to be investigated in the experimental campaign
- Optimization of blanket design
- Capability of predicting MHD flow phenomena in a DEMO reactor (derivation of extrapolation procedures of TBM data to DEMO conditions).

Magneto-hydrodynamic Pressure Drops in Geometric Elements forming a HCLL Blanket Mock-up

The helium cooled lead lithium (HCLL) blanket concept is one of the designs that will be tested and validated in the experimental reactor ITER. The liquid metal that is slowly circulated in the blanket interacts with the magnetic field confining the plasma leading to modifications of velocity and pressure distributions compared to the ones in hydrodynamic flows. Experiments have been performed to investigate the magneto-hydrodynamic flows in a scaled mock-up of a HCLL blanket. The design features that cause the highest pressure drops are identified and the effects of flow rate and magnetic field strength on the various contributions to the total pressure head are discussed.

The test section consists of 4 breeder units with internal plates, fed and drained by circular pipes and manifolds. Here the liquid metal flows mainly in direction perpendicular to the imposed magnetic field. Fig. 6a shows an open view on the mock-up whose main dimensions are 176(rad)×409(poI)×93(tor) mm³. In Fig. 6b the liquid metal flow path in the test section is illustrated: after entering the distributing manifold the model fluid fills boxes 1 and 3, it changes direction at the first wall to enter the adjacent unit (2 and 4, respectively) by flowing through a small opening. The liquid metal is then collected at the back plate by the second manifold. The test section has been manufactured from stainless steel and NaK is used as model fluid. Since all walls are electrically conducting, currents induced in the fluid domains may close through the mock-up solid structure leading to a complex electric flow coupling. During the experimental campaign pressure differences have been measured between couples of points on the test section. In Fig. 6c a radial-poloidal section of the mock-up is sketched and typical liquid metal flow paths, along which the pressure distribution is record-

ed, are displayed. In Fig. 7 the normalized pressure is plotted for the MHD flow at $Ha = 1000$ and various Reynolds numbers as a function of the coordinate l that varies along the characteristic paths. It is possible to identify the main contributions to the total pressure head: in the inlet circular pipe (path A1- B) a significant pressure difference Δp_{in} occurs, then the liquid metal flows in the distributing manifold (B -C) and part of it passes through the narrow gap in the back plate (B -D1) and enters breeder unit 1 resulting in an additional pressure drop Δp_{BP} .

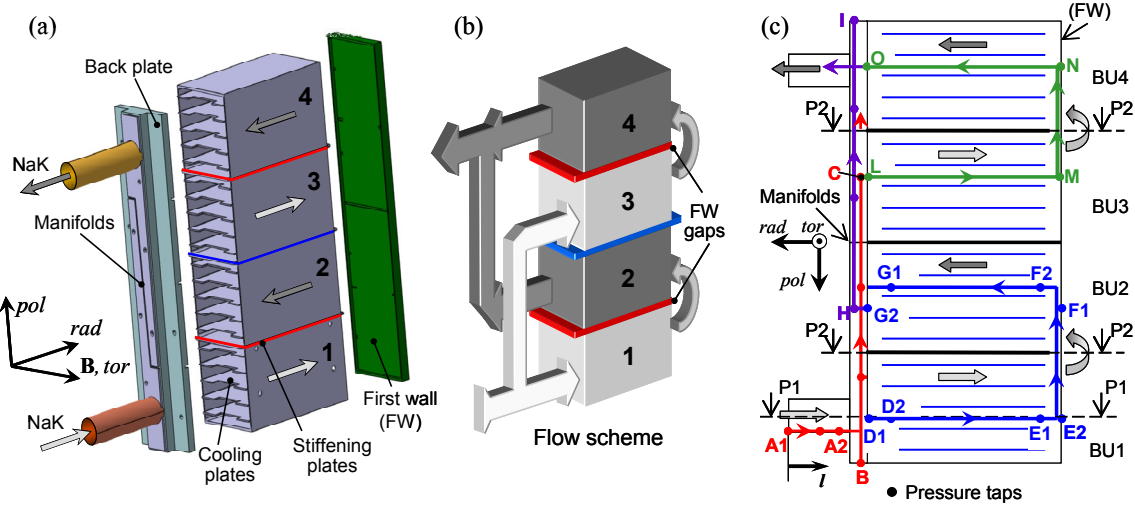


Fig. 6: (a) Test section design: it consists of 4 breeder units (BUs) fed and drained by poloidal manifolds. The BUs are connected hydraulically two by two at the first wall.
(b) Scheme of liquid metal flow in the mock-up.
(c) Flow paths along which the pressure distribution is measured.

Along the breeder units the pressure remains practically constant due to the small liquid metal velocities compared to the ones in pipes and manifolds. When the liquid metal turns in poloidal direction to enter the connected box (path E2- F1) inertia forces become stronger owing to the reduction of the cross-section along the flow path. The gap at the first wall is quite small and it yields an increased velocity. As a consequence an additional pressure head Δp_{FW} is observed. The liquid metal is then collected by a second manifold that transports the fluid out of the test section (H - I). The largest pressure differences Δp_{M1} and Δp_{M2} are measured along the manifolds. For this moderate Hartmann number there is an evident influence of inertia. If stronger magnetic fields are applied the pressure distribution in the mock-up becomes practically unaffected by inertia [7].

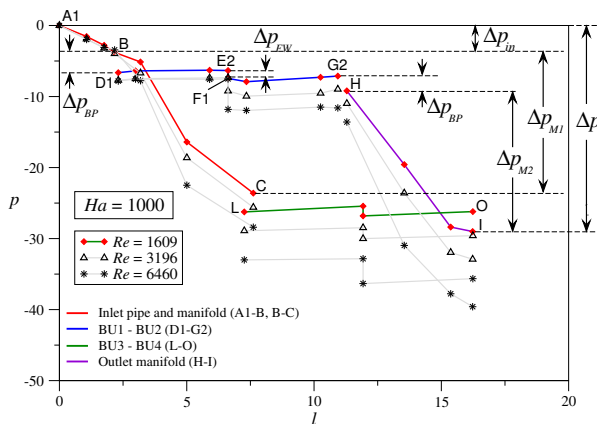


Fig. 7: Pressure distribution along typical flow paths for MHD flow at $Ha = 1000$ and different Reynolds numbers.

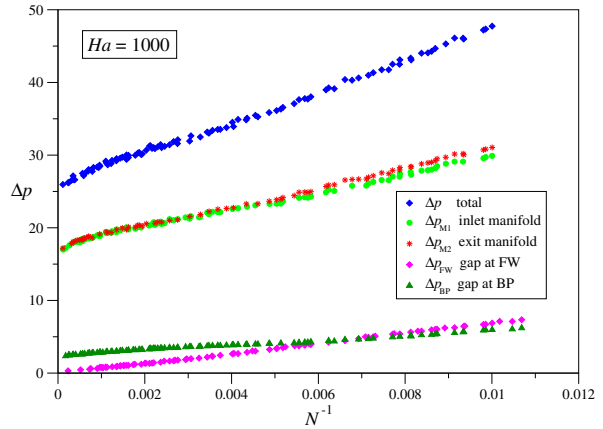


Fig. 8: Contributions to the total pressure drop Δp , which occur in various parts of the test section. Results for $Ha = 1000$.

Let us consider the described contributions to the total pressure drop that occur in various geometric elements that form the test section. They are plotted in Fig. 8 as a function of the inverse interaction parameter N (N^{-1} denotes the ratio of inertia to electromagnetic forces) for the flow at $Ha = 1000$ (Ha is a nondimensional measure for the strength of the magnetic field). It can be observed that all the contributions vary as N^{-1} . The pressure heads along the manifolds Δp_{M1} and Δp_{M2} represent about 65% of the total one. For large flow rates additional inertial effects increase the pressure drop in the outlet manifold compared to the one in the inlet distributing system ($\Delta p_{M2} > \Delta p_{M1}$). Across the gap at the back plate (B -D1 in Fig. 7), which connects the breeder units with the manifold, the pressure difference gives a contribution of 10 -13% depending on the Reynolds number. However, it remains quite stable showing that it is determined mainly by MHD phenomena. This can be explained considering that, when passing through this opening, the liquid metal expands along magnetic field direction to redistribute in the large box. This kind of flow is characterized by strong MHD effects due to the occurrence of internal viscous layers aligned with the magnetic field. Instead the pressure drop Δp_{FW} across the gap at the first wall reduces progressively with N^{-1} , i.e. it is mostly related to the action of inertia forces due to the increased velocity through the smaller opening cross-section.

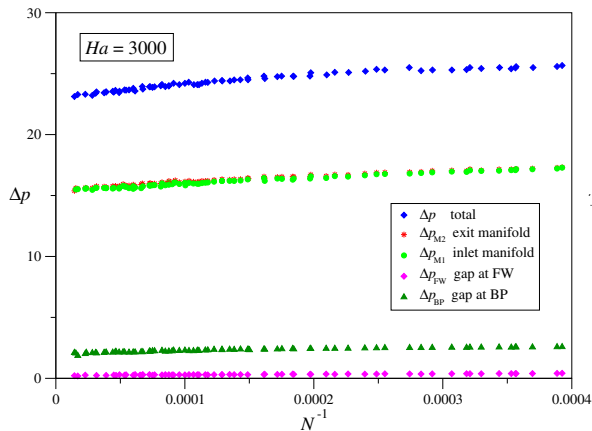


Fig. 9: Main contributions to the total pressure drop Δp .
Results for $Ha = 3000$.

Staff:

H.-J. Brinkmann
L. Bühler
S. Horanyi
C. Mistrangelo
K. Starke

Literature:

- [1] A. Aiello, L. Bühler, Ciampichetti, D. Demange, L. Dörr, J.F. Freibergs, B. Ghidersa, M. Ilic, G. Laffont, G. Messemer, I. Platnieks, G. Rampal, and A. Tincani. Mockup testing facilities and qualification strategy for EU ITER TBMs. In Proceedings of the 9th International Symposium on Fusion Nuclear Technology, 11.-16. November, Dalian, China. 2009.
- [2] L. Bühler. On the origin of super-rotating layers in magnetohydrodynamic flows. *Theoretical and Computational Fluid Dynamics*, 23:491-507, 2009. DOI 10.1007/s00162-009-0111-z.
- [3] L. Bühler and S. Horanyi. Measurements of time-dependent liquid metal magnetohydrodynamic flows in a flat rectangular duct. *Fusion Engineering and Design*, 84:518-521, 2009.
- [4] L. Bühler and C. Mistrangelo. Emergency draining of a HCLL TBM under the influence of a strong magnetic field: First estimates. In Proceedings of the 23rd Symposium on Fusion Engineering, SOFE 2009. June 2009.

For larger Hartmann numbers, in the range of a flow rate that can be investigated experimentally, the pressure drop contribution at the first wall is very small and tends to zero when reducing the flow rate. This can be seen in Fig. 9 where the various contributions to the total pressure head in the mock-up are displayed as a function of N^{-1} for the flow at $Ha = 3000$.

- [5] D. K. Fidaros, L. Bühler, A. P. Grecos, and N. S. Vlachos. Numerical modeling of rotating tangential layers (jets) in shells under strong uniform magnetic field. International Journal for Numerical Methods in Fluids, 2009, DOI 10.1002/fld.2036.
- [6] C. Mistrangelo and L. Bühler. Influence of helium cooling channels on magnetohydrodynamic flows in the HCLL blanket. Fusion Engineering and Design, 84:1323-1328, 2009.
- [7] C. Mistrangelo and L. Bühler. Experimental analysis of MHD pressure drop in a HCLL blanket mock-up. In Proceedings of the 23rd Symposium on Fusion Engineering, SOFE 2009. June 2009.
- [8] C. Mistrangelo and L. Bühler. Perturbing effects of electric potential probes on MHD duct flows. Experiments in Fluids, 2009. DOI 10.1007/s00348-009-0710-x.
- [9] C. Mistrangelo and L. Bühler. Liquid metal MHD in fusion technology. In EPM Madylam Seminar Grenoble, March 25-27. 2009.
- [10] C. Mistrangelo and L. Bühler. List of MHD experiments for HCLL TBM to be performed in ITER. Technical Report F4E Number, 05.6 TBMCA.2009.D2PT.0003 d1.0, Forschungszentrum Karlsruhe - Fusion for Energy, 2009.
- [11] C. Mistrangelo. Experiments and numerical simulations of MHD flows. 2009. Invited talk at ABB Corporate Research, Västerås, Sweden, September 16.
- [12] M.-J. Ni, L. Bühler, N. Morley, and M. Abdou. Direct simulations of 3D MHD flows in a sudden expansion using a consistent and conservative scheme. In Proceedings of the 9th International Symposium on Fusion Nuclear Technology, 11.-16. November, Dalian, China. 2009.
- [13] S. Smolentsev, R. Moreau, L. Bühler, and C. Mistrangelo. MHD thermofluid Issues of liquid metal blankets: Phenomena and advances. In Proceedings of the 9th International Symposium on Fusion Nuclear Technology, 11.-16. November, Dalian, China. 2009.
- [14] K. Starke, L. Bühler, and S. Horanyi. Experimental MHD - flow analyses in a mock up of a test blanket module for the ITER. Fusion Engineering and Design, 84(7-11):1794-1798, 2009.

Contribution to Division 2 (CEA leadership):

6. Non-destructive Testing (NDT)

Objectives

Qualification of adequate NDT (non-destructive testing) techniques for detecting cracks particularly in the welded areas of TBM components built from EUROFER 97 and to realise it with an automated NDT testing procedure.

Task current status

Within the reporting time period an automated ultrasonic scanning system with focused immersion transducers was installed. The system, KC 200 by GE Sensing & Inspection Technologies, has an immersion tank with a 3D scanning unit and allows automated ultrasonic inspection on TBM components with large dimensions (90 cm×50 cm×40 cm). The system was used within the EFDA-task TW6-TTMS-005 D5 to determine the minimum detectable flaw size in different EUROFER 97 welded joints.

In addition a collaborative working programme between KIT and CEA collecting the expertises of these two associations in the field of ultrasonic testing was formulated. In this programme different tasks are identified to be required for reliable non-destructive testing of TBMs. With the use of experimental and simulation techniques the inspectability of the differ-

ent TBM welds shall be assessed and improved by optimisation of the inspection procedures and tools as well as eventual changes in the weld design.

Staff:

T. Martin
S. Knaak
J. Aktaa

Contribution to Division 3 (ENEA leadership):

7. Breeder Blanket and Tritium Technology Group

Background

The Test Blanket Modules (TBM) in ITER will offer the unique possibility to perform integrated tests of both breeder blanket options for the DEMO machine: the Helium Cooled Pebble Bed (HCPB) and Helium Cooled Lithium Lead (HCLL) concepts. Based on the know-how accumulated over many years of R&D, the objectives are now to define the experiments to be performed in ITER, and accordingly prepare the R&D road map until the test phase in ITER.

From the tritium point of view, a design review is launched on the concepts for the tritium processes in both helium loops (extraction and coolant) that need now to be consolidated. In parallel, the mechanisms for the tritium release from the solid breeder should be better understood in support to the design activities. Within this first Grant managed by the European Consortium of Associates for the Test Blanket Modules (CA-TBM), the Tritium Laboratory Karlsruhe (TLK) is contributing to these topics.

Conceptual designs of the tritium processing in the helium loops

In collaboration with ENEA acting as task coordinator, the TLK is participating to the ongoing activities focussing on the design of Tritium Extraction System (TES) and the Coolant Purification System (CPS) for HCLL and HCPB.

Based on the know-how accumulated over many years of R&D and previous concepts proposed by TLK and ENEA, the processes used in these tritium systems are assessed with emphasis on performances (tritium removal efficiency, tritium decontamination factors), operation (reliability, maintenance, interfaces), and load to the accountancy stage as interface with the ITER tritium plant.

The design review for CPS has been completed. For the tritium processing requirements, the HCLL concept is the more demanding so that it is considered as the design limiting case. The proposed solution is a three stage process constituted by an oxidiser to convert molecular tritium (Q_2) into tritiated water vapour (Q_2O), followed by an adsorption step performed on molecular sieve at room temperature to remove Q_2O , and a final step performed on a heated getter to remove residual impurities. For the first stage, it is foreseen an over-estimation of the bed in order to avoid the complex procedure of regeneration. For the second stage, zeolite 5A has been proposed as adsorption material, while the third stage will adopt a getter based on a zirconium alloy working at about 400 °C. Compared with previous options, the last stage has been changed with the main benefit to avoid the use of cryogenic temperatures.

The design review of TES for HCPB is in progress. Based on the design review performed for CPS, the possibility to replace the adsorption of molecular hydrogen on zeolite at liquid nitrogen temperature by a reversible hydrogen getter is being evaluated. From the thermodynamic point of view, ZrCo is a good candidate, but the kinetic might be the limiting factor. At the moment in time, both options remain and additional tests will be required to validate the use of a getter bed. The design review for TES HCLL will be performed early next year.

For the instrumentation, it has been highlighted that online tritium measurement based on ionisation chambers will fulfil the required measurement range for the control and operation of all the tritium systems. However, such measurements shall not be enough accurate to provide quantitative results used for validation of neutronics calculation, and for tritium tracking between the TBM tritium systems and the tritium plant. Therefore an additional and dedicated accountancy stage shall be installed with collection of gas tritium and dedicated tritium concentration measurement. Among the conventional techniques for tritium analyses, gas chromatography is here the most adapted, but requires liquid nitrogen temperature to separate the 6 different hydrogen isotopologues. The alternative use of optical methods such as Laser Raman spectroscopy could greatly simplify and improve the accountancy procedure (no sampling, no liquid nitrogen). Further R&D focussing on such improvement is in progress at TLK.

Tritium release coupled phenomena in solid breeder concept

Within the Predictive Tools Group (PTG), TLK is coordinating a task focusing on the “tritium coupled phenomena” looking in detail at the tritium behaviour in the solid breeder functional materials (ceramic breeder + neutron multiplier). The objectives for this study are as follows: Define experiments to be performed in ITER, provide the state of the art for tritium behaviour in the breeder zone, and define the work plan for the next years.

Tritium release is a fundamentally complex function of many material parameters and operating conditions. The chemical composition (bulk and surface) and micro/macro-structure of the ceramic material will be subject to modifications along the life-time of the blanket under severe operating conditions with long term operation. Such ageing effects have to be carefully studied in terms of tritium inventory, tritium release rate, and tritium self-sufficiency, which are the major concerns for the design and operation of the DEMO machine.

Experiments in ITER have been proposed to tackle these issues. In-line tritium measurements combined with post irradiation examinations should be able to answer the following questions:

- A. Does the tritium production and release rate (dramatically) change over long time operation?
- B. If yes, what material parameter is responsible for this change?
- C. If yes, what is changed from the tritium point of view: residence time, tritium release chemistry, i.e. HT/HTO ratio?
- D. If yes, what are the consequences (countermeasures) on the breeder blanket design, and the corresponding tritium processing systems?

In synergy with these experiments, the tritium coupled phenomena and ageing effects shall be modelled and simulated in order to end up with predictive capabilities for DEMO.

A deep literature survey is being completed to evaluate the state of the art for experiments and model for tritium release and coupled phenomena. A huge amount of experimental results for tritium behaviour in breeder blanket has been produced for different materials by in-pile measurements and complementary out-of-pile studies including material characterisation. However, at this moment in time, the predictive capability for ITER remains very limited.

This is primarily due to the difficulty to extrapolate the tritium behaviour observed on previous materials to the new ceramics that are currently produced with a totally different production route based on melt-spraying. Moreover, little efforts have been put on model and simulation detailing tritium release and coupled phenomena.

Therefore, prior to the experiments in ITER, the following work plan is recommended:

- Produce a wide range of materials (silicate and titanate, with different porosity and grain size) using the newest fabrication techniques;
- Irradiate these new materials for tritium measurements (in- and out-of-pile) and perform post irradiation examinations for mechanical and chemical characterisations including residual tritium inventory;
- In parallel, develop models and simulation tools for tritium release at the pebble scale, first with input from former experimental data on tritium release and coupled phenomena, correlation relation, then progressively use new data to refine and calibrate the numerical tools;
- In addition, develop tritium analytical techniques other than ionisation chambers to be used in ITER experiments for real time measurements, enabling the discrimination between different chemical forms of tritium.

This future R&D plan should take benefit of the wide range of expertise and huge potential in Europe for material production, irradiation, post characterisation, simulation, and tritium measurements. Last but not least, the synergy between these fields shall be reinforced in the future.

Staff:

D. Demange
E. Fanghanel

Literature:

[15] A. Ciampichetti, A. Aiello, G. Coccoluto, I. Ricapito, K. Liger, D. Demange, C. Moreno: "The Coolant Purification System of the European Test Blanket Modules: preliminary design", 9th ISFNT October 11-16, 2009, Dalian, China (to be published in Fusion Engineering and Design)

[16] N. Ghirelli, D. Demange, O. Gastaldi, T. Gilardi: "Calculations of Tritium mass transfer in HCPB concept TBM and impact on systems for DEMO scale up", 9th ISFNT October 11-16, 2009, Dalian, China (to be published in Fusion Engineering and Design)

[17] A. Aiello, L. Bühler, A. Ciampichetti, D. Demange, L. Dörr, J.F. Freibergs, B. Ghidersa, M. Ilic, G. Laffont, G. Messemer, I. Platnieks, G. Rampal: "Mockup testing facilities and qualification strategy for EU ITER TBMs", 9th ISFNT October 11-16, 2009, Dalian, China (to be published in Fusion Engineering and Design)

Acknowledgement

This work was supported by Fusion for Energy under the grant contract No. F4E-2008-GRT-09(PNS-TBM)-01 with collaboration by CEA, France; ENEA, Italy; CIEMAT, Spain; KFKI-RMKI, Hungary and NRI Řež, Czech Republic. The views and opinions expressed herein reflect only the author's views. Fusion for Energy is not liable for any use that may be made of the information contained therein.

Fusion Researcher Fellowships

WP08-FRF-FZK/Cismondi

The objective of this Fusion Researcher Fellowship in KIT (former FZK) is the design of the 1:3 mock up of the Helium Cooled Pebble Bed Test Blanket Module (HCPB TBM). Due to the necessity to provide a vertical HCPB TBM (instead of horizontal) for the connection to one ITER equatorial port, the HCPB TBM global design has been at the beginning of the fellowship revised and adapted.

Once the full scale TBM design is validated, a coherent design of the 1:3 functional mock-up can be developed. In particular the detailed engineering design including the definition of fabrication routes and technologies and the definition of the mock-up experiment has to be performed. The work has been split in the following way:

- First year: preliminary design of the new vertical full scale HCPB TBM. Definition of the experimental plan for the 1:3 mock-up and preliminary approach to the mock-up design.
- Second year: design of the 1:3 functional mock-up based on the new vertical HCPB TBM. Start of the detailed design of the full scale HCPB TBM.

Other than the design of the TBM itself, the activity should deal with the TBM installation in ITER. Other than being compatible with both the two European TBM systems (HCPB and HCLL), the installation system developed must follow the general requirement of a limited number of interfaces, required by ITER organization and validated by F4E. For these reasons during this year a 5 months mobility has been organized in the frame of this Fusion Researcher Fellowship in order to participate in the development of the TBM installation inside ITER Equatorial Port with all the interfaces constraints and maintenance requirement. The host association of this mobility action has been CEA Cadarache (IRFM) and the engineering group working on the integration of the Port Plug in ITER.

Other than the mobility activities described below in more details, the technical activities during this 2nd year have been concentrated on the detailed design of the full scale HCPB TBM and on the preliminary design of the 1/3 HCPB TBM mock-up. In particular, the experiments to be performed on the 1/3 mock-up have been studied, proposing an experimental campaign and the thermo hydraulic behavior and relevance of the First Wall of the 1/3 mock-up have been studied in details. The next paragraph will describe shortly the activities performed during the mobility in Cadarache.

In relation with the global development plan of the TBM system, the technical work has been limited for this mobility to the Port Plug installation and to the two interfaces, between Shield and TBM box (Interface I) and between Port Plug and Shield (Interface II).

Three tasks have been identified in the Technical work plan proposed:

1. **Development of the TBM attachment to the shield** (interface I): development of a generic design compatible with HCLL and HCPB systems.
2. **Design of the shield attachment to the port plug.**
3. **Development of the generic shield** (for the HCLL and HCPB systems) with its cooling system. An important point to be developed in this context concerns the layout of TBM piping in the TBM shield.

The three tasks identified in the Technical Work plan have been developed as follows.

1. Development of the TBM attachment to the shield

A preliminary design of the TBM attachment has been proposed. In order to optimize the attachment geometry minimizing the stresses under typical loading conditions, eight different geometrical configuration of the preliminary attachment version have been studied, identifying the best geometrical configuration. The analyses have been carried on taking into account the different loading conditions: weight of the TBM, thermal expansion, electro magnetic loads and a case combining all the mentioned loads.

Once identified the best geometrical configuration, the optimal attachment has been integrated in a more complete FE model including the TBM back plate and the shield plate.

The analyses of the complete model need a clear definition of the boundary conditions to be applied. The TBM attachment system has to withstand the mechanical, thermal and electromagnetic loads of the TBM box in normal operation but also in case of off normal plasma operations. In particular the attachment are the connecting point between TBM box and shield and have to withstand the strong Electromagnetic forces and torques originated by a plasma disruption. An important effort has been dedicated to the clear definition of the boundary conditions. In this context the vicinity with the CEA team studying the Port Plug integration and the ITER team has facilitated and accelerated the exchange of information.

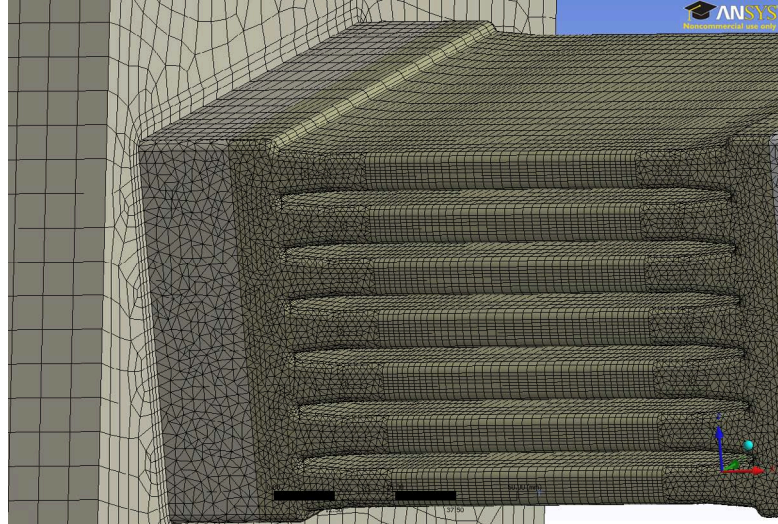


Fig. 1: Optimal geometry of the attachment system.

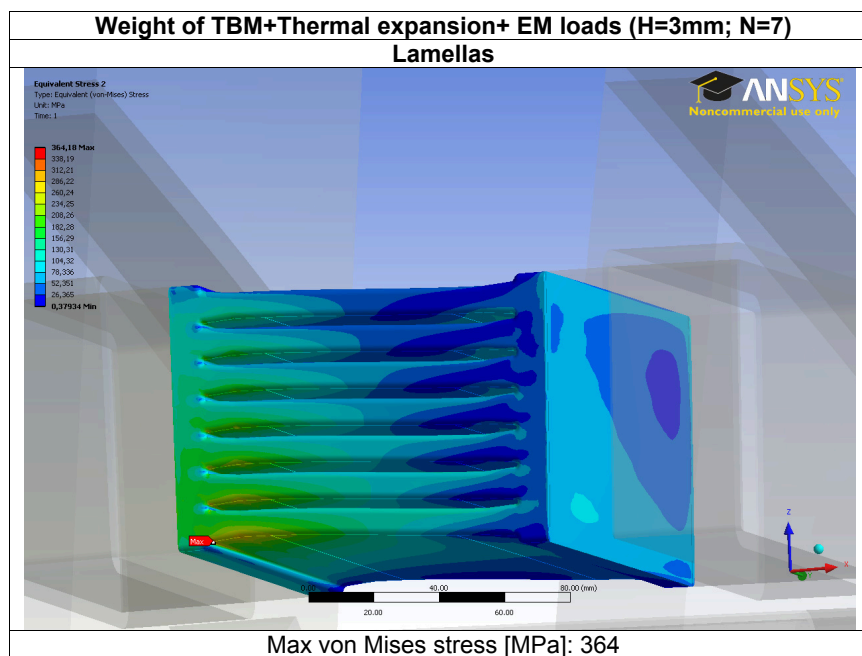


Fig. 2: Von Mises stress in the attachment system.

A 1/4 scaled model of the TBM attachment system has been built including the TBM box back plate and the shield plate. The helium coolant outlet pipe, the by pass pipe and the purge gas pipe have been included in the model.

The optimized geometry is proposed in Fig. 1, while Fig. 2 reports the results obtained applying simultaneously the different loads identified on the 1/4 model with the improved attachment geometry.

2. Design of the Shield attachment to the port plug

This point has been mainly developed contributing to the shield/Port Plug/Pipe Forest design with information about the TBM design and piping system.

An important model for the further development of the attachment system has been developed with the aim to evaluate the radiation effect on the thermal stress distribution in the attachment. The development of FE model in ANSYS taking into account the radiation effect requires a careful handling of the ANSYS tools and commands: the conclusion of this study is that, considering typical ITER operation and radiation temperatures, the maximal expected temperature difference between a model including the radiation effect and a model implementing only the conductive effect would be about 4%. Assuming typical radiation temperature, the radiation effect can be disregarded.

3. Development of the generic shield (for the HCLL and HCPB systems) with its cooling system

The main contribution in defining the interface in between TBM box and shield, other than the design of the attachment system, concerns the definition of the piping layout. The pipe dimensions and position in the HCPB TBM box have been defined in collaboration with experts of the HCS, identifying in the codes and standard the pipes closer to the design specifications. The shield designers have implemented these values in the shield conceptual design, transferring the information to the Pipe Forset designers for the space allocation.

Staff:

F. Cismondi

Acknowledgement

This work, supported by the European Communities under the contract of Association between EURATOM and Karlsruhe Institute of Technology, was carried out within the framework of the European Fusion Development Agreement. The views and opinions expressed herein do not necessarily reflect those of the European Commission.

Goal Oriented Training Programme “Breeding Blanket Developments for Fusion Reactors” (WP08-GOT-EUROBREED (FU07-CT-2008-00047))

The overall objective of the goal oriented training (GOT) Programme EUROBREED is helping to provide the necessary broad expert basis to successfully conduct the European breeding blanket development programme along with ITER and the developments beyond ITER, i.e., for a fusion power reactor, comprising the development of the optimum breeder and neutron multiplier materials, the design of specific breeder blanket components for future fusion reactors, and testing the breeding blanket in ITER. The training programme proceeds along, and enhance, already existing projects in the framework of the European Breeder Blanket Programme, and of supporting activities in the associations. The EUROBREED programme, jointly conducted by KIT, AEUL, CEA, CIEMAT, ENEA, FOM/NRG, HAS, and CCFE, consists of eight work packages (WP), two of them are hosted at KIT. Each of the WPs represents a training programme unit for a trainee that is employed in the WP leader association. Other associations are involved in a WP giving support and hosting the trainee for a certain period in a related field of work. The list of the different Work Packages and of the involved associations is summarised in Table 1.

Table 1: Work Packages in EUROBREED Network

WP Id	Leader Org.	Other organisations in the WP training	WP Description
WP1	KIT	CEA	Design, procurement and test of solid breeder units
WP2	KIT	NRG	Pebble bed development and testing for the EU solid breeder blanket
WP3	CEA	KIT, CEA, CIEMAT	Neutronics and radiation protection shielding design of the HCLL reactor
WP4	CEA	KIT, HAS	TBM integration in Port Plug with engineering design and interfaces management
WP5	HAS	KIT, CEA, CIEMAT	Measurement techniques development for breeder blankets
WP6	NRG	CAE, NRG	Pebble bed nuclear performance testing
WP7	CIEMAT	CEA, NRG	Tritium transport predictive modelling tool for Breeding Blanket design analyses and system modelling
WP8	AEUL	KIT, CCFE	Properties and diffusion of tritium accumulated in fusion reactor materials
HCLL: Helium Cooled Lithium Lead			

At KIT a concept of a solid breeder blanket, the EU Helium Cooled Pebble Bed (HCPB), is under development for future fusion reactors. In particular the KIT design group is responsible for the design of the EU HCPB Test blanket Module (TBM) to be irradiated in ITER and of the design of its validation mock-ups. The EU breeding blanket programme also includes the development of tritium breeder materials and neutron multiplier for the TBM.

In **work package No. 1**, the technical goal of the trainee is to design, procure and test a BU mock-up. In particular the trainee will follow the industrial production in a company and co-ordinate an experimental campaign in a Helium facility. In order to attend the overall objective, the technical programme of the trainee has been split in the following five parts. (1) Design of a BU mock-up including relevant parameters; (2) procurement of the structural components of the BU mock-up; (3) preparation of an experiment plan including selection of parameters, selection and installation of dedicated diagnostic systems and experimental devices; (4) supervision during experimental operation; (5) evaluation of the results of the experiments and comparison with the analysis performed.

The trainee WP1 started on August 24th 2009. The candidate is involved in the BU design activities in the HCPB TBM design team. He presently performs thermal hydraulic analyses of the helium coolant in the BU Cooling Plates. This includes a training period dedicated to the engineering tools for FE analyses (ANSYS ICEM, ANSYS classic and ANSYS CFX). In order to be able to select relevant BU mock-up fabrication processes and evaluate welding samples, the trainee has acquired knowledge in fabrication technologies, welding and mounting strategies. The required close collaboration with manufacturing and material experts in KIT will be completed next year by two months mobility in CEA, Saclay.

Other than the foreseen mobility in the Saclay Welding Laboratory close collaboration with WP2 and WP6 are necessary to get the trainee involved in key topics of the Breeding Blanket development.

As intended in the trainee program the basis of the necessary background to be involved in the design of Breeder Blanket components has been gained attending the Summer School on Fusion Technology in KIT and the lectures on Fusion Technology at the University of Karlsruhe. At the same time the trainee's background has been enriched by attending courses in management of complex projects, risk management and cross-cultural communication.

In **work package No. 2**, the technical programme of the trainee consists of three parts: the fabrication and characterization (1) of lithium orthosilicate pebbles as ceramic breeder and (2) of beryllium/beryllium alloy pebbles as neutron multiplier, and (3) the experimental testing of TBM Breeder Unit (BU) mock-ups in collaboration with WP 1. The parts will be successively pursued, beginning with part 1. During a research visit of two months at NRG, Petten, which is scheduled for autumn 2010, the trainee will additionally work on in-pile irradiation tests and post-irradiation examinations of pebble beds.

The trainee for WP 2 started on April 15th 2009 and is responsible for selected tasks within the development of ceramic breeders. He supervises the investigations aiming at a modified melt-based process for lithium orthosilicate pebbles and is in charge for the quality control of the produced pebbles. From preliminary results, received at a small test facility, it can be deduced that air inclusions in the pebbles can be avoided, and the crush load can be increased. The trainee has already acquired an extensive knowledge in characterization techniques of functional ceramics as on-the-job training during the characterization of lithium orthosilicate pebbles. The investigation of corrosion phenomena of Pt-alloy crucibles, which is an issue for the fabrication of lithium orthosilicate pebbles, also trained him in the characterization of metals.

As intended in the training programme, the trainee attended various training courses. The courses covered technical and management issues, as well as topics to further improve the soft skills of the trainee.

Staff:

L.V. Boccaccini
F. Cismondi
U. Fischer
F.A. Hernández González (trainee, WP 1)
R. Knitter
M. Kolb (trainee, WP 2)
A. Möslang

Acknowledgement

This work, supported by the European Communities under the contract of Association between EURATOM and Karlsruhe Institute of Technology, was carried out within the framework of the European Fusion Development Agreement. The views and opinions expressed herein do not necessarily reflect those of the European Commission.

Helium Cooled Pebble Bed: Breeder and Neutron Multiplier Materials

The most relevant properties of Be-Ti alloys besides their ability as neutron multiplier are their thermo-physical, chemical and tritium release properties. In particular, Be_{12}Ti is considered to be one of the promising materials for neutron multipliers in future fusion power plants. Laboratory-scale tests aimed to produce Be_{12}Ti samples and the study of their relevant properties were performed.

Sintering tests under different gas atmospheres (Ar/H_2 and pure Ar) and pressures (from 10^{-5} mbar up to 10 bar) aiming to fabricate Be_{12}Ti rod were performed. The mixture of fine-milled Be-Ti powders was used as an initial material in this process. This powder metallurgical method of production has been chosen due to a possibility to control precisely the chemical composition of fabricated rods. Also, the use of fine powders with a big specific surface area intensifies the diffusion of Be in Ti. One of the aims of Be_{12}Ti rod production is its future use as a target material for Be_{12}Ti pebble production by melting in the inert gas atmosphere.

Beryllide samples (two charges of Be_{12}Ti and two charges of Be_{12}V) delivered by Company Brush Wellman Inc., USA, were investigated. The programme of characterisation included the study of their tritium release characteristics after preliminary hydrogen – 50 appm tritium gas mixture loading, investigations of microstructure by means of optical microscopy, SEM, TEM and compression tests under constant loads in the temperature range from room temperature up to 900 °C.

Also, investigation of properties of Be_{12}V samples (Brush Wellman, Inc.) and pure beryllium pebbles supplied by Bochvar Institute, Russia, and Company NGK, Japan, was done.

Part 1: Equipment for overpressure sintering of fine Be-Ti powders

The process of overpressure sintering (the pressure of ambient inert gas atmosphere is up to 10 bar) allows to decrease the evaporation rate of beryllium at elevated temperatures and, thus, provides better sintering conditions of fine metal particles.

The ceramic (Al_2O_3) tube was connected by a flange to inner wall of a glove-box and placed into an electric-resistant furnace (Fig. 1). Gas transducers provided a controlled pressure of gas atmosphere inside a tube. Fig. 2 shows Nb tube with Be-Ti rod inside after sintering at 1250 °C for 2 hours in Ar/H_2 atmosphere. The stoichiometric mixture of fine Be-Ti powders (70 wt.% Ti and 30 wt.% Be) was sintered to 83% density of its theoretical value.



Fig. 1: The view of the closed ceramic tube in the glove-box.



Fig. 2: Be-Ti rod after overpressure sintering inside of Nb tube.

Part 2: Tritium release experiments

The study of parameters of tritium release was performed after preliminary loading of beryllium-containing specimens with hydrogen – 50 appm tritium gas mixture at 850 °C under 4 bar. Then, these specimens were put into release section and tritium desorption was detected using proportional counter.

The measured activity of tritium has been depicted by two different curves: one curve shows release rate in Bq/g*s and another depicts the changes of temperature during the experiment.

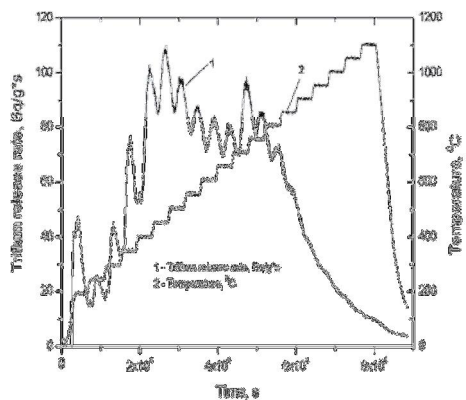


Fig. 3:: Tritium release from Be_{12}Ti fine-grained samples.

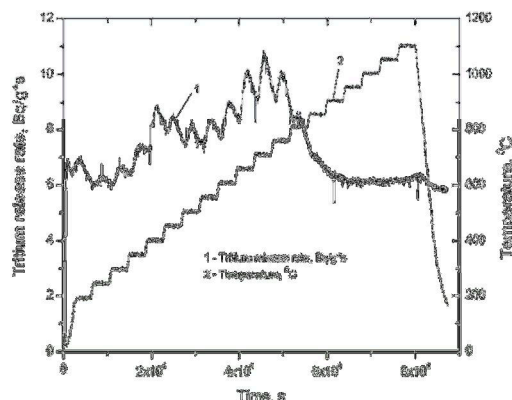


Fig. 4: Tritium release from two-phase α -Be- Be_{12}Ti samples.

Fig. 3 and Fig. 4 show the characteristic tritium release peaks of Be_{12}Ti specimens produced by Goraieb Versuchstechnik. The parameters of tritium release depend on the micro structural characteristics of investigated samples (grain size, phase composition, impurity content, etc.)

Part 3: Investigations of microstructure

Micro structural characteristics of pure beryllium and beryllide specimens were investigated by means of different technique. In particular, Fig. 5 shows optical micrograph of 1 mm pure Be pebbles from NGK, Japan, after micro hardness indentation tests and Fig. 6 shows a microstructure of polished Be_{12}Ti specimen provided by company Brush Wellman Inc.

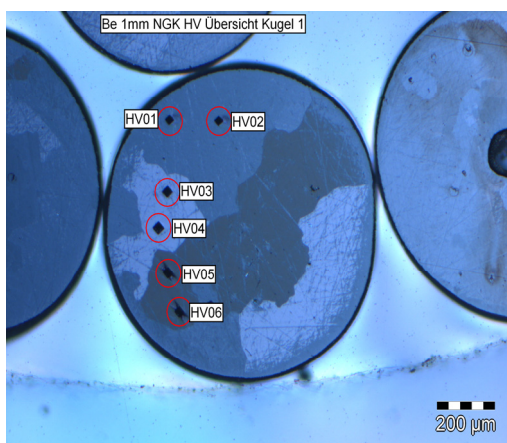


Fig. 5: Optical micrograph of 1 mm Be pebbles from NGK (polarized light).

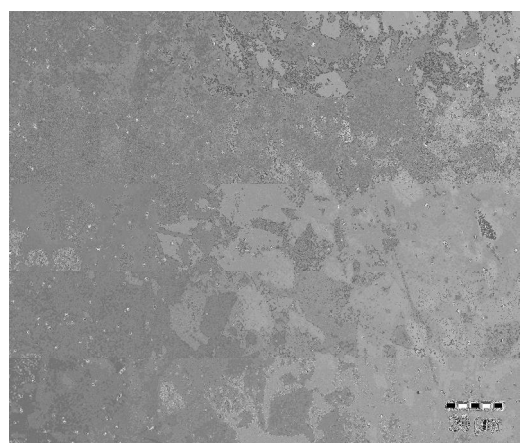


Fig. 6: Microstructure of Be_{12}Ti specimen from Brush Wellman, Inc.

Investigations of Be_{12}Ti specimens from Brush Wellman Inc. made by means of Transmission Electron Microscope are shown in Fig. 7 and Fig. 8.

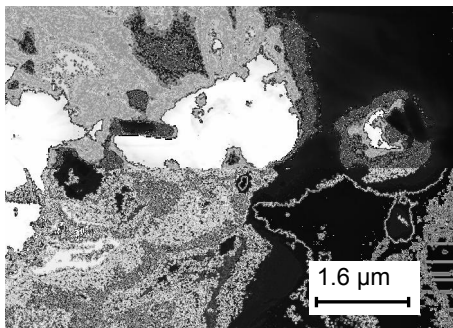


Fig. 7: Bright Field TEM Image of Be_{12}Ti sample from Brush Wellman, Inc.

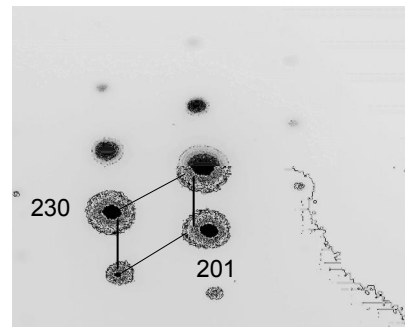


Fig. 8: Electron diffraction image with [-326] zone axis.

Part 4: Uniaxial compression tests

The mechanical properties of solid breeder materials have been identified as one of the key issues for the Helium Cooled Pebble Bed blanket design.

Cylindrical Be_{12}Ti and Be_{12}V specimens which have diameters of 3 mm and heights ranging from 2,6 to 4 mm were loaded at different temperatures (from room temperature up to 900 $^{\circ}\text{C}$) by constant loads (500 N and 1000 N).

Fig. 9 shows brittle performance of Be_{12}Ti specimen and two-phase $\alpha\text{-Be-Be}_{12}\text{Ti}$ specimen with improved ductile properties (Fig. 10) after testing at 900 $^{\circ}\text{C}$ with 1000 N.

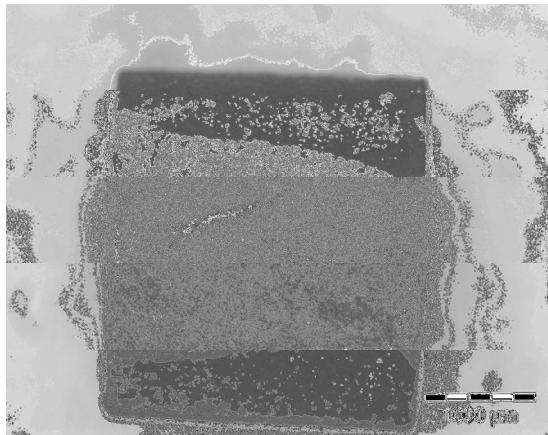


Fig. 9: Be_{12}Ti specimen (Brush Wellman, Inc.).

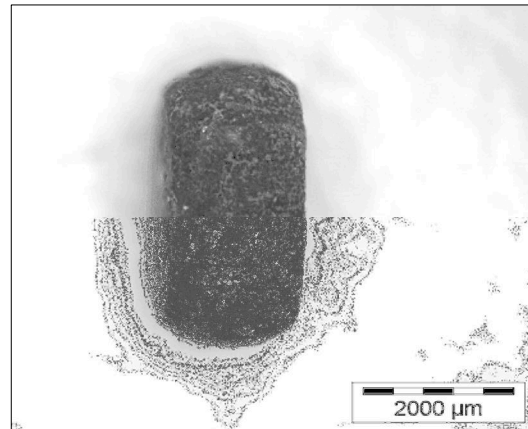


Fig. 10: Two-phase $\alpha\text{-Be-Be}_{12}\text{Ti}$ specimen (Goraieb Versuchstechnik).

Staff:

P. Kurinskyi
A. Möslang

Modelling of Pebbles and Pebble Beds

The modelling of pebbles and pebble beds has been developed using both simulations of collective behaviour of pebble beds and crush load experiments on single pebbles.

Statistical analysis of crush events inside ceramic breeder pebble beds

A framework for analyzing crush events of individual ceramic pebbles in solid breeder blankets is developed by means of probabilistic methods [2, 3]. As a brittle material, ceramic breeder pebbles show considerable scatter in crush strength for single pebbles. The combination of the discrete element method (DEM) [4] and experimental data of crush loads provides the possibility to obtain the overall crush probability of a pebble bed under compression. Micro-macro relations are used to correlate the crush probability of pebbles with the overall stress level of the bed. Analysis of uniaxial compression of a mono-sized lithium-orthosilicate pebble bed is presented here to demonstrate the application of this tool, see Fig. 1.

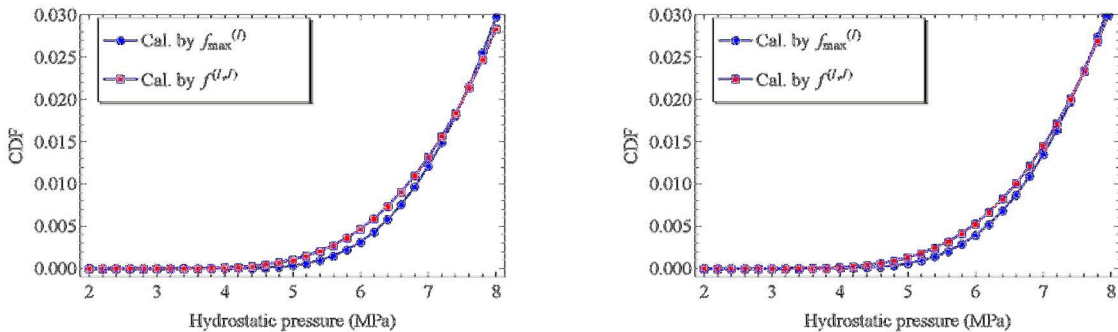


Fig. 1: Cumulative distribution functions for crush of individual pebbles inside the bed: (left) as-fabricated pebbles; (right) conditioned pebbles, as functions of macroscopic stress state, calculated by (1) maximum contact forces and (2) all inter-particle contact forces.

Computer simulation of packing structure

In HCPB blankets, pebble beds are composed of nearly spherical particles in the state of random closed packing. The packing structure is important to understand the response of pebble beds, e.g., mechanical stresses and effective thermal conductivity. In this investigation, an algorithm for random close packing of polydisperse particles is developed to reproduce the microstructure of a packed bed [1]. Both bulk and near-wall regions of pebble beds are considered in this work. Computer-generated samples are compared to recent X-ray tomography results of compressed and non-compressed pebble beds consisting of spherical particles, including packing factor and coordination number. Initial configurations obtained by this method can be used in DEM simulations of random configurations of pebbles to investigate the overall behaviour of pebble beds under fusion-relevant conditions [4].

Crush load tests of single pebbles

A modified statistic model was used to study the influence of the stiffness of the compression plate on the failure probability of Li_4OSi_4 pebbles based on two crush tests. The failure probability of pebbles with pebble-pebble contact was predicted with this model together with the experimental data of another crush test done at Fusion Material Lab (FML). The predicted probability with respect to absorbed energy was applied to DEM simulation of pebbles failure initiation and propagation. First, the initial load level for failure was identified with two methods. Second, the effect of failure propagation on the stress strain relation and the distribution of crushed spheres were studied. For both cases, parameter studies were carried out.

Staff:

Y. Gan
M. Kamlah
S. Zhao

Literature:

- [1] Gan, Y.; Kamlah, M.; Reimann, J. Computer simulation of packing structure in pebble beds. *9th International Symposium on Fusion Nuclear Technology (ISFNT-9)*, Dalian, China. October, 2009.
- [2] Gan, Y.; Kamlah, M. Statistical analysis of crush events inside ceramic breeder pebble beds in fusion blankets. *14th International Symposium on Applied Electromagnetics and Mechanics (ISEM09)*, Xi'an, China, 2009.
- [3] Gan, Y.; Kamlah, M.; Riesch-Oppermann, H.; Rolli, R.; Liu, P. Crush probability analysis of ceramic breeder pebble beds under mechanical stresses. *14th International Conference on Fusion Reactor Materials (ICFRM-14)*, Sapporo, Japan. September, 2009.
- [4] Gan, Y.; Kamlah, M. (2009) Discrete element modelling of pebble beds: With application to uniaxial compression tests of ceramic breeder pebble beds. *Journal of the Mechanics and Physics of Solids*. in press.
- [5] Gan, Y.; Kamlah, M. (2009) Thermo-mechanical modelling of pebble bed-wall interfaces. *Fusion Engineering and Design*. in press.
- [6] Gan, Y.; Kamlah, M. (2009) Thermo-mechanical analyses of HELICA and HEXCALIBER mock-ups. *Journal of Nuclear Materials*. 386-388: 1060-1064.

Procurement and Quality Control of Lithium Orthosilicate Pebbles – OSi 08

In collaboration with Schott AG, Mainz, the Karlsruhe Institute of Technology is developing and investigating slightly hyperstoichiometric lithium orthosilicate pebbles to be used in the HCPB blanket. The pebbles with a surplus of 2.5 wt% SiO₂ are produced by melting a mixture of LiOH·H₂O and SiO₂ powders and then spraying the liquid material in air. The characteristics of the final product are influenced by the batch wise melt-spraying process, which is rather difficult to control in the small facility. Consequently, the reproducibility from one production run to the other is not very high, and it is therefore necessary to control the quality of each batch of pebbles received from the industrial producer, in order to provide a well-defined standard material in all experimental activities with pebbles or pebbles beds.

The 4 kg of Li₄SiO₄ pebbles (OSi 08/1) were delivered in three batches of 0.92-1.62 kg. The pebbles with diameters ranging from 250 to 630 µm were characterised in the initial state according the standard test program for quality control (Table 1). Only the compressive crush load tests were carried out on 500 µm pebbles. For conditioning, the lithium orthosilicate pebbles were annealed at 970°C for 1 week under air to obtain the thermodynamically stable phases, lithium ortho- and metasilicate and a homogeneous microstructure in all pebbles. The results obtained for the conditioned pebble batches are summarised in Table 2 (OSi 08/1c).

The results of the chemical analysis revealed a SiO₂ excess of 2.7-2.8 wt% for all three pebble batches. This is in agreement with the desired value of 2.5 wt%. The impurities of the OSi 08/1 batches are quite low and well within the specification for the HCPB. To determine the phases in the delivered pebbles, X-ray powder diffraction was carried out for every batch. As expected, the pebbles consist of Li₄SiO₄ as the main constituent and the high-temperature phase Li₆Si₂O₇ as a minor constituent. During annealing, the high-temperature phase is decomposed into ortho- and metasilicate.

The appearance and microstructure of the OSi 08/1 batches were examined by optical and scanning electron microscopy. In all batches the pebbles appear 'pearl white', most of them are well, spherically shaped, but there are also some irregularly shaped particles (Fig. 1). A few pebbles exhibit a pockmarked or blistered surface, which was not observed in former batches. The reason for this appearance is unknown.

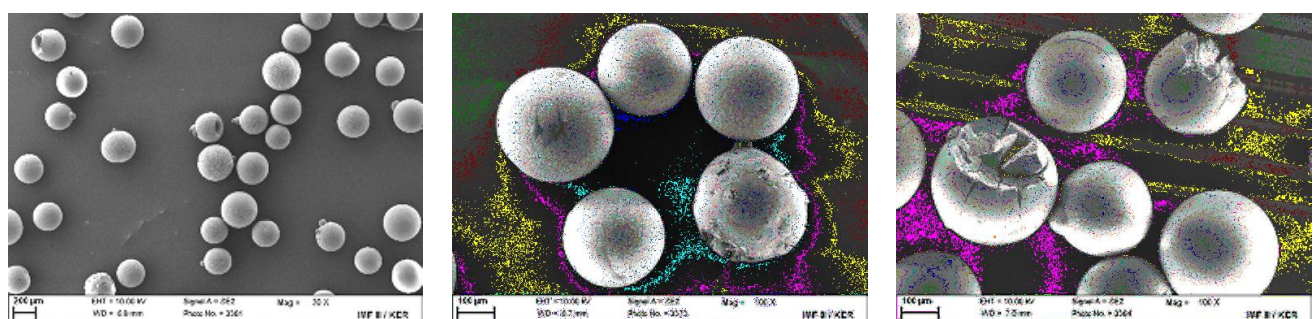


Fig. 1: Pebble morphology of lithium orthosilicate pebbles OSi 08/1 in the initial state (SEM).

Most of the pebbles display the expected, typical solidification microstructure of orthosilicate dendrites with small inclusions of the high-temperature phase Li₆Si₂O₇ at the surface as well as at etched cross-sections (Fig. 2). The orthosilicate dendrites often spread out over the whole pebble and contain a network of small interdendritic pores. The optical investigations at cross-sections display the usual amount of cracks and pores in the pebbles (Fig. 3). But there are also quite a few pebbles with large central pores in each batch due to gaseous inclusions in the melt droplets that were probably trapped during the solidification process. All batches also exhibit an amount of irregularly shaped pebbles.

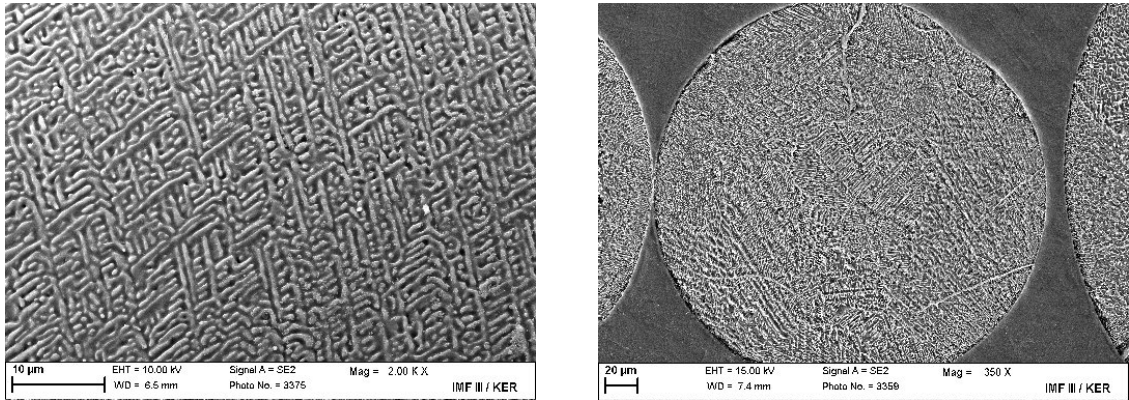


Fig. 2: Surface (left) and cross-section (right) of OSi pebbles in the initial state (SEM).

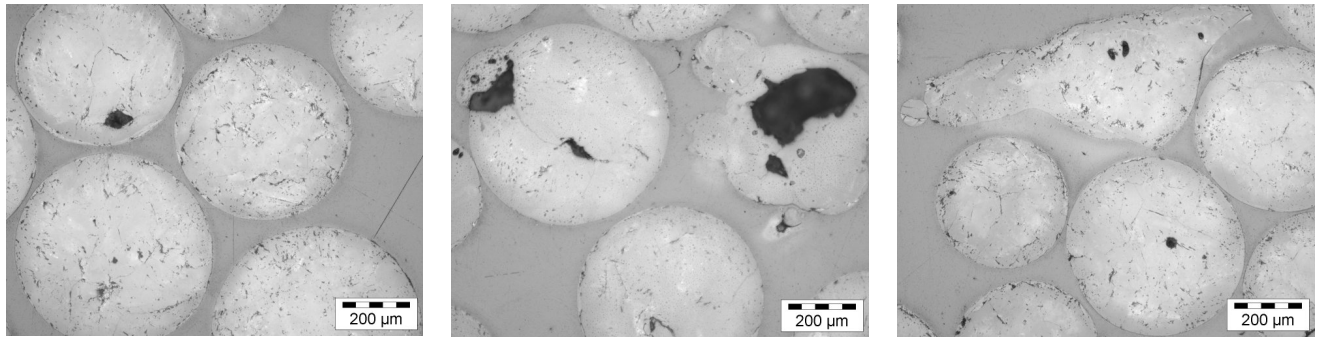


Fig. 3: Cross-sections of OSi pebbles in the initial state (OM).

The appearance of the pebbles after annealing is very similar to that in the initial state. The microscopic investigations display the usual amount of cracks and pores in the pebbles (Fig. 4). The pebble morphology is not altered by the heat treatment, so that deformed or blistered pebbles are still to be found in the conditioned batches (Fig. 5). At the surface of most pebbles lithium metasilicate grains can be observed, which result from the decomposition of the high-temperature phase $\text{Li}_6\text{Si}_2\text{O}_7$ into the equilibrium phases, lithium orthosilicate and metasilicate, during annealing (Fig. 5, right).

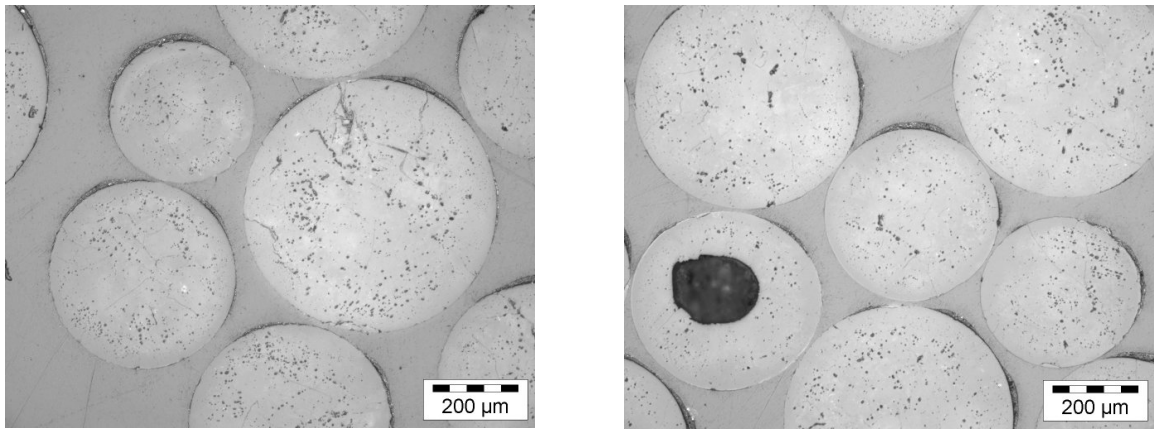


Fig. 4: Cross-sections of the lithium orthosilicate pebbles OSi 08/1c (970°C / 1 week) (OM).

At etched cross-sections the pebbles exhibit the expected microstructure of lithium orthosilicate grains and inter- and intragranular inclusions of metasilicate (Li_2SiO_3) (Fig. 6). Simultaneously, a rearrangement of pores and a coarsening of the microstructure take place. All

pebbles of the examined batches exhibit a homogeneous microstructure after annealing, however, the expected sintering microstructure is often less pronounced than usual.

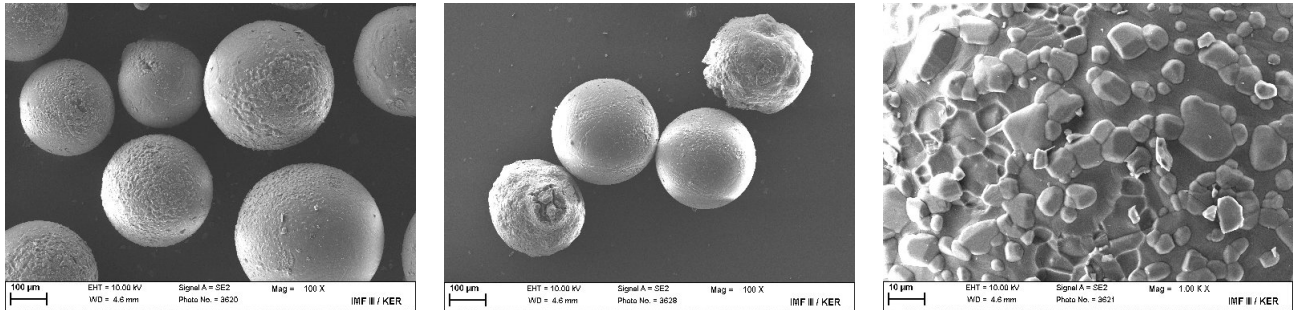


Fig. 5: Pebble morphology and surface appearance of OSi 08/1c (970°C / 1 week) (SEM).

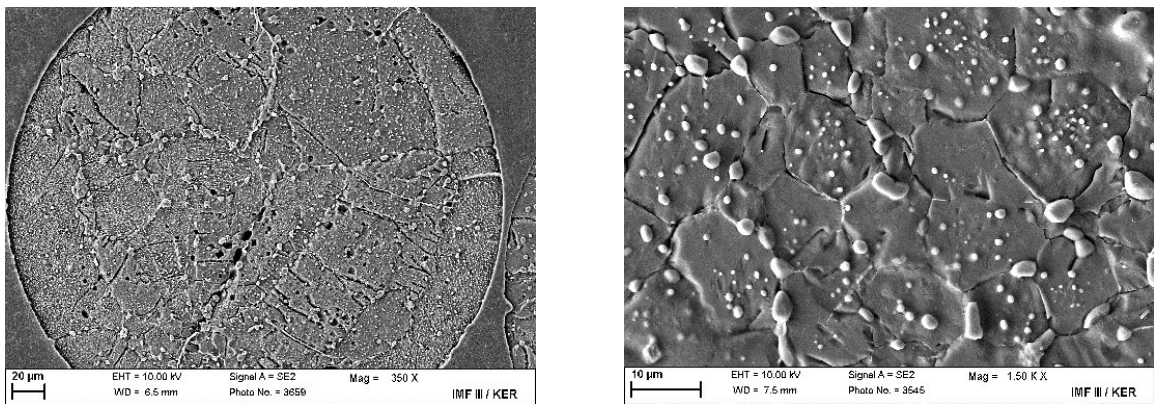


Fig. 6: Microstructure of OSi 08/c at etched cross-sections (970°C / 1 week) (SEM).

The delivered pebbles were screened to a diameter range of 250 – 630 µm, resulting in fractions with a mean particle diameter (d_{50}) of 310 µm for all three pebble batches OSi 08/1 (Fig. 7). The maximum of the distribution in each case is asymmetrically shifted to smaller diameters.

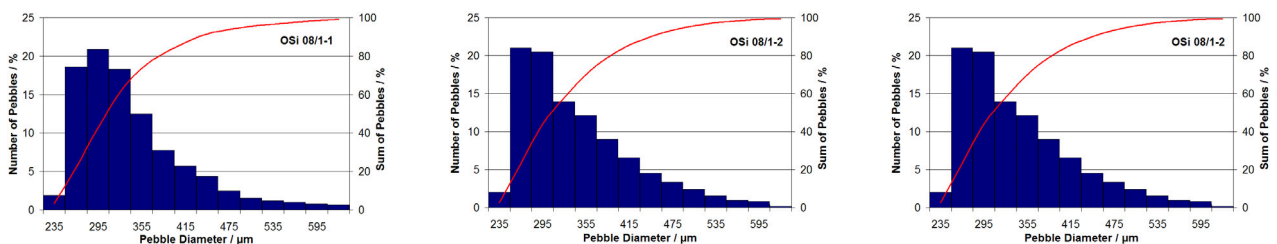


Fig. 7: Diameter distribution of the lithium orthosilicate pebbles OSi 08.

Porosity and density of the orthosilicate pebbles were measured by He-pycnometry and Hg-porosimetry (Table 1). A closed porosity of 0.4-05 % was determined by He-porosimetry. By Hg-porosimetry a density of approx. 94-95 %TD and an open porosity of 4-5 % were measured (TD = 2.40 g/cm³).

After annealing, for all samples a closed porosity of 0.6 % was measured by He-pycnometry (Table 2). The density of the pebbles is slightly increased to about 96 %TD after annealing. This is due to a decrease of the open porosity to about 3 %. The tap density of the pebbles before and after annealing amounts to 60-61 % TD.

Table 1: Properties of lithium orthosilicate pebbles OSi 08/1

Batch	OSi 08/1-1	OSi 08/1-2	OSi 08/1-3
Principal Constituents / wt% (Schott)			
Li ₂ O	48.18	48.05	48.13
SiO ₂	51.18	51.07	51.17
excess SiO ₂	2.74	2.76	2.78
Size Distribution			
d ₅₀ / μm	310	310	310
He-Pycnometry			
closed porosity (calc.) / %	0.5 \pm 0.0	0.4 \pm 0.0	0.4 \pm 0.0
Hg-Porosimetry			
density / g cm ⁻³	2.26 \pm 0.02	2.28 \pm 0.01	2.29 \pm 0.02
density / % TD*	94.1 \pm 0.9	94.9 \pm 0.2	95.2 \pm 0.8
open porosity / %	4.3 \pm 0.5	4.7 \pm 0.2	4.0 \pm 0.1
Pebble Bed Density			
tap density / g cm ⁻³	1.45 \pm 0.01	1.46 \pm 0.01	1.44 \pm 0.01
Crush Load Tests			
mean crush load / N	7.1 \pm 1.0	5.8 \pm 1.2	5.9 \pm 1.5

* A theoretical density of 2.4 g/cm³ was assumed for the OSi material.

Table 2: Properties of lithium orthosilicate pebbles OSi 08/1c (970°C / 1 week).

Batch	OSi 08/1-1c	OSi 08/1-2c	OSi 08/1-3c
He-Pycnometry			
closed porosity (calc.) / %	0.6 \pm 0.0	0.6 \pm 0.0	0.6 \pm 0.0
Hg-Porosimetry			
density / g cm ⁻³	2.31 \pm 0.02	2.32 \pm 0.01	2.31 \pm 0.01
density / % TD*	96.4 \pm 0.6	96.5 \pm 0.4	96.2 \pm 0.5
open porosity / %	2.8 \pm 0.1	2.9 \pm 0.4	3.2 \pm 0.7
Pebble Bed Density			
tap density / g cm ⁻³	1.46 \pm 0.01	1.45 \pm 0.01	1.45 \pm 0.01
Crush Load Tests			
mean crush load / N	5.5 \pm 1.3	5.5 \pm 1.3	5.4 \pm 1.1

* A theoretical density of 2.4 g/cm³ was assumed for the OSi material.

To investigate the differences in the mechanical stability of the pebbles, for each batch crush load measurements were performed on 40 pebbles with a diameter of 500 μm . Mean values of 7.1 N, 5.8 N and 5.9 N with standard deviations of 1.0-1.5 N were determined for OSi 08/1-1, 08/1-2 and 08/1-3, respectively (Fig. 8). While the values of the batches OSi 08/1-2 and 08/1-3 correspond to the crush load results of the OSi 07 mixture, the crush load of the first batch is slightly higher. The difference cannot be explained by the microscopic observation or by the density of the pebbles.

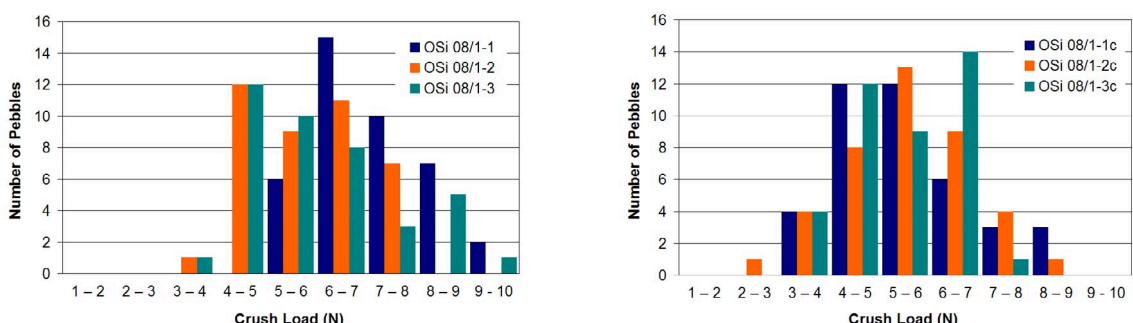


Fig. 8: Crush load measurements of lithium orthosilicate pebbles before and after annealing.

By thermal annealing, the crush load of the pebbles decreased to about 5.5 N with standard deviations of about 1.3 N. The average crush load of all annealed samples is consistent with the values determined for the annealed samples OSi 07/1c.

For testing of Breeder Unit mock-ups 4 kg of Li_4SiO_4 pebbles were procured in three batches and completely characterised. The quality control assured satisfactory properties of the recently fabricated OSi pebbles and the results are comparable to the quality of the mixture OSi 07/1. The properties of the investigated pebble batches of OSi 07/1 and 08/1 are within the specification of the reference material, but the mechanical properties – examined by crush load tests – are at the lower limit of the acceptable range.

Activation of Lithium Orthosilicate Breeder Ceramics

The fabrication of lithium orthosilicate (OSi) pebbles by melt-spraying enables a facile reprocessing of irradiated material by direct remelting [1]. The cost effectiveness of a direct remelting of breeder pebbles, however, strongly depends on the activation of the used breeder material and the necessity of a purification step. The impurities of as-prepared OSi pebbles mainly result from the raw materials, only Pt originates from the crucible used in the fabrication process [1]. These impurities are the main source for the activation of the lithium orthosilicate, which is otherwise a genuine low activation material [2]. The recycling of lithium orthosilicate has been simulated for a fusion power reactor with a helium cooled pebble bed blanket to assess the possible accumulation of radiologically relevant nuclides and to prove the possibility of a multiple reprocessing of OSi by remelting without any sumptuous, wet-chemical reprocessing [3]. An averaged inventory of the breeder pebbles was considered, i.e. the simulation of multiple reprocessing was based on the assumption that a mixing of pebbles of all breeder units can be accomplished. The nuclide inventory was calculated for lithium orthosilicates pebbles with their actual impurities [2] and an irradiation time of 3 full power years (fpy). For the simulation, the recycling was assumed to take place 10 years after shutdown. The recycling process was simulated by adding new ${}^6\text{Li}$, and additional impurities were considered in relation to the amount of new ${}^6\text{Li}$. Additionally, platinum from the crucible was added to the melt according to an equilibrium equation assuming that the platinum concentration may increase up to 500 $\mu\text{g/g}$. Afterwards, the material was assumed to be irradiated again under reactor conditions. This procedure was repeated for 15 cycles, so that the total irradiation time amounts to 45 fpy (Fig. 9).

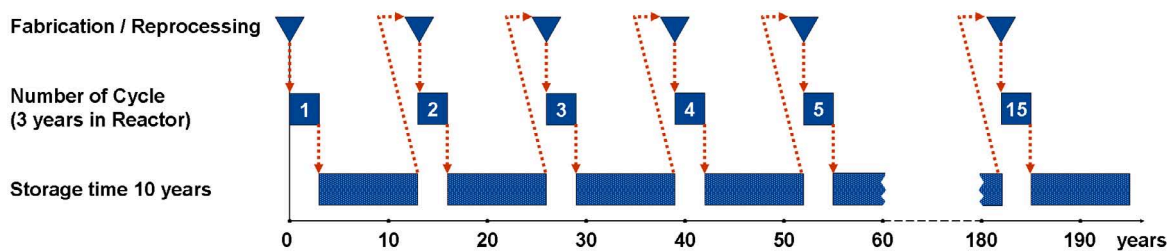


Fig. 9: Schematic representation of the simulated multiple recycling.

It was shown that there is no severe accumulation of radionuclides over the cycles and no deterioration of the breeder tritium breeding performance. The contact dose rate of the OSi pebbles after various cycles is shown in figure 10. After the first cycle the remote level of the averaged inventory is already reached in less than 1 hour, while it takes less than 30 years to reach the hands-on level. The waiting time for the hands-on level is dominated by ${}^{60}\text{Co}$, originating from the assumed amount of 1 $\mu\text{g/g}$ Co, while the actual amount of Co in OSi pebbles is below the determination limit in chemical analysis. The activities resulting from ${}^{193}\text{Pt}$ and ${}^{26}\text{Al}$ are irrelevant for the waiting time as they are well below the hands-on level. With increasing number of cycles, the waiting time for the remote level is increased from several hours to approx. 1 day, mainly due to an increasing amount of ${}^{24}\text{Na}$. The waiting time for the hands-on level, however, is barely changed to approx. 35 years even after cycle 15. In spite

of the assumed increasing amount of platinum, the activity resulting from ^{193}Pt is still below the hands-on level.

The calculation was also used to determine the change in the amount of impurities with increasing irradiation time. Starting from a total amount of impurities of the OSi pebbles of about 0.12 wt%, the accumulated impurities even after 15 cycles (45 fpy) were calculated to be below 1 wt%. Due to the high solubility of various elements in lithium orthosilicate, no new phase is expected to result by the relatively small increase of impurities.

The results reveal that numerous cycles of a three-year-use of the tritium breeder pebbles with subsequent remelting seem to be possible without any wet-chemical reprocessing, if a mixing of the pebbles of all breeder units can be accomplished. It is thus concluded that the multiple recycling of irradiated lithium orthosilicate is possible under remote conditions short time after discharge.

Staff:

C. Adelhelm
B. Dörzapf
U. Fischer
S. Herber
U. Kaufmann
R. Knitter
M. Kolb
B. Löbbecke
C. Odemer
M. Offermann
B. Wagner

Literature:

- [1] R. Knitter, B. Löbbecke, Reprocessing of lithium orthosilicate breeder material by remelting, *J. Nucl. Mater.* 361 (2007) 104-111.
- [2] R. Knitter, U. Fischer, S. Herber, C. Adelhelm, Reduction of impurities and activation of lithium orthosilicate breeder materials, *J. Nucl. Mater.* 386-388 (2009) 1071-1073.
- [3] S.C. Herber, U. Fischer, R. Knitter, E. Foßhag, Simulation of multiple recycling of breeder ceramics in fusion power reactors, 14th Int. Conf. on Fusion Reactor Materials (ICFRM-14), Sapporo, Japan, Sept. 2009, to be published in *J. Nucl. Mater.*
- [4] K. Munakata, T. Shinozaki, K. Inoue, S. Kajii, Y. Shinozaki, R. Knitter, N. Bekris, T. Fujii, H. Yamana, K. Okuno, Tritium release from lithium silicate pebbles produced from lithium hydroxide, *Fus. Eng. Des.* 83 (2008) 1317-1320.
- [5] T. Shikama, R. Knitter, J. Konys, T. Muroga, K. Tsuchiya, A. Moeslang, H. Kawamura, S. Nagata, Status of development of functional materials with perspective on beyond-ITER, *Fus. Eng. Des.* 83 (2008) 976-982.

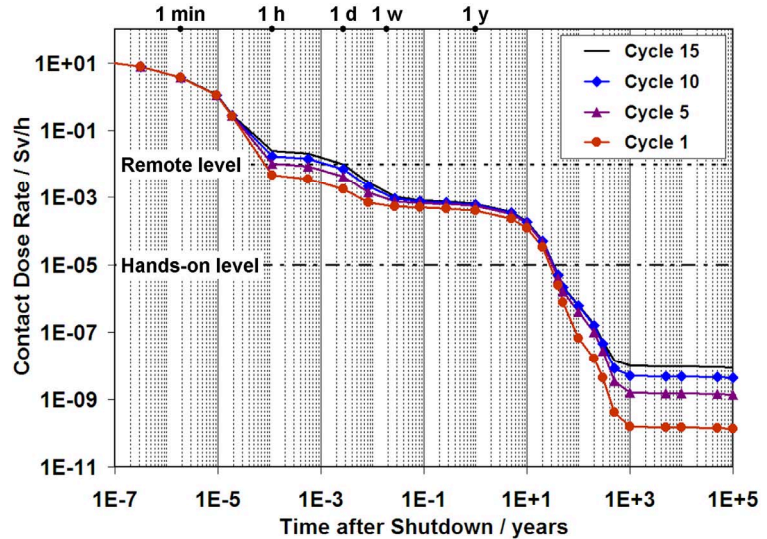


Fig. 10: Contact dose rate of OSi pebbles after cycle 1, 5, 10, and 15 versus time after shutdown.

- [6] B. Löbbecke, R. Knitter, M. Rohde, J. Reimann, Thermal conductivity of sintered lithium orthosilicate compacts, *J. Nucl. Mater.* 386-388 (2009) 1068-1070.
- [7] K. Munakata, T. Shinozaki, K. Inoue, S. Kajii, Y. Shinozaki, T. Takeishi, R. Knitter, N. Bekris, T. Fujii, H. Yamana, K. Okuno, Tritium release from lithium orthosilicate pebbles deposited with palladium, *J. Nucl. Mater.* 386-388 (2009) 1091-1094.
- [8] R. Knitter, Status of lithium orthosilicate pebbles fabricated by melt-spraying, 15th Int. Workshop on Ceramic Breeder Blanket Interactions (CBBI-15), Sapporo, Japan, Sept. 2009.
- [9] K. Mochizuki, K. Munakata, T. Shinozaki, R. Knitter, N. Bekris, T. Fujii, H. Yamana, K. Okuno, Tritium release from ceramic breeder materials deposited with noble metals, 14th Int. Conf. on Fusion Reactor Materials (ICFRM-14), Sapporo, Japan, Sept. 2009, to be published in *J. Nucl. Mater.*
- [10] M. Zmitko, Y. Poitevin, L. Boccaccini, J-F. Salavy, R. Knitter, A. Moeslang, A.J. Magielsen, J.B.J. Hegeman, R. Lässer, Development and qualification of functional materials for the EU test blanket modules: strategy and R&D achievements, 14th Int. Conf. on Fusion Reactor Materials (ICFRM-14), Sapporo, Japan, Sept. 2009, to be published in *J. Nucl. Mater.*
- [11] K. Mochizuki, K. Munakata, T. Wajima, K. Hara, K. Wada, T. Shinozaki, T. Takeishi, R. Knitter, N. Bekris, T. Fujii, H. Yamana, K. Okuno, Study of isotope exchange reactions on ceramic breeder materials deposited with noble metal, 9th Int. Symp. on Fusion Nuclear Technology (ISFNT-9), Dalian, China, Oct. 2009, to be published in *Fus. Eng. Des.*

DEMO Divertor: Fabrication, Joining, and High Heat Flux Component Testing (WP08-09-MAT-WWALLOY, Activity 1)

Introduction

A modular He-cooled divertor concept for DEMO has been developed at KIT. The design goal is to achieve a DEMO-relevant heat flux of 10 MW/m^2 . The reference design [1] is based on the use of small cooling finger modules (Fig. 1) made of tungsten and tungsten alloy. The finger modules are cooled by helium impinging jets. During the past years 2006-2008, three series of high heat flux (HHF) experiments [2, 3, 4] were successfully performed in a combined helium loop [5] and electron beam facility (Fig. 2) which was built at Efremov for verification of the design. The design principle and the performance of the divertor have been confirmed by these tests. The last tested mock-ups survived outstandingly more than 200 cycles at 10 MW/m^2 and were available for further tests which is part of the subject of the upcoming test series. In parallel, study on high precision fabrication of the mock-up parts and on W joining technologies has been launched at KIT.

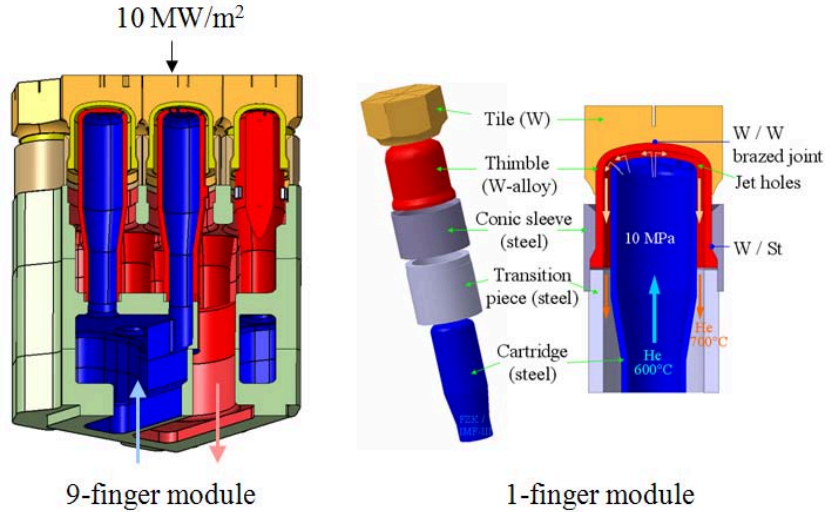


Fig. 1: Reference He-cooled divertor concept HEMJ, heat flux 10 MW/m^2 , T_{\max} , tile $1700 \text{ }^{\circ}\text{C}$, T_{\max} , thimble $1170 \text{ }^{\circ}\text{C}$ [1].

and electron beam facility (Fig. 2) which was built at Efremov for verification of the design. The design principle and the performance of the divertor have been confirmed by these tests. The last tested mock-ups survived outstandingly more than 200 cycles at 10 MW/m^2 and were available for further tests which is part of the subject of the upcoming test series. In parallel, study on high precision fabrication of the mock-up parts and on W joining technologies has been launched at KIT.

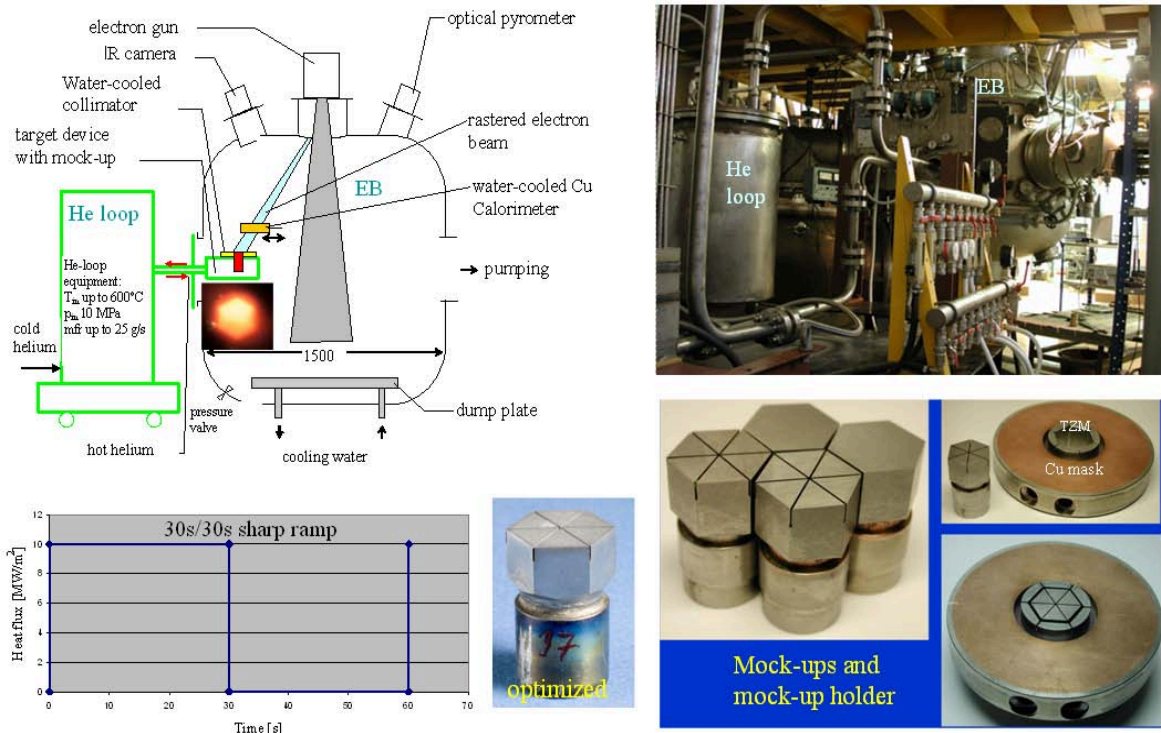


Fig. 2: Combined He loop and TSEFEY test facility at Efremov.

Divertor Finger Module Fabrication: Machining & Joining

Chosen materials

The current reference design HEMJ (He-cooled modular divertor with jet cooling, Fig. 1), reference case: 10 MW/m^2 , $T_{\max, \text{tile}} 1700 \text{ }^{\circ}\text{C}$, $T_{\max, \text{thimble}} 1170 \text{ }^{\circ}\text{C}$, is based on impingement cooling with multiple helium jets at 10 MPa , $600 \text{ }^{\circ}\text{C}$.

Tungsten is considered the most promising material [6] which is low-activating and can withstand the specified high heat load because it possesses a high melting point, high thermal conductivity, and relatively low thermal expansion. On the other hand, it has a small operation temperature window restricted by the ductile-brittle transition temperature (DBTT) at the lower boundary and the recrystallisation temperature (RCT) at the upper boundary. Further disadvantages are high hardness and high brittleness, which make the fabrication of tungsten components comparatively difficult. The RCT and machinability of tungsten can be improved by adding fine oxide particles, with WL10 being regarded a suitable option for the divertor design at present. The design window range of WL10 structural parts under fusion neutron irradiation is assumed between $600 \text{ }^{\circ}\text{C}$ and $1300 \text{ }^{\circ}\text{C}$.

Machining of tungsten and tungsten alloy parts

The motivation for this work came from the observation during the HHF tests of the divertor cooling fingers at Efremov that micro cracks initiated by EDM (electro discharge machining) and/or conventional machining with insufficient surface quality seriously could lead to crack growths in tile and thimble during thermal cyclic-loading. The depth of micro cracks in the tungsten initiated by machining lie between 30 and $200 \mu\text{m}$ [7] depending on machining type. Generally, requirements on high accuracy and excellent surfaces are important for reaching high performance, high reliability, and high functionality of the divertor. Machining of tungsten or tungsten alloy is a very challenging task which requires experience because of high hardness and brittleness (460 HV 30) [8] of tungsten.

We started to investigate turning and milling for W tile and WL10 thimble on a universal machining centre (Traub TNA 300), which enables both turning and milling without any repositioning, as well as on a milling machine (DMU 50 eVolution). The latter offers more options and flexibility, e.g. higher number of revolutions, possibility for performing dry milling (i.e. milling without liquid cooling), large number of tools (36), flexible clamp as well as 5-axis machining techniques. For the assessment Plansee's deformed W-rod $\varnothing 25 \text{ mm}$ for tile and deformed WL10 rod $\varnothing 21.5 \text{ mm}$ for thimble machining, respectively, were used.

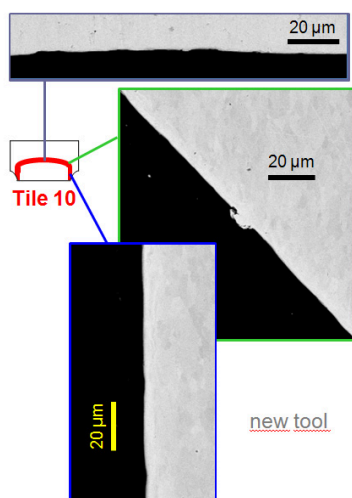


Fig. 3: Crack-free surfaces achieved by milling with a new tool.

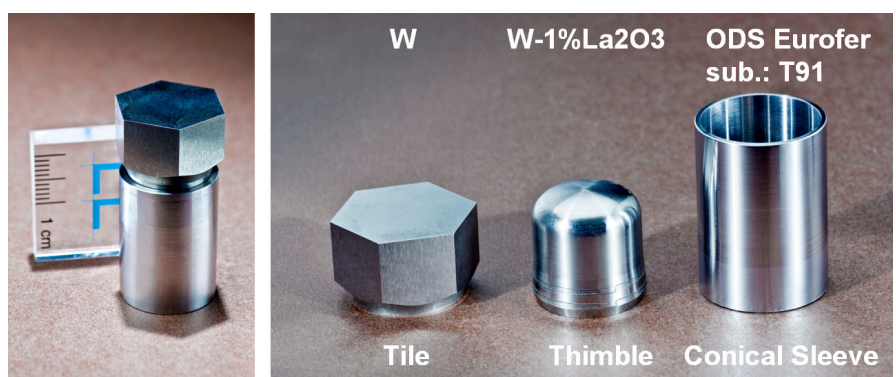


Fig. 4: W tile, WL10 thimble, and steel conical sleeve manufactured at the KIT.

The first tests for assessing the cutting parameters were performed in cooperation with the company of Sandvik Coromant. Parameters, such as cutting speed, feed, depth of cut, and kind of cutting inserts (positive vs. negative, coated vs. uncoated, sintered vs. ground), were tested for rough machining and finishing. A following case study was performed comparing turning to milling of tungsten tile. The interior of the tile can be machined either by turning or milling, the latter to be differentiated between front and peripheral milling. The aim is to select technology for reaching the best surface quality and smallest tool wear. The hexagonal flanks as well as the top plasma facing surface of the tile can be machined by either front or peripheral milling. The overall results show: a) generally, excellent micro-crack free surface quality was achieved by both turning and milling (Fig. 3, milling result) suitable for manufacturing high quality cooling fingers, b) dry milling has an in self-removal of most of the frictional heat by flying chip which helps reduce cutting tool wear when compared to turning, c) milling was found to be optimal procedure for W tile production since it offers shorter processing time by a factor of 4 than turning, d) for the hexagon contour circular front milling is recommended due to its higher accuracy, whereas machining the top surface to be carried out in a "from the edge to the center" manner to avoid break out of the edges. While machining W tile is a challenge, machining WL10 thimble is not a problem because it has a simple cylindrical shape suitable for turning. Fig. 4 illustrates the individual parts of a complete cooling finger (tile, thimble and conic sleeve) manufactured in such a way which will be assembled and HHF tested in the next test series at Efremov.

Taking into account the economical point of view mass oriented production techniques have to be assessed. For this reason deep drawing or roll pressing of WL10 thimble is under investigation at KIT. Deep drawing technique also offers the possibility of achieving a uniform grain orientation along the thimble contour suitable for load-oriented function and increasing the crack growth resistance of the thimble. This work was started systematically with deep drawing of stainless steel (V4A 1.4571) thimble in the first step followed by TZM molybdenum alloy containing titanium and zirconium in the second step. The current machining set up (Fig. 5a, 5b) includes a butane gas heater that should heat up the tungsten plate up to 400 °C, measured by pyrometer (red LED light spot). A higher temperature is not desired due to oxidation of tungsten. During the machining process the temperature is documented online by a pyrometer. This step was successfully performed. Fig. 5c shows good results of roll pressing thimbles of steel and TZM materials without failure. Deep drawing of thimble from a cross rolled tungsten sheet will be the next step.

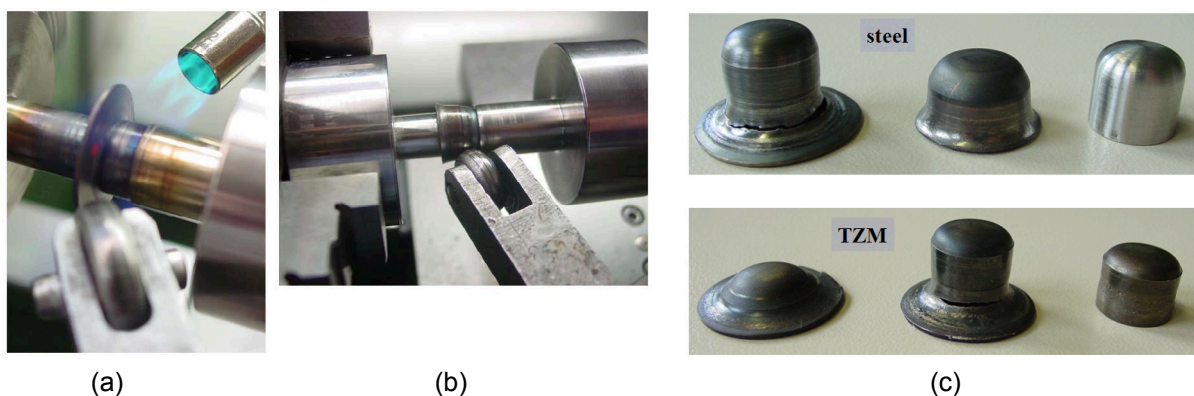


Fig. 5: Roll pressing steel and TZM thimbles: (a, b) pre-heating and pressing, © roll pressed thimbles.

Joining of divertor parts

Brazing W tile to WL10 thimble for the first mock-ups was earlier performed at Efremov [9] using STEMET®1311 filler metal (amorphous Ni based alloy, brazing temperature $T_{br} = 1050^\circ\text{C}$). During the first HHF tests tile and thimble detachment (top surface melting of the W tile as a consequence) was observed when ramping up the HHF beyond 13 MW/m². This failure was assumed to be caused by overheating of the brazed joint. This motivates us to

investigate a new brazing filler with T_{br} lying above the expected operation temperature at this joint of ~ 1200 °C (Fig. 6a). For this reason new brazing technology for the elevated brazing temperature has to be studied, taking into account the recrystallisation temperature of WL10 material (1300 °C). The literature research results in PdNi40 (liquidus temperature $T_{lq} = 1238$ °C) as a suitable filler for the W-WL10 joint.

For the brazing of WL10-Steel joint (working temperature ~ 700 °C) CuPd18 filler ($T_{lq} = 1100$ °C) was found suitable. The brazing procedure begins with a preparation step (sand blasting, acetone ultrasonic bath (Fig. 6b) before braze joining the parts in the furnace (Fig. 6c) under a $10^{-5} - 10^{-4}$ mbar vacuum.

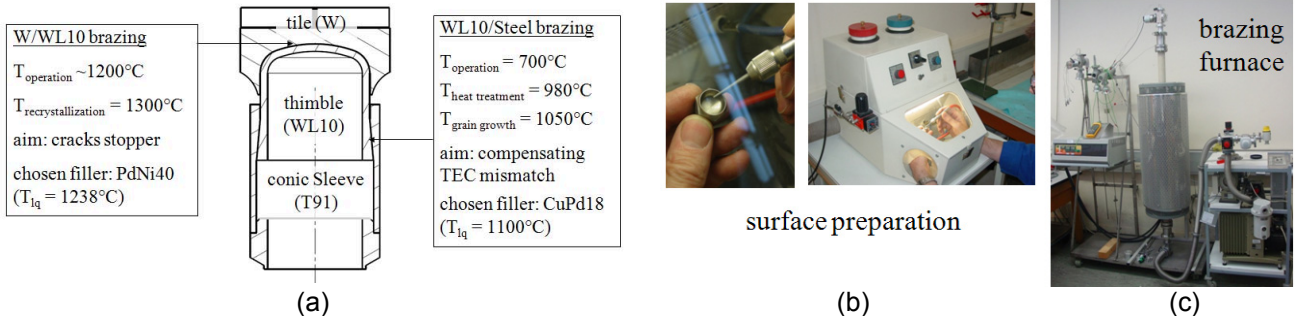


Fig. 6: Divertor parts brazing: a) boundary conditions; b) surface preparation; c) brazing furnace.

Fig. 7a and 7b illustrate the successful brazing results for the W-WL joint with PdNi and WL-steel joint with CuPd, respectively. In both cases a good adhesion of brazing fillers to the basic materials was achieved.

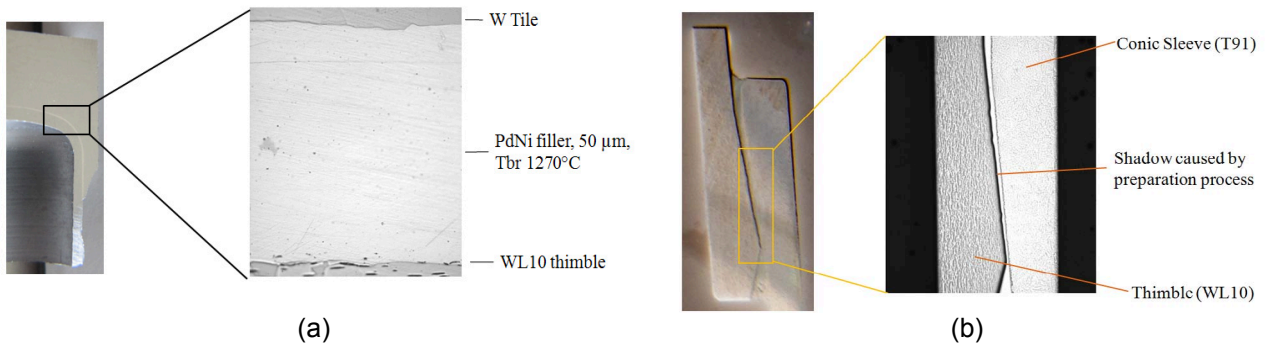


Fig. 7: Good brazing: a) W tile - WL10 thimble with PdNi40, b) WL10 thimble-steel with CuPd18.

Status of the HHF experiments

Upgrade of the EB unit of the HHF test facility

A combined test facility consisting of a helium loop [5] and an EB unit (60 kW, 27 keV) (Fig. 2, left) was originally built at the Efremov Institute St. Petersburg, Russia during 2004-2005. This facility enables mock-up testing under DEMO relevant conditions, i.e. at a nominal helium inlet temperature of 600 °C, an internal pressure of 10 MPa. The mass flow rate can be varied in a range of ~ 5 – 15 g/s. The temperature cyclic loading was simulated by means of switching periodically the beam on and off (variations 30 s/60 s, 30 s/30 s, and 60 s/60 s).

The EB unit has now been upgraded to 200 kW steady state heat removal and 40 keV beam energy (Fig. 8). Maximal density of the absorbed heat flux of 30 MW/m² can be reached. The upgrade was done to meet the requirement of the ITER divertor tests to be performed at the same facility. These ITER testing activities will cause a shift of our DEMO divertor testing schedule of at least 3-4 months.



Fig. 8: Test facility upgrade with a new electron beam gun (200 kW, 40 keV) installed (Efremov).

Conclusions and outlook

The current step of work is aimed at technological study on fabrication, integration, and HHF tests of divertor 1-finger and 9-finger mock-ups to demonstrate their fabricability and to prove the design performance. The tests were performed in a combined electron beam and He loop facility at Efremov. Three HHF test series were successfully performed till now. Neither sudden destruction and/or completely broken mock-ups (brittle failure) nor recrystallisation of W thimble was observed in any mock-up in all tests. The results of the first test series 2006 through 2008 already confirmed the performance of the divertor module under 10 MW/m^2 , where the mock-ups were successively further improved in view of thermal stress reduction as well as the manufacturing quality of the parts. The last successfully tested mock-ups survived outstandingly total more than 200 cycles under 10 MW/m^2 without any damages.

Altogether, these initial test results confirm the high heat flux capability of this concept and serve as a strong stepping stone for further development of the material and concept and more integrated testing. The upcoming HHF 1-finger test series 2010 ff will aim at reaching the breakthrough of 10 MW/m^2 and 1000 cycles by continuing testing the mock-ups from last test series, as well as testing new mock-ups manufactured with sophisticated technology in KIT and Efremov. Future HHF tests on 9-finger modules will be performed with real W cooling fingers. The EB test facility at Efremov has now been upgraded to 200 kW steady state heat removal and 40 keV beam energy. Maximal density of the absorbed heat flux of 30 MW/m^2 can be reached.

Staff:

S. Antusch
M. Ekat
A. Lerner
P. Norajitra
H.-J. Ritzhaupt-Kleissl
L. Spatafora
V. Widak

Literature:

- [1] P. Norajitra, R. Giniyatulin, W. Krauss, V. Kuznetsov, I. Mazul, I. Ovchinnikov, J. Reiser, M. Rieth, V. Widak, He-Cooled Divertor Development Towards DEMO, *Fusion Science and Technology*, Volume 56, Number 2, August 2009, Pages 1013-1017.
- [2] P. Norajitra, A. Gervash, R. Giniyatulin, T. Ihli, G. Janeschitz, W. Krauss, V. Kuznetsov, A. Makhankov, I. Mazul, I. Ovchinnikov, He-cooled divertor development: Technological studies and HHF experiments for design verification, *Proceedings of the 21st IAEA Fusion Energy Conference*, Chengdu, 16-21 October 2006, ISBN 92-0-100907-0 / ISSN 0074-1884.
- [3] P. Norajitra, A. Gervash, R. Giniyatulin, T. Hirai, G. Janeschitz, W. Krauss, V. Kuznetsov, A. Makhankov, I. Mazul, I. Ovchinnikov, J. Reiser, V. Widak, Helium-cooled divertor for DEMO: Manufacture and high heat flux tests of tungsten-based mock-ups, *Journal of Nuclear Materials* 386–388 (2009).
- [4] P. Norajitra, R. Giniyatulin, T. Hirai, W. Krauss, V. Kuznetsov, I. Mazul, I. Ovchinnikov, J. Reiser, G. Ritz, H.-J. Ritzhaupt-Kleissl, V. Widak, Current status of He-cooled divertor development for DEMO, *Fusion Engineering and Design* 84 (2009) 1429–1433.

- [5] I. Ovchinnikov, R. Giniyatulin, T. Ihli, G. Janeschitz, A. Komarov, R. Kruessmann, V. Kuznetsov, S. Mikhailov, P. Norajitra and V Smirnov, Experimental study of DEMO helium cooled divertor target mock-ups to estimate their thermal and pumping efficiencies, *Fusion Engineering and Design* 73 (2005) 181–186.
- [6] P. Norajitra, L.V. Boccaccini, A. Gervash, R. Giniyatulin, N. Holstein, T. Ihli, G. Janeschitz, W. Krauss, R. Kruessmann, V. Kuznetsov, A. Makhankov, I. Mazul, A. Moeslang, I. Ovchinnikov, M. Rieth, B. Zeep, Development of a helium-cooled divertor: Material choice and technological studies, *Journal of Nuclear Materials* 367–370 (2007) 1416–1421.
- [7] G. Ritz, T. Hirai, J. Linke, P. Norajitra, R. Giniyatulin, L. Singheiser, Postexamination of helium-cooled tungsten components exposed to DEMO specific cyclic thermal loads, *Fusion Engineering and Design* 84 (2009) 1623–1627.
- [8] <http://www.plansee.com/tungsten-and-its-alloys-tungsten.htm>.
- [9] R. Giniyatulin, A. Gervash, W. Krauss, A. Makhankov, I. Mazul, P. Norajitra, Study of technological and material aspects of He-cooled divertor for DEMO reactor, 23rd SOFT, Venice, Italy, 20.–24.9.2004.

Acknowledgement

This work, supported by the European Communities under the contract of Association between EURATOM and Karlsruhe Institute of Technology, was carried out within the framework of the European Fusion Development Agreement. The views and opinions expressed herein do not necessarily reflect those of the European Commission.

Structural Materials – Development and Characterisation

Investigation of Options to Reduce Critical Elements in Low Activation Ferritic/Martensitic Steels (EFDA/05-1244 (TW4-TTMS-RedAct))

During the last few years considerable improvement has been made in the definition and fabrication of 'reduced activation' ferritic-martensitic steels (RAFM). Three batches of a 9CrWVTa-steel called EUROFER 97, EUROFER 97-2, and EUROFER 97-3 respectively, including 17 heats and a total of 22 tons of different semi-finished were produced by Boehler in 1999 and by SaarSchmiede in 2003 and 2009. A third batch of about 11 tons was delivered end of March 2009 and is being used for technological fabrication investigations (cf. TW6-TTB-EUROFER). A metallurgical and mechanical characterisation is underway.

These productions have demonstrated that RAFM steels can successfully be produced at industrial scale. The steels, nominally according to the same specification, actually differ in the detailed contents of minor alloying elements and of impurities. All met the goal of an overall low content of those elements which have a detrimental effect on the long-term activation behaviour. Thereby, a remarkable step is achieved towards the final goal of the production of 'low activation' steels for the use in a DEMO (demonstration reactor).

Studies for further reduction of impurities as a generic property of RAFM steels were performed within in the frame of this EFDA task TW4-TTMS-RedAct.

The objectives of this task were

- To identify a number of critical elements that should be further reduced for the EUROFER 97 technical specification and to which level.
- To assess in cooperation with steel producers the technical feasibility.
- To define the specifications of a new heat (or a series of heats) to be produced.
- To determine in cooperation with the steel producers the uncertainty range in the concentrations of the various elements (alloying elements and impurities) in the heat.
- To determine the different and likely increasing costs of the heats with reduced impurity levels.
- To produce this material by industry at the smallest amount that is acceptable.
- To analyse by different laboratories (i.e. the steel producers and qualified EU/EFDA associations) and different methods, the chemical composition of the material produced up to now and from the new melts.

In order to qualify laboratories well in advance a Round Robin was organized where in a 'blind test' samples of different heats had to be analysed for a list of critical elements which were specified in advance.

Status of work

A comparison of the chemical composition as specified in the technical specification for EUROFER 97-1 and EUROFER 97-2 and the results achieved in the industrial production of the different products has been performed and the reasons for occurring deviations from the specifications have been analysed.

A web-based version of the FISPACT 2005 code has been implemented and numerous calculations with varied compositions of EUROFER have been performed to check the influence of different radiologically undesired elements [1,2] (Nb, Mo, Al, Ni, Cu, Co) on the activation behaviour of the steel.

The calculations showed that only EUROFER 97-1, passing the Low Level Waste activation level after about 100 years, can be regarded as reduced activation material. EUROFER 97-2

needs about 30,000 years to fall below this limit. The main originator for this behaviour is Niobium, where the specified content which was used for the calculations is 5 times higher for EUROFER 97-2 than for EUROFER 97-1. Calculations for EUROFER 97-2 with a systematic variation of the Nb content and unchanged contents of the other alloying elements showed, that the Nb content should be well below 10 ppm to assure "low level waste" properties.

On the basis of the above mentioned calculations trial heats could be specified. Input for a separate Art. 7 contract for the cooperation with steel manufacturers was given. A call for tender was launched and a manufacturer, experienced in the production of RAFM steels, was selected as industrial partner for the production of trial heats and performance of the above mentioned study. Due to budgetary reasons the manufacture of trial heats was postponed and only the study was performed. In the course of this study the different pathways on which the above mentioned detrimental elements come into the final RAFM steel product were analysed. These findings were used in the production of the new 11 ton EUROFER 97-3 heat and lead to a considerable reduction of the Nb content.

A Round Robin experiment for the chemical analysis of the radiologically undesired elements (Nb, Mo, Al, Ni, Cu, Co) was performed under the participation of six different industrial and research laboratories. After prior analytical homogeneity checks, samples of EUROFER 97-2 and EUROFER 97-3 were investigated applying ICP-OES (inductively coupled plasma optical emission spectrometry) or ICP-MS (ICP - mass spectrometry) methods, in one case GDMS (glow discharge mass spectrometry) for comparison. It was demonstrated that with both ICP methods experienced analytical laboratories are able to analyse in good agreement the above mentioned elements. Contents below 1 $\mu\text{g/g}$ of the most detrimental element Nb could be determined by all laboratories in good agreement.

Staff:

C. Adelhelm
T. Kaiser
R. Lindau

Literature:

- [1] Lindau, R.; Möslang, A.; Rieth, M.; Klimiankou, M.; Materna-Morris, E.; Alamo, A.; Tavassoli, A.-A. F.; Cayron, C.; Lancha, A.-M.; Fernandez, P.; Baluc, N.; Schäublin, R.; Diegele, E.; Filacchioni, E.; Rensman, J.-W.; v.d. Schaaf, B.; Lucon, E.; Dietz, W.; Present Development Status of EUROFER and ODS-EUROFER for Application in Blanket Concepts, *Fusion Engineering and Design*, 75-79 (2005) p.989-996
- [2] S. Kelzenberg; Berechnung und experimentelle Verifizierung von Materialaktivierungen in D-T Fusionreaktoren, Dr.-Thesis, FZKA Report 5836 (November 1996) p. 48.

Acknowledgement

This work, supported by the European Communities under the contract of Association between EURATOM and Karlsruhe Institute of Technology, was carried out within the framework of the European Fusion Development Agreement. The views and opinions expressed herein do not necessarily reflect those of the European Commission.

Support and Follow-up of the EFDA/06-1903 Art. 7 Contract for Procurement of EUROFER for the TBM Fabrication Technology Trials and Mock-ups (EFDA/06-1520 (TW6-TTB-EUROFER))

The main objective of this task was to support the EFDA Art. 7 contract 06-1903 for the procurement of app. 11 tonnes of EUROFER 97 RAFM steel in various semi-finished product forms. This material is foreseen to be used for fabrication technology trials and to build various components and mock-ups of Test Blanket Modules (TBM). An additional goal was to check the reproducibility of properties compared to two batches of EUROFER 97 available from the previous fabrications and to assess the achievable limits of reduction of detrimental impurities like Nb, Mo, Ni, Cu, Al, Co.

In order to follow-up the EUROFER fabrication process, several meetings with the steel manufacturer have been organised.

Status of work

After a Europe-wide call for tender for the production of about 11 tonnes of EUROFER 97 RAFM steel in various product forms (see table 1) Saarschmiede in Völklingen, Germany was assigned for the production according to the technical specification, which is close to the specification for the recent production of EUROFER 97-2. Table 2 gives the specified chemical composition of the material to be produced.

The main manufacturing steps were

- A. Melting in a 16 t Vacuum Induction Furnace
- B. Remelting using a Vacuum Arc Remelting Furnace
- C. Forging of 450x120 mm and 650x120 mm billet material in a 1000 t-Press
- D. Rolling of the plates
- E. Inspection of the plates according to the requirements of the referring specification

Table 1: Dimensions and quantity of semi-finished products.

Semi-finished product	Thickness	Area	Length	Mass	Total Mass
	mm	m^2	mm	kg	kg
Plates *)	1	14		109	
	8	5		312	
	10	5		390	
	12	14		1310	
	16	15		1872	
	20	4		624	
	25	10		1950	
	32	10		2496	
	35	3		819	
	48	1		374	
					10256
Forging/billet	100 x 100 mm ²		3000	234	
					234
					10490

*) All plates 1000 x 2000 mm

Table 2: Specified chemical composition.

Element	Min. Value (wt%)	Max. Value (wt%)	Remarks
Carbon	0.090	0.120	Target 0.11
Manganese	0.20	0.60	Target 0.4
Phosphorus		0.005	
Sulphur		0.005	
Silicon		0.050	
Nickel		0.01	ALAP
Chromium	8.50	9.50	Target 9.0
Molybdenum		0.005	ALAP
Vanadium	0.15	0.25	
Tantalum	0.10	0.14	Target 0.12
Tungsten	1.0	1.2	Target 1.1
Titanium		0.02	
Copper		0.01	ALAP
Niobium		0.005	ALAP
Aluminium		0.01	ALAP
Nitrogen	0.015	0.045	Target 0.030
Boron		0.002	ALAP
Cobalt		0.01	ALAP
As+Sn+Sb+Zr		0.05	Target
Oxygen		0.01	

The rolling of the billets to plates was performed by a subcontractor, Böhler Bleche in Mürzzuschlag, Austria, who also performed the inspection and testing of the plates.

The material was delivered to FZK (now KIT) end of March 2009 and is ready for characterisation and use according to the intended purpose.

Staff:

R. Lindau

Acknowledgement

This work, supported by the European Communities under the contract of Association between EURATOM and Karlsruhe Institute of Technology, was carried out within the framework of the European Fusion Development Agreement. The views and opinions expressed herein do not necessarily reflect those of the European Commission.

Characterisation of Reference EU-ODS-EUROFER Batch: Optimisation of Heat Treatment, Ageing Behaviour and Microstructural Characterisation (TW5-TTMS-006 D 10)

Introduction

The efficiency of future fusion reactors will strongly depend on the operating temperature allowed by selected structural materials. With this respect, ODS steels are attractive candidates since they would allow to increase the operating temperature by approximately 100 °C. The reduced activation martensitic steel EUROFER-97 (8.9Cr, 1.1W, 0.2 Ta, 0.42 Mn 0.11 C wt%), which is currently considered as a European reference for structural application, has been selected as a base material. Based on the experience with a precursor a 50 kg EU-ODS-EUROFER batch has been specified and produced (TW3-TTMS-006 D1a). Within this task an optimum heat treatment should be determined. The influence of different heat treatments on microstructure was also investigated.

The improvement of the mechanical behaviour should be achieved by different annealing procedure. The different annealing conditions have been applied on the specimens with studying the hardness and microstructure. Additionally the influence of cooling conditions on the mechanical behaviour and should be verified. The results of the different heat treatments on the hardness are given in Figure 1.

Method

The microstructural examinations included transmission electron microscopy (TEM) method. The TEM investigations were performed using a FEI Tecnai 20 F microscope equipped with a Gatan image filter for EELS measurements as well as with an HAADF detector for scanning TEM (STEM). The microscope was operated at 200 kV accelerating voltage with a field emission gun. The EELS experiments were performed in the STEM mode with a probe size of ≥ 3 nm and a probe current of 0.1 nA (6×10^8 e/s). The experimental conditions were chosen such that the collection semi-angle was 13 mrad and the beam convergence angle was 10.5 mrad. For the EELS measurements, an energy resolution of 1.1 eV and dispersions of 0.1 eV/channel were employed.

Results

The hardness measurements

The Vickers hardness of all ODS alloys in the interesting temperature range between 550 and 850 °C is very similar. According to the good mechanical behaviour of the precursor ODS-EUROFER steel, 1100 °C 30 min air-/ water-quenching + 750 °C 2 h air-cooling was chosen as reference heat treatment. Figure 1 shows the hardness depending on the annealing temperature T_A for 2 hours annealing time. (Hardening, $T_A=0$ h).

Above 850 °C a re-austenitisation starts with martensitic transformation after quenching. So the interesting range for technical application is between 600 and 800 °C in order to have a safety margin of about 50 °C.

Due to a higher C-content (0.13 wt.-%) of the EU-batch compared to the pre-cursor alloys, air-quenching instead of water-quenching can be applied. The higher hardness of water-quenched samples between RT and 500 °C is of no technical relevance.

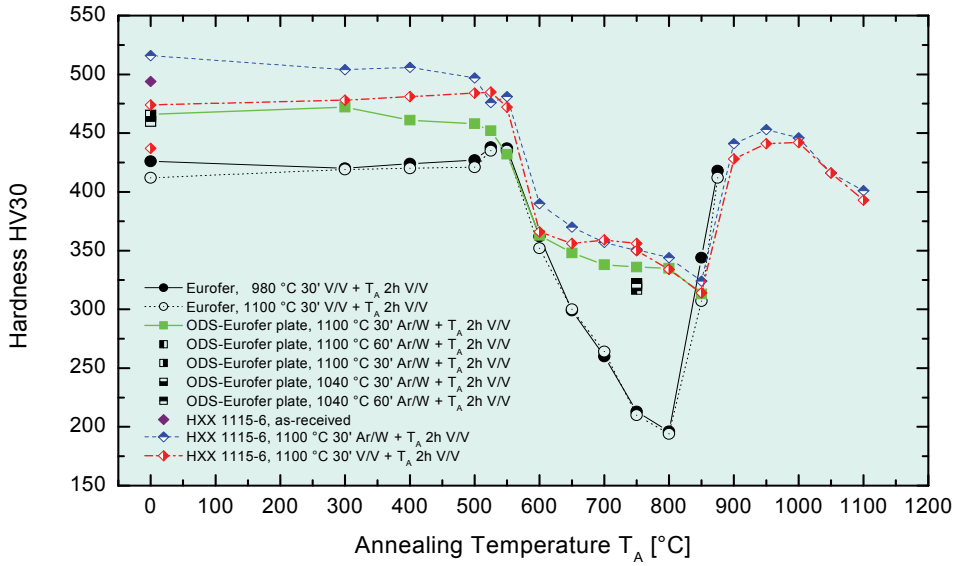


Fig 1: Vickers hardness HV30 in dependence of the annealing temperature.

Microstructural analysis

The microstructure and presence of different precipitates was investigated using conventional bright field TEM imaging and spatially resolved analytical TEM. In Fig. 2 is presented the TEM bright field image of the “as-delivered” EU EUROFER material. The grains have obviously an elongated form with 1-3 μm length and 0.2-0.5 μm width. Inside the grains numerous defects such as dislocation lines are visible. The defects and elongated forms come possibly from the rolling procedure.

The scanning transmission electron microscopy with HAADF detector has been used for analytical study of precipitates and inclusions in the material. Figure 3 presents the spatially resolved analytical investigations of the large area in the specimen. STEM investigations using the HAADF detector show the presence of well visible precipitates with a darker contrast (Fig. 3a). The precipitates have a round shape and their size varies from 30 nm to 300 nm. According to statistical evaluations, their spatial density amounts to $(3\pm2)\times10^{13} \text{ cm}^{-3}$. In most cases, the precipitates are statistically embedded in the matrix. However, areas in which they are ordered along the lines have also been observed. These lines often extend to a length of more than 10 μm – the entire TEM transparent area on the specimen edge. Apparently, these lines are not coincident with the previous austenitic grains. In Fig. 3c-f are presented the Fe, V, Cr and Y elemental maps. It is obvious that the round inclusions consist of V - Cr composition. The Y map shows the formation of small amount of Y_2O_3 particles.

The specimens were thermally treated in vacuum at 1100 °C. Some specimens were additionally annealed at 750 °C.

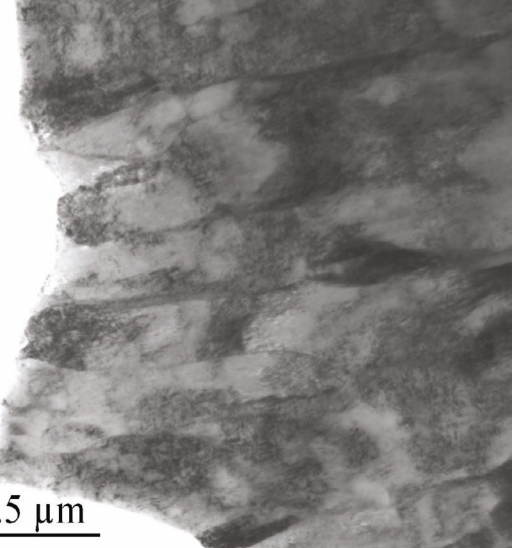


Fig 2: Bright field TEM image show the grain structure of the as-delivered material.

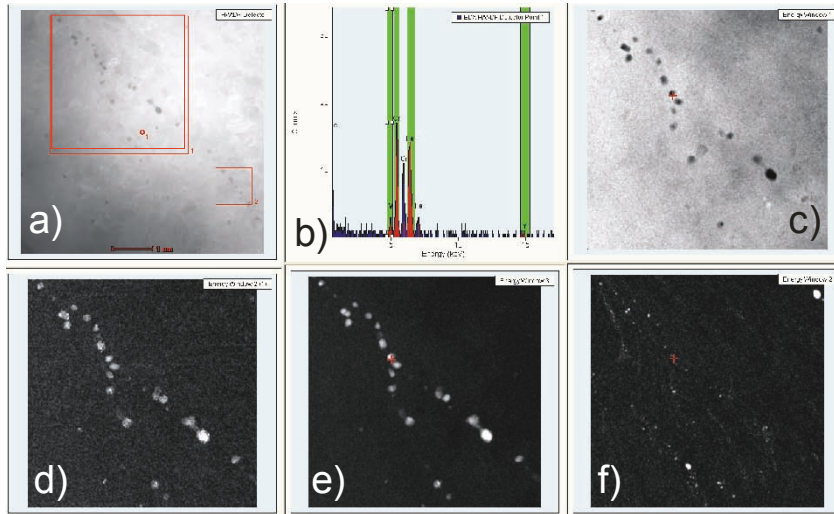


Fig. 3: Spatially resolved analytical investigations. Part a) is the HAADF image with marked investigated area. Part b) shows one EDX spectrum of a visible inclusion. Parts c), d), e) and f) show the spatial distribution of Fe, V, Cr and Y elements in the marked area.

Fig. 4 presents the results of analytical TEM characterisation of the specimen after treatment at 1100 °C for ½ h and cooling in vacuum. The investigated area is imaged in Fig. 4a. The Cr and Fe elemental maps show the presence of round oxide inclusions, whose microstructure and chemical composition correspond to $(\text{Mn},\text{Fe})(\text{Cr},\text{V})_2\text{O}_4$ oxide. The Y map shows that particles are not homogeneously distributed in the specimen. They are ordered along lines which were presumably formed during mechanical alloying. In Fig. 5 the results of elemental mapping of the 6 $\mu\text{m} \times 4 \mu\text{m}$ area are shown. In the Fe and Cr map numerous Cr-rich M_{23}C_6 precipitates are visible. The precipitates are often located on the grain and lath boundaries. In the V-map numerous V rich precipitates which are presumably V carbides and large oxide precipitates are visible.

The TEM investigations of the specimen after 1100 °C treatment with following rapid cooling in water (Fig. 5) show that the treatment does not change the visible grain structure of the material compared to the as-delivered state. In the specimen large oxide precipitates and ODS particles were found. M_{23}C_6 precipitates were not detected. Detailed investigation of oxide particle does not reveal significant changes of the microstructure of large oxide precipitates.

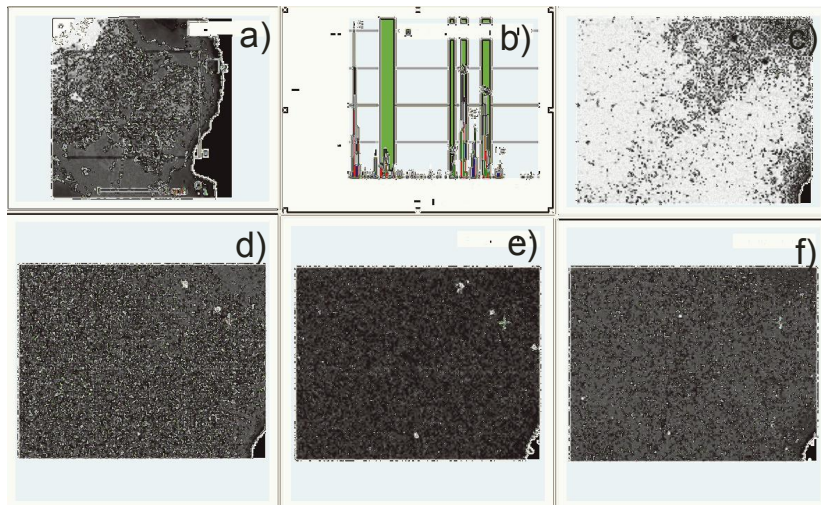


Fig. 4: HAADF image of an area in the specimen (a) and Fe, Cr, V, and Y elemental maps in figures (c)....(f), respectively.

The microstructure of the material shows the major changes after additional annealing at 750°C in water. The TEM investigations reveal the formation of numerous quite large carbide precipitates in the matrix (Fig. 5) which can be attributed to the higher Cr-content. The precipitates could have an influence on the hardness, strength and toughness of the material.

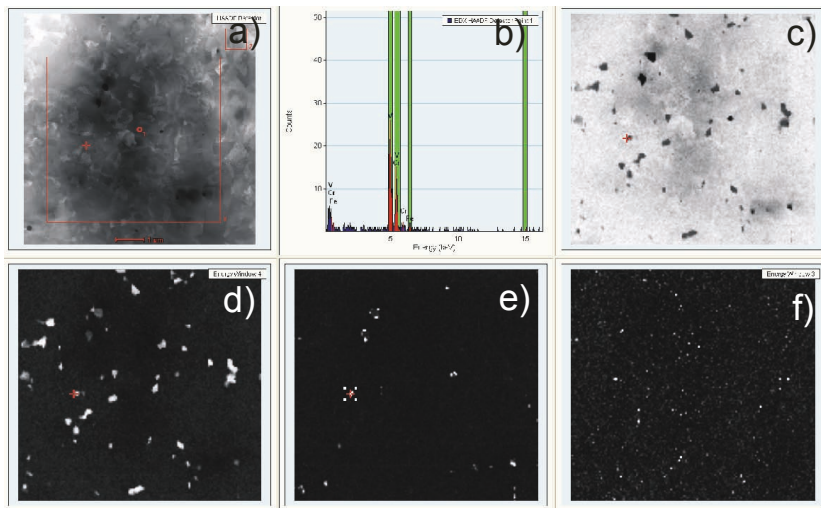


Fig. 5: HADF image of an area in the specimen with marked investigated area (a) and Fe, Cr, V, and Y elemental maps in figures (c)....(f), respectively.

Conclusions

The analytical TEM characterisation of specimens of EU ODS-EUROFER heat after different thermal treatments procedures was performed. The EDX mapping show the presence of large oxide precipitates of $(\text{Mn},\text{Fe})(\text{Cr},\text{V})_2\text{O}_4$ composition, which were possibly formed due to the excess of oxygen in the matrix. The precipitates have often a complex multi-phase structure which does not change during different thermal treatment procedures. It was shown that the additional tempering at 750 °C and 800 °C leads to the formation of carbide precipitates. This is intended to reduce the lattice distortion and inner stresses and to improve ductility. On the other hand, these carbides should not be too large, because they may act as crack initiator thus degrading the mechanical properties.

Staff:

U. Jäntschi
M. Klimenkov
R. Lindau
E. Materna-Morris
A. Möslang

Acknowledgement

This work, supported by the European Communities under the contract of Association between EURATOM and Karlsruhe Institute of Technology, was carried out within the framework of the European Fusion Development Agreement. The views and opinions expressed herein do not necessarily reflect those of the European Commission.

Fabrication and Irradiation of FE-54 Enriched Samples to Study the Influence of He/dpa Ratio on Materials Degradation up to Medium Dose Level (TW4-TTMS-001 D 1, TW5-TTMS-001 D 2)

Overview

The structure components of future fusion reactors will suffer from specific irradiation damage, i.e. the ratio of helium production (in appm) to displacement rate (in dpa) varies around 10 appm He/dpa. Due to the lack of appropriate high energy neutron sources there seems to be only one promising way to generate such irradiation damages in a RAFM steel with common in-pile fission reactor irradiation experiments: If the content of natural iron would be replaced by the stable isotope Fe-54, helium production would be stimulated by the according (n, alpha) reactions. A significant advantage over the alternative boron-10 helium production technique would be a uniform helium distribution through the whole matrix.

Therefore, the goal of the task is to produce a heat similar to EUROFER using Fe-54 instead of natural iron. Then miniaturized Charpy and tensile specimens with cores of Fe-54 substituted EUROFER steel have to be fabricated. Finally, an appropriate irradiation programme has to be planned and managed.



Fig. 1: Left: Bottle with 391 grams of Fe54 Isotope, as delivered. Right upper and lower image: Before and after arc melting the isotope powder to pellets.

Achievements 2005

- Development and optimization of the fabrication process steps for the production of small EUROFER 97 heats using natural iron.
- Delivery of 391 grams of Fe54 isotope in October (with a delay by 3 month).
- Quality assurance: chemical composition (purity) and weight measurement.
- Revision of the induction furnace.

2006

- Since the amount of Fe54 isotope necessitates a production of at least two batches, a final test production (with natural iron) of two 200 gram plates of EUROFER 97 with low impurities and acceptable outer dimensions were successfully performed, before the actual production with the isotope.
- Production of the first batch with Fe54 isotope (see Fig. 1): During the final melting process in the induction furnace the crucible cracked and the melt flow over a graphite part (see Fig. 2).

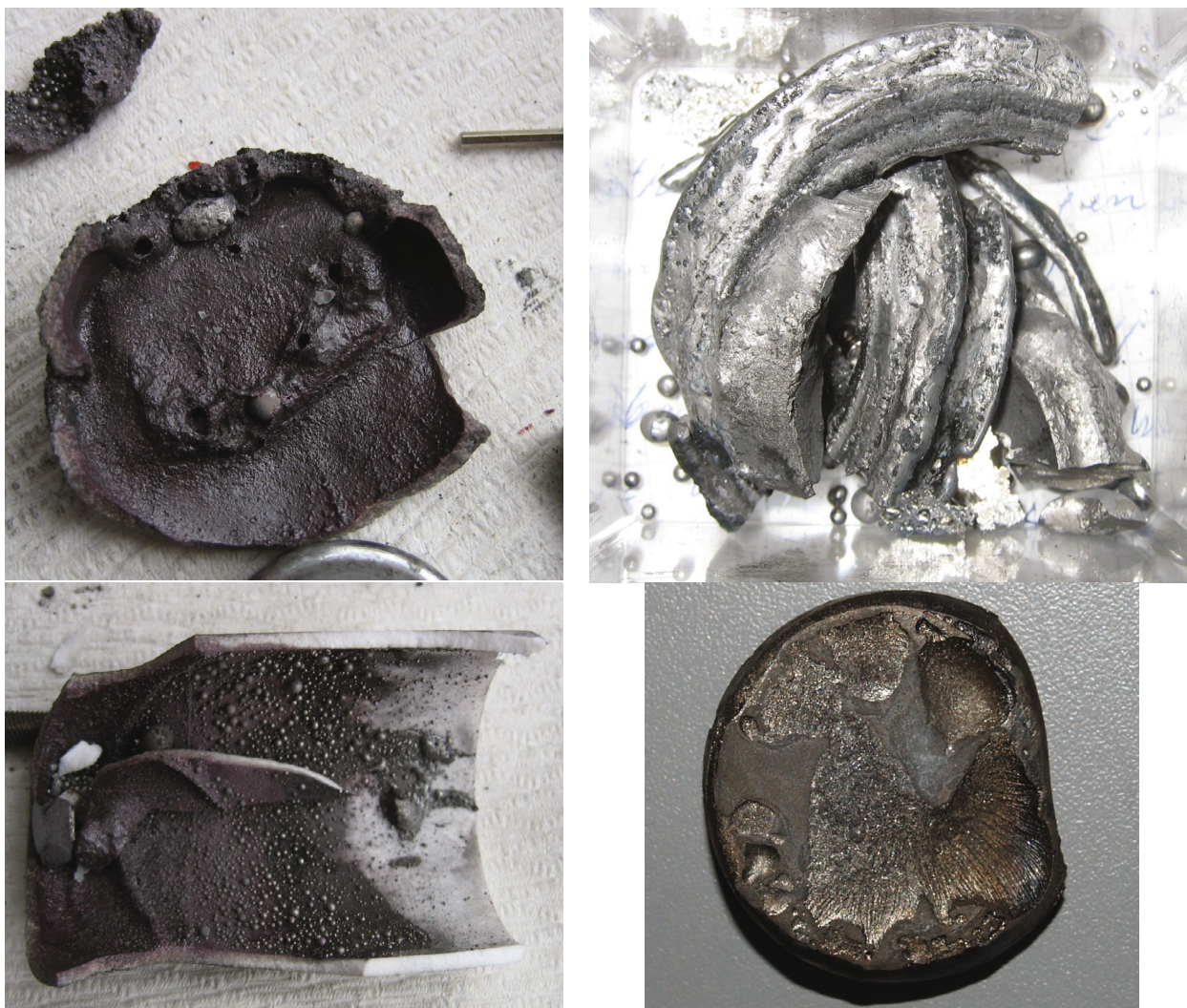


Fig. 2: Left upper and lower image: The remains of the broken aluminium-oxide crucible. Right upper image: Some parts of the melt which could be recovered. Right lower image: The recovered parts after repeated remelting under different reducing atmospheres to lower the carbon content.

- Analysis of the accident: The ceramics (aluminium-oxide) crucible most probably had a fabrication fault (this never happened during the production of the test batches). Only 90% of the heat could be restored. The restored material had a carbon content of about 4 weight percent (due to the contact with the graphite part).
- Counter measures: To avoid similar accidents, the aluminium-oxide crucibles were replaced by boron-nitride crucibles which can be operated at even higher temperatures. In addition, all graphite parts in the induction furnace were replaced by tantalum parts.
- Successful production of the second batch with Fe54 isotope.

2007

- Decarbonisation of the accidental heat by repeated melting under purge gas (mixture of argon and hydrogen) atmosphere. Result: After some weeks of repeated melting the carbon content could be lowered to 0.1 wt.% (see Fig. 2).
- Successful production of another Fe54- EUROFER batch with the remaining (and now decarbonised) material.
- Successful completion of the whole fabrication process for the specimen production. That is, welding and fabrication processes of Charpy and tensile specimens with cores of Fe54- EUROFER 97 were applied and demonstrated using the produced test batches. A characterisation of the mechanical properties showed agreeable results.
- Analysis of the chemical composition of the Fe54- EUROFER 97 batches: >0.3wt.% boron content.
- Conclusions: The use of boron-nitride crucibles for casting the Fe54-Eurofer97 batches led to a significant contamination. Normally, this would have a negligible effect on the material properties. But this material would be neutron irradiated to produce a homogeneous helium production due to the transmutation of the Fe54 isotope. Since boron transmutes also to helium, and since boron is concentrated at grain boundaries, the analysed amount of more than 0.3% boron would have a contra-productive effect. Therefore, all produced Fe54-Eurofer batches had to be considered as useless. Therefore, the next step would be to develop a suitable cleaning method.

2008

- Extensive discussions with leading experts in the field of purification of metals led to the conclusion that the removal or reduction of boron is only possible by chemical cleaning.
- Further literature studies and discussions with experts led to the following theoretical cleaning process: (1) A complete solution of the material in a mix of acids. (2) Neutralizing with leach for oxide precipitation. (3) Separation of the iron oxide by a centrifuge.
- Successful solution tests with different mixtures of acids have been performed using EU-ROFER 97 flakes.
- Two heats were produced with natural iron in boron-nitride crucibles to get test material with the same amount of boron.
- Different cleaning processes were performed with the test material. But the chemical analysis showed still too high amounts of boron.

Status

All material production steps are developed and qualified. For the further casting of the plates, high quality aluminium-oxide crucibles were purchased and tested successfully.

The whole specimen fabrication processes are developed and qualified: Electron beam welding of stripes of EUROFER 97 to core plates of Fe54- EUROFER to spare the valuable isotope material, then heat treatment and specimen fabrication by EDM and turning.

But for a continuation of the present task, it is absolutely necessary to remove the boron from the contaminated isotope cast materials.

Progress

A new evaluation of the situation led to the following results: One idea was to send the material back to Russia for a repeated isotope separation. But the costs would be unacceptable high. A second idea came from the analytical chemistry group in FZK: A long time ago, for the determination of boron in steels, a special distillation process was used. Possibly the same procedure could be applied for cleaning the isotope material.

Again, test material was produced by the same method as before using boron-nitride crucibles. Then the cleaning process was investigated and step-by-step developed using standard EUROFER 97 which was artificially contaminated by different amounts of boron acid.

Finally, using 10 grams of the test material, it could be demonstrated that the cleaning process by distilling works very well. The boron content could be reduced to the ppm range.

Conclusions and Outlook

A feasible cleaning method was developed. It is readily available but time consuming. To apply it to the contaminated isotope material, chemical laboratory equipment for handling larger quantities is necessary and has to be purchased.

The further steps will be: (a) Chemical cleaning, (b) reducing the boron-free oxide in a hydrogen sinter furnace, (c) final chemical analysis of the isotope material, (d) production of two (or more) Fe54-Eurofer batches, (e) chemical analysis.

Only after a successful boron removal of the failed heats, the specimen fabrication may be completed and planning for irradiation campaigns may be started. The irradiation is foreseen to take place in the HFIR reactor of ORNL and, if possible, in the Petten HFR. A detailed irradiation program will be elaborated after the specimen fabrication is completed.

Staff:

C. Adelhelm
B. Dafferner
A. Falkenstein
S. Heger
U. Jäntschi
A. Möslang
M. Rieth
P. Vladimirov
H. Zimmermann

Acknowledgement

This work, supported by the European Communities under the contract of Association between EURATOM and Karlsruhe Institute of Technology, was carried out within the framework of the European Fusion Development Agreement. The views and opinions expressed herein do not necessarily reflect those of the European Commission.

Tomographic Atomic Probe Analysis of EUROFER Material Irradiated in the ARBOR Irradiation Campaign (TW5-TTMS-001 D 4)

Introduction

The aim of this task is to investigate atomic scale microstructure of EUROFER steel before and after irradiation. The ECOTAP (Energy Compensated Optical Tomographic Atom Probe) which is able to reconstruct atom positions within investigated sample seems to be appropriate for this task. This report contains the data for irradiated EURODShip (EUROFER +0.5%Y₂O₃) steels.

The principle of three dimensional atomic probe (3DAP) is based on the evaporation of surface atoms induced by strong electric field pulses. Some fraction of the evaporated and ionized atoms (usually ~50%) fly to a detector where they are registered and their final position is fixed. Their initial position in the lattice can be recalculated using known electric field distribution. The analysis of the measured time of flight of each atom from the tip of the probe to the detector provides information on the charge to mass ratio, which is usually sufficient to determine uniquely the nature of evaporated chemical specie. The necessity of high electric fields requires the preparation of the samples in form of very thin needles with a sharp tip with a radius of ~10-50 nm.

Experimental

Materials and irradiation

Mechanically alloyed EUROFER 97 with 0.5% Y₂O₃, developed for higher creep-rupture resistance on the base of reduced activated ferritic/martensitic steel was investigated in this study. EUROFER ODS steel was manufactured in a powder metallurgical route from gas atomised EUROFER 97 powder by mechanical alloying of the steel powder with Y₂O₃ followed by hot isostatic pressing (HIP) as consolidation process. The specimen designation in the ARBOR experiment is EURODShip, heat HXN 958/3. The chemical composition is given in Table 1. Specimens were irradiated in a fast neutron flux of 1.8×10^{19} n/m² s (>0.1 MeV) up to ~ 30 dpa. In this work two states ODS-EUROFER 97 irradiated at 330° C were studied. The first one labelled as EO01 was investigated in as-irradiated state while the second – EO04 was irradiated and then additionally annealed at 500° C for 3 hours to achieve nearly total mechanical properties recovery.

Table 1: Chemical composition of ODS-EUROFER 97 (at.-%).

Material	C	Si	Mn	Cr	B	N	V	W	Ta	Y	O
EURODShip	0.514	0.160	0.378	9.65	0.0	0.029	0.209	0.33	0.27	0.25	0.37

Tomographic atom probe (TAP)

This investigation was carried out by Energy Compensated Optical Tomographic Atom Probe (ECOTAP) installed at ITEP. Some technical details were presented in [4]. Atom probe investigations were performed in high vacuum $< 1 \times 10^{-9}$ Torr. The specimens were cooled down to cryogenic temperatures at 40 ÷ 80 K; the pulse repetition rate had the maximum value of 1.6 kHz. The pulse fraction was within 15-23% and was changed correspondingly to the specimen temperature for better performance. The dependence of the pulse evaporation efficiency on pulse fraction and specimen temperature for Cr was observed, while other elements were not influenced by these parameters within used ranges. Optimal results were obtained at 70 K and 19% pulse fraction.

Atom probe needles were prepared from the parts of broken Charpy bar specimens after mechanical tests. The preparation of the specimens was carried out in two steps. The first

step consisted of billets preparation from bulk material using electro-erosion cutting in water. The second step was electropolishing (thinning) of the billets by the method of anodic etching in electrolyte. The diameters of TAP needle tips varied from 30 nm to 250 nm, while the optimal parameters for atom probe investigations are 25 nm – 100 nm for tip diameter and 100-150 nm for tip length, as was shown by our investigation. Diameter and shape of specimen tip were checked by transmission electron microscopy. Although, the referred above billet dimension $0.3 \times 0.3 \times 10 \text{ mm}^3$ is standard for our preparation technique, due to the high specimen activity additional modification of etching procedure was required.

Results of TAP study

The first results of TAP investigations on irradiated EUROFER 97 are presented in this paper. Two different states - irradiated and irradiated plus annealing after irradiation - were characterized (see typical mass spectrum in Fig. 1). This mass-spectrum shows the presence of peaks at 33.95, 34.43 and 32.93, which can be interpreted as CrO^{+2} evaporated ions. These peaks were also observed in the unirradiated state, however, after irradiation they are more strongly pronounced. On atom maps these ions are mainly positioned in areas enriched with Y, O – referred hereafter as Y-O-clusters. The number of events in these peaks is in the same proportion as for chromium isotopes, whereas the mass-to-charge value is in a good agreement with each chromium isotope plus oxygen masses.

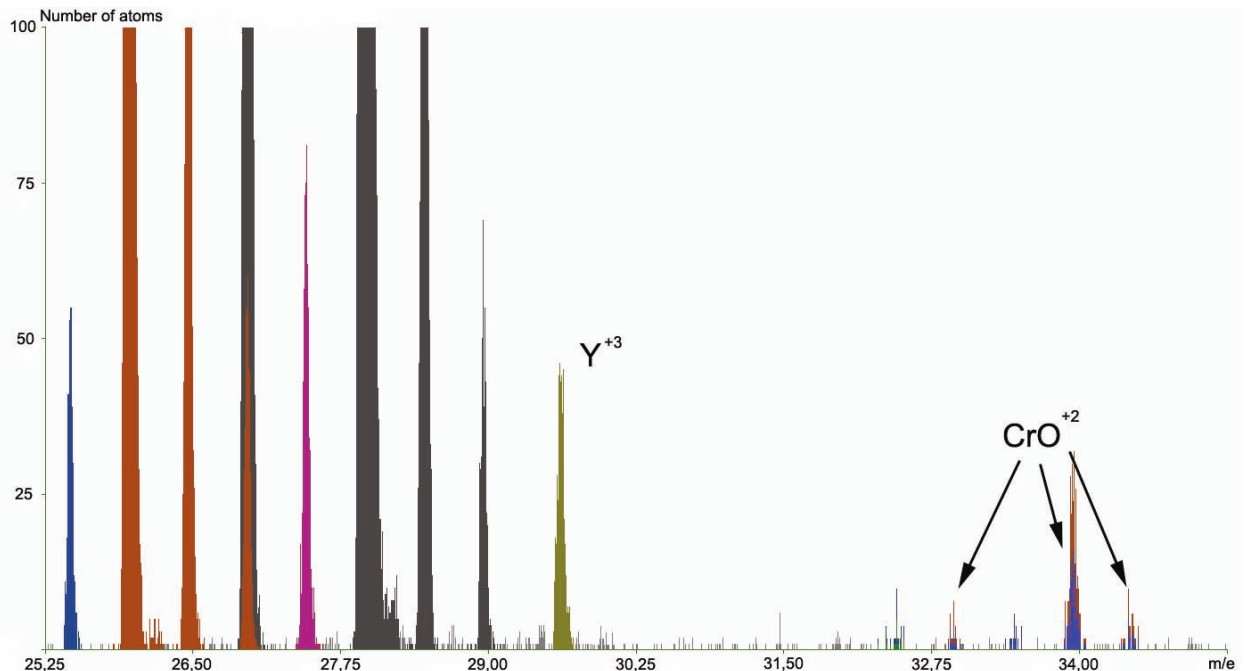


Fig. 1: Mass-spectrum of the ODS-EUROFER 97 irradiated at 330°C up to 30 dpa.

Normally, evaporated molecular ions indicate a strong affinity between atoms that form this ion in solid solution in material. It should be noted that the peak at 32.5 which is interpreted as VN^{+2} is slightly visible, and that at 33.45 which is inferred as VO^{+2} is absent. Both peaks were observed in unirradiated material. No other differences in comparison with the unirradiated state were detected. 3D reconstructions of two volumes for EO01 state are presented in Fig.2 a,b. The spatial distribution of each element in the same analyzed volume is shown separately for the sake of better visual perception. The average values of the element concentration in the matrix and the volume are shown in Table 2.

Table 2: Element concentrations in matrix and average values* EO01 and EO04.

Material (at.-%)		C	Si	Mn	Cr	N	V	W	Y	O
ODS-EUROFER 97	bulk	0.51	0.16	0.38	9.65	0.03	0.21	0.33	0.25	0.37
ODS-EUROFER 97 irradiated at 330° C (EO01)	average	0.08	0.24	0.43	9.65	0.02	0.21	0.22	0.30	0.32
	matrix	0.08	0.23	0.40	9.54	0.02	0.21	0.22	0.15	0.26
ODS-EUROFER 97 irradiated& an- nealed (EO04)	average	0.06	0.18	0.28	7.53	0.02	0.21	0.14	0.11	0.19
	matrix	0.06	0.17	0.27	7.4	0.02	0.21	0.15	0.07	0.15
Unirradiated ODS- EUROFER 97 [4]	average	0.07	0.23	0.25	7.6	0.03	0.20	0.23	0.05	0.10
	matrix	0.06	0.22	0.25	7.5	0.02	0.14	0.23	0.02	0.06

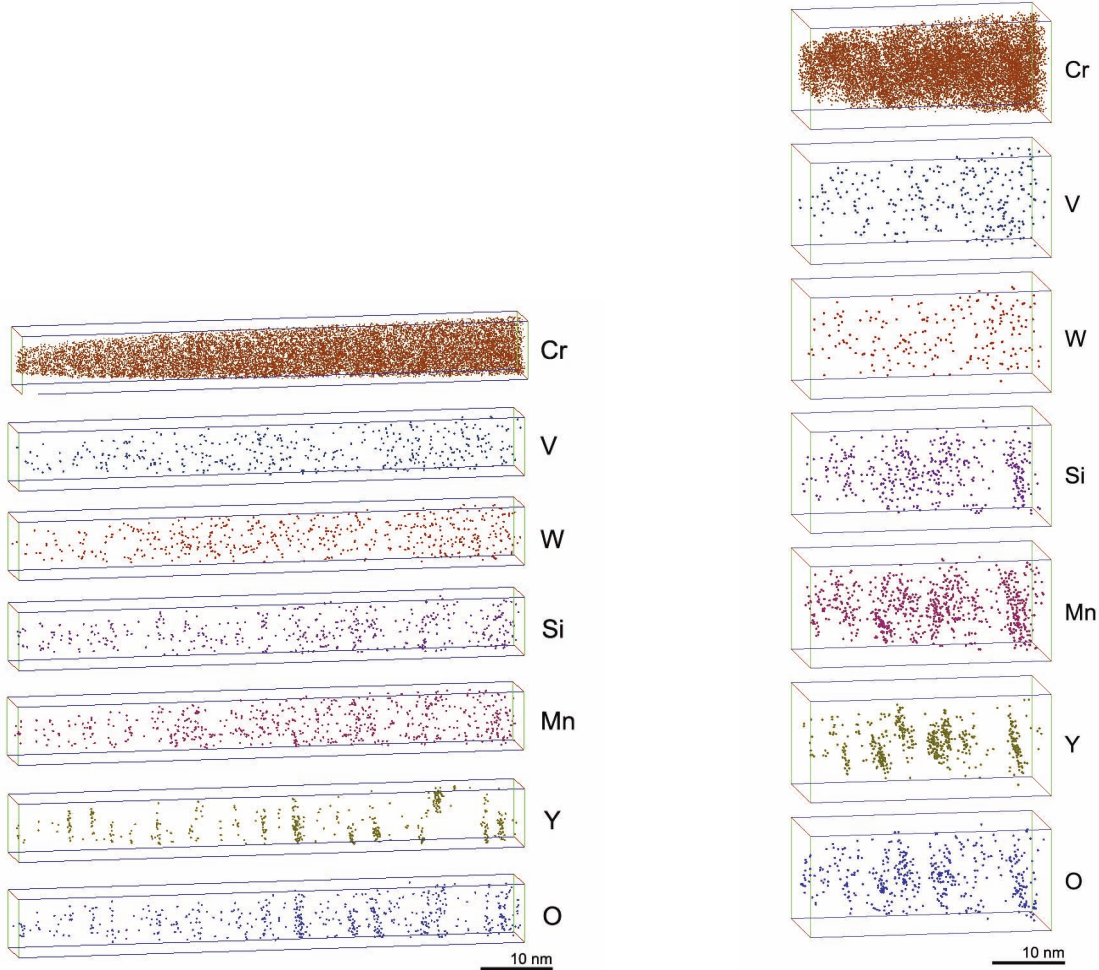


Fig. 2: Atom maps of the solute distribution in the ODS-EUROFER 97 irradiated at 330° C up to ~ 30 dpa (EO01 state). The investigated volumes are about 13×13×78 (left hand side), and 13×13×32 (right hand side).

The atom distribution analysis of the investigated volumes revealed areas enriched with oxygen, yttrium, chromium and manganese. These areas can be easily detected visually by notable enrichment in yttrium and oxygen. The cluster identification procedure was carried out using the maximum separation method. For volumes shown in Fig. 2-3 the typical parameters - separation distance d_{\max} and N_{\max} were set to 8 angstrom and 5 atoms respectively. The particles sizes were determined as double gyration radius calculated for each solute-

enriched cluster. For the annealed state there were volumes where some clusters were identified manually using radial distribution of element concentration as they were too diffuse.

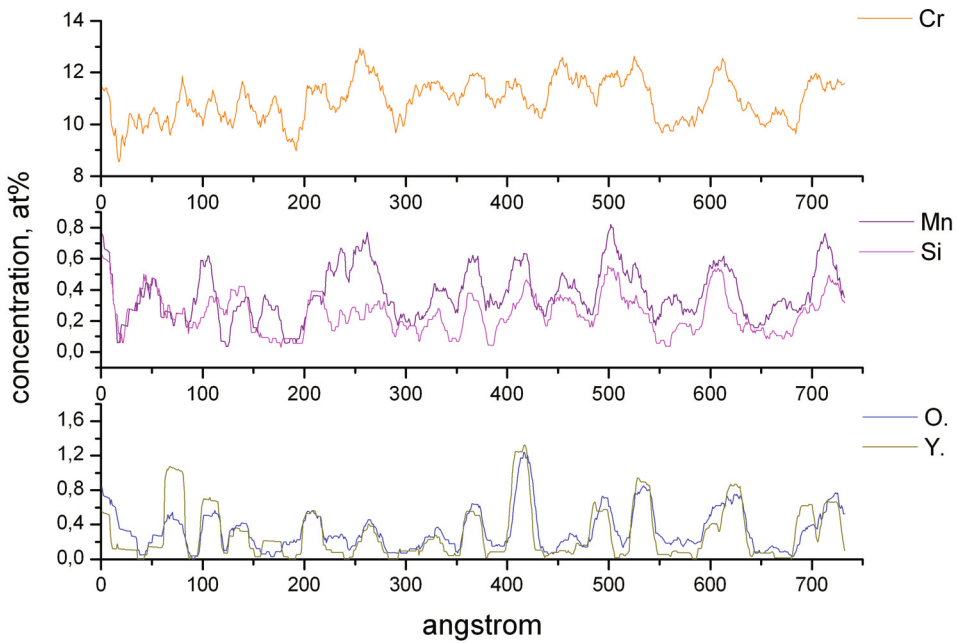


Fig. 3: Distribution of chemical elements along the evaporation axis in the volume from Fig. 2a (EO01 specimen). Enriched areas can be easily distinguished.

The typical size of the Y-O clusters for EO01 state varies from 1 to 5 nm with an average value of 3 nm. The estimated number density of these clusters in investigated volumes lies within $3.5 \div 5 \times 10^{24} \text{ m}^{-3}$ with an average value of $\sim 4 \times 10^{24} \text{ m}^{-3}$.

The distribution of elements along the evaporation axis of an irradiated sample is shown in Fig 3. A considerable enrichment compared to the matrix in O, Y (7 and 10 times higher correspondingly) and a moderate one in Cr (about 1.3 - 1.5 times) at some depths can be seen. Moreover, a correlation between Mn and Si concentration peaks and Y-enriched areas is visible. After the cluster identification procedure the parameters of Y-clusters were determined: chemical composition of each cluster and its Guinier radius. The element concentrations of observed clusters for both EO01 and EO04 states are presented in Fig. 5.

Atom maps for the EO04 state are presented in Fig. 4 a,b . Element concentrations in the matrix and average values (over matrix and clusters) are shown in Table 2. Concentrations of O and Y atoms in EO04 specimens are lower than in EO01. In Fig. 4a, b some areas enriched in yttrium and oxygen (Y-O clusters) are visible. Their typical sizes are 1.0÷2.5 nm with an average value of 1.5 nm. The estimated number density in this volume is $2 \times 10^{24} \text{ m}^{-3}$. The element concentrations in Y-clusters are presented in Fig. 5 and are similar to that of EO01. A considerable enrichment in O, Y and partly in Cr is also detected. However, in the annealed state a second kind of peculiarities were found. They are more diffuse and have absolutely different composition (see clusters 34-36 in Fig 5). These peculiarities consist of a far less number of solutes but still could be visually distinguished. Probably, they are nothing but remnants of Y-O clusters that were observed earlier. According to the bar histogram of the cluster composition, shown in Fig. 5, the concentration of minor solutes varies in a wide range while the elements like Y, O, Si and Mn are always present. Moreover, their total concentration in Y-O-clusters is within 6-9 at.-% and no visible enrichment at the cluster-matrix interface by light element can be seen.

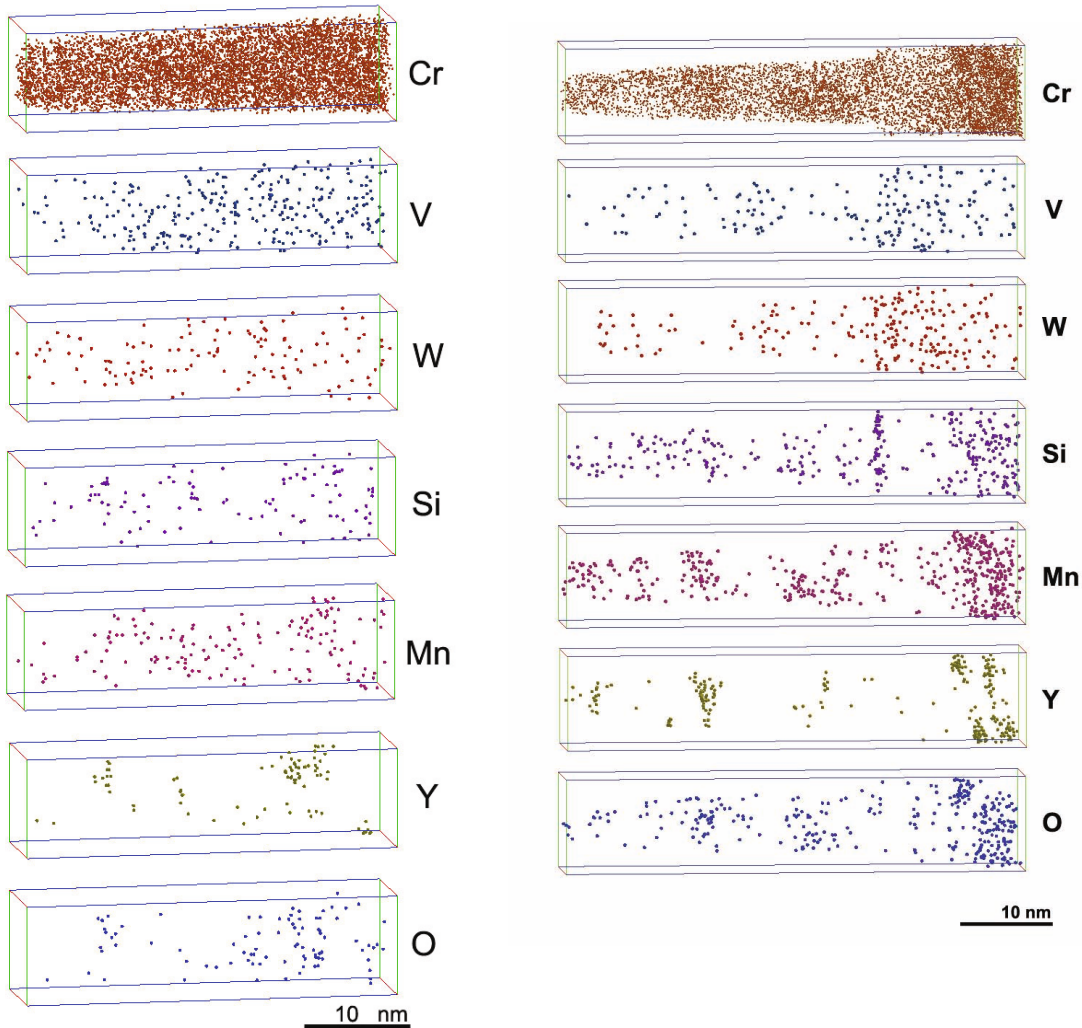


Fig. 4: Atom maps of the solute distribution in the ODS-EUROFER 97 irradiated at 300° C up to ~ 30 dpa and then annealed at 500° C for 3 hours (EO04 state). The investigated volumes are about 13×13×34 (left hand side) and 12×12×64 (right hand side).

The data processing also revealed that under irradiation a matrix depletion in some chemical elements took place. The slight difference in element concentration between our data and data obtained by other techniques could be caused by radiation-induced segregation. The detected concentration of Cr notably depends on the pulsed-to-DC voltage ratio and, as we decreased this parameter for better performance, the measured concentration was underestimated.

Discussion

The stability of the nanostructure of ODS steels under irradiation is essential for their radiation resistance. The investigations performed on ODS-EUROFER 97 samples irradiated up to 30 dpa at 300° C and with additional post-irradiation annealing at 500° C for 3 hours, revealed changes in its nanostructural state. The main difference for both states was in the nanoparticles composition. In the unirradiated state clusters are enriched in V, Y, O and N, whereas after neutron irradiation the V and N contents in the particles decrease and on the other hand the concentration of Y, Cr and Mn increased. The composition of formed Y-O clusters differs from that of pure yttria particles which core had the stoichiometry of $(Y_{1.8}Mn_{0.2})O_3$. The calculated ratio of Y+Mn to O was about 3 for clusters formed under irradiation and stayed the same after annealing.

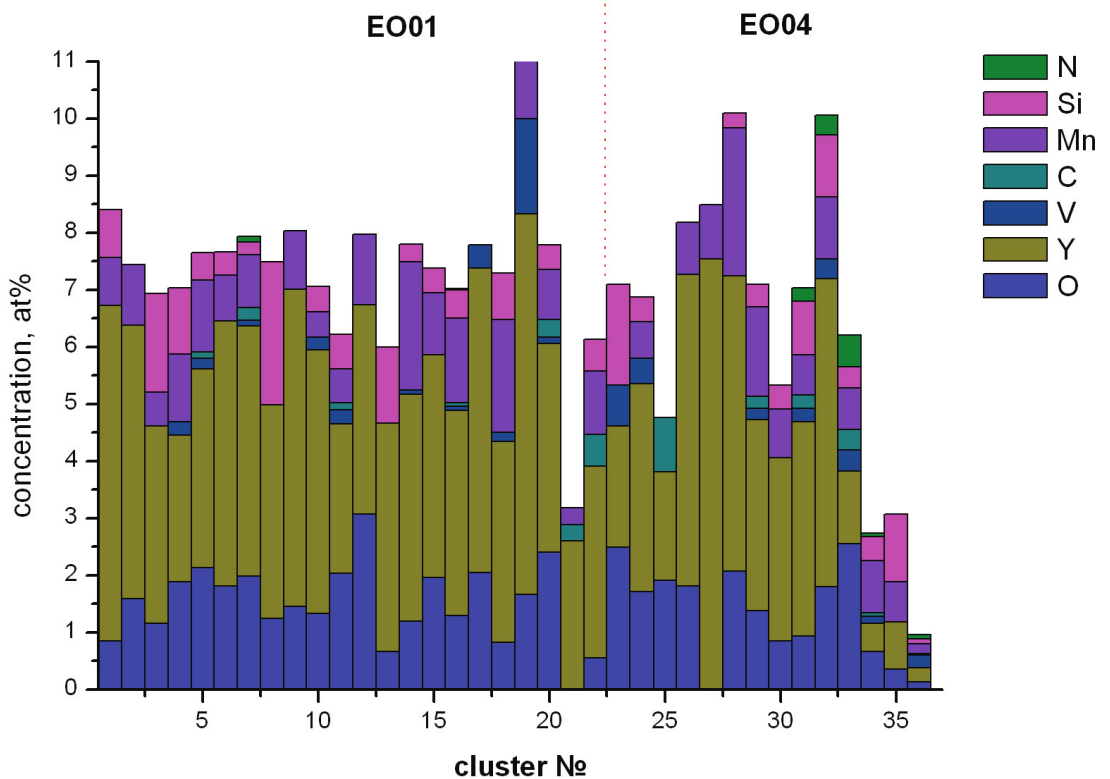


Fig. 5: Histogram of element concentrations in Y-O-clusters observed in EO01 and EO04 states. Each element concentration is equal to the height of the visible part of a corresponding bar.

It should be noted that in the observed clusters chromium had probably the highest affinity to oxygen. This assumption is supported by analysis of evaporated ion mass-spectra. Among ions evaporated from the cluster area, besides YO molecular ion, CrO ions were detected. Such drastic changes in the cluster composition in comparison with unirradiated state could be caused by the presence of vacancies. Their influence on the stoichiometry of Ti-Y-O particles was described in an earlier annual report.

The obtained data sets are relatively small and, therefore, are not fully statistically representative. Anyway, even a limited insight into the atomic structure of ODS steels might be important for the understanding of the mechanisms occurring under irradiation.

The cluster number density in the irradiated state is estimated to be about $4 \times 10^{24} \text{ m}^{-3}$ which is slightly higher than that for unirradiated one ($\sim 2 \times 10^{24} \text{ m}^{-3}$). The average cluster sizes for both un- and irradiated at 330° C states are close and equal to $\sim 3 \text{ nm}$, while after annealing it is $\sim 2 \text{ nm}$ and the number density is close to the unirradiated state. It is believed that fine cluster formation under irradiation could lead to irradiation induced hardening and increases ductile-to-brittle transition (DBTT) temperature. A similar behaviour was observed for EUROFER ODS steel where the increase of DBTT after irradiation [6] correlate with the increase of nanoscale cluster number density.

Important information can be derived from comparison of the local material chemical composition obtained for un- and irradiated states (Table 2). Vanadium that was found mainly in clusters in the initial material moved into matrix under irradiation. Considerable redistribution of yttrium and oxygen also occur: the yttrium concentration was six times higher and the value for oxygen three times. Post irradiation annealing at 500° C decreases this effect: Y and O concentrations in the matrix decrease to double values for un-irradiated state. An increase of manganese within the particles in the irradiated specimens was also observed.

Since the concentration of elements was increased after irradiation both in the clusters and in the surrounding matrix one can suppose that this increase resulted from dissolution of larger yttria particles. Thus, the data shown indicate that bigger particles (≥ 10 nm), not seen in this tomographic atom probe investigation, but observed routinely with TEM (see e.g.), may be not stable under irradiation and at least partly dissolve.

Conclusion

Oxide dispersion strengthened ferritic-martensitic steel ODS-EUROFER 97 irradiated at 330° C up to ~ 30 dpa in fast neutron reactor BOR-60 was studied by topographic atom probe in the as-irradiated state and after additional annealing at 500° C. A high number density $2\div4\times10^{24} \text{ m}^{-3}$ of ultra fine $\sim 1\text{-}3$ nm in diameter nanoclusters enriched in yttrium, oxygen, manganese and chromium were observed. The composition of detected clusters differs from that for the unirradiated state. Irradiation by fast neutron resulted in escaping vanadium from clusters into the surrounding matrix. The concentration of yttrium and oxygen in the matrix increases several times after irradiation. This effect can be explained by the dissolution of the yttrium oxide particles with sizes larger than 10 nm that cannot be detected by tomographic atom probe due to the limited size of the needle, but observed by TEM. The recovery annealing at 500° C for 3 hours decreases the number density of observed clusters compared to the pre-irradiated state. However, the composition of Y-O clusters after annealing was closer to the irradiated state than to the unirradiated.

Staff:

A. Möslang

P. Vladimirov

S.V. Rogozhkin (Institute for Theoretical and Experimental Physics, Moscow, Russia)

A.G. Zaluzhnyi (Institute for Theoretical and Experimental Physics, Moscow, Russia)

References

- [1] P. Vladimirov, A. Möslang, R. Lindau, M. Klimenkov, C. Eiselt, R. Coppola, A.A. Aleev, A.V. Karpov, O.N. Makeev, S.V. Rogozhkin, A.G. Zaluzhnyi. Workshop on Structural Materials for Innovative Nuclear Systems (SMINS), Karlsruhe, Germany, 4-6 June 2007.
- [2] A.A. Aleev, N.A. Iskandarov, M. Klimenkov, R. Lindau, A. Möslang, A.A. Nikitin, S.V. Rogozhkin, P. Vladimirov, A.G. Zaluzhnyi, Investigation of oxide particles in unirradiated ODS-EUROFER by tomographic atom probe. Submitted to Journal of Nuclear materials, 2009
- [3] M. Klimenkov, R. Lindau and A. Möslang, Journal of Nuclear Materials 386-388 (2009) 553-556.
- [4] S. Rogozkin, A. Chernobaeva, A. Aleev, A. Nikitin, A. Zaluzhnyi, D. Erak, Ya. Shtrombakh, O. Zabusov, L. Debarberis and A. Zeman. The effect of post-irradiation annealing on VVER-440 RPV materials mechanical properties and nano-structure under re-irradiation, Proceedings of PVP2009, 2009 ASME Pressure Vessels and Piping Division Conference, July 26-30, 2009, Prague, Czech Republic, PVP2009-78128.

Acknowledgement

This work, supported by the European Communities under the contract of Association between EURATOM and Karlsruhe Institute of Technology, was carried out within the framework of the European Fusion Development Agreement. The views and opinions expressed herein do not necessarily reflect those of the European Commission.

TEM Examination of Microstructure & Nano-Chemistry of Neutron Irradiated EUROFER 97 Specimens (15 dpa HFR) (WP08-09-MAT-REMEV, Activity 5)

Method

Specimens of EUROFER97 prepared of impact tests have been irradiated up to an average dose of 16.3 dpa at irradiation temperatures of 250 °C, 300 °C, 350 °C, 400 °C and 450 °C. The neutron irradiation was performed in the HFR (High Flux Reactor, Petten, Netherlands). Neutron flux was $3.99 \times 10^{18} \text{ m}^{-2}\text{s}^{-1}$ ($E > 0.1 \text{ MeV}$). The TEM specimens were prepared and analyzed in the FML (Fusion Materials Laboratory) of the Hot Cell facility of KIT.

For the preparation by electrochemical etching the Tenupol-3 jet polisher was used with a 20% H_2SO_4 + 80% CH_3OH solution as electrolyte. A voltage of 10-12 V was applied for etching. The investigations were performed using a FEI Tecnai 20 F microscope suitable for analysing of active specimens. The microscope was operated at 200 kV accelerating voltage with a field emission gun by strong electric field pulses. Some fraction of the evaporated and ionized atoms (usually ~50%) fly to a detector where they are registered and their final position is fixed. Their initial position in the lattice can be recalculated using known electric field distribution. Analysis of the measured time of flight of each atom from the tip of the probe to the detector provides information on the charge to mass ratio, which is usually sufficient to determine uniquely the nature of evaporated chemical specie.

Results

Microstructural analysis

The bright and dark field images of small dislocation loops in a specimen after irradiation at 250 °C are shown in Fig. 1 as an example. Both images were obtained near [001] zone axis. The diameter of the defects ranged from 2-5 nm to the 15 nm dislocations loops, where the fraction of 15 nm loops is very low. In the case of small (2-5 nm) defects it is sometimes difficult to definitely determine whether

they are small dislocation loops or point defects. In the weak beam dark field image $g(4g)$ $g=\{020\}$ numerous small white dots and few loops are visible (Fig. 1b). The concentration of the detected visible defects was estimated to $2 \pm 0.5 \times 10^{15} \text{ cm}^{-3}$ (Tab. 1). The dislocation loops have a $\frac{1}{2}\langle 111 \rangle$ Burgers vector as it can be determined using standard $\mathbf{g} \cdot \mathbf{b} = 0$ invisibility criteria. For this measurement the specimen was imaged near the [001] zone axis.

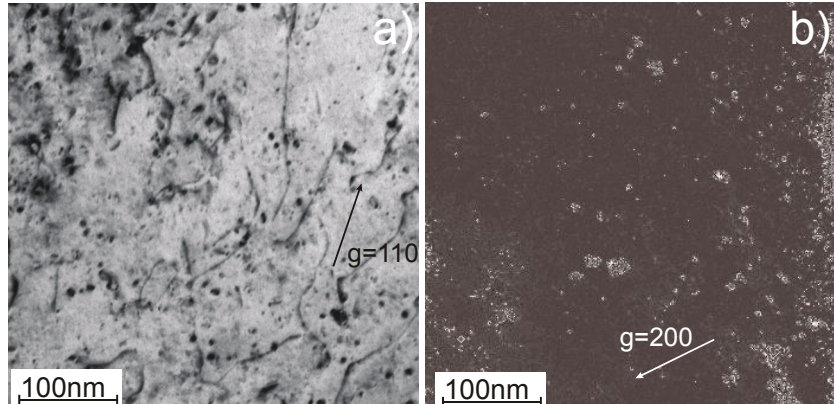


Fig. 1: TEM image of the specimen irradiated at 250 °C using $g=110$ (a) and weak beam image $g(4g)$ $g=200$ (b).

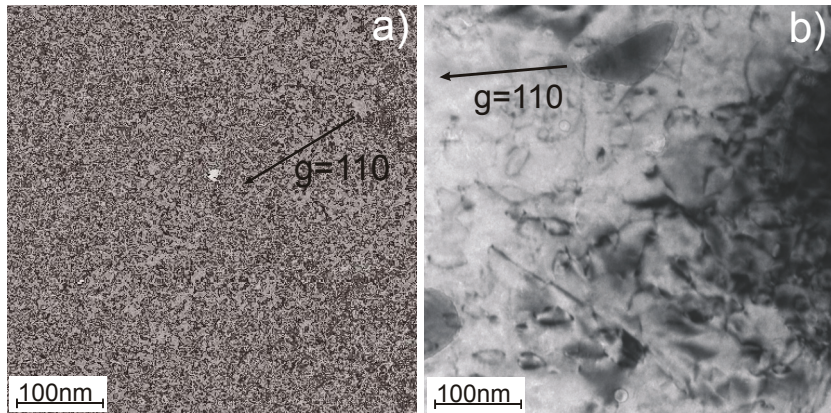


Fig. 2: TEM image of the specimen irradiated at 300 °C (a) and 350 °C (b) using $g=110$ for the both images.

typically around 10 nm, only a few grow up to a diameter of 25 nm. Above an irradiation temperature of about 300 °C, the spatial concentration of irradiation induced defects strongly decreases, as shown in Fig. 2b: After an irradiation at 350 °C dislocation loops with diameters up to 70 nm have been observed. $\frac{1}{2}\langle 111 \rangle$ Burgers vector have been determined for all loops formed during neutron irradiation at 300 and 350 °C.

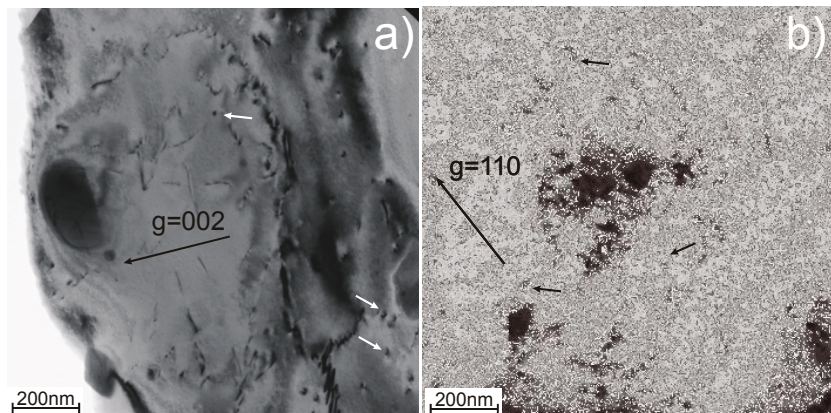


Fig. 3: TEM images of the specimens irradiated at 400 °C (a) using $g=002$ and 450 °C (b) using $g=110$. The dislocation loops are marked by the arrows.

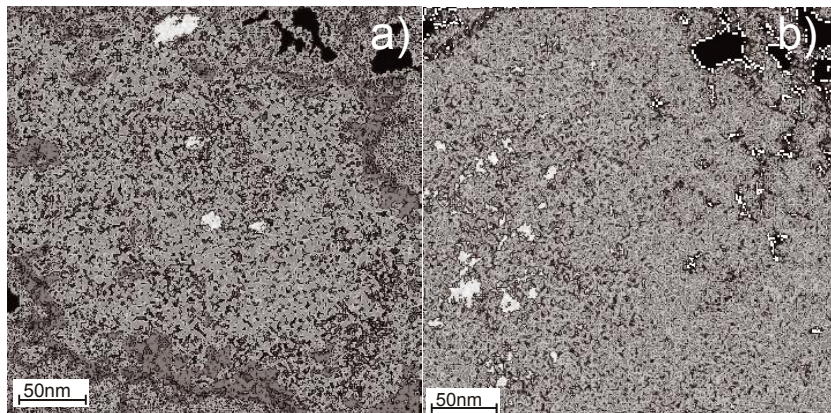


Fig. 4: Bright field TEM micrographs of He bubbles in the specimen irradiated at 350 °C.

ROFER 97, the total helium concentration can be estimated to ≤ 10 appm. The very inhomogeneous distribution of the rare cavities suggests that they can be interpreted as helium bub-

Fig. 2 reveals bright field images showing dislocation loops in the specimens irradiated at 300 °C (a) and 350 °C (b). Obviously both, the irradiation induced defect density and defect size are remarkably higher at 300 °C compared to 250 °C. At an irradiation temperature of 300 °C, the total concentration of visible defects amounts to $4 \pm 0.8 \times 10^{15} \text{ cm}^{-3}$, and the diameter of dislocation loops is

Fig. 3 shows TEM microstructures of specimens irradiated at 400 °C and 450 °C, respectively. Loops with diameters typically between 5-10 nm were detected; however the density of radiation induced defects is significantly smaller compared to the lower temperature irradiations (Table 1).

In the specimens irradiated at 350 °C and 400 °C a very small number density of voids or helium bubbles has been detected. Fig. 4 shows examples after 350 °C irradiation. Statistically, such voids or He bubbles are very seldom and many TEM micrographs do not show any of them. However, if they show up, a couple of them can be detected within local areas of 200 nm x 200 nm (Fig. 4a or 4b). Due to the very low boron content of EU-

bles in the surrounding of boron rich precipitates. The density of bubbles in specimens irradiated at 400 °C decreases rapidly compared to the specimen irradiated at 350 °C

Table 1: Statistical analysis of size and concentration of dislocation loops.

T_{irr}	250 °C	300 °C	350 °C	400 °C	450 °C
Defects concentration cm^{-3}	2×10^{15}	4×10^{15}	3×10^{14}	5×10^{13}	1×10^{13}
average size nm	7	14	35	12	10

Table 1 contains statistical data from the analysis of TEM micrographs. Here the measured densities and average sizes of dislocation loops and He bubbles are presented. In the present specimens only loops with $\frac{1}{2}\langle 111 \rangle$ Burgers vector have been detected. This

result correlates with literature where the formation of dislocation loops with $\langle 100 \rangle$ Burgers vector was observed only in the specimens with lower Cr concentration and higher irradiation temperature.

Correlation of dislocation density with tensile and DBTT data

Tensile results from the same irradiated EUROFER 97 material reveal at $T_{\text{irr}} = 300$ °C an ultimate tensile strength R_m of ~ 880 MPa while at $T_{\text{irr}} = 250$ °C the later is only ~ 795 MPa. At a first glance, this behaviour can be explained with the Orowan mechanism by the smaller irradiation induced defect density of the 250 °C specimens. The fact, that with decreasing irradiation temperature the tensile strength does not show saturation around 300 °C but decreases again towards lower temperatures has been recently also observed already after 2.5 dpa. The authors of that publication showed for about 10 RAFM steels a maximum in R_m and a minimum of total elongation A at 300 °C. Even in instrumented Charpy tests, the ductile to brittle transition temperature DBTT seems to have a maximum around an irradiation temperature of 300 °C, although the data scatter is larger in this case.

Descriptions on the origin of the abnormal temperature dependency of the dislocation density and on structure property relations taking into account diffusion kinetics and hardening mechanisms will be given in a forthcoming publication.

Conclusions

After neutron irradiation of EUROFER 97 between 250 and 450 °C up to 16.3 dpa density, size and orientation of irradiation induced defects have been analyzed by TEM. All loops investigated showed a Burgers vector of $\frac{1}{2}\langle 111 \rangle$. While the defect density revealed a strong decrease from 300 °C towards 400 °C as expected, an abnormal density decrease from 300 °C to 250 °C has been observed. However, this observation correlates with recent tensile and Charpy results that showed a maximum of irradiation hardening and embrittlement also around 300 °C. Very few and completely non-homogeneously distributed voids or helium bubbles have been found that can be attributed to the production of helium from segregated boron.

Staff:

M. Klimenkov
E. Maternal-Morris
A. Möslang
R. Rolli
H.-C. Schneider

Acknowledgement

This work, supported by the European Communities under the contract of Association between EURATOM and Karlsruhe Institute of Technology, was carried out within the framework of the European Fusion Development Agreement. The views and opinions expressed herein do not necessarily reflect those of the European Commission.

Nano Composited Ferritic Steels for HT Application: Identification of Promising Candidate Alloy Compositions and Respective Fabrication Routes According to the Outcome of the 2004 Study. Production and Characterisation of Different Laboratory Batches (14%Cr) (TW5-TTMS-006 D 5, TW6-TTMS-006 D 7)

Advanced blanket concepts like the HCPB (Model C) or gas cooled divertor concepts require allowable operational temperatures of 700 to 750 °C or even more. Reduced activation ferritic (RAF) ODS-steels such as Fe-(12-14)Cr-(2-3)W-(0.2-0.5)Ti-(0.2-0.5)Y₂O₃ being developed in USA and Japan for fission and fusion application seem to be promising in fulfilling the requirements and presently also form the basis for EU efforts.

Within this task, two master alloys containing 13-14% Cr and 1.0-1.2% W and varying Ti contents were ordered and inert gas atomised. These steel powders formed the basis for the production of different ODS steels with varying Y₂O₃ and Ti contents by mechanical alloying in a high-energy attritor mill. Hot-Isostatic-Pressing was applied to consolidate the MA powder. Powders and hipped samples of the different alloys were screened by appropriate methods like metallography, SEM, XRD, HRTEM, and chemical analyses. Tensile and charpy tests on miniaturised specimens are used for the mechanical characterisation of these alloys.

In terms of continuing the general studies on the properties of 13Cr-1W-0.3Ti-0.3Y₂O₃ ferritic ODS-alloy the microstructural stability was examined by various analyses: Firstly the ODS-particles within the material's matrix were analysed by performing HAADF, EDX and EELS line scans on as hipped (HIP parameters: $p_{\text{hip}} = 1000$ bar, $T_{\text{hip}} = 1150$ °C, $t_{\text{hip}} = 2$ h) as well as aged specimens of 13Cr-1W-0.3Ti-0.3Y₂O₃ for determination of decompositon and segregation effects and appearance of a V-Cr-O rich shell on the ODS-Particle/matrix boundary as detected for ODS-EUROFER in earlier investigations [1]. As aging temperatures $T_{\text{aging}} = 850$ °C and 950 °C and as aging times $t_{\text{aging}} = 3000$ h and 1000 h were chosen in this context. Secondly for determination of creep and fatigue properties long term creep experiments in vacuum at two temperatures $T = 650$ °C, $T = 750$ °C with varying stresses as well as fatigue tests at a temperature of $T = 550$ °C with different strain variation ranges were conducted, both with rolled specimens of 13Cr-1W-0.3Ti-0.3Y₂O₃ (Roll parameters: $T_{\text{rolling}} = 800$ °C, $\varphi = -0,6$).

Figure 1 a)-c) contains the HAADF images together with the according EDX line scan results for ODS-particles, which can be recognized as round dots of dark contrast, with diameters of 12-14 nm in the as hipped state (a), as well as in the two aged states (b,c). Those were taken over the line scan distance x. The according K_α-intensity profiles show, that the K_α-intensities for the analysed elements iron and chromium decrease, while those for titan and yttrium parallelly increase, as soon as the line scan leaves the matrix and enters the particle for all tested states. The conditions are vice versa, when the particle is passed. This behaviour is more profound in the as hipped state, but also detectable in the aged versions and the particles are therefore spectroscopically verified. The particle's morphology does also not differ much between the analysed states. Due to the phenomenon of so called peak overlapping for certain important elements such as K_α-intensities of oxygen with titan, vanadium and chromium L₁₋₃-peaks as well as for the vanadium K_α-intensities with titan K_β-intensities and the manganese K_α-peaks with chromium K_β-intensities, EDX does not provide a sufficient spectroscopical differentiation of the element's intensity distributions [2]. Therefore EELS analyses were performed: The higher energy resolution of EELS- analyses allows a better separation of EELS intensity profiles or "edges" and can therefore provide more detailed information concerning a possible shell formation [3]. Figure 2 shows a HAADF-image and the corresponding series of EELS-spectra according to the line scan distance x for the as hipped state.

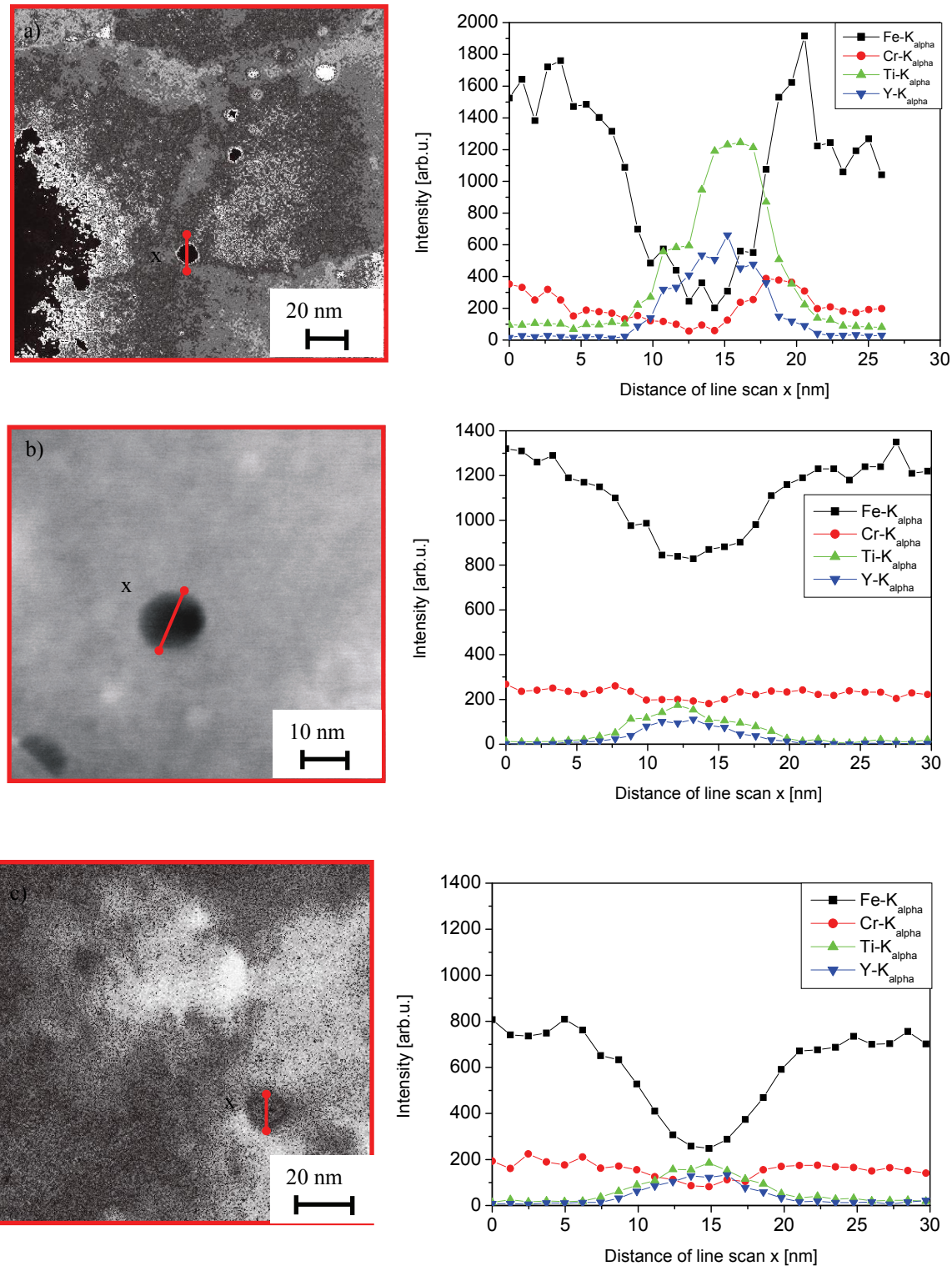


Fig. 1: HAADF-images of 13Cr-1W-0.3Ti-0.3Y₂O₃ and according K_α- intensity profiles of EDX line scans in dependence of the line scan distance x for a) as hipped state, b) after aging with t=3000 h, T=850 °C, c) after aging with t=1000 h, T=950°C.

ODS-particles with diameters of 17-19 nm have been selected for the analyses. The edges of the interesting elements are located in the high energy loss region of the EELS spectrum (550 eV-730 eV), therefore the zero loss peak and the low energy loss regions are not displayed. These intensities only allow qualitative interpretations of the elements and not any quantitative statements about the element's concentrations. In Figure 2 the O-K, Cr-L_{2,3} and the Fe-L_{2,3} intensities are clearly visible. Furthermore the cross-over between the base material's matrix and the ODS-particle can be recognized, when the Fe- L_{2,3} and Cr- L_{2,3} intensities decreases, while the O-K peak intensities increase in the middle part of the EELS-spectra series. The O-K peaks stand for the oxygen, which is bonded within the ODS-particles. Therefore the ODS-particle positions correspond to the peak position within the spectra.

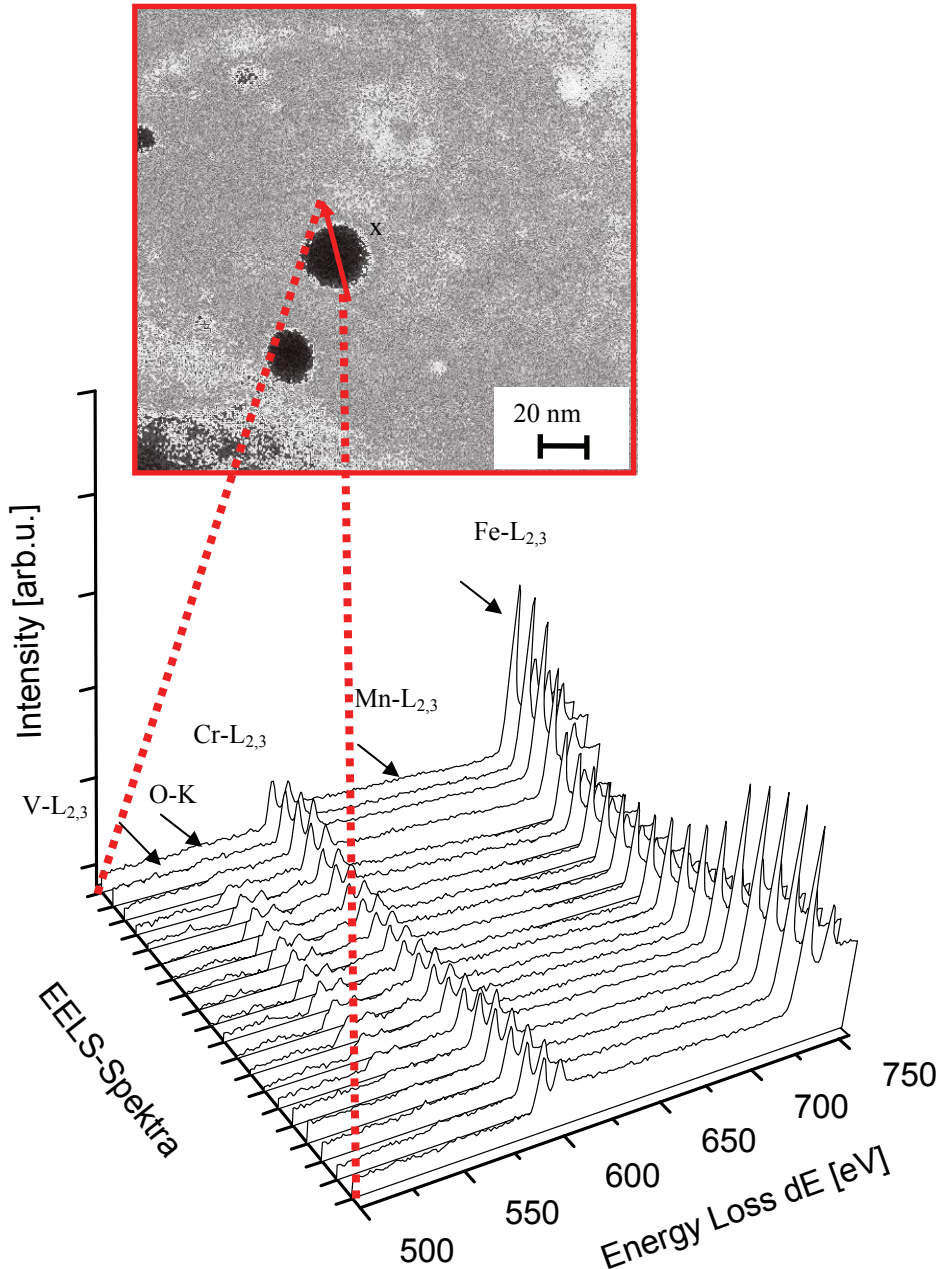


Fig. 2: HAADF-image of 13Cr-1W-0.3Ti-0.3Y₂O₃ (as hipped state) and according EELS- intensity profiles in dependence to the line scan distance x.

On the contrary to [1] no V- $L_{2,3}$ as well as Mn- $L_{2,3}$ edges can be detected on the ODS-particles of 13Cr-1W-0.3Ti-0.3 Y_2O_3 , despite a higher resolution of the EELS-analyses and missing peak overlapping. Significant concentration gradients are therefore not existent on the particle's edges as well as within the particle's volume. Consequently a V-Cr-O rich shell and manganese enrichment within the particles, as shown in [1] for ODS-EUROFER, does not exist for 13Cr-1W-0.3Ti-0.3 Y_2O_3 .

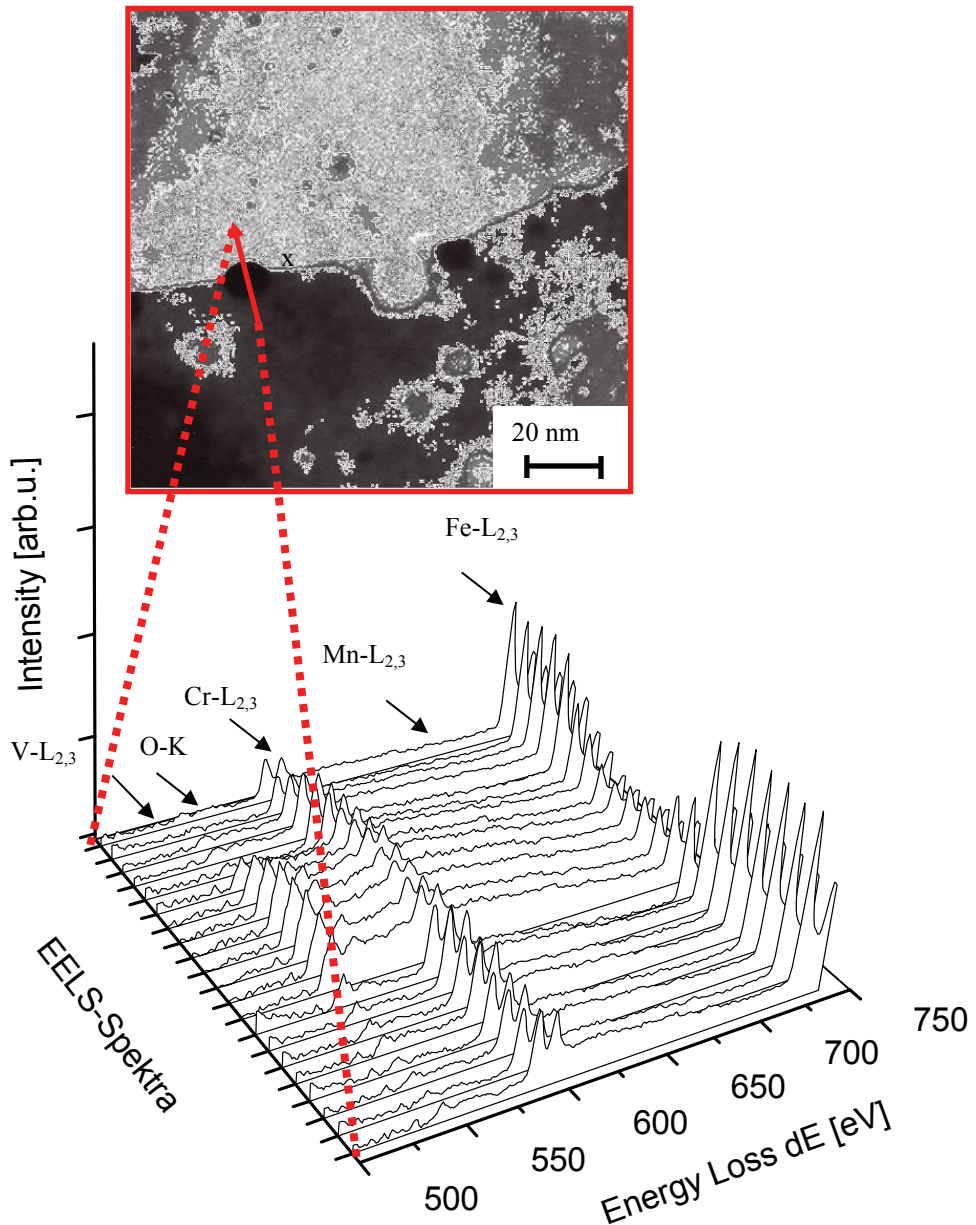


Fig. 3: HAADF-image of 13Cr-1W-0.3Ti-0.3 Y_2O_3 ($t=3000$ h, $T_{\text{Alterung}}=850$ °C) and according EELS- intensity profiles in dependence to the line scan distance x.

Figure 3 contains the spectra series for an ODS-particle on the grain boundary of an aged version ($T_{\text{aging}}=850$ °C, $t_{\text{aging}}=3000$ h) of 13Cr-1W-0.3Ti-0.3 Y_2O_3 . The O-K, Cr- $L_{2,3}$ and the Fe- $L_{2,3}$ intensities and the particle-matrix crossovers are also clearly detectable, while equally V- $L_{2,3}$ as well as Mn- $L_{2,3}$ edges are totally absent. Even for an increased aging temperature $T_{\text{aging}}=950$ °C but reduced aging time $t_{\text{aging}}=3000$ h (the spectra are not displayed here) the situation is very similar. Due to this reason no evidence and even no indications for decom-

position or segregation effects on the ODS-particles in the as hipped as well as for the aged versions of 13Cr-1W-0.3Ti-0.3Y₂O₃ can be derived with the applied analyses tools. The assumption, that ODS-particles serve not only as a trapping center for argon, which is frequently used as a milling atmosphere during mechanical alloying, but also as a trapping center for vanadium [1], cannot be confirmed for of 13Cr-1W-0.3Ti-0.3Y₂O₃. A possible explanation could be a lower vanadium as well as manganese content in the alloy compared to ODS-EUROFER. However, the appearance of a Cr-O rich shell, leaving out vanadium, cannot be fully excluded: in all conducted analyses Cr and O peaks exist parallel at the particle-matrix crossovers. The Cr-content of 13% could also serve as a support for this conclusion. As a whole five line scans for each version of 13Cr-1W-0.3Ti-0.3Y₂O₃ have been carried through, which all lead to similar results: therefore the developed 13Cr-1W-0.3Ti-0.3Y₂O₃ alloy shows a strong microstructural as well as phase stability within the applied parameter fields.

Figure 4 shows a Larson Miller diagram, which connects the parameters stress, temperature and time to rupture of long term creep experiments and therefore allows the comparison of different materials tested with alternating parameter sets. In Figure 4 the long term creep tests for the rolled 13Cr-1W-0.3Ti-0.3Y₂O₃, which have been conducted at T=650 °C and 750 °C, are compared to the non particle hardened steel EUROFER as well as ODS-EUROFER. It can be seen, that the levels of both ODS-materials are a lot higher than for EUROFER. The mechanism of particle strengthening is therefore an effective option to increase the creep rupture strength in this context. ODS-EUROFER is displayed in two different versions, in the as delivered state, as well as after thermomechanical treatments [4] which have been tested at T=600-700 °C. For 13Cr-1W-0.3Ti-0.3Y₂O₃ only the milling atmosphere during MA was initially altered from argon to hydrogen. It can be recognized, that the creep strength levels of the two versions of 13Cr-1W-0.3Ti-0.3Y₂O₃ for stresses in the range of 110–200 MPa is relatively near to ODS-EUROFER alloys but does not yet reach it fully. In the stress range of 70 MPa to 100 MPa the ferritic ODS-alloy has a slightly higher level than ODS-EUROFER. In both cases the version of 13Cr-1W-0.3Ti-0.3Y₂O₃ originally produced in a hydrogen atmosphere during MA shows a little higher level than the argon processed version. An exception is only detectable at the lowest tested stress of 70 MPa.

Figure 5 shows the maximum stress levels of the rolled 13Cr-1W-0.3Ti-0.3Y₂O₃ in dependence of different strain variation ranges, fatigue cycles and the applied temperature of 550°C. Generally the maximum stresses decrease with lower strain variation ranges as expected. Furthermore it can be clearly seen, that the ferritic ODS-alloy does not exhibit any significant material's softening independently from the applied strain variation ranges, because the maximum stresses remain constant until the specimen rupture. From these results it can also be concluded, that 13Cr-1W-0.3Ti-0.3Y₂O₃ has a high microstructural stability. The properties of the microstructure stay the same until the specimen breaks.

Staff:

C. Adelhelm
S. Baumgärtner
C. Eiselt
P. Graf
M. Klimenkov
T. Kaiser
R. Lindau
A. Möslang
U. Jäntschat
R. Ziegler
H. Zimmermann

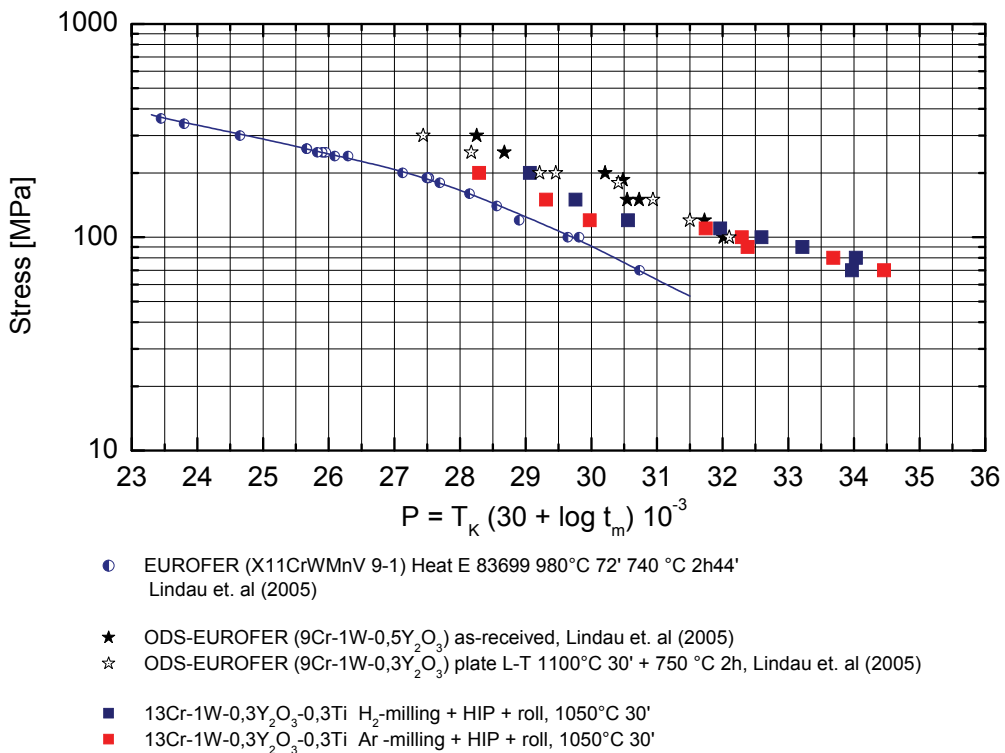


Fig. 4: Creep strength (Larson-Miller-Plot) of 13Cr-1W-0.3Ti-0.3Y₂O₃ compared to standard EUROFER steel and ODS-EUROFER steels in dependency of the production parameters.

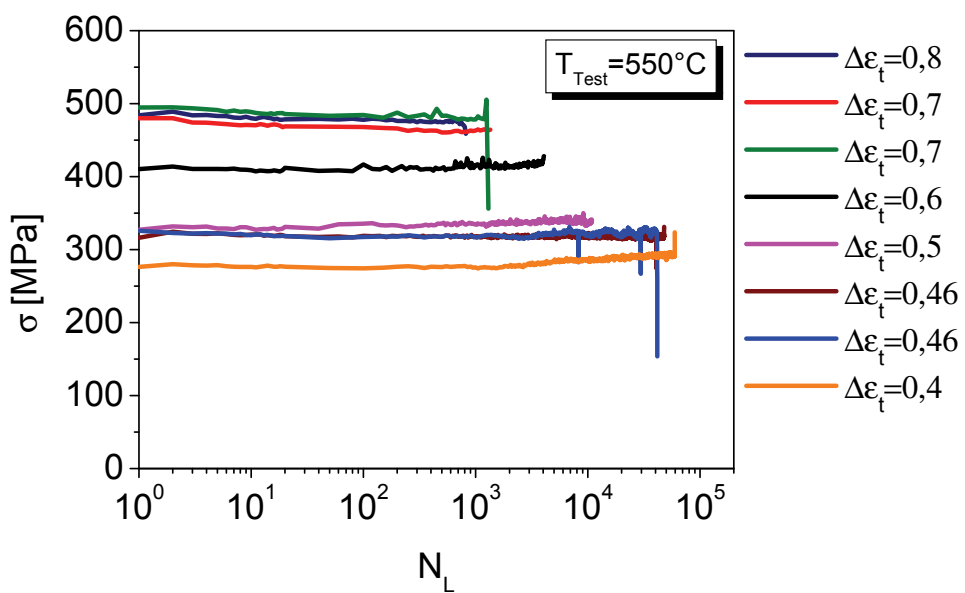


Fig. 5: Maximum stress levels of the alloy 13Cr-1W-0.3Y₂O₃-0.3Ti over number of fatigue cycles in dependence of the applied temperature.

Literature:

[1] M. Klimenkov, R. Lindau, A. Möslang: New insights into the structure of ODS-particles in the ODS-EUROFER alloy, Journal of Nuclear Materials 386-388 (2009), pp. 553-556

- [2] G.G. Johnson, E.W. White: X-ray Emission Wave length and KEV tables for Nondiffractive analyses, ASTM Data Series DS46, USA, (1970). S. 1-2
- [3] C.C.Ahn, O.L.Krivanek: EELS Atlas – A reference guide of electron energy loss spectra covering all stable elements. Gatan Inc. Warrendale PA 15086 USA (1983). S.1.
- [4] R. Lindau, A. Möslang, M. Rieth, M. Klimiankou, E. Materna Morris et al.: Present development status of EUROFER and ODS-EUROFER for application in blanket concepts. Fusion Engineering and Design 75-79 (2005), pp. 989-996.

Acknowledgement

This work, supported by the European Communities under the contract of Association between EURATOM and Karlsruhe Institute of Technology, was carried out within the framework of the European Fusion Development Agreement. The views and opinions expressed herein do not necessarily reflect those of the European Commission.

Developing the Present Generation of ODS Nano-structured Ferritic Steels (WP08-09-MAT-ODSFS, Activity 1)

Overview

The main objective of this activity is to develop the present generation of ODS nano-structured ferritic steels that are able to withstand the high neutron and heat fluxes for sufficiently high neutron fluences of at least $10 - 15 \text{ MW y m}^{-2}$ corresponding to a component lifetime of at least five years. The plate supporting the W tiles of the dual-coolant tritium breeding blanket and the cartridge within the finger-like concept of the He-cooled divertor are presently the foreseen applications of ODS ferritic steels. Both require materials that have sufficient creep strength in the temperature range of up to $\sim 750 \text{ }^{\circ}\text{C}$ with reasonable fracture toughness. In recent years considerable work has been performed worldwide to develop these types of alloys. Since the only commercial producer for ODS alloys in Europe has given up the production, special emphasis of the developmental work is also focussed on the transferability from laboratory to industrial scale.

In order to develop or improve the present generation of reduced activation 14 Cr ferritic ODS steel, the production process was analysed and the different fabrication steps were investigated. The production route includes the mechanical alloying of gas-atomised powder, consolidation by hot isostatic pressing and a thermo-mechanical treatment which consists either of a deformation step like extrusion or a rolling. The latter two steps are followed by a thermal treatment to adjust the desired microstructure, which in turn has a strong impact on the mechanical properties.

Also under the aspect of scalability, a horizontal high energy attritor produced by ZOZ with a 200 g powder capacity was chosen for the mechanical alloying (MA) investigations. ZOZ produces similar high energy ball mills with capacities up to 10 kg powder. The MA process was optimised with respect to the milling parameters like milling time, rotation speed and also to the powder to ball ratio. The problem is to adjust these parameters in order to get a good alloying and a small particle size of the MA powder which allows a good filling of the HIP canister. An additional goal is to minimise the wear of the components like the rotor and the steel balls which can contaminate the MA powder. It is known from earlier investigations, that mechanical alloying under argon atmosphere, which should avoid or minimise the oxidation of the powder during milling, leads to an uptake of Ar into the material. This noble gas tends to precipitate into bubbles at the yttria particles. To avoid this noble gas uptake, alternative milling atmospheres like hydrogen were tested. Fig. 1 shows a picture of the ZOZ attritors installed at KIT.

The effect of all these different process parameters on the micro/nanostructure were investigated applying light microscopy (LM), scanning electron microscopy (SEM) and advanced analytical methods transmission electron microscopical (TEM) methods. The mechanical properties were determined by tensile and Charpy impact tests using small scale test technologies.

The next step in the production route is the encapsulation and degassing procedure. The MA powder is filled into stainless steel containers which are evacuated at elevated temperature



Fig. 1: ZOZ Simoyer CM01-2L.

for some hours. The degassing temperature and time depends on the protective gas used in the MA process. After the degassing procedure the suction pipe is being crimped and afterwards seal-welded. Hot isostatic pressing in an industrial device is used to consolidate the MA powder. As HIPping pressure the maximum available pressure was chosen while the temperature was optimised with respect to density and grain size. Low HIP temperatures lead to a smaller yttria particle size but bear the risk of higher porosity whereas a too high temperature can lead to grain coarsening. As experience with earlier ODS developments at KIT shows, hot rolling and subsequent heat treatment can improve the high temperature tensile ductility and impact behaviour significantly. In order to check, whether this is also valid for the ferritic ODS steels, this kind of thermo-mechanical treatment was also applied to the test pieces.

Mechanical testing, results and discussion

A few results of the mechanical testing are given in the following figures. Fig. 2 and 3 give the results of tensile testing of samples, prepared under different conditions. The test temperature was varied from RT to 750 °C. Fig 2 shows the ultimate tensile strength R_m of samples mechanically alloyed under argon or hydrogen as protective gases. As a second parameter the HIPping temperature was varied from 950 to 1150 °C. The results are compared to the reference structural steel EUROFER 97 and its ODS variant, as well as the American ferritic RAF 12Cr ODS steel 12YWT. Compared to the 9Cr RAFM ODS steel ODS- EUROFER, developed at KIT, the RAF 13Cr ODS steel has a higher ultimate tensile strength than the RAFM 9Cr ODS steel. Above a testing temperature ODS of 400 °C the tensile strength of the ferritic alloy decreases continuously and reaches the values of the ferritic martensitic 9Cr ODS steel. Neither the milling atmosphere nor the HIP temperatures seem to have a significant influence on the tensile strength. Especially above 400 °C the values don't scatter very much. The ferritic American 12Cr ODS steel shows a significantly higher tensile strength than the 13Cr ODS steels.

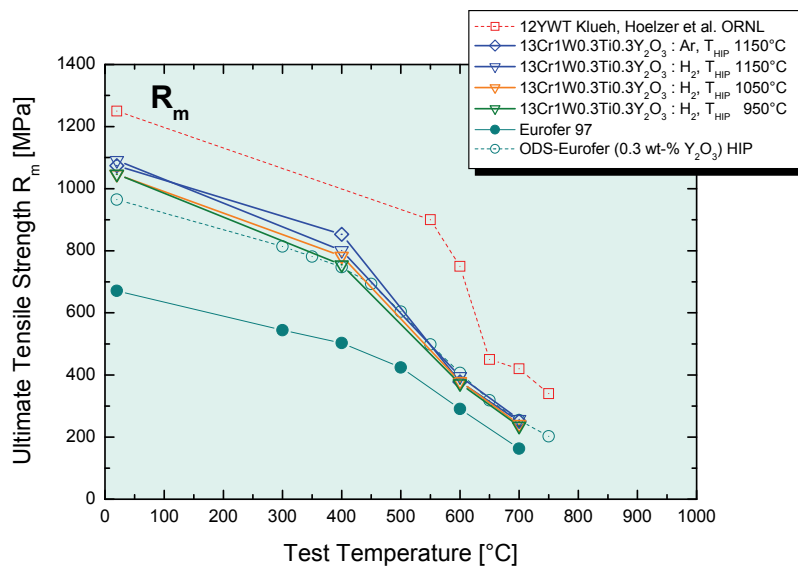


Fig. 2: Ultimate tensile strength of 13Cr ODS steels produced under different conditions in comparison with the RAFM reference steel EUROFER 97, ODS- EUROFER and 12YWT.

The uniform elongation $R_{p0.2}$ shows an analogous behaviour. The results are not displayed here. Fig. 3 gives a comparison of the total elongation of the same alloys under the same preparative and testing conditions. To demonstrate the effect of thermo-mechanical treatments, data of thermo-mechanically treated ODS- EUROFER are added for comparison.

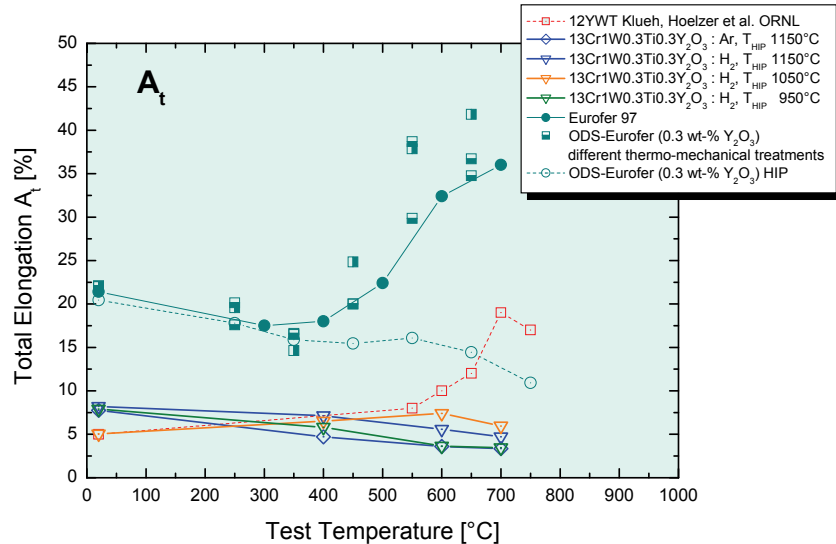


Fig. 3: Total elongation A_t of 13Cr ODS steels produced under different conditions in comparison with RAFM reference steel EUROFER 97, ODS- EUROFER and 12YWT.

It can be clearly seen, that the purely ferritic alloys have significantly lower total elongations. The values for the 13Cr alloys reach at least only half the values for the hipped 9Cr ODS steel. Thermo-mechanical treatment of the 9Cr ODS improves significantly the total elongation above 400 °C. The extruded 12YWT shows between 400 and 700 °C the same tendency, but at much lower values. Also in this plot there is no big scatter between the different milling atmospheres and HIP temperatures. The tensile curves of the 13Cr alloys show also that there is only little work hardening whereas the 9Cr ODS steel shows pronounced work hardening. Rolled and heat treated material was also tested, but they show the very same behaviour as described before. The reason could be an insufficient degree of deformation in the rolling process due to the limited geometrical dimensions of the HIP capsules which did not allow higher deformation. Otherwise, much smaller samples would have been necessary at the expense of comparability with available data.

Besides the tensile behaviour, fracture toughness and impact behaviour are important material properties for the suitability as structural materials for blanket and divertor applications in future nuclear fusion reactors. Figure 4 gives the comparison of the impact properties of different ODS steels produced under different conditions with the RAFM steel EUROFER 97. Since no cast 13Cr steel with similar composition is commercially available, hipped 13 Cr steel powder was used as reference for the 13Cr ODS steel. The impact energy A_v of the hipped ferritic 13 Cr ODS steel is very low compared to all other steels. The upper shelf energy of the 13 Cr ODS steel is independently from the milling atmosphere about one third of the hipped 13 Cr Steel and one fifth of the hipped 9Cr ferritic martensitic ODS- EUROFER steel. It is difficult to determine a ductile to transition temperature (DBTT). If one takes as usual half the difference between upper and lower shelf energy a DBTT of about 50 °C can be given. A thermo-mechanical treatment, i.e. hot rolling plus subsequent heat treatment, which improved the impact behaviour of the 9Cr ODS- EUROFER significantly, did not have the same effect for the 13 Cr ODS steel. The uppers shelf energy is increased only slightly. The reasons for the poor impact properties of the 13Cr ODS steel can be manifold. The hipped base material itself has comparably poor impact behaviour which could be material-inherent. This is speculative since no cast material with comparable composition is available. That there is no effect of hot working can be due to the low degree of deformation. This was unavoidable due to the given capsule und specimen size. Also no effect of the milling atmosphere was found. It could be that the expected effect of Ar bubbles at the yttria particles on the mechanical behaviour was overestimated. Whether other factors like too high oxygen contents play an important roll is still under investigation.

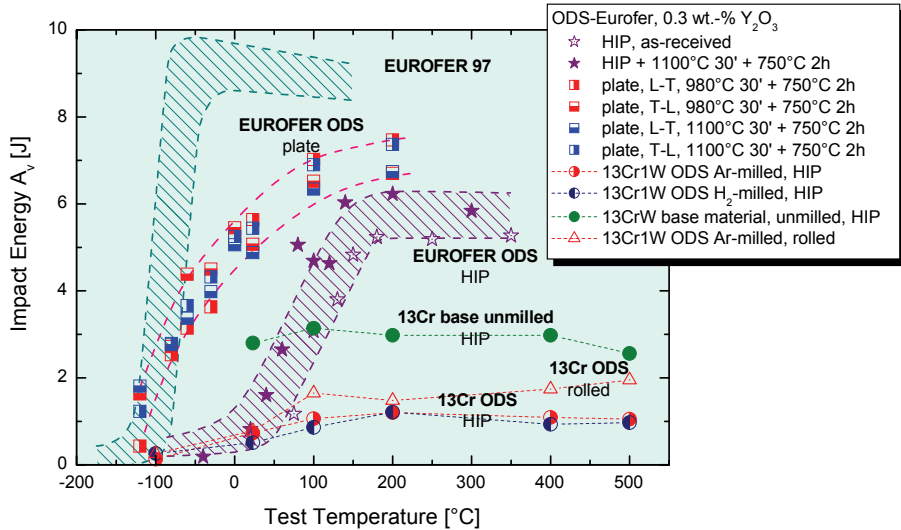


Fig. 4: Impact properties of 13Cr ODS ferritic steels produced under different conditions in comparison with RAFM reference steel EUROFER 97, ODS- EUROFER and 12YWT.

Conclusions

In order to improve the currently developed ferritic 13Cr ODS steel, the production parameters were varied and the effect on the microstructural and mechanical behaviour was investigated. The material shows good tensile and creep strength, but all ductility related properties are not satisfying. The reasons for that behaviour cannot be clearly identified. From these findings it is impossible at the moment to propose a common specification for a joint European ferritic 13-14Cr ODS steel. Further investigations how to improve the unsatisfactory material properties have been launched.

Staff:

C. Adelhelm
S. Baumgärtner
B. Dafferner
C. Eiselt
U. Jäntschat
T. Kaiser
M. Klimenkov
R. Lindau
A. Möslang
R. Ziegler
H. Zimmermann

Acknowledgement

This work, supported by the European Communities under the contract of Association between EURATOM and Karlsruhe Institute of Technology, was carried out within the framework of the European Fusion Development Agreement. The views and opinions expressed herein do not necessarily reflect those of the European Commission.

Coordination of the EFDA Fusion Materials Topical Group and Fundamental Studies on Mechanical Properties of W-alloys (WP08-09-MAT-WWALLOY)

Coordination for EFDA Fusion Materials Topical Group

During the reporting period the EFDA programme 2008-2009 on tungsten and tungsten alloys development was compiled and evaluated. The according proposals were assessed. During seven working and monitoring meetings the progress was monitored and discussed. The results of the Topical Group were presented. The final activity was the formulation of the next program for 2010 and the assessment of the proposals.

Introduction

The most critical issue of tungsten based alloys in connection with structural applications is the required ductile-to-brittle transition temperature (DBTT) of less than 600 °C after irradiation (measured by EU standard mini-Charpy tests). A comprising study has been performed to characterize different tungsten materials with respect to their applicability for structural divertor parts.

Fabrication and testing Charpy specimens has been performed according to the EU standards DIN EN ISO 148-1 and 14556:2006-10. That is, small size specimens (27 mm x 3 mm x 4 mm, 1mm notch depth, 22 mm span) have been used for instrumented Charpy tests. The specimens were fabricated by electrical discharge machining (EDM). For investigating the influence of machining, the notches of some specimens were fabricated by a diamond wire saw. The notches were all fabricated perpendicular to the rolling direction. This is important and has to be kept in mind for the evaluation of the Charpy results, since this orientation is the most favorable for energy and DBTT values.

Materials, Study and Results

By comparing the Charpy test results of the tungsten based alloys with those of TZM it becomes obvious that only TZM shows the usual embrittlement behavior which is typical for most body-centred cubic metals. That is, (1) there is a clear transition from brittle (at lower temperatures) to ductile (at higher temperatures) fracture, and (2) there is an extended regime of ductile fracture (the so-called upper shelf). In the case of TZM the DBTT lies between 200 °C (fully brittle) and 400 °C (fully ductile fracture) and the upper shelf energy varies from 9 to 10 J.

The tungsten based alloys don't show this single transition. Moreover, only specimens of pure tungsten and WVM show an upper shelf starting at 1000 °C and 900 °C. All other rod materials did not fracture in a fully ductile manner within the whole test temperature range. However, all materials tend to exhibit brittle fracture at temperatures below 600 °C. Above that temperature, the specimens show fractures which (partly) propagate along the rod axis, that is, parallel to the specimen's long side and perpendicular to the notch (see Fig. 1). This is comparable to the fracturing of fiber reinforced materials and it is called delamination.

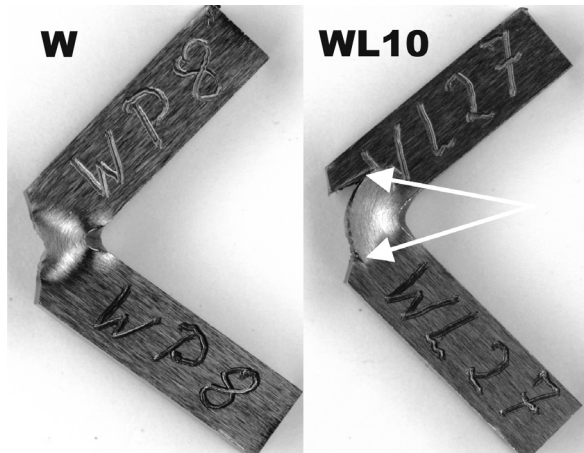


Fig. 1: Fracture of pure tungsten and WL10 at 1000°C. The tungsten specimen fractured ductile while the WL10 specimen shows delamination (indicated by the arrows).

In summary, there are three types of fractures (brittle, delamination, and ductile) which are obviously linked by a brittle-to-delamination transition and a delamination-to-ductile transition. The brittle-to-delamination transition temperature (defined in analogy to DBTT) varies around 500 ± 50 °C for all tungsten based alloys while the delamination-to-ductile transition temperature is about 900 °C for tungsten and about 1000 °C for WVM.

The other materials (WL10, WL10opt, and W1Re1La2O₃) show slightly increasing energies with temperature, but they do not show an additional transition (the slight step in the W1Re1La2O₃-curve cannot be related to a change in fracture type).

The test results of the plate materials are shown in Fig. 2. Compared to the results of the rod materials the energies are lower by more than 50% and all plate materials (even molybdenum) don't show fully ductile fractures at test temperatures up to 1100 °C. The reason for the severe reduction of Charpy energy is pronounced delamination fracture as can be seen in Fig. 3.

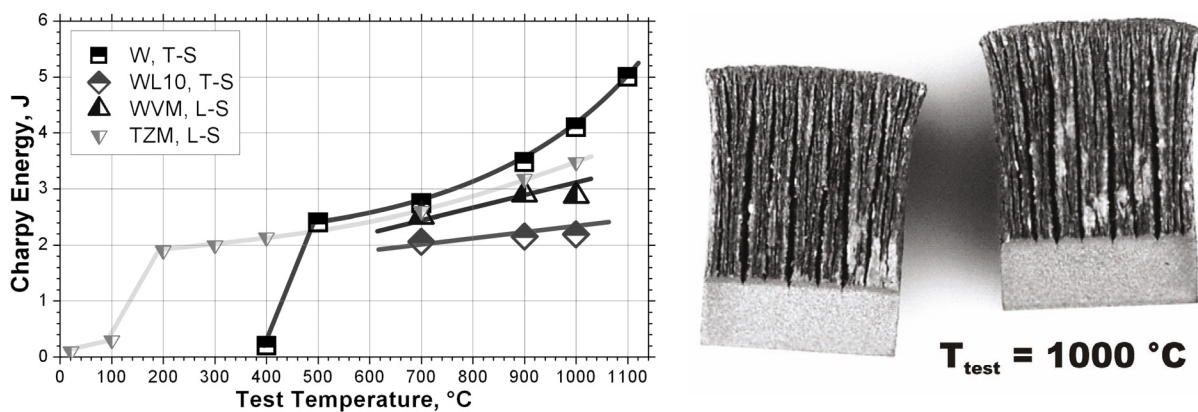


Fig. 2: Charpy test results of the plate materials.

Fig. 3: Typical fracture surface of plate material after delamination.

Figure 4a (right image) shows a simple model of a rod specimen just after delamination initiation. At this point, the upper layer of about 1 mm thickness (colored grey in Fig. 4b) doesn't contribute significantly to the bending strength of the specimen. Therefore, the analogy between a delaminated and un-notched specimen (Fig. 4c) is obvious. That is, the energies of notched and un-notched specimens should be approximately at the same level, provided, the delamination crack initiation is negligible.

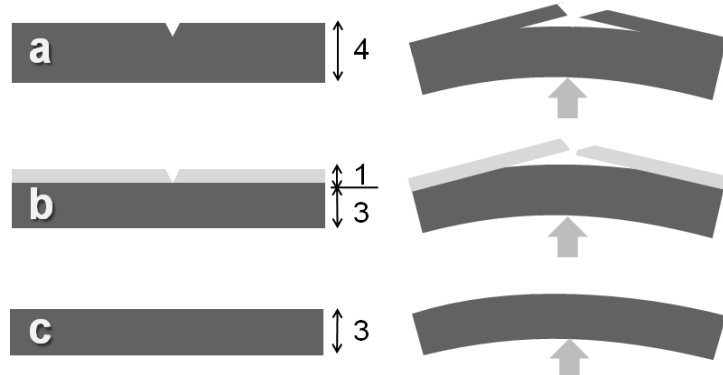


Fig. 4: Analogy between a delaminated and un-notched specimen (see also Fig. 1).

The results presented in Fig. 5 confirm that at 800 °C there is indeed no difference between an un-notched Charpy specimen and a sample with a notch fabricated by EDM. The un-notched tungsten specimens show the usual fracture behavior with a sharp DBTT at 450 °C.

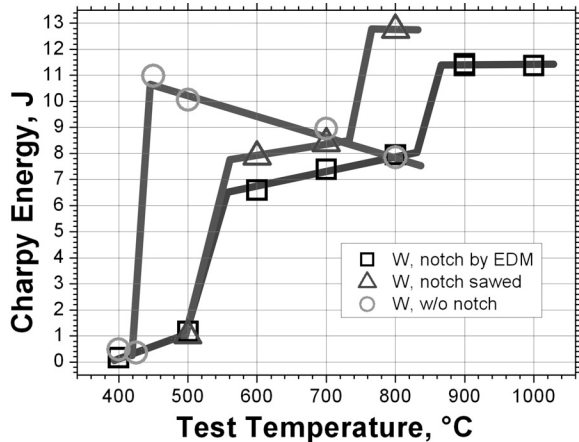


Fig. 5: Influence of notch fabrication on delamination and fracture modes of pure tungsten rod specimens.

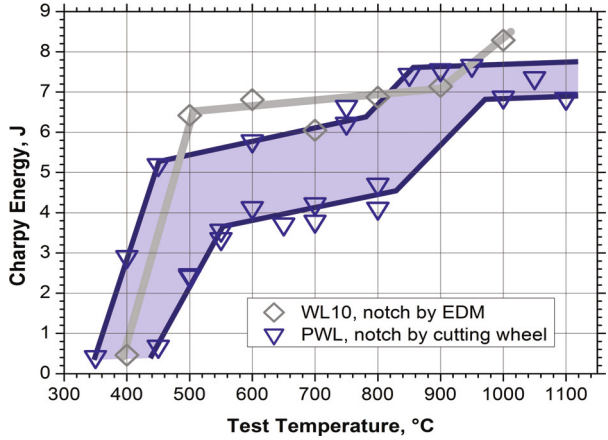


Fig. 6: Scattering as a result of notch fabrication and material production.

Figure 5 demonstrates also the influence of different notch fabrication methods. Compared to EDM, sawed notches lead to an improvement of the delamination-to-ductile transition by about 100 °C. Also, delamination takes place at higher energies by about 1 J. This coincides also with the result of the un-notched specimen at 700 °C. The brittle-to-delamination transition, however, seems not to be influenced by the fabrication process.

In a further study the extend of scattering of the Charpy tests has been determined. Therefore, specimens have been fabricated from a WL10 rod of 20 mm diameter (PWL) and tested in the temperature range from 350 °C up to 1100 °C. The results are plotted together with the previous WL10 results in Fig. 6. Here it is important to note that the notch of the PWL specimens has been fabricated by a diamond cutting wheel. Therefore, the notch root radius is almost twice as large compared to the EDM fabricated WL10 specimens. However, there is significant scattering in the PWL Charpy results which has been characterised by a lower and upper boundary line in the diagram (Fig. 6). But strangely, the results are either on the upper or on the lower boundary, and never between these limits. How can this be explained?

Figure 7 shows two typical fractures of specimens tested at 750 °C and 800 °C which should result in almost the same energy value (either 4-5 J or 6-7 J). But the test at 750 °C (PWL22) led to about 7 J while the test at 800 °C (PWL21) resulted only in 4 J. The fracture photo shows clearly that in one case (PWL22) the specimen fractured symmetrically with small delamination cracks on both sides of the notch root. In the other case (PWL21), the fracture developed in only one direction which obviously led to a slip of the specimen on the anvil. The same fracture behaviour was observed for the other tests: The higher energy results can be assigned to symmetrical fractures while the lower energy results can be attributed to onesided fractures.



Fig. 7: Different fractures of the Charpy specimens.
PWL21: 800 °C/4.1 J; PWL22: 750 °C/6.6 J.

At a closer look, the results of the EDM fabricated specimens of all other rod materials show single deviations, but only in the order of about 1 J. In all cases these deviations coincide also with unidirectional delamination fractures. Obviously, a larger notch root radius increases the extend (and probability) for a single-sided delamination crack propagation.

Conclusions

The known benefits of lanthanum-oxide particles in tungsten are (1) an improvement of the processability, (2) the suppression of recrystallisation, and (3) a slight strengthening in creep. On the other hand, the present study proves that the already insufficient fracture characteristic of pure tungsten is further reduced by the addition of lanthanum oxide (also by potassium, but to a lesser degree).

The study reveals furthermore that all considered tungsten rod materials show brittle fracture below about 600 °C. Earlier studies on commercial 8 mm weld electrode materials revealed brittle transition temperatures of more than 900 °C. Compared to that, the presently tested thin tungsten rod materials from PLANSEE confirm an improvement with respect to ductile fracture. Anyway, it could also be demonstrated that (rolled) plate materials in general perform worse than (rolled) rod materials. This could be attributed to the different microstructures which develop during material production.

The reason for the still high ductile transition temperature is not brittle fracture but an extended range of delamination fracture. Additional examinations revealed that notches prepared by electro discharge machining produce more surface micro-cracks than notches produced by sawing or milling. That such micro-cracks promote delamination fracture has been demonstrated by a comparison with un-notched specimens and with specimens without micro-cracks (notch fabrication by sawing).

Furthermore, it could be seen that all Charpy tests show a binary scattering which is due to asymmetric crack propagation and which depends on the notch root radius. The sharper the notch root, the smaller the scattering.

Staff:

C. Adelhelm
S. Baumgärtner
B. Dafferner
S. Heger
U. Jäntsch
M. Klimenkov
A. Möslang
P. Lukits
M. Rieth
M. Rohde
R. Ziegler
H. Zimmermann

Literature:

- [1] M. Rieth, A. Hoffmann, B. Dafferner, S. Heger, Impact Bending Tests on Selected Tungsten Materials, 1st International Conference on New Materials for Extreme Environments, June 2-4, 2008, San Sebastián, Spain. Published in: Trans Tech Publ., 2009, S.101-04 (Advanced Materials Research ; 59), ISBN 978-0-87849-344-9.
- [2] M. Rieth, A. Hoffmann, B. Dafferner, S. Heger, E. Materna-Morris, H. Sandim, H. Zimmermann, *Mechanical properties of different refractory materials for nuclear fusion applications*, Materials Science and Engineering, Sept. 1-4, Nürnberg, Germany.
- [3] M. Rieth, A. Hoffmann, *Fracture behavior of tungsten materials depending on microstructure and surface fabrication*, 18th Topical Meeting on the Technology of Fusion Energy (TOFE-18), San Francisco, Calif., September 28 - October 2, 2008.
- [4] M. Rieth, A. Hoffmann, M. Rohde, *Tungsten as Structural Material for Power Plant High Heat Flux Components*, Int. High Heat Flux Components Workshop, San Diego, Calif., December 10 - 12, 2008.

- [5] M. Rieth, A. Hoffmann, B. Dafferner, S. Heger, U. Jäntschi, M. Klimenkov, P. Lukits, M. Rohde, H. Zimmermann, *TUNGSTEN AS STRUCTURAL DEMO DIVERTOR MATERIAL*, Jahrestagung Kerntechnik 2009, 12.-14. Mai, Dresden, Germany.
- [6] Raffray, A.R.; Nygren, R.; Whyte, D.G.; Abdel-Khalik, S.; Dörner, R.; Escourbiac, F.; Evans, T.; Goldston, R.J.; Hölzer, D.T.; Konishi, S.; Lorenzetto, P.; Merola, M.; Neu, R.; Norajitra, P.; Pitts, R.A.; Rieth, M.; Rödig, M.; Rognlien, T.; Suzuki, S.; Tillack, M.S.; Wong, C.; High heat flux components - readiness to proceed from near term fusion systems to power plants; 36th International Conference on Plasma Science (ICOPS) and 23rd Symposium on Fusion Engineering (SOFE-23), San Diego, Calif., May 31 - June 5, 2009
- [7] Rieth, M.; Snead, L.L.; The challenges of high heat flux components in fusion reactors with respect to material selection; 36th International Conference on Plasma Science (ICOPS) and 23rd Symposium on Fusion Engineering (SOFE-23), San Diego, Calif., May 31 - June 5, 2009.
- [8] Rieth, M.; Boutard, J.L.; Review of the EFDA programme on divertor materials technology and science; 14th Internat. Conf. on Fusion Reactor Materials (ICFRM-14), Sapporo, Japan, September 7-12, 2009.
- [9] M. Rieth, A. Hoffmann, *Influence of microstructure and surface fabrication on impact bending properties of tungsten materials*, 17th PLANSEE SEMINAR, 25-29 May 2009, Reutte, Austria.

Acknowledgement

This work, supported by the European Communities under the contract of Association between EURATOM and Karlsruhe Institute of Technology, was carried out within the framework of the European Fusion Development Agreement. The views and opinions expressed herein do not necessarily reflect those of the European Commission.

Developing of Improved W-alloys for Application in a Power Plant with He Cooled Divertor (TW4-TTMA-002 D 2, TW5-TTMA-002 D 2)

Objectives

Intense R & D work was carried out on testing commercially available W alloys to create a data base with reliable properties acting as a reference point for the development of W alloys with improved properties for future application of these alloys in a helium-cooled divertor. The performed testing work of state-of-the-art products showed that they might not fulfil the requirements which are deducted from the actual divertor design indicating an application in the temperature range of 600 °C to 1300 °C. The most critical features will be the ductile to brittle transition and the recrystallization behaviour which are also affected by fast neutrons.

The development of new tungsten alloys with improved properties was conducted under the tasks TW4-TTMA 002 and TW5-TTMA 002. The chosen processing route to synthesize these tungsten alloys was mechanical alloying applying a ball milling system. The intention was to disperse oxide powders in tungsten to fabricate an ODS-tungsten precursor with nano-scale features. During the subsequent adopted compaction steps (e.g. pressing and sintering) the powders should be consolidated to compacts with interlinked grains and controlled morphology. The idea was to compare the properties of the improved W-alloys with the ones of standard, commercially available WL10 grades.

Actual status

Determination of tungsten alloy properties (tensile properties, microstructure) was continued by applying raw materials (rods) in the usual (state of the art) way. The tested alloys, pure W and WL10 (W-1%La₂O₃), exhibit large longitudinally elongated grains partially with a rather big diameter of approx. 20 µm for W grains. This is a result of the processing route. The ODS particles are not homogeneously dispersed in the WL10 quality. The performed tests [1] indicate that DBTT of both materials, pure W and WL10, lays at higher levels than claimed by the lower boundary of 600 °C, as a result from design analyses. The detected microstructure implies that the grain structure and the ODS distribution is not optimized adequately for a structural material and affects the properties. Thus finer grains and a more homogeneous ODS distribution may improve mechanical and physical properties.

Experimental

As processing route under these tasks mechanical alloying was selected to fabricate tungsten based precursors for synthesizing W bulk parts with improved properties. The milling process of W powder blended with La₂O₃ was performed in an attritor ball milling system, for which the correct working was demonstrated by processing of ODS-EUROFER steel powder. However, in the first processing of W powders the system was heavily damaged due to permeation of fine W powder into the feed through system for the drive of the attritor panel. A repaired and redesigned system was build up and used for the next milling tests. The first new test series were performed with smaller vessel filling (half of the powder amount) compared to the first test. The problem concerning the feed through was eliminated but strong heating up of the milling container still remained during mechanical alloying under these parameters. Thus, in a next step the powder to ball ratio was reduced to 1 to 10. Only under this measure the heating up of the milling container could be accepted and controlled. All tests were performed with a milling container and balls fabricated from Cr-steel whereas the plaids of the attritor propeller were hard metal plaited.

Results

Fig.1 shows the SEM picture of a W-1%La₂O₃ mixture after 10 h ball milling. The formed particles exhibit morphology known from milling of other refractory alloys. The agglomerates

reached dimensions up to roughly 50 μm as can be seen in Fig. 1. The particles have a spattered structure. This raw material was used for densification by cold pressing in steel dies of 12 mm. Densification pressure was varied between 400 and 700 MPa. The compacts were sintered under Ar-atmosphere at temperatures between 1000 and 1400 °C. Fig. 2 shows a sample after sintering at 1100 °C for 1 h. At this rather low temperature compared to the melting point of tungsten ($T_{\text{MP}} \sim 3400$ °C) first sintering necks were formed between the powder particles.

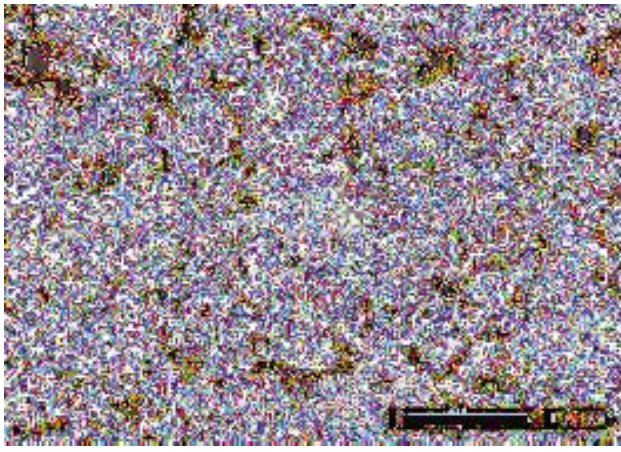


Fig. 1: SEM picture of W1% La_2O_3 powder mixture after mechanical alloying in attritor mill for 10 h.

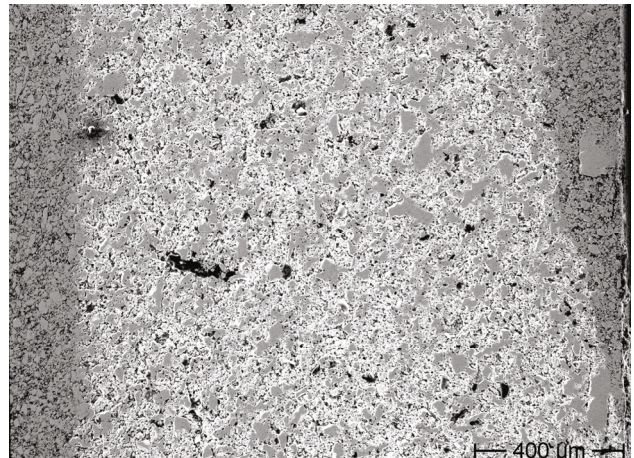


Fig. 2: Consolidated MA powder after sintering at 1100 °C. The cold pressed sample had an thickness of roughly 2 mm.

Fig. 3 gives the element analyses of the sintered sample by EDX line scanning. Still visible is the added amount of La_2O_3 with a very constant distribution over the whole compact indicating that the desired fine distribution of the ODS particles was achieved in the milling process. The line scan shows additionally that a high amount of Fe and Cr is present in the sintered sample. This is an indication that also under these 'optimised' processing conditions with reduced milling ball to powder ratio still very high abrasion of the steel container is present. More on concentration focused Fe analyses revealed Fe concentrations of 5 to 10% in the processed tungsten powder. Compared to earlier milling tests no significant reduction in Fe contamination was found.

Conclusions

The performed milling tests of W / La_2O_3 powder mixtures using the attritor milling system led to a fine distribution of the oxide particles in the processed W-powder. The milled powder shows agglomerated structure as known from processing of other refractory metal combinations [3]. However, in contrast to these softer and more ductile materials no coating of the milling vessel and the ball was observed which leads to a passivation of abrasion effects and stops contamination of the powder by components coming from the processing unit. Variations of processing parameters e.g. ball to powder ratio or filling level of the milling vessel did not show a significant impact on the Fe contamination. The Fe amount was always in the range 5 to 10%. Using this type of equipment tungsten – iron heavy metal powder is synthesized but not the desired improved W powder for fabrication of advanced W alloys. The resume is that this medium sized equipment in the present layout status is not applicable for the intended alloy development. This is no general statement concerning mechanical alloying for synthesis of improved W alloys. In small ball milling units nearly contamination free W processing is possible. However, this technique is not suitable for the planned work to prepare batch sizes necessary for subsequent testing of mechanical parameters.

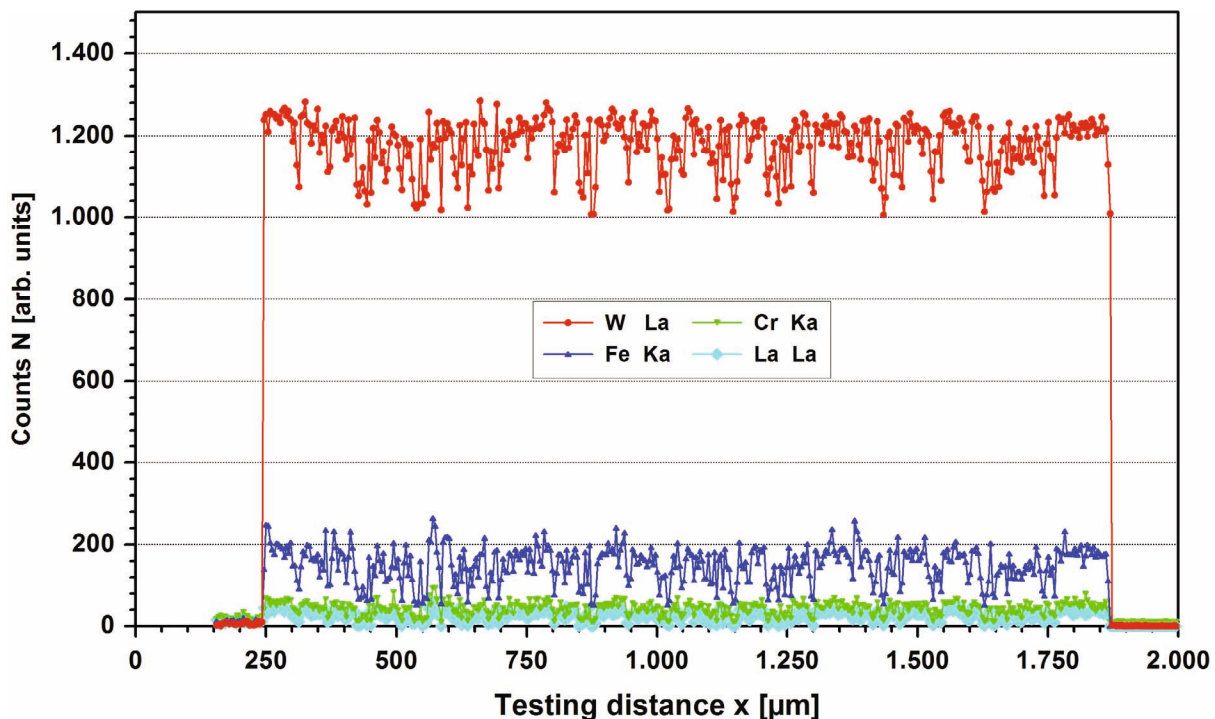


Fig. 3: EDX analyses of W-La₂O₃ sintered sample. Clearly visible is the high contamination by steel-elements coming from the milling vessel and balls.

The applied attritor system – a commercially available unit for fabrication of roughly 500 g batches as demonstrated in ODS-steel processing - build up for the ball milling of W-precursors needs extensive technological upgrades to open a chance for synthesising of pure – Fe free – W-ODS precursors. Alternative ball milling systems with vessels without rotating feed through and W based hard metal coating may be a development line with smaller risk in powder contamination by abrasion. Some newer results from development work in electrochemical tungsten processing and coating technology may also open additional paths for the goal of fabrication of W-alloys with improved properties.

Staff:

C. Eiselt
J. Konya
W. Krauss
R. Lindau
J. Lorenz
A. Möslang
M. Rieth

Literature:

- [1] M. Rieth, B. Dafferner, Limitations of W and W-1%La₂O₃ for use as structural materials, J. Nucl. Mat. 342 (2005) 20 - 25
- [2] W. Krauss, N. Holstein, J. Konya, Development and fabrication aspects regarding tungsten components for a He-cooled divertor, Fus. Eng. Design 75-79 (2005) 775 - 778
- [3] W. Krauss, C. Politis, P. Weimar, Preparation and compaction of mechanically alloyed amorphous materials, Metal Powder Report, 43 (1988), 231-38
- [4] M. Rieth, A. Hoffmann, Fracture behaviour of tungsten based alloys depending on microstructure and notch fabrication method, Fusion Science and Technology, 56 (2009) S.1018-22

- [5] W. Krauss, J. Konys, N. Holstein, J. Lorenz; Electrochemically based machining and joining development for He-cooled divertor; ICFRM-14, Sapporo, Japan, September 7-12, 2009
- [6] W. Krauss, N. Holstein, J. Konys; Advanced electrochemical processing of tungsten components for He-cooled divertor application, ISFNT-9, Dalian, China, October 11-16, 2009

Acknowledgement

This work, supported by the European Communities under the contract of Association between EURATOM and Karlsruhe Institute of Technology, was carried out within the framework of the European Fusion Development Agreement. The views and opinions expressed herein do not necessarily reflect those of the European Commission.

Structural Materials - Mechanical Behaviour and Reliability

Fast Reactor Irradiation up to 30 dpa, at 340°C of Tensile, Charpy and LCF RAF/M Specimens, Completion of the PIE (TW2-TTMS-001b D 9)

Objectives

In an energy generating fusion reactor structural materials will be exposed to very high levels of irradiation damage of about 100 dpa. Due to the fact, that fast reactor irradiation facilities in Europe are not available anymore, a cooperation with the Russian institution JSC "SSC RIAR" has been implemented. The irradiation project is named "ARBOR 1" (Latin for tree). Impact, tensile and low cycle fatigue specimens of Reduced Activation Ferritic/Martensitic steels, e.g. EUROFER 97, F82H mod., OPTIFER IVc, EUROFER 97 with different boron contents and ODS-EUROFER 97 have been irradiated in a fast neutron flux (> 0.1 MeV) of 1.8×10^{19} n.m $^{-2}$ at a temperature less than 340°C up to ~ 30 dpa. Mechanical PIE is terminated at SSC RF RIAR

Status end of 2008

All reasonable impact, tensile and LCF tests of the selected different materials irradiated in the ARBOR 1 irradiation had been performed and the final report is under preparation. The transport of irradiated ARBOR 1 specimens was organized and performed between SSC RF RIAR and KIT.

Specimens of ARBOR 1 reached FZK

For a detailed analysis of the implication of irradiation damage on mechanical properties a sophisticated microstructural analysis of the damaged specimens is necessary, therefore a series of deformed and undeformed specimens of different materials was transported to the hot cells of FZK. The transport was performed during 2009 and the specimens are examined under a new EFDA task (WP08-09-MAT-REMEV) for microstructural analysis in the hot cells of FZK.

On the basis of the mechanical post irradiation examination results the final report is ready as FZKA report 7517 end of 2009.

Staff:

C. Petersen
H.-C. Schneider

Literature:

- [1] C. Petersen, A. Povstyanko, V. Prokhorov, A. Fedoseev, O. Makarov and M. Walter: "Tensile and Low Cycle Fatigue Properties of different Ferritic/Martensitic Steels after the Fast Reactor Irradiation "ARBOR 1"" , Journal of Nuclear Materials 386 – 388 (2009) 299 – 302.
- [2] C. Petersen, "Post irradiation examination of RAF/M steels after fast reactor irradiation up to 33 dpa and $< 340^\circ\text{C}$ (ARBOR 1)" Final Report for TW2-TTMS-001b, D 9, FZKA-Report 7517, Dec. 2009.

Acknowledgement

This work, supported by the European Communities under the contract of Association between EURATOM and Karlsruhe Institute of Technology, was carried out within the framework of the European Fusion Development Agreement. The views and opinions expressed herein do not necessarily reflect those of the European Commission.

Mechanical Post Irradiation Examinations of FZK-Specimens Irradiated in the ARBOR 2 Experiment in the BOR 60 Reactor (TW5-TTMS-001 D 10)

Objectives

In the framework of the ARBOR 2 irradiation programme (the successor of ARBOR 1) EUROFER 97, selected RAFM steels (F82H-mod, OPTIFER XI, OPTIFER XII, BS-EUROFER, OPTIMAX), EUROFER ODS HIP, EUROFER based boron doped steels and technological specimens (diffusion welded EUROFER, EB welded EUROFER) have been irradiated in the BOR-60 experimental fast reactor of JSC "SSC RIAR" to reach an irradiation damage dose up to 70 dpa (up to 80 dpa for CEA specimens). KIT specimen matrix included 290 KLST, miniaturized tensile and LCF specimens for quantification of neutron irradiation induced embrittlement, hardening and changes in the fatigue behaviour.

PIE of ARBOR 2

The post irradiation Charpy impact and tensile testing of the specimens from ARBOR 2 has been finished in 2008 at the material science laboratory of SSC RIAR. In addition the influence of the post irradiation annealing on the mechanical properties has been studied.

In the course of 2009 the majority of the LCF specimens irradiated to a damage doses between 47 and 70 dpa have been tested with an electro-mechanical testing machine of INSTRON-DOLI 1362 type equipped with a 100 kN load cell, a three-zone furnace and high-temperature extensometer, installed in the K-12 hot cell of the SSC RIAR. Miniaturized cylindrical specimens of 7.6 mm gauge length and 2 mm diameter were used for the investigation of LCF properties. The strain controlled push-pull (LCF) loading was performed at a constant temperature of 330 °C with different total strain ranges ($\Delta\varepsilon_{\text{tot}}$) between 0.8 and 1.2% and at common strain rate of $3 \times 10^{-3} \text{ s}^{-1}$. The number of cycles to failure (N_f) was defined at a point where the peak tensile stress within a cycle decreased by 30% from its value at a point marking the termination of the linear dependence of peak tensile stress on the number of cycles (N). In addition, inelastic strain amplitudes ($\Delta\varepsilon_{\text{inelastic}}$) at $N_f/2$ were determined for given total strain amplitudes from the hysteresis loops.

Fig. 1 shows the fatigue behaviour for EUROFER 97 (980 °C/0.5 h + 760 °C/1.5 h) steel in the unirradiated condition and after neutron irradiation up to 70 dpa at 330 - 337 °C. The neutron irradiation (47 and 70 dpa) has only a minor influence on the number of cycles to failure (N_f) in the intermediate range (0.9 - 1.0 %) of the total strain amplitude in Fig. 1a. For a total strain range of the 1.1% the 70 dpa irradiated specimen shows a reduced lifetime in comparison to the unirradiated state and at the same time a non-monotonic evolution of the peak tensile stress with the number of cycles was observed. The fatigue behaviour for adequate inelastic strain amplitudes is shown in Fig. 1b. The neutron irradiation to 47 and 70 dpa has only a minor influence on the number of cycles to failure for inelastic strain ranges below 0.5%, whereas for inelastic strain ranges above 0.5% a noticeable reduction of the fatigue life can be recognized. The detailed analysis of the hysteresis loops of a specimen irradiated to 47 dpa and tested at $\Delta\varepsilon_{\text{tot}} = 1.1\%$ ($\Delta\varepsilon_{\text{inelastic}} = 0.55\%$ at $N_f/2$) indicated inelastic deformation already after the first quarter cycle. Under these circumstances, subsequent inelastic cyclic deformation is expected to occur within the grains in narrow slip bands which become cleaned from radiation defects e.g. dislocation loops by moving dislocations. As a result the deformation in these slip bands is enhanced and yields rapid strain softening. Thus, the reduction of the fatigue life in irradiated specimens at high strain amplitudes might be related to the micro crack initiation and the accumulation of fatigue damage in narrow slip bands. In addition irradiation enhanced stresses compared to the unirradiated state for adequate inelastic strain might also accelerate the fatigue damage accumulation.

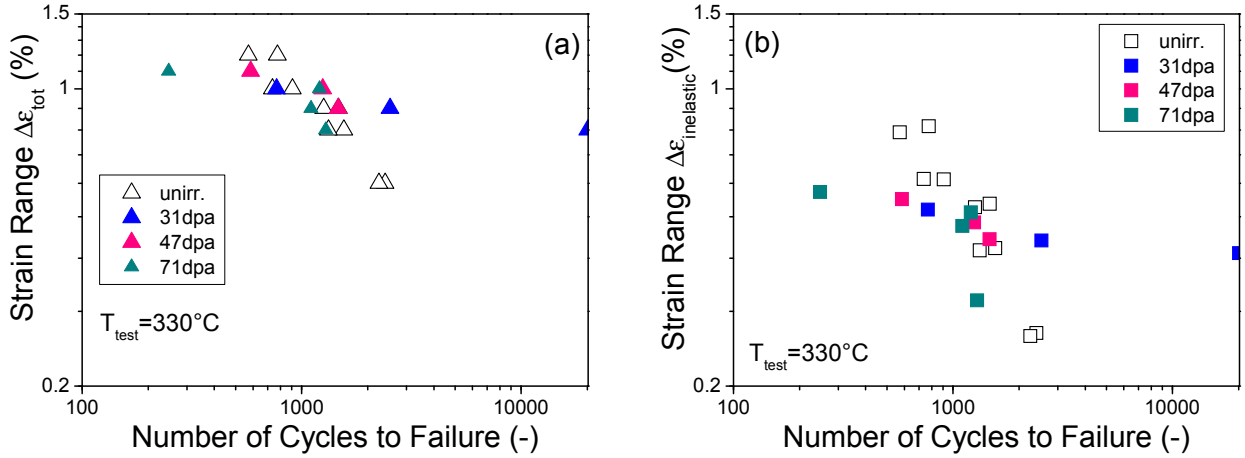


Fig. 1: Fatigue lifetime of EUROFER 97 (980°C/0.5h + 760°C/1.5h) vs. a) total strain range and b) inelastic strain range.

Fig. 2 shows the fatigue behaviour of pre-irradiation heat treated EUROFER97 HT (1040 °C/0.5 h + 760°C/1.5 h) steel in the unirradiated condition and after neutron irradiation up to 70 dpa at 330 - 337 °C. The neutron irradiation has qualitatively different influence trends for 47 and 70 dpa specimens for adequate total strain ranges in Fig. 2a. The 47 dpa irradiated specimens show if any only slight decreases of the lifetime in comparison to the unirradiated state. The 70 dpa irradiated specimens show in contrast an increase of the lifetime for adequate total strain amplitudes which is more pronounced for low strain amplitudes. In terms of the adequate inelastic strain amplitudes, see Fig. 2b, the 47 dpa specimens show clear decrease of the lifetime compared to the unirradiated state, whereas the lifetime of the 70 dpa specimens remains nearly unchanged. The apparent increase of the lifetime for 70 dpa irradiated specimens in Fig. 2a is thus mainly related to the irradiation induced strong material hardening.

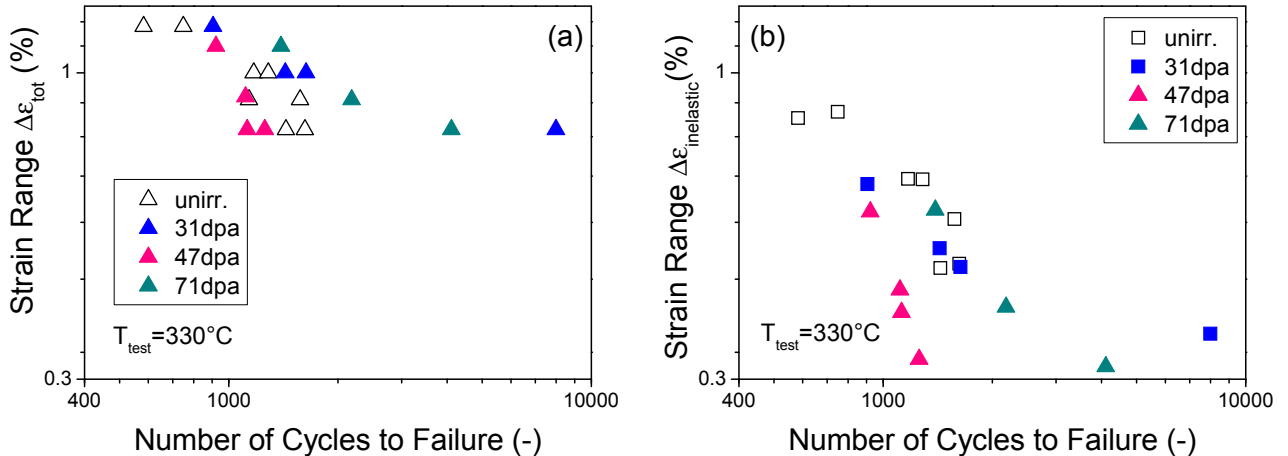


Fig. 2: Fatigue lifetime of EUROFER97 HT (1040°C/0.5h + 760°C/1.5h) vs. a) total strain range and b) inelastic strain range.

Fig. 3 shows the fatigue behaviour of F82H-mod. (1040 °C/38 min + 750 °C/2 h) steel in the unirradiated condition and after neutron irradiation up to 47 dpa at 330 - 337 °C. The neutron irradiation to 47 dpa leads to the increase of the lifetime in comparison with unirradiated state for adequate total strain amplitudes. For adequate inelastic strain amplitudes, however, the lifetime increase is observed for the inelastic strain ranges above 0.57% only. For low inelastic strain ranges the lifetime remains nearly unchanged in comparison to the unirradiated state.

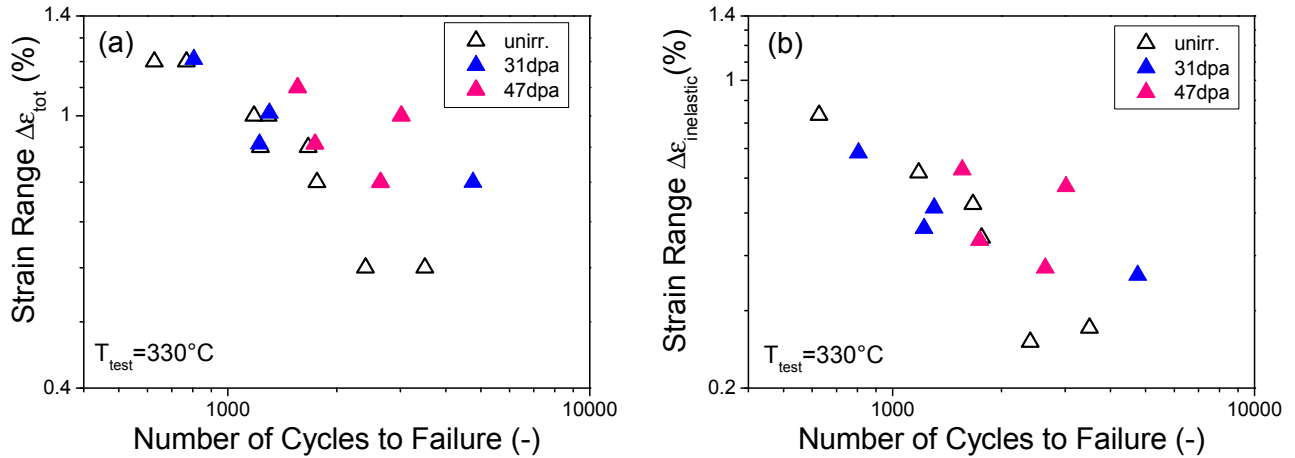


Fig. 3: Fatigue lifetime of F82H-mod. (1040°C/38min + 750°C/2h) vs. a) total strain range and b) inelastic strain range.

Summary and outlook

The influence of the neutron irradiation on fatigue behaviour was determined for EUROFER 97 (980 °C/0.5 h + 760 °C/1.5 h), EUROFER 97 HT (1040 °C/0.5 h + 760 °C/1.5 h) and F82H-mod. (1040 °C/38 min + 750 °C/2 h) steels for total strain ranges between 0.8 and 1.1%. The comparison with the corresponding results in the reference unirradiated state has been performed both for the adequate total and inelastic strain amplitude. The limited number of available irradiated specimens does not allow detailed statistical analysis.

Fractographic and microstructural investigations should shed more light on the fatigue behaviour of the irradiated specimens. The state of the specimen surface quality and its possibly different influences on the fatigue behaviour in the unirradiated and irradiated conditions have to be also addressed.

The LCF testing of the remaining specimens will be finished in the course of 2010. Tensile testing of the mini-specimens machined from the diffusion welded EUROFER mock-up with cooling channels will be performed.

Staff:

U. Bürkle
E. Gaganidze
M. Klotz
C. Petersen

Literature:

- [1] E. Gaganidze, C. Petersen, E. Materna-Morris, C. Dethloff, O. J. Weiß, J. Aktaa, A. Povstyanko, A. Fedoseev, O. Makarov, V. Prokhorov, Mechanical properties and TEM examination of RAFM steels irradiated up to 70 dpa at BOR-60, Proceedings of the 14th International conference on Fusion Reactor Materials, September 6-11, 2009, Sapporo, Japan
- [2] J. Aktaa, C. Petersen, Modeling the Constitutive Behavior of RAFM steels under Irradiation Conditions, Proceedings of the 14th International conference on Fusion Reactor Materials, September 6-11, 2009, Sapporo, Japan

Acknowledgement

This work, supported by the European Communities under the contract of Association between EURATOM and Karlsruhe Institute of Technology, was carried out within the framework of the European Fusion Development Agreement. The views and opinions expressed herein do not necessarily reflect those of the European Commission.

Creep-fatigue Lifetime Prediction Rules for Irradiated EUROFER (TW2-TTMS-005b D 4)

Objectives

The aims of this task are the modification of the lifetime prediction model developed in TW2-TTMS-005a D4 for RAFM steels under creep fatigue conditions taking into account the irradiation influence and the verification of the modified model by applying it to EUROFER 97 in the post-irradiated state.

Task current status

Within the reporting time period the coupled viscoplastic deformation damage model modified taking into account the irradiation induced hardening and its recovery due to inelastic deformation and/or high temperature annealing is applied to describe the behaviour of the RAFM steels, EUROFER 97 and F82H mod, observed in post irradiation examinations of the irradiation programs ARBOR 1 and ARBOR 2. Thereby tensile and low cycle fatigue tests are considered determining the material and temperature dependent parameters of the model and verifying its prediction capability.

A precondition for the application of the model is that sufficient data are available for the determination of the model parameters. In former applications on the RAFM steels EUROFER 97 and F82H mod the major parts of the parameters, particularly those relevant for describing the material behaviour in the un-irradiated state, were identified for different temperatures [1]. In addition the parameters required for describing the irradiation induced hardening were determined for EUROFER 97 at selected temperatures assuming that the irradiation induced hardening is dominated by one obstacle type [2]. With the same assumption the application is extended to F82H mod in the irradiated state considering data obtained from post irradiation examinations performed within the irradiation programmes ARBOR I and II as well as data from the literature and determining the parameters for describing the irradiation induced hardening at temperatures in the range 300 °C-350 °C [3, 4]. With these parameters values fairly good descriptions are obtained for the irradiation hardening dependence on the irradiation dose as well as for the decrease of the irradiation induced hardening due to inelastic deformation (see Figure 1 and Figure 2, respectively).

The model application is expanded by considering the LCF tests performed on irradiated EUROFER 97 [3, 4]. Figure 3 shows a comparison between the model predictions and the experimental results. For discussion the model predictions for the fatigue lifetimes of the unirradiated EUROFER 97 at the same temperature are illustrated in addition. It can be recognized that at high strain ranges a decrease of the fatigue lifetime due to irradiation is expected by the model. This is mainly attributed to the higher stresses resulting from the irradiation induced hardening which are that high that the lower inelastic strain within a cycle and thus its reduced influence on the fatigue damage are compensated. With lower strain ranges the inelastic strain within a cycle is strongly reduced and even vanishes resulting in fatigue lifetimes higher than those of the un-irradiated material (see figure 3) which tends to infinity due to the lack of damage evolution [3, 4]. In addition, it can be recognized in figure 3 that the predicted influence of irradiation on the LCF lifetime saturates toward higher irradiation doses (the calculated curves for irradiation doses higher than 31 dpa lie very close to each other, see figure 3). The experimental LCF lifetimes verify the model predictions whereas except for one data point only the experimentally observed lifetimes are within a range of factor of two in comparison to those predicted by the model (see figure 3).

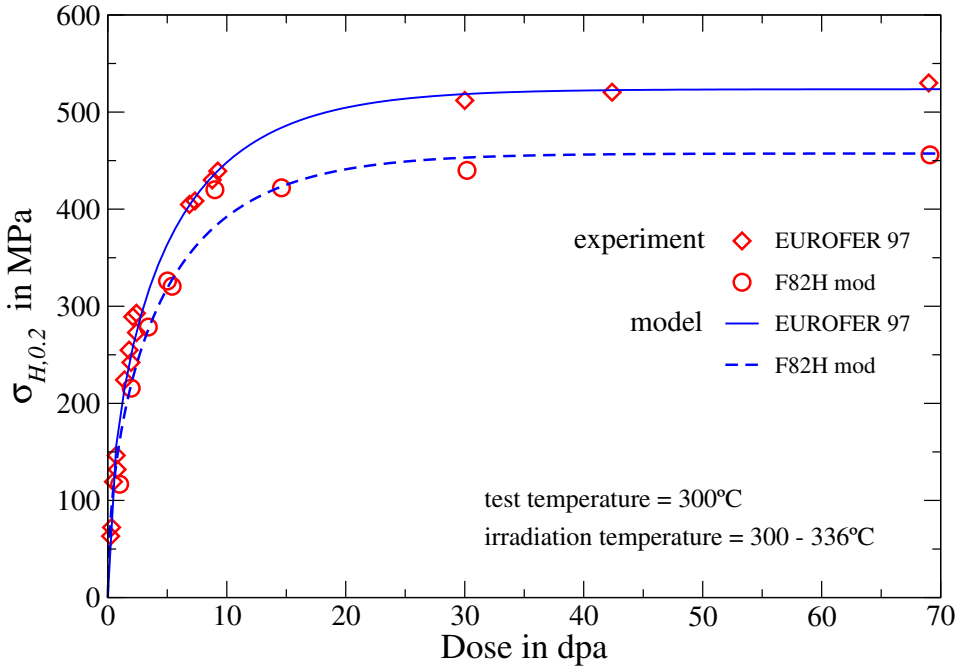


Fig. 1: Irradiation induced hardening as a function on irradiation dose, comparison between experimental data (markers) and model description (solid line) [2, 3].

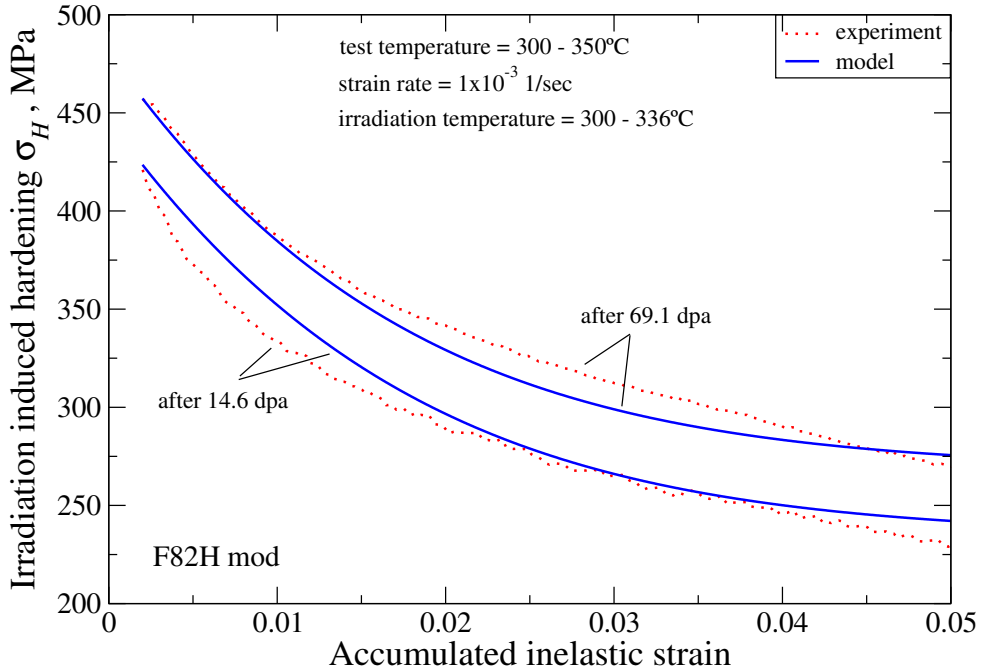


Fig. 2: Influence of inelastic deformation on irradiation induced hardening of F82H mod; comparison between experimental data (dotted lines) and model description (solid lines) [3, 4].

Conclusions

The model developed provides a powerful tool for the prediction of the constitutive deformation damage behaviour of RAFM steels under creep-fatigue and high dose irradiation conditions. It allows fairly good description of the mechanical behaviour of EUROFER 97 and F82H mod observed in post irradiation examinations. Thereby further model parameters for F82H mod could be determined particularly those required for describing its irradiation induced hardening. Applying the model to predict the low cycle fatigue behaviour of irradiated EUROFER 97 the negative influence of irradiation on the fatigue lifetime at high strain ranges could be fairly well reproduced. At low strain ranges the model predicts higher fatigue life-

times and even endurance for irradiated EUROFER 97 which however is not yet verified by the experiments.

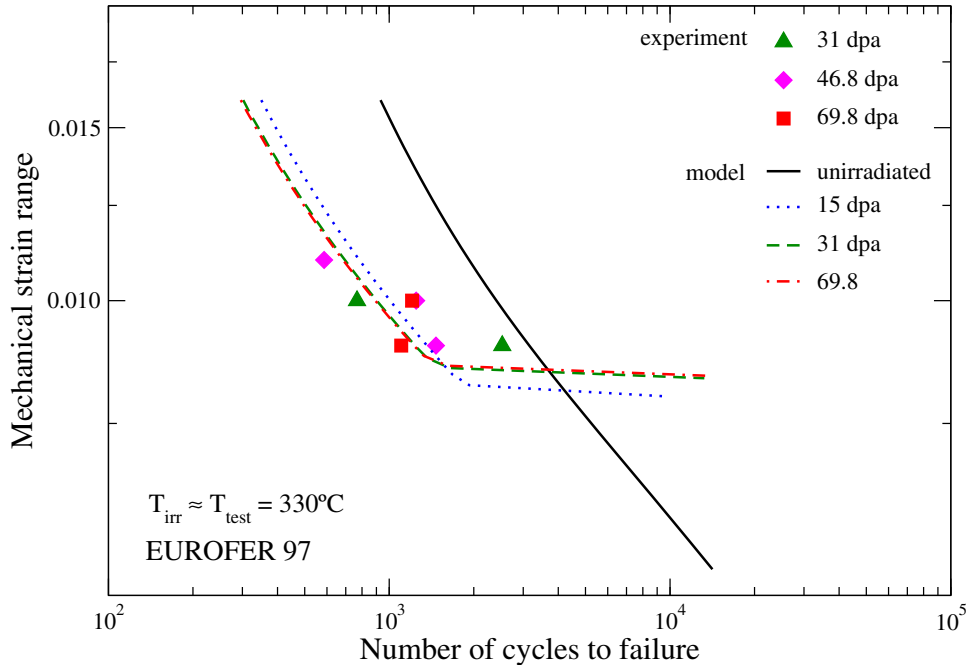


Fig. 3: Influence of high dose irradiation on the low cycle fatigue of EUROFER 97; comparison between experimental data (makers) and model prediction (lines) [3, 4].

Staff:

J. Aktaa

Literature:

- [1] J. Aktaa and R. Schmitt, Fusion Engineering and Design, 81 (2006) 2221-2231.
- [2] J. Aktaa and C. Petersen: "Modeling the influence of high dose irradiation on the deformation and damage behavior of RAFM steels under low cycle fatigue conditions", Journal of Nuclear Materials 389 (2009) 432-435.
- [3] J. Aktaa and C. Petersen: "Modeling the constitutive behavior of RAFM steels under irradiation conditions", ICFRM-14, Sapporo, Japan 2009.
- [4] J. Aktaa and C. Petersen: "Deformation and lifetime prediction model for RAFM steels under creep-fatigue and high dose irradiation conditions", FZKA 7451, Forschungszentrum Karlsruhe, 2009.

Acknowledgement

This work, supported by the European Communities under the contract of Association between EURATOM and Karlsruhe Institute of Technology, was carried out within the framework of the European Fusion Development Agreement. The views and opinions expressed herein do not necessarily reflect those of the European Commission.

Quantitative TEM & SEM Investigation of Irradiated Specimens from SPICE (HFR) and ARBOR 1 (BOR-60) (WP08-09-MAT-REMEV, Activity 5)

Objectives

The current task aims at analysis of neutron irradiation induced evolution of microstructure in a RAFM steel EUROFER 97 addressing (a) irradiation dose dependence of *sizes* and *volume densities* of radiation defects (e.g. defect clusters, dislocation loops, precipitates); (b) neutron fluence rate dependence of *sizes* and *volume densities* of radiation defects. The long term goal is the correlation of the neutron irradiation changes in the microstructure to the changes in the mechanical properties as well as development of phenomenological model for description of evolution of radiation defects in RAFM steels. The specimens to be studied in this task stem from SPICE (15 dpa, HFR, NRG, Petten), WTZ (15 dpa, Bor-60, JSC "SSC RIAR", Dimitrovgrad) and ARBOR 1 (32 dpa, Bor-60, JSC "SSC RIAR", Dimitrovgrad) irradiation programmes.

Task Current Status

Quantitative analysis of the microstructure of RAFM steel specimens in the reference unirradiated state has been performed with a high resolution FEI Tecnai G² F20 X-TWIN TEM installed in the hot cells of FML. Compositional analysis of precipitates has been performed with EFTEM, EELS and EDX techniques.

Fig. 1a) shows a BF TEM image of ADS3, a EUROFER 97 based model alloy doped with 83 wppm ¹⁰B. Several precipitates of about one hundred nm size are visible. The EFTEM elemental map in Fig. 1b) reveals that they consist predominantly of Cr and Fe (and also carbon, not shown). Regarding the mechanical properties it is important to know if boron is homogeneously distributed or located at grain boundaries or in precipitates. Because the boron content is 10 times lower than the detectable limit of about 0.5 at-%, no signal can be seen in the EFTEM map in Fig. 1c). However, Auger analysis revealed that there are a few but large precipitates with high boron and nitrogen content. Indeed EFTEM analysis of a larger specimen area confirmed the presence of a few BN-containing precipitates exemplarily shown in Fig. 2.

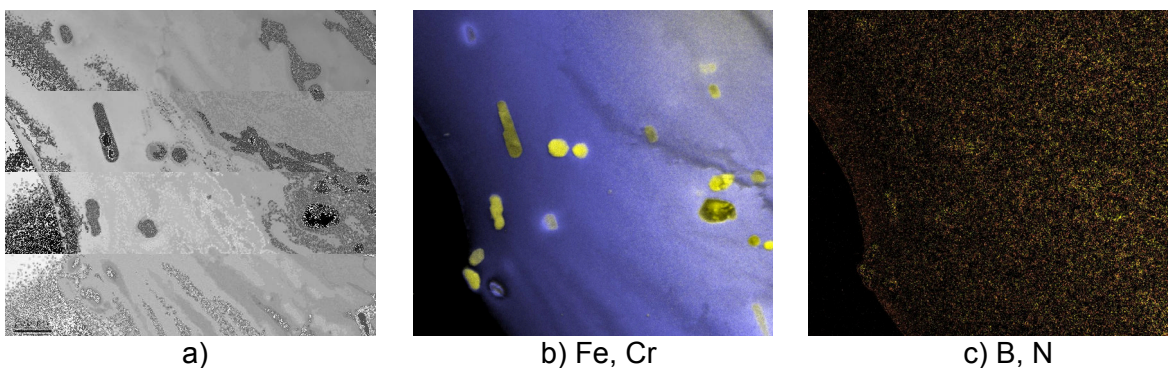


Fig. 1: a) BF TEM image of ADS3 region with several precipitates.
b) Colored overlay of iron and chromium EFTEM elemental maps taken from the same region as a) Fe is displayed in blue and Cr in yellow.
c) Overlay of boron and nitrogen elemental maps. Since the B and N concentrations are below the detectable limit, the picture shows only noise.

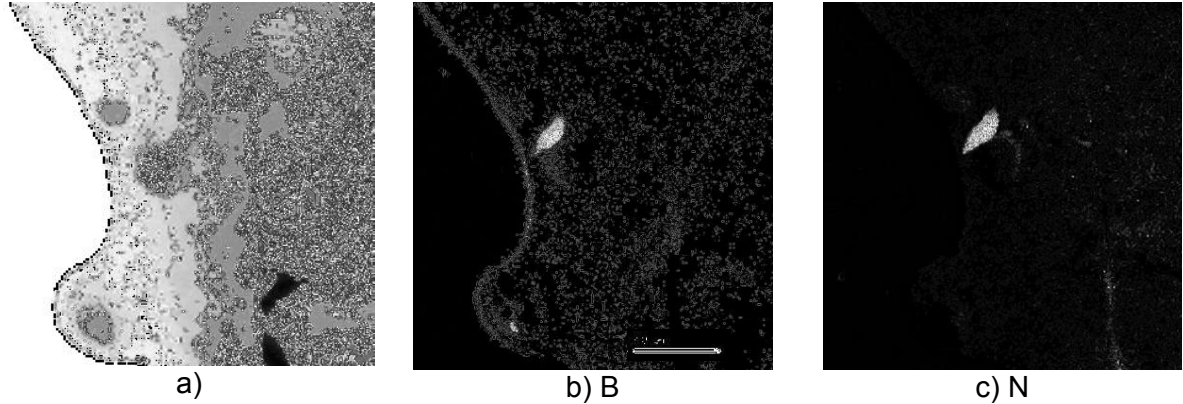


Fig. 2: a) BF TEM image of ADS3.
b), c) Elemental maps of boron and nitrogen respectively.
The EFTEM analysis reveals the presence of a BN-precipitate inside a grain.

By using EELS in the STEM mode it was possible to quantify the boron and nitrogen densities of the precipitate in Fig. 2a) & b), yielding 21.6 and 22.2 nm^{-3} for B and N, respectively. After estimating the volume of the BN precipitate and taking into account the specimen boron content it became clear, that in the investigated specimen section ($1.75 \times 1.75 \mu\text{m}^2$) the most of ^{10}B atoms are located in a single BN precipitate.

For the modeling of the nucleation and growth of He-bubbles in the boron doped steels, quantitative assessment of different microstructural sink defects (e.g. line dislocations, grain boundaries) is required. The line dislocations were made visible by tilting the ADS3 sample to a low-index zone-axis diffraction condition. Subsequently detailed pictures of the dislocation structure were taken and the sample thickness was measured by CBED. Finally the pictures were analyzed using an overlaid grid, counting the intersections with dislocations as displayed in Fig. 3. Eight detailed images from two different grains were analyzed, yielding a dislocation density ρ of $1.3 \times 10^{14} \text{ m}^{-2}$.

Within a HRJRG-13 project a phenomenological model is developed to describe helium cluster/bubble growth kinetics under irradiation. The evolution of the helium clusters with irradiation time is described by using the Fokker-Planck approach to the rate theory for clusterization. The calculation of the cluster size dependent kinetic coefficients was performed with the helium diffusion coefficient as free parameter. Assuming a homogeneous nucleation the size distributions of helium clusters were obtained by numerical solution of the Fokker-Planck equation implemented in a FORTRAN code. Fig. 4 shows the evolution of the helium clusters in the 83 wppm ^{10}B doped alloy with irradiation time up to the end of SPICE experiment ($6.67 \times 10^7 \text{ s}$). Model calculation is done with dpa and helium production rates characteristic for the SPICE experiment yielding a total amount of 432 appm helium already after 10^7 s . A simulated final cluster size distribution obtained with a diffusivity of $4.32 \times 10^{-12} \text{ cm}^2/\text{s}$ is peaked at a cluster size of 410 helium atoms corresponding to a bubble size of 2.1 nm which is in a good qualitative agreement with microstructural observations.

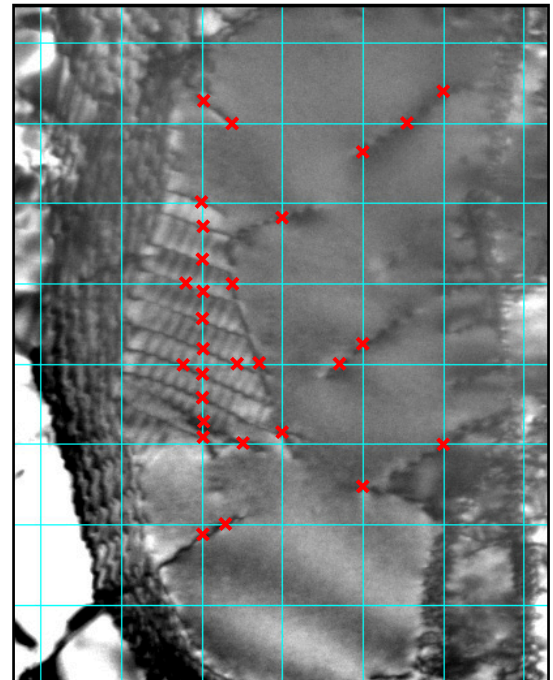


Fig. 3: Method of intersecting grid: A 100 nm grid with random offset is overlaid the TEM image and the intersections with dislocations are counted.

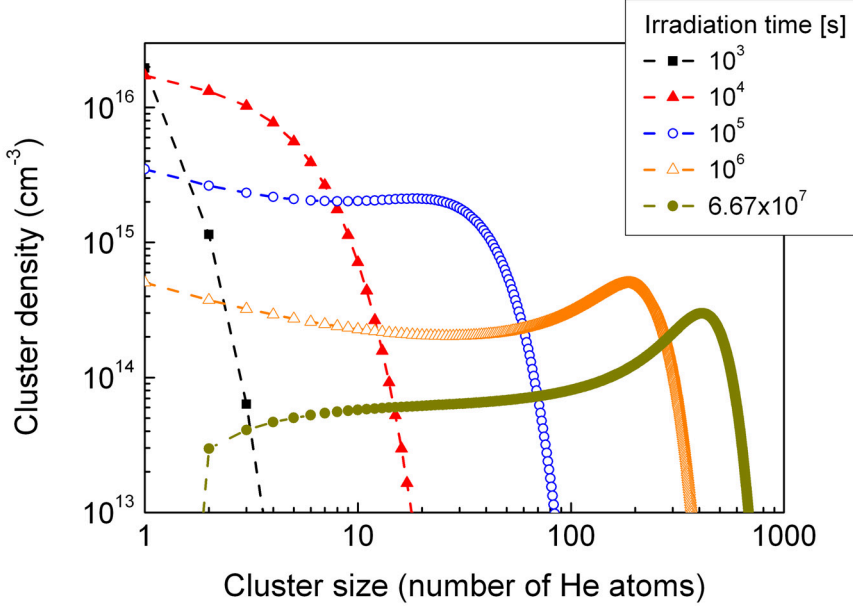


Fig. 4: Evolution of helium clusters with irradiation time in 83 wppm ^{10}B doped model alloy. Model calculation is done with dpa and helium production rates characteristic for the SPICE irradiation experiment.

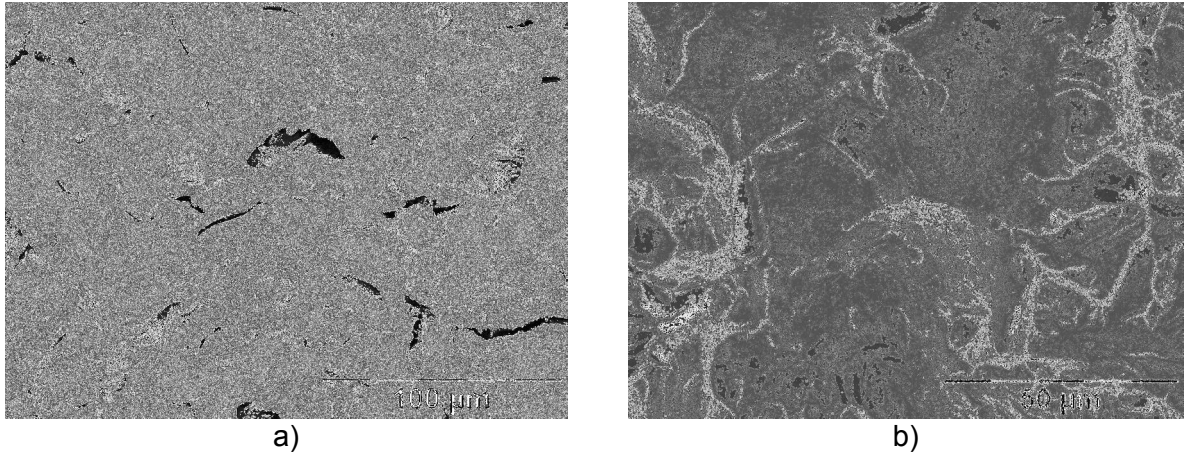


Fig. 5: SEM images of irradiated and fractured ADS3 charpy specimens
a) Typical quasi-cleavage fracture,
b) Evidence for intergranular fracture.

Conclusion and Outlook

Qualitative and quantitative analysis of the microstructure of unirradiated RAFM steel specimens has been performed. It was shown that in a few cases the bulk-concentration of boron in ADS3 is reduced due to the presence of large BN precipitates. The fracture surface of irradiated samples shows typical quasi-cleavage fracture like in Fig. 5a). Since only a single evidence for intergranular fracture like in Fig. 5b) could be found, it can be concluded so far, that the BN precipitates are not preferentially located at grain boundaries.

The concentration of solved boron is too low to be detected by EFTEM analysis. Irradiated TEM samples of ADS3 will be prepared to check the spatial distribution of He-bubbles. Also bubble size and distribution will be quantified to support the model describing nucleation and growth of He-clusters.

Irradiated EUROFER 97 specimens will be prepared and characterized with respect to sizes and volume densities of radiation induced defects (e.g. defect clusters, dislocation loops, precipitates).

Staff:

C. Dethloff
E. Gaganidze
O. Weiß

Literature:

[1] E. Gaganidze, C. Petersen, E. Materna-Morris, C. Dethloff, O. J. Weiß, J. Aktaa, A. Povstyanko, A. Fedoseev, O. Makarov, V. Prokhorov, Proceedings of the 14th International Conference on Fusion Reactor Materials, September 7-12, 2009, Sapporo, Japan

Acknowledgement

This work, supported by the European Communities under the contract of Association between EURATOM and Karlsruhe Institute of Technology, was carried out within the framework of the European Fusion Development Agreement. The views and opinions expressed herein do not necessarily reflect those of the European Commission.

Qualification of Welded Joints by LCF Testing (TW6-TTMS-004 D 3)

Overview

According to the current design for the European Helium Cooled Pebble Bed (HCPB) ITER Test Blanket Module (TBM) there are basically six subcomponents which have to be fabricated and assembled: first wall, caps, stiffening grid, breeding units, back plates/manifolds, and attachment system. The main technologies needed for blanket fabrication are joining of parts (particularly production of plates with internal cooling channels and welding at inaccessible component areas) and applying suitable post weld heat treatments. Both steps together are the key technologies that determine the mechanical strength of the blanket, the ductile-to-brittle transition temperature (DBTT) which is important under neutron irradiation, and the potential for a compact design. While it is certain that the structural material will be EUROFER, most joining technologies and/or procedures have still to be developed, adapted, or qualified.

The designated welding techniques may be divided into two groups: diffusion or solid phase welding, and fusion welding, whereas the first is either performed in a hot isostatic press (HIP) or in a uniaxial hydraulic press, both after different specific joint preparations. Fusion welding may be performed either by electron beam (EB), laser beam, hybrid MIG/laser, or by tungsten inert gas (gas tungsten arc) welding with filler wire.

The general objective is to support the fabrication development in the blanket areas and to improve the reliability of the materials and joints according to the TBM design. Even though welds play an important (if not dominant) role for the mechanical behaviour of TBMs, fatigue test results of typical joints have not been reported so far. But due to the pulsed operation of tokamaks, a comprising characterisation of the EUROFER alloy including welded joints by low-cycle fatigue (LCF) tests would be highly desirable.

The present work contributes at least to the basic LCF characterization of the base material EUROFER 97 and its TIG welded joints. However, further and more comprising studies are still necessary for the prediction of the long-term behaviour of TBM components during pulsed thermo-mechanical operation modes.

Initial Status

For the investigations on base material the new EUROFER 97-2 heat 993393 (14 mm plate) was used while a TIG weld was fabricated of the EUROFER 97 heat 83698 (also a 14 mm plate). Preparation, orientation, and TIG welding was performed for the 10 mm plate. That is, the weld was produced in half V geometry with a root distance of 1 mm. The 1 mm filler wire consisted of heat D83350.

The LCF specimen gauge dimensions are 2 mm in diameter with a length of 7.6 mm. The fabrication, however, was performed in two steps. First, cylindrical parts with the correct overall length (27 mm) were produced from the base material and from the weld. The position relative to the weld is shown in Fig. 1, i.e. for the present case, the heat affected zone was positioned at the specimen's center. In a second step the final shape was produced by turning.

It is well known that LCF test results are rather sensitive to the specimen surface. This is especially true for miniaturized samples used for the present investigation. Therefore, all surfaces have been treated as outlined in Fig. 2 by grinding and finally electro-chemical polishing.

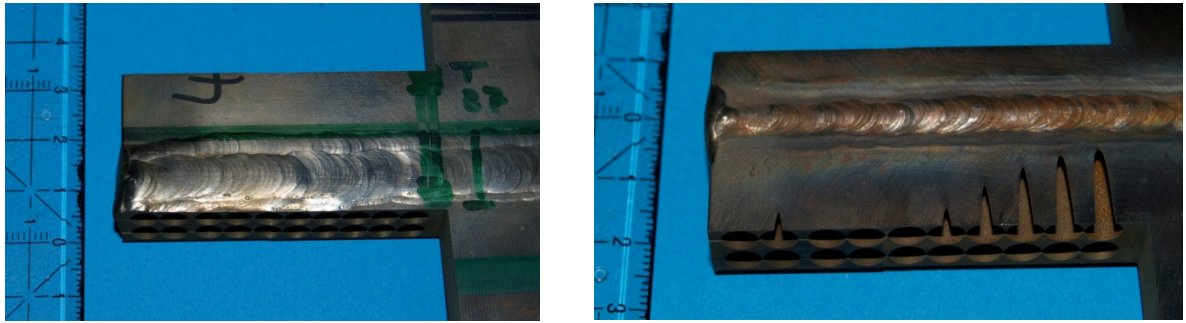


Fig. 1: First step in LCF specimen fabrication. Left: view from top. Right: bottom view.

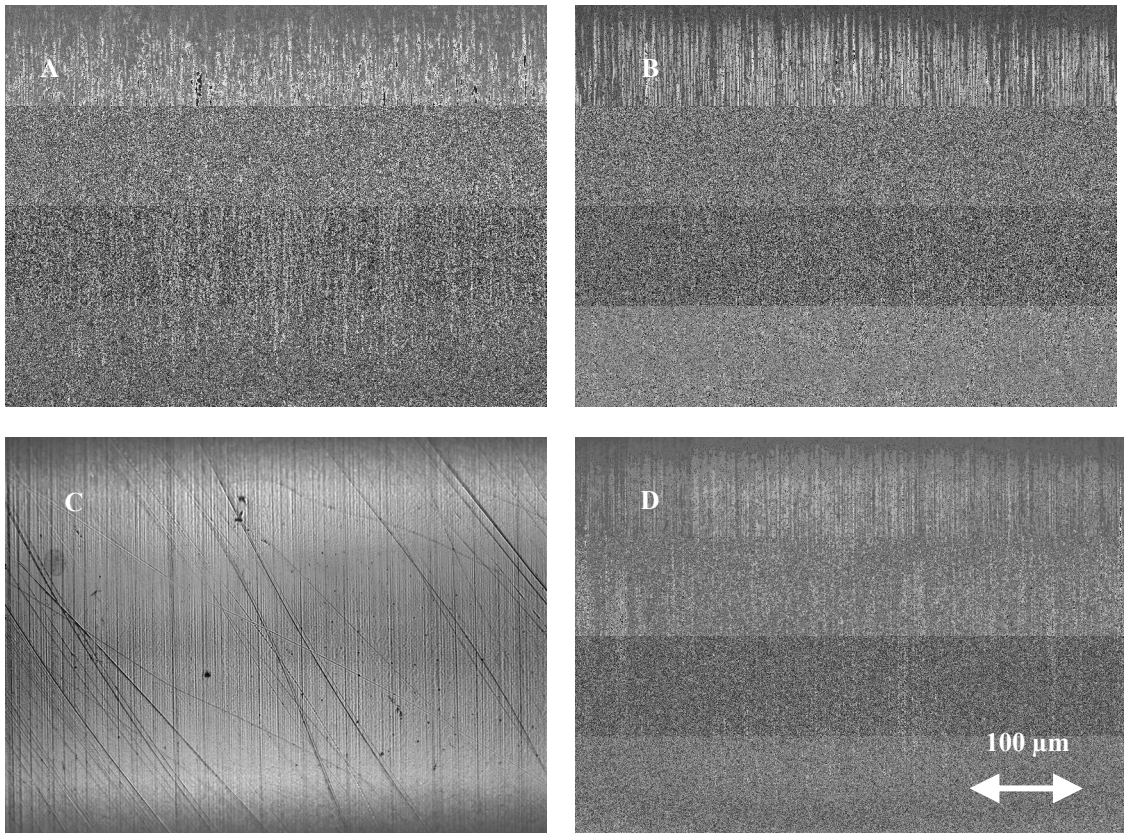


Fig. 2: Specimen surface after different treatments as observed by microscope. (A) After turning. (B) After grinding with diamond paste of 15 µm grit. (C) After grinding with diamond pastes of 15 µm and 6 µm grit. (D) After grinding with diamond pastes of 15 µm and 6 µm grit followed by electro-chemical polishing [2].

Table 1: Results of the LCF tests ($T=550^{\circ}\text{C}$).

Sample	Total strain	Cycles to failure
B	1%	4800
D	0.9%	3100
A	0.8%	3277
E	0.7%	6435
G	0.6%	9258
C	0.5%	19231
F	0.45%	62000

Strain controlled low-cycle fatigue tests have been performed in the strain interval from 0.4% up to 1% at 550 °C (the maximum operation temperature of EUROFER). The softening with increasing cycles can be seen quite clearly. The hysteresis curves are also getting wider which indicates the increase in plastic strain. It is remarkable that the softening behavior of all specimens is similar, independent of the strain amplitude. After only about 100 cycles the softening curves are practically the same.

The softening is also extensive which is reflected by the fact that the maximum stress drops down to about 170 MPa after 10000 cycles. The initial stresses vary between 250 and 300

MPa. The main results, however, are the cycles to failure for different strain amplitudes. The results with the base material are compiled in Table 1.

Progress

Welded specimens have been tested at 550 °C in two different post welding conditions. One was the condition without further heat treatment, the other after tempering at 750 °C for two hours.

Unfortunately most specimens without PWHT failed by necking in the weld zone (see Fig. 3). This affected the strain measurement which, in turn, led to invalid results. A typical example is specimen 0972. Therefore, the test series for specimens without PWHT was cancelled after 6 LCF tests and only 2 suitable results that are listed in Table 2.

Table 2: Results of the LCF tests with WIG welded joints without PWHT.

Sample	Total strain	Cycles to failure
0972	0.8%	n/a
1002	0.6%	4457
0973	0.5%	8835

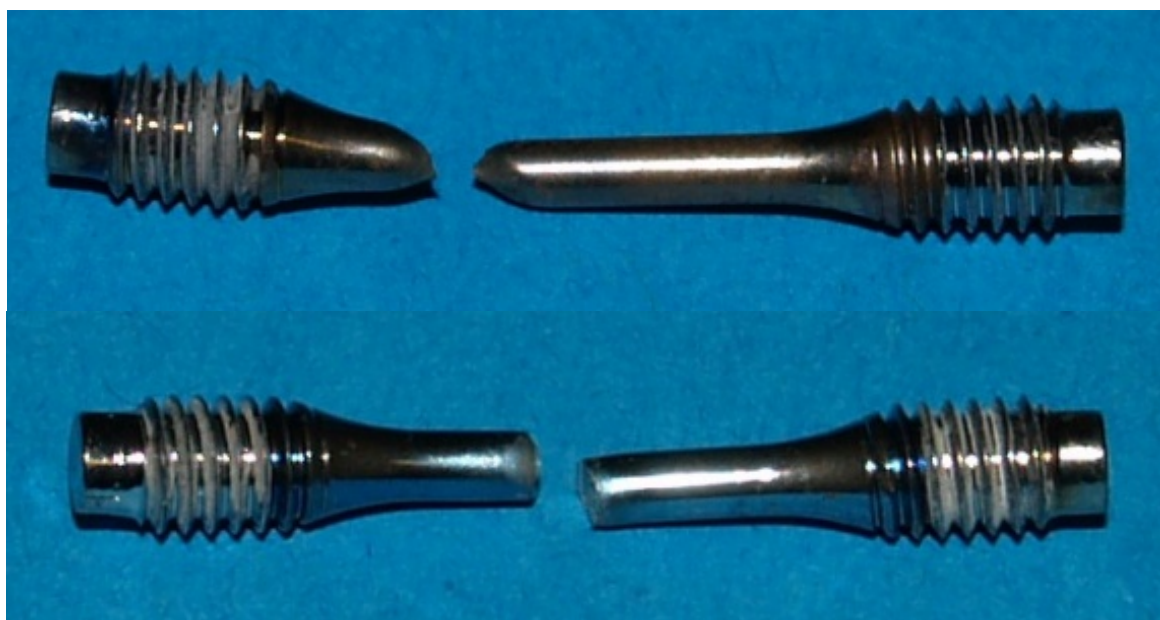


Fig. 3: Upper photograph: Distinct necking was observed for many cases of TIG welded specimens without PWHT. Lower image: Typical fracture of TIG welded specimens after PWHT of 750 °C/2 h. It is comparable to the fracturing of the base material specimens.

The tempered specimens, however, showed a fracture behavior similar to that of the base material. That is, distinct necking was never observed. But in some cases the fracture appeared near the strain measurement clip which corrupted the test results. Table 3 shows the valid test data.

Table 3: Results of the LCF tests with WIG welded joints after PWHT of 750 °C/2 h.

Sample	Total strain	Cycles to failure
0968	0.9%	578
0970	0.8%	3129
0971	0.6%	4463
0969	0.5%	17480

Compared to the base material tests, scattering in the test results of welded specimens is clearly higher. Figure 4 shows the cycles to failure for all tests with welded specimens.

It is possible to some degree to approximate the results of the tempered specimens (PWHT at 750 °C/2 h) by a straight line. For the results with specimens without a PWHT, however, just a trend to lower cycles to failure can be derived.

The softening behaviour is plotted in Fig. 5 for the tempered specimens. It is evident that the softening behavior of all specimens is similar. Independent of the strain amplitude after about 100 cycles the softening curves are nearly identical. The curves of the specimens without a PWHT are not shown here, but they are also similar and only slightly higher than the results of the tempered specimens.

The maximum stress drops down to a value of about 180 MPa after 10000 cycles. This is accompanied by a significant amount of plastic strain which is plotted in the lower diagram of Fig. 5.

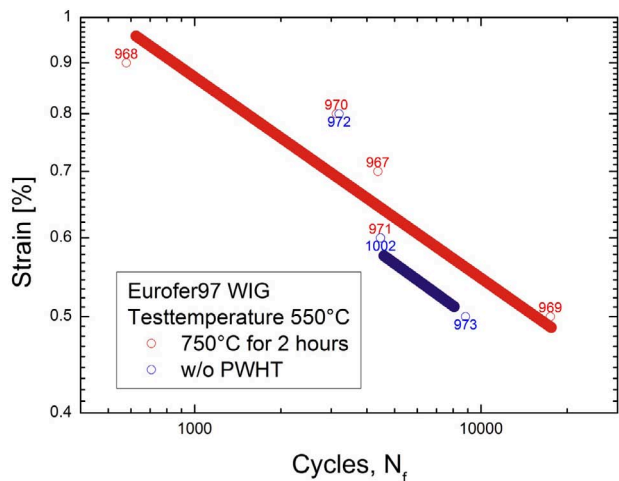


Fig. 4: Cycles to failure at 550 °C for different conditions of the TIG welded specimens.

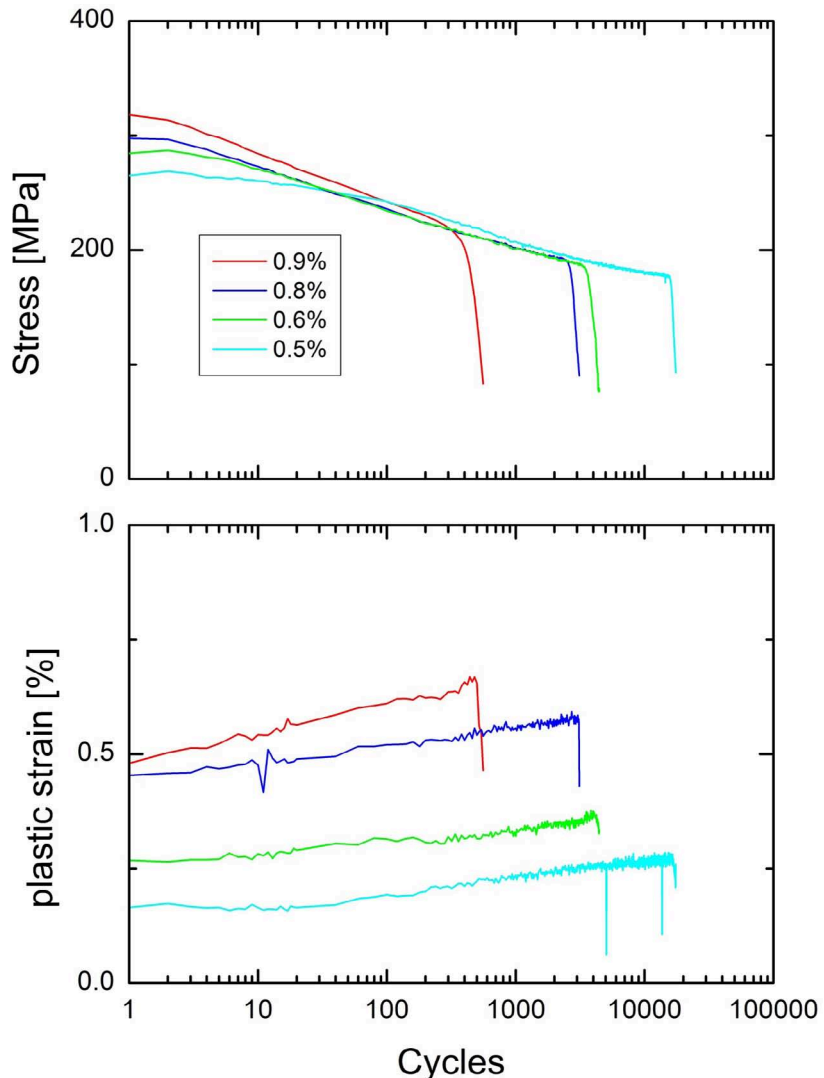


Fig. 5: Upper diagram: The maximum stress per cycle vs. cycle number. Lower diagram: plastic strain vs. cycle number.

Conclusions and Outlook

The aim of this task was to determine the low cycle fatigue behaviour of welded EUROFER joints. Due to availability and technical problems of the testing machine and due to some welding equipment failure it was not possible to include as much different welds as planned. It was also impossible to study an extensive parameter set of post welding heat treatments.

However, the performed tests on TIG welds in two different conditions show clear trends and the results allow drawing some basic conclusions:

- LCF tests on TIG welded specimens without PWHT led to rather high failure rates of the strain measurement which invalidated the tests. This was mainly due to deformation in the vicinity of the strain measurement clips. Therefore, the miniaturized specimens used for the present investigations are clearly not suitable to perform LCF tests on TIG welded joints since the lateral extension of these joints is too large.
- The test results of TIG welded joints after tempering at 750 °C for 2 hours show a broad scattering of the cycles to failure. But a clear tendency to lower cycles to failure compared to the base material results is recognizable (see Fig. 6). This can be explained by the fact that a mere tempering PWHT softens the martensite but does not restore the coarse microstructure of the weld zone.
- The permanent fatigue strength of EUROFER begins approximately at strain amplitudes of about 0.45% with cycles to failure of more than 20,000.
- The initial maximum stress of all specimens (welded and base material) varies between 250 and 300 MPa depending on the strain amplitude. After about 100 cycles, however, the softening behaviour is practically identical for all base material tests and for all welded specimens.
- The softening of the base material is slightly higher than that of the TIG welded specimens. After 10,000 cycles the maximum stress drops down to 170 MPa for the base material and to 180 MPa for the welded specimens.

In summary, the present study shows that the degradation of low-cycle fatigue strength due to TIG welding can be as severe as the shift in DBTT determined by Charpy tests. A full recovery of the microstructure of the welding zone (and, therefore, LCF strength) can only be achieved (if at all) by a two-step PWHT, that is, by an austenitization and quenching, followed by tempering.

Especially for LCF tests with TIG welds, larger specimens are better suited for investigating the failure mechanisms (crack initiation and propagation). Larger specimens would also guarantee a more reliable strain measurement.

Finally, larger specimens would also be useful for a more detailed parameter study on PWHTs and microstructure correlation.

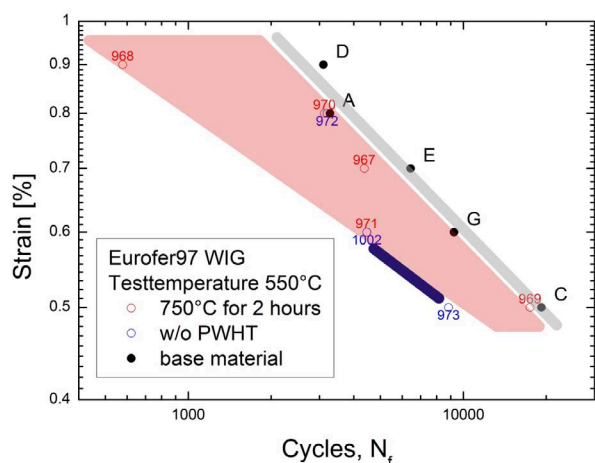


Fig. 6: Comparison of cycles to failure for TIG welded joints and for the base material. The scatter band for the heat treated TIG welded specimens is rather broad – especially at high strain amplitudes.

Staff:

A. Baumgärtner
B. Dafferner
S. Heger
U. Jäntschn
M. Klimenkov
M. Rieth
R. Ziegler
H. Zimmermann

Acknowledgement

This work, supported by the European Communities under the contract of Association between EURATOM and Karlsruhe Institute of Technology, was carried out within the framework of the European Fusion Development Agreement. The views and opinions expressed herein do not necessarily reflect those of the European Commission.

Experimental Determination of the Slip Systems and Dislocation Glide Properties of Pure α -Fe (WP08-09-MAT-REMEV, Activity 4)

Alloyed steel in particular when irradiated can have a very complex mechanical behaviour. In order to develop an understanding of this behaviour and to develop tools for modelling, experimental data is needed. The fundamentals of deformation can be investigated by considering a strongly simplified system. Here α -Fe was used. It has a bcc crystal lattice in which dislocations may glide on different glide planes. Within this project experiments were performed to observe deformation in this metal.

Development and optimization of mechanical experiments and preparation methods for micrometer sized Fe samples

Microcompression tests were performed on micromachined specimens made from high purity (<20 ppm C) α -Fe (alpha aesar, Dillinger Hütte). The samples were produced using a focused ion beam microscope (FIB) where material could be selectively removed by a 30 keV Ga ion beam. The micro columns (figure 1a) were made inside individual grains so that single crystalline samples resulted. The crystal orientation of the columns was determined by electron backscatter diffraction (EBSD). After production, the samples were mechanically tested under compression in a nanoindenter equipped with a flat punch. Load-displacement curves were recorded and the deformed columns were investigated by SEM before and after the tests (figure 1b). FIB machining of α -Fe is not problematic and different ways of machining columns were successfully tested. The preparation route consisted of mechanical polishing, subsequent electropolishing and a 2 h anneal under vacuum at 900 °C which was performed in order to allow for grain growth and to remove preparation defects. Columns with round, square and rectangular cross sections were produced by FIB. Ion milling from the top resulted in columns with small taper angle of a few degrees. By using a lathe like production method where the columns were milled from the side, columns without taper could be made. This was rather time consuming and in most cases tapered columns were used.

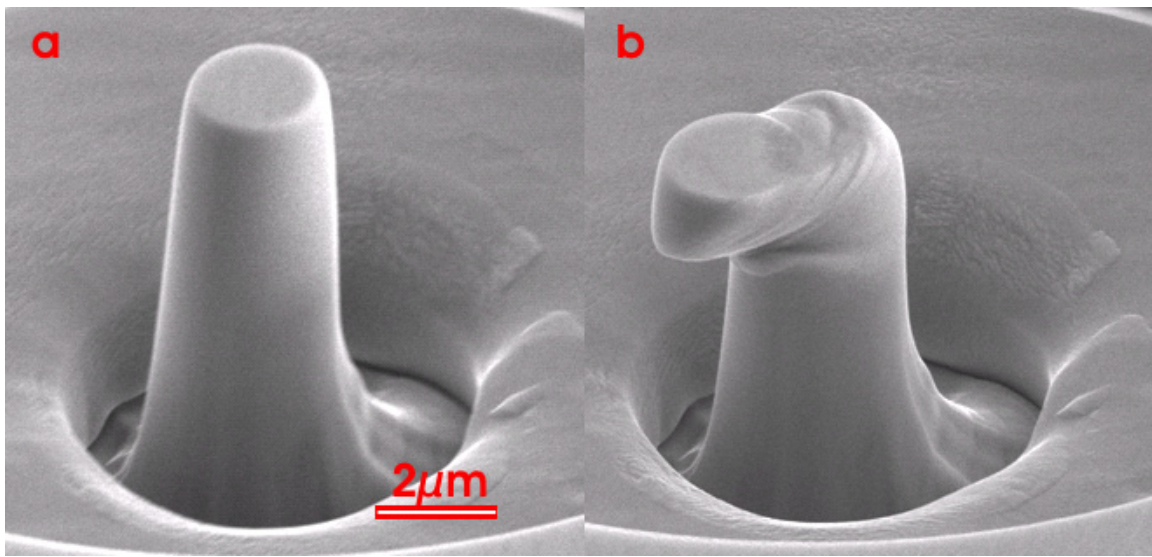


Fig. 1: Micro column machined into a grain of an α -Fe sample. (a) before and (b) after the compression experiment.

Microscopic observation of the plastic flow of Fe micro columns

Columns of different diameters were produced and mechanically tested. Figure 2 shows the size dependent stress strain behaviour. As typically observed in fcc metals, smaller samples show higher stresses and an increasing number of disruptive deformation events. This is often attributed to the statistical nature of deformation.

Although α -Fe has a bcc crystal structure, the shape of the deformed columns was similar to that of columns made from fcc metals. In many cases there were no clearly identifiable slip traces and instead weak and soft distortions (e.g. barrel shaped distortions)

occurred. Such deformations are often explained by dislocation interactions and glide occurring on different slip systems simultaneously. The size dependence of the flow stresses in figure 3 is also in accordance with what is found in fcc metals where the flow stress depends on the column diameter by a power law with an exponent in the range of -0.8 to -0.5. This is in contrast to typical bcc materials where the size dependence is weaker (exponents btw. -0.5 and -0.2) and where deformation is controlled by screw dislocations [1]. This is not surprising given the fact that at room temperature screw dislocations are very mobile in α -Fe.

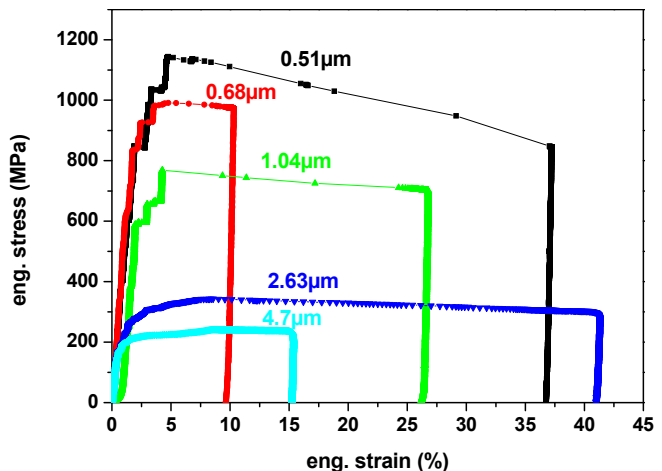


Fig. 2: Stress-strain curves of α -Fe columns.

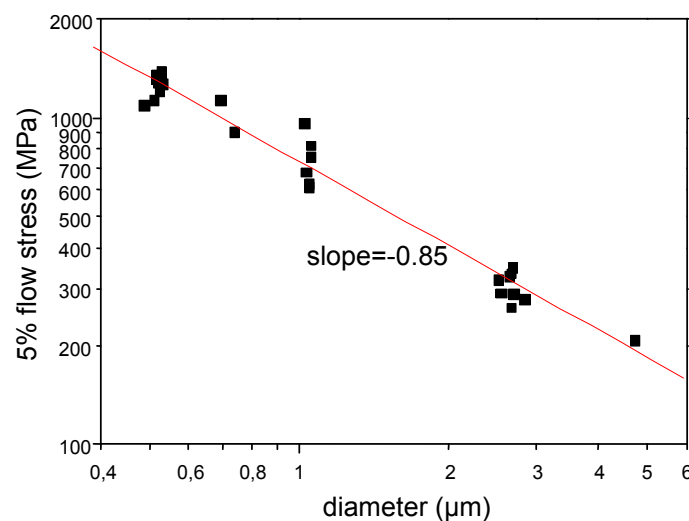


Fig. 3: Size dependence of the flow stress.

Micro columns from α -Fe can be easily tested by microcompression experiments. Although α -Fe is a bcc metal which has different slip systems and fundamental dislocation mechanisms from fcc metals, its size scaling and the deformed shapes are similar. For the tested orientations no particular anisotropies were obvious. Deformation rates were varied by two orders of magnitude and no rate dependence of the flow stress became apparent at RT.

Staff:

D. Kaufmann
R. Mönig
S. Schendel

Literature

[1] A. S. Schneider, D. Kaufmann, B. G. Clark, C. P. Frick, P. A. Gruber, R. Möning, O. Kraft, and E. Arzt, "Correlation between Critical Temperature and Strength of Small-Scale bcc Pillars", *Phys. Rev. Lett.* 103, 105501 (2009)

Acknowledgement

This work, supported by the European Communities under the contract of Association between EURATOM and Karlsruhe Institute of Technology, was carried out within the framework of the European Fusion Development Agreement. The views and opinions expressed herein do not necessarily reflect those of the European Commission.

Define and Perform Accompanying Experiments to D 5 (e.g. creep crack growth at 550 °C) (TW5-TTMS-005 D 6)

Background and Objectives

For TBM's licensing, in order to establish design rules for the materials, joints and specific sub-components, a broad set of R&D activities have been launched within the WP 2002. These activities will continue with emphasis on implementation in DSCD (Demo structural design code) and verification and validation experiments. Additional rules for HT (high temperature) fatigue-creep interaction need to be formulated, in particular for fracture mechanics.

The low ductility of EUROFER (in particular after irradiation) gives very conservative limits for design against fast fracture and local flow localization. Some experiments are required in support of special design code activities that could lower very conservative assumptions in existing frameworks. In addition, development of small scale test techniques in fracture mechanics will continue including transferability of the small size specimen tests to the behaviour of the TBM's sub-components.

The objective of this subtask is to perform long time creep crack growth experiments on EUROFER to determine the da/dt (crack velocity) - C^* (C^* -integral)- behaviour at the temperatures 500 and 550 °C. The results are needed for the determination of material parameters in HT fracture mechanical rules.

Status

The assembling of the experimental set-up has been finished. Preliminary tests with the set-up for the DC potential method were done in order to determine the correct correlation between voltage and crack length in the relevant temperature range. Parallel to these tests, special clip gauges were developed and fabricated to measure the crack opening during the main experiments. In 2009 new specimens with incipient fatigue cracks were fabricated and after removing the side-notches, the main experimental set-up for the long time creep crack growth tests was configured. For that purpose, the rods of two creep testing machines were modified to implement the specimens and the measurement devices, respectively, within the test facilities. To measure the crack opening during the experiments, special developed clip gauges were adapted and configured for the HT application.

Upon completion of the test set-up, which is shown in Fig. 1, the functionality of all electronic measurement devices was checked in pre-tests under different load conditions at 550 °C. Afterwards, the time-consuming tests to determine the suitable load cases for the long term experiments were started. Actually, they are still running.

Conclusion and Outlook

The main experimental set-up for the long time creep crack growth tests was configured and the tests to determine the suitable load cases for the long term experiments were started. After finishing these pre-tests, the main experiments will start.

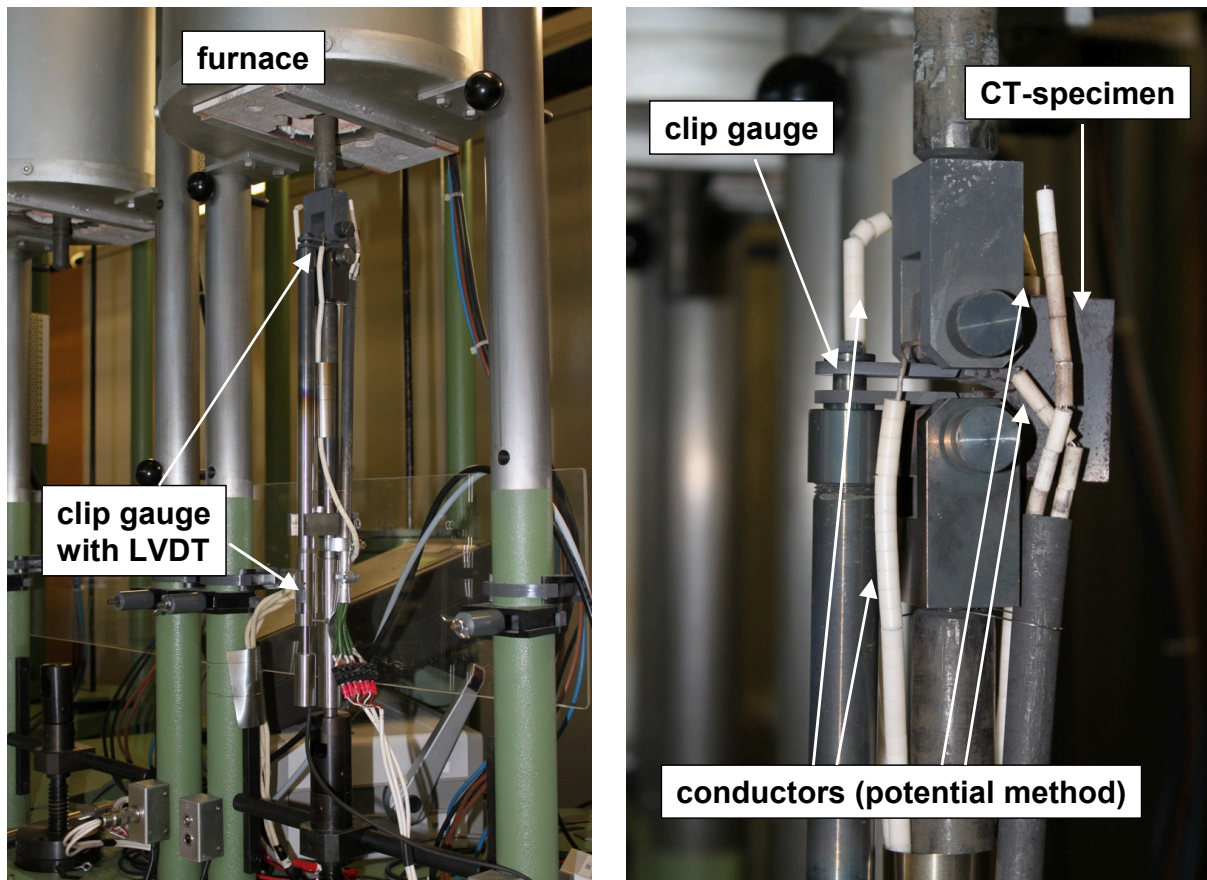


Fig. 1: Complete test set-up for the long time creep crack growth experiments.

Staff:

M. Klotz
St. Knaak
M. Walter

Acknowledgement

This work, supported by the European Communities under the contract of Association between EURATOM and Karlsruhe Institute of Technology, was carried out within the framework of the European Fusion Development Agreement. The views and opinions expressed herein do not necessarily reflect those of the European Commission.

Qualification of NDT (non-destructive testing) for Evaluation of Limits of Detectable Cracks (TW6-TTMS-005 D 5)

Objective

The objectives of this task are to find out an adequate NDT (non-destructive testing) technique for detecting cracks particularly in the welded areas of blanket components built from EUROFER 97 and to realise it with an automated NDT testing procedure.

Status

The assessment of different non-destructive testing techniques within the activities of this task yielded the selection of ultrasonic testing as suitable method for non-destructive inspection of welds in blanket components. Within the reporting time period an automated ultrasonic scanning system with focused immersion transducers was installed. The system, KC 200 by GE Sensing & Inspection Technologies, has an immersion tank with a 3D scanning unit and allows automated ultrasonic inspection on TBM components with large dimensions (90 cm×50 cm×40 cm).

Results

The system was used for to determine the minimum detectable flaw size in different EUROFER 97 welded joints. Therefore EUROFER 97 parts with different shapes and three different welding seam types (diffusion bonding, electron-beam welding and TIG - welding) are produced. The welding seams of these parts were furnished with differently arranged artificially defects, whose size was also varied to determine the minimum detectable flaw size. In essence, the artificially introduced defects were longitudinal and lateral drilled holes with diameters in the range 0.2 mm to 1.0 mm as well as tungsten wires with diameters in the range 0.2 mm to 1.0 mm. To derive the DAC curves (Distance Amplitude Correction) for defects of 0.2 mm and 0.1 mm in size EUROFER 97 samples with appropriate drilled holes at varying depths are additionally prepared.

The ultrasonic testing was performed with straight and angle beam examinations by longitudinal and transverse waves from sensors of different resolution. The measurement results showed that in welding seems of typical blanket structures flaws of 0.2 mm in size are detectable with automated immersion ultrasonic testing. In diffusion bonded seems the limit of detectable flaw size can be even 0.1 mm provided the distance between the surface and the diffusion bonded seem is less than 5 mm.

Staff:

T. Martin
S. Knaak
J. Aktaa

Acknowledgement

This work, supported by the European Communities under the contract of Association between EURATOM and Karlsruhe Institute of Technology, was carried out within the framework of the European Fusion Development Agreement. The views and opinions expressed herein do not necessarily reflect those of the European Commission.

SSTT: Continuation of the Modeling of the Ductile Region – Development of Models for Transferability of Small Size Specimens to Standard Size and FW Applications (TW6-TTMS-005 D 12)

Objectives

Small specimen testing technology (SSTT) is currently under development for mechanical fracture testing of irradiated RAFM steels. This technology is needed due to the limited irradiation volume provided by IFMIF and other irradiation facilities. The fracture mechanical small testing specimens (pre-cracked KLST) for RAFM steels do not meet the requirements needed for standard tests. Therefore it is necessary to develop a method which allows transferring data from small specimen to standard one. Chosen approach is based on the cohesive zone model used in finite element simulations. The objective is to perform finite element simulations of three point bending tests on small testing specimens and optimize the parameters of cohesive zone model that it will be possible to replicate $J-\Delta a$ data obtained by experiments. Given parameters will be then used for predictions of standard specimen tests.

Task current status

Within the reporting time period finite element calculations with cohesive zone model were performed to simulate the 3 point bending fracture toughness test with KLST specimens made of EUROFER 97 steel. The parameters of cohesive zone model were obtained by an optimization procedure which was based on the fitting of computed force displacement curves to the experimental curve. Better fit was achieved for a linear hardening model for EUROFER 97 with the hardening modulus taken as a fitting parameter and thus considered in the optimization. Simulations with a non-linear hardening model for EUROFER 97 yields results with larger differences to the experimental data. The simulations over predict the value of the J -Integral at the onset of crack propagation (J_{IC}) and consequently later crack initiation in comparison to the experiment is observed. Subsequent crack growth is faster in simulations compared to experimental data. These two effects are contradictory in the used model and therefore cannot be successfully solved within its framework. Also the assumption of a straight crack propagating in symmetry plane seems to be a very significant simplification with respect to the propagation of the real crack. Therefore the quantitative prediction of experimental data is not satisfactory within the given model and geometry.

In order to get more suitable predictions some possible improvements of the simulations are proposed. The investigation of the stress triaxiality influence could be the further step. Stress triaxiality changes along the crack front as well as in the direction of crack propagation [1]. The crack front variation is minimized by side grooving but the variation in propagation direction is still present. The cohesive zone parameters can be closely related to the triaxiality so that consequently the parameters may have different values during crack initiation and crack propagation.

Another important aspect in simulations on KLST specimens is the compliance or violence of small-scale yielding conditions. The equality between the separation energy and the critical value of the J -integral J_{IC} is valid only for such conditions. Therefore the relation between yielding conditions and separation energy could be also investigated.

Used cohesive interface approach works with a priori determined crack path. The presence of cohesive elements changes the mechanical characteristics of the structure at given location before it is influenced by the crack tip [2]. This could be eliminated by increasing the stiffness of cohesive zone elements prior the crack initiation according to the proper stiffness evolution law. Such conditions have to be taken into account if the non symmetrical tilted crack will be simulated. The predefined crack path could not influence the stress-strain behavior of the structure before the crack initiation. Simulation with tilted crack must be performed for whole size structure which increases the computational effort.

The most advanced approach is the application of embedded discontinuity approach, where the cohesive properties are implemented in continuum elements. This approach is able, together with relevant remeshing rules, to simulate the crack growth according to actual global and local loading conditions. In the other hand its application needs high computational efforts.

Staff:

J. Aktaa
F. Siska

Literature:

- [1] C.R. Chen, O. Kolednik, J. Heerens, F.D. Fischer, Engineering Fracture Mechanics 72 (2005), 2072.
- [2] R. de Borst, Engineering Fracture Mechanics 70 (2003), 1743.

Acknowledgement

This work, supported by the European Communities under the contract of Association between EURATOM and Karlsruhe Institute of Technology, was carried out within the framework of the European Fusion Development Agreement. The views and opinions expressed herein do not necessarily reflect those of the European Commission.

Fracture-mechanical Characterization of W-Alloys (W-Ti, W-V, W-Ta) in the Interesting Temperature Window for Fusion Applications (RT-1300 °C) (WP08-09-MAT-WWALLOY, Activity 2)

Objectives

Inherent low fracture toughness of tungsten combined with the high DBTT are major drawbacks for structural application of tungsten alloys. Furthermore, FM properties are expected to exhibit strong anisotropy due to (i) different grain shape/orientation with respect to the rolling direction and (ii) texture. The current task aims at FM characterization of different laboratory and industry scale W-alloys (W-Ti, W-V, W-Ta) in the interesting temperature window for fusion applications (RT-1300 °C). Emphasis is put on the investigation of microstructure and load rate dependence of the fracture toughness (K_{IC}). The investigations should be accompanied by fractographic and microstructural investigations.

Performed Work

FM investigations have been carried out on commercially available rolled polycrystalline W and its ODS variant WLa_2O_3 alloys produced in a powder metallurgical route from PLANSEE Metall GmbH, Reutte/Austria. Three point bending tests have been performed on pre-cracked rectangular SENB specimens with dimensions of 3x6x27 mm and 3x4x27 mm. V or U shaped notches have been machined in the specimens prior introduction sharp crack starter notches by means of a razor blade polishing. This method allowed reduction of the notch radius down to 20 μm . During the experiments, force, displacement and temperature were recorded. The FM experiments have been performed over the temperature range of -150 °C to 950 °C. Tests above 350 °C were performed in high vacuum to avoid any oxidation of the specimens and in a cooling nitrogen atmosphere below room temperature. The fracture toughness K_{IC} has been calculated following the ASTM E399 standard using the overall notch depth as a crack length.

The microstructure of polycrystalline W was characterized by elongated grains with an aspect ratio of roughly 1:3 in the rolling direction and a $<110>$ -fiber texture. To take the anisotropic microstructure into account, the W specimens were extracted in three different kinds of crack orientations (see Fig. 1).

Fig. 2 shows the fracture toughness obtained on polycrystalline rolled tungsten for all three investigated crack orientations over a wide temperature range. All tests were performed in displacement controlled regime at a fixed loading rate of 1 $\mu m/s$. All specimen types failed by brittle fracture at low temperatures and a transition from brittle to ductile fracture behaviour can be observed with increasing temperature marked by a steep increase of fracture toughness. As K loses validity with increasing ductile behaviour, the calculated values above the transition regime give only a lower bound and are denoted by open symbols. The anisotropic microstructure clearly manifests itself in a strong anisotropy of the DBTT and the absolute reached fracture toughness values. The two transverse specimens of types I and II exhibit a much lower fracture toughness in the lower shelf and a much higher DBTT compared to the longitudinal specimens of type III.

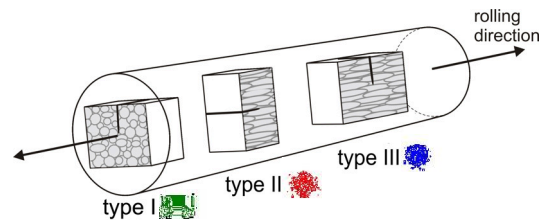


Fig. 1: Illustration of crack orientation and texture of the investigated tungsten specimens.

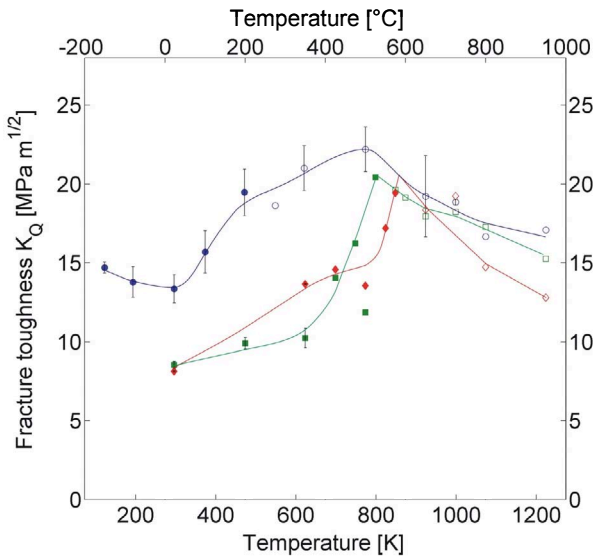


Fig. 2: Fracture toughness of tungsten for the three different crack orientations with respect to the RD. Values denoted by open symbols do not satisfy the ASTM E399 conditions.

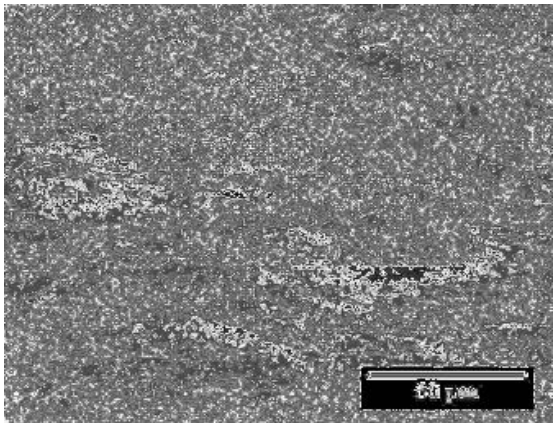


Fig. 3: SEM image of a type I tungsten specimen tested at room temperature. The crack growth (top to bottom) and rolling direction (horizontal) were perpendicular to each other.

At low temperatures the specimens of type I and II exhibit a stable crack growth after crack initiation but this fracture behaviour becomes less pronounced with increasing temperature. Examination of the fracture surfaces show that both specimen types fail predominately by intergranular fracture and only a small amount of transgranular cleavage surfaces could be observed (Fig. 3 and Fig. 4). Partially pulled out grains could be regularly found at the fracture surfaces. No significant change of the fracture morphology was observed with increasing temperature till at 950 °C first local traces of ductile fracture appeared.

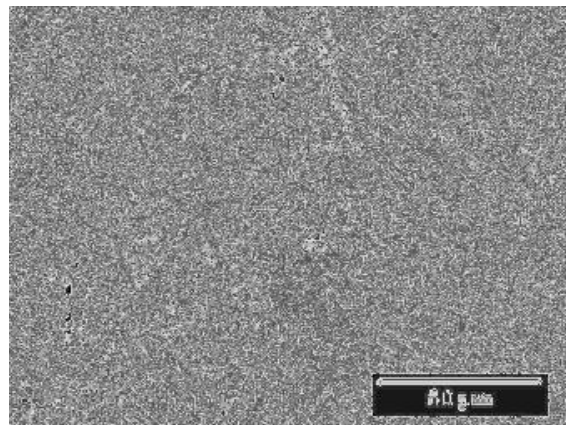


Fig. 4: SEM image of a type II tungsten specimen tested at room temperature. The crack growth (top to bottom) and rolling direction (vertical) were parallel to each other.

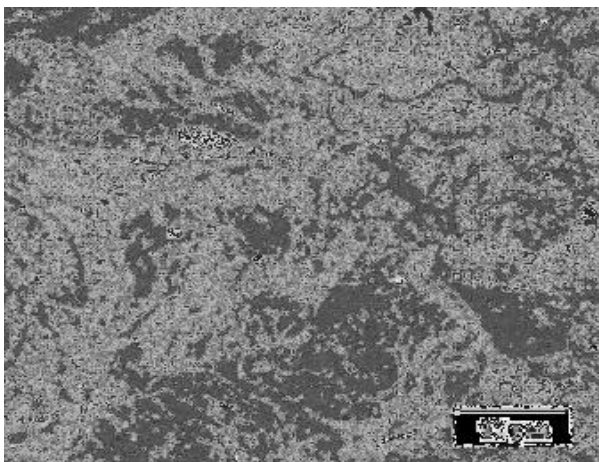


Fig. 5: Type III tungsten specimen tested at 100 °C. The crack switched locally from transgranular cleavage to intergranular fracture leading to a crack deflection in the RD.

The type III specimens extracted along the RD show completely different fracture behaviour in the brittle regime as they fail by almost entirely transgranular cleavage. Furthermore, in contrast to the two transverse specimen types, the fracture behaviour changed significantly with increasing temperature. Examination of the fracture surfaces after FM testing at 100 °C revealed that the crack switched locally from transgranular cleavage to intergranular fracture along the elongated grain boundaries in the RD as shown in Fig. 5. In-situ FM experiment performed at a test temperature of 350 °C revealed that crack initiation occurred ahead of the notch, not oriented along the symmetry plane of the specimen

but perpendicular to it, which corresponds to the RD. With increasing load the crack propagated by intergranular fracture along the elongated grain boundaries in both directions and the remaining ligament between the notch root and the transverse crack finally failed by shear fracture.

The loading rate dependence of the fracture behaviour of polycrystalline tungsten has been studied for all three specimen orientations in Fig. 1. Figures 6a and 6b show the fracture toughnesses of the two transverse specimen types I and II as a function of the temperature for three different stress intensity rates. The DBTT of both specimen types is clearly shifted to higher temperatures with increasing loading rate and a strong dependence of the fracture toughness on the loading rate can be observed in the semi-brittle regime. At low temperatures, in contrast, the fracture toughness is almost independent of the loading rate. The analysis of the temperature dependence of the DBTT in terms of the Arrhenius law:

$$dK / dt = A \exp\left(-\frac{E_{BDT}}{k_B T_{BDT}}\right)$$

yielded the apparent activation energies of $E_{BDT} = 1.32$ eV for the type I specimens and $E_{BDT} = 1.44$ eV for the type II specimens. The apparent activation energies for the BDT suggest that the crack tip plasticity is controlled by the mobility of screw dislocations. For longitudinal orientation (type III) no results are shown as the variation of the loading rate dependence showed no clear trend. This is probably due to the scatter in the experimental data. Furthermore, it is very likely that the rate dependence is obscured by the observed change of fracture mode, which occurred just in the semi-brittle regime, where the largest effect of loading rate is expected.

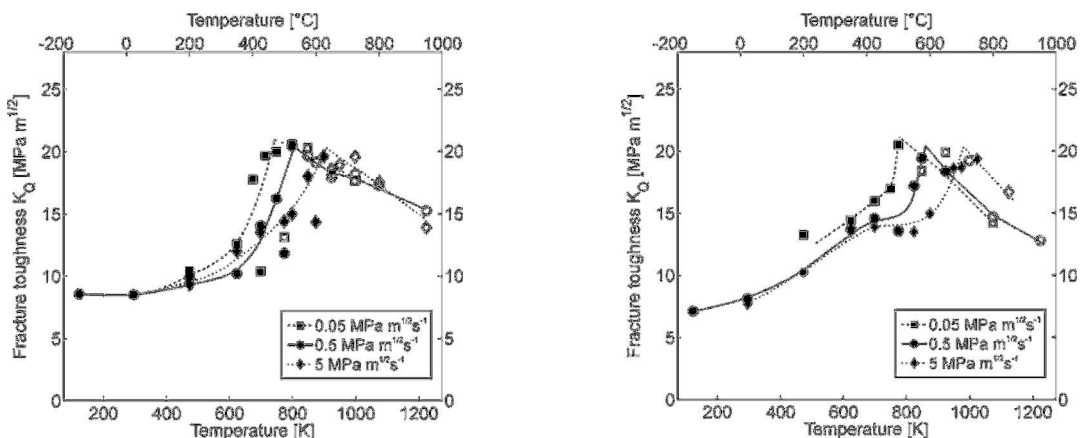


Fig. 6: Loading rate and temperature dependence of fracture toughness: a) type I specimen; b) type II specimen.

Fig. 7a shows load displacement curves on polycrystalline rolled W-1%La₂O₃. The FM specimens have been machined in the type III configuration. After introducing the crack starter notches by a razor blade the sharp cracks have been produced by compression fatigue. The FM tests were performed in displacement control at a fixed loading rate of 1 μm/s. At RT the load displacement curve showed a load drop at about 185 N accompanied by a drastic reduction of the load level being characteristic for an unstable crack growth. The corresponding SEM image in Fig. 7b reveals almost entirely transgranular cleavage. Estimation of the fracture toughness according to ASTM E399 standard yields 11 MPa m^{1/2}. At 500 °C the load level corresponding to the first drop increased to 390 N indicating increase of the fracture toughness. This load drop, however, was not accompanied by a drastic load reduction, rather a further increase of the load with increasing the displacement was observed. The observed behaviour does not allow the estimation of the fracture toughness according to ASTM E399 standard. The examination of the specimen in Fig. 7c revealed multiple crack emission and propagation preferably along the rolling direction.

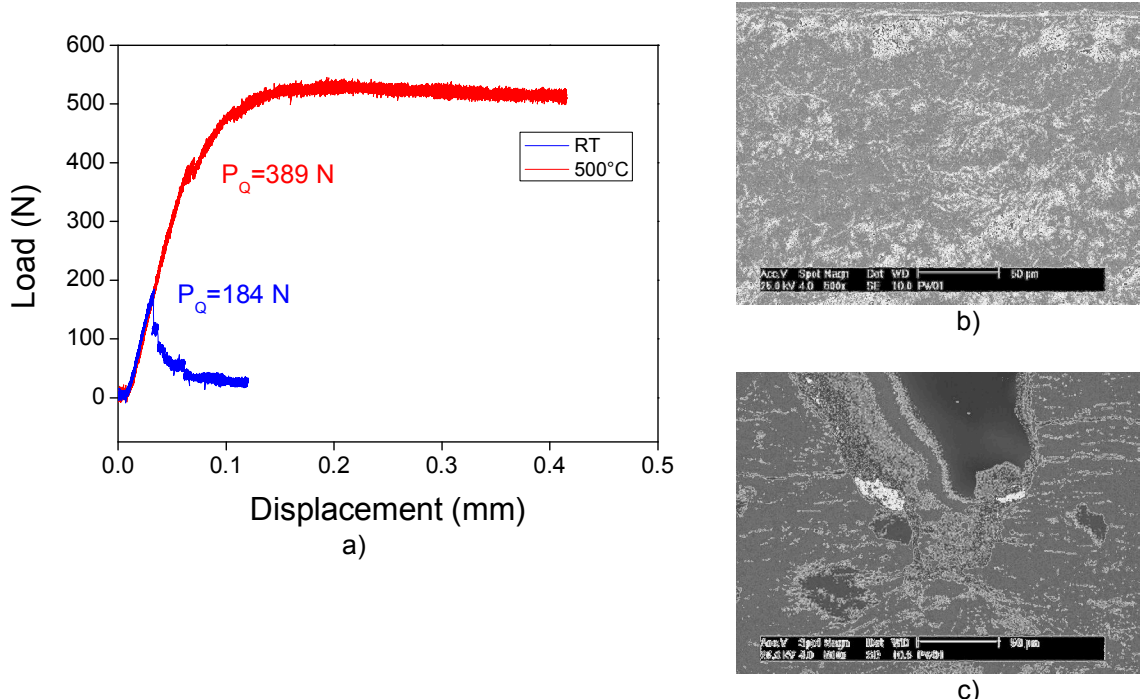


Fig. 7: FM investigation on W-1% La_2O_3 . a) Load displacement curves at RT and 500 °C; b) SEM image of the fracture surface after testing at RT; c) Side view of the specimen after testing at 500 °C.

Conclusion and Outlook

The anisotropic microstructure of the polycrystalline rolled tungsten has a strong influence on the fracture behaviour. The largest fracture toughness and the lowest DBTT are observed for the specimens extracted in the longitudinal orientation when the crack propagates transverse to RD through the elongated grains yielding a transcrystalline cleavage. In the two investigated transverse orientations observed lower fracture toughness in contrast is related to the propagation of the crack along weak grain boundaries yielding an intergranular fracture. In the case of the type I and type II specimens, the DBTT strongly depends on the loading rate, giving an activation energy for the DBTT of $E_{\text{BDT}} = 1.32 \text{ eV}$ and $E_{\text{BDT}} = 1.44 \text{ eV}$, respectively. In contrast to these two transverse orientations, no clear trend was identifiable for the longitudinal orientation. The anisotropy of polycrystalline rolled W-1% La_2O_3 revealed strong influence on the fracture behaviour. At 500 °C for the type III configuration the observed propagation of the crack along the RD indicates presence of very weak grain boundaries.

FM characterization of different novel laboratory and industry scale W-based structural materials (W-Ti, W-V, W-Ta) that are being developed under EFDA “Tungsten and Tungsten Alloys Development” Task Agreement will be performed in the interesting temperature window for fusion applications (RT-1300 °C). Emphasis will be put on the investigation of microstructure and load rate dependence of the fracture toughness (K_{IC}). FM experiments will be accompanied by fractographic and microstructural investigations. To avoid an expected influence of the loss of the stress concentration at the notched crack tips on the fracture toughness a method for introducing sharp controlled pre-cracks will be developed.

Staff:

U. Bürkle
E. Gaganidze
S. Knaak
D. Rupp
O. Weiss
S. Weygand

Literature:

- [1] D. Rupp, S. M. Weygand, Fracture toughness and microstructural characterization of polycrystalline rolled tungsten, Proceedings of the 17th Plansee Seminar, 2009.
- [2] D. Rupp, S. M. Weygand, Loading Rate Dependence of the Fracture Toughness of Polycrystalline Tungsten, Proceedings of the ICFRM 14, 2009.

Acknowledgement

This work, supported by the European Communities under the contract of Association between EURATOM and Karlsruhe Institute of Technology, was carried out within the framework of the European Fusion Development Agreement. The views and opinions expressed herein do not necessarily reflect those of the European Commission.

Preliminary RT Test of Unirradiated Specimens Thin Foil Tensile Specimens in View of Future PIE – Comparison to Standard Tensile Test (TW5-TTMA-002 D 5)

Background and Objectives

High Z high temperature alloys (such as tungsten) are assumed to be primary materials candidates for divertor structural application. However, these materials suffer from embrittlement at “low temperature” after irradiation. The DBTT (ductile-brittle-transition temperature) strongly depends on the irradiation dose and could also depend strongly on the material processing. A first irradiation experiment has been launched in TW3 to determine the design limits at two temperature levels (600 and 1000 °C).

Investigations to improve, produce and characterise different W alloys will be carried out during this period. Emphasis will be put on improved alloys and improved thermal and mechanical treatment, such as nano-structured materials produced by severe plastic deformation and/or mechanical alloying with special thermo-mechanical treatments. The effect of the grain size and of the interstitial content on the microstructure stability (re-crystallisation), the mechanical properties and the irradiation performance will be emphasised. Investigations on the joining to ODS (ferritic or EUROFER type) steels will be started.

The objective of the subtask is to evaluate the mechanical properties at RT of W specimens (WVM) out of thin foil in tensile tests and to compare the results with results from experiments with standard specimens.

Status

The specimens were sent from CEA at the beginning of the 4th quarter 2009. Additionally, some thin foil WL10 tensile specimens and some WVM and WL10 KLST specimens, respectively, were sent. After consulting EFDA it was decided to test all specimens – the tensile specimens as proposed at room temperature (RT) and the KLST specimens at different temperatures to determine the ductile to brittle transition temperature (DBTT) of the materials. Actually, the impact tests will be carried out at IMF I using a HT-HV impact testing facility.

The tensile tests on WVM and WL10 were performed. In general, both materials failed without really observable plastic deformation. The tensile strength (= fracture stress) shows values between 789 and 993 MPa at elongations after fracture between 0.19 and 0.24%.

Based on missing stress-strain curves from experiments on standard specimens at RT, some round solid specimens will be fabricated at the moment. They will be tested within the near future to compare the results.

Conclusion and Outlook

The tensile tests at RT on thin foil WWM- and WL10 specimens were performed. Additional tests at RT on standard tungsten specimens will be performed as soon as the specimens are fabricated. The impact tests on the KLST specimens to determine the DBTT are running.

Staff:

B. Dafferner
M. Rieth
M. Walter

Acknowledgement

This work, supported by the European Communities under the contract of Association between EURATOM and Karlsruhe Institute of Technology, was carried out within the framework of the European Fusion Development Agreement. The views and opinions expressed herein do not necessarily reflect those of the European Commission.

Mechanical Characterisation of W-Armour Materials (WP08-09-MAT-WWALLOY, Activity 3)

Background and Objectives

Tungsten and tungsten alloys are presently considered for helium cooled divertor and possibly for the protection of the helium cooled first wall in DEMO designs, mainly because of their high temperature strength, good thermal conductivity, and low sputter rates. There are two types of applications for these materials which require quite different properties: one is the use as plasma-facing armour or shield component, the other is for structural purposes. An armour material needs high crack resistance under extreme thermal operation condition while a structural material has to be ductile within the operation temperature range. Both material types have also to be stable with respect to high neutron irradiation doses and helium production rates.

The part protection materials development is focussed on an optimisation of armour materials and high heat flux testing. Candidate materials have to be characterised by fatigue and shock tests for an assessment of their possible lifetimes. Additionally, basic mechanical characterisations have to be performed on new developed materials, to support the alloys optimisation processes.

Activity 2, Structural Material Development, Characterisation of W-Ti, W-V and W-Ta alloys: The objective is a mechanical characterization of the selected W-ODS materials, based on tensile tests, LCF tests and TMF tests in the interesting temperature region for fusion applications (up to 1600 °C).

Status

The first new developed W-ODS material (W-2%Y) was recently provided by PSI – CRPP in the form of one small sintered ingot ($d = 26$ mm, $l = 36$ mm) and 10 prefabricated V-notched miniaturized Charpy specimens. To determine the ductile to brittle transition temperature, these specimens will be tested at IMF I using a HT-HV impact testing facility for the investigations. The ingot will be used to fabricate small tensile specimens. Actually, it will be figured out if it is possible to fabricate the tensile specimens by turning (a fabrication by EDM technique will lead to very high costs).

Conclusion and Outlook

The first new developed W-ODS material is now available, the specimen fabrication has been started and the mechanical tests will probably start within the next weeks.

Staff:

B. Dafferner
M. Rieth
M. Walter

Acknowledgement

This work, supported by the European Communities under the contract of Association between EURATOM and Karlsruhe Institute of Technology, was carried out within the framework of the European Fusion Development Agreement. The views and opinions expressed herein do not necessarily reflect those of the European Commission.

Operation of the Fusion Materials Laboratory (Underlying Technology)

The Fusion Materials Laboratory (FML) provides the infrastructure for the performance of tasks defined in the EFDA and F4E work programmes related to the characterisation and testing of irradiated and non-irradiated materials. Methods such as optical and electron microscopy, tritium adsorption and desorption, He pycnometry and Hg porosimetry, crush load, micro hardness, creep, charpy impact, tensile, LCF and instrumented indentation tests as well as long-time annealing tests are applied. The work includes Post Irradiation Examinations (PIE) of Reduced Activation Ferritic Martensitic (RAFM) steels (reference material for DEMO and ITER-TBMs) and investigations on materials relevant for the HCPB blanket (ceramic breeder materials, beryllium).

PIE on selected samples from the HFR IIB and BOR 60 experiments were performed. For this purpose, Charpy impact tests, tensile tests, and LCF tests were performed and the density of irradiated and unirradiated materials was compared. Tested specimens' small cuts were prepared for light optical, scanning and transmission electron microscopy and examined. Broken halves of Charpy specimens were prepared for instrumented indentation and served for identifying material parameters and Vickers hardness. The aim of the investigations was to study the irradiation effects on the mechanical and structural properties of these materials and to investigate the possibilities of a post-irradiation heat-treatment in order to reduce irradiation defects.

The investigation of blanket materials was continued. Lithium orthosilicate pebbles were investigated by light optical microscopy and their porosity and deformation hardness were determined. Different batches of materials were characterised with respect to the influence of parameters of the fabrication process on the mechanical and structural properties. Tritium adsorption/desorption tests and creep tests were done on beryllium, beryllium vanadium, and beryllium titanium alloys and on BeO-doped beryllium.

Adsorption and desorption experiments were also done with unirradiated beryllium titanium pebbles. Furthermore different beryllium titanium alloys were characterized by light optical microscopy and porosity measurements and creep tests were performed. Activated beryllium was investigated by light optical and scanning electron microscopy, by densiometry, and specimens were prepared for SANS experiments.

Detailed results and consecutive analysis of the measurements are reported in the respective chapters of this report.

For the PIE the following equipment was used:

- Charpy impact, LCF and tensile testing devices
- Indentation device for instrumented ball-indentation and Vickers hardness-test
- Light optical, scanning electron and transmission electron microscopes with analysis of chemical elements
- Desorption device with high temperature furnace for tritium and helium release measurements
- He-pycnometer and Hg-porosimeter
- Sphere crush and creep testing apparatus

In the frame of our upgrading programme, a new 200 kV high resolution transmission electron microscope for investigation of radioactive material down to atomic scale started operation with highly radioactive specimens. First results, identifying the irradiation temperature's influence on the damage mechanisms, could be published. A new pycnometer was installed in a hot cell and started hot operation.

Future activities:

Continuation of measurements as referred to above:

- PIE of the HFR II B irradiation phase, 15 dpa
- PIE of the BOR 60 irradiation campaign, 15 – 30 dpa
- PIE of the OSIRIS FURIOSO high temperature irradiation, WL10-tungsten, 5 dpa
- Installation of a new mass spectrometer for use in the tritium desorption device
- Installation of a device for instrumented indentation at elevated temperatures
- Characterization of new batches of ceramic breeder materials and beryllium
- Operation of a gamma-ray spectrometer to study the activation of RAFM steels

Staff:

P. Barié
J. Ehrmann
A. Erbe
M. Gilpert
M. Holzer
H. Jackisch
S. Lautensack
G. Mangei
W. Nägele
H. Ries
M. Rietschel
R. Rolli
G. Rösch
I. Sacksteder
R. Schmidt
H.-C. Schneider
H. Steinle

Literature:

- [1] Materna-Morris, E.; Möslang, A.; Rolli, R.; Schneider, H.C.: Effect of helium on tensile properties and microstructure in 9%Cr-WVTa-steel after neutron irradiation up to 15 dpa between 250 and 450 °C. *Journal of Nuclear Materials*, 386-388(2009).422-25
- [2] Materna-Morris, E.; Schneider, H.C.; Gaganidze, E.; Rolli, R.; Möslang, A.: The influence of helium on material properties of 9% Cr-alloys (EUROFER) after neutron irradiation. *Jahrestagung Kerntechnik 2009*, Dresden, 12.-14.Mai 2009, Berlin : INFORUM GmbH, 2009, CD-ROM Paper 804
- [3] Sacksteder, I.; Schneider, H.C.; Materna-Morris, E.: Determining irradiation damage and recovery by instrumented indentation in steel. *14th Internat. Conf. on Fusion Reactor Materials (ICFRM-14)*, Sapporo, J, September 7-12, 2009, paper to be published in proceedings
- [4] Bekris, N.; Coad, J.P.; Widdowson, A.; Erbe, A.; Ehrmann, J.; Kloppe, B. ; JET- EFDA Contributors Assessment of the flash-lamp photon-cleaning detritiation method tested at JET. *Journal of Nuclear Materials*, 390-391(2009) 614-17
- [5] Gan, Y.; Kamlah, M.; Riesch-Oppermann, H.; Zhao, S.; Rolli, R.: Crush probability analysis of ceramic breeder pebble beds under mechanical stresses. *14th Internat. Conf. on Fusion Reactor Materials (ICFRM-14)*, Sapporo, J, September 7-12, 2009, paper to be published in proceedings
- [6] Kurinskiy, P.; Chakin, V.; Möslang, A.; Rolli, R.; Goraieb, A.A.; Harsch, H.; Alves, E.; Franco, N.: Characterisation of titanium beryllides with different microstructure. *Fusion Engineering and Design*, 84(2009) 1136-39

Structural Materials – Processing and Compatibility

Corrosion Resistance of EUROFER in Liquid PbLi

Introduction

Reduced activation ferritic-martensitic steels are considered as structural materials in HCLL blanket development for DEMO and for TBM's tested in ITER. In the past, corrosion testing was performed at moderate temperatures of about 480 °C and showed acceptable homogeneous corrosion behaviour [1, 2]. However, in the mean time the envisaged temperature limits increased to around 550 °C for TBM's. Due to large uncertainties in extrapolations of the corrosion behaviour from 480 to 550 °C, new tests were initiated and are under execution, inclusively the development of modelling tools and analyzing for the first time in more detail transport and precipitation phenomena.

The long-term based tests up to 12,000 h exposure time indicated dramatically high corrosion rates with 400 µm/year steel dissolution at flow velocities of 0.22 m/s and slightly increased temperature to 550 °C. Precipitation of dissolved material at cooler loop sections rose to a serious problem with loop blockages after short operation time of roughly 3000 h. All evaluated data were also used for validation of the modelling tools integrated into the developed code MATLIM [3] a tool describing corrosion attack under various flow and temperature conditions in a Pb-15.7Li system with forced convection. MATLIM gives also assistance in the field of transport of corrosion products by the Pb-15.7Li breeder and forming of precipitates at cooler loop sections. A high degree of consensus between measured and calculated corrosion attack values was obtained.

Both activities, corrosion testing in PICOLO loop and model development are nowadays focused on the change to smaller flow velocities to generate a higher overlap with scenarios present in TBM ITER testing. Due to the fact that this causes a change from high flow velocities with clearly turbulent behaviour to velocities near 1 cm/s with laminar flow conditions, intermediate testing is in the foreground to generate a homogeneous data base and validate modelling tools step by step towards the new demands. The testing at 0.1 m/s is under progress and shows still high corrosion attack.

Parallel to the testing of bare EUROFER steel in contact with flowing Pb-15.7Li, where dramatically material dissolution was found, the development of electro-chemically deposited Al-based scales on EUROFER was intensified for production of corrosion resistant and T-permeation barriers. Two deposition lines were meanwhile developed named ECA and ECX. The first is specialized for Al deposition from organic electrolyte and the second can handle more metals and uses a new electrolyte class of ionic liquids.

Corrosion testing

The corrosion testing of bare EUROFER 97 samples was performed in flowing Pb-15.7Li with a flow velocity of 0.22 m/s or 0.10 m/s in the PICOLO loop. The highest temperature in the loop was present in the test section with 550 °C. The coolest sections were the electromagnetic pump and magnetic trap devices with roughly 350 °C. Fig. 1 shows a schematically view of the PICOLO loop with the main components. The fresh test samples had a diameter of 8.0 mm and were mounted concentrically in the test section with inner diameter of 16 mm. The flow velocity of 0.22 m/s is the calculated value for the fresh "un-corroded" configuration. The longest exposed sample was removed after nearly 12,000 h and the smallest exposure time was 500 h. Due to the high corrosion attack at 550 °C a high amount of precipitates was present in the loop which caused a first plugging after about 3,000 h of operation. The blockage appeared in the mounted magnetic trap section which is installed to collect precipitates and prevent the electromagnetic pump from damages. Replaced fresh magnetic traps had in the following an average life time of around 3,000 to 4,000 h.

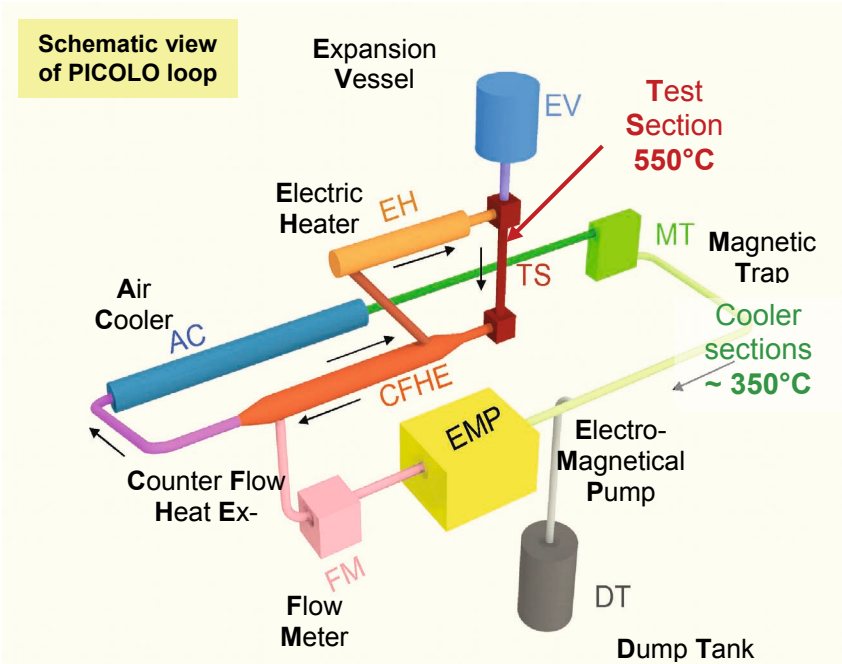


Fig. 1: Schematic view of PICOLO loop with temperature in hot test section and cooler loop parts.

Corrosion attack

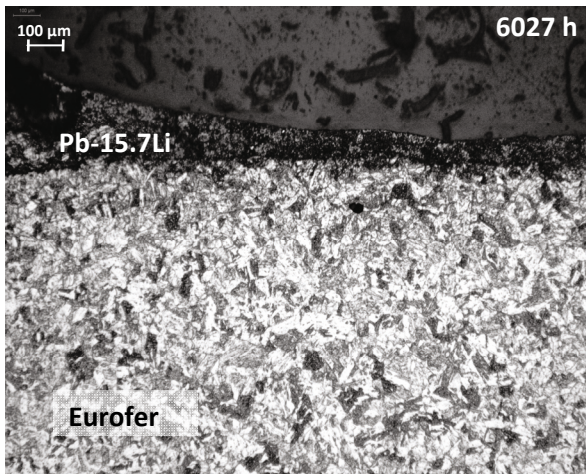


Fig. 2: The micrograph exposed more than 6,000 h to Pb-15.7Li at 550 °C shows a smooth surface in contact area to Pb-15.7Li indicating a homogeneous corrosion attack.

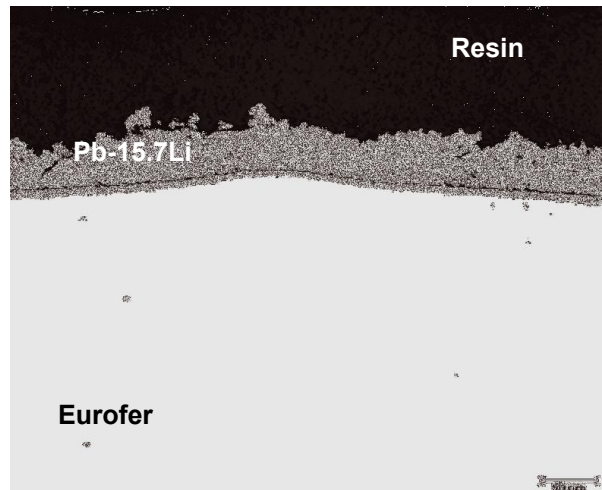


Fig. 3: Micrograph of Eurofer exposed at 0.10 m/s to Pb-15.7Li at 550 °C for 1,500 h.

The corrosion testing of RAFM steels performed at 480 °C in PICOLO loop in earlier test campaigns showed that dissolution of e.g. Fe, Cr out of the steel matrix is the acting corrosion mechanism which leads to a corrosion rate at 480 °C of roughly 90 μm/year at 0.22 m/s. The new tests performed at 550 °C delivered for EUROFER the same corrosion mechanisms and showed also a homogeneous attack of the surfaces at longer exposure times as can be seen in the micrograph depicted in Fig. 2. The whole testing program was running up to about 12,000 h and showed always a good wetting of the surfaces and a homogeneous corrosion. Compared to 480 °C, only insignificant changes in the surface structure may be present. No evidence was found in metallographic analyses for leaching or cracking off of complete martensitic needles in shape of particles as can be concluded from Fig. 2. Similar corrosion behaviour was also found for the reduced flow velocity of 0.10 m/s near the boun-

dary range to mixed flow conditions. After 1,500h a almost cylindrical surface shape of the samples is present indicating homogeneous attack and smoothing of some roughness caused by incubation effects in the time range up to 500 h exposure.

Corrosion rate

The corrosion rate = material loss of each sample was determined by measuring the diameters of each sample before and after exposure to the flowing Pb-15.7Li. The half difference of these diameters stands for the corrosion rate. Diameter measurements of fresh samples were done mechanically. Some specially prepared cuts of such samples were used as reference standards for calibration of the optical measurement process which is applied for determination of the diameter from the metallurgical cuts of Pb-15.7Li exposed samples. The cuts of all Pb-15.7Li exposed samples showed a symmetrical spherical attack within the resolution limits of about 5 μm of the used measurement process.

Extrapolations done by samples removed at 550 °C test temperature and flow velocity 0.22 m/s deliver rather high corrosion values of about 400 $\mu\text{m}/\text{year}$ with more emphasis to the values evaluated for the long term exposed samples up to 12,000 h. Fig. 4 gives an overview of mass loss due to corrosion attack of samples exposed to flowing Pb-15.7Li in dependence of flow velocity and temperature. The measured values for corrosion attack in PICOLO are given for the temperatures 480 and 550 °C. Also indicated is the regime for new PICOLO tests at reduced flow velocities roughly in the range 10 to 1 cm/s. The correlation of Sannier [4] based on experimental values is integrated to show that PICOLO values are correctly lying in the corrosion regimes of steels for both 480 and 550 °C. This underlines also the correctness of the observed high corrosion values and the amount of transported corrosion products in the loop.

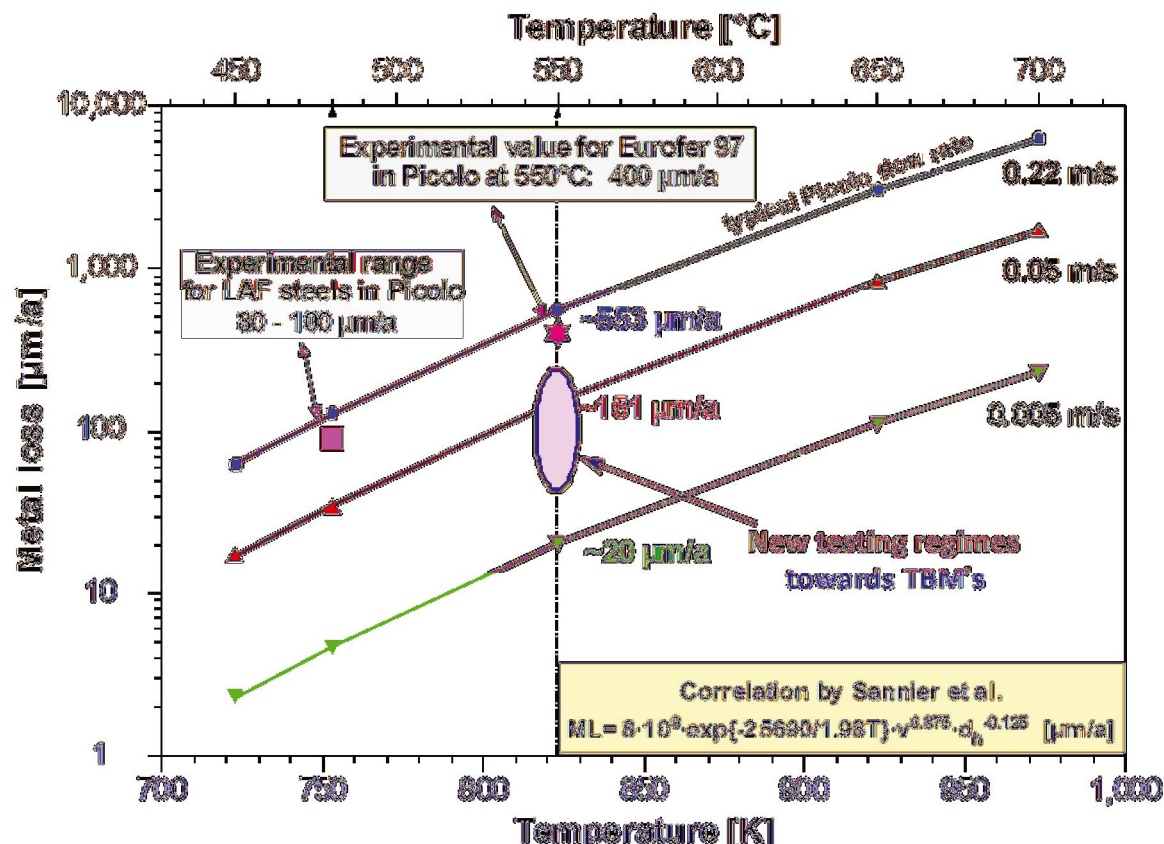


Fig. 4: Overview on corrosion regimes and positioning of PICOLO tests.

In the area of 0.1 m/s flow velocity the corrosion testing was started shortly ago. Up to now, only some values in the short to medium term testing range are available. The corrosion attack evaluation was performed in the same manner as for the samples exposed at 0.22 m/s. The evaluated mass loss is given in Fig. 5 vs. exposure time. Extrapolation to longer times reveals an attack of roughly 300 $\mu\text{m}/\text{year}$. This is still a high value and produces similar amounts of corrosion products as testing at 550 °C. This implies that corrosion attack and the corrosion products will only be hardly manageable and that one possibility may be the application of corrosion barriers to solve this.

Corrosion and T-permeation barriers by electro chemical Al coating

Earlier performed development work by Hot Dip Aluminisation [5] showed that protective scales can be formed on EUROFER steel by appropriate metallurgical reaction and heat treatment which can withstand flowing Pb-15.7Li attack without visible damage. However, the coating of the EUROFER by dipping into an Al melt had shown some technological restrictions, especially in the fields of homogeneity and industrial application with complex geometries. Thus, a search for more flexible and reliable processes was started. This evaluation process indicated that electro chemical coating may overcome these lacks if a deposition method can be developed which is working at low temperature and without water as part of an electrolyte. Thus general electro chemical analyzes were performed to evaluate the conditions for deposition of Al from electrolytes near room temperature. In Fig. 6, the limits for aqueous and aprotic based electrolytes are depicted together with the standard potential of several metals. From water systems, elements like Cu or Ni can be deposited but never Al. Electrolytes for handling Al have to be based always on organic water-free systems.

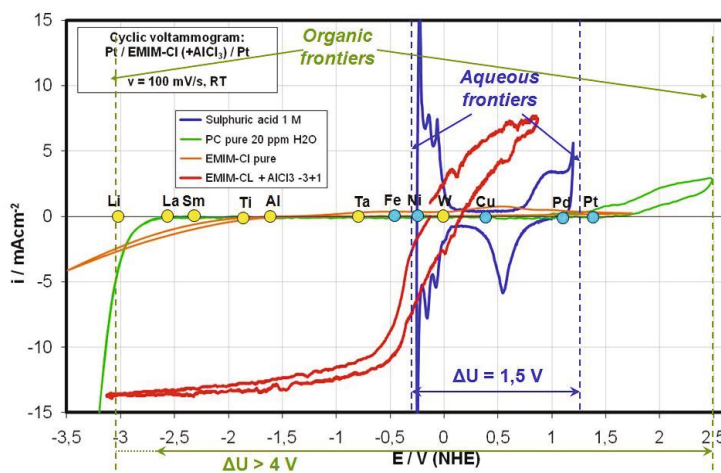


Fig. 6: Voltammogram with operation area for aqueous and organic electrolytes incl. potential of major elements.

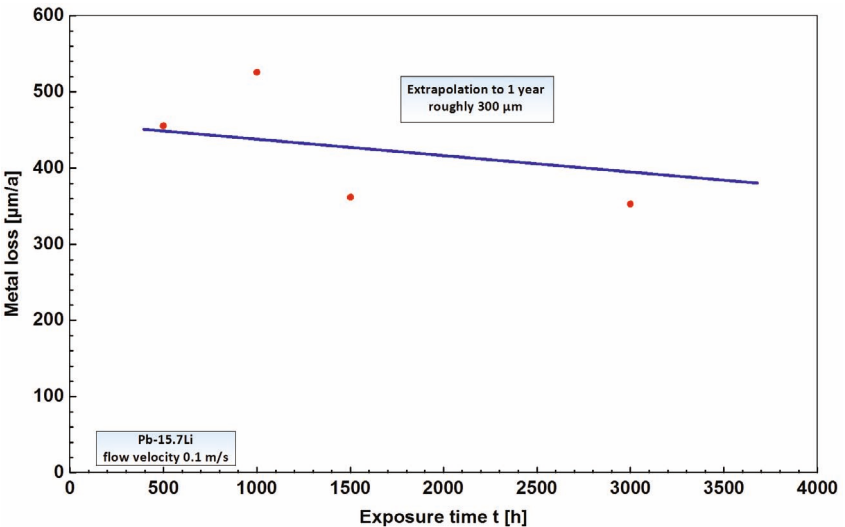


Fig. 5: Corrosion attack of EUROFER 97 at 550 °C test temperature and flow velocity 0.10 m/s vs. exposure time.

Two different Al-deposition processes were developed in the meantime named ECA (Electro Chemical Al deposition working with a Toluol-ether base) and ECX standing for different X-element deposition by Electro-Chemical method using ionic liquid EMIM-Cl (Ethylamidazolium-chlorid). With ECA Al scales with roughly 20 μm were deposited on PICOLO test samples of diameter 8 mm (Fig. 7, left) and heat treated at 980 °C and 760 °C for 0.5 and 1.5 h, respectively to generate the

protective surface scales. Some first samples were exposed to flowing Pb-15.7Li in PICOLO loop for some 1,000 h. Fig. 7 (right side) gives the microcut of a test sample exposed for roughly 5,300 h. No visible attack of the sample can be found indicating the desired corrosion barrier function.

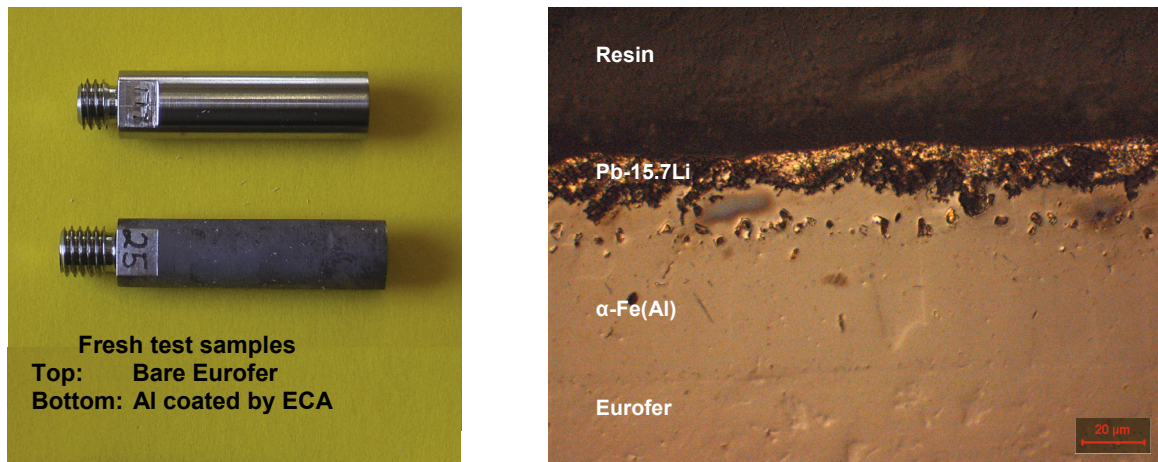


Fig. 7: Bare and ECA coated test sample after heat treatment for PICOLO testing (left) and micrograph of sample after 5,300 h exposure to Pb-15.7Li

The development of the ECX process is rather new and the evaluation of optimized electrolyte and deposition parameters are in the foreground. From the ionic liquid EMIM-Cl and the salt AlCl_3 , an electrolyte suitable for Al deposition could be synthesized. From such a solution Al deposition on substrates is possible by DC power as illustrated in Fig. 8. This electrolyte is liquid and stable over a wide temperature range and deposition was performed at about 150 °C. The ionic scattering behaviour of ECX is more effective than that of ECA resulting in coatings with similar thicknesses on front and rear sides of substrates by applying only a plate anode in front of the substrate. The deposited scale thickness can be easily controlled by deposition time and current. The scale homogeneity is excellent as can be seen from the micrograph depicted in Fig. 8 right side. The protective surface scales concerning barrier function have also been generated by a subsequently performed heat treatment.

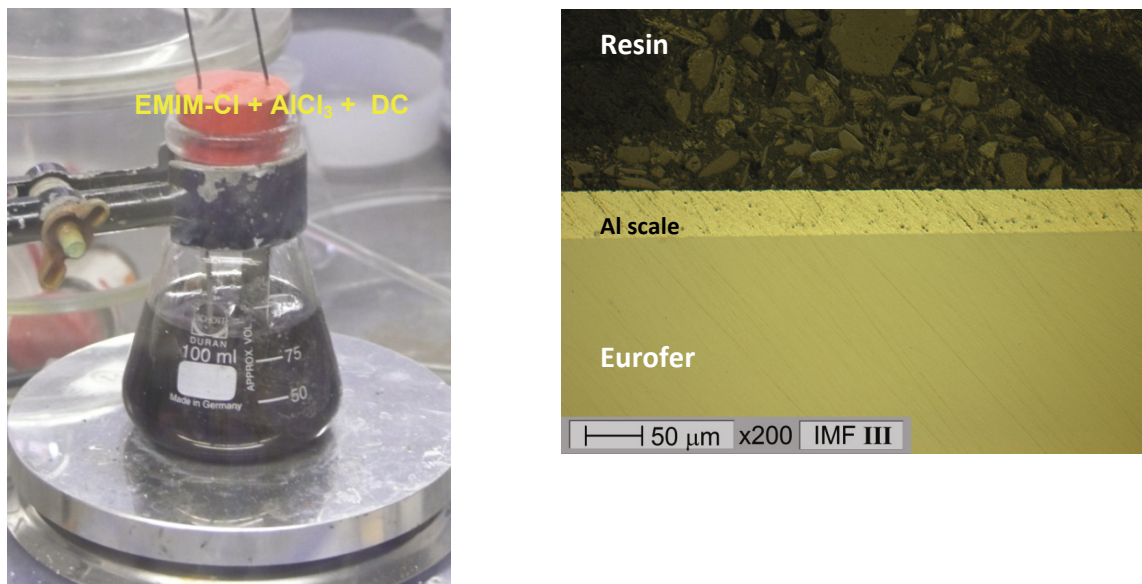


Fig. 8: Glass container with electrolyte EMIM-Cl + AlCl_3 (left side) and an Al scale deposited on EUROFER at about 150 °C

Conclusions

The corrosion testing program of EUROFER which reached at flow velocities of 0.22 m/s exposure times of 12,000 h was successfully enlarged at same testing temperature of 550 °C conditions at a flow velocity of 0.1 m/s. The modelling activities were continued by integrating the developed tools into MATLIM code inclusively the validation vs. the measured data. Both, calculated and measured values of corrosion attack are in good agreement. At both flow velocities a high amount of precipitations are formed in cooler loop section always with the ability to form loop blockages. At 0.22 m/s first changes of the magnetic trap were necessary after about 3,000 h to gain Pb-15.7Li flow again. This suggests that transportation and precipitation phenomena should be more considered than up to now.

With the development of electro-chemically based deposition technologies ECA and ECX a clear step towards industrially relevant coating technologies was done. With ECA first protective scales on EUROFER were successfully prepared and a qualification in PICOLLO loop was successfully done. No corrosion attack was observed at exposure times up to ca. 5,300 h. ECX can also deposit Al scale as demonstrated, however, with higher flexibility and better scattering behaviour. Both processes show excellent industrial relevance. Surely, additional development work is absolutely necessary e.g. in the field of metallurgical heat treatment and optimization of electrolyte parameters with special view on reduced but homogeneous Al scale thickness.

Staff:

M. Heck
N. Holstein
J. Konys
W. Krauss
J. Lorenz
J. Novotny
A. Skrypnik
O. Wedemeyer

Literature:

- [1] H. Glasbrenner, J. Konys, H. D. Röhrlig, K. Stein-Fechner, Z. Voss; Corrosion of ferritic-martensitic steels in the eutectic Pb-15.7Li, *J. Nucl. Mat.*, 283-287, (2000), 1332.
- [2] J. Konys, W. Krauss, Z. Voss, O. Wedemeyer, Corrosion behavior of EUROFER steel in flowing eutectic Pb-15.7Li alloy, *J. Nucl. Mat.*, Vol. 329-333, Part 2, (2004), 1379-1383.
- [3] H. Steiner, W. Krauss, J. Konys, Calculation of Dissolution/Precipitation Rates in Flowing Eutectic Pb-17Li with the MATLIM code, *J. Nucl. Mat.*, Vol. 386-388, (2009) 675-677
- [4] J. Sannier, T. Flament, A. Terlain, Corrosion of martensitic steels in flowing Pb17Li, *Proc. 16th Symp. Fusion Technology*, 3-7 Sept., (1990), London, UK, 901-905.
- [5] J. Konys, W. Krauss, Z. Voss and O. Wedemeyer, Comparison of corrosion behavior of bare and hot-dip coated EUROFER steel in flowing Pb-17Li, *J. Nucl. Mat.*, Vol. 367-370, (2007), 1144-1149
- [6] J. Konys, W. Krauss, H. Steiner, J. Novotny, A. Skrypnik, Flow rate dependent corrosion behavior of EUROFER-steel in Pb-15.7Li, ICFRM-14, Sapporo, Japan, September 6-11 (2009).
- [7] W. Krauss, J. Konys, N. Holstein, H. Zimmermann, Al-based anti-corrosion and T-permeation barrier development for future DEMO blankets, ICFRM-14, Sapporo, Japan, September 6-11 (2009).
- [8] J. Konys, W. Krauss, N. Holstein, Development of advanced processes for Al-based anti corrosion and T-permeation barriers, ISFNT-9, Dalian, China, October 11–16 (2009)

PM Production and PIM of Tungsten and Tungsten Alloys (WP08-09-MAT-WWALLOY, Activity 2)

Objectives of the task

A He-cooled divertor design [1] for future fusion power plants has been developed at Karlsruhe Institute of Technology. Tungsten and tungsten alloys have been chosen as functional and structural materials, respectively. The most important design criteria in particular for the divertor structure material are low ductile-brittle transition temperature (DBTT), high thermal conductivity, high strength, and sufficient ductility. The advantages of tungsten based materials are their high melting points, high thermal conductivity, low thermal expansion, and low activation. But on the other hand their disadvantages are high hardness and brittleness. This mismatch can be potentially minimized by a new kind of material which can be developed on the basis of Powder Injection Moulding (PIM), which offers a large potential for mass production of near-net-shape parts with high precision as well as the possibility for adjusting important material properties like the thermal conductivity.

State of the art PIM R&D

The R&D work programme is divided into two different routes: a) powder metallurgical (PM) investigation of the basis refractory material alloy to understand its fundamental properties followed by b) application of the gained knowledge from a) on the first PIM test step to learn and optimize the complete process and to produce in this way small specimens for the material characterization. After the successful preparatory step, the actual PIM process for the end product, i.e. to produce the divertor parts, will follow with the starting steps of rheology simulation, optimization, construction and manufacturing of the new PIM tool. The motivation for this work is to manufacture the W tile by PIM in view of mass production aspects.

First successful experiences with W-PM were made in the last year. The manufactured samples reaching a final density of approximately 90% TD and a Vickers-hardness of 430HV0.1 [2]. The knowledge gained from the PM trials (e.g. powder preparation and mixing) is applied on the PIM development route. This process route comprises powder preparation; feedstock (powder and binder) formulation; injection moulding process; debinding; sintering and HIP. The results shall be discussed below.

Results

Powder Injection Moulding of W-parts

The knowledge of W-powder preparation and mixing from PM was very useful for the first PIM step: development of a new feedstock. To provide a W-feedstock with a solid load of 50 vol.-% and a low viscosity for replication of complex shaped components a binary W-powder system with a grain size distribution in a range of 0.7 μ m to 1.7 μ m FSSS and a binder system, also 50 vol.-%, based on a wax/thermoplastic mixture was developed and used. Fig. 1 shows the green part after injection moulding (left) and finished disk after the pre-sintering and HIP-cycle (right). The shrinkage is nearly 20%.

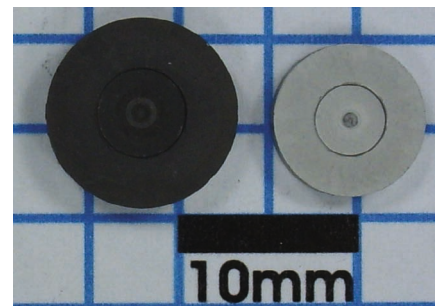


Fig. 1: Green part (left) and finished disk after pre-sintering + HIP (right).

Debinding was done in a two step procedure, first solvent debinding in n-Hexane followed by a thermal debinding step. Samples were pre-sintered (1650 °C; 2 h; H₂) in order to reach the closed porosity necessary for the HIP treatment. After pre-sintering the samples showed a density of 94.7%TD and a Vickers-hardness of 417HV0.1.

Fig. 2 (a) shows the microstructure of the sample after pre-sintering. These samples were used for an optimization of HIP parameters regarding grain growth and final density. By applying a suitable HIP-cycle (1600 °C; 3 h; Ar; 250 MPa) samples were compacted, thus reaching values near the theoretical density (97.6%TD), a Vickers-hardness of 457HV0.1 and a grain size of approximately 5 µm, the corresponding microstructure is shown in Fig. 2 (b).

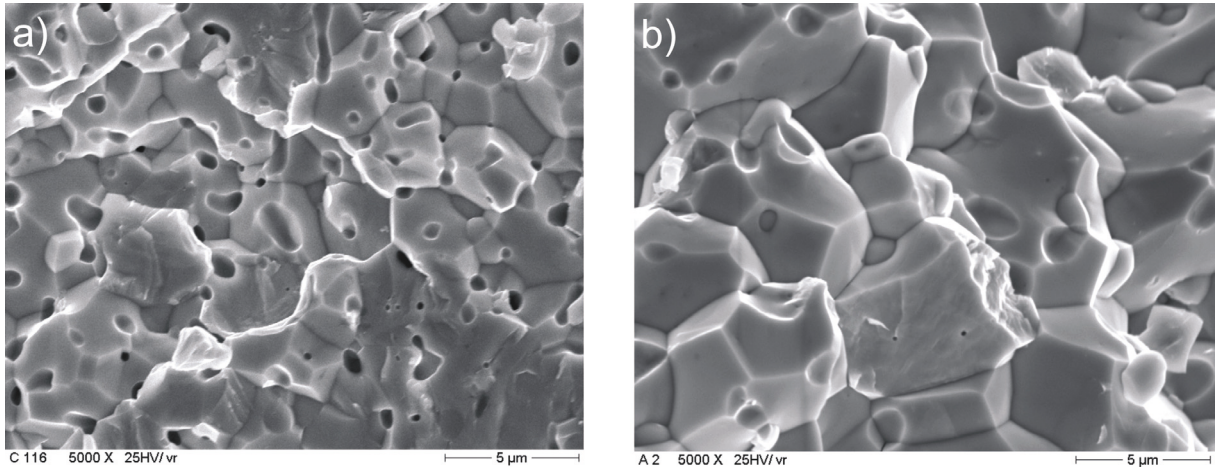


Fig. 2: Microstructure of a (a) pre-sintered and (b) pre-sintered + HIPed tungsten sample prepared by PIM.

Design of a new injection moulding tool

The development steps such as simulation, optimization, construction, and manufacturing of the new PIM tool for the W tile have been realized in parallel. The new tool was delivered in November 2009 and the first tests are on going.

Conclusions and outlook

A new feedstock with 50 vol.-% solid load of a binary W-powder particle system was successfully developed. First W-PIM experiments showed a good mouldability of microparts. Also a suitable pre-sintering and HIP process chain has been developed. The finished samples show a high density and hardness. In parallel, the work (simulation; design; construction; manufacturing) on a new PIM tool for the W tile was also successful and the tests are going on.

The future work will focus on injection moulding with the new tool for the W tile including tests and characterization of the product. The W-tiles produced in such a way will undergo high heat flux tests at Efremov within the frame of divertor finger mock-up tests.

Staff:

S. Antusch
P. Holzer
T. Mueller
P. Norajitra
V. Piotter
K. Plewa
H.-J. Ritzhaupt-Kleissl
R. Vouriot
H. Walter

Literature:

- [1] P. Norajitra, R. Giniyatulin, T. Hirai, W. Krauss, V. Kuznetsov, I. Mazul, I. Ovchinnikov, J. Reiser, G. Ritz, H.-J. Ritzhaupt-Kleissl, V. Widak, Current status of He-cooled divertor development for DEMO, *Fusion Engineering and Design* 84 (2009) 1429–1433.
- [2] S. Antusch, P. Norajitra, V. Piotter, H.-J. Ritzhaupt-Kleissl, PIM application for mass production of He-cooled divertor parts, 14th International Conference on Fusion Reactor Materials, Sapporo, Japan, September 7-12, 2009, to be published in *Journal of Nuclear Materials*.

Acknowledgement

This work, supported by the European Communities under the contract of Association between EURATOM and Karlsruhe Institute of Technology, was carried out within the framework of the European Fusion Development Agreement. The views and opinions expressed herein do not necessarily reflect those of the European Commission.

W-Alloy Development for Structure Application and Characterisation (WP08-09-MAT-WWALLOY, Activity 2)

High temperature alloys (such as tungsten) are assumed to be primary materials candidates for structural application in the divertor. A modified commercial indentation device installed in a hot cell of a Fusion Materials Laboratory (FML) in combination with a neural network based analysis method allows identifying the material parameters of a unified viscoplasticity model with nonlinear isotropic and kinematic hardening from small metal specimens.

Different tungsten materials will be base characterised at RT by instrumented indentation. Registering hardness tests (Vickers, Rockwell, and Berkovich) are performed. Furthermore, determination of a complete set of tensile parameters as well as fracture mechanics tests will be performed.

Tungsten materials will be characterised by instrumented indentation at elevated temperatures up to 1000 °C with two new indentation devices. Hardness tests, parameter-identifying creep tests, and identification of the ductile-to-brittle transition will be done.

The applicability of the method for bulk material and even for porous tungsten coatings could be demonstrated with indents made in a cross-section of a polished W-coating deposited on a EUROFER substrate (plasma-spray, material furnished by IPP Garching). The micrographs in Fig. 1 indicate several difficulties when indenting the W-coating, which do not occur using bulk material. The indent should have sufficient distance to the interface (left micrograph) as well as to big pores (right micrograph) in the plasma deposited coating. The height of the coating is about 2 mm and therefore sufficient material is available for the about 100 µm wide imprints. The middle micrograph shows an indent in a typical area for which good results have been obtained.

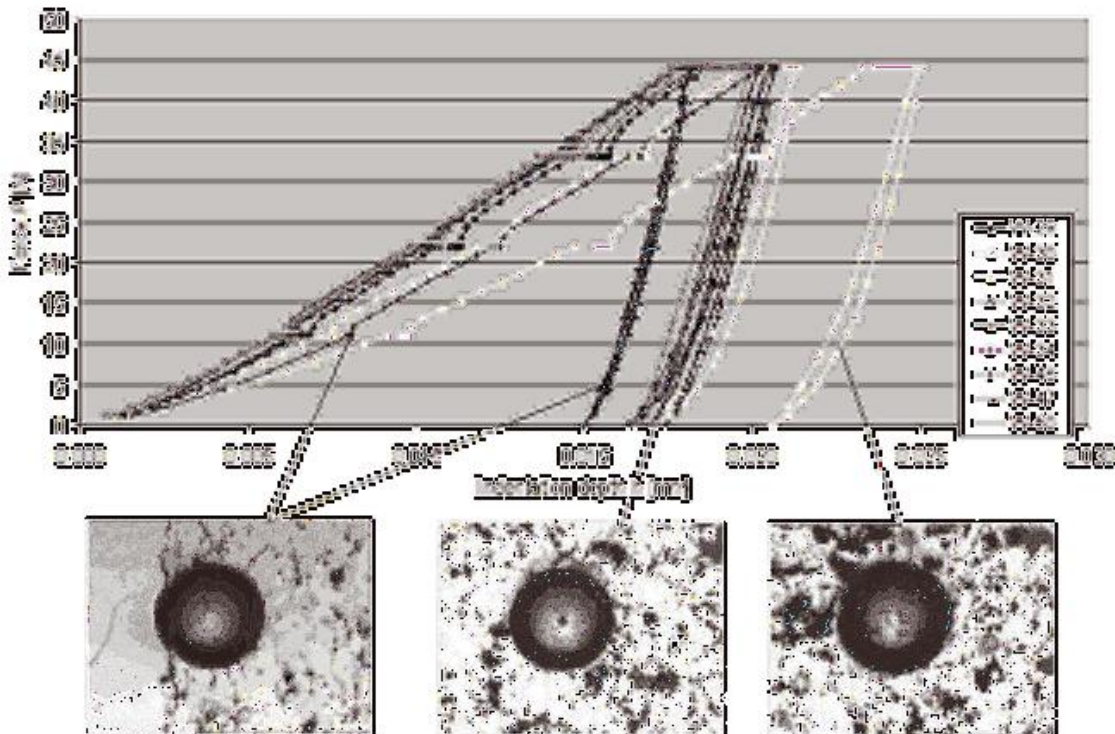


Fig. 1: Load-depth curves for a porous W-coating deposited on EUROFER by plasma-spray. The interface between tungsten and EUROFER can be seen in the lower left micrograph.

Future activities:

- Basic Characterisation of different tungsten materials
- Installation of two different high temperature indentation devices
 - Device 1 for temperatures up to 650 °C and forces up to 200 N
 - Device 2 for temperatures up to 1000 °C and forces up to 2 N

Staff:

S. Lautensack
H.-C. Schneider
I. Sacksteder

Acknowledgement

This work, supported by the European Communities under the contract of Association between EURATOM and Karlsruhe Institute of Technology, was carried out within the framework of the European Fusion Development Agreement. The views and opinions expressed herein do not necessarily reflect those of the European Commission.

Electro-chemical Machining (ECM) of Tungsten and Tungsten Alloys (WP08-09-MAT-WWALLOY, Activity 1)

Introduction

As application in a fusion power system, a helium cooled divertor concept is investigated, which is envisaged to remove heat loads of up to 15 MW/m^2 . This divertor design is based on a modular arrangement of cooling fingers, which is to be fabricated from a heat resistant material like tungsten (alloys). But shaping of tungsten, a hard and brittle material, is by the state of the art only possible by applying spark erosion methods (EDM), which systematically introduces microstructural defects into the bulk or by rather cost intensive milling technology which is also not risk-free concerning microcracks. Looking at the divertor structures and symmetries of some parts, it is obvious that only erosive machining methods can be used. EDM can surely produce such structures e.g. in steel, but not in W-alloys with the required quality. Beyond needed excellent surfaces without any damages and microcracks, economical costs are also an important figure which pushes the development of advanced technologies for processing of tungsten [1, 2].

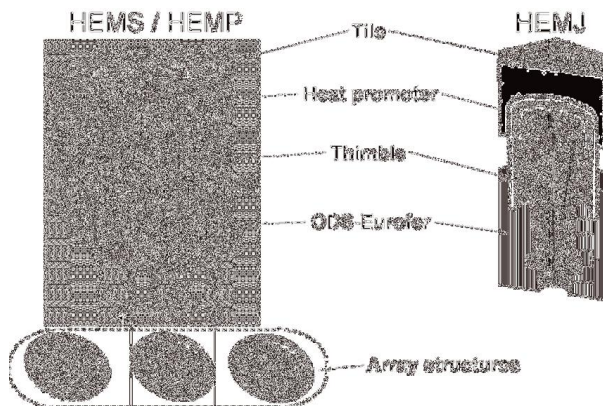


Fig. 1: Design variants HEMJ and HEMS / HEMP of cooling fingers. Especially in the later ones, micro-structurally shaped W-arrays are integrated into the thimble made of WL10 (W1%La2O3) to enhance heat transfer. The shown array structures are: pin, straight slot and curved slot arrays with groove dimensions of approx. $1.5 \times 0.3 \text{ mm}$ (H x W) and a total diameter of approx. 12 mm.

Innovative ECM technology can produce defect-free surfaces and high precision parts at low costs by guided and directed anodic dissolution [3] of material as e.g. applied in steel processing. However, any application in W-alloy processing is missing and tests of industrial ECM process equipment working with electrolytes adapted to steel shaping failed due to passivation effects. In the first development step tungsten behaviour in contact with electrolytes was analyzed and passivation of tungsten was successfully eliminated by development of a suitable electrolyte. This opened the path for the anodic dissolution of tungsten as possible application for divertor parts and the evaluation of different ECM processing routes.

Development of electrolytes and physical aspects for ECM (Electro-chemical Machining) of tungsten

Tungsten is, given by its pure properties, in theory less stable than iron in acidic etching solutions, but in reality, tungsten forms, after an initial electro-chemical oxidation, completely insulating oxide layers and the tungsten scales are totally insoluble in commercial ECM electrolytes. Standard and hardly changeable electrolytes for the electro-chemical etching of steel work with pH values between 5 and 7 and cannot remove those passivation layers from tungsten by dissolution. This is the reason why shaping of W failed in industrial electrolytes. The electrolyte systems, their intensive basic electrochemical investigations and properties are the basis for development of W machining by ECM. All results shown here were

achieved in aqueous two-component systems (TCEE) and the focus was set on drastic optimization of EDM-machined surfaces.

Developed ECM process variants

The evaluation of the general electro-chemical behavior of tungsten and the development of specific electrolytes opened the path for the development of ECM processing variant adapted to special needs in W machining. As process variants were identified three different branches in electrochemical machining and called M-ECM, C-ECM and S-ECM. The prefixes **M** and **C** are standing for the synonyms "Mask" assisted shaping and "**Cathodic**" / "**Copy**" deep etching structuring process method and **S** for "Surface" treatment processes [4].

S-ECM surface finishing

As generally known tungsten is a hard and brittle material at least at room temperature. Surfaces processed by conventional methods (e.g. EDM, milling) exhibit easily surface defects (microcracks) which will influence dramatically the life time in application due to crack growth at such positions. The structuring by M-ECM had shown that smooth surfaces were produced without any crack initiation centres. Based on this result a tool free surface was aspired by adapting ECM to these needs. The main difference to M-ECM is, that S-ECM is EC-etching of free, unmasked surfaces in order to achieve a smoothing effect of the affected surface by ablation of layers in dimensions of micrometers; this is also known as electro-polishing.

As depicted in Fig. 1 the required W components have very different shapes and sometimes also high geometrical complexity e.g. castellation with high aspect ratios, macroscopic curved shapes and different grain orientations. Already in M-ECM processing the impact of current intensity on shaping quality was shown. Deducted from these results it is obvious that parts with mixed geometrical surface components required specially developed parameter sets to obtain a homogeneous material removal at all position e.g. on the flat surface and inside of narrow gaps.

As reference geometries for the S-ECM development were selected:

a) Plain surfaces, b) pyramidal structures and c) gaps with high aspect geometries.

Because of the fact, that the performance of tungsten surfaces revealed as an important aspect, and based on the demand of corresponding suitable manufacturing methods, surface finishing was set in the focus of tungsten ECM in the report period.

Plain surfaces

The macroscopic geometric uniformity of plain surfaces (aspect ratio as quotient depth/width = 0) allow to adopt the current densities for electro-polishing up to the necessary maximal values. High currents allow minimizing the process time. The samples (disks, cylinders) required for qualifying the S-ECM process as surface finishing tool were cut from W-rod material of diameter 16 mm. Two types of conventional shaping, EDM (electro-discharge machining) and rough milling, were applied with the intention to produce significant defects. This type of raw material with additionally EDM machined trenches was also used for analyzing the applicability in finishing of castellated parts.

For evaluation of morphology effects S-ECM finishing was also performed with rough machined cuts from single crystals. S-ECM machining of crystals had the aim to produce mirror like surfaces and to demonstrate that a homogeneous material removal can be realized by appropriate selection of process parameters.

Fig. 2 gives the surface structure of the sample (PM-material, rough machined) as delivered with the clearly visible machining scratches and after S-ECM processing with slight materials removal by electrochemical erosion. The electrolyte was of type TCEE [5] and the applied current was 10 mA/cm^2 . It can be seen, that the machining scratches disappeared as desired however a slightly rough structured surface remained. This indicates that only in macroscopic scales (some μm) homogeneity was obtained and that top levels were not dissolves preferably. One of the reasons may be here the anisotropy of the material and the soft (low current) polishing. However, the dangerous microcracks (crack centers under operational load) introduced by mechanical machining were completely removed.

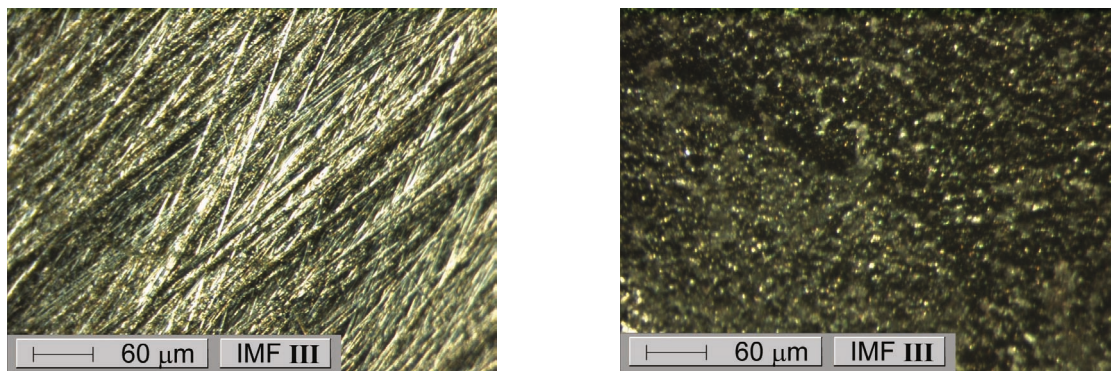


Fig. 2: Rough polished surface, a) before and b) after S-ECM with a removal of $50 \mu\text{m}$.

At the surfaces of single-crystal tungsten samples, differences in the effects of electro-polishing became evident, which is caused by the different metallurgical structure / morphology. For S-ECM of such surfaces, the suitable parameters for S-ECM elaborated at PM-processed rod samples, had shown a significant different impact. Mirror-like surfaces could be obtained in machining (Fig. 3) by variation of current densities to higher levels.

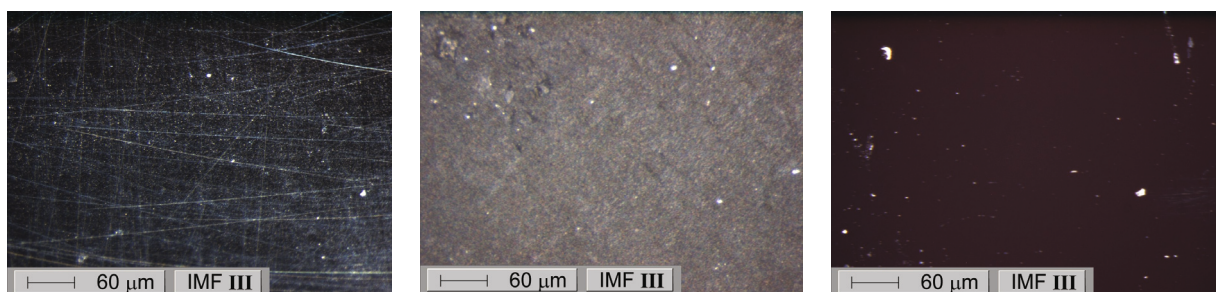


Fig. 3: Electrochemical surface machining of single crystals
a.) blank and ground surface as delivered;
b.) S-ECM, same parameters as for sample in Fig. 2 b,
c.) Mirror-like surface by S-ECM with higher current density by factor 10.

The depicted surface views of PM-material and W single crystal demonstrate successfully, that surfaces with several defects and/or traces from fabrication can be smoothed and that dangerous cracks can be removed.

Surfaces with three-dimensional structures

In contrast to plain samples, structured surfaces are much more challenging in processing. A special case is the electro-chemical treatment of "triangular", low aspect ratio surface structures, i.e., three-dimensional pyramidal structures, were the surface consisted of pyramids of $0,5 \times 0,5 \times 0,5 \text{ mm}$ (Fig. 4). They had been manufactured by EDM from the cross section surface of 16 mm rods. Besides the demand of removal of the EDM-typical known defects, a further problem to be solved was the incorporation of copper from the EDM tool into the structured tungsten metal surface.

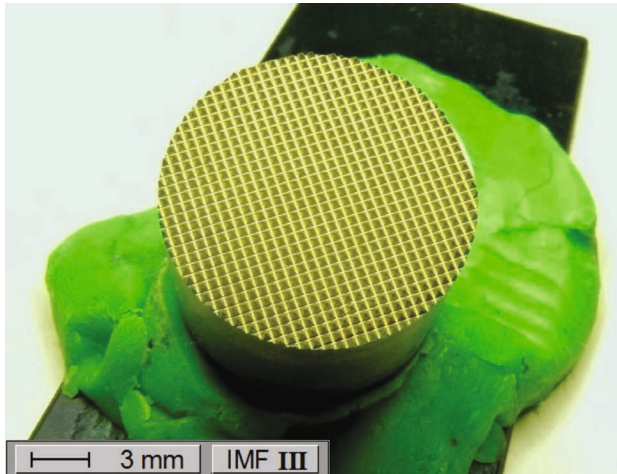


Fig. 4: Three-dimensional structured surface by an array of 580 tetragonal pyramids (each $0.5 \times 0.5 \times 0.5$ mm). Copper of the EDM causes yellow colour on tungsten surface.

To perform surface finishing by S-ECM, the electrolyte has to fulfil the requirements in combining the ability of copper dissolution with the ability of a homogeneous surface ablation, but without general smoothing to an unstructured flat plate. The electrolyte of type TCEE showed the ability to remove the Cu contamination in parallel. However the additional challenge from the electrochemical view was the request of contour accuracy. The sharp vertices of the pyramids describe highly accentuated positions, were dissolution under S-ECM conditions would occur preferentially (the basic principle of flattening in electro-polishing); but in the case of the pyramidal structure, this has to be avoided.

Consequently, the approved and established S-ECM parameters as described above for flat surfaces could not be used. Also reductions of concentrations in the TCEE agent were not appropriate, due to the needed feasibility of copper dissolution. Thus other parameters more acting with the physical nature of the ECM process had to be changed for a suitable combination to increase surface dissolution between the pyramids and the ground under preservation of the three-dimensional structure.

First good results appeared by application of reduced current densities in a fitting combination with forced convection. Fig. 5 depicts the view on a pyramidal structured W piece as machined by EDM with the Cu coating and after processing by S-ECM with small current densities. Clearly visible are the dissolution of the Cu scale and the retention of the sharp pyramids structure.

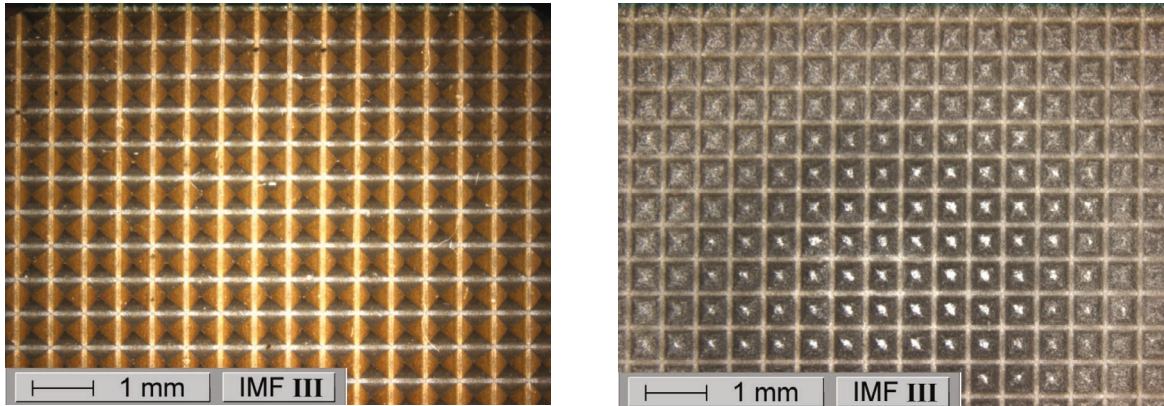


Fig. 5: Three-dimensional structured before and after S-ECM.

High aspect ratio structures

The reference design of the He-cooled divertor depicted in Fig. 1 has as direct plasma facing component a castellated tile worked from pure tungsten. The castellation has cuts with depth of roughly 3 mm and trench widths of 0.3 mm. Performed HHF tests, compare ref [1], had shown that defects with dimensions of up to 100 μm , introduced by conventional machining, lead to early failure. Especially EDM cut trenched in tiles were recognized as starting points for cracks. Compared to flat or also the pyramidal structured surfaces, castellated tiles exhibit a structure of high aspect ratio (HAR). Although the basics of C-ECM technique are quite the

same, there was the need to elaborate new sets of parameters for the electro-polishing of work-pieces in complex geometries with high aspect ratio >10: The electro-chemical challenge arises by the transition from convection into pure diffusion control, which reduces ECM dissolution rates by a factor of 5.

The trench width of 150 µm (depicted in Fig. 6) does not allow any convection in deeper regions or especially at the ground of the trenches, were the typical dangerous EDM defects are situated. The limiting boundary of diffusion does not allow applying the usually high currents as in S-ECM of flat samples, because an overrun of the limited current would increase the electric potential and therefore, initiate automatically the next possible electrochemical reaction. This is the anodic decomposition of water, with evolution of gas, which blocks the trenches by gas bubbles.

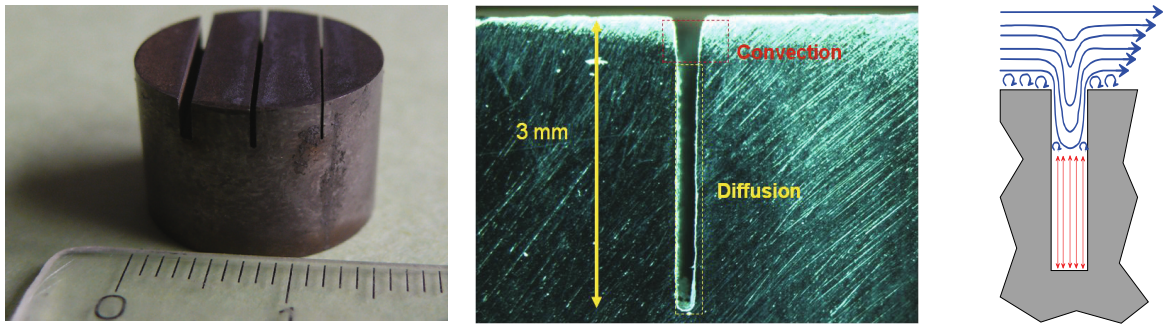


Fig. 6: HAR tungsten sample and electrolyte transport therein.

In this application currents have to be adapted also to diffusion parameters of the erosion products in the electrolyte (which is in M-ECM or plain S-ECM absolute not relevant). Optimized S-ECM by a development of a combination of reduced currents with the process time was observed in trenches with aspect ratio of 20. In the first series with currents reduced under the critical voltage of gas evolution, it could be proven, that a removal of tungsten takes place down to the lateral positions.

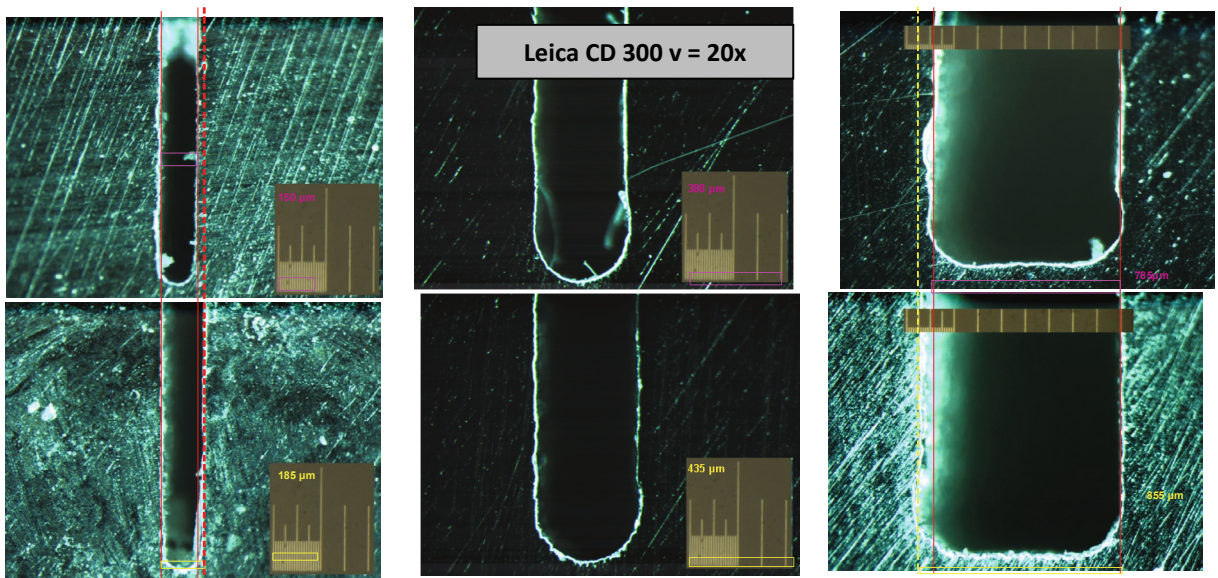


Fig. 7: Series of S-ECM in trenches.

Fig. 7 depicts the cut trough a trench machined by EDM (top line) and subsequently finished by S-ECM (bottom line). Clearly visible is (e.g. from pictures in the centre) that a homogeneous broadening of the trenches takes place by roughly 20%. The removal of material at the bottom of the trench was measured to be above 100 µm; enough to remove microcracks.

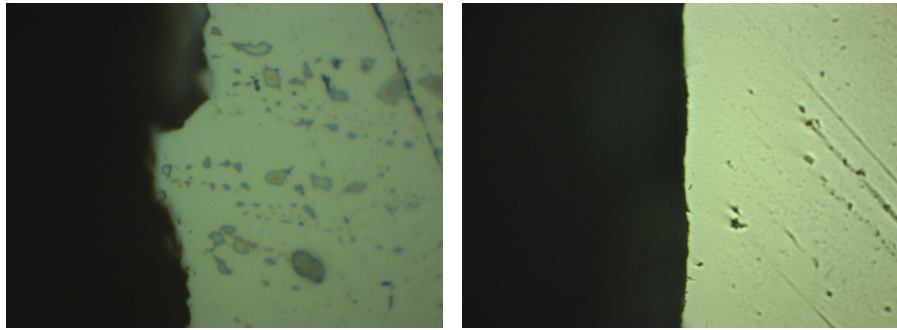


Fig. 8: Smoothing of wall surfaces in the trenches, left EDM machined, right S-ECM finished.

The micrographs given in Fig. 8 illustrate the vertical structure of the trench wall before and after S-ECM processing. The top levels are dissolved and a smooth wall surface is produced. Due to required optimization (working with low current densities and forced convection) the whole finishing of trenches is determined mainly by the process time. Applying a sufficient processing time lead to the complete removal of cracks in the lateral ground regions of the trenches as can be seen in Fig. 9.

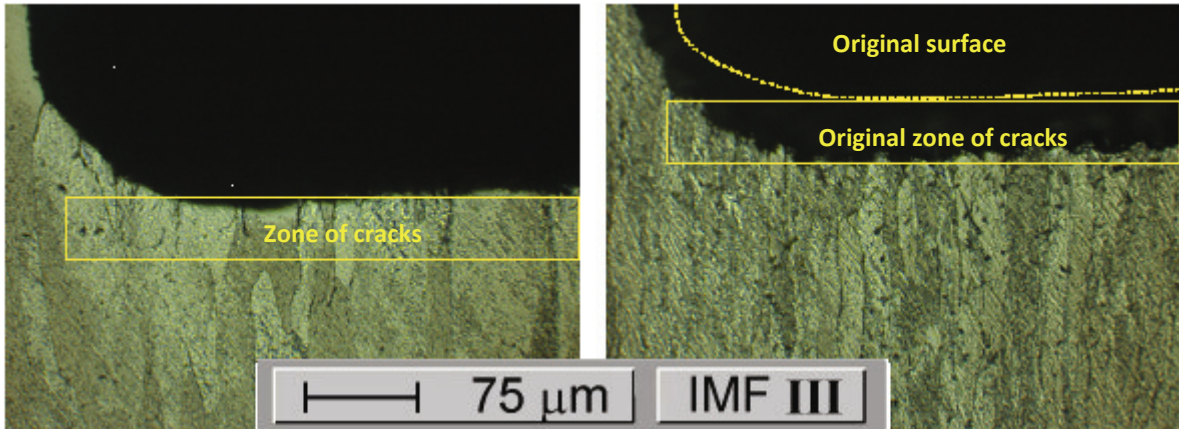


Fig. 9: Effect of S-ECM in the ground of trenches.

Conclusions

The development of the two component electrolyte (TCEE) opened the path for large area processing and shaping of tungsten for the first time. Meanwhile three different branches in ECM processing were selected and developed. Due to the different main application fields (surface finishing by S-ECM, mask assisted surface structuring M-ECM and 3D shaping by cathode tool dissolution C-ECM) the processing parameters have to be adapted to each processing line separately. The development of C-ECM and S-ECM showed that a variation of the electric regime, e.g. pulse sequences will be the right path for process optimization. This is the main (mid-term) objective in the current research program on S-ECM and C-ECM.

The general result of investigations concerning electro-polishing (S-ECM) are, that tungsten surfaces in different geometrical features can be optimized by suitable parameters, which were demonstrated by selection of the concrete structure element. It was additionally shown that surface layers remaining from pre-shaping by EDM or mechanical tooling can be removed in parallel. The essential benefit by soft ECM processing was the electro-chemical abrasion of damaged / microcracks containing surface near areas and this also at the ground of deep cuts.

The use of HF pulse currents lead to a drastic advancement in processing time and of the accuracy of shaping. This pulsed current processing will be further developed in the next time especially in C-ECM.

The future aim is to make ECM technology available for industrial fabrication of all W components as innovative and reliable process. For this purpose, first contacts to ECM manufacturers were realized.

Staff:

N. Holstein
J. Konys
W. Krauss
J. Lorenz

Literature:

- [1] P. Norajitra, R. Giniyatulin, T. Ihli, G. Janeschitz, W. Krauss et al., He cooled divertor development for DEMO, Fus. Eng. Design 82 (2007) 2740-2744
- [2] W. Krauss, N. Holstein, J. Konys, I. Mazul, Investigation of the impact of fabrication methods on the micro-structure features of W-components of a He-cooled divertor, Fus. Eng. Design, Vol. 81, 1-7, (2006), pp. 259-264.
- [3] W. König, F. Klocke, Elektrochemisches Abtragen (ECM), Fertigungsverfahren, Vol. 3, Springer, (1997), pp. 91-121.
- [4] N. Holstein, W. Krauss, J. Konys; Structuring of tungsten by pulsed ECM processes for He-cooled divertor application; Fus. Eng. Design, 83 (2008) 1512–1516
- [5] W. Krauss, J. Konys, N. Holstein, J. Lorenz, Electrochemically based machining and joining development for He-cooled divertor; IEA-W-Satellite Meeting at ICFRM-14, Sapporo, Japan, 8th September 2009.
- [6] N. Holstein, W. Krauss, J. Konys, Advanced electrochemical processing of tungsten components for He-cooled divertor application, ISFNT-9, Dalian, China, , 12-16. Oct. 2009

Acknowledgement

This work, supported by the European Communities under the contract of Association between EURATOM and Karlsruhe Institute of Technology, was carried out within the framework of the European Fusion Development Agreement. The views and opinions expressed herein do not necessarily reflect those of the European Commission.

Development of W-EUROFER & W-W Brazed Joints. Commercial Joints Deposited by Electro-chemical Methods: (i) Aqueous Electrolytes and (ii) Organic Electrolytes (WP08-09-MAT-WWALLOY, Activity 1)

Introduction

For application in a fusion power system a helium cooled divertor concept is investigated, which is projected to remove heat loads of up to 15 MW/m^2 . This divertor design is based on a modular arrangement of cooling fingers, which is to be fabricated from a heat resistant material like tungsten alloys. From the plasma facing material (tile) with the highest temperature (approx. 1700°C at the surface), the heat is transferred via tungsten alloy e.g. WL10 (acting as structural material) to the cooling gas He. In the lower part the W-alloys are connected to the steel base fabricated from pure or ODS EUROFER.

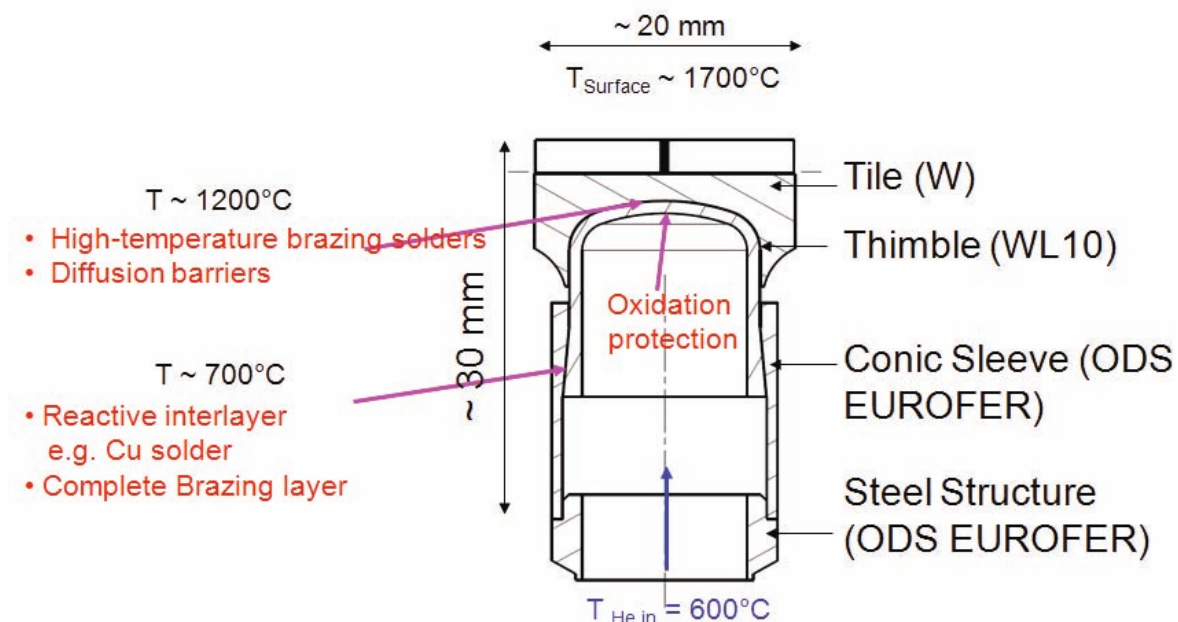


Fig. 1: Positions in the divertor finger lay out for brazing layers.

For such a purpose all these components must be connected precisely, and also must withstand high mechanical and thermal stresses without any danger of failure. This duty shall be done by brazing materials, where the solders besides a force-fit connection guarantee also a certain ability to compensate mechanical stresses coming from the highly different thermal expansion coefficients.

Two positions in the divertor are of special interest:

- The connection between Tungsten tile and tungsten/WL10 thimble in the upper part of the finger design. This connection has functional characters and must withstand temperatures of approx. 1250°C ; here exists a high chemical metallurgical similarity of the both metal sides, but the high temperatures reduce drastically the choice of convenient materials for brazing.
- The connection between tungsten thimble and steel sleeve (ODS EUROFER) at lower position. The operation temperatures are about 700°C ; but here the connection underlies high pressure forces (80 bar cooling gas pressure). The connection must be gastight, furthermore stable also under cyclic conditions with repeated cold-warm changes. Fig. 2 shows the cross section of such an arrangement.

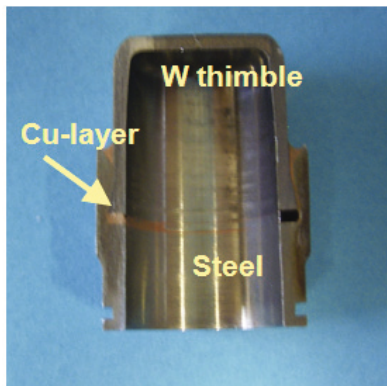


Fig. 2: Cross section of a joined thimble-steel combination by copper casting.

Here, the differences in thermal expansion coefficients are drastic, and the metals with completely different chemical properties have to be connected by a solder with a contact affinity to both sides. In the illustrated assembling the Cu is casted into the gap but no brazing to tungsten takes place. If Cu should be used as filler metal a functional scale on top of the tungsten part is required to allow a metallurgical reaction and alloy formation for good adherence. Nickel may be such a metal which has affinity to both copper and tungsten.

For the suitable brazing solders materials arises the question to manufacture the layers selectively at the desired positions, even with a high degree of uniformity and reproducibility. In the light of the needed numbers of divertor units, which have to be produced in mass-production, also economic aspects are not negligible.

Electrochemical metal deposition

Electro-chemistry allows the deposition of metallic layers on a solid substrate from a liquid system. Galvanic depositions from aqueous systems generally take place in temperature regions of $< 100^{\circ}\text{C}$. So far, the electroplating does not affect the substrate by thermal forces. Moreover, because of the fact, that the deposition takes place from a liquid system under normal pressure without any further force (besides the electric voltage), the solid substrate material is not affected by any mechanical stresses; which is important for brittle substrate materials. Electro-chemical deposition is also one of the few techniques, where deposition on the surface all over the substrate can take place simultaneously.

Liquid media (electrolytes) in electro-chemical technology are mostly based on aqueous systems, and for some other metals liquid organics, but aprotic media, are used. The first group comprises the transition metals e.g. iron, copper, silver, nickel and chromium, which are used in electro chemical coating technology and electroforming since long times, so that there is a high degree industrial application and the mass production logistic. But this counts only for standardized applications with tasks to deposit such metals on common substrate materials (related transition metals or alloys). Tungsten and its alloys are in electro chemical coating technique not such a common material. All technical electrolytes used in industrial coating technique exhibit mostly acidic pH-values, in which tungsten easily forms passivating oxide layers.

Targets of brazing development

For the task of joining investigations were carried out comprising following aspects:

- Development of electro-chemical technologies based on commercially known filler compositions from aqueous systems for brazing of divertor components. The main goals are here analyzing deposition on tungsten and brazing conditions incl. the metal / filler reactions under load.
- Development of surface conditioning tools for coating of tungsten, multi-layer deposition of e.g. Ni and Cu, as well as analyzing of inter-diffusion during heat treatment up to 1100°C .
- The third main step is development of electro-chemical coating technologies for deposition of 'refractory metals', suitable for designing advanced brazing metals under fusion aspects. The name 'refractory metals' indicate here elements like W, Ta to Ti which cannot be deposited from aqueous electrolytes due to their chemical and electrochemical nature. The technological challenge is to evaluate appropriate electrolytes of type ionic liq-

uids (IL) and IL-metal combinations in conjunction with adjusted concentrations and current/voltage parameters for deposition.

Results

Substrate surface characterization and pretreatment

The nature of the tungsten substrates, which commonly are cut by EDM, became an important aspect for the deposition. EDM cuts reveal often a very distorted surface, as can be seen in Fig. 3 a / left side, with cracks of about 30-100 μm and reacted surface layers. These surface films have to be removed to guarantee a good wetting by the electro-chemically deposited scales. Thus, a pre-treatment process based on (electro) chemical etching technology for the machined tungsten parts was analyzed. Valuing process stability, availability in industries and environmental aspects an etching media based on $\text{K}_3[\text{Fe}(\text{CN})_6] \cdot \text{KOH}$ was selected, which showed best homogeneous scale removal and only small surface roughing. The electrochemical Ni deposition using an electrolyte with excellent moulding behaviour as proven in micro system technology shows clearly the still present microcracks introduced by EDM processing. The deposited nickel infiltrates the fine cracks and pronounces their presence as illustrated in Fig. 3 right side.

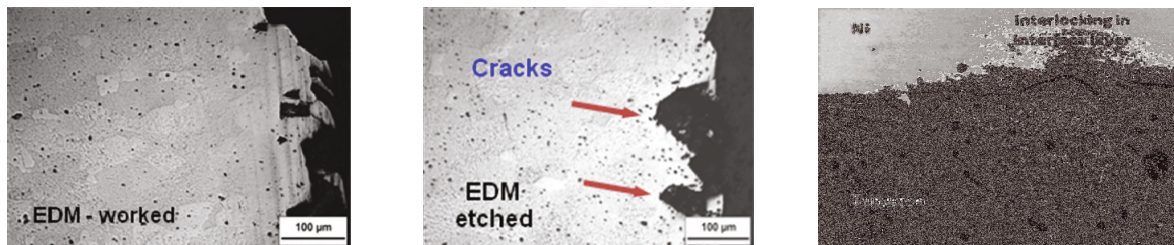


Fig. 3: Tungsten surfaces in dependence of processing steps.
Left: Tungsten surface as EDM-cut; Centre: Tungsten surface after additional short time etching with some still visible microcracks;
Right: EDM machined and etched tungsten surface with electro chemically deposited Ni scale.

From aqueous systems deposited nickel on tungsten

The pre-treatment of tungsten parts was done applying an alkaline hexcyanoferrate solution as suitable etchant for the nickel deposition. The electrolyte for nickel deposition consisted of a mixture of 410 ml/l commercial nickelsulphamate (76 g/l Ni^{2+}), 35 g/l Boric acid, 0.15 g/l fluorinated tensile and a non dimension-stable nickel anode. Further deposition parameters were $T = 52^\circ\text{C}$ and $\text{pH} = 3.3\text{--}3.5$. The current density with homogeneous coating behaviour was found to be in the range $I = 10 \text{ mA/cm}^2$. The scale thickness is adjustable easily by deposition time in the range 5 to 100 μm depending on the requirements of joining.



Fig. 4: Nickel layers on tungsten deposited from aqueous electrolyte.

The sequence of micro cuts given in Fig. 4 illustrate the high uniformity and good adherence of deposited Ni-coatings on tungsten. Especially the picture in the centre of Fig. 4 indicates

the excellent coating of corners and the high scattering ability of the electrolyte by applying only flat nickel anode for scale deposition on the cathodically switched work piece. The whole evaluation of electrochemical Ni deposition showed that the pre-treatment by etching is essential to obtain homogenous scale deposition.

From aqueous systems deposited Cu-Ni multilayers on tungsten

Due to the immiscibility of copper and tungsten it is not possible to use copper on tungsten as a brazing layer. Therefore it had to be investigated, how copper cold be bound via an intermediate metal e.g. Ni (as model substance), which is miscible with tungsten. A condition was, to deposit only the minimal necessary amount of Nickel, due to its "high" activation under neutron radiation. To analyze in general the processes and mechanisms occurring under thermal treatment (annealing, brazing) the scale thickness of the Ni scale was set in first tests to approx. 200 μm in thickness. Later on scale thickness was reduced step by step to roughly 5 μm to evaluate minimal thickness limits.

On this functional nickel layer the filler metal copper was deposited from a sulphuric acid electrolyte. Optimal copper layers were achieved from 120 g/l CuSO_4 in 120 g/l H_2SO_4 ; 0.19 ml/l HCl; 10 ml tensile Solution Primus CD KN 438021. A copper anode was applied to keep Cu concentration stable in the electrolyte; the used current density was 30 mA/cm^2 at room temperature.

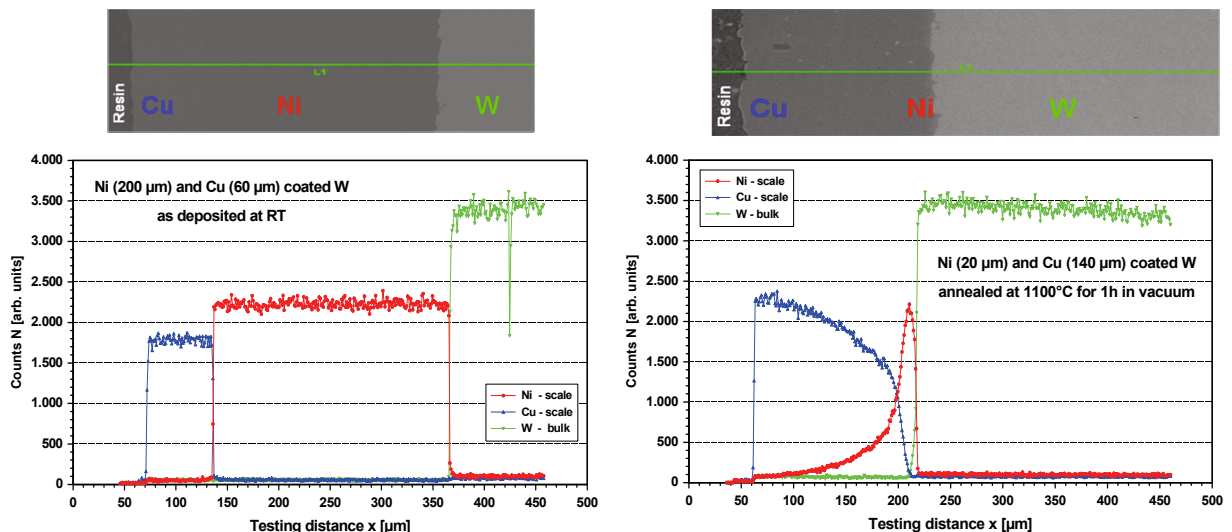


Fig. 5: Line scans and REM pictures of Ni-Cu multilayer deposited on tungsten before and after heat treatment.

EDX-linescans of multilayer coating are given in Fig. 5 for the conditions as deposited and after heat treatment. The scan of the sample as deposited shows a clear separation of the different metals (no diffusion zone) and delivers together with the REM picture the information that a good adherence is present without pores or gaps. The pictures given on the right side of Fig. 5 illustrate the situation under joining conditions using a functional Ni scale of 20 μm on tungsten and brazing by copper at 1100 °C. A small reaction is visible in the W-Ni boundary with diffusion of tungsten into the Ni-scale. A good mixing and alloy formation took place at the boundary copper to nickel. Roughly half of Ni diffused into the filler metal Cu. This indicates that the thickness of the functional Ni scale should not be much below 10 μm if complete brazing process lasts about 30 min. REM picture and line scan indicate a successful joining behaviour. In the next step the tungsten will be joined by this electro chemically deposited multilayer system to EUROFER.

Deposition from non-aqueous electrolytes e.g. W deposition

In comparison to transition metals like Fe and Ni, tungsten is by its electrochemical standard potentials much more noble, and therefore, should be in theory better applicable in electrochemical deposition technology. But the standard reaction is bound to a reaction with water and intermediate formation of tungsten hydroxides. As result, the aqueous deposition of tungsten from water is more or less workable, but the deposition of pure tungsten metal not realizable, due to incorporation of a high percentage of oxides.

Here the absence of water during deposition is afforded. Such aprotic electrolytes were mostly molten salt systems in the past with all the disadvantages of high temperature electrolyte systems. Electrolytes of type ionic liquids (IL), which are also molten salt systems, but with drastic reduced melting temperatures, can open new paths in electrochemical deposition if a suitable combination of IL and metal salt can be designed / evaluated for deposition of refractory metal e.g. W, Ta or Ti. Due to the good knowledge of tungsten behaviour in ECM processing (Electro Chemical Machining) tungsten was selected as model alloy out of the refractory metals for deposition from the new class of electrolytes.

The used Ionic Liquid was the first commercial available IL, Ethyl-Methyl-Imidazolium Chloride (EMIM-Cl), which revealed already as a suitable electrolyte type for Al-deposition on EUROFER for formation of corrosion and tritium permeation barriers [2].

The investigation of the EMIM-Cl tungsten systems revealed drastic differences to Al systems. The mixed EMIM-Cl and WCl_6 as tungsten carrier does not form a room temperature liquid, but rise the melting point up to 120 °C (pure EMIM-Cl: 80 °C). As consequence, low viscous solutions can not be handled below 150 °C working temperature.

The affinity of tungsten deposition from such systems is higher as for Al from Al-systems (measured as the mole ratio solvent to salt), so it was possible to deposit metallic layers from the system EMIM-Cl / WCl_6 = 1 / 0.5 for the first time. Fig. 6 shows the top view on a successfully deposited tungsten scale with a thickness of roughly 20 µm. This result indicates that the electrolytes of type IL open the path for electro-chemical deposition of refractory metals which can be used as diffusion barriers in brazing or as filler metals directly. It has to be considered in the next steps of the development work that EMIM-Cl has not to be the best IL in coating development and that additional potentiometric measurements are absolutely necessary to determine optimized deposition parameters for improved scales.

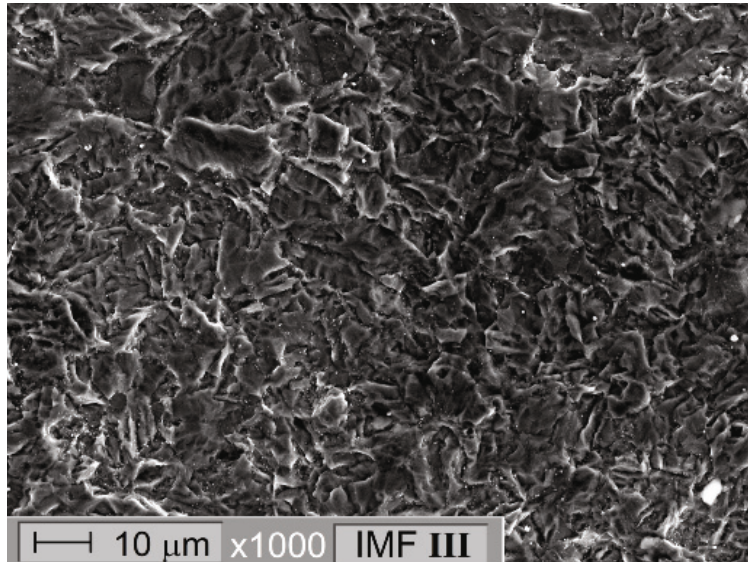


Fig. 6: SEM of tungsten layer on EUROFER steel.

Conclusion

The development of suitable and long term stable joints for He cooled divertor fingers is essential for the successful operation of this design. Challenging are both required joints the steel / W alloy combination due to the high expansion mismatch and the strong differences in alloy characteristics and the high temperature brazing of the W alloys between tile and thimble. The general screening has shown the needs for functional interlayers to allow brazing instead of only casting or to suppress unacceptable diffusion reactions and last not least the homogenous coating and complete wetting of surfaces to be joined.

Driven by this facts and requirements of He cooled finger joining the development of electro-chemical coatings was started. In the first step commercially used filler metal combinations were selected for the deposition process. As electrolytes water based systems were investigated. The performed tests showed that especially tungsten has to undergo a surface cleaning and conditioning due to oxide / hydroxide scales before any coating is performed. It was demonstrated that copper brazing instead of only casting of tungsten can be applied if functional scales were deposited on tungsten. Performed heat treatments and pre-brazing studies imply that such scales may be in the dimension of roughly 10 µm. A homogeneous coating of tungsten was successfully achieved by Ni deposition as functional inter layer which was subsequently electro chemically coated by a Cu layer which acts as filler metal in tungsten – EUROFER brazing. The performed analyses indicate a high rate of reproducibility and excellent wetting of the joining parts a condition for defect free brazing. This positive results in application of electro chemical deposition of coatings point out that this technology can be applied in combination with fusion relevant alloys like tungsten and EUROFER steel. Modification of filler metals and functional scales (e.g. Fe instead of Ni) will be the focus of next steps in the development of electro chemical brazing tools from aqueous systems.

Diffusion barriers and high temperature fillers require combinations of / or with refractory metals (e.g. W, Ta or Ti type). However, these elements can not be deposited from aqueous electrolytes due to e.g. oxide formation. Thus an alternative and innovative development line in electro chemical deposition technology based on the use of novel ionic liquids as electrolytes was started to have access to the unique properties of these elements in high temperature application. For first evaluation of the applicability of IL as electrolytes the aprotic component EMIM-Cl was selected. Basic potentiostatic investigations were performed in combination with metal salts e.g. WCl_6 to demonstrate and verify the applicability and syntheses of electrolytes suitable for metal deposition in general. Based on these successfully performed pre-tests tungsten deposition from electrolytes liquid near room temperature could be performed for the first time. The deposited tungsten scales had a thickness of roughly 20 µm and good adherence to the base material EUROFER steel. The further development in aprotic systems will include also other IL and refractory metals with focus high temperature W&W alloy brazing.

Staff:

N. Holstein
J. Konys
Dr. W. Krauss
J. Lorenz

Literature:

- [1] N. Holstein, W. Krauss, J. Konys, Development of advanced processes for Al-based anti corrosion and T permeation barriers, Fus. Eng. t be published
- [2] W. Krauss, N. Holstein, J. Konys, H. Zimmermann, Al-based anti-corrosion and T-permeation barrier development for future DEMO blankets, Fus. Eng. to be published

- [3] W. Krauss, J. Konys, N. Holstein, J. Lorenz Electrochemically based machining and joining development for He-cooled divertor; IEA Implementing Agreement for Fusion Materials Development, W-Satellite Meeting, 8th September 2009, ICFRM-14 Sapporo, Japan
- [4] W. Krauss, J. Konys, N. Holstein, J. Lorenz, Alternative processing routes – Electrochemical processing and coating techniques, 17th European Fusion Physics Workshop, Hungary, 7th to 9th December 2009

Acknowledgement

This work, supported by the European Communities under the contract of Association between EURATOM and Karlsruhe Institute of Technology, was carried out within the framework of the European Fusion Development Agreement. The views and opinions expressed herein do not necessarily reflect those of the European Commission.

Nuclear Data

Nuclear Data: Benchmark Experiments to Validate EFF/EAF Data (EFDA/07-1704-1631 (TW6-TTMN-002B))

Overall objective: The overall objective of Task TW6-TTMN-002B was to provide the experimental data base required for the validation of the nuclear data libraries EFF (European Fusion File) and EAF (European Activation File) developed in the frame of Task TW6-TTMN-001B of the EU Fusion Technology Programme. According to the programme orientation on ITER (TBM) and IFMIF, the focus was on activities devoted to the experimental validation of TBM design calculations by means of a neutronics mock-up experiment and cross-section validation experiments relevant for IFMIF.

Deliverable 2

Measurements of the tritium production and neutron and gamma spectra in the neutronics HCLL TBM mock-up by a second experimental team

Background

A dedicated neutronics experiment [1 -3] has been previously performed on a mock-up of the Helium-Cooled Pebble Bed (HCPB) Test Blanket Module (TBM) with the objective to validate the capability of the neutronics codes and nuclear data to predict nuclear responses, such as the tritium production rate (TPR), with qualified uncertainties. In the frame of TW6-TTMN-002B, a follow-up experiment on a mock-up of the Helium-Cooled Lithium-Lead (HCLL) TBM has been performed [4]. Fig. 1. shows schematic views of the HCLL mock-up prepared at ENEA Frascati with LiPb bricks.

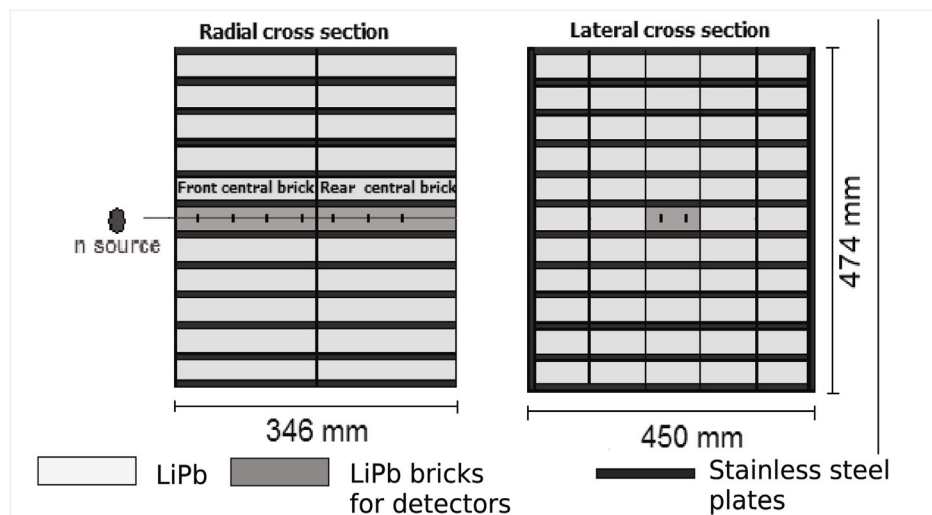


Fig. 1: Experimental LiPb assembly (2D schematic views).

Experiment

The TPR was measured at the Frascati Neutron Generator (FNG) laboratory of ENEA Frascati and the HCLL mock-up was then shipped to the TU Dresden (TUD) neutron laboratory for measurements of the fast neutron and γ -ray flux spectra.

Tritium production rates were measured with two methods:

1. a procedure involving pellet detectors made of Li_2CO_3 and liquid scintillation counting techniques.
2. a combination of LiF thermoluminescence detectors (TLD) with natural isotopic composition of Li and enriched in ^{7}Li (99.99%).

The TPR value was obtained from the dose deposited in the LiF TLD which is mostly due to the tritons and α -particles emitted in the tritium producing reactions. A combination of LiF-TLDs of natural lithium composition and others depleted in ^{6}Li was used to cancel contributions from γ -rays etc. in each measurement position. This method is considered more sensitive than the TPR measurement technique with the Li_2CO_3 pellet detectors and allows for faster detector processing after irradiation. Fig. 2 compares the tritium production rates measured in the Li_2CO_3 pellets by the ENEA and TUD teams as function of the penetration depth in the mock-up and calculated by the MCNP code with JEFF-3.1 data.

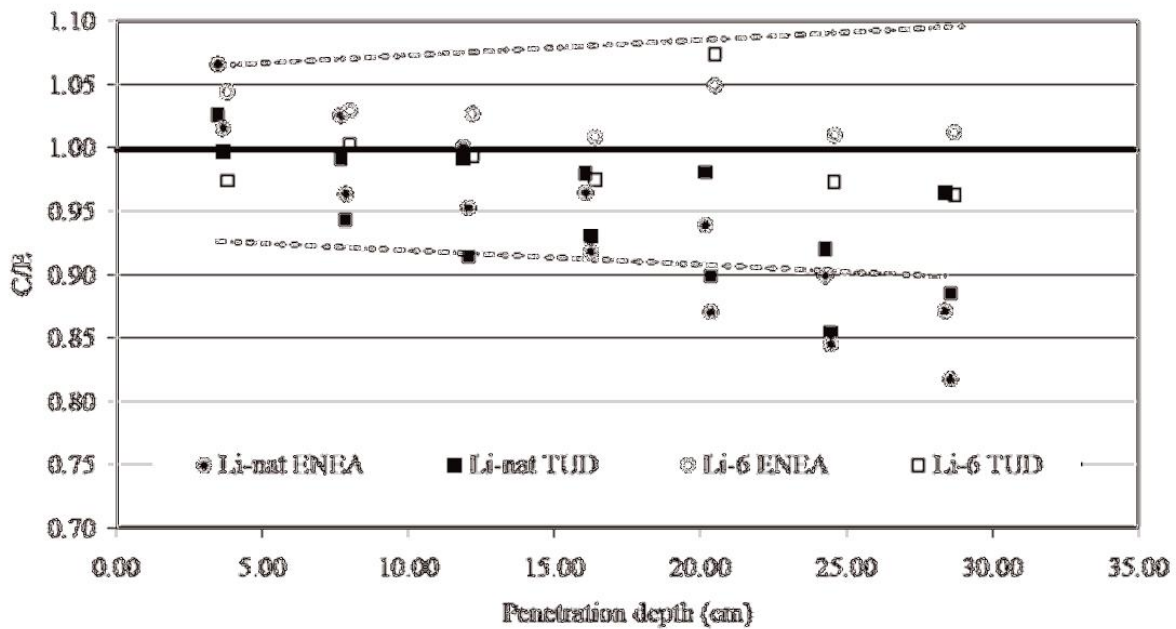


Fig. 2: Calculation/Experiment (C/E) comparison of the tritium production rate measurements using Li_2CO_3 pellets and the JEFF-3.1 nuclear data library.

Fast neutron and gamma-ray flux spectra were measured at the TUD neutron laboratory using a slightly modified mock-up assembly as compared to the tritium production rate measurements performed at FNG: The central channel, which accommodated the tritium detectors, was replaced by solid LiPb bricks. A dedicated channel with a square cross section of $5 \times 5 \text{ cm}^2$ was prepared perpendicular to the central axis of the mock-up (as defined by the deuterium beam of the neutron generator) from five bricks of LiPb. This channel served to accommodate the NE-213 detector and the ^3He proportional counter. By exchanging the rear bricks with the front bricks of the middle lithium-lead layer, two separate measurement positions A and B, 16.5 and 18.1 cm from the front of the assembly, respectively, were realized.

Fast neutron and gamma ray flux spectra were obtained by means of the cylindrical NE-213 scintillator with 3.25 cm diameter and thickness. The scintillator was coupled to a photomultiplier with a 50 cm long waveguide. Pulse shape discrimination techniques together with multi-parameter acquisition were used to separate recorded neutron events from events caused by gamma rays. The raw pulse height spectra obtained were unfolded with the MAXED code and response matrices experimentally obtained for this detector.

Figures 3 and 4 show the resulting experimental spectra in comparison with those calculated by the MCNP code using JEFF-3.1 nuclear cross-section data.

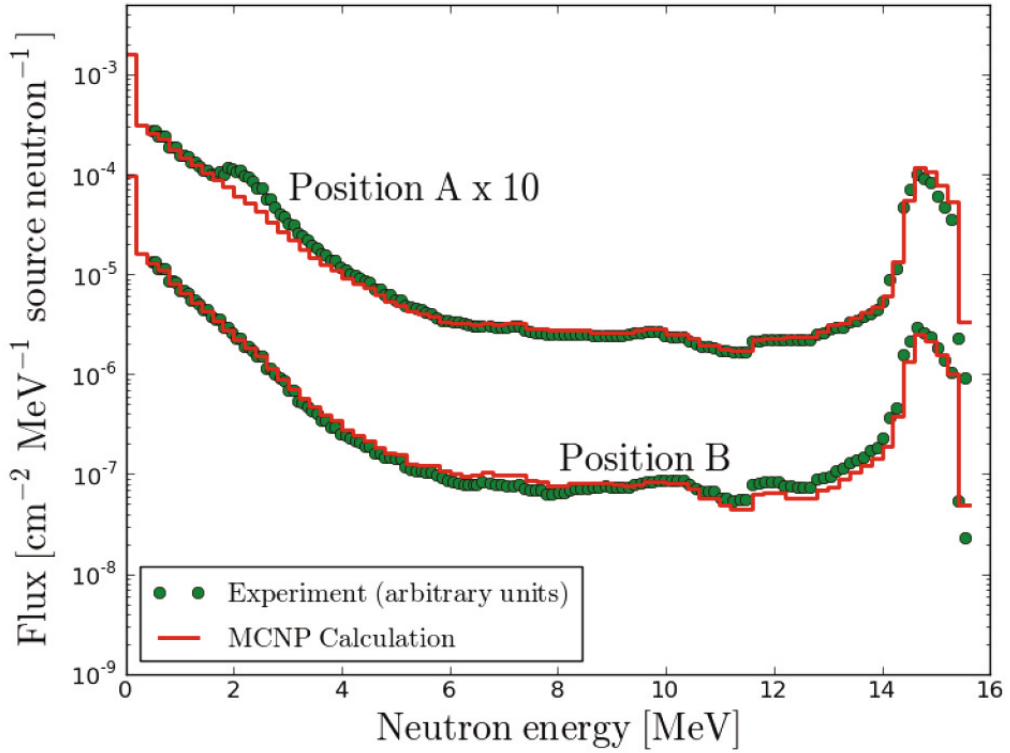


Fig. 3: Unfolded neutron spectra measured in the LiPb assembly for the positions A and B compared to the results of MCNP calculations with FENDL-2.1 data.

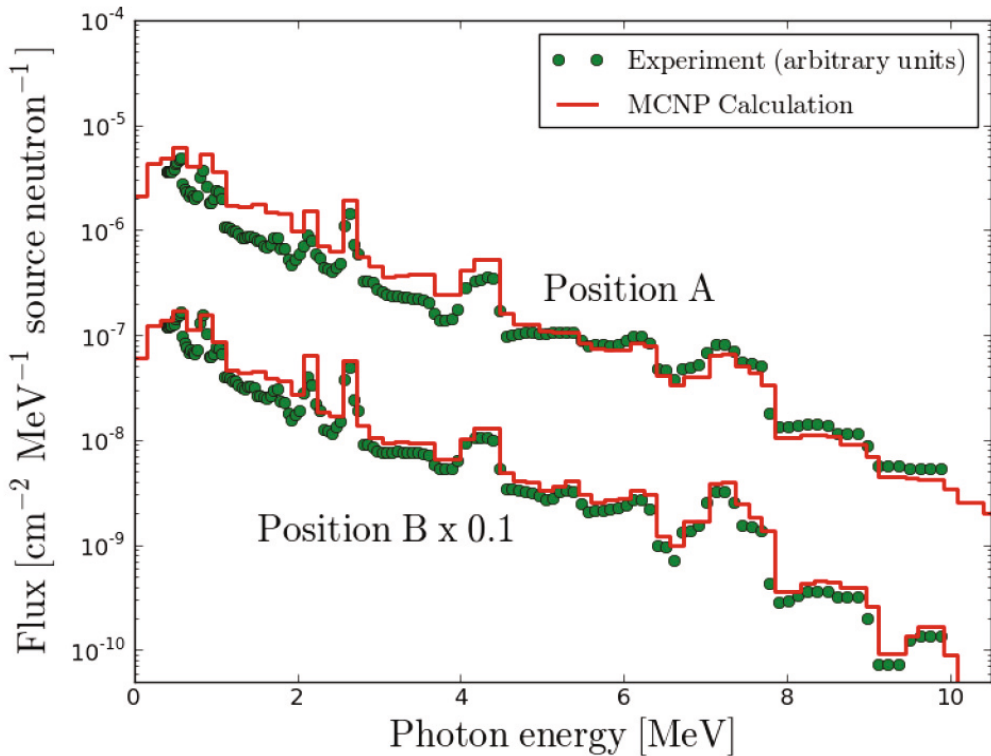


Fig. 4: Unfolded photon spectra measured in the LiPb assembly for the positions A and B compared to the results of MCNP calculations with JEFF-3.1 data.

Staff:

J. Henniger (TU Dresden)
A. Klix
D. Lebrun-Grandié
M. Sommer (TU Dresden)

Literature:

- [1] K. Seidel, P. Batistoni, U. Fischer, et.al., "Measurement and analysis of neutron and gamma-ray flux spectra in a neutronics mock-up of the HCPB Test Blanket Module", Fus.Eng.Des. 82 (2007) 2212-2216
- [2] D. Leichtle, U. Fischer, I. Kodeli, et.al., "Sensitivity and uncertainty analyses of the tritium production in the HCPB breeder blanket mock-up experiment", Fus.Eng.Des. 82 (2007) 2406-2412
- [3] P. Batistoni, M. Angelone, L. Bettinali, et.al., "Neutronics experiment on a helium cooled pebble bed (HCPB) breeder blanket mock-up", Fus.Eng.Des. 82 (2007) 2095-2104
- [4] P. Batistoni et al, "Neutronics experiments on HCPB and HCLL TBM mock-ups in preparation of nuclear measurements in ITER", 9th Int. Symp. on Fusion Nuclear Technology (ISFNT-9), Dalian, China, October 11-16, 2009
- [5] A. Klix, H. Freiesleben, J. Henniger, et.al., "Blanket mock-up experiment with a LiAlPb assembly irradiated with 14 MeV neutrons in preparation of the HCLL-TBM neutronics experiment", Fus.Eng.Des. 83 (2008) 1813-1817
- [6] A. Klix , P. Batistoni, R. Böttger, D. Lebrun-Grandié, U. Fischer, J. Henniger, D. Leichtle, R. Villari, Measurement and Analysis of Neutron Flux Spectra in a Neutronics Mock-up of the HCLL Test Blanket Module, 9th Int. Symp. on Fusion Nuclear Technology (ISFNT-9), Dalian, China, October 11-16, 2009

Deliverable 4

Monte Carlo based transport and sensitivity/uncertainty pre-analysis of neutron flux spectra and tritium production measurements in the neutronics HCLL TBM mock-up

The objective of this deliverable was to perform computational analyses of the neutron flux spectra and of tritium production rates (TPR) in Li_2CO_3 pellets of the HCLL mock-up experimental setup at the Frascati Neutron Generator. It comprises neutron transport, sensitivity and uncertainty calculations based on a Monte Carlo approach.

The analyses of the TPR proceeded in the following way: (i) Calculation of the TPR in the pellets using a detailed three-dimensional geometry model of the experimental set-up including the neutron generator, the HCLL mock-up with measurements equipments, assembly support and experimental hall; (ii) Sensitivity calculations for the pellets stacks to assess the sensitivity of the TPR to the reactions cross-sections of the involved nuclides and to provide the sensitivity profiles required for the uncertainty analyses; (iii) Calculations of the uncertainties of the calculated TPR due to uncertainties of the underlying nuclear data.

The neutron flux spectra as well as the TPR in the Li_2CO_3 pellets have been obtained by transport calculations employing the Monte Carlo code MCNP, Version 5, using nuclear data from the Joint European Fusion File JEFF-3.1 (reference case) and Fusion Evaluated Nuclear Data Library FENDL-2.1. The TPR were obtained as per second and source neutron. The specific activities during the irradiation are based on a fluence of $5 \cdot 10^{15}$ neutrons.

The MCNP model made use of a detailed three-dimensional geometry model of the experimental set-up including neutron generator, HCLL mock-up with measurements equipments, assembly support and experimental hall provided by ENEA Frascati (Fig. 5). The mock-up consists of alternating layers of LiPb bricks and EUROFER-97 plates. Two additional thin

layers and a back reflector of Polyethylene have been introduced to optimize the neutron flux distribution with regard to the ITER TBM situation.

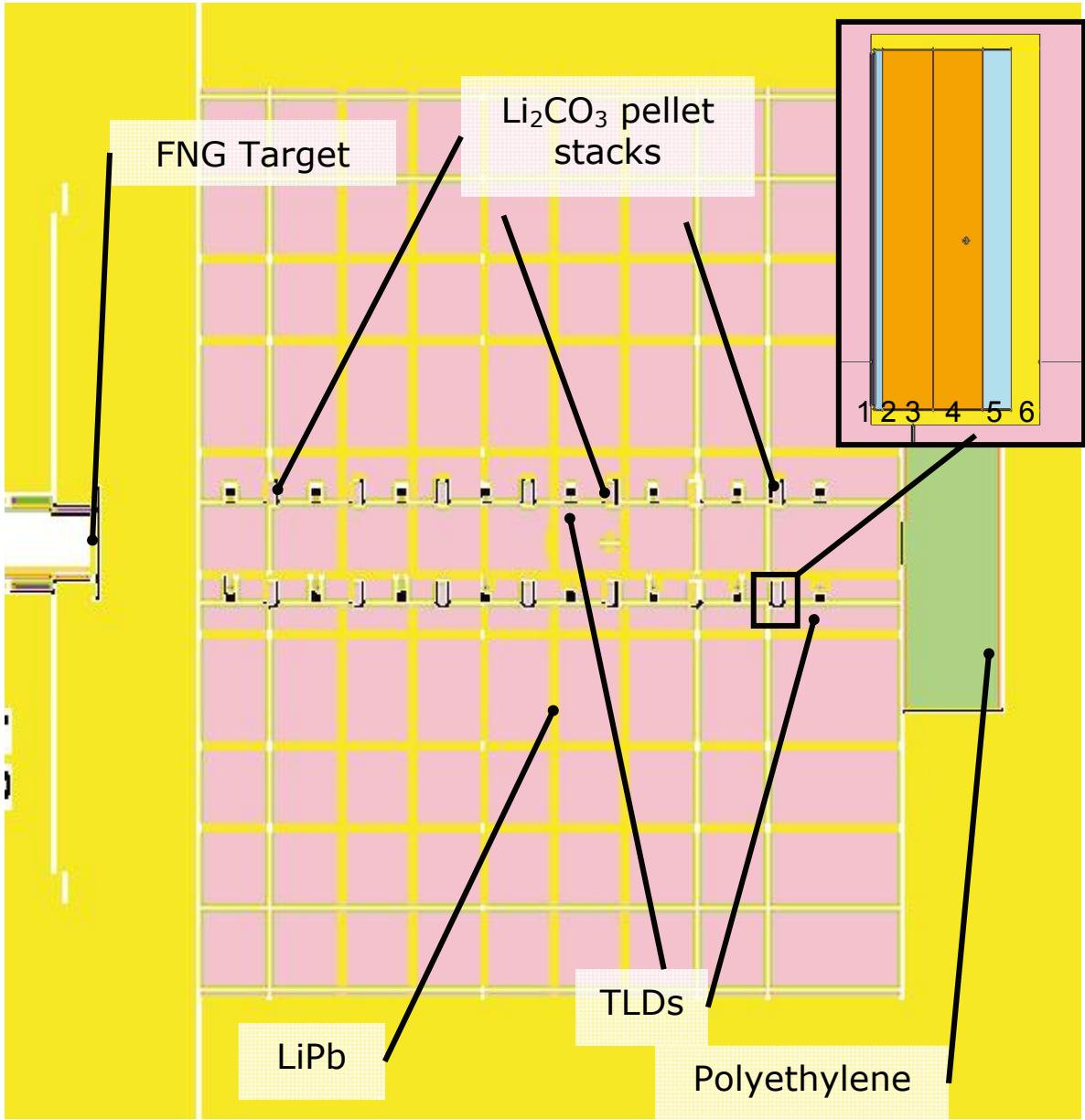


Fig. 5: MCNP model of the TBM-HCLL mock-up. Horizontal cut through the centre of the block, showing the two sets of symmetrical detectors (TLD = Thermoluminescence detector). One pellet stack is enlarged to show the sequence of foils and pellets: (1) Nb, (2) Al, (3) Li_2CO_3 nat., (4) nat., (5) enriched, (6) air.

The TPR responses in the HCLL mock-up have been obtained for pellets both with natural lithium (7.5 % ^6Li) and with Li enriched in ^6Li (95 % ^6Li). Sets of 3 pellets with 1.3 cm diameter and thicknesses of 0.18 / 0.18 / 0.10 cm have been introduced at 7 radial positions starting from 3.65 cm to 28.55 cm in the mock-up (cf. Fig. 4). As in the previous experiment on the HCPB mock-up, the variation of the ^6Li -content allows for a better tailoring of the measured TPR to the conditions in the real TBM of ITER, and to separate computationally the contributions from both lithium isotopes. As for the LiPb brick material composition, it has been revealed in the experiment that the actual lithium content is about half the nominal value of 15.7 at%. The lithium content used for the analyses was adjusted accordingly. The TPR in the pellets varies due to flux depression and moderation within the mock-up. The contribution from ^7Li amounts up to 54% in the front position for the natural pellets, elsewhere its contribution is much smaller, even negligible in the case of enriched lithium pellets.

The sensitivities of the TPR with respect to variations of the nuclear reaction cross sections were studied using the MCSEN code and its track length estimator feature. Sensitivity profiles were calculated in the VITAMIN-J 175 group structure to enable the calculation of data related uncertainties by making use of the covariance data provided in the same energy group structure. The tritium production from ${}^6\text{Li}$ is most sensitive to Pb (elastic and (n,2n)), H (elastic) and ${}^6\text{Li}(n,t)$ cross-sections. The sensitivities are decreasing at deeper positions in the mock-up. The tritium production from ${}^7\text{Li}$ is most sensitive to the ${}^7\text{Li}(n,n'\alpha)t$ reaction (about 1 %/%) itself. Additional significant negative sensitivities are due to (n,2n) cross sections in Pb.

For the calculation of uncertainties in the TPR due to uncertainties of the underlying nuclear data, the covariance data were taken from different sources, mainly from ENDF/B-VI.8, and the ZZ SCALE6.0/COVA-44G libraries, available at OECD/NEA Databank. The SCALE-6 covariances were developed for criticality calculations and for this reason, the covariance data do not cover some reactions which are of importance for fusion applications. For Pb isotopes, we have used ENDF/B-VI.8 as well as SCALE6.0 covariances. For ${}^6\text{Li}$ the data source is IRDF02, for ${}^7\text{Li}$ ENDF/B-VII, and for ${}^1\text{H}$ ENDF/B-V. During the processing and checking of the covariance libraries the quality was found to be relatively poor in some cases. Matrices with small negative eigenvalues and even unreal matrices were detected. The following covariance data should be revisited: Pb-isotopes, MT51-53 (ENDF/B-VI.8), Pb-208, MT17 (ENDF/B-VI.8), Li-7, MT2,4,852 (ENDF/B-VI.8). Furthermore, unrealistically large standard deviations of some non-elastic cross sections of Pb isotopes have been observed. In particular, the processing of ENDF/B-VI.8 covariances for the inelastic scattering on ${}^{207}\text{Pb}$ lead to uncertainties of up to more than 70 % and were discarded, accordingly. In a similar way, the Pb(n,3n) have been discarded.

Tab. 1 summarizes the uncertainty results at two detector positions. Generally, the uncertainties to individual isotopes are quite low, usually below 2 %. For the TPR contribution from ${}^7\text{Li}$ the uncertainties increase with depth, but since its contribution to the total TPR becomes negligible, it is not significant to the total response. For the response in ${}^6\text{Li}$ the main uncertainties are from Pb, H, and ${}^6\text{Li}$. The uncertainties to the total TPR as calculated by MCSEN are in the range of 0.7 % to 2 %. The results obtained are comparable to an analysis performed with deterministic calculations. Both computational approaches provide similar results, with a few exceptions. Those refer to sensitivities of the TPR from ${}^7\text{Li}$, where the results of Pb(elast) and of ${}^6\text{Li}(n,t)$ are differing significantly between the two approaches at the rear position.

Table 1: Total uncertainties (1σ , in %) of TPR due to uncertainties of nuclide reaction cross sections. Results for Pb are from ENDF/B-VI.8 and SCALE6.0 covariance data, respectively.

Mat	TPR from ${}^{95}\text{Li}$ at 3.65 cm	TPR from ${}^{95}\text{Li}$ at 28.55 cm	TPR from ${}^{\text{nat}}\text{Li}$ at 3.65 cm	TPR from ${}^{\text{nat}}\text{Li}$ at 28.55 cm
${}^{206}\text{Pb}$	1.1/1.0	0.8/0.6	0.4/0.2	0.5/0.4
${}^{207}\text{Pb}$	-/0.8	-/0.3	-/0.2	-/0.4
${}^{208}\text{Pb}$	1.4/1.6	1.2/0.8	0.4/0.3	1.2/1.0
${}^6\text{Li}$	0.1	<0.1	0.1	<0.1
${}^7\text{Li}$	<0.1	<0.1	0.4	<0.1
${}^1\text{H}$	0.4	0.4	0.2	0.4

Staff:

U. Fischer
D. Leichtle
A. Klix

Literature:

- [7] P. Batistoni, M. Angelone, U. Fischer, D. Leichtle, A. Klix, et al., Design optimisation and measuring techniques for the neutronics experiment on a HCLL-TBM mock-up, Proc. Symposium of Fusion Technology, 15-19 Sept. 2008, Rostock, Germany, Fus. Eng. Des. 84 (2009) 430-434
- [8] D. Leichtle, U. Fischer, I. Kodeli, R.L. Perel et al., Sensitivity and Uncertainty Analyses of the HCLL Mock-up Experiment, 9th Int. Symp. on Fusion Nuclear Technology (ISFNT-9), Dalian, China, October 11-16, 2009.

Deliverable 7

Analyses of the validation experiments for Bi cross-sections up to 35 MeV in a quasi-monoenergetic neutron spectrum

The objective of this subtask was to perform computational pre-analyses for the optimization of the set-up for the Bi activation experiments in a quasi-monoenergetic neutron spectrum extending up to 35 MeV [9] and, after completion of the experiment, to perform the computational post-analysis to check the relevant activation cross-section data and, in case of discrepancies, identify the responsible cross-sections.

Pre-calculations were performed with the MCNPX code and LA-150h cross section data for the $\text{Li}(\text{p},\text{xn})$ reaction to predict the intensity and the spectral shape of the quasi monoenergetic neutron source employing a thin lithium target and a carbon proton beam stopper. The comparison of calculations with available experimental data has shown that MCNPX with LA-150h library predicts satisfactorily the energy-angular distributions of the neutrons emitted from the Li/C target.

The activation of Bi samples was performed at the isochronous cyclotron U120M in NPI/Rez in the frame of the EFDA task TW6-TTMN-002B, D6 [9]. The neutron target consisted of a thin ^7Li foil backed by a carbon beam stopper and cooled by flowing water. The measurements have been performed at incident proton energies of 22.1, 27.1, 32.1 and 36.5 MeV, which produced neutron spectra having peaks at the energies 19.6, 24.3, 29.6 and 34.3 MeV, respectively. The Bi foils were located at 4.8 and 8.8 cm distance from the target and were activated during 17-20 hours. The samples were analysed off-line by the gamma-spectroscopy technique employing two calibrated HPGe detectors with an energy resolution of 1.8 keV at 1.3 MeV. The unstable decaying isotopes were identified on the basis of the half-lives $T_{1/2}$, the γ -ray energies and the intensities. The measurement period of decaying gammas ranged from minutes to 100 days.

For the Monte Carlo transport calculations, the NPI target set-up (Fig. 6) was modelled in detail including the 40 mm (diameter) \times 2 mm (thickness) lithium foil, 20 mm \times 8 mm carbon beam stopper, 4 mm thick alcohol coolant, steel target container and aluminium holder for the bismuth foils (Fig. 7). The neutron spectra calculated by means of MCNPX/LA-150h are shown in Fig. 8 for proton energies of 22.1 and 36.5 MeV. The spectra of neutrons generated in the Li foil alone are displayed separately, to demonstrate that the neutron generation in the carbon stopper and multiple scattering on the whole target assembly contribute below 5-15 MeV. This means that these parasitic neutrons do not affect the measured bismuth activation reactions having a threshold above 14 MeV.

The finite diameter of the foils and the close location to the neutron source result in a non-uniform irradiation. In the worst case, at 48 mm distance from the $\text{Li}(\text{p},\text{xn})$ source, the foils are exposed within a cone with 9° opening angle which yields a variation of the neutron flux by 30% and of the energy by 0.14 MeV over the foil area. Nevertheless, the main factor limiting the energy resolution is the proton energy loss in the 2 mm thick lithium which equals to 1.50 MeV.

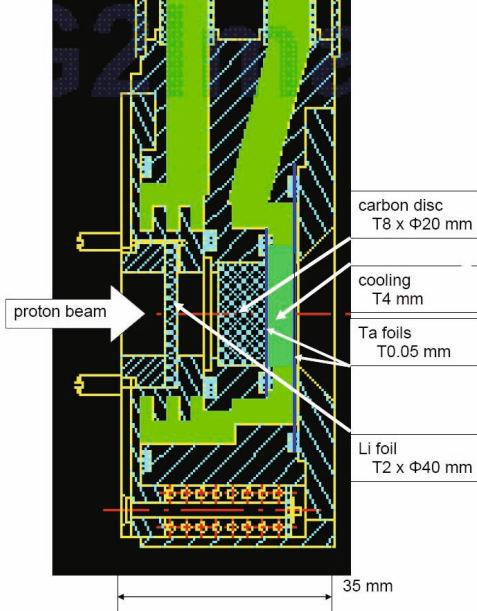


Fig. 6: The ${}^7\text{Li}/\text{C}$ neutron source set-up at NPI/Řež [9]

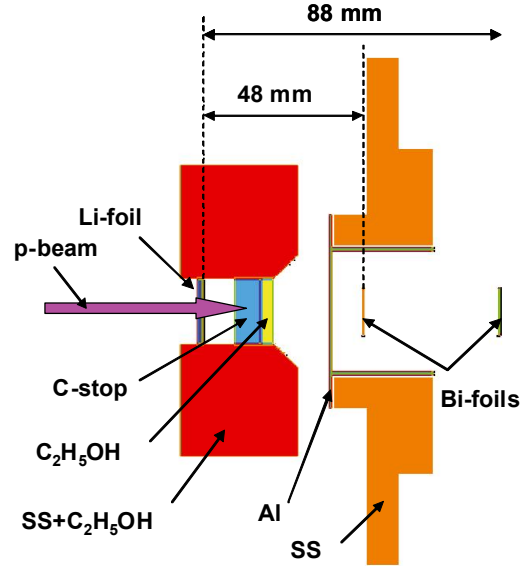


Fig. 7: The MCNPX model of the NPI/Řež neutron source.

The energy spectra were calculated and represented in a histogram form using a 211 group structure called VITAMIN-175+, as employed in the EAF-2007 library, to store and collapsing the activation cross sections up to 55 MeV. As seen in Fig. 5, the energy groups are extremely broad for representing the mono-energetic peak. This is especially true for the group 17.3325 to 19.6403 MeV (width 2.3 MeV) and 1 MeV groups above 20 MeV.

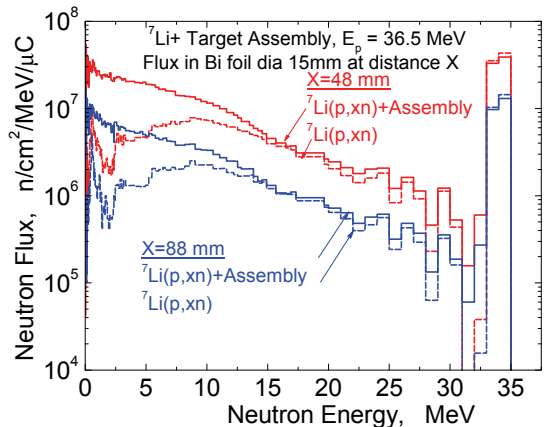
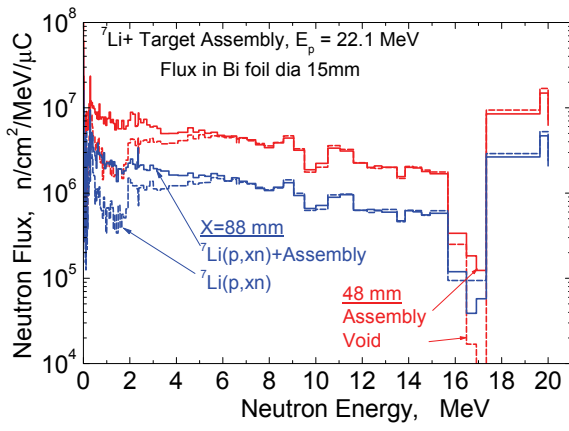
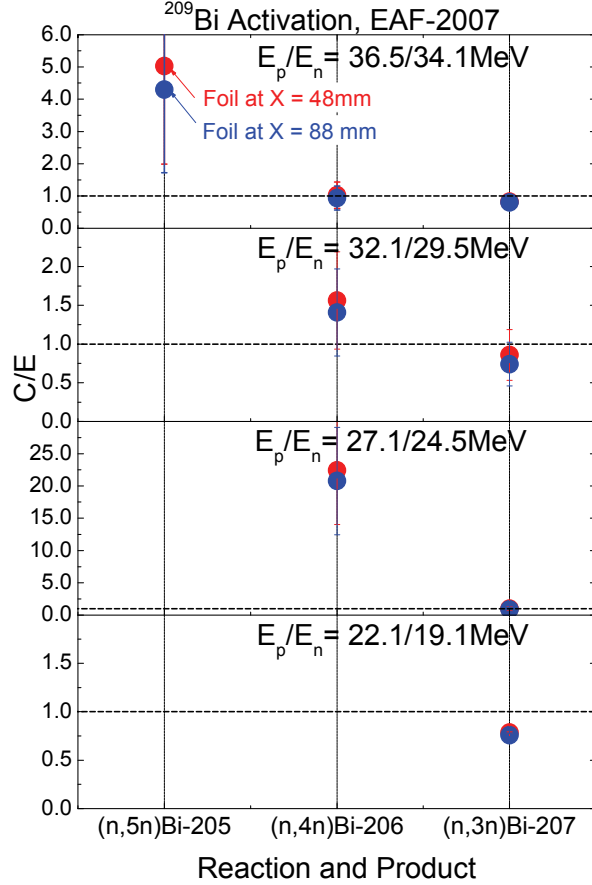


Fig. 8: Calculated neutron energy differential fluxes in the volume of the Bi foils located at 48 and 88 mm from the ${}^7\text{Li}/\text{C}$ neutron source at incident proton energies 22.1 MeV (left) and 36.5 MeV (right).

The activation calculations have been performed with FISPACT/EAF-2007 using the neutron spectra calculated by MCNPX as explained above. Fig. 9 compares calculated and measured radio-activities (in terms of C/E ratios) for the 3 unstable isotopes detected in the irradiated Bi samples at 4 proton energies. As can be seen, the most essential differences were observed for the cases where the energy of the main peak slightly exceeds the reaction threshold.



E_p MeV	E_n MeV	$(n,5n)205\text{Bi}$ $E_{\text{thr}}=29.62\text{MeV}$	$(n,4n)206\text{Bi}$ $E_{\text{thr}}=22.55\text{MeV}$	$(n,3n)207\text{Bi}$ $E_{\text{thr}}=14.42\text{MeV}$
36.5	34.1	6.80 ± 1.80	0.98 ± 0.04	0.83 ± 0.02
32.1	29.5	-	1.48 ± 0.08	0.80 ± 0.06
27.1	24.5	-	21.6 ± 0.80	0.93 ± 0.05
22.1	19.1	-	-	0.77 ± 0.02

Fig: 9: Graphical (top) and tabulated (bottom) representation of C/E ratios for specific γ -activities induced in Bi (calculated with EAF-2007 activation data).

As an example, Fig. 10 (left) displays the cross section for the $^{209}\text{Bi}(n,5n)205\text{Bi}$ reaction together with spectra of neutrons incident on the foil. Only the mono-energetic peak (34.1 MeV) is above the kinematic reaction threshold (29.2 MeV), whereas all other neutrons produced in the target are below. In this case the cross section can be derived directly from the C/E ratios resulting in the new experimental values for two energy groups as shown in the right half of Fig. 10.

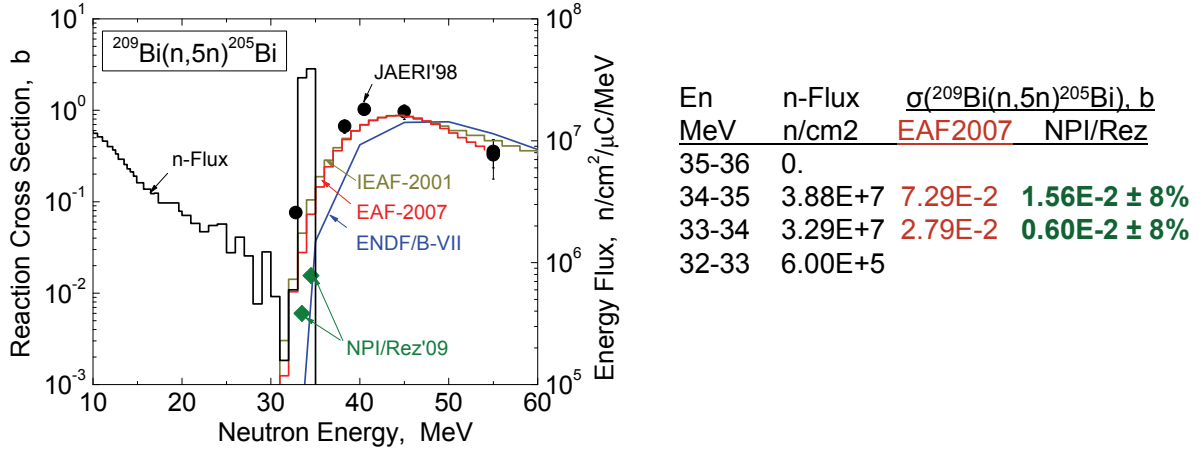


Fig. 10: Left: Activation cross sections for $^{209}\text{Bi}(n,5n)^{205}\text{Bi}$ reactions: symbols – measured in the present work and, curves – evaluations from EAF-2007, ENDF/B-VII and IEAF-2001. Neutron spectrum at 36.5 MeV proton energy – black histogram.
Right: Energy groups and cross sections from EAF-2007 and present measurements (NPI/Rez)

A more complicated situation is observed for the $^{209}\text{Bi}(n,3n)^{207}\text{Bi}$ reaction, Fig. 11: the neutron spectra measured at 4 proton energies cover the activation cross sections from threshold up to 34 MeV, i.e. well above the maximum for this reaction located around 25 MeV.

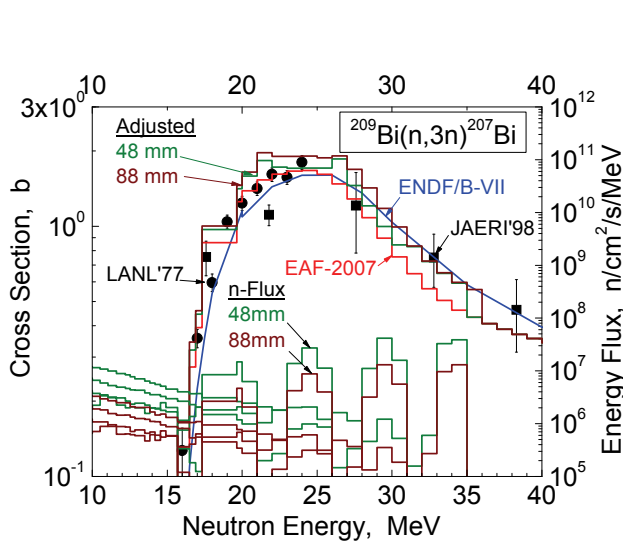


Fig. 11: Left: Activation cross sections for $^{209}\text{Bi}(n,3n)^{207}\text{Bi}$ reactions. Symbols – measured data points, curves – evaluations EAF-2007, ENDF/B-VII and adjusted for the foils at the distances 48 mm (green) and 88 mm (brown).
Right: Energy groups and cross sections from evaluation (EAF-2007) and from the present experiment at NPI/Rez (average from the adjustment at 48 mm and 88 mm).

To derive the cross section, a modified version of the SAND-II code for the neutron spectrum adjustment was used. In the present case, the procedure was reversed: the neutron spectra in the foil were supposed to be known and fixed, whereas the activation cross section was allowed to vary in order to bring the C/E ratio close to unity at all four proton energies. The cross sections for the $^{209}\text{Bi}(n,3n)^{207}\text{Bi}$ reaction, adjusted to the ^{207}Bi specific activities and measured at distances of 48 and 88 mm, are shown in Fig. 8 (left). The iteration procedure converges and provides correct results only in the energy bins which contain the mono-energetic peaks. This is why the new experimental cross section finally is presented only there, as shown in the right half of Fig. 11. The listed uncertainties include experimental un-

certainties as well as the deviations between the adjustment results obtained for the two Bi samples located at different distances. Additionally, 10% (as discussed above) should be summed up in square to get the total estimated uncertainty.

Staff:

U. Fischer
S. P. Simakov

Literature:

- [9] P. Bém, V. Burjan, M. Götz, M. Honusek, U. Fischer, V. Kroha, J. Novák, S.P. Simakov and E. Šimečková, Experimental validation of Bi cross-sections up to 35 MeV in a quasi-monoenergetic neutron spectrum, Final report TW6-TTMN-002B, Deliverable 6, September 2009.
- [10] SAND-II-SNL Neutron Flux Spectra Determination by Multiple Foil Activation-iterative Method, RSICC Shielding Routine Collection PSR-345, Oak Ridge 1996
- [11] R.A. Forrest, J. Kopecky, J-Ch. Sublet, The European Activation File: EAF-2007 neutron-induced cross section library, Report UKAEA FUS 535, Culham, 2007

Acknowledgement

This work, supported by the European Communities under the contract of Association between EURATOM and Karlsruhe Institute of Technology, was carried out within the framework of the European Fusion Development Agreement. The views and opinions expressed herein do not necessarily reflect those of the European Commission.

**Improvement of Nuclear Data, Development of Tools and Experiments/
Validation in Support of ITER Activities
(F4E-2008-GRT-014-01 (ES-AC), Action 1, NUDATA_Files)**

Overall objective: The overall objective of the grant agreement is to further contribute to the development of a qualified nuclear data base and validated computational tools for nuclear calculations of fusion reactors. The related tasks are devoted to the evaluation, processing, application, and benchmarking of required nuclear cross section and uncertainty data as well as the development of computational tools for uncertainty calculations.

Task 3

Finalise updating and testing of the MCSEN code and prepare in a format so that it can be used by general users of the MCNP code. Prepare documentation

The objective of this task is to prepare a release version of the Monte Carlo sensitivity code MCSEN. To this end, the code with its extended capabilities, developed and implemented under several EFDA subtasks in the last years, shall be tested, finalised and documented.

MCSEN allows efficient calculation of sensitivities of different types of responses (tallies), e.g. point-detectors, track length estimators, to many (multi-bin) parameters, e.g. reaction cross sections and Legendre moments. The applied algorithms are based on Hall's differential operator method and have been implemented into the MCNP code, version 4C.

Several MCNP routines have been changed accordingly, e.g. hstory, colidn, tallyd, transm. In addition, some new routines have been added. The MCSEN version of MCNP changes also the "common" decks, so that many more routines are (indirectly) affected. The specific additional input to MCSEN makes use of the general input tools supplied by MCNP. The specific input is done with the standard MCNP input options "fu" (user tallies) and "idum". In the user-tally, the boundaries of the sensitivity energy bins (groups) are given. In the "idum" input, information about the required sensitivity isotope and reactions is entered.

Basically, MCSEN uses the regular MCNP sources. However, for special purposes, dedicated versions of MCSEN with special source routines have been created - such as the source routine for the FNG fusion neutron source, or a source routine for the ITER plasma source.

The code and its different capabilities as given above are currently tested rigorously by recalculation and comparisons of several fusion neutronics experiments, such as the FNG TBM mock-up experiments as well as integral experiments of fusion material benchmarks. A general source code assessment is aimed to provide consistent coding as well as documentary comments.

The current work includes also the preparation of a package that enables a user to create the MCSEN code, using a patch on a standard MCNP code package. The package will include input instructions and test runs.

Staff:

U. Fischer

D. Leichtle

R. Perel (Hebrew University of Jerusalem)

Task 4

Produce cross-section data evaluations for the ^{50}Cr , ^{53}Cr and ^{54}Cr isotopes interacting with neutrons up to the energy of 150 MeV and prepare general purpose files from these evaluations in ENDF format

Task 5

Analyze suitable chromium integral benchmark experiments using the MCNP code, test the recent chromium evaluations and provide feedback to improve the evaluations

The objectives of these tasks are to provide general purpose nuclear data evaluations and files describing the interaction of neutrons with the Cr isotopes 50, 53, and 54 up to 150 MeV neutron energy (Task 4), to test the chromium evaluations, including the one performed for ^{52}Cr in the frame of the previous EFDA Task TW6-TTMN-001, D4, against suitable benchmark experiments and provide feedback to improve the data evaluations (Task 5).

The nuclear data calculations were performed with the nuclear model code TALYS of NRG Petten. This code provides the possibility of performing calculations with various nuclear models that are included in the code as different options. In case of massive nuclear model calculations TALYS has a great advantage, namely: it has a huge data base for default calculations. In this case the average agreement with experimental data is quite acceptable. For the present work, the focus was put on the improvement of the quality of the produced nuclear data. Instead of using default nuclear model options, a search of the optimal parameters needs to be made in order to reach good agreement with available experimental data.

The optical model calculations in TALYS are based on the global optical model potentials (OMP) elaborated for incident neutrons and protons. For all other charged particles the folding approach is used in the code as default option. Following this approach, the OMPs for the incident complex charged particles are calculated as a certain combination of the OMPs for neutrons and protons. This approach shows, however, worse accuracy as compared to the use of the OMPs elaborated specifically for the particular species. To overcome this deficiency, the global OMPs for deuteron and alphas were used for the calculations. For tritons and helions, the specifically elaborated OMPs were implemented. The results of the optical model calculations with TALYS are shown in Fig. 1 for ^{50}Cr .

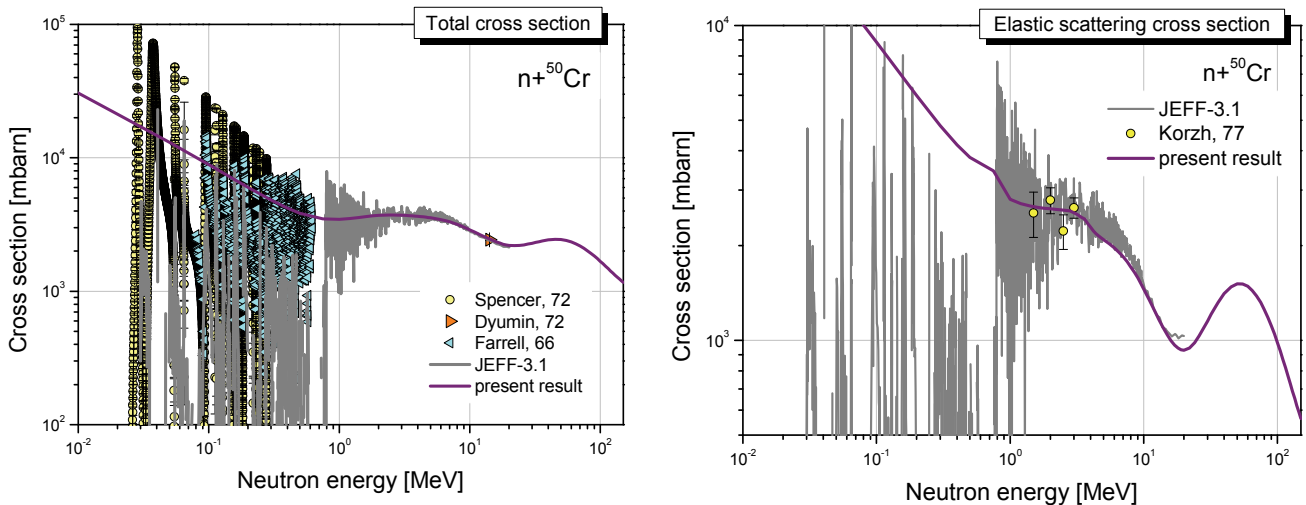


Fig. 1: Neutron total and elastic scattering cross sections for ^{50}Cr .

The results of the nuclear model calculations are very sensitive to the choice of the level density parameters for the residual nuclei considered in the calculations. The detailed analysis performed within this work shows advantages of the superfluid model for the level density

parameter calculations. This model is integrated in TALYS and was used during calculations for chromium isotopes instead of the default one. The results of the cross section evaluations for $^{53,54}\text{Cr}$ are shown in Figs.2 and 3. In these figures, there are included as well the data from TENDL-2008 data library prepared by NRG Petten on the basis of the default nuclear model parameters of the TALYS code.

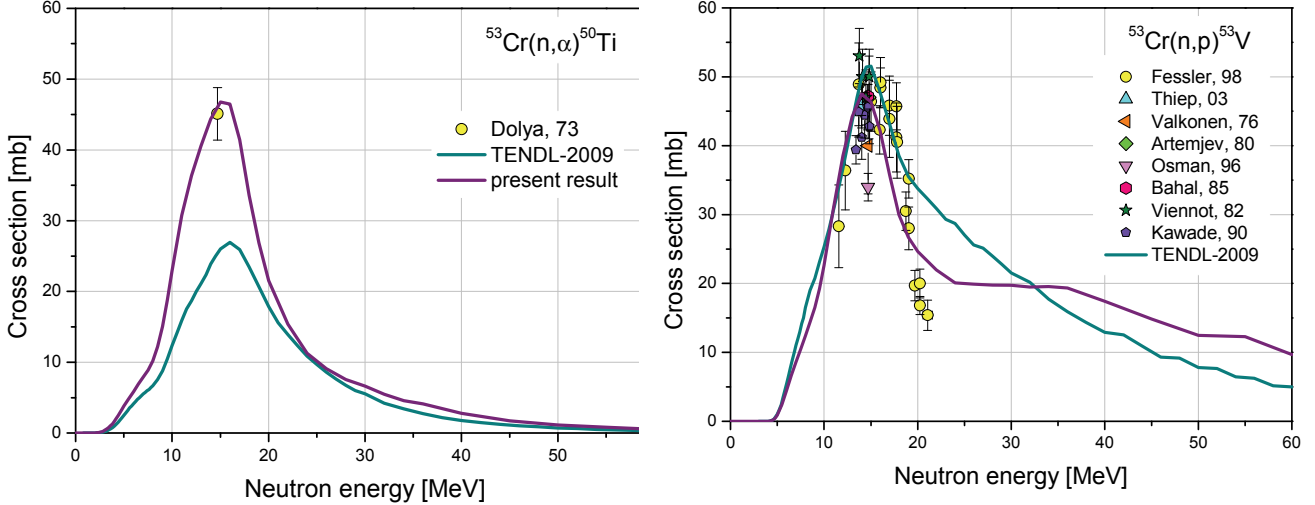


Fig. 2: Examples of neutron cross sections evaluations for ^{53}Cr .

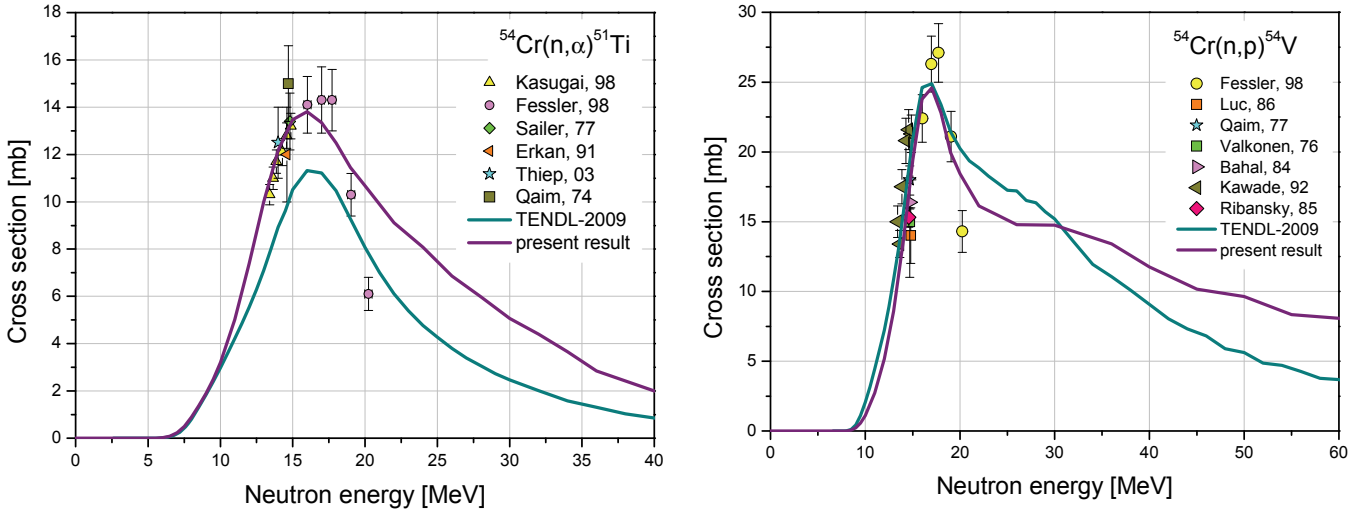


Fig. 3: Examples of neutron cross sections evaluations for ^{54}Cr .

The pre-analysis performed with TALYS showed a certain deficiency of the pre-equilibrium models implemented in the code. To overcome this problem, the GDH (geometry dependent hybrid) pre-equilibrium model was implemented in TALYS as a new option. This permits more accurate evaluations of the particle emission spectra (especially for emitted deuterons, tritons, He-3 and alphas) at the pre-equilibrium stage of the nuclear reactions.

With the GDH model, experimental gas production cross sections can be reproduced much better, as shown in Fig. 4 for the proton and alpha production cross sections of natural chromium.

Results for the particle emission spectra evaluation are shown in Fig. 5. The inclusion of the GDH model in TALYS again provides much better agreement with experimental data for the alpha emission spectra.

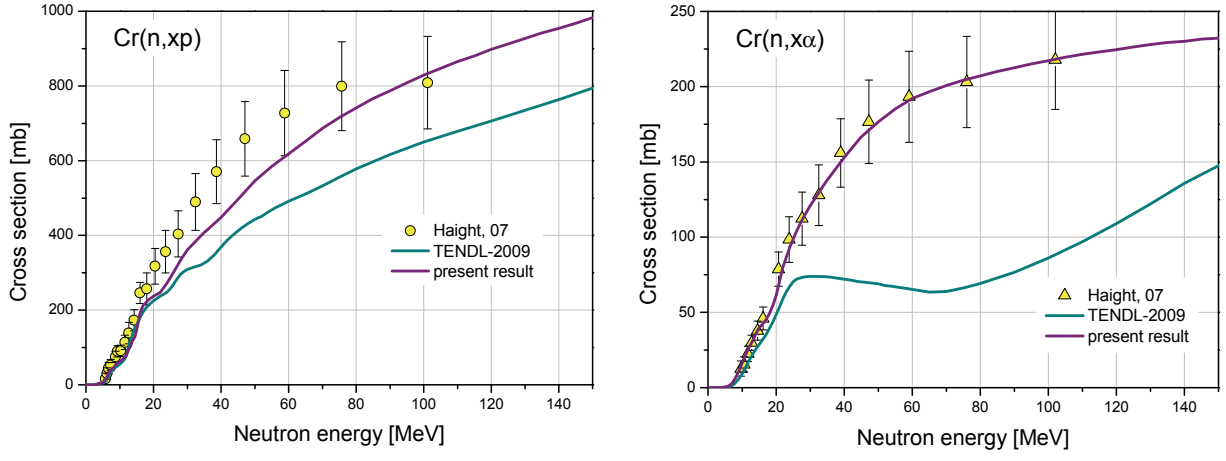


Fig. 4: Proton and alpha production cross sections for natural chromium.

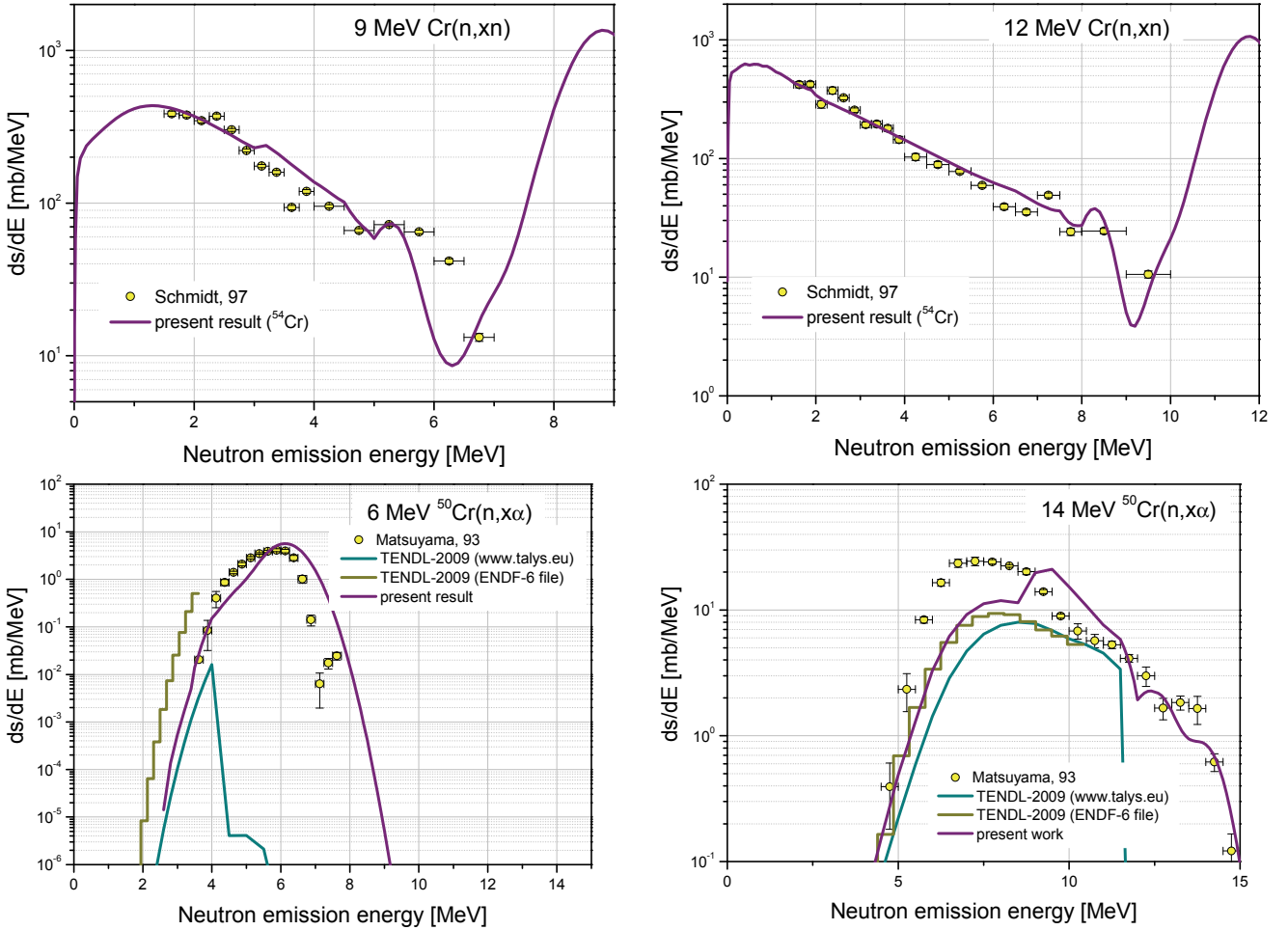


Fig. 5: Evaluated particle emission spectra for natural chromium.

The methodology adopted for the evaluation of the neutron cross-section data of the $^{50,53,54}\text{Cr}$ isotopes has several important features. First, the GDH model was implemented as a new option in TALYS to improve the pre-equilibrium reaction model. Second, various global OMPs were used in the optical model calculations instead of the simple folding approach approximation. A set of optimal nuclear model parameters was determined for each isotope. This approach allows very accurate TALYS calculations providing results that are in very

good agreement with available experimental data and finally result in a higher quality of the evaluated nuclear data.

Staff:

U. Fischer
P. Pereslavtsev
S. P. Simakov

Literature:

[1] P. Pereslavtsev, A. Konobeyev, U. Fischer, Status of the evaluation and benchmarking of the Cr-50,53,54 neutron cross-section data up to 150 MeV, EFF/EAF Nuclear Data Monitoring Meeting, NEA Data Bank, Paris, November 25 – 27, 2009, EFF-DOC-1083.

Acknowledgement

This work was supported by Fusion for Energy under the grant contract No. F4E-2008-GRT-014-01 (ES-AC) with collaboration by CCFE, United Kingdom; NRG, Netherlands; IFIN HH, Romania; TU Wien, Austria and JSI, Slovenia. The views and opinions expressed herein reflect only the author's views. Fusion for Energy is not liable for any use that may be made of the information contained therein.

Nuclear Data Studies/Experiments in Support of TBM Activities (F4E-2008-GRT-014-02 (ES-AC), Action 2, NUDATA_Exper)

Overall objective: The overall objective of the grant agreement is to provide the experimental data base required for the validation of the nuclear data libraries EFF and EAF developed in the frame of the task TTMN-001 of the EU Fusion Technology Programme. The focus is on the experimental validation of ITER and TBM design calculations and cross-section validation experiments relevant for IFMIF.

Task 4

Monte Carlo based sensitivity/uncertainty analysis of the neutron flux spectra and TPR in the HCLL TBM in ITER for comparison to the TBM mock-up experiment

The objective of Task 4 is the computational analysis of the Helium Cooled Lithium Lead (HCLL) Test Blanket Module (TBM) in ITER using Monte Carlo techniques for transport and sensitivity/uncertainty calculations. The results will be compared to the corresponding analyses performed for the HCLL mock-up experiment conducted at the Frascati Neutron Generator in 2009. To this end, the MCSEN code will be employed for the Monte Carlo sensitivity calculations of neutron fluxes and tritium production on nuclear cross-sections. Available covariance data will be used to obtain nuclear response uncertainties related to nuclear data uncertainties.

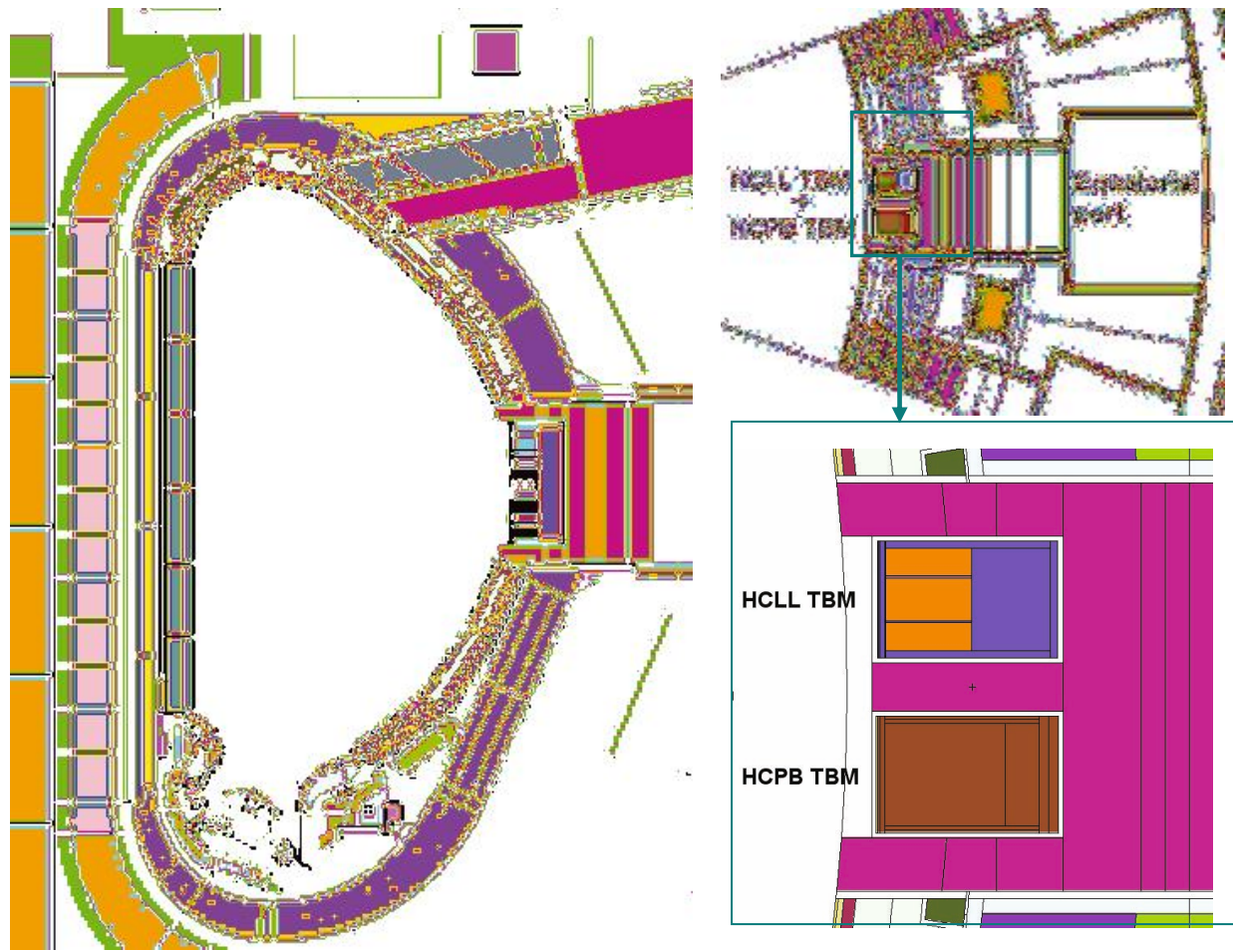


Fig. 1: Vertical (left) and horizontal (right) cuts of the A-lite ITER model with integrated HCPB and HCLL Test Blanket Modules

The MCNP transport and tritium production calculations are to be performed with the most recent ITER MCNP model called A-lite. This model represents a 40° torus sector including

various dummy ports for the integration of diagnostic tools, test objects, etc. The test blanket port of the A-lite model was modified to allow the integration of a TBM insert. It includes a water-cooled steel frame, the Helium Cooled Pebble Bed (HCPB) TBM in one vertical half of the frame compartment and a HCLL TBM in the other half. The HCPB TBM has been converted into MCNP geometry from a CAD model by the McCad software tool. For the HCLL TBM, a simplified model, developed in the frame of the EFDA task TW6-TTMN-002, D3, for benchmark analyses with the previous ITER "Brand" model has been utilized and adapted to the A-lite geometry.

Fig. 1 (left) shows a vertical cut of the A-lite model with the TBM integrated into the test blanket port. The horizontal cuts (Fig. 1, right), at the level of the torus mid-plane, show the test blanket port region at the outboard side of the ITER torus with steel frame and the HCPB and HCLL TBM in place. For comparison with the HCLL mock-up experiment, two representative positions in the front and the rear of the ITER TBM are selected. Pre-analyses of the mock-up experiment, performed in the frame of TW6-TTMN-002, D3, already showed that the neutronic characteristics in terms of neutron flux and tritium production spectra of the HCLL TBM in ITER can be well represented in the experiment. MCNP transport and MCSEN sensitivity/uncertainty calculations using JEFF nuclear data and the ITER A-lite model with integrated HCLL and HCPB TBM have been started and will be concluded on schedule in early 2010.

Staff:

U. Fischer

D. Leichtle

R. L. Perel (Hebrew University of Jerusalem)

A. Serikov

Task 7

Analyses of the validation experiments for Au cross-sections up to 35 MeV

The objective of this subtask was to perform a computational pre-analyses for the optimization of the set-up for the Au activation experiments in a quasi-monoenergetic neutron spectrum extending up to 35 MeV [1] and, after completion of the experiment, to perform the computational post-analysis to check the relevant activation cross-section data and, in case of discrepancies, identify the responsible cross-sections.

Pre-calculations were performed with the MCNPX code and LA-150h cross section data for the $\text{Li}(\text{p},\text{xn})$ reaction to predict the intensity and the spectral shape of the quasi monoenergetic neutron source employing a thin lithium target and a carbon proton beam stopper. The comparison of calculations with available experimental data has shown that MCNPX with LA-150h library predicts satisfactorily the energy-angular distributions of the neutrons emitted from the Li/C target.

The activation of Au samples was performed at the isochronous cyclotron U120M in NPI/Rez [1] in the frame of the F4E Contract F4E-GRT-014 (ES-AC), Task 6. The neutron target consisted of a thin ^7Li foil backed by a carbon beam stopper and cooled by flowing water. The measurements have been performed at 15 different incident proton energies ranging from 19.8 to 37.5 MeV, which produced neutron spectra having peaks at energies from 16 to 36 MeV, respectively. The Au foils were located at 4.8 and 8.8 cm distance from the target and were activated during 20 hours. The samples were analysed off-line by the gamma-spectroscopy technique employing two calibrated HPGe detectors with an energy resolution of 1.8 keV at 1.3 MeV. The unstable decaying isotopes were identified on the basis of the half-lives, the γ -ray energies and the intensities. The measurement period of decaying gammas ranged from minutes to 100 days.

For the Monte Carlo transport calculations, the NPI target set-up was modelled in detail including the 40 mm (diameter) \times 2 mm (thickness) lithium foil, 20 mm \times 8 mm carbon beam stopper, 4 mm thick alcohol coolant, steel target container and aluminium holder for the gold foils. The finite diameter of the foils and the close location to the neutron source result in a non uniform irradiation. In the worst case, at 48 mm distance from the Li(p,xn) source, the foils are exposed within a cone with 9° opening angle, yielding a variation of the neutron flux by 30% and of the energy by 0.14 MeV over the foil area. Nevertheless, the main factor limiting the energy resolution is the proton energy loss in the 2 mm thick lithium which equals to 1.50 MeV. The energy spectra were calculated by means of the MCNPX code with LA-150h transport cross section data and represented in a histogram form using a 211 group structure as employed in the EAF-2007 library [2] to store and collapsing the activation cross sections up to 55 MeV.

The Li/C source neutron spectra calculated at the locations of the Au sample have indicated that mono-energetic peaks account for 30-50% of the total flux, the rest being the low energy neutrons from the Li breakdown reaction and re-scattering on the target assembly. To derive the cross section, we used a modified version [3, 4] of the SAND-II code [5] for the neutron spectrum adjustment. In the present case, the procedure was reversed: the neutron spectra in the foil were supposed to be known and fixed, whereas the activation cross section was allowed to vary to get C/E ratio close to unity at all 15 proton energies. In such a way the cross sections for the $^{197}\text{Au}(n,xn)^{197-x-1}\text{Au}$ reactions were adjusted to the $^{197-x-1}\text{Au}$ specific activities, measured at the distances of 48 and 88 mm.

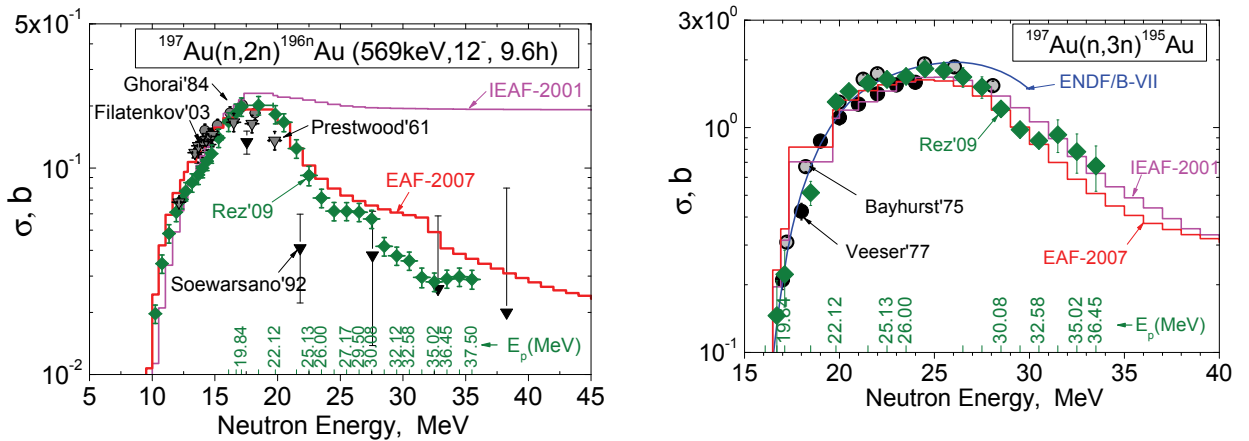


Fig. 2: The cross section for $^{197}\text{Au}(n,2n)^{196n}\text{Au}$ (left) and $^{197}\text{Au}(n,3n)^{195}\text{Au}$ (right) reactions obtained in the present work from measurements at NPI/Rez (green symbols) in comparison with available experimental and evaluated data.

The new experimental cross sections obtained are presented, as an example for the $^{197}\text{Au}(n,2n)^{196n}\text{Au}$ and $^{197}\text{Au}(n,3n)^{195}\text{Au}$ reactions, in Fig. 2. The total uncertainties include experimental uncertainties and the deviations between the adjustment results obtained for the two Au samples located at different distances, as well as, additionally, 10% due to the uncertainty of Li(p,n) yield simulation. Further details are available in [6].

Staff:

U. Fischer
S.P. Simakov

Literature:

- [1] P. Bém, V. Burjan, U. Fischer, M. Götz, M. Honusek, V. Kroha, J. Novák, S.P. Simakov, E. Šimečková, The NPI Cyclotron-based Fast neutron Facility, Int. Conf. on Nuclear Data for Sci. and Techn. (ND-2007), Nice 2007; EDP Sciences 2008, p. 555-558
- [2] R.A. Forrest, J. Kopecky, J-Ch. Sublet, The European Activation File: EAF-2007 neutron-induced cross section library, Report UKAEA FUS 535, Culham, 2007
- [3] S.P. Simakov, P. Bém, V. Burjan, M. Götz, M. Honusek, U. Fischer, V. Kroha, J. Novák, E. Šimečková, Development of activation foils method for the IFMIF neutron flux characterization, Fus. Eng. Des. 82 (2007) 2510
- [4] S.P. Simakov, P. Bém, V. Burjan, U. Fischer, R.A. Forrest, M. Götz, M. Honusek, V. Kroha, J. Novák, E. Šimečková, Determination of neutron spectrum by the dosimetry foil method up to 35 MeV, Proceedings of ISRD-13 (May 2008, Alkmaar); Reactor Dosimetry, State of the Art 2008, World Scientific, 2009, pp. 532-540
- [5] SAND-II-SNL Neutron Flux Spectra Determination by Multiple Foil Activation-iterative Method, RSICC Shielding Routine Collection PSR-345, Oak Ridge 1996
- [6] S.P. Simakov, U. Fischer, P. Bém, M. Honusek, M. Götz, J. Novák and E. Šimečková, Analyses of the validation experiments for Au cross-sections up to 35 MeV in a quasi-monoenergetic neutron spectrum, EFF-DOC-1093, JEFF/EFF Meetings, 25 - 27 November 2009, NEA, Paris

Task 8

Validation experiment for gamma activities of Ti / Li_2TiO_3 irradiated in fusion peak neutron spectrum

The objective of this subtask was to provide experimental data for the validation of activation cross-sections for Ti/ Li_2TiO_3 irradiated in a fusion peak neutron spectrum. To this end, samples of titanium were irradiated with fusion peak neutrons from a DT neutron generator, and the induced gamma activity was determined. The results were compared with calculations with the EASY-2007 [7].

Natural titanium consists of five isotopes which transmute mainly to scandium isotopes by (n,p), (n,d), and (n,np) reactions. The isotopic abundance of natural Ti is as follows: ^{46}Ti 8.2 at%, ^{47}Ti 7.4 %, ^{48}Ti 73.8 %, ^{49}Ti 5.4%, and ^{50}Ti , 5.2 %. A first survey revealed that especially the latter reactions play a significant role for the activation of titanium at neutron energies around the DT fusion neutron peak.

Experiment

A pre-analysis with EASY assuming fusion power plant conditions but with the emphasis on fast neutrons shows that for compound Li_2TiO_3 with a lower volumetric Ti concentration, the recycling and hands-on limits are reached after 3.2 years and 17.7 years, respectively. The recycling limit of pure Ti according to ICRP-60 [8] is reached approximately 4.4 years after shut-down, while the hands-on limit is reached approximately 109 years later.

One can easily identify three ranges where the contact dose rate is completely dominated by ^{48}Sc (until about 2 days after shut-down), ^{46}Sc (2000 days after shut-down), and ^{42}K until the hands-on-limit is reached. The results of these calculations are shown in Figure 3.

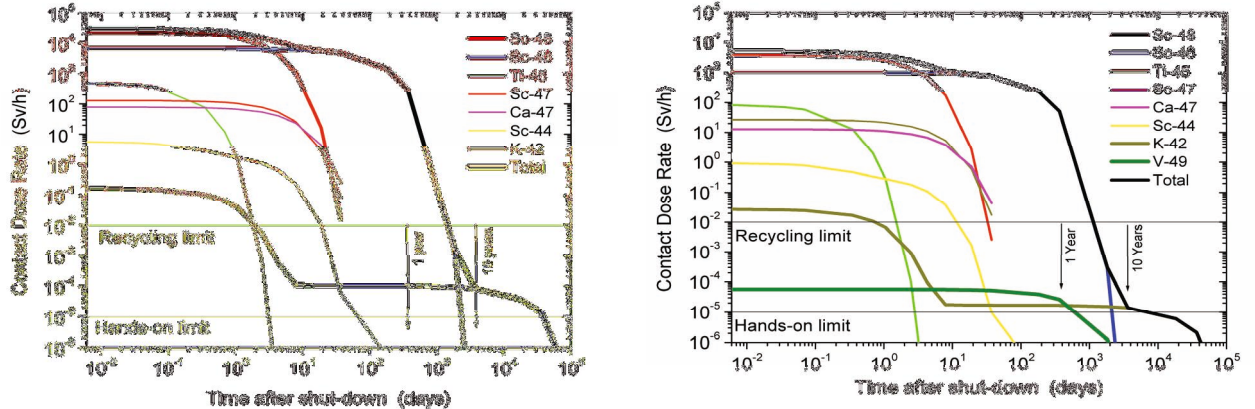


Fig. 3: Contact dose rate after irradiation of Li₂TiO₃ (left) and of Ti (right) with fusion peak neutrons of 1 MW/m² power density for one year as a function of decay time.

In the experiment, a sample of titanium with a purity of 99.99%, a mass of 0.2060 g, and a size of ca. 1 cm squared and 0.25 mm thickness was irradiated in the DT fusion peak neutron field of the neutron generator of TU Dresden. The neutron generator was operated at a deuteron energy of 320 keV bombarding a Ti-T target. The sample was arranged at an effective angle of 8 degrees with respect to the deuteron beam at a distance of approximately 7.5 cm from the neutron source. Two Nb and two Zr foils were sandwiched with the titanium foil for monitoring of the local neutron fluence. Nb served as the actual fluence monitor while Zr was used to determine the "effective" neutron energy at the position of the titanium sample following a method described in Ref. [9]. This information is required since some of the cross sections leading to the production of scandium isotopes do contribute significantly but have a threshold around 14~15 MeV.

The time profile of the irradiation was recorded with a silicon detector for the associated alpha particle from the DT reaction in the neutron source, and with a U-238 fission chamber. This time profile is used in the analysis to correct for decay of the produced isotopes during irradiation in cases of short-living isotopes such as ⁴⁸Sc but also the Zr foil monitors.

For the EASY calculation, an input neutron spectrum was computed with a detailed calculation of the neutron transport through the tritium target assembly of the neutron generator with the MCNP code [10]. Angle-dependent energy distributions of the neutrons generated in the DT fusion reaction were obtained with the DROSG code [11]. The neutron spectrum at the sample position from the calculation is an asymmetric peak with a maximum at 14.8 MeV and a full-with-at-half-maximum of approximately ± 0.3 MeV. The calculated spectrum at the sample position was validated by comparing the ratio of produced ⁸⁹Zr and ^{92m}Nb in the monitor foils to values from the MCNP calculation and activation cross sections from the IRDF-2002 library [12]. An "effective" neutron peak energy of 14.9 MeV was determined, measured and calculated values agreed within 1%. According to Ref. [9], the measured value can be expected within 0.04 MeV for a 68% confidence level.

The neutron fluence at the position of the Ti sample was obtained from the Nb foils using a cross section value of 464 mb [13] with an uncertainty of 4.2% for producing the metastable state of ⁹²Nb. This cross section is nearly flat between 14 and 15 MeV, and a fluence of 5.41×10^{11} cm⁻² was computed. The uncertainty of this value is estimated to be 5.2% taking into account the uncertainty of the activity determination of the niobium foil with 3.1%. The estimate represents the root-mean-square of the uncertainties of the gamma line intensity, the half-life of the sample (decay times during measurement and storage), the efficiency calibration, and gamma counting statistics, and the uncertainty of the ⁹³Nb(n,2n)^{92m}Nb cross section mentioned above. The uncertainty of the measurement of the gamma activity of the titanium sample for each case was approximately 4%.

The uncertainty estimate of the EASY calculation includes the half-life and cross section uncertainties, both from the EASY output.

Discussion

Not all nuclides contributing to the contact dose rate shown in Fig. 3 above could be investigated in this work, partly because irradiation times similar to a fusion reactor cannot be achieved with a neutron generator, but also because some of the radio-isotopes produced have only very low gamma line intensities.

The measured gamma activities were analyzed with the EASY-2007 code package consisting of the inventory code FISPACT-2007 and the EAF-2007 activation data library. They are presented together with their experimental and calculation uncertainties and the production pathways in Table 1.

There is a slight overestimation of the ^{46}Sc production by the EASY calculation as one can see from the calculated-to-experiment ratio (C/E). Approximately 80% of the ^{46}Sc is produced by (n,p) reactions on ^{46}Ti . In most cases, this reaction leads directly to the ground state of ^{46}Sc , or via the first excited state which has a half-life of 18.7 seconds and decays with a branching ratio of 1.0 into the ground state.

The production of ^{47}Sc is largely overestimated by the EASY calculation. Most of it is produced by (n,d) and (n,np) reactions on ^{48}Ti which is by far the most abundant Ti isotope. Both reaction cross sections have their threshold around 14~15 MeV and are therefore sensitive to the position of the DT neutron peak. However, the correct position of the peak for the input neutron spectrum for the EASY calculation has been validated by the simultaneous measurement of the Zr foil which applies a well-validated cross section [14]. The comparison of evaluated cross section data and experimental data shows a rather large spread of data around 14.8 MeV. However, the uncertainty of the cross section data which is suggested by this comparison does not appear to explain the the large overestimation of the ^{47}Sc production and is therefore subject of ongoing work.

The amount of ^{48}Sc in the sample was also overestimated by the EASY calculation. This isotope is mostly produced by (n,p) reactions on ^{48}Sc and, because of the lower isotopic abundance, to a small amount by (n,d) reactions on ^{49}Sc .

Table 1: C/E (Calculation/Experiment) comparison of measured and calculated (EASY) gamma ray activities. Half-lives, gamma energies and intensities are based on JEFF-3.1.1 data. The reaction contributions and the uncertainty of the calculation DC/C were taken from the EASY output. The experimental uncertainty DE/E is for the activity measurement of the sample. The (n,d) reaction in the *reaction contributions* column from the EASY output includes (n,np) and (n,d).

Radio-nuclide	Half-life	Eg (keV) / Ig	Reaction contribution (%)	C/E	DC/C (%)	DE/E (%)
^{46}Sc	83.79 d	889.3 / 1.00 1120.5 / 1.00	$^{46}\text{Ti}(\text{n},\text{p})^{46}\text{Sc}$ $^{46}\text{Ti}(\text{n},\text{p})^{46m}\text{Sc} \rightarrow \text{IT} \rightarrow ^{46}\text{Sc}$ $^{47}\text{Ti}(\text{n},\text{d})^{46}\text{Sc}$ $^{47}\text{Ti}(\text{n},\text{d})^{46m}\text{Sc} \rightarrow \text{IT} \rightarrow ^{46}\text{Sc}$	64.39 15.87 16.79 2.95	1.08	25.1 3.5
^{47}Sc	3.351 d	159.4 / 0.68	$^{47}\text{Ti}(\text{n},\text{p})^{47}\text{Sc}$ $^{48}\text{Ti}(\text{n},\text{d})^{47}\text{Sc}$	40.19 59.80	5.66	47.6 4.2
^{48}Sc	1.81958 d	983.5 / 1.00 1037.5 / 0.975 1312.1 / 1.00	$^{48}\text{Ti}(\text{n},\text{p})^{48}\text{Sc}$ $^{49}\text{Ti}(\text{n},\text{d})^{48}\text{Sc}$	99.01 0.99	1.39	10.0 4.1

Staff:

A. Domula (TU Dresden)
A. Klix
K. Zuber (TU Dresden)

Literature:

- [7] R.A. Forrest, The European Activation System: EASY-2007 overview, Report Culham Science Centre, UKAEA FUS 533, 2007.
- [8] ICRP recommendations, ICRP publication 60, Annals of the ICRP 21
- [9] V.E. Lewis, K.J. Zieba, A Transfer Standard for d+T Neutron Fluence and Energy, Nucl. Instr. Meth., Vol. 174, 1980, pp 141-144
- [10] MCNP—A General Monte Carlo N-Particle Transport code, Version 5, Report LA-UR-03-1987, Los Alamos, 2003
- [11] M.Drosg, DROSG-2000: Neutron Source Reactions, IAEA-NDS-87, IAEA Nuclear Data Section, May 2005
- [12] International Reactor Dosimetry File 2002 (IRDF-2002), IAEA Technical Report Series No. 452, 2006
- [13] K. Seidel, R. Eichin, R.A. Forrest, H. Freiesleben, S.A. Goncharov, V.D. Kovalchuk, et.al., Activation experiment with tungsten in fusion peak neutron field, J. Nucl. Mat., 329-333, 2004, pp. 1629-1632
- [14] K.I. Zolotarev, Evaluation of Cross-Section Data from Threshold to 40-60 MeV for Specific Neutron Reactions Important for Neutron Dosimetry Applications, part 1, INDC
- [15] A. Klix, A. Domula, R. Forrest, K. Zuber, Measurement and Analysis of Activation Induced in Ti/Li_2TiO_3 with Fusion Peak Neutrons, 14th International Conference on Fusion Reactor Materials, 7-11 September 2009, Sapporo, Japan

Acknowledgement

This work was supported by Fusion for Energy under the grant contract No. F4E-2008-GRT-014-02 (ES-AC) with collaboration by ENEA, Italy; AGH-UST, Poland; JSI, Slovenia and ASCR-NPI, Czech Republic. The views and opinions expressed herein reflect only the author's views. Fusion for Energy is not liable for any use that may be made of the information contained therein.

Assessment of the Suitability of Neutron and Gamma Detectors in the Future Experiment at JET for the Validation of Shutdown Dose Rate Prediction (JW9-FT-5.31)

Characterization of a CdTe Gamma-ray Detector for Measurements at JET

Deliverable 2

Calibration of the CdTe detector

Introduction

Local shut-down dose rate assessments for areas near a fusion reactor vessel are a necessary input for the design of maintenance schemes and the definition of accident scenarios, and hence are of importance for the licensing procedure. Two methods, the Rigorous 2 Step (R2S) method [1] and the Direct 1 Step (D1S) method [2], have been developed to perform such dose rate calculations. In order to establish these methods as standard tools, it is necessary to validate them experimentally in benchmark experiments.

Two attempts have been made in the past with a mock-up assembly irradiated with 14 MeV neutrons from the FNG neutron source at Frascati [3], and with dosimetry data and the known history of the experimental campaign at the JET facility [4]. The latter performed poorly, which is deemed due to insufficient knowledge of the composition of the activated reactor material. It was therefore decided to investigate the shut-down gamma-ray spectrum in different locations near the JET reactor vessel experimentally, to determine which gamma lines (and the isotopes causing them) are of importance for the dose rate.

A previous task (JW8-FT-5.28) was partly devoted to investigate the possibility of using a NaI scintillation detector and an HPGe detector to record the gamma-ray spectrum in the torus hall of JET. The NaI scintillator, although state-of-the-art and with improved performance as compared to earlier NaI detectors, did not provide the necessary energy resolution. The HPGe detector is well-suited for high-resolution gamma-ray spectra, however, the one available for these measurements would need N_{2L} cooling and thus is too heavy to be used in locations above the JET torus hall floor.

An alternative detector for the gamma-ray spectrum measurements, for use at least near the activated JET reactor vessel, could be a CdTe detector, although such type of detector does not perform equal to HPGe detectors. They are very small and light and therefore well-suited for measurements near the JET vessel, especially in places with very limited space.

Current status of the experiment and next steps

Calibration measurements have been performed with reference gamma-ray sources to obtain energy calibration curves and to determine the relative efficiency of the detector. It is known that the efficiency of a CdTe detector drops considerably with increasing energy. Fig.

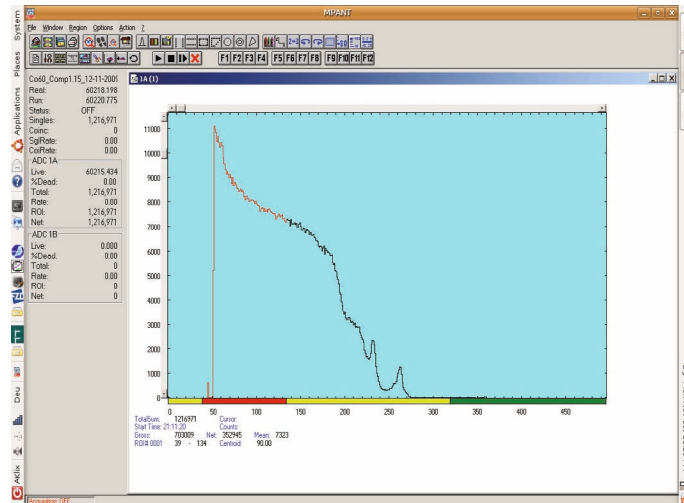


Fig. 1: Gamma-ray pulse height spectrum recorded with the CdTe detector and a ^{60}Co reference source of approximately 10 kBq activity.

2 shows the pulse height spectrum obtained from a ^{60}Co reference source with an activity of approximately 10 kBq, located adjacent to the CdTe detector.

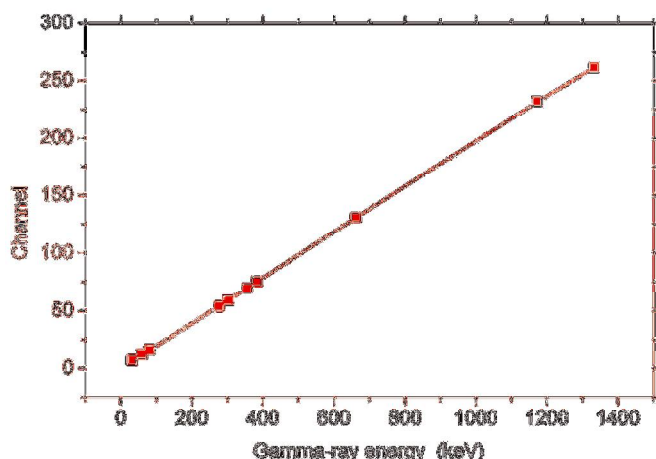


Fig. 2: Energy calibration curve for the CdTe detector system.

Other calibration sources included ^{137}Cs , ^{241}Am and ^{152}Eu . An excellent linearity was found for the energy calibration, see Figure 2. The determination of the relative efficiency curve is underway.

In the next step, material samples (EUROFER) irradiated in the 14 MeV neutron field of the neutron generator of Technical University of Dresden (TUD) will be examined with the CdTe detector. These measurements were delayed due to a shut-down of the neutron generator because of technical problems. The neutron generator came back into service end 2009.

Staff:

A. Klix^a
S. Villari^b

^a) Karlsruher Institut für Technologie (former Forschungszentrum Karlsruhe), Germany

^b) FNG / ENEA Fusion and Nuclear Technologies Department, Frascati, Italy

Literature:

- [1] Y. Chen, U. Fischer, "ITER-FEAT Shutdown Dose Rate Analysis by Rigorous Method", Final report, Sept. 2001
- [2] L. Petrizzi, H. Iida, D. Valenza, and P. Batistoni, "Improvement and benchmarking of the new shutdown dose estimation method by Monte Carlo code", Advanced Monte Carlo for Radiation Physics, Particle Transport Simulation and Applications. Proceedings of the MC2000 conference 23-26 Oct. 2000 Lisbon, Portugal. Springer Feb 2001 (865-870)
- [3] H. Freiesleben, D. Richter, K. Seidel, S. Unholzer, Y. Chen, U. Fischer, M. Angelone, P. Batistoni, M. Pillon, "Experimental Validation of Shut-down Dose Rates -- Measurement of dose rates, decay gamma-rays and neutron flux", Report TU Dresden, Institut für Kern- und Teilchenphysik, March 2001
- [4] M. Angelone, L. Petrizzi, M. Pillon, S. Popovichev, and R. Villari, "A dose rate experiment at JET for benchmarking the calculation direct one step method", Fus. Eng. Des. V. 82, Issues 15-24, Elsevier 2007, pp. 2805-2811

Acknowledgement

This work, supported by the European Communities under the contract of Association between EURATOM and Karlsruhe Institute of Technology, was carried out within the framework of the European Fusion Development Agreement. The views and opinions expressed herein do not necessarily reflect those of the European Commission.

**International Fusion Materials
Irradiation Facility
(IFMIF)**

Broader Approach Activity: IFMIF Test Cell and High Flux Test Module

Introduction

In the Engineering Validation and Engineering Design Activities (EVEDA) for the International Fusion Material Irradiation Facility IFMIF, which is an element of the Broader Approach activities launched jointly by several European countries and Japan, the german contribution includes engineering tasks for the IFMIF Test Cell and the IFMIF High Flux Test Module. This report covers tasks performed at the Institute for Neutron Physics and Reactor technology at the KIT attributed to the following foreseen procurement arrangements (PAs):

- PA TF-1.1 : Engineering design and Validation of the IFMIF High Flux Test Module
- PA TF-2: Irradiation in fission reactor (Responsible SCK-CEN, contribution by KIT)
- PA TF-6: Test Cell, Access Cell, Test Module Handling Cell and Technology Rooms

According to the planning for EVEDA, these tasks will be performed in the timeframe up to 12/2013. In this report, the progress for the year 2009 is described. For the High Flux Test Module, the design has been documented in the Definition Report, delivered 12/2009 to the IFMIF Project Team.

System Overview

The IFMIF Target- and Test Cell (TTC), containing the lithium target neutron source and the test modules, is shown in Fig. 1. Within a concrete pit, which has a radiation shielding function, there is the TTC vessel, which is gas tight to allow a controlled inner atmosphere, and to provide a barrier against hazardous materials, such as Lithium, NaK, and radioactive contaminants. Inside the TTC vessel, there is a positioning system (rails) which support the test modules. The vessel can be opened by removing the top cover. All connections, like gas supply, electrical power and signals, are connected to the outside world via a so called intermediate ring.

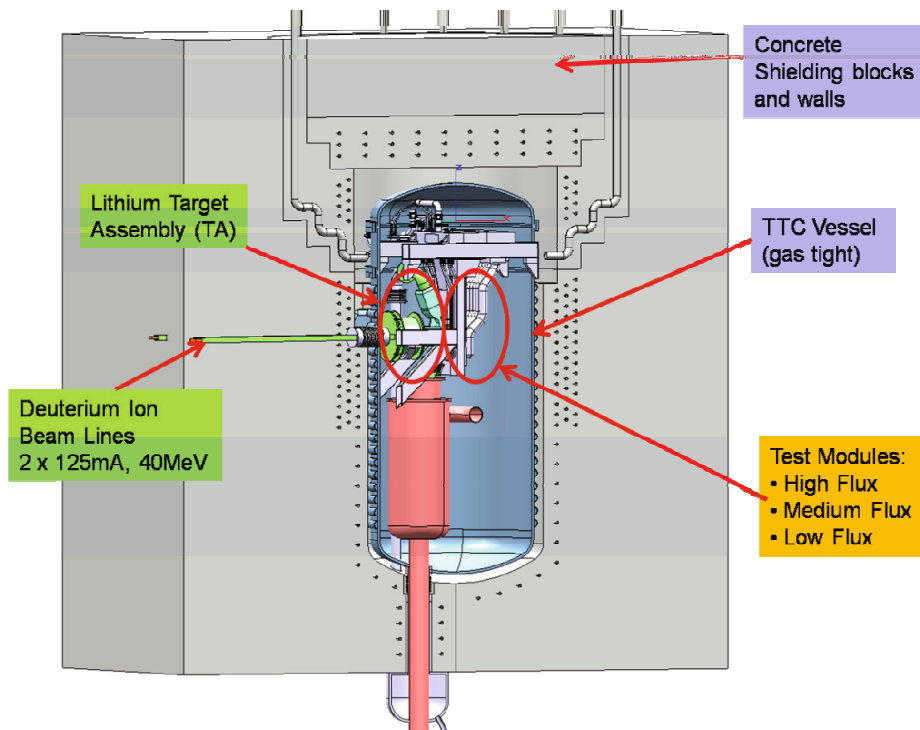


Fig. 1: Overview on the Target- and Test Cell (TTC).

The High Flux Test Module (HFTM) is the irradiation device for miniaturized SSTT samples. The radiation induced changes of the mechanical properties will be assessed after the irradiation (PIE) by several test methods. The HFTM is positioned immediately behind the neutron source inside the TTC. The HFTM is subdivided into eight so called compartments, each of which contains three irradiation rigs. Each rig contains a temperature controlled (heated) irradiation capsule, which can contain up to 80 SSTT samples. It is possible, to adjust individual temperatures for the specimen in each rig, in the range of 250 – 550°C (A high temperature option 650°C is additionally investigated). The HFTM, and three rigs from one compartment, are shown in Figure 2.

The HFTM and the other irradiation modules, together with the TTC and the assembly/disassembly hot cells must ensure an efficient logistics, to ensure a high facility availability. This considerably affects the design of the components.

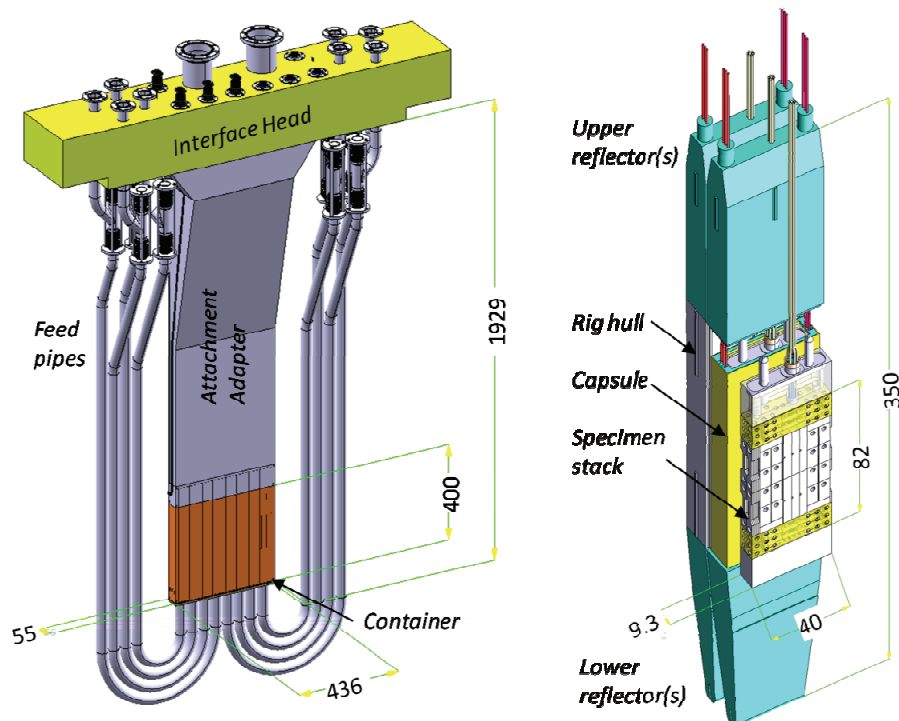


Fig. 2: Overview on the HFTM and the irradiation rigs

Engineering Design and Validation for the HFTM

1. Irradiation Capsule and Rig

The irradiation capsule, which contains a set of material specimen for irradiation inside the HFTM, was already developed and analyzed to a considerable degree of maturity. New efforts were concentrated on the fittings for the filling and emptying of the NaK liquid metal (employed to improve the heat conduction from the specimen to the capsule surface), the specimen insertion and retrieval procedure, and the placement and specification of the welding seams. These activities were a priority in the project, to launch the production of the irradiation capsules scheduled for delivery to the BR2 test reactor on purpose of the irradiation tests in the frame of PA TF-2.

In the operation of IFMIF, newly fabricated capsules will be loaded before every irradiation cycle with either new or previously irradiated material specimen. In the latter case, a portion of assembly steps and manufacturing procedures will have to be performed in radiation shielded hot cells by remote handling tools. The following general procedure is proposed:

1. In the conventional workshop: Joining of the capsule body with already brazed on heaters and the lower cap. Connection of the reflector to the lower cap. Prefabrication of the upper cap with the thermocouples. Ducting the heater and thermocouple wires through the rig hull and upper reflector, fixation of these parts on a building slip (assembly board). Soldering of the heater- and thermocouple wires to an electrical connector socket.
2. In the conventional workshop *or* inside the rig assembly hot cell: Assembly of the specimen stack (about 80 miniaturized SSTT samples) in an assembly tray together with the upper cap and the thermocouple rod. Insertion of this assembly from the assembly tray into the capsule.
3. Welding of the upper cap to the capsule body. First test for leak tightness.
4. Filling of NaK inside the capsule, closing the NaK filling fittings. Final check of leak tightness.
5. Slip the rig hull over the capsule and welding of the rig hull to the lower reflector. Welding the rig hull to the upper reflector.

Compliant with this procedure the following changes were implemented in the CAD design (Overview in Fig. 3):

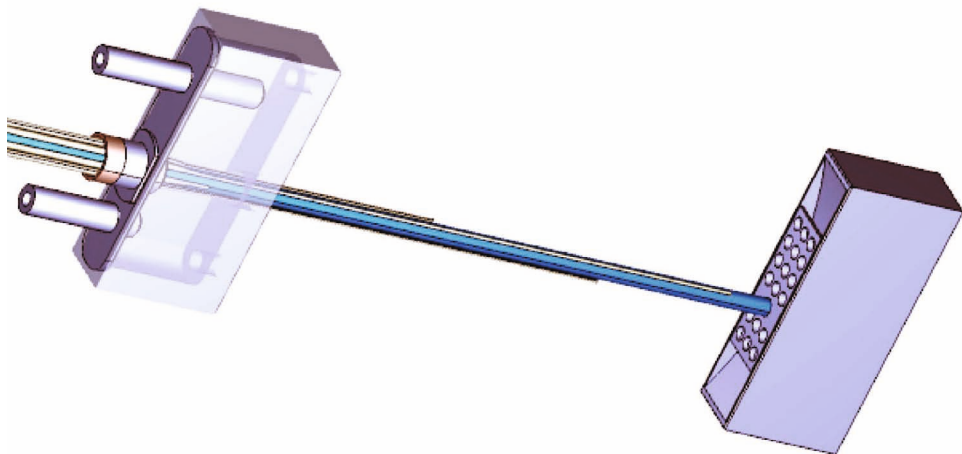


Fig. 3: Upper and lower cap of the irradiation capsule, with feedthrough for thermocouples and central rod.

A central NaK filling tube is leading from the feedthrough plug in the upper cap to the bottom of the capsule. A better, bubble free dispersion of the NaK within the specimen stack is expected from this arrangement in comparison with the previous design, where the NaK was spilt from above on the specimen stack. The thermocouples are now no longer sheathed by a common tube, but immersed directly in the NaK, to have a better measurement of the specimen temperature. A disadvantage is now the direct chemical contact of the thermocouple sheathing material with the NaK. However, according to literature, the compatibility several stainless steel grades with liquid NaK is assured. A dedicated experiment will address this issue directly in the near future.

There is a small insulation gap between the capsule and the rig, with a gap width in the range between 0.2 – 1.0mm. This gap is filled with stagnant helium, and represents the main thermal resistance between the heated specimen and the cooling helium flow. Constancy of this gap is a prerequisite for homogenous specimen stack temperatures. The HFTM-SR (single rig) experiment has been devised to assess the deformation of this gap in operation conditions. To this end, micro deformation sensors have been developed to withstand the high temperatures, and fit into the restricted space. This measurement method has been qualified by assessing sensitivities of several disturbances. The HFTM-SR flow channel(including dummy heaters) has been fabricated to a great extent (completion expected in 02/2010).

2. HFTM Container

The HFTM Container and the attachment adapter have been optimized for fabrication. Especially the weldability of the components has been improved, by adapting the material strengths. The new geometry has been taken as a basis for new CFD and FEM models. CFD calculations of the temperature fields in the structure have been performed for the standard case of specimen temperatures. This will be ensured by thermomechanical FEM calculations, to assess the mechanical stresses in the structures and to arrive at lifetime estimations.

The HFTM attachment adapter has been redesigned with respect to the assembly steps to be performed in the hotcell environment. It is now envisaged that the back cover is open during the insertion of the rigs, so that the adapter, which serves also as a cabling channel, is accessible for handling operations, for example to fix the instrumentation cables. Standing bolts now strengthen the attachment adapter plates against buckling. In the future, a further optimization of the assembly routine in hot cell environments will be pursued.

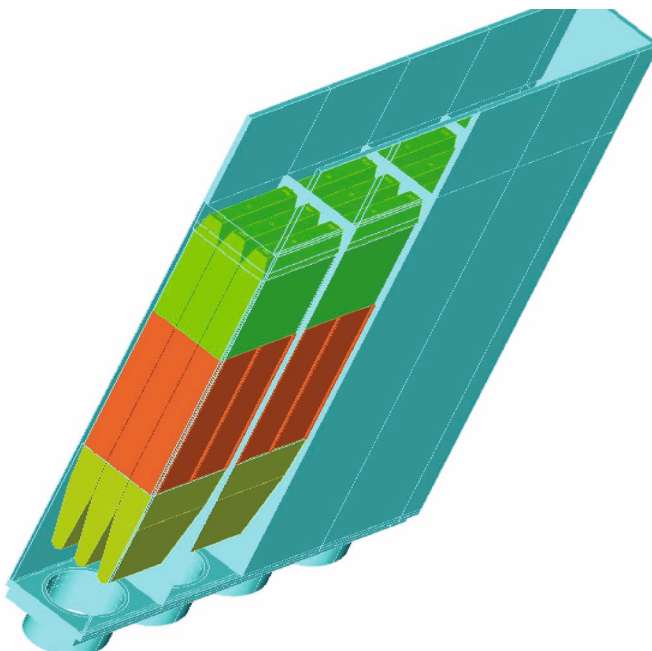


Fig. 4: STAR-CD Model for four compartments (1/2 HFTM) for the simulation of the temperature field of the HFTM.

Engineering Design of the Target- and Test Cell

The cylindrical vessel type test cell design (MTC) has been developed further. Starting from the original dimensions, the TTC vessel diameter has now been reduced from 4m to 3.2m. This significantly reduced the masses, which have to be moved by remote handling during the loading/unloading procedures between the irradiation campaigns, but still offers enough space for the test modules, their positioning system, and the Target Assembly (TA) to be accessible.

A major task is the arrangement of the many hundred electrical cable and gas pipes, connecting the test modules with the "outside world". The following requirements must be met by the connectors:

- Remote Handling Compatibility
- Radiation Resistance (excluding many plastic materials)
- Cooling ability, accommodation of thermal expansions
- High reliability /safety

For the HFTM with 10 gas pipes and approx. 350 electrical lines, an arrangement has been found and implemented into the CAD model, as shown in Fig. 5. A major issue is the choice of the insulation material to be employed for electrical connectors. The best choices are either PEEK or epoxy resins. A connector made of these materials would receive approximately the literature value for the maximum dose at the position of the HFTM interface head within one irradiation period of a half year. Improvement of the shielding of the connectors will be a major challenge for further TTC development.

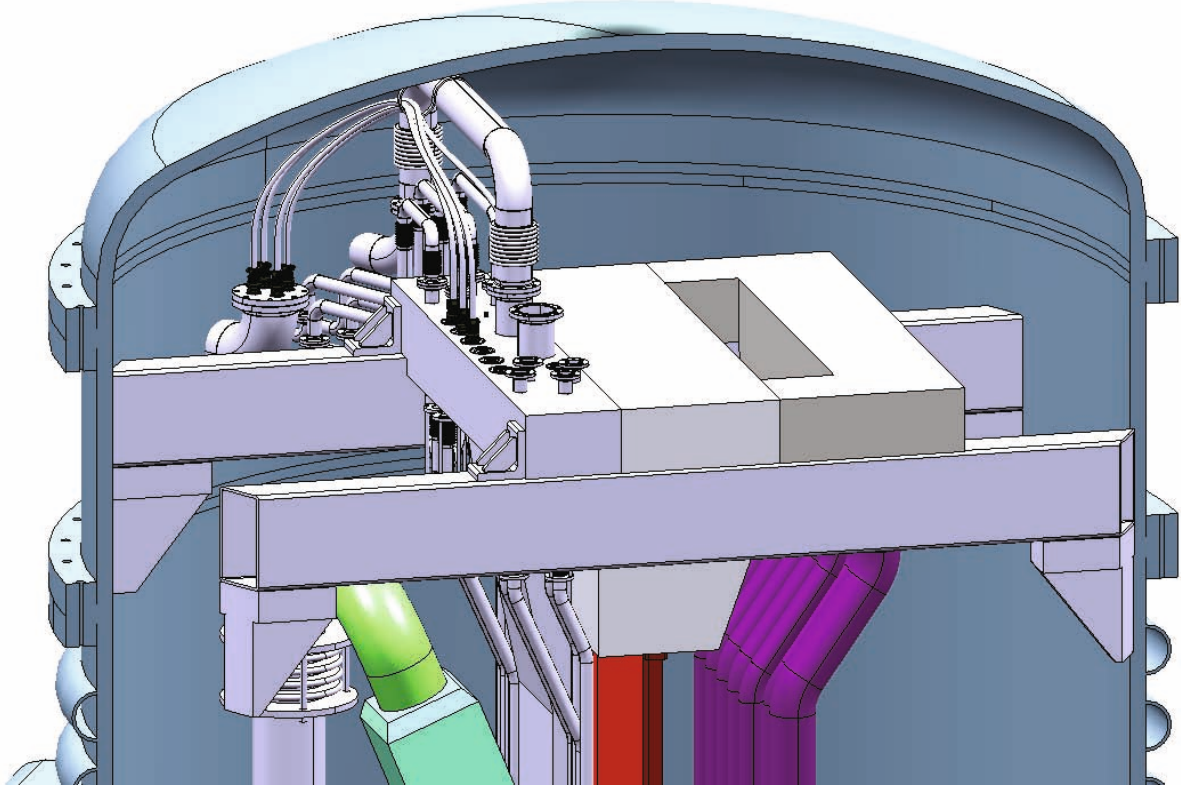


Fig. 5: Pipes and electrical cables (one half is shown) of the HFTM, being accommodated by feedthroughs through the Removable Intermediate Ring of the TTC. Remote handling requirements are met.

HELOKA-LP test facility

The HELOKA-LP test facility is dedicated to the test of the HFTM under 1:1 operation conditions. This facility has been constructed by the industry in cooperation with KIT-INR. In 2009, this facility has been finalized and tested. A view of the facility is given in Fig. 6. It was found, that an optimization concerning the startup and shutdown procedures could be reached, by arranging two buffer vessels at the low pressure end (compressor suction duct) instead one on the low pressure side, and one on the high pressure side. With this new configuration, also the stability of the process variables was improved.

It was proven, that the facility can sustain all specified operation points foreseen for the HFTM mockup, and stay within the given tolerances for mass flow, inlet pressure, and temperature. Fig 7 shows a transient of the process variables between idle mode to the nominal operation point of the HFTM. (0.3MPa inlet pressure, 0.11kg/s helium mass flow, and 50°C inlet temperature). It can be seen, that pressure and mass flow are stabilized after 15 minutes. The stabilization of the temperature takes considerably longer. Next steps are the training of the personnel and fine tuning of the facility, and the construction of the test section port, which will connect the HFTM mockups to the facility.

Staff:

F. Arbeiter

Y. Chen

B. Dolensky

T. Heupel

Chr. Klein

G. Messemer

A.-L. Muche

G. Schlindwein

N. Scheel

E. Stratmanns

K. Tian

K. Zinn



Fig. 6: View of the HELOKA-LP facility.

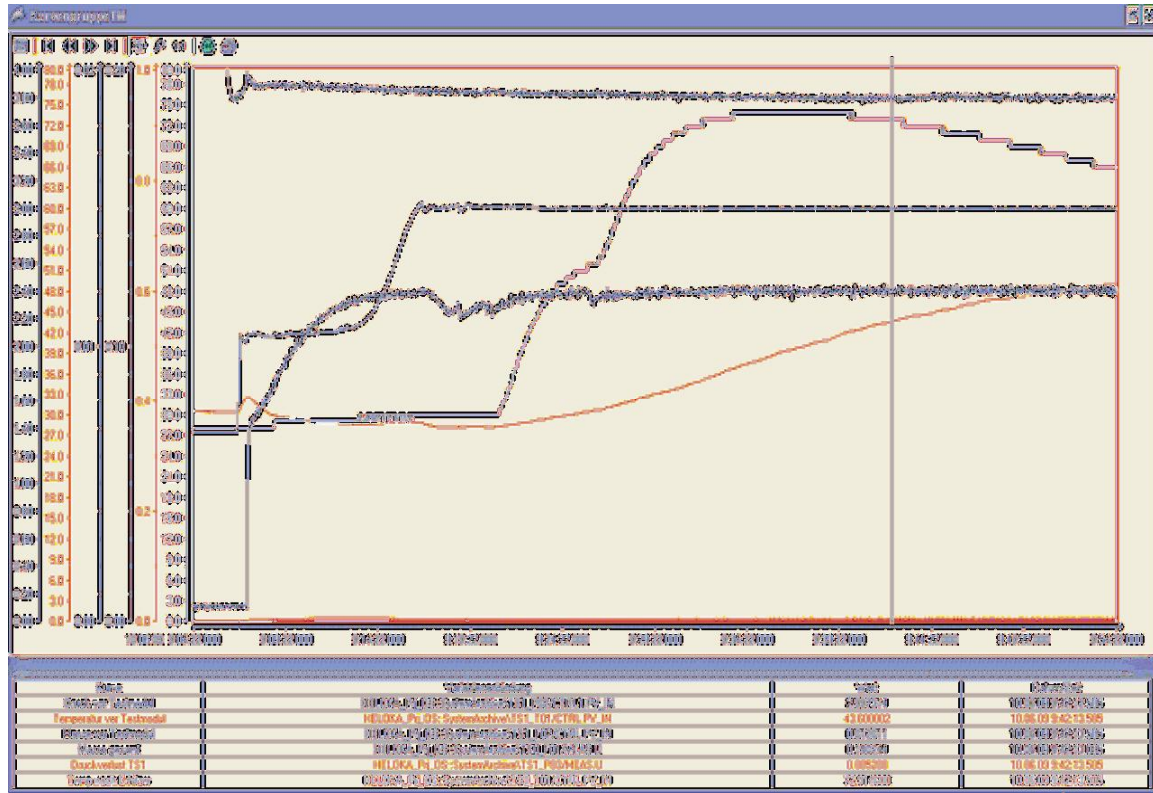


Fig 7: Transient of the HELOKA-LP facility from idle operation to nominal operation point for the HFTM.

Acknowledgement

This work was financially supported by the Ministry of Research and Education (BMBF) under the grant No. 03FUS0008 and is done in the Project IFMIF/EVEDA under the Broader Approach Agreement between Europe and Japan. The views and opinions expressed herein do not reflect necessarily those of the BMBF or the European Commission.

Broader Approach Activity:

IFMIF EVEDA

Material Responses in Creep-fatigue Samples and Heating Bodies irradiated at IFMIF CFTM

Introduction

International Fusion Materials Irradiation Facility (IFMIF) is a deuteron-beam based intense neutron source, which is designed to mimic as close as possible the irradiation conditions for structural materials in future fusion reactors. Besides express irradiation of structural materials to high doses in the IFMIF high flux test module, in-situ creep-fatigue and tritium release experiments are foreseen in the medium flux test module of IFMIF.

Controlling temperature of the samples during irradiation is very important for interpretation of the results, certification and licensing of fusion materials as well as for prediction of material behavior under irradiation. In the high-flux test module sample temperature will be controlled using a combination of electric heaters and helium cooling. Another approach was selected for the creep-fatigue test module (CFTM). Fatigue sample holders will be cooled by helium flow inside the holders, while the samples will be heated by tungsten heating bodies put over the sample holders. Heat inside heating bodies will be generated by nuclear reactions without additional electric heating.

The aim of this study is to assess the present CFTM design and provide the necessary data: material responses of creep-fatigue samples and tungsten heating bodies to neutron irradiation in IFMIF.

Method

The d-Li neutron source and neutron transport were simulated by Monte Carlo code MCDeLicious, which is an extension to MCNP5 with the capability of simulating the generation of neutrons, γ -rays and other d-Li reaction products on the basis of the evaluated Li(d,xn) reaction cross section data.

Comprehensive three dimensional IFMIF test cell geometry model for Monte Carlo calculations developed in the frame of Task TW4-TTMI-003 D5a was used in this study. The model was modified to reflect the latest design modifications of the CFTM.

Since d-Li IFMIF neutron source generates neutron spectrum extending up to 55 MeV, the neutron transport, activation and transmutation calculations require cross sections exceeding the traditional limit of 20 MeV.

CFTM Geometry

Side and front views of the IFMIF test cell with respect to the direction of the deuteron beam are shown in Figure 1. Arrangement of liquid lithium target, high-flux test module (HFTM) and creep-fatigue machine followed by tungsten spectral shifter plate and tritium release module is presented on left part of the figure. Three creep-fatigue specimens, hollow sample holders and tungsten heating bodies as well the frame of creep fatigue machine are shown on the right.

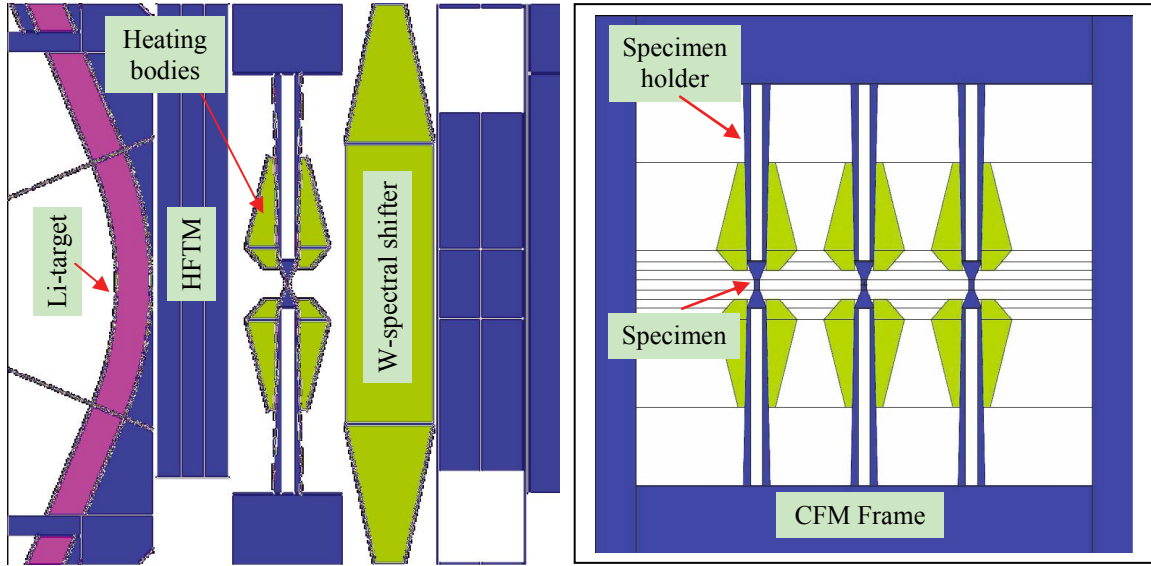


Fig. 1: IFMIF test cell: side (left) and front (right) views.

Results

Damage rate variation along sample length is shown in Figure 2. The average dose rate in the gauge region is around 13 dpa/fpy and 10 dpa/fpy for the central and peripheral samples respectively. The variation of the damage rate along the sample gauge is less than 10% of the average value excellently conforming to the IFMIF user requirements.

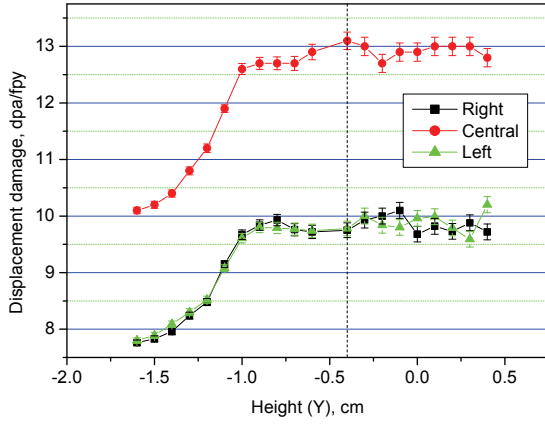


Fig. 2: Damage rate along the sample length calculated for central and two peripheral samples.

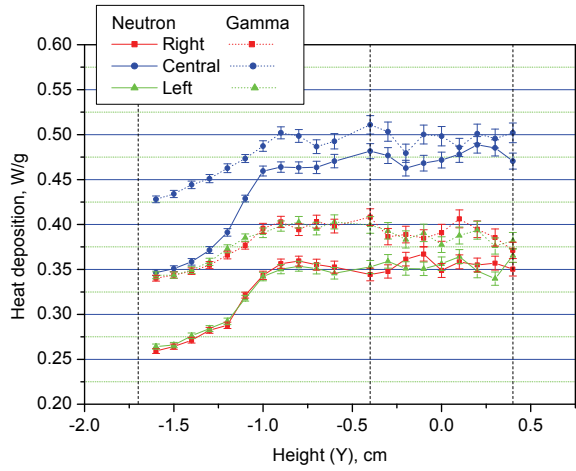


Fig. 3: Heat deposition along the sample length calculated for central and two peripheral samples.

Heat deposition produced by neutrons and gamma averaged over the sample gauge is 1 W/g and 0.75 W/g for the central and side specimens. Gammas and neutrons provide approximately equal contributions to the total heat deposition. Heat production in the heating bodies changes gradually with decreasing the distance from the beam centre from 0.3 to 0.7 W/g. In the case of tungsten more than 95% of the heating is produced by gammas.

Three dimensional heat distributions through the specimens and heating bodies necessary for the thermo- hydraulic analysis were obtained using a mesh tally capability of MCNP5 (see examples in Figures 4 and 5).

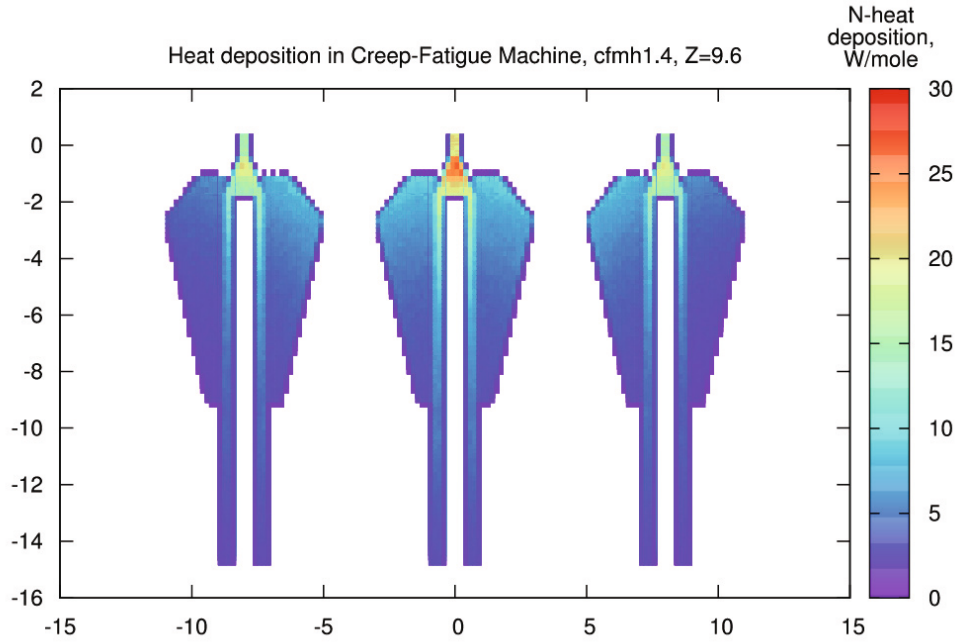


Fig. 4: Neutron heat deposition in W/mole generated in the middle cross section of the creep-fatigue samples.

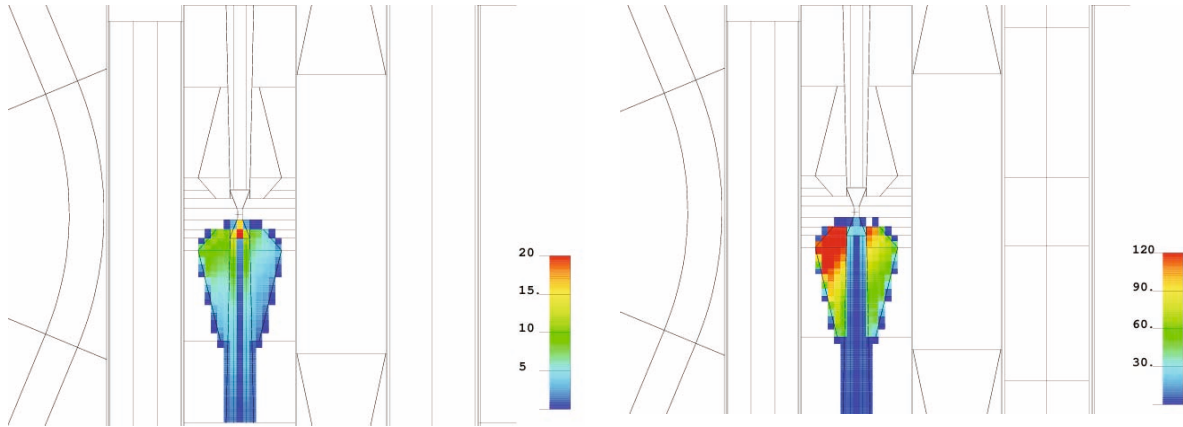


Fig. 5: Neutron (left) and gamma (right) heat depositions in W/mole generated in the middle cross section of the central creep-fatigue specimen (cut along the beam) imposed over the test cell geometry.

Conclusions

Some conclusions relevant for the IFMIF CFTM design can be drawn based on the results of this study.

- Major material responses show only moderate changes against fine details of CFM design, unless the distances from the back plate and between the samples are kept. Otherwise severe reduction of the irradiation dose seen by the creep-fatigue samples is expected.
- In particular, total heat deposition in the c/f samples is ~ 1 W/g in the central and 0.75 W/g in the peripheral samples (cf. 0.9 and 0.45 W/g in the previous version).
- Damage rates remain unchanged: 13 dpa/fpy and 10 dpa/fpy in the central and the peripheral samples respectively.
- Heat deposition in the heating bodies comes mainly due to gammas: 0.3-0.7 W/g in the central and 0.2-0.6 W/g in the peripheral bodies.

- Previous evaluation has shown that damage in the heating bodies is notably lower than in the c/f samples: 7.4 and 3.4 dpa/fpy, respectively. This is expected due to significantly larger threshold displacement energy for tungsten (40 eV, cf. with 25 eV for Fe).
- Our calculations have shown that the components installed at the height of 24 cm from the beam axis will be subjected to a radiation rate of 30 Gray/s, which gradually decreases with increasing height and is ~2–3 Gray/s at the fatigue actuator electric motor. The energy rate at the load cell in the PIREX *in situ* tests was 0.027Gray/s. The energy deposition rate in the IFMIF electro-mechanical components of CFTM will be about 100 times higher, even assuming that they will be mounted far enough from the specimens. Therefore, shielding of such components can be recommended.

Staff:

U. Fischer
A. Möslang
S. Simakov
P. Vladimirov

Literature:

- [1] P. V. Vladimirov, A. Möslang, P. Marmy, *Material Responses in IFMIF Creep-fatigue Testing Machine*, Fus. Eng. Design **83**(10-12) (2008) 1548-1552
- [2] P. Vladimirov, S. Bouffard, *Displacement damage and transmutations in metals under neutron and proton irradiation*, Eds.: J. L. Boutard, S. Dudarev and G. Martin, Fusion and Generation IV Fission Power Reactors: Behaviour of Materials Subjected to Fast Neutron Irradiation, Compt. rend. Phys. **9** (2008) 303-322
- [3] P.V. Vladimirov, A. Möslang, *Irradiation Conditions for Breeder Materials in Tritium Release Module of IFMIF*, 14th International Conference on Fusion Reactor Materials, September 6-11, 2009, Sapporo, Japan

Acknowledgement

This work was financially supported by the Ministry of Research and Education (BMBF) under the grant No. 03FUS0008 and is done in the Project IFMIF/EVEDA under the Broader Approach Agreement between Europe and Japan. The views and opinions expressed herein do not reflect necessarily those of the BMBF or the European Commission.

Fuel Cycle – Vacuum Pumping

Upgrade of TIMO Facility (TW5-TFFF-VP 58, F4E-2009-GRT-019-01)

Background and objectives

Following successful completion of the testing of the 50% scale ITER model pump, a full scale ITER torus pre-production torus cryopump (PPC) is being designed and constructed for testing in the TIMO facility. Certain features of the TIMO infrastructure need to be upgraded to accommodate the larger ITER-scale pump and to operate it according ITER requirements, and the scope of this task is to provide for the supply and installation of these features so as to have a replication of ITER conditions in many aspects for the new, bigger sized pumps in the same way as it was provided for the 50% scale model pump. The fully upgraded facility is called TIMO-2. In the reporting period, the enhancement activities towards TIMO-2 were continued and the work in most subsystems could be completed.

New cryotransfer line for TIMO-2

Preparing the future programme for TIMO-2, the facility was rearranged for the tests with the ITER prototype pump as well as a few of the serial torus and cryostat cryopumps. One step was the replacement of the rigid transfer line between the valve box and the pump by a flexible one, see Figure 1. With this new flexible transfer line the turnover time for the pump exchange operation will be reduced. A major advantage which helps to reach this shorter turn over time are the Johnston coupling connections integrated in the supply and return lines. The integration of the Johnston couplings follows the concept of the ITER cryo-jumper.

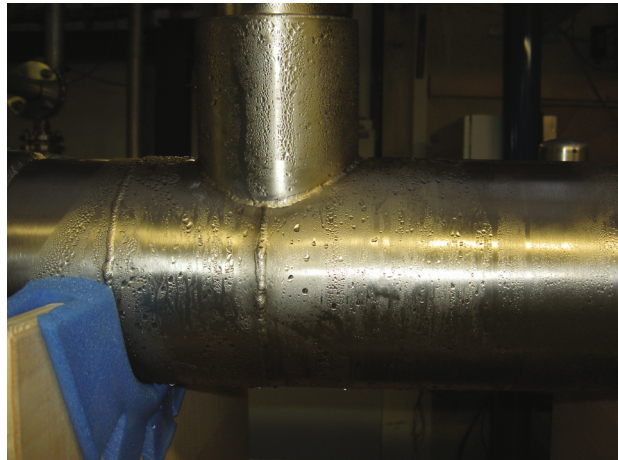


Fig. 1: Left: The new flexible TIMO-2 cryogenic transfer lines, equipped with heaters (for acceptance purposes). Right: Moisture condensation on top of the lines under cryogenic conditions inside due to inefficient insulation vacuum.

Following the assembly and installation of the line in TIMO the acceptance tests were started using a dummy bypass as cryogenic client. Caused by problems with the insulation vacuum, see Fig. 1 right, it was decided to replace the existing (typically used by the manufacturer NEXANS) metallic sealed closures by valves, which solved the problems. This solution gives also the possibility to check the pressure inside the insulation vacuum and to improve it if necessary.

Currently, detailed pressure drop measurements are being performed, to characterise the cryoline well, and to derive from that an estimate on the acceptable pressure losses downstream the cryogenic valve boxes at ITER. This is an essential information needed to design the cryopumps and not known at the moment, as ITER only specifies the integral pressure loss which combines the loss of the valve box, along the lines, and across the pump.

Adaptor flange for the TIMO-2 test vessel

Caused by different flange dimensions of the PPC and the ITER model pump an adaptor flange is necessary for the installation of the PPC into the TIMO-2 test vessel. For manufacturing, the information on the existing 3D TIMO flange dimension was measured very accurately, especially the area of the seal and the 72 screw holes. The measurement was carried out with a tactile method. The manufacturing order was given to the company DeMaCo already end of 2007, but could only be finished by April 2009, which meant a significant delay. During the acceptance tests at DeMaCo, the adaptor flange together with the flange support were checked. During this inspection a scratching spot on the sealing surface was detected, see Fig. 2 (right). This necessitated to re-work the sealing surfaces on the adaptor flange. After successful remachining of both sealing surfaces the adaptor flange was delivered in June 2009 to KIT.

The result of the acceptance tests at KIT was that the required sealing surface roughness is fulfilled. The adaptor flange together with the supporting frame, as shown in figure 2 is ready for use and stored at the ITEP.

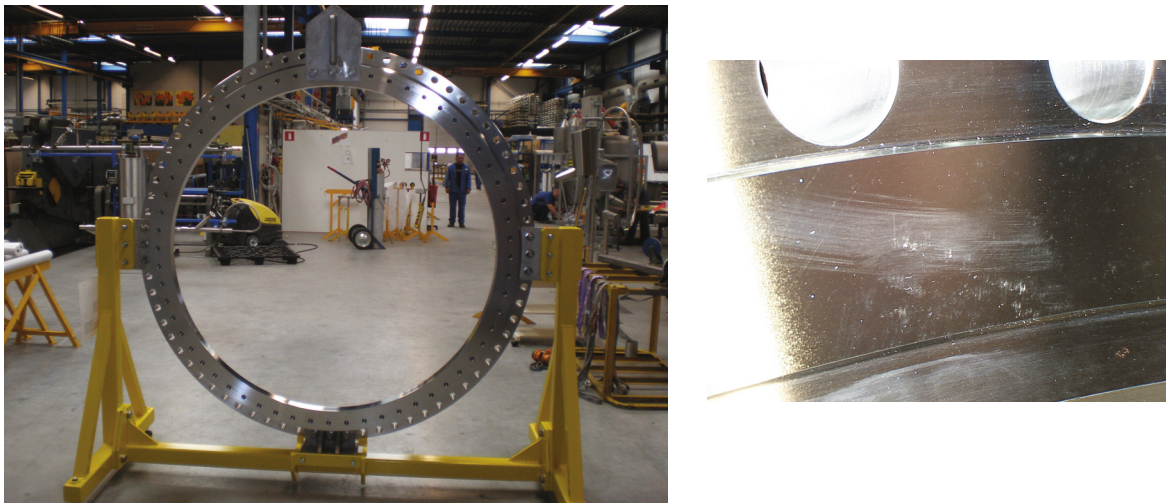


Fig. 2: Left: The final adaptor flange for the TIMO-2 test vessel installed in the supporting frame. Right: Scratching marks on the sealing surface which necessitated re-machining.

New pressure device for the TIMO-2 control cryostat

The FZK TIMO-2 facility is the only available EU facility capable of testing a real size ITER torus cryopump by providing the necessary cryogenic flow rates at different temperature levels between 4.5 K and 470 K. However, ITER now proposes to operate with lower inlet temperatures of 4.35 K. In order to accommodate such an inlet temperature reduction, the present TIMO-2 facility, used for testing the ITER model cryopump with 4.5 K supercritical helium (ScHe), must be upgraded. This is provided under the F4E Grant F4E-2009-GRT-019-01.

During the normal operation the ScHe flow is supplied by the 2 kW LINDE facility available at ITEP. The temperature adjustment is done by means of a control cryostat which is filled with ~ 3500 l liquid helium (LHe). The temperature of the ScHe provided to the TIMO-2 test com-

ponent is given by the thermodynamic condition of the boiling helium inside the control cryostat and the subsequent heat intake of the helium flow on the way from the control cryostat to the test component. For the provision of the cryogenic supply at 4.35 K with the TIMO-2 control cryostat some modifications at TIMO-2 and the 2 kW LINDE facility were necessary.

The temperature in the piping system inside the control cryostat can be reduced by reduction of the boiling pressure of the helium bath from 1.3 bar(a) down to close to ambient pressure. For this operation a new pressure measurement device for the gaseous helium volume in the control cryostat was installed. In the second step the available compressor units at the 2 kW LINDE facility were modified such that they can cope with these reduced intake pressures. For the control of this operation a new pressure transducer was installed (range between 0.1 mbar(a) and 2000 mbar(a)).

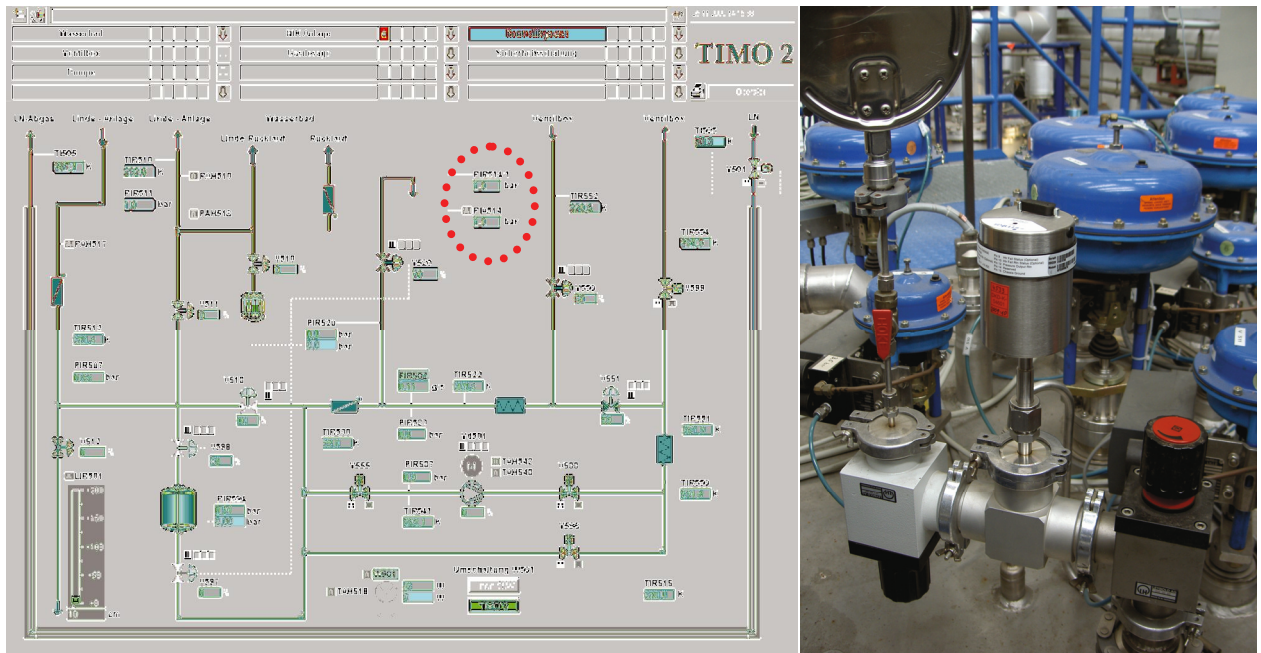


Fig. 3: The new pressure measurement device of type Baratron 627D (Company MKS) installed on top of the control cryostat (right side) is used for the new operation mode, integrated as pressure measurement device PIR 514_1 in the PLC PCS7 operation screen for the control cryostat.

The signal of the new pressure measurement, is integrated to the TIMO-2 PCS7 as well as to the PCS7 of the 2 kW LINDE facility and is used to control the pressure reduction inside the control cryostat by regulation of the compressors of the 2 kW LINDE facility. As a result of this new pressure control loop the temperature in the helium bath as well as in the piping of TIMO-2 cooling circuit can be reduced.

In addition to these activities works started to minimize the heat uptake along the cryogenic transfer lines between the control cryostat and the TIMO-2 valve box. Inside the valve box the piping system was checked and the superinsulation of different pipe sections was revised.

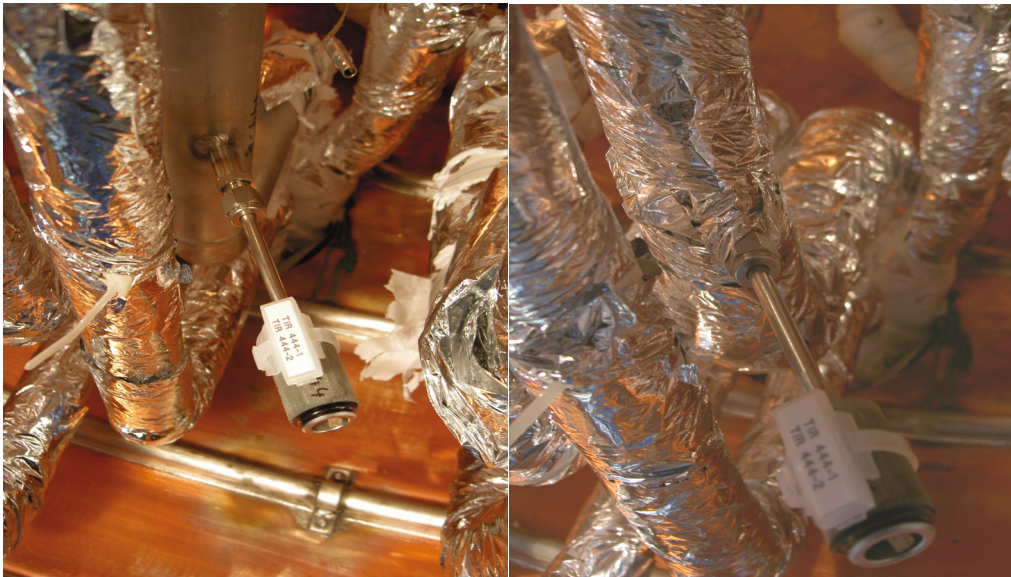


Fig. 4: Refurbishment of the superinsulation around the cryogenic piping inside the TIMO-2 valve box.

Conclusions

The TIMO upgrade project has progressed according to plan and will be accomplished during 2010. This is ready in time for the foreseen experimental campaigns with the PPC to be conducted in TIMO-2.

Staff:

Chr. Day
A. Demsooreanu
H. Haas
Th. Johann
R. Müller
P. Pfeil
M. Scannapiego
H. Strobel
H. Stump
J. Weinhold

Acknowledgements

This work, supported by the European Communities under the contract of Association between EURATOM and Karlsruhe Institute of Technology, was carried out within the framework of the European Fusion Development Agreement. The views and opinions expressed herein do not necessarily reflect those of the European Commission.

This work was supported by Fusion for Energy under the grant contract No. F4E-2009-GRT-019-01. The views and opinions expressed herein reflect only the author's views. Fusion for Energy is not liable for any use that may be made of the information contained therein.

Completion of Final Design for the Prototype Torus Cryopump and Testing in TIMO-2 to Qualify the Design (F4E-2009-GRT-018-01)

Background and objectives

The reference design of the ITER exhaust gas pumping includes 8 cryopumps to pump the torus via 5 ducts (increase from 4 to 5 is a recent design change in 2009). The design of these cryopumps has to consider the different requirements for vacuum pumping, remote handling and safety, and provides strong interfaces to the surrounding environment of the installation port plugs of the ITER machine.

The aim of this task is to provide the build-to-print design of the pre-production cryopump (PPC, formerly PTC), including the mechanical construction, the calculation of thermohydraulic properties, the definition of operational parameters and the assessment of all safety issues. The extensive data base which has been achieved during several years in the TIMO campaigns with the model cryopump has served as a very important reference. The basic concept of the cryosorption pumping philosophy realized in the PPC has been successfully validated in former test series at TIMO and JET as well as for NBI applications.

The PPC is a prototype device, which will be tested in the TIMO-2 facility at KIT. This test rig is an upgrade of the existing TIMO test bed which has already been used for the characterisation of the ITER model pump and has been upgraded under parallel activities (F4E-2009-GRT-019; TW5-TTFF-VP58). It is anticipated that the serial pumps and the PPC will be very similar; however, some minor additional features have been introduced to the PPC design to ease defined testing.

2009 ITER baseline requirements on the torus cryopump

Pumping: The requirements on pumping are defined by the different operation modes. The key requirement in plasma operation is to maintain a typical divertor pressure between 0.25 Pa and 10 Pa against the high exhaust gas throughput of up to 200 (Pa·m³)/s. Different calculations showed that in combination with the limited conductance of the pumping ducts, a pumping speed at the bellows in front of the pump inlet of 50 m³/s (D₂, 273 K) per pump is reasonable. The pumping requirements for conditioning of the vessel as well as the dwell pumping between the burn pulses are depending on the preceding operation history, which determines the outgassing of the wall materials. For the dwell pumping mode at the end of the 1400 s dwell period (maximum repetition rate condition) a terminal base pressure of 0.5 mPa is required. In view of these challenging requirements, the chosen design philosophy for the individual torus cryopump was optimised for maximum pumping speed in molecular flow regime.

Space and Remote Handling: The torus cryopump is classified as Remote Handling Class 2, which means that it does not have to be disassembled on a routine basis. The maximum possible outer cryopump diameter is 1780 mm. The available distance between the pump plug and the remote handling cask is limited to 250 mm. All parts having a length longer than that have to be designed such that they can be disassembled before starting any remote handling operation. The pumping duct provides a maximum length of 2248 mm for the cryopump.

Safety: The maximum amount of pumped hydrogen isotopes is given by the limitation of the deflagration pressure which would result inside the cryopump under a LOVA (Loss of vacuum accident) event. The maximum allowed deflagration pressure in ITER is set to 0.2 MPa, the design pressure of the duct, leading to a maximum gas hydrogen inventory of 1.5 mol/m³ hydrogen isotopes. The ITER torus cryopump will have a connection to the surrounding volume to reduce the hydrogen deflagration pressure by providing the larger volume of the port cell. Further, the maximum tritium inventory in all pumps is set to the admin-

istration limit of 180 g. The pump plug is also working as a radiation shield that limits the radiation behind the bioshield to less than 10 $\mu\text{S}/\text{h}$. A pump plug thickness of 270 mm is therefore required.

Design enhancement

The basic design of the torus cryopump as developed in 2007 is still maintained (shown in Fig. 1) [1, 2]. It is circular shaped with a maximum outer diameter of 1776 mm and a total length of about 2054 mm. The 4.5 K charcoal coated pumping surface of 11.2 m^2 is roughly three times larger as was for the ITER model pump. The outer 80 K shields and the louver baffle form an enclosure around the 4.5 K pumping panels against the heat radiation from inside and outside the cryopump. The pumping speed can be varied by throttling the main valve, which opens towards the torus with a maximum stroke of 500 mm. The valve inlet diameter is 800 mm. The prototype torus cryopump can be separated into four main sub-assemblies: the pump outer shell including the pump plug, the 80 K system, the 4.5 K system and the pump inlet valve.

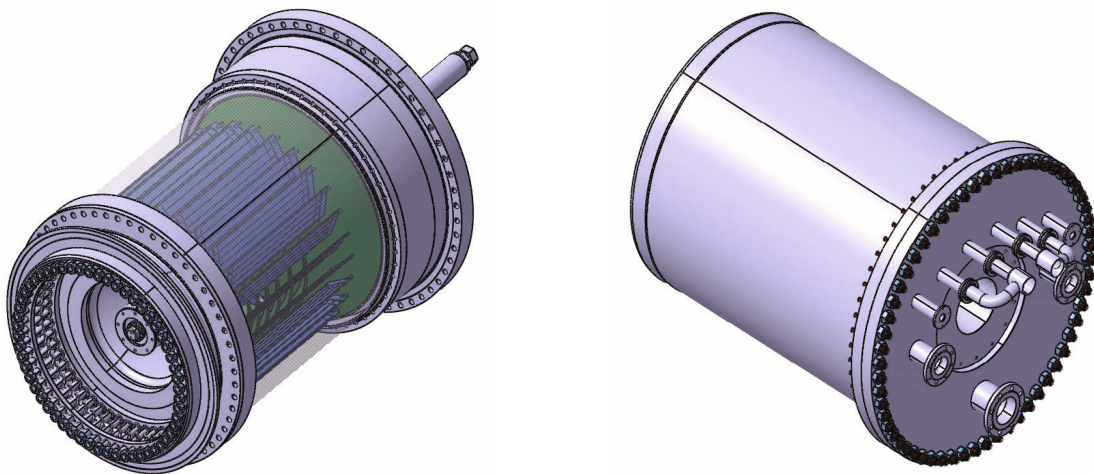


Fig. 1: Basic design of the torus pump as single unit (left without outer 80 K shield and housing).

Inside of this Grant the design will be adapted to the changed ITER requirements on the torus cryopumps. The design enhancements include the change of the 80 K und 4.5 K system to reduce the pressure loss as well as the design adaptation to the new remote handling supports and the new deflagration suppression system. A partly new design of the valve is needed due to change of the supply pressure from 1.8 to 0.8 MPa. In 2009 all needed design enhancements for the 80 K system were integrated, as described in the following.

The 80 K system: The 80 K system (see Fig. 2) includes six plain shields around the 4.5 K panels which protect the panels from the heat radiation of the housing and the inner valve parts and the inner baffle structure. The baffle subassembly consists of 11 louver panels with a 45° inclination for cooling the gas to be pumped and protecting the 4.5 K panels against heat radiation through the pump inlet. The shields and baffles are cooled by a forced flow of gaseous helium (GHe) at a temperature of about 80 K and a supply pressure of max. 1.8 MPa. Shields and baffles are connected in series to guarantee a uniform distribution of the coolant. All shields and baffles are made from hydroformed 2 mm thick stainless steel sheets in spot-welded quilted design to exclude any plastic deformation caused by high pressures during testing and operation.



Fig. 2: 80 K subassembly of the pre-production cryopump.

Therefore FEM calculations were started to determine the optimal design of such a flexible valve head. Fig. 3 shows the results of FEM calculation for a corrugated head design.

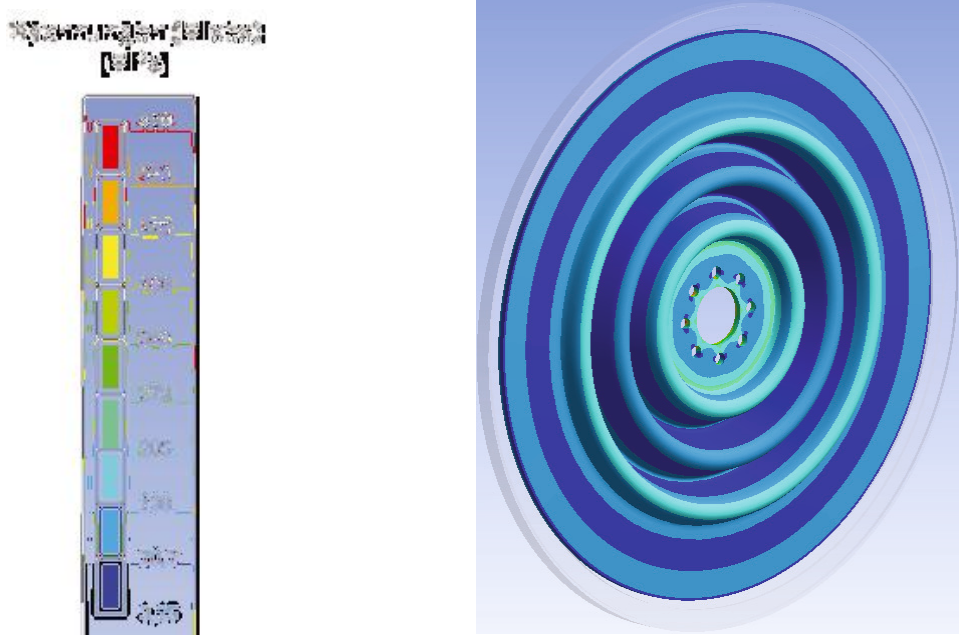


Fig. 3: FEM calculations of a corrugated PPC valve head design.

Outlook

The detailed build-to-print design of the PPC design will be fully elaborated during 2010. After that, the Technical Specification for manufacturing will be written and the manufacturing order will be tendered and placed. When manufactured, the Grant will be resumed and the complete PPC will be tested in the TIMO-2 facility to validate the design and measure the pressure drop in the 4.5 and 80 K circuits.

The design enhancements include the replacement of the active cooled inlet shield by a passive cooled one and a new routing of the 80 K pipes. The aim of these changes is the reduction of the overall pressure drop in the 80 K system. The outer shields were designed partly new to introduce larger gaps that are necessary to reduce the pump-out time of gas at regeneration.

A second design issue in 2009 was the valve head. The reduced gas supply pressure of the valve actuator requires a change in the valve head alignment. The alignment in the basic design was realised by a flexible part in the valve shaft. A new design option is a flexible valve head itself.

Staff:

Chr. Day
A. Demsooreanu
V. Hauer
P. Pfeil
M. Scannapiego
R. Simon
H. Strobel
H. Stump
M. Börsch, D. Örtig (Company WEKA, Switzerland, Third Party to KIT)
X. Sauge (Company SDMS, France, Third Party to KIT)

Literature:

- [1] V. Hauer, J.-C. Boissin, Chr. Day, H. Haas, A. Mack, D.K. Murdoch, R. Lässer, M. Wykes, Design of the ITER torus prototype cryopump, *Fusion Engineering and Design* 82 (2007) 2113–2119.
- [2] Chr. Day, A. Antipenkov et al., Numerical simulations of electromagnetic transients in ITER cryopumps with the use of TYPHOON code, *Int. Conf. On Mathematical Modeling and Comp. Physics*, Dubna, Russia, July 2009.

Acknowledgement

This work was supported by Fusion for Energy under the grant contract No. F4E-2009-GRT-018-01 with collaboration by SDMS S.A.S. La Chaudronnerie blanche, France and WEKA AG, Switzerland. The views and opinions expressed herein reflect only the author's views. Fusion for Energy is not liable for any use that may be made of the information contained therein.

Instrumentation for ITER Cryopumps and Cold Valve Boxes (F4E-2009-GRT-020-01)

Background and objectives

This task aims to support ITER IO in the definition of instrumentation for the cryopumps (torus, cryostat, NBI) and the Cold Valve Boxes (CVBs) reflecting the specific ITER requirements and conditions. The work will start with the definition of the number and location of sensors needed to fulfil the given ITER measurement tasks under normal and off-normal operation conditions. Then, a survey of suitable commercially available instrumentation will be given. A screening of them will be done to find matching solutions, and, where this can not be found, a programme for the development and qualification of novel sensors for ITER needs will be defined.

The scope includes measurement information for temperatures (in a very wide range incl. cryogenic, i.e. ~ 4 K to 500 K), pressures (in vacuum as well as above atmospheric for the pressurized cryogen, i.e. $\sim 10^{-10}$ mbar to 20 bar), cryogenic mass flows (up to ~ 200 g/s helium), gas composition, and pumped amounts.

Collection of 2009 ITER baseline system requirements

Starting point for this activity is to collect a defined input of the ITER environmental conditions and system requirements. This action was finalized in the reporting period 2009.

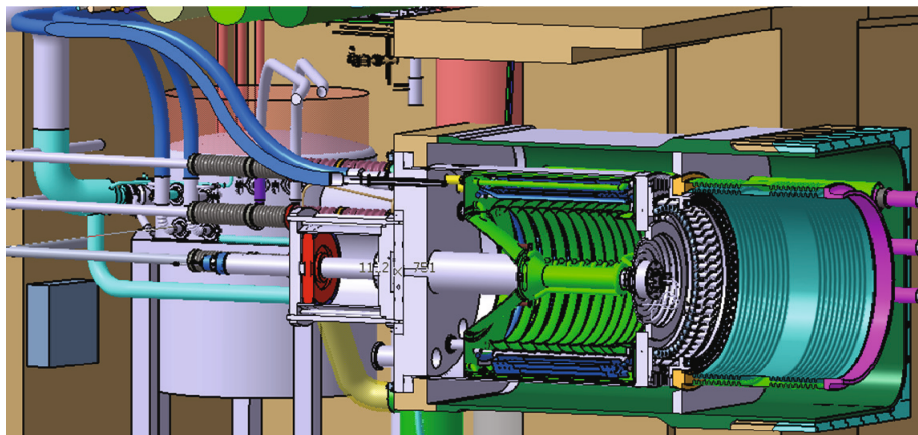


Fig. 1: Typical installation situation of one of the 8 torus cryopumps. Left is the CVB, right is the bellow connection towards the torus.

The geometric situations are shown in Figs. 1 and 2. The torus/cryostat cryopumps are within the bioshield whereas their dedicated CVBs are part of the port cell. The NBI itself is integral part of a dedicated NBI cell.

Table 1 summarizes the magnetic and radiation system requirements with which the instrumentation has to be compatible with.

Table 1: Summary of environmental conditions.

Requirement	Torus/ cryostat cryopump	NBI cryopump	Torus/ cryostat CVB	NBI CVB
Magnetic field strength [T]	0.55	0.15	0.125	0.05
Radiation, equivalent dose [Gy]	10^6	10^6	10^2	10^2

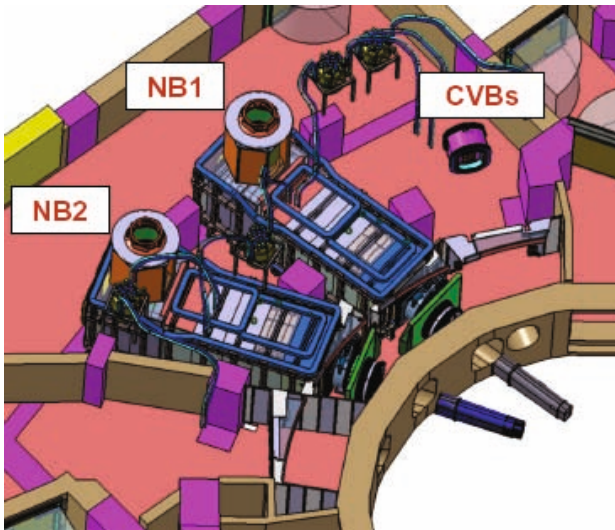


Fig. 2: Installation situation of the two first ITER NBI vessels (containing the NBI cryopump) with their dedicated CVBs.

as ultrasound) suffer from poor resolution at cryogenic conditions.

The task does also reflect the philosophy of ITER to operate the torus cryopumps on a flexible and intelligent automated regeneration pattern rather than according to a strict predefined scheme. This approach will provide a lot of flexibility, but is more demanding for instrumentation (e.g. to balance the pumped and released amount, and to identify when the capacity limit is approached). The instrumentation would provide data as part of a suite of measures capable to access pumped quantities to identify regeneration requirements. Several concepts have been developed and are currently further investigated. The most promising candidate is based on a prediction of the incoming flow as a function of pressure measurements in the duct and divertor and an accurate measurement of the valve position.

Once a sensor is identified, the whole measurement chain has to be assessed, including internal and external cabling as well as compatible feedthroughs.

Outlook

As next step, the type, position and number of measuring devices will be identified under the ITER specific requirements and limitations (access, maintenance). Furthermore, the necessary accuracies and ranges will be developed. Measurements that do not correspond to any commercially available device will be identified and possible R&D routes will be explained.

Staff:

Chr. Day

A. Demsooreanu
H. Haas
V. Hauer
P. Pfeil
H. Stump
J.-L. Marechal (CEA Cadarache, Third Party to KIT)

Acknowledgement

This work was supported by Fusion for Energy under the grant contract No. F4E-2009-GRT-020-01 with collaboration by CEA, France. The views and opinions expressed herein reflect only the author's views. Fusion for Energy is not liable for any use that may be made of the information contained therein.

One of the major challenges associated with temperature measurement is the wide range that has to be covered with especially high resolution of the order of 10 s of mK at around 4 K. At the same time, a high cycling stability (at around 30 000 cycles) has to be ensured. According to the first preliminary results, it looks as if this cannot be provided in one single sensor.

The major challenge of the vacuum gauges is in general their poor accuracy at pressures below the lower limit of diaphragm gauges and their strong dependence on residual magnetic fields.

The central challenge of cryogenic flow instrumentation is their unacceptable high pressure losses if direct measurements are implemented. Alternative methods (such

Conductance Modelling of ITER Divertor and Torus Pumping Duct (EFDA/06-1498 (TW6-TFFF-VP 68))

Background and objectives

The simulation of the ITER torus vacuum system was started under a previous EFDA Task (TW4-TTFF-VP 47). At that time, the results revealed a strong conductance limitation of the reference pumping duct. The calculated pressure profile of the duct identified the divertor pumping slots as the bottlenecks. This was one of the reasons for ITER to re-design the divertor.

The scope of this present task is to estimate the conductance of the re-designed ITER divertor and torus pumping ducts. This shall be achieved by intense use of the ITERVAC code [1].

ITERVAC full network model

Within this task, a comprehensive and very detailed model of the ITER torus vacuum system was built up for the first time. Only the maximum throughput for one gas species at isothermal conditions can be calculated, determined by the conductance of the individual elements. So, the calculated maximum throughputs can be larger than the real fuelling flow rate into the torus.

The real flow situation of a standard divertor cassette is illustrated in Fig. 1. The final ITER-VAC flow model for the full divertor system (54 cassettes, 4 pumping ducts) with about 1600 model ducts is shown in Fig. 2 [2]. The sections of the divertor system are logically split into channels with constant shapes, cross sections and length. The channel symbols in the models are linked with linking nodes. Linking nodes define the locations inside the model where the results have to be calculated. After a simulation the pressure and mass flow for every node is known. The total inlet cross section of the pumps is chosen to 680 m². The pumping speed of the plasma is assumed to be very large (above 20,000 m³/s), which is limited by ITERVAC in relation to the small opening inside the divertor dome and target plates supports and between the cassettes to the black hole pumping speed for the plasma pumps.

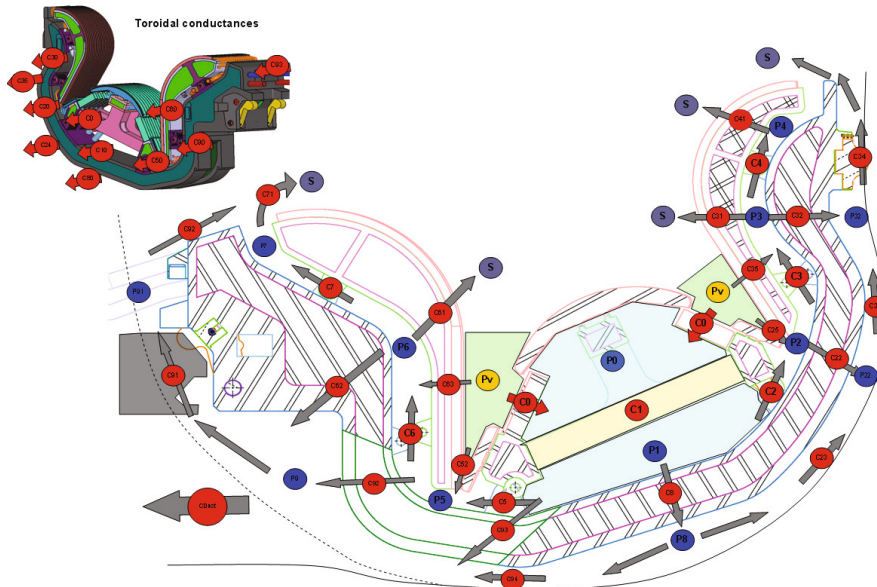


Fig. 1: Flow situation of a standard divertor cassette before simplification.

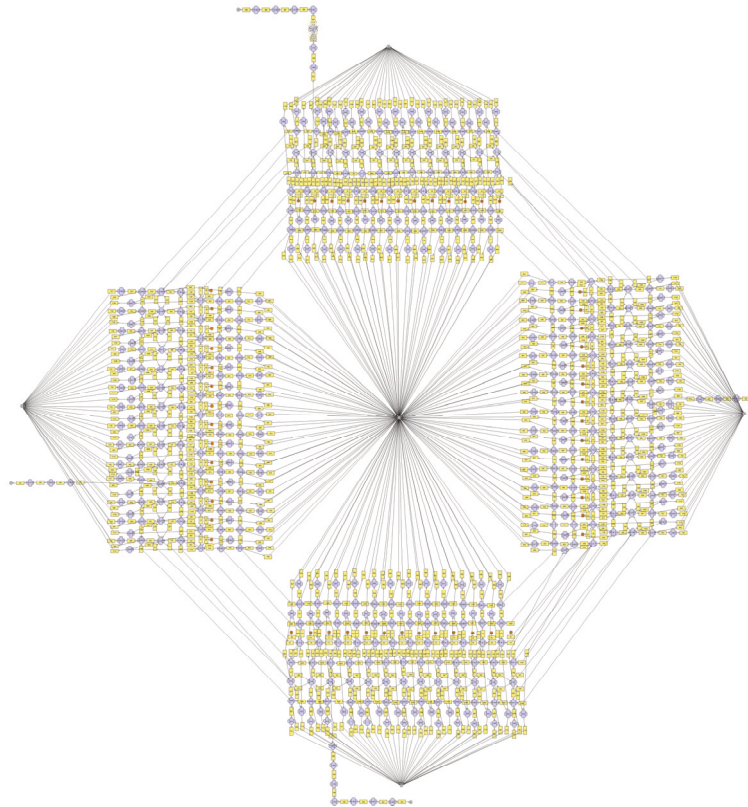


Fig. 2: ITERVAC model of the full ITER torus vacuum system.

The pressure inside the divertor dome was varied between 1 and 10 Pa for the burn phase and between 10^{-4} and 1 Pa for the dwell pumping. The simulation of dwell pumping needed a change of the model; the pumps simulating the plasma have to be replaced by gas sources. The inclusion of 4 additional pumping ducts is an option for simulation the dwell pumping with 8 torus pumps.

Typical simulation results (deuterium, 420 K)

From the start in 2006 on, the work performed under this task was complementary to and triggering further divertor design efforts inside ITER. Fig. 3 is illustrating the changes achieved between 2006 and 2007, by changing back from a three-finger connection of the pumping ducts to a more open divertor system with gaps in between all individual cassettes. One general significant improvement is an increase in conductance towards the torus (almost doubled compared to the old 2006 design, blue curve in Fig. 3). However, there is a significant recycle flow towards the plasma, which gets worse with increasing gap size as the directed flow towards the torus pumps is rather independent of the gap size. Fig. 4 is adding the 2008 design situation, which included diagnostic cassettes and considered that not all cassettes are identical in design. This is the most complete and most recent model which has been investigated under this task. It becomes obvious that the throughput towards the torus pumps could not be further increased, but, unfortunately the recycle flow path towards the plasma. All in all, the situation has become more difficult to control, as at higher divertor pressures, only 30% of the gas is exhausted by the pumps, whereas 70% is recycled back into the plasma.

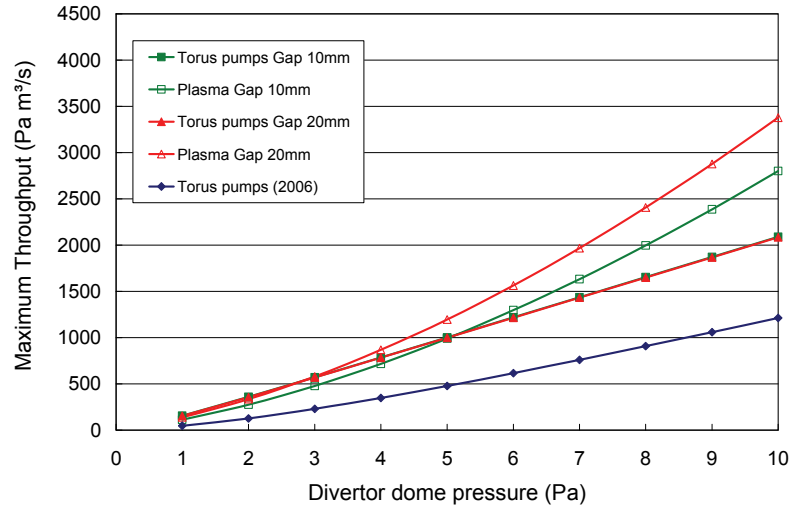


Fig. 3: Influence of introducing gaps between the divertor cassettes (comparison 2006-2007 design).

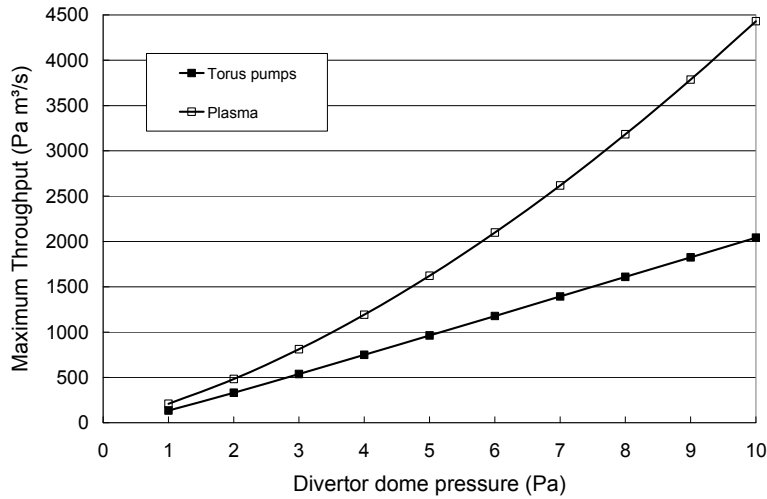


Fig. 4: Influence of introducing diagnostic cassette design (2008 design).

Status and outlook

This task has been closed. It has been found that to have a complete model of the divertor vacuum system is a very helpful tool in highlighting any design consequences on the system performance [3]. The high recycle flows which are expected for the present design are recommended to be re-iterated inside ITER.

Staff:

Chr. Day
V. Hauer

Literature:

- [1] Chr. Day, V. Hauer, G. Class, D. Valougeorgis, M. Wykes, Development of a simulation code for ITER vacuum flows, IAEA Fusion Energy Conference, Chengdu, China, Oct 2006.
- [2] V. Hauer, Chr. Day, Conductance modelling of ITER vacuum systems, Fusion Engineering and Design 84 (2009) 903-907.
- [3] Chr. Day, Recent developments in fusion vacuum flow modelling, ISFNT, Dalian, China, Oct. 2009.

Acknowledgement

This work, supported by the European Communities under the contract of Association between EURATOM and Karlsruhe Institute of Technology, was carried out within the framework of the European Fusion Development Agreement. The views and opinions expressed herein do not necessarily reflect those of the European Commission.

Development of a New Collisional Flow Monte Carlo Method

Background and objectives

The gas flow in a vacuum system is characterized by the Knudsen number $\text{Kn}=\lambda/d$, with λ being the mean free path of the molecules and d a characteristic size of the vacuum chamber. For an ultra high vacuum or a high vacuum system, the mean free path is greater than the size of the vacuum chamber, so $\text{Kn}>1$. In this case, the gas molecules seldom collide with each other and the gas flow is called as free molecular flow, which can be simulated by the so-called Test Particle Monte Carlo (TPMC) method [1]. If $\text{Kn}<0.01$, the gas can be usually considered as continuum fluid and the flow is called as viscous flow, which can be simulated by Computational Fluid Dynamics. The gas flow regime when $0.01<\text{Kn}<1$ is called as transition flow regime, which can be simulated by kinetic theory (solution of the Boltzmann equation) or the Direct Simulation Monte Carlo method (DSMC). However, the simulation of complex 3D vacuum system with DSMC or kinetic theory is still a challenging task because of the huge demand on computational memory and CPU time. Unfortunately, the gas flows in many ITER applications, for example, the gas flow inside the neutralizer of the Neutral Beam Injection system (NBI) or the gas flow upstream the torus cryopumps in certain scenarios are within the transition flow regime. Thus, the aim of this activity is to develop a new, versatile and quicker, collisional flow Monte Carlo simulation method and it is expected that such a tool, once available, will become a reference tool for the design of fusion systems.

Basic ProVac3D simulation code

ProVac3D is a test particle simulation program developed by KIT. The acronym stands for '3D density PROfile in VACuum systems'. ProVac3D uses the real 3D coordinates to define system components. Plenty of default geometries have been programmed and can be chosen from an entity library. The available entities are grouped in two types, namely plane components or rotational components, as listed in Table 1. In addition, we can consider each entity as an ordinary wall (diffuse or specular reflector), as a source, as a pumping surface, or even as a virtual surface. Sticking probability, transparent probability, temperature and thermal accommodation coefficient can be defined, too. With these components we can build up a true 3D simulation model of a complex system. Of course, additional entities will be developed in future, if the geometries to be modeled require it.

Table 1: Available entities of ProVac3D.

Plane component	Rotational component
Parallelogram	Cylinder
Triangle	Cone
Circle	Crown half sphere
Ellipse	Elliptic cylinder
Ring	Wedge
Hexagon with hole	3-way cross
Square with hole	4-way cross
Octagon with hole	5-way cross
	6-way cross

The trajectories of the molecule coming from the source are traced down until it hits a component. However, unlike a usual test particle simulation code, every molecule has real mass, temperature and velocity. This makes us able to calculate the time of flight. If we divide the volume of interest into cells, by the record of the accumulation of the time of flight of every molecules in each cell, we can derive the 3D density distribution by simulation of a high number of molecules based on the hypothesis that the density in one cell is proportional to the accumulation of time of flight of every molecule in this cell and inversely proportional to the cell volume.

ProVac3D is very suitable to simulate a vacuum system characterized by complex geometry, great temperature gradients and distributed gas loads. It has been successfully cross-checked in a former EFDA-Task (TW5-THHN-MONRF) and then been used in different applications in free molecular flow regime [2-5]. Recently, this program has been chosen as the

reference simulation code for the full scale NBI test facilities on site of Consorzio RFX in Padova, Italy.

Further development of ProVac3D including molecular collisions

The natural idea to extend ProVac3D into transition flow regime is to include the collision between gas molecules by considering appropriate interaction between the probe molecule and the gas background, which is described in Figure 1.

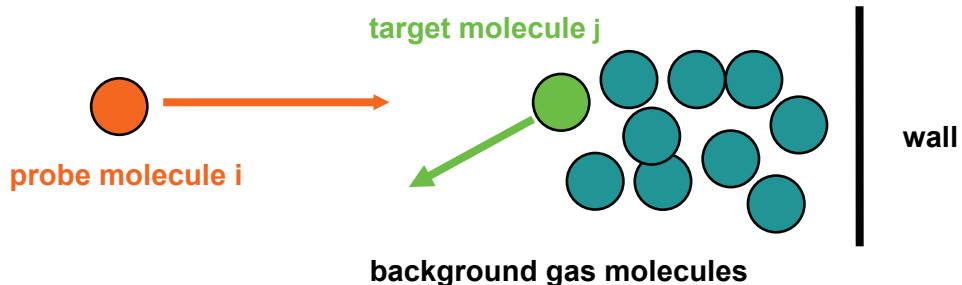


Fig. 1: The collision between the probe molecule and target molecule.

The collision time t can be calculated from the speed of the probe molecule and the properties (density and bulk speed) of the background gas; t is then compared with the collision time with the wall τ which results when no collision with the background is included. If $t < \tau$ the collision will happen with the target molecule; otherwise, it will happen with the wall.

Above mentioned collision mechanism has been recently implemented into ProVac3D.

Outlook and future work

In the next step, we will carefully compare the simulation results of ProVac3D with the simulation results of kinetic theory and DSMC. We believe that in this way we can find an alternative method to simulate the gas flow in transition flow regime, which can be used to some ITER applications with complex vacuum system at acceptable efforts.

Staff:

Chr. Day
X. Luo

Literature:

- [1] G. Saksaganski, Molecular Flow in Complex Vacuum systems, Gordon and Breach, New York, 1988.
- [2] Chr. Day, X. Luo, A. Conte, A. Bonucci and P. Manini, Determination of the Sticking Probability of the SAES St707 NEG Strip, J. Vac. Sci. Technol. A25 (2007) 824.
- [3] X. Luo, M. Dremel and Ch. Day, ProVac3D and Application to the Neutral Beam Injection System of ITER, RGD26, AIP Conference Proceedings 1084 (2009) 1099.
- [4] M. Dremel, Chr. Day, S. Hanke and X. Luo, Cryopump design development for the ITER Neutral Beam Injectors, Fusion Engineering and Design 84 (2009) 689.
- [5] X. Luo and Chr. Day, 3D Monte Carlo vacuum modeling of the Neutral beam Injection System of ITER, ISFNT-9, Dalian, China, October 2009, submitted to Fusion Engineering and Design

Design Activities for the first ITER HNB Injector (F4E-2008-GRT-011, F4E-2009-GRT-032)

Objectives

The 2009 activities performed at KIT in the area of the ITER Neutral Beams (NB) were focussed on two main aspects of the cryogenic pumping systems. Firstly, resulting from several changes of requirements and input parameters, the design of the HNB cryopump finalized in 2008 [1] had to be adapted and recalculations were performed. Secondly, the critical issue of the thermal hydraulic behaviour of the very complex 80 K shielding system which can not be predicted on a theoretical basis was further elaborated; here, an extensive experimental and analytical work was done to characterise the complex behaviour of the shielding circuit.

This work was organised under Grant F4E-2008-GRT-011, which was closed in spring 2009 and continued under the follow-up Grant F4E-2009-GRT-032. Whereas the former grant covered the design of the cryopumps for the NB test facility in Padua, the latter grant has been agreed to focus primarily on the ITER HNB system. It is aimed to minimize any differences between the two cryopumps.

Design development

For the ITER heating NBIs the cryopump design was advanced and refined to cover all requirements given by the latest injector design. To achieve this, the following stepwise approach has been taken:

1. Integration test in the MITICA vessel: Assumptions, base geometry, size and position of the cryopump in the given beam line vessel were agreed and frozen. Furthermore, a first collision test was performed to ensure the consistency of the pump and the feedthroughs of the water cooling pipes for the beam line components. This test was done with the current model of the pump and intended to verify the base for the ongoing detailed design of the MITICA beam line vessel. The resulting space envelopes for the cryopump are shown in Fig. 1.

2. Recalculations of the gas distribution profiles: Using the KIT vacuum code ProVac3D the density distribution profiles in the beam line were calculated for different gas baffle configurations along the beam line. These calculations lead to the proposal to use two baffles in a removable configuration.

The most important parameter required for these calculations are the gas fluxes from the different sources, especially from the neutralizer. To achieve a neutralization efficiency of 60% a gas target of $1.4 \cdot 10^{20} \text{ m}^{-2}$ is necessary for a 1 MeV deuterium beam. In the case of neutralization a protium beam of 870 keV (the same per nucleon) the gas target in the neutralizer must be increased to $2.2 \cdot 10^{20} \text{ m}^{-2}$ leading to a very demanding situation for the vacuum pumps. To perform this target thickness the gas flux out of the neutralizer had to be increased from $27 \text{ Pa} \cdot \text{m}^3/\text{s}$ ([1], June 2008) to $43 \text{ Pa} \cdot \text{m}^3/\text{s}$.

Beside this drastic change of gas flux out of the neutralizer also the gas fluxes from other components changed. All new gas fluxes have been taken into account and lead to new calculations and results of the pressure profile along the beam line, of the pumping speed, the pumping time and of the possible pressure limit. The new expected possible pressure at the neutralizer will be 0.024 Pa.

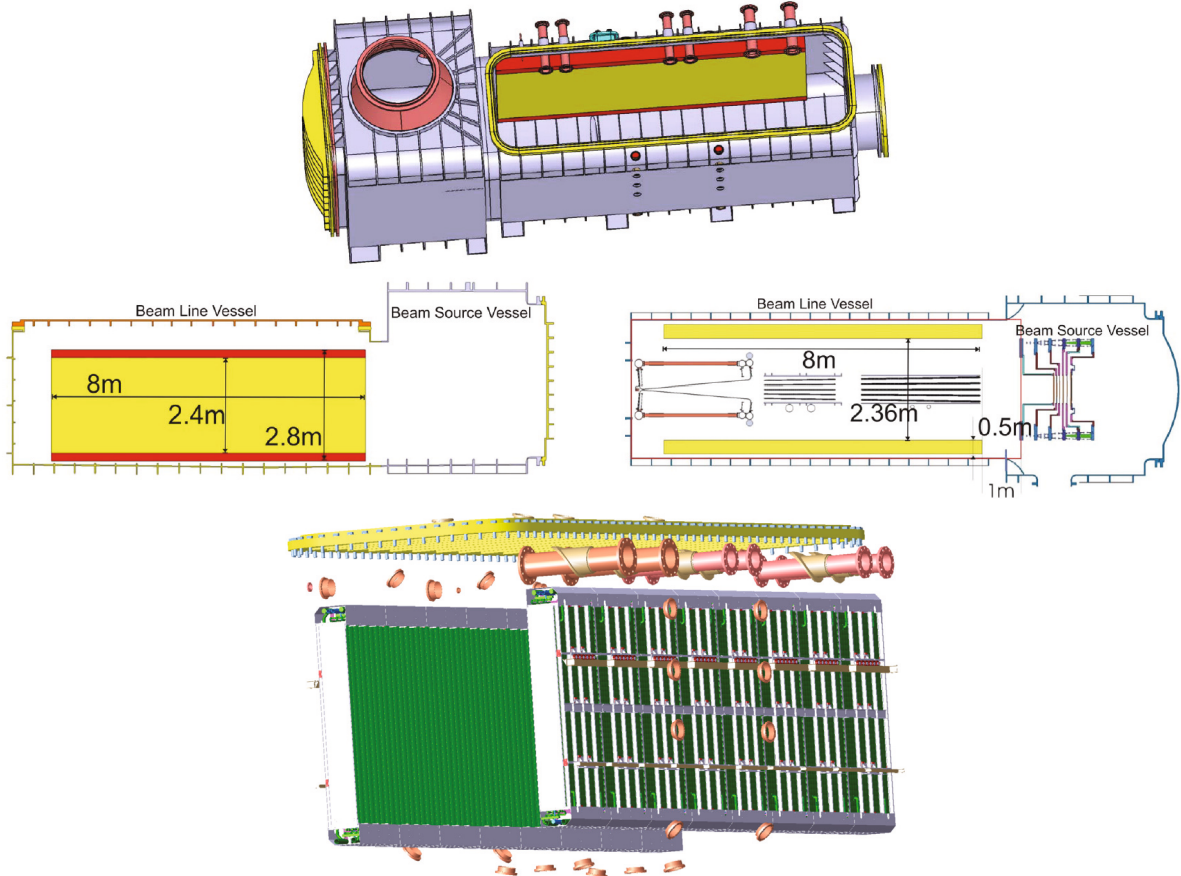


Fig. 1: Available geometric envelope for the HNB cryopumps and a view to the collision test with the feedthroughs of the MITICA beam line vessel.

3. Heat load and cryogenic detailed design:

The surface temperatures of the water-cooled beam line components decreased from 100 °C to 68 °C average, the effect of which was assessed. In Table 1 the reduced heat loads for the pulse operation scenario are listed. The heat load caused by electrons is not included but with assessed 12 kW of the same order and has to be calculated on the base of a future design of the electron dump.

Table 1: Heat loads for the ITER heating neutral beam cryopump in the case of unshielded beamline components (BLC), but without the heat load by electrons.

<i>T of BLC</i>	<i>Radiation Shields</i>	<i>Cryopanels</i>
373 K	11.7 kW	260 W
341 K	9.9 kW	225 W

4. Reassessment of flexible hoses: Due to the fact that the pump has to handle temperatures from 4 K up to 470 K, the thermal expansion of all panels has to be compensated. Therefore all cryopanels as well as all shielding panels are connected at both sides via flexible hoses with the supplying piping system. Because flexible hoses introduce a certain risk of leaks to the pump and because the pump consists of 384 shielding panels and 192 cryopanels every feasible reduction of the amount of needed compensators is a clear advantage concerning the reliability of the pump. Therefore, a first investigation was performed to redesign the piping with the aim of a significant reduction of the amount of compensators. This first approach was combined with a successful verification of its feasibility by FEM analyses of the remaining compensators and lead to a significant reduction.

5. Determination and optimization of the pressure loss behaviour: A critical issue of the cryogenic supply is the pressure loss in the 80 K radiation shielding. Due to the complexity of the internal structure, especially of the back wall panels, it is not feasible to solve this problem by calculation. To analyse the radiation shielding circuit of the pump, pressure drop measurements on 1:1 scaled panels were performed with the THEA facility (Figure 2).

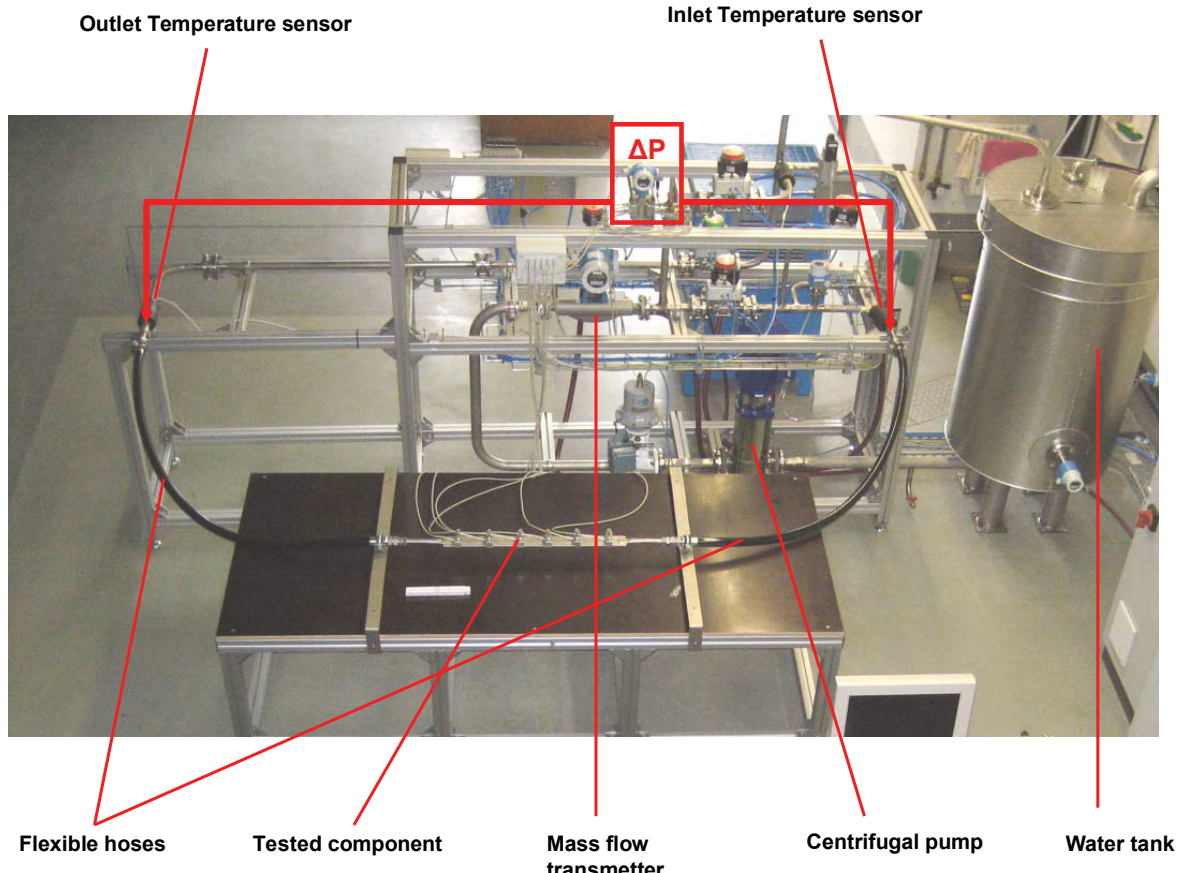


Fig. 2: The THEA facility for measurement of the pressure loss coefficients of 1:1 components of the 80 K shielding.

Figure 3 shows the determined pressure loss of the entire 80 K shielding system of the pump. Under an assessed total heat load of 30 kW every side of the pump has to handle 15 kW. The related mass flow to carry this heat load leads to the shown behaviour. Depending on the ΔT allowed for the 80 K circuit, different pressure losses will result. To achieve the goals of 10 K ΔT and at the same time maximum 2 bar pressure loss inclusive cryojumper and CVB, further design and optimization effort has to be made.

In addition, the distribution of the cryogenics and the resulting temperature distribution along the pump were determined, taking into account the unbalanced heat load along the beam line (Figure 4). The caused changes in flow, pressure and temperatures lead to a more detailed and reliable prediction of the behaviour of the entire shielding and are the base for the needed final optimizations in the future.

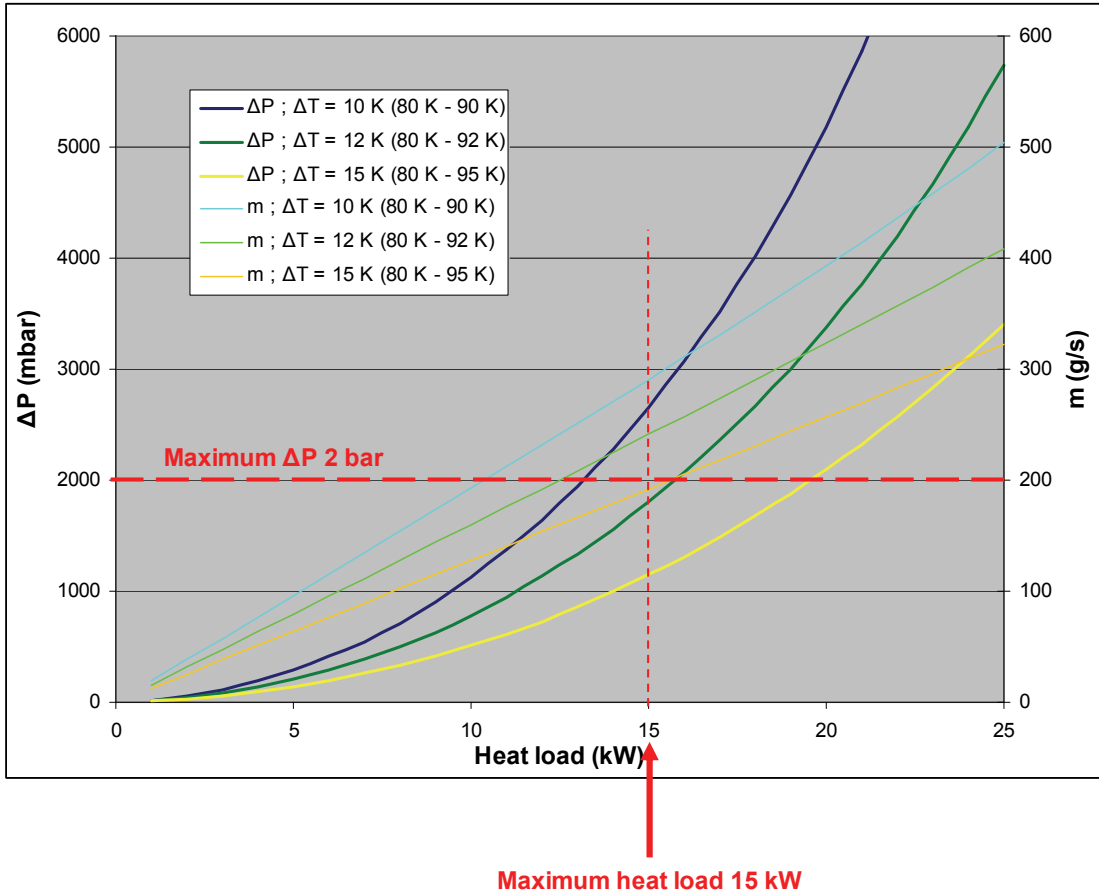


Fig. 3: The determined pressure loss behaviour of the 80 K shielding under the assessed averaged heat load of 15 kW on each side of the pump. The current requirements of 10 K temperature difference and a maximum pressure loss of 2 bar including supply and valve box are still incompatible but further design optimizations should achieve this goal.

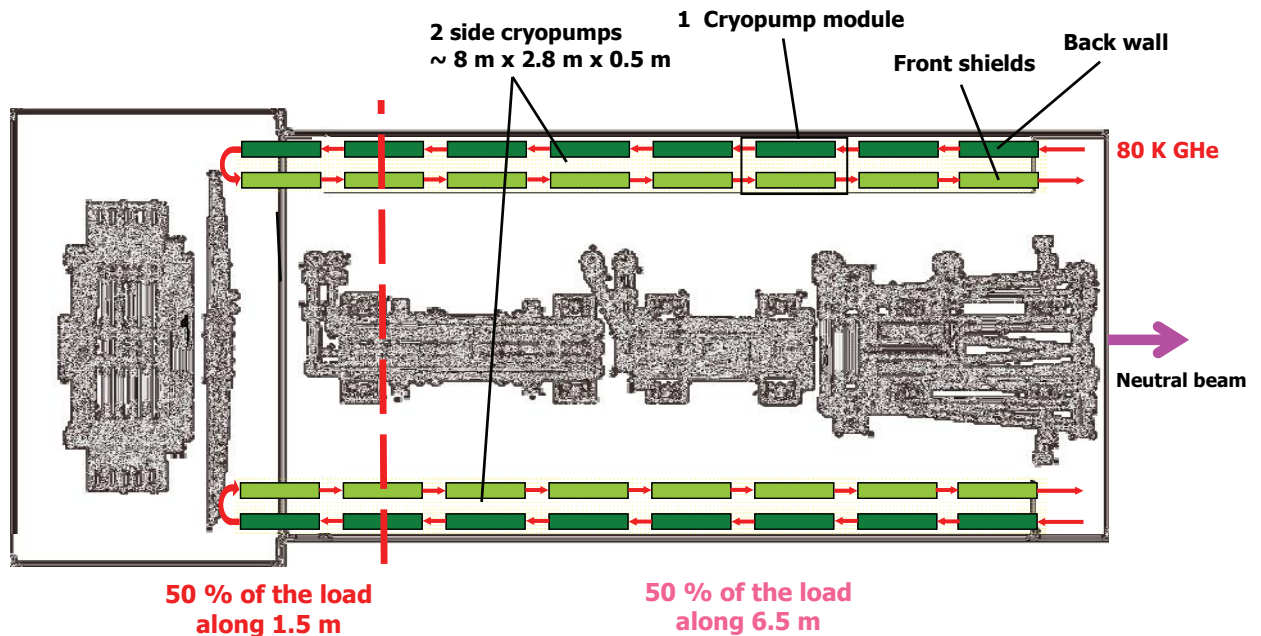


Fig. 4: The unbalanced heat load along the beam line leads to an unequal heat load deposition on the pump and has to be taken into account for a reliable prediction of the behaviour concerning pressure loss, temperature and flow distribution inside the shielding system.

Final status and future work

The scope of GRT-011 has been fully achieved and the task is now closed. But there are a series of open issues which remain to be performed in the running GRT-032:

- The running measurements and analyses of the pressure loss behaviour of the shielding system with THEA.
- Final design of the piping for optimization of pressure loss and flow distribution basing on the results on THEA. Consideration of all heat loads, especially the electron heat load to the pump which depends on the design of the electron dump at the beam source.
- Final design of the entire shielding- and cryocircuit, of the passive shieldings, thermal connectors and spacers.
- Final design of the mounting structure with a further reduction of the amount of thermal compensators.
- Recalculation of all pump properties basing on the finalized design.
- Compilation of operating and manufacturing procedures, of the technical specification and all other documents needed for a call for tender.

Staff:

Chr. Day
A. Demsoreanu
St. Hanke
V. Hauer
X. Luo
M. Scannapiego
R. Simon
H. Strobel

Literature:

[1] M. Dremel, Chr. Day, St. Hanke, X. Luo, Cryopump design development for the ITER neutral beam injectors, Fusion Engineering and Design 84 (2009) 689-693.

Acknowledgement

This work was supported by Fusion for Energy under the grant contracts No. F4E-2008-GRT-011 and No. F4E-2009-GRT-032 with collaboration by RFX, Italy; CEA, France; CNRS, France; IPP, Germany and CCFE, United Kingdom. The views and opinions expressed herein reflect only the author's views. Fusion for Energy is not liable for any use that may be made of the information contained therein.

Investigation of Vacuum Gas Flows for Nuclear Fusion Applications (Fusion Researcher Fellowships - WP08-FRF-FZK/Varoutis)

Background and objectives

Vacuum flows play a central role for several subsidiary systems of fusion reactors. In particular, there are three high vacuum pumping systems for evacuation and maintenance of the needed low pressure levels in the torus, in the cryostat and in the neutral beam injectors (NBI). The achievable pumping speed in all the aforementioned systems is of major importance and therefore a thorough and complete study of the flow conditions is mandatory, in order the optimum values to be achieved.

Each of the vacuum systems consists of networks of various channels with different lengths and cross sections. The flow in such channels varies from the free molecular regime up to the hydrodynamic limit. The aim is to study on numerical and experimental basis overall quantities of practical interest as for instance the mass flow rate and the conductance, for various lengths and cross sections and in the whole range of Knudsen number. This works continues from the previous EFDA task TW5-TTFF-VP57.

Experimental set-up

To compare with the calculations and to enlarge the existing and still very scarce data base of transitional flows, a large scale test facility has been set up under EFDA-Task TW5-TTFF-VP57. The basic principle of the TRANSFLOW test rig (Transitional Flow Range Experiments, see Figure 1) is the measurement of the conductance of different channels in the transitional and near transitional flow regime at isothermal conditions. TRANSFLOW is based on the direct dynamic approach, where a constant flow is adjusted and the pressure difference is measured. The constant flow into the test rig is provided by a dosing unit. The temperature and pressure of the injected gas can be measured in the dosing dome, which is directly connected to the dosing unit. The test channel is following the dosing dome in flow direction. On the downstream end it is connected with the pump dome. The pump dome serves to measure temperatures and pressures at the outlet side of the test channel. It is also equipped with turbomolecular pumps, which are further connected to the forepumps, to maintain the vacuum conditions inside the system. For the experimental work, several short and long channels with various cross sections have been already used [1].

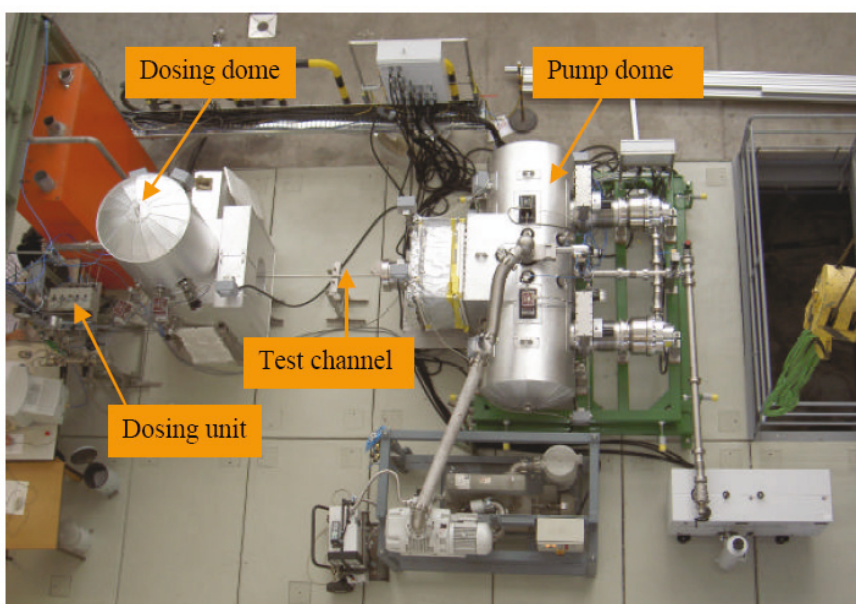


Fig. 1: TRANSFLOW test rig.

Gas flows in long channels using discrete velocity algorithms

Over the years, it has been shown that simulation of gas flows in low, medium and high vacuum based on discrete kinetic theory models is a very powerful methodology yielding accurate results within reasonable computational time in the whole range of the Knudsen number. In that framework, numerical codes have been already developed for the simulation of rarefied gas flows through circular, square, triangular and trapezoidal ducts, implementing the BGK model in the case of single gases. All codes are based on the Discrete Velocity Method [1,2]. Using the discrete velocity algorithm, comparisons between computational kinetic theory results and corresponding experimental results obtained from TRANSFLOW experimental facility for the four above channels, have been performed with considerable success [1]. Figure 2 exemplifies the results for the long circular tube with a length/diameter ratio of 80 in terms of conductance vs. Knudsen number. In parallel, numerical results from the ITERVAC code [3] have been also compared with corresponding experimental and kinetic results. The ITERVAC code is an essential empirical code, which was developed in KIT-Forschungszentrum Karlsruhe for the validation of proposed design changes to the ITER vacuum systems (neutral beams, torus exhaust, cryostat high vacuum systems and dedicated forepump trains). The benchmarking of ITERVAC was successful in the whole range of Knudsen number for the cases of channels with infinite length.

Gas flows in channels of finite length using DSMC

The flow of rarefied gases through channels of finite length due to a pressure gradient is investigated by the Direct Simulation Monte Carlo (DSMC) method. The DSMC method simulates a random sample of computational molecules, which move, interact with solid boundaries and collide with each other. At each time step the process is splitting between streaming and collisions. The state of the system is defined by the position and the velocity vectors of the particles. Each model particle in the simulation represents a large number of real molecules in the physical system. Particle motions are modelled deterministically, while the collisions are treated statistically. The core of the DSMC algorithm consists of four primary processes: free particle motion, index and cross-reference of the particles, simulation of collisions, and sampling of the flow field. The main objective is to calculate the detailed flow field of the channel including also the mass flow rate, in terms of flow and geometric parameters like the Knudsen number, the length-to-radius ratio and the pressure ratio. Several comparisons between corresponding experimental results obtained from TRANSFLOW and numerical results have been performed for the case of short tubes and excellent agreement has been observed (see for example Figure 3) [4,5].

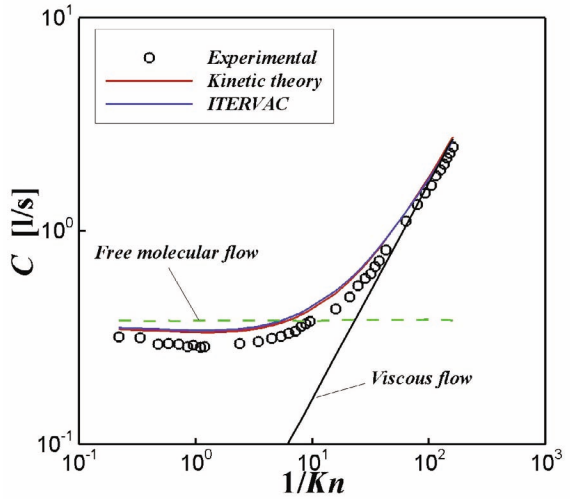


Fig. 2: Experimental and computational conductance in terms of the Knudsen number for long tubes (gas nitrogen, average temperature 296 K).

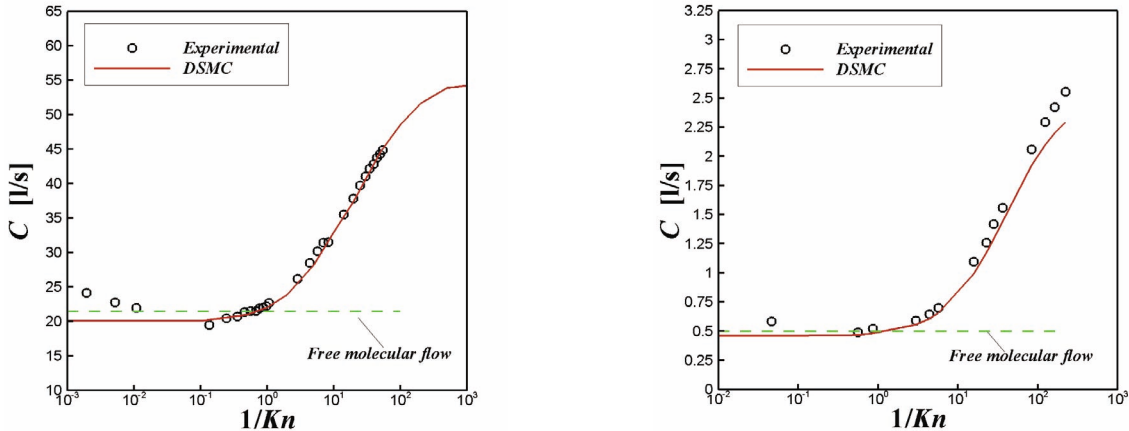


Fig. 3: Experimental and computational conductance in terms of the Knudsen number for short tubes with $L/D=1$ (left) and $L/D=4.28$ (right).

Conclusions and outlook

It was successfully demonstrated that numerical methods are available to calculate vacuum flows for the whole range of Knudsen number and for developed flow (i.e. through long channels) and developing flow cases (i.e. short channels). Software codes have been developed and the agreement with the experiments is very good.

In the future, additional channels will be calculated and measured in TRANSFLOW including rectangular ducts with a wide aspect ratio, which are known to provide very significant Knudsen minima. Moreover, typical vacuum piping elements such as bellows and pipe connectors will be investigated. Finally, it is planned to apply the DSMC method to model an ITER torus cryopump, which is most challenging from geometry complexity point of view.

Staff:

Chr. Day
 S. Efdanitis (Guest scientist, University Thessaly, Volos, Greece)
 Th. Giegerich
 V. Hauer
 S. Pantazis (Guest scientist, University Thessaly, Volos, Greece)
 P. Pfeil
 H. Stump
St. Varoutis

Literature:

- [1] S. Varoutis, S. Naris, V. Hauer, Chr. Day, D. Valougeorgis, Computational and experimental study of gas flows through long channels of various cross sections in the whole range of the Knudsen number, *J. Vac. Sci. Technol. A* 27(1) (2009) 89-100.
- [2] S. Naris and D. Valougeorgis, Rarefied gas flow in a triangular duct based on a boundary fitted lattice, *European Journal of Mechanics B/Fluids* 27 (2008) 810-822.
- [3] Chr. Day, V. Hauer, G. Class, D. Valougeorgis, M. Wykes, Development of a simulation code for ITER vacuum flows, *IAEA Fusion Energy Conference*, Chengdu, China, Oct 2006.
- [4] S. Varoutis, D. Valougeorgis and F. Sharipov, Simulation of gas flow through tubes of finite length over the whole range of rarefaction for various pressure drop ratios, *J. Vac. Sci. Technol. A* 27(6) (2009) 1377-1391.
- [5] S. Varoutis, Experimental and numerical investigation in flow configurations related to the vacuum systems of fusion reactors, *ISFNT*, Dalian, China, Oct. 2009, accepted for publication in *Fusion Engineering and Design*.

Acknowledgement

This work, supported by the European Communities under the contract of Association between EURATOM and Karlsruhe Institute of Technology, was carried out within the framework of the European Fusion Development Agreement. The views and opinions expressed herein do not necessarily reflect those of the European Commission.

Fuel Cycle – Tritium Plant

Endurance Tests of Water Detritiation System (TW6-TTFD-TR 64)

The Water Detritiation System (WDS) and the Vent Detritiation Systems (VDS) are the only systems in ITER which have direct interface with the environment and therefore evaluation of time behaviour of the critical components, such as the catalyst/packing mixture of the Liquid Phase Catalytic Exchange (LPCE) columns and the SPM electrolyte of the electrolysis unit is compulsory in order to implement an appropriate management and maintenance scheme in the ITER WDS.

The so-called TREN TA facility, in support of R&D activities for the design of ITER WDS and ISS, contains a Combined Electrolysis Catalytic Exchange (CECE) process employing a LPCE column which was commissioned for tritium processing. The CECE process of TREN TA facility is in operation on long term basis aiming for process performance studies and endurance tests of critical components.

Beside the investigation on the influence of the ratio gas to liquid on the decontamination factor along the LPCE column, the influence of the temperature of the column on the decontamination factor has been studied as well. The variation of the decontamination factor versus the temperature of the LPCE column is shown in figure 1.

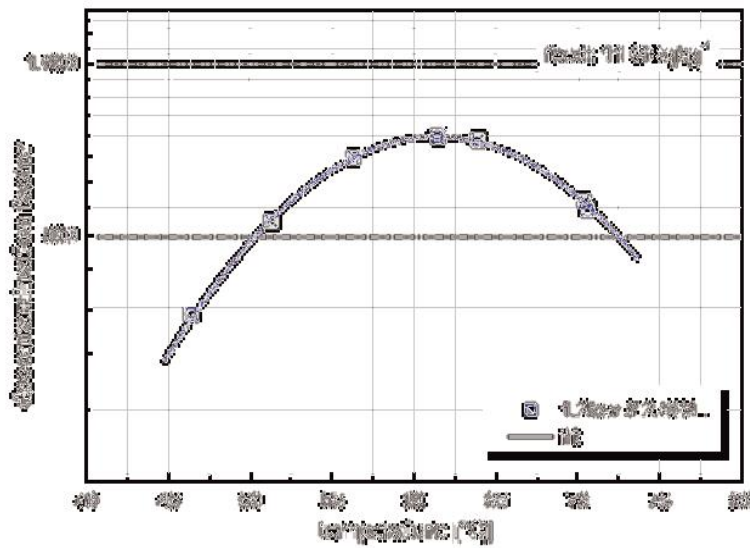


Fig. 1: Variation of decontamination factor versus temperature.

One concern related to the catalyst developed by ICIT Romania – TLK was the chemical stability, and the release of fluorine under tritiated water exposure. Several experimental campaigns were performed within TREN TA test facility. The main goal was to determine the decontamination factor of tritiated hydrogen gas. The time behaviour of the separation performance can also be used as an indication of the tritium compatibility and possible catalyst-packing degradation during tritiated water processing over longer time period.

The performance studies showed that the level of decontamination performance is stable over the time. This indicates in specific that there is no loss in performance or degradation of the responsible catalyst/packing mixture material of the LPCE column determined over the years. The last separation performances measured in the period 20.11.2008 –20.12.2008, after almost three years on tritium service, are shown in figure 2. The decontamination factor was in the range of 10³-10⁵ depending on the operation conditions. Since no degradation could be measured, this confirms the stable decontamination performance of the LPCE column internals.

In addition to the decontamination factor of the LPCE performance, the water processed in the LPCE column was analysed in respect of any impurities which could indicate the degradation of the catalyst/packing material caused by the tritiated conditions. The focus was on the catalyst material, hence the water was chemically analysed for fluorine and chlorine ions and for various metals from the packing materials like iron and chromium. The experimental data does not show evidence of release which may cause any technological troubles.

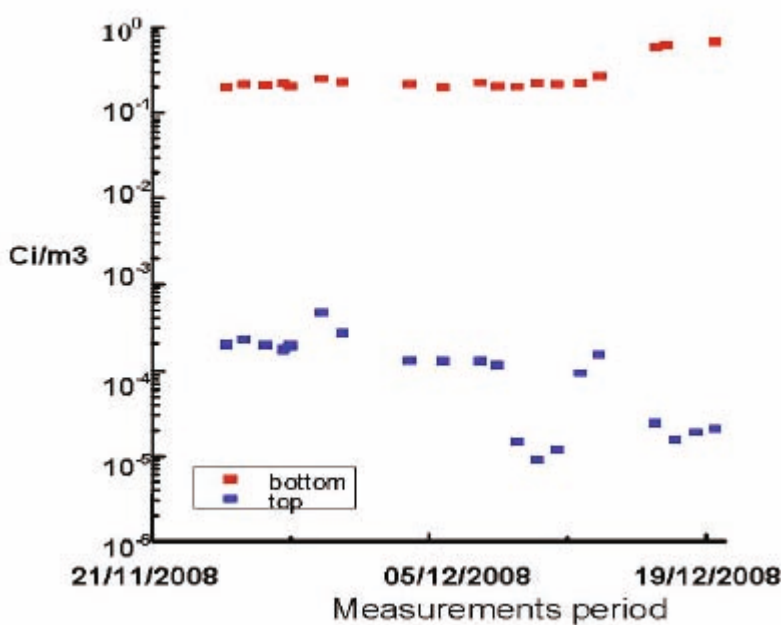


Fig. 2: Separation performances of the 8 m LPCE column.

Solid Polymer Electrolyte (SPE) electrolyser units based on Nafion® membranes as electrolyte have been selected and implemented into the TRENTA facility. Furthermore, the investigations were performed to study the long-term operation of the electrolyser systems under ITER-like conditions. In addition, two small electrolyser units have been in operation with highly tritiated water for one year each. These special long-term experiments give more detailed information about the expected lifetime and applicability of Nafion® materials for tritiated water processing. After one

year of operation the cells were disassembled and the membranes have been investigated and analysed by different methods. The mechanical investigations have been carried out to reveal the possible changes in membrane structural backgrounds. The methods comprised tests of membranes tensile strength and the analysis of the surface morphology. Besides the mechanical methods, the evaluations of the long-term tests were broadening by specific chemical analysis of the process water and the general monitoring of the cell performances over the whole period of operation.

These investigations gave no direct evidence that the tritium decay caused any structural deterioration of the membrane surface. The tritiated membrane seems to have less structural degradation relative to the reference membrane which represents the normal wear and tear after water electrolysis operations over a long period.

Staff:

I. Cristescu
R. Michling
S. Welte
W. Wurster

Acknowledgement

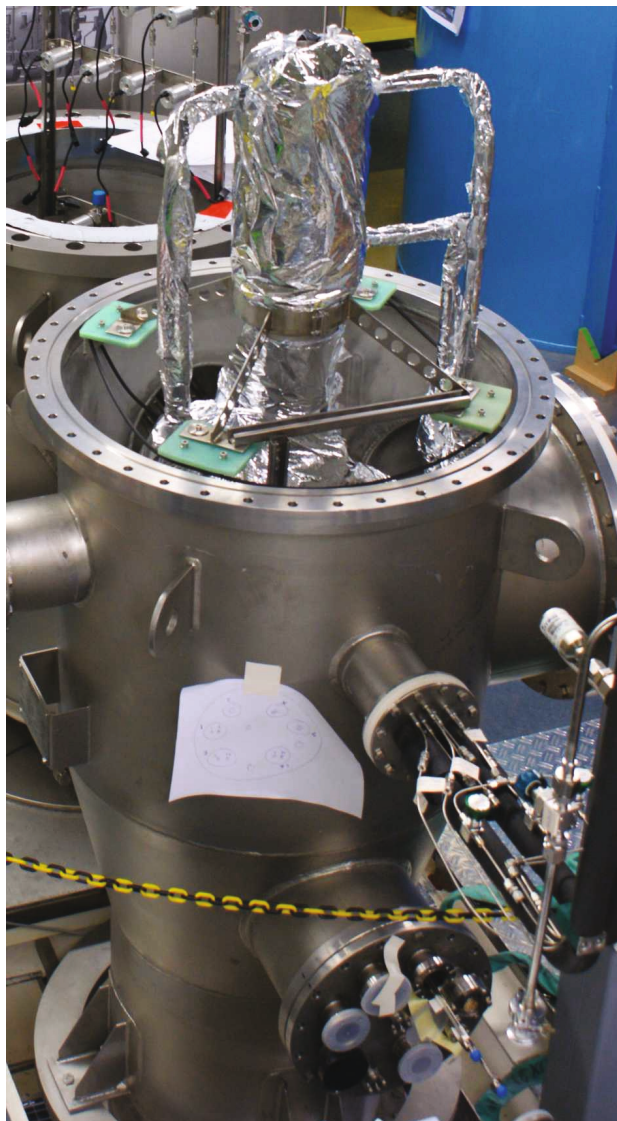
This work, supported by the European Communities under the contract of Association between EURATOM and Karlsruhe Institute of Technology, was carried out within the framework of the European Fusion Development Agreement. The views and opinions expressed herein do not necessarily reflect those of the European Commission.

Functional and Performance Evaluation of Sulzer CY Packing in View of ITER-ISS (F4E-2009-GRT-023-01)

The ITER Isotope Separation System (ISS) consists of a cascade of up to four Cryogenic Distillation (CD) columns and aims at processing two main gas streams: one from Torus exhaust and the other from the Water Detritiation System (WDS). The ISS shall supply five streams with various tritium, deuterium and hydrogen compositions [1]. The top product of CD1 of the ITER ISS, which may contain tritium at a level that is not directly dischargeable to the environment, will be returned to the bottom of the Liquid Phase Catalytic Exchange (LPCE) column of the WDS for further processing [2].

The tritium inventories in the Fuel Cycle of ITER and the amount of tritium released to the environment have a significant impact on ITER licensing. According to the current configuration of the fuel cycle, the tritium/hydrogen inventory in the cryogenic ISS is the largest among all fuel cycle subsystems. Minimisation of the tritium/hydrogen inventory in the ITER ISS can be achieved both by operation of the columns at appropriate loadings and by using a packing or combinations of packings with low tritium/hydrogen inventory and high separation performance. Therefore, various kinds of packings were tested in the CD column of the TRENTA facility at the Tritium Laboratory Karlsruhe (TLK). The major objective of this Grant is to determine the liquid hold-up and separation performance of a CD column equipped with packing of SULZER CY type and to compare the results with the ones available for CD columns equipped with HELIPACK-C and SULZER EX packings. The latter two were previously investigated under the EFDA-task TW6-TTFD-TR56.

The work within the scope of this Grant started after the kick-off meeting on June 18th, 2009. Due to the high impact on ITER safety considerations, a report on the methodologies employed during the investigations was requested by the ITER Organisation (IO). The goal was to identify possible uncertainties in the measurement method and weaknesses in the equipment which could later give rise to questions from the French regulatory authorities responsible for licensing of ITER. During a meeting with representatives from F4E and IO, the experimental procedures laid out in this report were deemed to be appropriate and applicable.



The opened Cold-Box with a view on the condenser which is attached to the top of the CD column.

Simultaneously to the preparation of the report, laboratory work started with finalising the experimental installation: It consists of a CD column of ~3 m length and 5 cm inner diameter equipped with SULZER CY packing to which a condenser is attached at the top and a reboiler (or heater) at the bottom. The column is located inside a vacuum containment (Cold-Box) for thermal insulation during operation in the temperature range 16-26 K (see figure). The condenser is cooled by a cold helium stream from the LINDE refrigerator installed at TLK. A buffer vessel of 0.6 m³ is available for preparation of different hydrogen mixtures and injection to the CD column.

After finalising the experimental setup and calibrating the Quadrupole Mass Spectrometer (QMS) used for measuring the composition of gas samples taken along the CD column, the first experimental run was carried out with pure deuterium end of August. Further runs followed in September and October, where the hydrogen content in the injection mixture was increased stepwise (up to 30%). Four runs were conducted in total, each lasting approximately five days with 24 h shifts. During the runs the so-called Flooding Point was determined first. The Flooding Point is defined by the heating power in the reboiler that leads to such a high vapour velocity of evaporated hydrogen from the reboiler that the liquid flowing down from the condenser cannot reach the reboiler any more. The reboiler empties and essentially all liquid stays in the packed section of the column. Afterwards, the liquid hold-up was measured at 70% of the heating power that corresponds to the Flooding Point. The hold-up can be calculated from the total amount of hydrogen fed to the system subtracting the liquid amount in the condenser and the reboiler. The latter two were first estimated from the hydrostatic pressure drop in the reboiler and from geometric considerations. Later, the estimates were verified by removing the CD column from the Cold-Box and measuring with condenser and reboiler alone. The liquid hold-up was found to be in the range 0.015-0.017 mol/cm³ for the SULZER CY packing. The separation performance of the SULZER CY packing could not yet be determined at 30% hydrogen content since the separation is so good that no hydrogen was found in the reboiler.

The liquid hold-up results for the SULZER CY packing are quite similar to those of HELI-PACK-C [3]; approximately three times larger than the values given in the 2001 Baseline Design [1]. The SULZER EX packing showed thermodynamic instabilities and could not be stably operated at all. These packings are seemingly not appropriate for operation with liquid hydrogen when keeping the minimisation of inventory in view. Therefore, it was decided to abort the current investigation and change the Grant in such a way to include testing of additional packing materials. Several promising candidates were identified and the change proposal is currently under development (in agreement with F4E and IO). An intermediate report is being prepared summarizing the experimental results obtained so far.

Staff:

D. Adami
C.-G. Alecu
E. Cilbir
I. Cristescu
F. Eichelhardt
R. Michling
C. Pluszczyk
R. Schön
S. Welte
W. Wurster

Literature:

- [1] ITER DDD 2001 – Isotope Separation System
- [2] ITER SRD 2008 – Isotope Separation System
- [3] I. Cristescu, L. Dörr, F. Eichelhardt, K. Liger, R. Michling, T. Pinna, M. Zamfirache, S. Welte, W. Wurster, Design and R&D Activities in EU in Support of ITER Water Detritiation and Cryogenic Distillation Systems as in Kind Contribution, to be published in Fusion Engineering and Design

Acknowledgement

This work was supported by Fusion for Energy under the grant contract No. F4E-2009-GRT-023-01. The views and opinions expressed herein reflect only the author's views. Fusion for Energy is not liable for any use that may be made of the information contained therein.

Testing of Isotope Separation System (ISS) with the WDS (TW6-TTFD-TR 63)

In view of mitigation the concern over tritium release into the environment during pulsed operation of the Torus, the Water Detritiation System (WDS) and the Isotope Separation System (ISS), based on cryogenic distillation (CD), will operate in such way that WDS will be a final barrier for the processed protium waste gas stream discharged from the ISS. To investigate the capability of the WDS to achieve this goal, the influence of the additional basically hydrogen stream from ISS and its feeding location into the WDS, the separation performances of Liquid Phase Catalytic Exchange process has to be investigated and accurately mathematically modeled.

In order to develop the experimental data base needed for design of ITER WDS and ISS, the following modes of operation have been considered during the design of the combination WDS-ISS:

- Operation of the LPCE column with composition fluctuation in the stream returned from the CD column
- Operating of the CD column with composition and flow rate fluctuations in the feeding stream
- Operation in different dynamic modes in order to validate and bench mark the TRIMO code

To support the research activities, an experimental facility called TRENTA has been constructed and is in operation at TLK. The design of the facility was developed to allow carry out the experimental programme mainly focused to investigate the process performances of the combination WDS-ISS during isotopic and thermal transitory regimes. Therefore, a detailed investigation of the control system and separation performances of the CECE process when working as a final barrier of the top product of the CD column to be discharged into the environment is under investigation.

In support of the above program the following activities have been carried out in 2009:

- The manufacturing of the heat exchangers which shall provide the required temperature of the feeding streams of the cryogenic distillation column has been completed; the pressure and the tightness tests has been performed as well.
- Detailed design concerning the installation of the heat exchangers in view of thermal stress and heat load minimization has been carried out and the preparation for installation is well advanced.
- The installation of the hardware within the glove box has been completed. Following the requirements for the tritium processing plants, the X ray checking of 50% of the welds has been completed and the unaccepted welds have been redone.
- The installation of the isolation valves within the valve box has been completed and commissioned.
- The electrical and automation cabinet has been delivered, installed and commissioned.

The status of the valve box and the glove is shown in Figure 1.

Staff:

I. Cristescu
F. Eichelhardt
R. Michling
S. Welte
W. Wurster

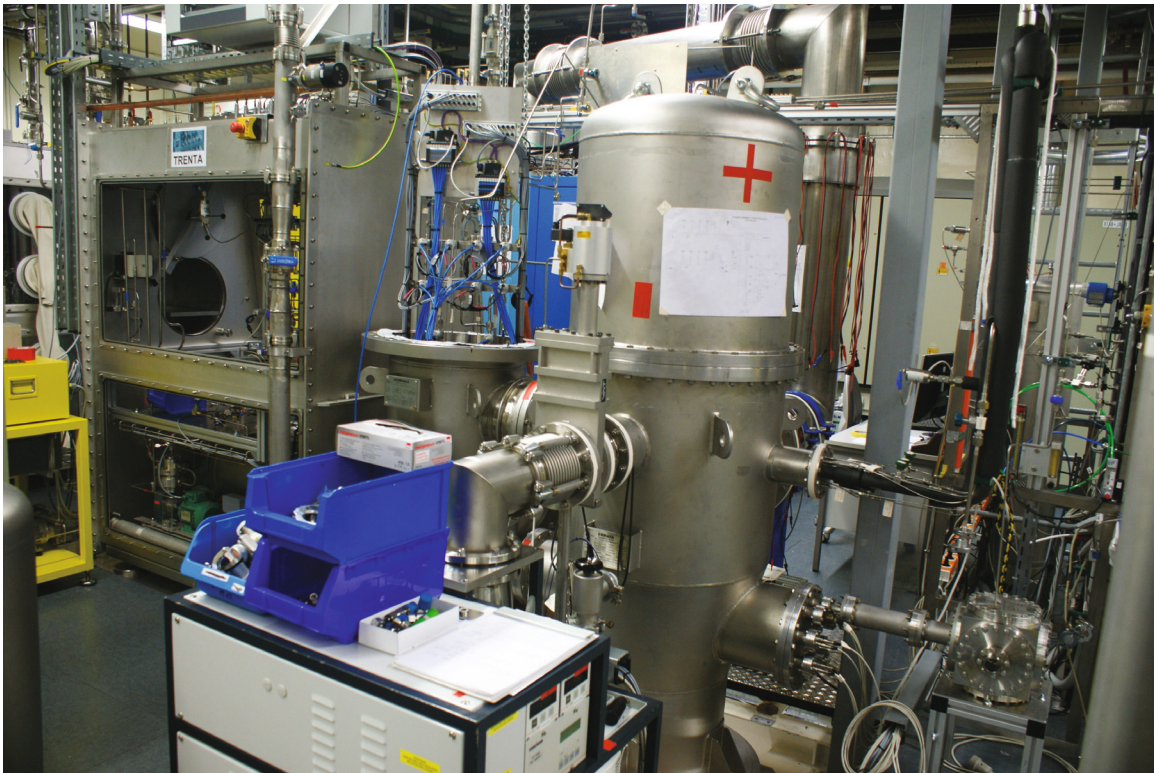


Fig. 1: Installation of the components within the valve box and glove box.

Acknowledgement

This work, supported by the European Communities under the contract of Association between EURATOM and Karlsruhe Institute of Technology, was carried out within the framework of the European Fusion Development Agreement. The views and opinions expressed herein do not necessarily reflect those of the European Commission.

Update of ITER ISS-WDS Process Design - 1 (EFDA/06-1510 (TW6-TTFD-TPI 55))

The R&D activities have been conducted in view of updating the process design of the ITER ISS and WDS as documented in the 2001 FDR (Final Design Report). The activities performed during 2009 have been focused on the evaluation of the impact of the new requirements from ITER IO as a result of design integration activities.

The update of ITER ISS-WDS design was developed on the basis that the ISS and the WDS will be integrated by routing the top product stream from the WDS to a feed point near the bottom end of the WDS Liquid Phase Catalytic Exchange (LPCE) Column. In this respect the evaluation of the optimum position of the feed points, hydrogen stream from ISS and the combined “low tritium” feed stream which includes the WDS electrolyser Q₂ stream and the NBI regeneration gas and (possibly) pellet injector propellant, has been established. The design update took into account the results and recommendations of the FMEA report generated under Task TW5-TSS-SEA4.2, and experimental results from ongoing R&D tasks. Extensive research activities have been carried out related to Water Detritiation System (WDS) and Isotope Separation System (ISS) as components allocated to EU PT. The experimental data base achieved on the performances of several components, such as electrolysis unit and oxygen purification system allows revision and enhancement of the configuration of WDS-ISS.

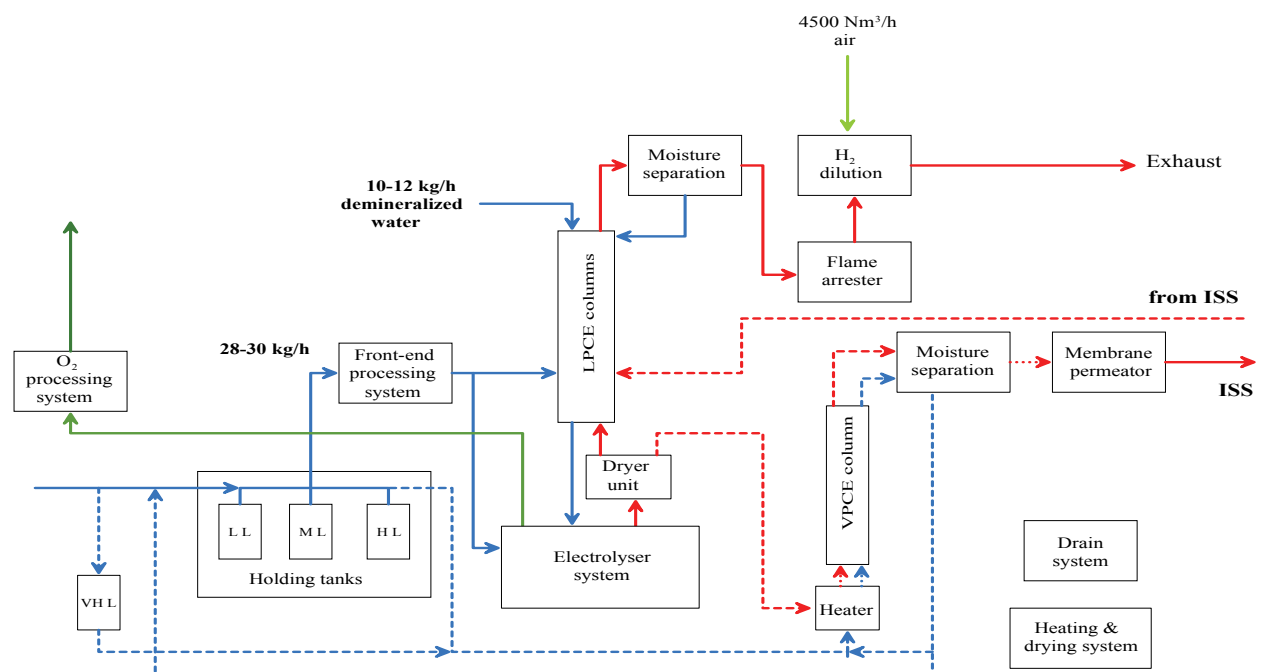


Fig. 1: Enhanced configuration of the ITER WDS.

The main achievements of the completed task are:

1. Detailed investigation of the WDS-ISS configuration which allows reduction of the tritium activity in water to be fed in the CECE process. The new configuration, Figure 1, allows also to process the highly tritiated water which shall be produced during high temperature regeneration of the cryopumps or other detritiation systems.
2. Detailed investigation of the cryogenic distillation cascade; a cascade of three cryogenic distillation columns instead of four columns was found to be feasible for the new approach of the combination between the WDS and ISS. In addition a three cryogenic distillation columns cascade allows producing the deuterium and tritium required for the Torus by only two products:

- A deuterium stream of high quality: protium <0.5% and tritium <0.02%, which will allow feeding both the NBI and gas fuelling systems
- A tritium product of quality higher than 90% which mixed with deuterium of high quality allows feeding Torus with various mixtures
- The quality of product streams is matching the ITER requirements, as shown in figure 2.

3. The P & IDs and proposal for installation within the Tritium Plant building have been provided to ITER IO.

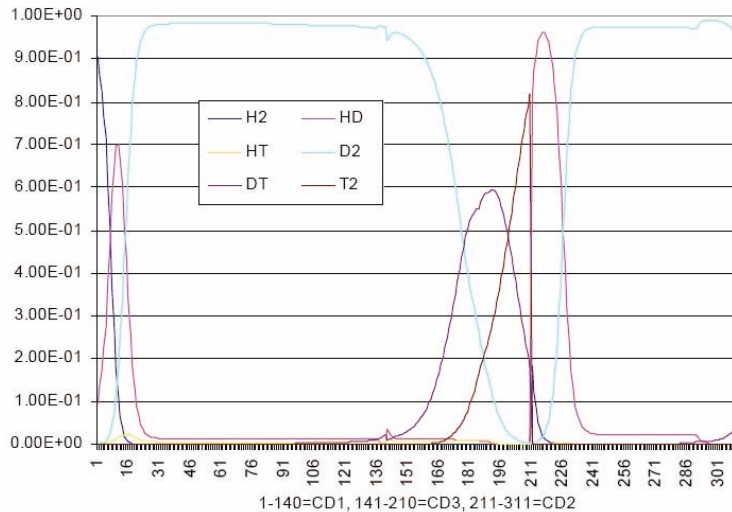


Fig. 2: Profiles of the molecular species along the 3 CD columns.

Staff:

I. Cristescu
W. Wurster
A. Lazar (ICSI-Rm. Valcea – Romania)

Acknowledgement

This work, supported by the European Communities under the contract of Association between EURATOM and Karlsruhe Institute of Technology, was carried out within the framework of the European Fusion Development Agreement. The views and opinions expressed herein do not necessarily reflect those of the European Commission.

Development and Customization of CATIA V5 for Tritium Plant Systems (EFDA/06-1514 (TW6-TTFD-TR 65))

Background

The Computer Aided Three Dimensional Interactive Application (CATIA) is a multi-platform commercial software suite intended for computer aided design, engineering and manufacturing of mechanical, electrical and fluid systems. The wide range of applications (P&ID, HVAC diagrams and equipment arrangement) provides the ability for a upstream design process from functional 2-D to a 3-D detailed design including a consistent and structured data base containing all necessary information for system components.

The Project Resource Management (PRM) system and the standard parts catalogue required for customisation of the CATIUA data base and the design tools for tritium plants were developed within the previous task TW5-TTFD-TPI 51. However, a facilitation of the design work on the ITER Fuel Cycle systems layout within the ITER Tritium Building required a further development of the CATIA PRM. This development includes an implementation of the numbering systems (for example the ITER numbering system), design methods reflecting the plant breakdown structure and using ENOVIA remote participation. Another important task was the implementation of ISOGEN software for the production of piping isometric drawings necessary for manufacturing. Since ISOGEN is not included in the CATIA package, such implementation requires customisation of E&S PRM in order to allow for seamless integration of additional tools into the CAD system.

Status and results of TR 65

The CATIA software has been successfully applied to a project at the Tritium Laboratory Karlsruhe (TLK) to confirm its suitability for application in the design of the ITER fuel cycle components within the ITER Tritium Building. Project Resource Management and standard parts catalogues previously developed were used and the ISOGEN software incorporated.

Conclusions of the work: A further development of standard parts catalogues is necessary. Furthermore an intensive training of a design personal for creation of the systems in the specific tritium plants boundary conditions is strongly recommended. For example, a person skilled in CATIA but without any idea how to work at gloveboxes will never be able to make a design which can be used in reality. One need to know how the people work at the boxes, which tools are used, which space needs to be available for mounting systems or exchange defect parts as e.g. pumps and valves.

The results of TR 65 have been compiled in an official EFDA report, which was submitted in the reporting period.

Staff:

B. Bornschein

Acknowledgement

This work, supported by the European Communities under the contract of Association between EURATOM and Karlsruhe Institute of Technology, was carried out within the framework of the European Fusion Development Agreement. The views and opinions expressed herein do not necessarily reflect those of the European Commission.

Goal Oriented Training Programme “Tritium Technologies for the Fusion Fuel Cycle” (WP08-GOT-TRI-TOFFY (FU07-CT-2008-00047))

Background

The overall objective of the project is to support EU activities in the Deuterium-Tritium Fuel Cycle area for ITER by the training of six Early-Stage Researchers. The training programme is developed along existing projects in the framework of the European procurement package for the ITER Fuel Cycle with the main focus on water detritiation (WDS) and isotope separation (ISS) systems, detritiation processes, gas analytics and tritium measurements (see overview table: List of Work Packages). The participating Associations are: KIT, CEA, ENEA, HAS/MTA ATOMKI, MEdC/ICIT and CCFE.

No.	Title	Partners involved
1	Combined operation of WDS and ISS	KIT (ICIT, CCFE)
2	Detritiation of waste	CEA (KIT, CCFE)
3	Technologies for tritium recovery and trapping	ENEA (KIT, CCFE)
4	Calorimeter with large sample volume	MTA ATOMKI (KIT, CCFE)
5	Experimental Pilot Plant for Tritium and Deuterium Separation	ICIT (KIT, CCFE)
6	Participation in JET operation	CCFE (KIT)

The project was started in late 2008. It was planned to finalize the process of recruitment of trainees until 3rd quarter of 2009, so that all trainees should have started their employment in 2009.

Status of project

All recruitments have been done except in the case of MTA ATOMKI where the candidate has been chosen but the working contract is foreseen to start 1st of March 2010. Also the CCFE Trainee was recruited 2 months too late to allow for a full 36 months training period. Therefore, an extension in time of the network task agreement will be necessary. The Personal Training Schemes of the five already employed trainees have been fixed and these five trainees have started their training at their home institutions.

Outlook

In the next reporting period all trainees shall have finished their home based introductory training and shall be able to contribute to R&D activities.

Programme Coordinator:

B. Bornschein

Acknowledgement

This work, supported by the European Communities under the contract of Association between EURATOM and Karlsruhe Institute of Technology, was carried out within the framework of the European Fusion Development Agreement. The views and opinions expressed herein do not necessarily reflect those of the European Commission.

Safety

Combined Hydrogen and Dust Explosion and Mitigation Experiments and Model Development. Validation and Application to ITER and New Analysis of Explosion Reference Events (F4E-2008-GRT-01-01 (ES-SF))

Introduction

In the ITER wet bypass accident scenario, water leakage, air ingress and hot dust (Be, W, C) could generate combustible hydrogen-air-steam mixtures which may threaten the integrity of the ITER structure and lead to radiological release. To prevent energetic hydrogen combustions, a nitrogen injection system in the vacuum vessel (VV) and hydrogen recombiners in the pressure suppression tank (ST) were proposed. In previous work the hydrogen-air-steam distribution in the ITER sub-volumes has been studied and the capability of the nitrogen injection system to make fully inert the atmosphere in the VV and the ST has been investigated. The 3D computational fluid dynamics (CFD) code GASFLOW was used to calculate the evolution of the mixtures and to evaluate the hydrogen combustion risks in the different ITER sub-volumes. The results indicated that the proposed hydrogen risk mitigation systems will generally prevent the risks of hydrogen detonation and fast deflagration. However, the atmosphere in ITER sub-volumes cannot be completely made inert at the early stage of the scenario. Slow deflagrations could still generate quasi-static pressures above 1 bar in the VV. Therefore, the details of the dust mobilisation and of the low pressure regimes, as well as the structural impact of thermal and pressure loads generated by these hydrogen combustions are investigated in the current work program.

Progress – Combustion Simulations

For the first sub-task the three most relevant scenarios have been identified. The decision was based on the previous work [1] and supported by the information provided by the ITER organisation [2].

Hydrogen combustions in the ITER vacuum vessel under accident scenarios were simulated with the CREBCOM model in the CFD combustion code COM3D. The analyses were dedicated to conservatively estimate the pressure and thermal loads on the ITER structure due to the combustion. The effects of various hydrogen inventories, ignition locations, ignition times and flame speeds on the pressure and thermal loads were studied.

A wedge shaped stoichiometric H_2 -air mixture was ignited at various locations with various flame speeds in a simplified plasma chamber in Cases 1 to 4 (see Figure 1). The local connections to the NBIs and cryo- and pump ports were not considered in such a dynamic and rapid process. The global pressure after the combustion in the VV is around 2.4 bar which is close to the AICC pressure in Cases 1-4. For low flame speed cases, no pressure peak was observed. There is a standing pressure wave along the arc of the Torus. For detonation cases, local pressure peaks over 10 bars occur inside the H_2 -air cloud and in surface S5 due to the pressure wave collision. High temperature over

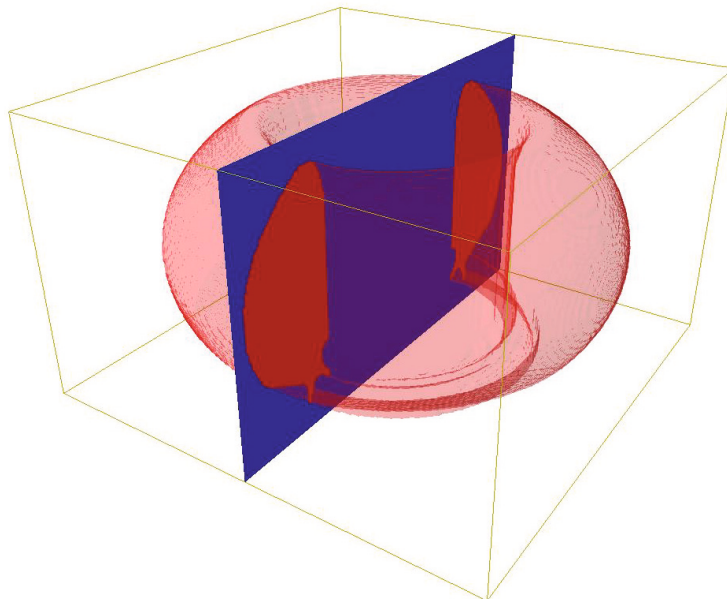


Fig. 1: Geometry model for the Case 1-4.

2000 K was observed in the H₂ cloud and its adjacent region. Variations of ignition locations could affect the local pressure and thermal loads. The effect of various ignition locations on the global loads is small.

The hydrogen distribution under an ITER wet bypass scenario was calculated with GASFLOW. Two cases were analyzed in this study. A nitrogen injection system was installed in Case 5, and in Case 6 no nitrogen mitigation measure was taken. The GASFLOW calculation results were imported into COM3D as initial conditions for the combustion simulations. The H₂-rich mixtures were ignited when the pressure in the VV reached 0.7 bar. A subsonic flame speed was set in the CREBCOM model in COM3D. The total H₂ mass is 20 kg, and the total O₂ mass is 64 kg and 80 kg in Case 5 and 6, respectively. After the complete combustion, the pressure in the VV is around 2.4 bars and 2.9 bars in Case 5 and 6 (see Figure 2). The local temperatures vary from 700 K to 2400 K. The local pressure and thermal loads are strongly dependent on the local H₂ and O₂ concentrations. It indicates that the nitrogen mitigation system will not only dilute the H₂ mixture but also pressurize the volume to reduce the total mass of oxygen in the VV.

More parametric analyses will be performed under the wet bypass scenario in the future study, such as various air ingress locations, various hydrogen inventories, various flame speeds and so on. Structural impact will be analyzed based on the results of this study.

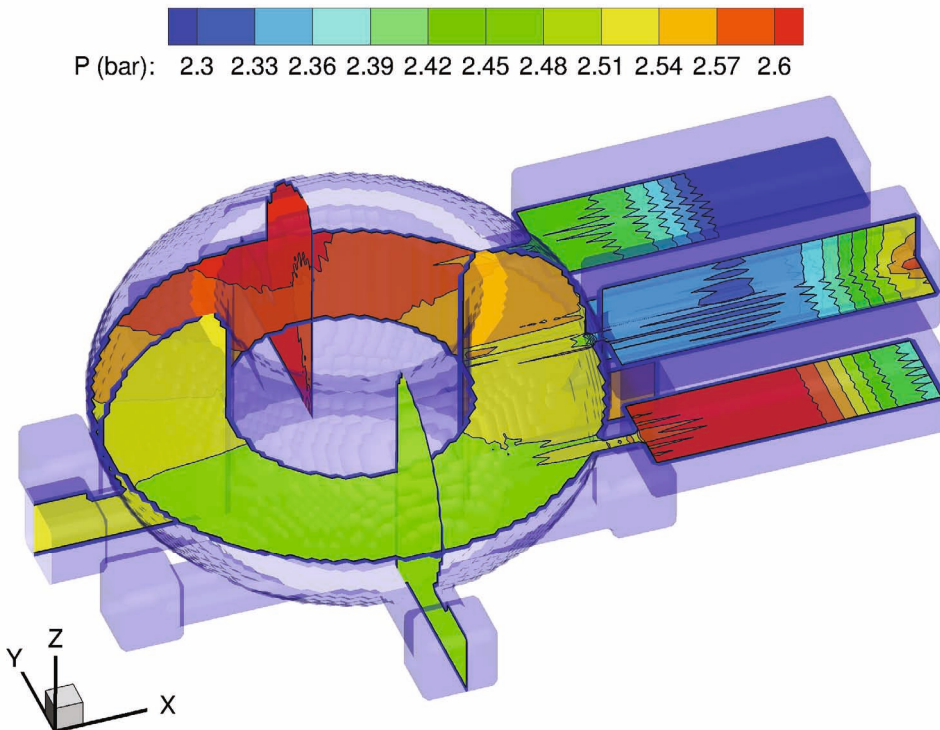


Fig. 2: Pressure contours in the VV at 257.34 ms in Case 5.

Progress – Data for Hybrid H₂/Dust-Explosions

The DUSTEX II facilities have been set-up for hybrid mixtures. The first commissioning tests were done in August 2009. The full testing program has started in 2009 and will be finalized in spring 2010.

Progress – Data for Dust Mobilisation

An expert meeting was held on June 25, 2009 in Frascati, Italy. The participants discussed the ITER relevant properties and contributed to a list of suggested benchmarks. They agreed on a list of suitable benchmarks.

The selected benchmarks are:

- A. TDMX (with or without dust); data by ENEA
- B. Jet injection (all partners); data by KIT
- C. STARDUST (CFD with and without dust); data by ENEA

The responsible partners, as indicated above, provided a detailed description of the benchmark and all required input data, like initial conditions, meshing etc. The discussion on the relevance for ITER revealed that there is generally no pressure level studied close to the ITER initial conditions, that there are no details available on the re-suspension, and that there is no light metal dusts studied so far which could be a model dust for the ITER specific dust. Moreover, no study highlighted surface roughness and humidity effects.

Besides, first design concepts for small and large scale experiments for mobilisation and combustion have been discussed at KIT and at ENEA. The work progress is corresponding to the planning.

Outlook

The work in particular related to the reactive characterization of the hybrid mixtures and hydrogen at low sub-atmospheric pressure will be continued in 2010. It is intended to apply for a continuation of the work in a second phase possibly starting in 2010.

Staff:

W. Breitung
A. Denkevits
T. Jordan
A. Kotchourko
M. Kuznetsov
A. Lelyakin
B. Oechsler
F. Prestel
J. Xiao
Z. Xu

Literature:

- [1] J. Xiao, J.R. Travis, W. Breitung, T. Jordan: "Feasibility study of possible prevention of hydrogen combustion in ITER by injection of inert gas" (FZK report, Feb 2008)
- [2] "H₂ explosion scenarios and modelling"; S. Reyes, ITER Organization, ES&HS, F4E, presentation for an advanced meeting in Barcelona, November 19, 2008
- [3] J. Xiao; J.R. Travis; W. Breitung; T. Jordan: Feasibility study of nitrogen injection system to mitigate hydrogen risks under ITER wet bypass scenario. (2009),. 9th IAEA Technical Meeting on Fusion Power Plant Safety, Wien, A, July 15-17, 2009

Acknowledgement

This work was supported by Fusion for Energy under the grant contract No. F4E-2008-GRT-01-01 (ES-SF) with collaboration by CEA, France and ENEA, Italy. The views and opinions expressed herein reflect only the author's views. Fusion for Energy is not liable for any use that may be made of the information contained therein.

Appendix I: KIT Departments Contributing to the Fusion Programme

KIT Department	KIT Institut/Abteilung	Director	Ext.
Institute for Materials Research	Institut für Materialforschung (IMF)	I. Prof. Dr. O. Kraft (Acting Head) II. Prof. Dr. O. Kraft III. Prof. Dr. H. Haußelt	4815 4815 2518
Institute for Pulsed Power and Microwave Technology	Institut für Hochleistungsimpuls- und Mikrowellentechnik (IHM)	Prof. Dr. M. Thumm	2440
Institute for Nuclear and Energy Technology	Institut für Kern- und Energietechnik (IKET)	Prof. Dr. T. Schulenberg	3450
Institute for Neutron Physics and Reactor Technology	Institut für Neutronenphysik und Reaktortechnik (INR)	Dr. R. Stieglitz	2550
Institute for Technical Physics	Institut für Technische Physik (ITeP)	Prof. Dr. M. Noe	3500
- Tritium Laboratory Karlsruhe	- Tritiumlabor Karlsruhe (TLK)	Dr. B. Bornschein	3239
Institute for Data Processing and Electronics	Institut für Prozessdatenverarbeitung und Elektronik (IPE)	Prof. Dr. M. Weber	5612

Appendix II: Fusion Programme Management Staff

Head of the Research Unit	Dr.K. Hesch (Acting Head)	ext. 5460 e-mail: klaus.hesch@kit.edu
Secretariat:	Mrs. A. Knoll	ext. 5461 e-mail: anja.knoll@kit.edu
	Mrs. Maria-Elena Tuzia	ext. 2435 e-mail: maria-elena.tuzia@kit.edu
Program Budget, Administration, Reports, EU-Affairs	BW. M. Henn	ext. 5547 e-mail: michael.henn@kit.edu
	Mrs. I. Pleli	ext. 8292 e-mail: ingrid.pleli@kit.edu
Blanket and Divertor Development, HELOKA, IFMIF, Public Relations	Dr. D. Radloff	ext. 8750 e-mail: dirk.radloff@kit.edu
Fuel Cycle, Structural Materials, Superconducting Magnets, CAD-Office	DI. S. Gross	ext. 5468 e-mail: sigurd.gross@kit.edu
Plasma Heating Technology, Safety Studies, Neutronics, Physics	Dr. K. Hesch	ext. 5460 e-mail: klaus.hesch@kit.edu
Quality Management Resource Loaded Planning, Document Management	Dr. J. Gafert	ext. 2923 e-mail: juergen.gafert@kit.edu
	Mrs. DI. Ch. Schweier	ext. 8325 e-mail: christine.schweier@kit.edu
	Mrs. DI. B. Keim	ext. 4194 e-mail: birgit.keim@kit.edu

Address:

**Karlsruhe Institute of Technology
Nuclear Fusion Programme Management**

Post Office Box 3640, D - 76021 Karlsruhe / Germany

Telephone No:

07247-82- Extensions

Telefax No:

07247-82-5467

world wide web:

<http://www.fusion.kit.edu>

Appendix III: Glossary

AC	Alternating Current
AISS	Adiabatic Isochoric Complete Combustion
Ar	Argon
ARBOR-1	Fast Reactor Irradiation from FZK in BOR 60
ARBOR-2	Fast Reactor Irradiation from FZK and CEA in BOR 60
ASDEX	Axial-Symmetrisches Divertor-EXperiment
ASG	ASG Superconductors, Italy (former Ansaldo Superconduttori)
ASTM	American Society for Testing and Materials
BDT	Brittle-to-Ductile Transition
BF	Bright-Field
BN	Boron Nitrite
BOR 60	Fast Reactor at SSC RF RIAR, Dimitrovgrad, Russia
BSM	Blanket Shield Module
CAD	Computer Aided Design
CATIA	Computer Aided Three Dimensional Interactive Application
CBED	Convergent Beam Electron Diffraction
CCFE	Culham Centre for Fusion Energy, UK
CD	Cryogenic Distillation
CEA	Commissariat à l'Énergie Atomique, Saclay (France)
CECE	Combined Electrolysis Catalytic Exchange
CFC	Carbon Fibre Composite
CFD	Computational Fluid Dynamic
CFTM	Creep Fatigue Test Module
CICC	Cable in Conduit Conductor
CIEMAT	Centro de Investigaciones Energeticas Medioambientales y Tecnologicas
CNR	Consiglio Nazionale delle Ricerche, Milano, Italy
CPS	Capillary Porous System
CPS	Coolant Purification System
CRPP	Centre de Recherces en Physique des Plasmas, Lausanne, Switzerland
CS	Central Solenoïd
Cu	Copper
CuLTKa	Current Lead Test Facility Karlsruhe
CVB	Cold Valve Box
CVD	Chemical Vapor Deposition

CW	Continuous Wave
DBTT	Ductile-to-Brittle Transition Temperature
DEMO	Demonstration Power Station
dpa	Displacement per atom
DSMC	Direct Simulation Monte Carlo
DT	Deuterium Tritium Fusion Process
DWE	Deggendorfer Werft und Eigenbau
EAF	European Activation File
EASY	European Activation System
EB	Electron Beam
ECA	Electro-Chemical Aluminium Deposition
ECCD	Electron Cyclotron Current Drive
ECH	Electron Cyclotron Heating
ECH&CD	Electron Cyclotron Heating and Current Drive
ECHULA	Electron Cyclotron Heating Upper Launcher Associations
ECM	Electrochemical Machining
ECRF	Electron Cyclotron Range of Frequencies
ECRH	Electron Cyclotron Resonance Heating
EDM	Electric Discharge Manufacturing
EDX	Energy Dispersive X-ray Analysis
EELS	Electron Energy Loss Spectroscopy
EFDA	European Fusion Development Agreement
EFF	European Fusion File (by EU)
EFTEM	Energy Filtered TEM
EGYP	European Gyrotron Consortium
ELM	Edge Localized Mode
EM	Electro Magnetic
ENDEP	Code Name
ENDF	Evaluated Nuclear Data File
ENDF/B-VII	Evaluated Nuclear Data File, B, Version VII (USA)
ENEA	Ente per le Nuove Tecnologie, l'Energia e l'Ambiente, Italy
ENOVIA	Software package for supporting work with CATIA
EU	European Union
EUROFER	European RAF/M Steel
EVEDA	Engineering Validation Engineering Design Activities
F4E	Fusion for Energy

F82H mod.	Japanese RAF/M steel
FDU	Fast Discharge Unit
FEM	Finite Element Method
FENDL	Fusion Evaluated Nuclear Data Library
FISPACT	Nuclear Inventory and Activation Code (by UKAEA Culham)
FM	Fracture-Mechanical
FML	Fusion Materials Laboratory
FNG	Frascati Neutron Generator
FOM	Institute for Plasma Physics Rijnhuizen
FOREV	Code Name
fpy	full power year
FSSS	Fisher Sub Sieve Size
FTU	Name of Tokamak
FW	First Wall
FWP	First Wall Panel
FZK	Forschungszentrum Karlsruhe
GDH	Geometry Dependent Hybrid (nuclear model)
HAADF	High Angle Annular Dark Field (detector)
HAS	Hungarian Academy of Sciences
HAZ	Heat Affected Zone
HCLL	Helium Cooled Lithium Lead
HCPB	Helium Cooled Pebble Bed
He	Helium
HEBLO	HElium BLOwer (Helium facility at FZK)
HELLAS	A synonym for the collaborating Greek institutions National Technical University of Athens, Greece and the National and Kapodistrian University of Athens, Greece
HELOKA	Helium Loop Karlsruhe
HEMJ	Helium-cooled Divertor Concept with Multiple Jet Cooling
HETRA	HEat TRAnsfer Experiment
HFIR	High Flux Isotope Reactor
HFR	High Flux Reactor, Petten, Netherlands
HFTM	High Flux Test Module
HHF	High Heat Flux
HIP	Hot Isostatic Press
HNB	Heating Neutral Beam
HPGe	High Purity Germanium (detector)
HRJRG-13	Helmholtz Russia Joint Research Group-13

HT	High Temperature
HT	Tritiated Gas
HTO	Tritiated Water Vapour
HTS	High Temperature Superconducting
HV	High Voltage
HVAC	Heating, Ventilating and Air Conditioning
ICRP	International Commission on Radiological Protection
IEAF-2001	Intermediate Energy Activation File 2001
IFMIF	International Fusion Materials Irradiation Facility
ILSS	Interlaminar Shear Strength
IO	ITER Organisation
IPE	Institute for Data Processing and Electronics, Karlsruhe Institute of Technology
IPF	Institut für Plasmaforschung, Universität Stuttgart
IPP	Max-Planck Institute for Plasma Physics, Garching
IRDF	International Radiation Dosimetry File
ISOGEN	World' leading solution for the total automation of piping isometric drawing production (de factor standard CAD system)
ISS	Isotope Separation System
ISSP	Institute of Solid State Physics, Riga, Latvia
ITER	International Thermonuclear Experimental Reactor
ITERVAC	Code for Vacuum Gas Flows
JEFF	Joint European Fission Fusion File
JSC "SSC RIAR"	Joint Stock Company "State Scientific Centre Research Institute of Atomic Reactors"
KFKI	Research Institute of Particle and Nuclear Physics of the Hungarian Academy of Science
KIT	Karlsruhe Institute of Technology
KLST	Kleinlast Impact Specimen
Kn	Knudsen number
LARA	Laser Raman Spectroscopy
LCF	Low Cycle Fatigue
LHT	Launcher Handling Test Facility
LLL	Liquid Lithium Limiter
LOVA	Loss of Vacuum Accident
LPCE	Liquid Phase Catalytic Exchange
MA	Mechanical Alloying
MAN	Maschinenwerke Augsburg Nürnberg
MAXED	Maximum Entropy Deconvolution Code for Spectrum Unfolding
MBWG	Multi-beam Waveguide

McCad	Software for the conversion of CAD to Monte Carlo geometry
MCNP	Monte Carlo code for neutron and photon transport simulations
MCNPX	Monte Carlo Code for Neutral and Charged Particle Transport Simulations
MCSEN	Monte Carlo Sensitivity Code based on MCNP
MDIT	Management Support and Design Integration Team
MEMOS	Code Name
MGI	Massive Gas Injection
MHD	Magneto Hydrodynamic
NB	Neutral Beam
NBI	Neutral Beam Injector
NC	Normal Conducting
NDT	Non-Destructive Testing
NPI	Nuclear Physics Institute (Řež)
NRG	Nuclear Research and Consultancy Group, Petten, Netherlands
NRI	Nuclear Research Institute Řež, Czech Republic
NTM	Neo-classical Tearing Mode
ODS	Oxygen Dispersion Strengthened
OFHC	Oxygen-free High Conductivity
OM	Optical Microscopy
OMP	Optical Model Potential
OPTIFER IVc	German RAF/M steel
ORNL	Oak Ridge National Laboratory
OSi	Lithium Orthosilicate
P&ID	Process and Instrumentations Diagram
PCB	Printed Circuit Board
PDR	Preliminary Design Review
PEGASUS	Code Name
PF	Poloïdal Field
PFC	Plasma Facing Components
PICOLO	Pb-Li Corrosion Loop
PID controller	Proportional-Integral-Differential Controller
PIE	Post Irradiation Examination
PIM	Powder Injection Molding
PLC	Programmable Logic Control
PM	Powder Metallurgy
PMW	Projekt Mikrowellenheizung for W7X

PPC	Pre Production Cryopump
ProVac3D	KIT code for vacuum flow calculations
PSI	Paul-Scherrer-Institute, Switzerland
PWHT	Post Weld Heat Treatment
PWI	Plasma Wall Interaction
QD	Quench Detection
QDU	Quench Detector Unit
QMS	Quadrupole Mass Spectrometer
QSPA-T, QSPA-Kh50	Plasma Guns Names
RACC	Roebel-cables Assembled from Coated Conductors
RAF	Reduced Activation Ferritic (steel)
RAFM	Reduced Activation Ferritic Martensitic (steel)
RD	Rolling Direction
REM	Raster Electron Microscope
RF	Radio Frequency
RT	Raleigh-Taylor (instability)
RT	Room Temperature
SAND-II	Spectrum Unfolding Code
SANS	Small Angle Neutron Scattering
SBWG	Single-beam Waveguide
SCK-CEN	Studiecentrum voor Kernenergie, Mol, Belgium
SEM	Scanning Electron Microscopy
SENB	Single Edged Notched Bar
SOL	Scrape-off Layer
SPICE	<u>S</u> ample <u>H</u> older for <u>I</u> rradiation of <u>M</u> iniaturized <u>S</u> teel <u>S</u> pecimens
SS	Stainless Steel
SSP	Separatrix Strike Position
SSTT	Small Scale Test Techniques
STEM	Scanning Transmission Electron Microscope
TALYS	Nuclear model Code (NRG)
TAP	Tomographic Atom Probe
TBM	Test Blanket Module
TBM-CA	Test Blanket Module Consortium of Associate
TCEE	Two Component ECM Electrolyte
TD	Theoretical Density
TED	Thales Electron Devices, Vélizy

TEM	Transmission Electron Microscopy
TENDL	TALYS Evaluated Nuclear Data Library (by NRG)
TEP	Tokamak Exhaust Processing
TES	Tritium Extraction System
TF	Toroidal field
THEA	<u>T</u> hermohydraulic <u>E</u> xperimental <u>A</u> rrangement
TIG	Tungsten Inert Gas
TIMO	Test Facility for ITER Model Pump
TLD	Thermo Luminescence Detector
TLK	Tritium Laboratory Karlsruhe
TMF	Thermo-Mechanical Fatigue
TOKES	Code Name
TOSKA	Torusspulen Testanordnung Karlsruhe
TPMC	Test Particle Monte Carlo
TPR	Tritium Production Rate
TQ	Thermal Quench
TSEFEY	Electron-beam Testing Facility
TTC	Target- and Test Cell
TUD	Technical University of Dresden
TZM	Molybdenum, stabilized by small amounts of titanium and zirconium
UPP	Upper Port Plug
USE	Upper Shelf Energy
VDE	Vertical Displacement Event
VDS	Vent Detritiation System
W	Tungsten
W7-X	Wendelstein 7-X stellarator project, Greifswald, Germany
WDS	Water Detritiation System
WL10	Tungsten with 10 % of La ₂ O ₃

